Disease Markers

# Neuroimaging Biomarkers for Chronic Diseases 2022

Lead Guest Editor: Yi Shao
Guest Editors: Xi-jian Dai, Wensi Tao, and Pei-Wen Zhu

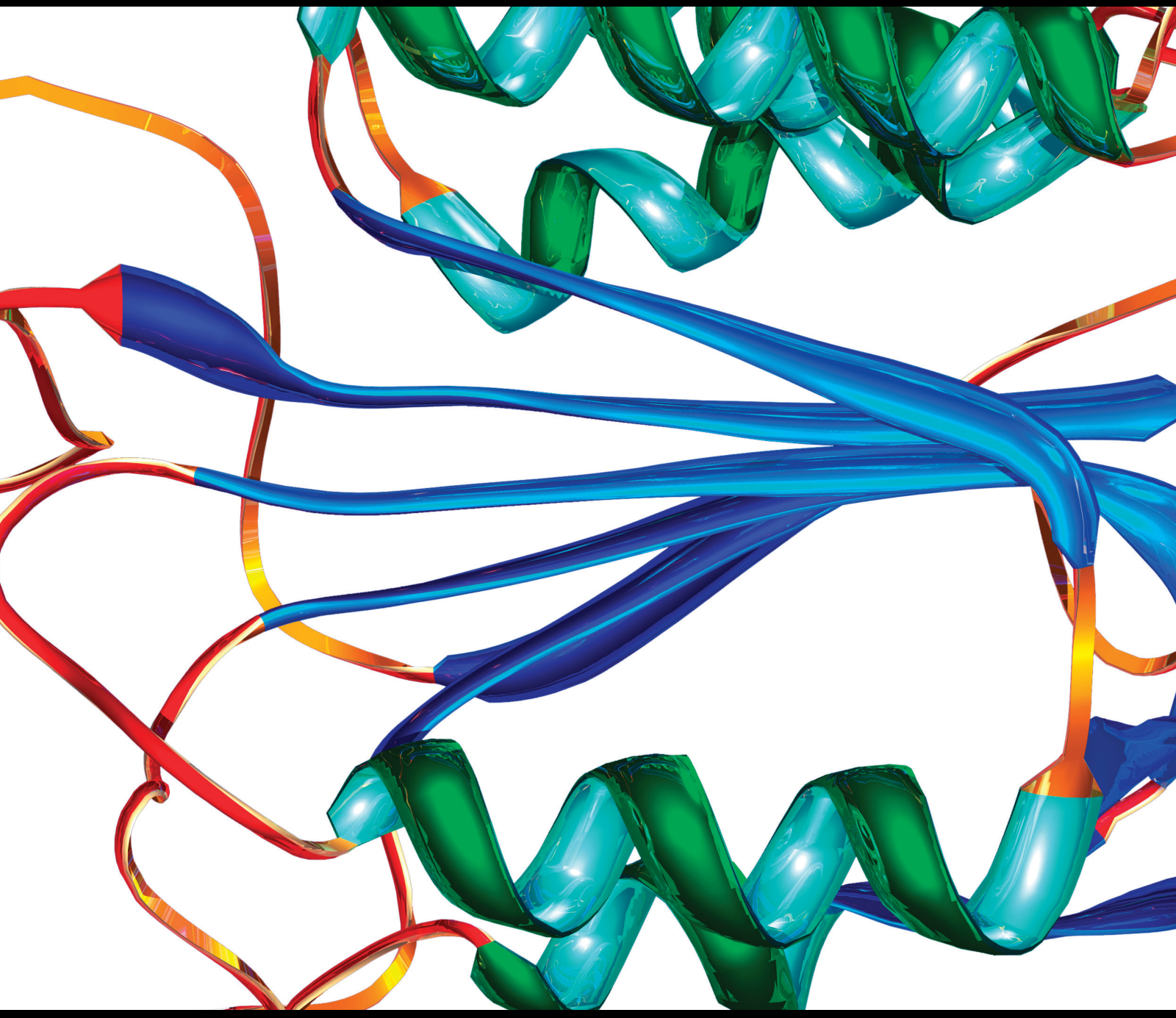

# Neuroimaging Biomarkers for Chronic Diseases 2022

Disease Markers

# Neuroimaging Biomarkers for Chronic Diseases 2022

Lead Guest Editor: Yi Shao
Guest Editors: Xi-jian Dai, Wensi Tao, and Pei-Wen Zhu

# Contents

# Contents

Hindawi
Disease Markers
Volume 2022, Article ID 8270100, 11 pages
https://doi.org/10.1155/2022/8270100

*Research Article*

# Changes in Degree Centrality and Functional Connectivity after the First Cycle of Neoadjuvant Chemotherapy in Newly Diagnosed Breast Cancer: A Longitudinal Study

**Yixin Hu,[1] Daihong Liu,[1] Yongchun Deng,[2,3] Feng Yu,[2,3] Hong Yu,[1] Yong Tan,[1] Xiaoyu Zhou,[1] Jiang Liu,[1] Weiwei Lei,[4] Xiaohua Zeng,[2,3] and Jiuquan Zhang[1]**

[1]*Department of Radiology, Chongqing University Cancer Hospital & Chongqing Cancer Institute & Chongqing Cancer Hospital, Chongqing 400030, China*
[2]*Department of Breast Cancer Center, Chongqing University Cancer Hospital, Chongqing, China*
[3]*Chongqing Key Laboratory for Intelligent Oncology in Breast Cancer (iCQBC), Chongqing University Cancer Hospital, Chongqing, China*
[4]*Department of Intensive Care, Chongqing University Cancer Hospital & Chongqing Cancer Institute & Chongqing Cancer Hospital, Chongqing 400030, China*

Correspondence should be addressed to Xiaohua Zeng; zxiaohuacqu@126.com and Jiuquan Zhang; zhangjq_radiol@foxmail.com

Received 3 March 2022; Revised 17 May 2022; Accepted 6 October 2022; Published 28 November 2022

Academic Editor: Carlo Cervellati



*Purpose*. To evaluate the longitudinal changes of brain degree centrality (DC) and functional connectivity (FC) in breast cancer patients after the first cycle of neoadjuvant chemotherapy (NAC). *Methods*. Thirty-five breast cancer patients were included in the NAC group. Resting-state functional magnetic resonance imaging (rs-fMRI) and neuropsychological test were performed at baseline before NAC (time point 0, TP0) and after the first cycle of NAC (time point 1, TP1). The healthy controls (HC) included 30 healthy subjects and received the same rs-fMRI scan and neuropsychological test as the above-mentioned NAC group at one time point. DC and FC analyses were conducted to assess brain connectivity of all participants. Receiver operating characteristic (ROC) curve was used to assess the ability of DC and FC in distinguishing patients before and after chemotherapy. *Results*. In the NAC group, the Self-Rating Anxiety Scale scores decreased significantly over time. At TP0 and TP1, the Digital Span Test forward score of the NAC group was significantly lower than that of the HC group. In the NAC group, DC in the right middle frontal gyrus and left precentral gyrus/middle frontal gyrus decreased significantly at TP1, and FC between the left precentral gyrus/middle frontal gyrus and bilateral precuneus was significantly reduced at TP1. Through ROC analysis, we found that the area under the curve (AUC) of DC, FC, and the combined model in distinguishing patients in TP0 or TP1 was 0.7886, 0.7665, and 0.8278, respectively. *Conclusions*. Brain connectivity, involving executive and motor function related brain areas, changes in the short term after NAC treatment in breast cancer patients.

## 1. Introduction

Breast cancer is the most prevalent cancer worldwide according to the International Agency for Research on Cancer GLOBOCAN cancer statistics for 2020 [1]. As an essential and effective treatment, chemotherapy is associated with cognitive impairment in breast cancer patients, with 8.1%-75% of survivors suffering from this side effect [2]. Cognitive problems present major challenges to patient care and quality of life. Elucidating the underlying neurological mechanisms of chemotherapy-related cognitive impairment may enable early diagnosis and treatment.

Comprehensive cognitive domains are involved in chemotherapy-induced cognitive impairments, including attention, memory, executive function, and information processing speed [3]. The potential mechanisms underlying the cognitive deficits have been explored in previous studies. For instance, postchemotherapy patients exhibit high levels of

proinflammatory cytokines and oxidative stress, which have been suggested to be associated with cognitive deficits [4]. In addition, the neurotoxicity of chemotherapeutic agents can cause neurogenesis inhibition and impaired white matter integrity [5]. Other potential factors should also be taken into consideration, including DNA damage, mitochondrial dysfunction, and aberrant neurotransmitter levels [5, 6]. These interrelated factors may coordinately contribute to the development of cognitive impairment. However, the mechanism is only beginning to be explored. Neuroimaging is also an essential approach for the exploration of chemotherapy-associated large-scale neuronal abnormalities that may underlie cognitive impairment in breast cancer patients.

Functional magnetic resonance imaging has been proven to be an informative neuroimaging method to determine brain function alterations in patients receiving chemotherapy. Systemic chemotherapy for breast cancer is inferred to comprehensively influence the brain. Among the neuroimaging measurements, degree centrality (DC) is a measurement method based on graph theory, which quantified the number of links connected to a node and used to assess the importance of each node in brain network, in terms of its connectivity number to every voxel [7], this underlies the importance of the local region, termed the "brain hub" [8]. It reduces the possible bias caused by selecting brain regions according to the priori assumption and exhibits relatively high test-retest reliability [9]. Recently, the DC approach has been successfully used to disclose the neurobiological mechanism for several diseases, such as obsessive compulsive disorder [10], Alzheimer's disease [11], and major depressive disorder [12]. Breast cancer survivors have been reported to have reduced DC of gray matter networks in the frontotemporal regions, which may be associated with impairments of memory and executive functioning [13]. Furthermore, FC analysis enables an exploration of the particular edges that showed aberrant connections to these nodes, as we demonstrated previously [8]. A recent study combined DC and FC to derive that the dorsolateral prefrontal cortex may play a key role in multiple system atrophy with cognitive impairment [14]. These results indicate that DC and FC are feasible methods to explore the damage of the whole brain neural network in the resting state. However, as far as we know, there is a lack of relevant studies using the above methods to explore the damage of the whole brain neural network in breast cancer patients. The characteristics of DC and FC anomalies caused by NAC remain to be further studied.

Previous neuropsychological studies suggest that cancer patients have cognitive dysfunction at all stages of the disease course, and subjective complaints are most frequently reported one month after the end of chemotherapy [15], and the time point of most neuroimaging studies is also one month after the end of chemotherapy [16, 17]. A recent study showed a sharp decline in cognitive function of breast cancer patients within three months after chemotherapy [18]. However, the short-term changes in brain connectivity caused by NAC remain to be studied. In this study, breast cancer patients completing the first circle of NAC were enrolled to investigate the short-term effect of chemotherapy on the brain and exclude the potential influence of surgery. We hypothesized that the aberrant brain connectivity may contribute to the development of cognitive impairment in breast patients receiving chemotherapy. We used the regions that showed significant alterations in DC, combined with secondary seed-based FC analysis to explore the changes of brain connectivity after the first circle of NAC in breast cancer patients. Finally, the receiver operating characteristic (ROC) curve analysis based on logistic regression was constructed to assess the ability of DC values and FC $z$ scores to distinguish patients between before and after chemotherapy.

## 2. Materials and Methods

*2.1. Participants.* This prospective longitudinal study was approved by the Ethics Committee of Chongqing University Cancer Hospital (approval number: czls2021042-A). All participants provided written informed consent. Thirty-five female breast cancer patients (NAC group) were recruited from our institution, and thirty female healthy controls (HC group) were recruited from communities between January 2021 and June 2021. The inclusion criteria of the NAC group in this study were as follows: (1) stage I-III breast cancer patients between the ages of 20 and 70 and scheduled for NAC before surgery and (2) right-handedness. Exclusion criteria were as follows: (1) organic brain abnormalities (brain metastases, trauma, stroke, or a history of brain surgery); (2) history of neurological or psychiatric diseases (major depressive disorder, dementia, multiple sclerosis, schizophrenia, and epilepsy); (3) metal implants; and (4) contraindication of MR examination. We recruited HC groups matched by age, gender, and education level. None of them had a history of cancer or chemotherapy, and the remaining exclusion criteria were the same as those in the NAC group.

In the NAC group, the baseline assessment was performed before NAC (time point 0, TP0), including a brain rs-fMRI scan and neuropsychological test. Follow-up evaluation was performed after the first cycle of NAC (time point 1, TP1). The HC group underwent the same brain rs-fMRI scan and neuropsychological test at one time point. Demographic information of the study participants, including age, education, body mass index (BMI), blood pressure, and menstrual status, was obtained through a self-report questionnaire. In addition, we obtained disease stage and treatment information, such as the chemotherapy regimen, from the NAC group through medical record abstraction.

*2.2. Neuropsychological Test.* All participants underwent a battery of neuropsychological test in a fixed order that assessed their global cognitive level and major cognitive subdomains. The major cognitive subdomains were evaluated with the following test: (1) the Trail Making Test (TMT, Part A) for executive function and psychomotor speed [19], (2) the Verbal Fluency Test (VFT) for mental flexibility [20], and (3) the Digit Span Test (DST, forwards and backwards) for working memory [20]. We used the Functional Assessment of Cancer Therapy Cognitive Function Version 3 (FACT-Cog) (version 3, simplified Chinese) [21] to evaluate

self-perceived cognitive function. FACT-Cog is designed for cancer patients 18 years and older with chemotherapy-induced cognitive problems. It assesses cognitive complaints over the last seven days. The higher the score, the lower the cognitive complaints. The FACT-Cog includes four subscales: perceived cognitive impairment (PCI), comments from others (Oth), perceived cognitive abilities (PCA), and impact on quality of life (QOL). The Self-Rating Anxiety Scale (SAS) and Self-Rating Depression Scale (SDS) were used to assess anxiety and depression in the emotional test.

*2.3. Magnetic Resonance Imaging.* MRI sequences were acquired with a 3.0 T scanner (Magnetom Prisma; Siemens Health care, Erlangen, Germany) equipped with a 64-channel head-neck coil. Subjects were instructed to close their eyes, stay awake, and avoid thinking about any topics. Earplugs and cushions were used to alleviate noise influence and restrict head motion, respectively. The rs-fMRI data were acquired using rapid gradient echo-planar pulse imaging with the following parameters: repetition time = 2000 milliseconds (ms), echo time = 30 ms, flip angle = 70°, field of view = $240 \times 240\,mm^2$, slices = 36 (interleaved), matrix = $80 \times 80$, and voxel size = $3 \times 3 \times 3\,mm^3$. From each participant, 240 volumes were acquired over 8 minutes and 8 seconds. High-resolution T1-weighted structural images were scanned by three-dimensional magnetization prepared rapid gradient echo, and the parameters were as follows: repetition time = 2100 ms, echo time = 2.26 ms, flip angle = 8°, field of view = $256 \times 256\,mm^2$, slices = 192, matrix = $256 \times 256$, and voxel size = $1 \times 1 \times 1\,mm^3$. The total scanning time was 4 minutes and 53 seconds.

*2.4. Neuroimaging Processing.* Rs-fMRI data were preprocessed using Data Processing & Analysis for Brain Imaging (DPABI_V5.1) based on MATLAB R2016a [22]. The preprocessing process is as follows: (1) all DICOM files were converted to NifTI files. (2) The first 10 time points of the functional image were removed to ensure high homogeneity of the remaining image. (3) Slice timing was performed to correct the time differences between slices. (4) Realignment was performed to correct head motion, and a report of head motion was created. Any subjects with head motion > 3.0 mm in any direction of $x$, $y$, and $x$ or >3.0° at any angle were excluded from the subsequent statistical analyses. (5) The Friston 24-parameter model was applied to regress out head motion effects. Other nuisance variables, including white matter signal and cerebrospinal fluid signal, were regressed out. Individual functional images were normalized into the Montreal Neurological Institute (MNI) space for intersubject comparison [23]. (6) The data were bandpass filtered (0.01–0.10 Hz) to reduce physiological noise at other frequency bands.

Based on preprocessing, DC calculations were performed using DPARSF in a voxel-wise manner with a threshold of $r > 0.25$ in accordance with previous studies [24, 25]. The weighted DC of each voxel was divided by the global mean weighted DC of each subject to achieve standardization. After calculation, all the resulting DC maps were spatially smoothed (full-width at half maximum = 6 mm). According to the follow-up statistical results, brain regions with significantly altered DC were used as seed regions including the brain regions with significant differences in DC over time in the NAC group and the brain regions with significant differences in DC between the NAC group and the HC group. Then, gray matter volume from seed regions was extracted. On the basis of preprocessed data with smoothing (full-width at half maximum = 6 mm), the time series correlation coefficient between seed region and other brain voxels was calculated, and the FC pattern of each subject was obtained. Fisher's $r$-to-$z$ transformation was performed to improve the normality of the correlation coefficient values of FC.

*2.5. Statistical Analysis.* SPSS software (22.0 version, IBM Corp., Armonk, NY) was used to analyze the numerical data, including demographic data and neuropsychological test scores. First, the Kolmogorov-Smirnov test was used to check whether the data conformed to a normal distribution. Then, according to the results of the test, comparison analyses were carried out. For the intergroup comparison of the NAC group and HC group (TP0 vs. HC, TP1 vs. HC), an independent sample $t$-test was used for the data conforming to the normal distribution, and the Mann–Whitney $U$ test was used for the abnormal distribution. For the intragroup comparison (TP0 vs. TP1) of the NAC group, a paired sample $t$-test was used to analyze the data conforming to a normal distribution, and the Wilcoxon signed-rank test was used to analyze the data with a nonnormal distribution.

Analyses of DC and FC maps were conducted in the Statistical Analysis module of DPABI V5.1 software. First, one-sample $t$-test was performed to check the distribution patterns of DC and FC of each group (compared to "0"). For the intergroup comparison of the NAC group and HC group (TP0 vs. HC, TP1 vs. HC), an independent sample $t$-test was used to compare the DC and FC maps. For the intragroup comparison (TP0 vs. T1) of the NAC group, a paired sample $t$-test was used to compare the distribution of DC and FC. Age, years of education, and head motion parameters were included as covariates. The results were corrected for multiple comparisons using Gaussian random-field theory (voxel level $P < 0.001$ and cluster level $P < 0.05$, two tailed). The gray matter volume of seed regions was compared by paired sample $t$ test using SPSS software. The mean DC values and FC $z$ scores of significant altered brain regions in NAC group were extracted, and the receiver operating characteristic (ROC) curve analysis based on logistic regression was applied to identify different imaging characteristics of the corresponding groups. Diagnostic accuracy was indicated by the area under the curve (AUC), with values between 0.5 and 0.7, 0.7 and 0.9, and >0.9 having low, moderate, and high accuracy, respectively.

We calculated the average DC values and FC $z$ scores of aberrant brain regions and used Spearman correlation analysis to evaluate the correlation between these two parameters and neuropsychological test scores with significant differences. $P < 0.05$ was considered statistically.

Table 1: Clinical characteristics.

| Characteristics | NAC group ($n = 35$) | HC group ($n = 30$) | $P$ value |
|---|---|---|---|
| Age (years) | 50.11 ± 9.19 | 50.77 ± 9.55 | 0.78 |
| Education (years) | 9.14 ± 3.75 | 10.03 ± 3.19 | 0.31 |
| BMI (TP0) | 24.05 ± 2.87 | 32.28 ± 44.03 | 0.32 |
| Hypertension/nonhypertension (TP0) | 6/29 | 3/27 | 0.49 |
| Premenopausal/postmenopausal (TP0) | 14/21 | 14/16 | 0.59 |
| Stage | | | |
| cIIA/cIIB | 2/4 | N/A | N/A |
| cIIIA/cIIIb/cIIIc | 17/5/7 | N/A | N/A |
| Regimen | | | |
| AC-T | 9 | N/A | N/A |
| EC-T | 3 | N/A | N/A |
| TCbHP | 7 | N/A | N/A |
| TCbHB | 4 | N/A | N/A |
| TAC | 12 | N/A | N/A |

Distribution data are reported as means ± SD. For the intergroup comparisons of age, education, and BMI, the $P$ value was obtained using the independent sample $t$-test. For the intergroup comparisons of blood pressure and menstrual status, the $P$ value was obtained using the $\chi^2$ test. Abbreviations: BMI: body mass index; AC-T: epirubicin, cyclophosphamide, and paclitaxel; EC-T: doxorubicin, cyclophosphamide, and paclitaxel; TCbHP: paclitaxel, carboplatin, pertuzumab, and trastuzumab; TCbHB: paclitaxel, carboplatin, trastuzumab, and pyrotinib; TAC: docetaxel, doxorubicin, and cyclophosphamide; N/A: not applicable.

Table 2: Comparison of the neuropsychological test results between the NAC group at TP0 and the HC group.

| Neuropsychological test | NAC TP0 ($n = 32$) | HC group ($n = 30$) | $P$ value |
|---|---|---|---|
| General cognition | | | |
| FACT-Cog | 113.05 (101.65, 118.60) | 110.45 (94.95, 117.10) | 0.28 |
| PCI | 60.30 (57.83, 64.80) | 59.40 (51.30, 63.23) | 0.12 |
| Oth | 16.00 (15.00, 16.00) | 16.00 (14.00, 16.00) | 0.42 |
| PCA | 21.00 (16.30, 21.80) | 20.61 (16.13, 21.80) | 0.96 |
| QOL | 16.00 (12.25, 16.00) | 16.00 (15.00, 16.00) | 0.28 |
| Executive function and psychomotor speed | | | |
| TMT-A | 56.50 (34.25, 90.00) | 42.00 (30.00, 57.75) | 0.11 |
| Mental flexibility | | | |
| VFT | 37.00 (31.00, 42.75) | 32.50 (27.00, 39.25) | 0.10 |
| Working memory | | | |
| DST forwards | 7.00 (6.00, 8.00) | 10.00 (8.75, 12.00) | <0.001 |
| DST backwards | 4.00 (4.00, 5.00) | 4.00 (4.00, 6.00) | 0.63 |
| Anxiety and depression | | | |
| SAS | 27.50 (26.00, 32.00) | 27.50 (25.00, 31.25) | 0.79 |
| SDS | 26.00 (25.00, 30.00) | 26.00 (25.00, 30.00) | 0.94 |

Nonnormal distribution data are reported as [$M$(QR)]. For the intergroup comparison, the $P$ value was obtained using the Mann–Whitney $U$ test. Abbreviations: FACT-Cog: Functional Assessment of Cancer Therapy-Cognitive Function; PCI: perceived cognitive impairments; Oth: comments from others; PCA: perceived cognitive abilities; QOL: impact on quality of life; TMT-A: Trail Making Test A; VFT: Verbal Fluency Test; DST: Digital Span Test; SAS: Self-Rating Anxiety Scale; SDS: Self-Rating Depression Scale.

## 3. Results

*3.1. Demographic Characteristics and Clinical Data.* Thirty-eight breast cancer patients were recruited in this study. Three of the patients were excluded, one patient had head movement greater than 3 mm during baseline scanning, one patient had head movement greater than 3 mm in the follow-up scanning, and another patient had a history of schizophrenia. Therefore, 35 patients were finally enrolled for data analysis. Among them, three patients refused neuropsychological test at TP0, and three patients refused neuropsychological test at TP1, but they agreed to conduct rs-fMRI data collection and analysis. A total of 29 patients underwent neuropsychological test at both TP0 and TP1.

Table 3: Comparison of the neuropsychological test results between the NAC group at TP1 and the HC group.

| Neuropsychological tests | NAC TP1 ($n = 32$) | HC group ($n = 30$) | $P$ value |
|---|---|---|---|
| General cognition | | | |
| FACT-Cog | 110.40 (105.05, 115.80) | 110.45 (94.95, 117.10) | 0.99 |
| PCI | 62.55 (58.50, 63.90) | 59.40 (51.30, 63.23) | 0.12 |
| Oth | 16.00 (16.60, 16.00) | 16.00 (14.00, 16.00) | 0.05 |
| PCA | 19.05 (16.30, 21.00) | 20.61 (16.13, 21.80) | 0.33 |
| QOL | 15.00 (14.00, 16.00) | 16.00 (15.00, 16.00) | 0.13 |
| Executive function and psychomotor speed | | | |
| TMT-A | 46.50 (30.50, 71.50) | 42.00 (30.00, 57.75) | 0.50 |
| Mental flexibility | | | |
| VFT | 38.50 (28.50, 45.75) | 32.50 (27.00, 39.25) | 0.14 |
| Working memory | | | |
| DST forwards | 7.00 (6.00, 8.00) | 10.00 (8.75, 12.00) | <0.001 |
| DST backwards | 4.00 (4.00, 5.00) | 4.00 (4.00, 6.00) | 0.88 |
| Anxiety and depression | | | |
| SAS | 26.00 (25.00, 28.00) | 27.50 (25.00, 31.25) | 0.20 |
| SDS | 27.00 (25.00, 31.00) | 26.00 (25.00, 30.00) | 0.83 |

Nonnormally distributed data are reported as [$M$(QR)]. For the intergroup comparison, the $P$ value was obtained using the Mann–Whitney $U$ test.

Table 4: Comparison of the neuropsychological test results between the TP0 and TP1 in the NAC group.

| Neuropsychological tests | NAC TP0 ($n = 29$) | NAC TP1 ($n = 29$) | $P$ value |
|---|---|---|---|
| General cognition | | | |
| FACT-Cog | 112.50 (102.30, 118.60) | 109.50 (104.55, 115.80) | 0.60 |
| PCI | 60.30 (57.15, 64.80) | 62.10 (58.05, 63.90) | 0.95 |
| Oth | 16.00 (15.00, 16.00) | 16.00 (16.00, 16.00) | 0.15 |
| PCA | 16.00 (12.50, 16.00) | 15.00 (14.00, 16.00) | 0.37 |
| QOL | 21.00 (16.30, 21.80) | 19.40 (16.30, 21.40) | 0.57 |
| Executive function and psychomotor speed | | | |
| TMT-A | 60.00 (31.00, 90.00) | 48.00 (30.00, 72.50) | 0.24 |
| Mental flexibility | | | |
| VFT | 36.00 (30.50, 40.50) | 39.00 (27.00, 46.00) | 0.11 |
| Working memory | | | |
| DST forwards | 7.00 (6.00, 8.00) | 7.00 (6.00, 8.00) | 0.43 |
| DST backwards | 4.00 (4.00, 5.00) | 4.00 (4.00, 5.00) | 0.50 |
| Anxiety and depression | | | |
| SAS | 30.00 (26.00, 32.00) | 26.00 (25.00, 27.50) | 0.003 |
| SDS | 26.00 (25.00, 31.00) | 27.00 (25.00, 31.00) | 0.56 |

Nonnormal distribution data are reported as [$M$(QR)]. For the intragroup comparison, the $P$ value was obtained using the Wilcoxon signed-rank test.

The median time interval between the TP0 and TP1 moments of the MRI scan was 27 days (range 19–46 days). In addition, age, education, BMI, blood pressure, and menstrual status of the HC group were not significantly different from those of the NAC group ($P > 0.05$). The clinical stages and preoperative chemotherapy regimens in the NAC group are detailed in Table 1.

*3.2. Neuropsychological Test Comparison.* The DST forward scores of the NAC group at two time points were significantly lower than those of the HC group (Tables 2 and 3). In the NAC group, the SAS scores decreased significantly over time ($P < 0.05$) (Table 4).

*3.3. DC and FC Analysis.* After correcting the Gaussian random field, the distribution patterns of DC and FC for each group are shown in Figure 1 according to the results of the one-sample $t$-test. It was found that high DC values mainly occurred in the bilateral prefrontal cortex, the precentral gyrus, the postcentral gyrus, and parietal cortex. The left

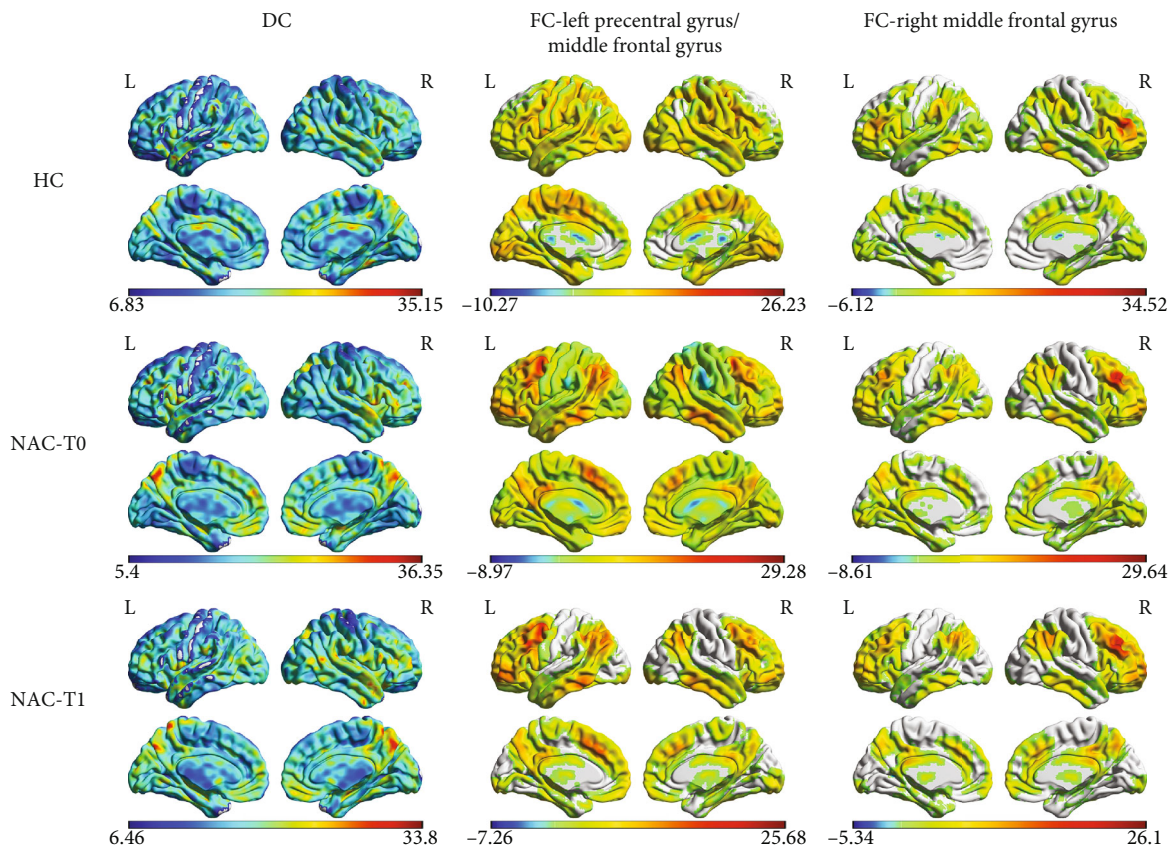


Figure 1: Degree centrality (DC) and functional connectivity (FC) distribution in the HC group and NAC group (one-sample $t$-test). The DC and FC spatial distributions in the NAC group (both time points) were similar to those of the HC group. $P < 0.05$ (corrected with Gaussian random-field theory). The color bar denotes the $t$-value. R: right; L: left.

precentral gyrus/middle frontal gyrus mainly connected to the bilateral prefrontal cortex and the temporal lobe and parietal cortex. The right middle frontal gyrus mainly connected to the prefrontal cortex, the parietal cortex, and the temporal lobe. The spatial distributions of DC and FC in the NAC group (both time points) were similar to those of the HC group.

There was no significant intragroup statistical difference in the DC values of the HC group and the NAC group at the two time points. In the NAC group, the DC values of the patients' right middle frontal gyrus and left precentral gyrus/middle frontal gyrus decreased significantly over time from TP0 to TP1 (Figure 2, 3(a) and Table 5). We selected the above regions as the seed regions and compared the gray matter volumes of seed regions in the NAC group. The results showed that the gray matter volumes of the right middle frontal gyrus and left precentral/middle frontal gyrus were $0.39 \pm 0.06\,cm^3$ and $0.38 \pm 0.06\,cm^3$ at TP0 and $0.30 \pm 0.05\,cm^3$ and $0.29 \pm 0.05\,cm^3$ at TP1, respectively. The gray matter volume of these two regions was significantly different at both times ($t = 2.913$, $P = 0.006$; $t = 2.513$, $P = 0.017$). Afterwards, the FC between the seed region and the whole brain voxel was analyzed. The results showed that FC between the left precentral gyrus/middle frontal gyrus and bilateral precuneus was significantly reduced from TP0 to TP1 (Figures 2 and 3(b) and Table 6). No brain regions with altered connectivity were detected in the right middle frontal gyrus in the NAC at TP1.

*3.4. ROC Curve.* According to ROC curve analysis, the AUC of DC values and FC $z$ scores to distinguish the status of breast cancer patients before and after chemotherapy (TP0 and TP1) were 0.7886 ($P < 0.001$; 95% CI: 0.6794-0.8978) and 0.7665 ($P < 0.001$; 95% CI: 0.6546 - 0.8785), respectively; the AUC of combined model of DC values and FC $z$ scores was 0.8278. ($P < 0.001$; 95% CI: 0.6226-0.8607). (Figure 4).

*3.5. Correlation Analysis.* Previous results showed that the DC values and FC $z$ scores of the right middle frontal gyrus and left precentral gyrus/middle frontal gyrus were significantly different between TP0 and TP1. We performed spearman correlation analysis between neuropsychological test scores (SAS) and average DC values of these two brain regions, as well as FC $z$ scores. There was no significant correlation between them ($P > 0.05$).

## 4. Discussion

In the present study, DC and FC were used to assess intrinsic brain connectivity in breast cancer patients after the first cycle of NAC. These patients exhibited aberrant DC in the

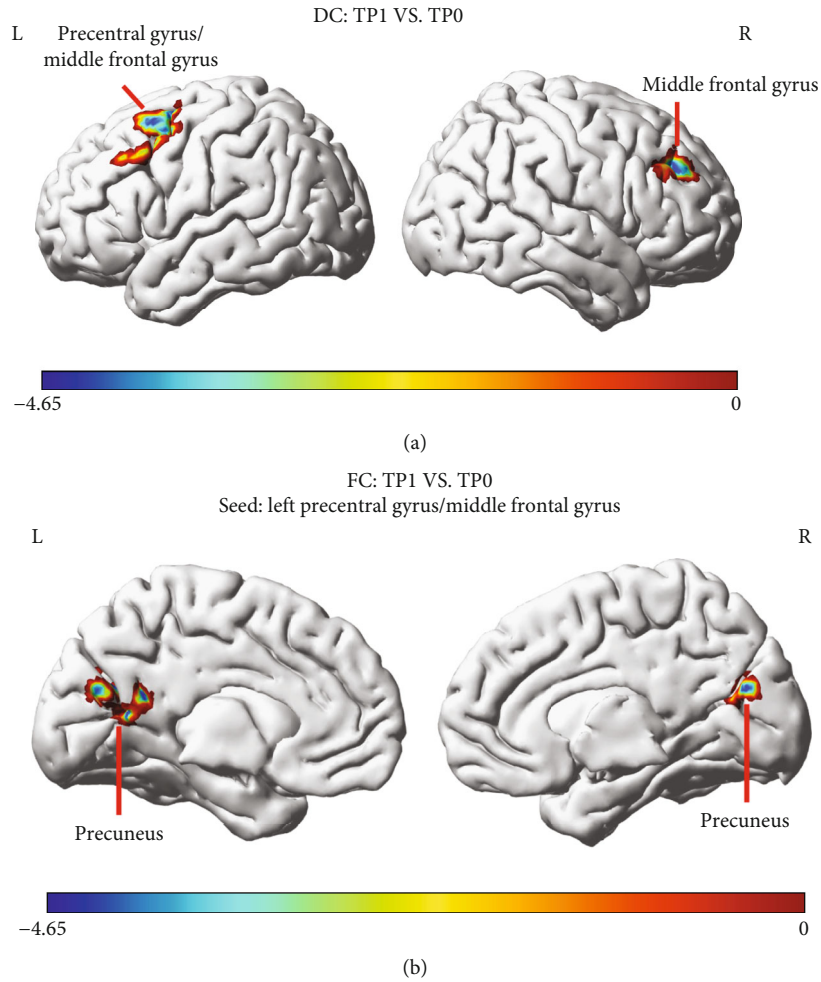


Figure 2: Comparisons of DC and FC distribution between TP0 and TP1 in the NAC group (paired sample $t$-test). (a) The DC in the right middle frontal gyrus and left precentral gyrus/middle frontal gyrus decreased significantly from TP0 to TP1. (b) The FC between the left precentral gyrus/middle frontal gyrus and bilateral precuneus was significantly reduced from TP0 to TP1. $P < 0.05$ (corrected with Gaussian random-field theory). The color bar denotes the $t$-value. R: right; L: left.

right middle frontal gyrus and left precentral gyrus/middle frontal gyrus. Taking the above brain regions as seed regions for whole-brain voxel-wise FC analysis, we found that FC between the left precentral/middle frontal gyrus and bilateral precuneus gyrus was reduced after the first cycle of NAC. Furthermore, the brain function indexes of altered brain region show satisfactory performance to distinguish between the patients before and after chemotherapy. These findings may help to improve the understanding of the mechanism of acute brain injury caused by NAC in breast cancer patients.

According to neuropsychological test, in the NAC group, we found that SAS was significantly reduced at TP1 compared to TP0, which was similar to the results of most previous studies [26–28]. Breast cancer patients who suffer more negative effects from the disease and treatment in the beginning experience a higher level of anxiety [29]. Over a period of time, breast cancer patients will gradually come to terms with the disease and the treatment procedures [30]. Moreover, a proportion of patients were relieved and showed lower anxiety levels due to the diminished lump size and reduced pain [31]. Even SAS scores were significantly different in TP0 and TP1 in the NAC group; the scores of all patients were less than 50, indicating that they had no anxiety experience and belonged to a normal state; it may be the underlying reason for the lack of anxiety-related changes in brain function. In addition, the DST forward scores of the NAC group at TP0 and TP1 were significantly lower than those of the HC group. The DST forwards is related to short-term memory. Previous studies have reported that cancer-related cognitive impairment includes short-term memory that occurs at various stages, including before, during, and after cancer treatment [32, 33]; this may be mediated by cancer-related posttraumatic stress [34].

Previous studies have proven that impaired executive function is one of the main manifestations of cognitive impairment in chemotherapy patients [3]. Although abnormalities of executive function were not reflected by neuropsychological test in our study, functional changes occurred in the brain areas related to executive function in patients. We observed a significant decrease in DC in the

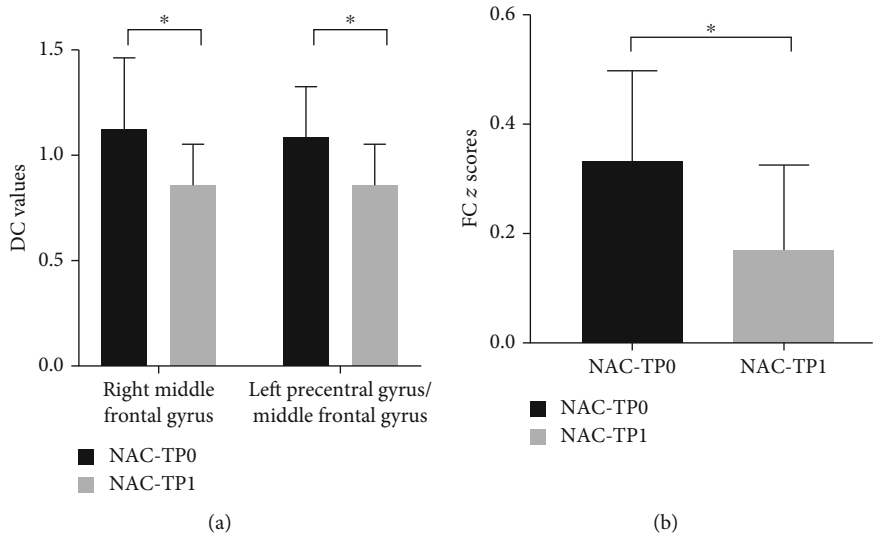


Figure 3: Comparisons of DC and FC between TP0 and TP1 in the NAC group (paired sample $t$-test). (a) Comparison of DC in the right middle frontal gyrus and left precentral gyrus/middle frontal gyrus between the TP0 and TP1 NAC groups. (b) Ordinates represent FC $z$ scores between the left precentral gyrus/middle frontal gyrus and bilateral precuneus. $^{*}P < 0.05$ (corrected with Gaussian random-field theory). Error bars define the SD.

Table 5: Brain regions with significant DC differences between TP0 and TP1 in the NAC group.

| Brain regions | BA | Peak MNI coordinates | | | $t$-value | Cluster (voxels) |
|---|---|---|---|---|---|---|
| | | $x$ | $y$ | z | | |
| Right middle frontal gyrus | 46 | 42 | 39 | 33 | -4.0392 | 56 |
| Left precentral gyrus/middle frontal gyrus | 6 | -45 | 3 | 54 | -4.285 | 100 |

MNI: Montreal Neurological Institute; BA: Brodmann area; $P$ values were corrected with Gaussian random-field theory.

Table 6: Brain regions showing significant functional connectivity differences within the seed between TP0 and TP1 in the NAC group.

| Seed regions | Brain regions | BA | Peak MNI coordinates | | | $t$-value | Cluster (voxels) |
|---|---|---|---|---|---|---|---|
| | | | $x$ | $y$ | $z$ | | |
| Right middle frontal gyrus | None | | | | | | |
| Left precentral gyrus/middle frontal gyrus | Bilateral precuneus | Not applicable | -12 | -63 | 30 | -4.649 | 137 |

MNI: Montreal Neurological Institute; BA: Brodmann area; $P$ values were corrected with Gaussian random-field theory.

bilateral middle frontal gyri, which have been demonstrated to be critical to executive function [35]. We speculated that the brain may maintain relatively normal executive function through the compensatory effect in a short time after NAC. It is also possible that the scale is not sensitive to subtle differences in cognitive function [36]. Generally, the present study indicated that MRI can detect brain damage caused by chemotherapy earlier than scales, which is consistent with previous studies [37–39].

We also found reduced DC in the left precentral gyrus/middle frontal gyrus after the first cycle of NAC. The left precentral gyrus is one of the main motor areas in the cerebral cortex, and it is associated with other motor areas, such as the middle frontal gyrus, to plan and perform actions [40]. Previous studies on schizophrenia suggested that the precentral gyrus was associated with motor-related cognitive function [41]. The decreased DC of the left precentral gyrus/middle frontal gyrus after short-term NAC suggested that motor-related cognitive function may be vulnerable to chemotherapy attack.

To better understand the neural mechanisms underlying chemotherapy-induced brain damage, it is essential to consider how the brain regions work together rather than studying them in isolation [42]. The results showed that the DC distribution changed significantly in the brain area, and their gray matter volume also decreased significantly. Therefore, it is reliable to use these two brain regions as seed regions for whole-brain functional connectivity analysis. After the first cycle of NAC, we found that FC between the left precentral gyrus/middle frontal gyrus and bilateral precuneus was decreased in breast cancer patients. The precuneus is a critical node in the default mode network (DMN) [43]. Our results suggest that the balance between the DMN network and motor (precentral gyrus) and execution-related (middle

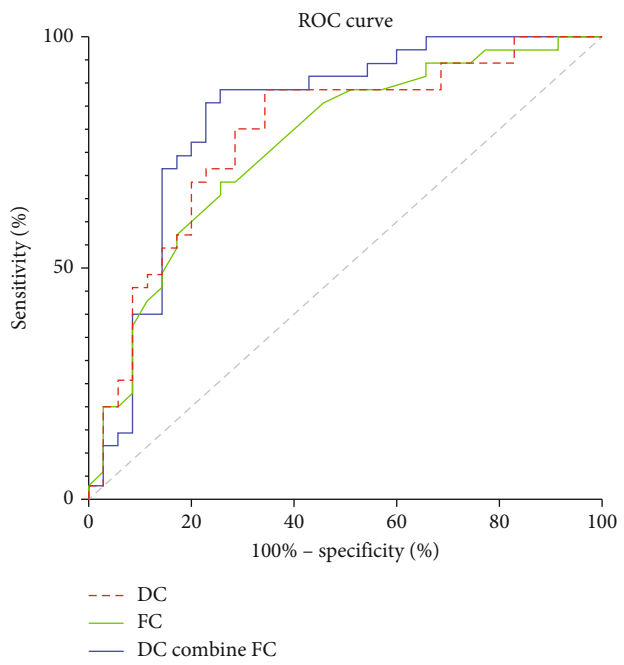


Figure 4: ROC curve analysis of the DC values and FC $z$ scores for altered brain regions. The AUC of DC values in altered brain regions to distinguish between TP0 and TP1 was 0.7886 ($P < 0.001$; 95% CI: 0.6794-0.8978). The AUC of mean FC $z$ scores to distinguish between TP0 and TP1 was 0.7665 ($P < 0.001$; 95% CI: 0.6546-0.8785). The AUC of combined DC values and FC $z$ scores to distinguish between TP0 and TP1 was 0.8278 ($P < 0.001$; 95% CI: 0.6226-0.8607).

frontal gyrus) brain regions may be disrupted, indicating that chemotherapy may reduce the ability to prepare for future task execution in patients with breast cancer. According to ROC curve results, brain function parameter DC and FC values can reflect the brain injury caused by chemotherapy and may be potential neuroimaging markers. However, this needs to be confirmed in subsequent longitudinal studies.

In our study, we observed significant changes in DC distribution in the NAC group in longitudinal comparison (TP0 vs. TP1) and nonsignificant differences in cross-sectional comparison (TP0 vs. HC; TP1 vs. HC). This may be due to the presence of confounding variables. Though there were no differences in important confounding variables (such as age, education, BMI, blood pressure, and menstrual status) between the HC and NAC groups at baseline, there may still exist other uncontrolled confounding variables. In addition, these findings might be underpowered to detect reliable cross-sectional associations owing to the small sample size. And longitudinal studies require far fewer participants than do cross-sectional studies to detect small changes in the brain [44, 45].

There are several limitations of this study. First, patients with breast cancer in this study received a variety of chemotherapy regimens, and they have different menstrual statuses. In addition, there was no significant correlation between neuropsychological test scores and brain function indicators, which may also be attributed to the above factors. The research cohort needs to be further expanded in future studies and grouped for further exploration. Second, the HC group did not receive scan at TP1, since the interval between the two scans was relatively short. Previous studies suggested that the brain function of HC did not change in a short time [16]. Therefore, we only scanned the HC group at TP0 and assumed that the brain function did not change with time. However, in future longitudinal studies, this should be treated more cautiously.

## 5. Conclusion

In the present study, DC and FC were used to characterize the pattern of brain dysfunction in breast cancer patients after the first cycle of NAC. We found that breast cancer patients exhibited aberrant brain connection in the right middle frontal gyrus and left precentral gyrus/middle frontal gyrus, which may be involved in executive function and motor-related cognitive function. Our results support the notion that changes in brain functional connectivity may precede changes in cognitive performance. However, these findings need to be further validated with larger cohorts and longer follow-up in future studies.

## Abbreviations

| | |
|---|---|
| AUC: | Area under the curve |
| BMI: | Body mass index |
| DC: | Degree centrality |
| DST: | Digit Span Test |
| DMN: | Default mode network |
| FACT-Cog: | Functional Assessment of Cancer Therapy-Cognitive Function |
| FC: | Functional connectivity |
| HC: | Healthy control |
| NAC: | Neoadjuvant chemotherapy |
| Oth: | Comments from others |
| PCA: | Perceived cognitive abilities |
| PCI: | Perceived cognitive impairments |
| QOL: | Impact on quality of life |
| ROC: | Receiver operating characteristic |
| Rs-fMRI: | Resting-state functional magnetic resonance imaging |
| SAS: | Self-Rating Anxiety Scale |
| SDS: | Self-Rating Depression Scale |
| TMT: | Trail Making Test |
| TP: | Time point |
| VFT: | Verbal Fluency Test. |

## Data Availability

The study data may be available from Jiuquan Zhang (zhangjq_radiol@foxmail.com) upon reasonable request.

## Conflicts of Interest

The authors have no conflicts of interest to declare.

## Authors' Contributions

Yixin Hu and Daihong Liu are joint first authors.

## Acknowledgments

This work was supported by the Natural Science Foundation of Chongqing (Grant Nos. CSTB2022NSCQ-MSX0951, cstc2021jcyj-msxmX0313, and cstc2021jcyj-msxmX0319), National Natural Science Foundation of China (Grant no. 82071883), Chongqing Medical Research Project of Combination of Science and Medicine (Grant No. 2021MSXM035, 2021MSXM085), 2020 SKY Imaging Research Fund of the China International Medical Foundation (Project No. Z-2014–07–2003–24), Talent Program of Chongqing (Grant No. CQYC20200303137), and Clinical Research Special Fund of Wu Jieping Medical Foundation (320.6750.2020-20-13).

## References

[1] J. Ferlay, M. Colombet, I. Soerjomataram et al., "Cancer statistics for the year 2020: an overview," *International Journal of Cancer*, vol. 22, no. 9, 2021.

[2] Y. Feng, X. D. Zhang, G. Zheng, and L. J. Zhang, "Chemotherapy-induced brain changes in breast cancer survivors: evaluation with multimodality magnetic resonance imaging," *Brain Imaging and Behavior*, vol. 13, no. 6, pp. 1799–1814, 2019.

[3] M. Lange, F. Joly, J. Vardy et al., "Cancer-related cognitive impairment: an update on state of the art, detection, and management strategies in cancer survivors," *Annals of Oncology*, vol. 30, no. 12, pp. 1925–1940, 2019.

[4] T. C. Alexander and K. R. Krull, "Effects of chemotherapy for acute lymphoblastic leukemia on cognitive function in animal models of contemporary protocols: a systematic literature review," *Neuroscience and Biobehavioral Reviews*, vol. 129, pp. 206–217, 2021.

[5] M. Vitali, C. I. Ripamonti, F. Roila et al., "Cognitive impairment and chemotherapy: a brief overview," *Critical Reviews in Oncology/Hematology*, vol. 118, pp. 7–14, 2017.

[6] J. Du, A. Zhang, J. Li et al., "Doxorubicin-induced cognitive impairment: the mechanistic insights," *Frontiers in Oncology*, vol. 11, p. 673340, 2021.

[7] X. N. Zuo, R. Ehmke, M. Mennes et al., "Network centrality in the human functional connectome," *Cerebral Cortex*, vol. 22, no. 8, pp. 1862–1875, 2012.

[8] D. Liu, S. Duan, C. Zhou et al., "Altered brain functional hubs and connectivity in type 2 diabetes mellitus patients: a resting-state fMRI study," *Frontiers in Aging Neuroscience*, vol. 10, p. 55, 2018.

[9] X. N. Zuo and X. X. Xing, "Test-retest reliabilities of resting-state FMRI measurements in human brain functional connectomics: a systems neuroscience perspective," *Neuroscience and Biobehavioral Reviews*, vol. 45, pp. 100–118, 2014.

[10] M. Gottlich, U. M. Kramer, A. Kordon, F. Hohagen, and B. Zurowski, "Resting-state connectivity of the amygdala predicts response to cognitive behavioral therapy in obsessive compulsive disorder," *Biological Psychology*, vol. 111, pp. 100–109, 2015.

[11] Z. Guo, X. Liu, H. Hou, F. Wei, J. Liu, and X. Chen, "Abnormal degree centrality in Alzheimer's disease patients with depression: a resting-state functional magnetic resonance imaging study," *Experimental Gerontology*, vol. 79, pp. 61–66, 2016.

[12] Y. Shen, J. Yao, X. Jiang et al., "Sub-hubs of baseline functional brain networks are related to early improvement following two-week pharmacological therapy for major depressive disorder," *Human Brain Mapping*, vol. 36, no. 8, pp. 2915–2927, 2015.

[13] S. M. Hosseini, D. Koovakkattu, and S. R. Kesler, "Altered small-world properties of gray matter networks in breast cancer," *BMC Neurology*, vol. 12, no. 1, p. 28, 2012.

[14] H. Yang, X. Luo, H. Yu et al., "Altered resting-state voxel-level whole-brain functional connectivity in multiple system atrophy patients with cognitive impairment," *Clinical Neurophysiology*, vol. 131, no. 1, pp. 54–62, 2020.

[15] T. Tong, C. Pei, J. Chen, Q. Lv, F. Zhang, and Z. Cheng, "Efficacy of acupuncture therapy for chemotherapy-related cognitive impairment in breast cancer patients," *Medical Science Monitor*, vol. 24, pp. 2919–2927, 2018.

[16] B. T. Chen, T. Jin, S. K. Patel et al., "Intrinsic brain activity changes associated with adjuvant chemotherapy in older women with breast cancer: a pilot longitudinal study," *Breast Cancer Research and Treatment*, vol. 176, no. 1, pp. 181–189, 2019.

[17] J. A. Dumas, J. Makarewicz, G. J. Schaubhut et al., "Chemotherapy altered brain functional connectivity in women with breast cancer: a pilot study," *Brain Imaging and Behavior*, vol. 7, no. 4, pp. 524–532, 2013.

[18] L. I. Wagner, R. J. Gray, J. A. Sparano et al., "Patient-reported cognitive impairment among women with early breast cancer randomly assigned to endocrine therapy alone versus chemoendocrine therapy: results from TAILORx," *Journal of Clinical Oncology*, vol. 38, no. 17, pp. 1875–1886, 2020.

[19] C. R. Bowie and P. D. Harvey, "Administration and interpretation of the Trail Making Test," *Nature Protocols*, vol. 1, no. 5, pp. 2277–2281, 2006.

[20] A. Diamond, "Executive functions," *Annual Review of Psychology*, vol. 64, no. 1, pp. 135–168, 2013.

[21] Y. T. Cheung, S. R. Lim, M. Shwe, Y. P. Tan, and A. Chan, "Psychometric properties and measurement equivalence of the English and Chinese versions of the functional assessment of cancer therapy-cognitive in Asian patients with breast cancer," *Value in Health*, vol. 16, no. 6, pp. 1001–1013, 2013.

[22] Y. Chao-Gan and Z. Yu-Feng, "DPARSF: a MATLAB toolbox for "pipeline" data analysis of resting-state fMRI," *Frontiers in Systems Neuroscience*, vol. 4, p. 13, 2010.

[23] C. G. Yan, B. Cheung, C. Kelly et al., "A comprehensive assessment of regional variation in the impact of head micromovements on functional connectomics," *NeuroImage*, vol. 76, pp. 183–201, 2013.

[24] J. C. Beucke, J. Sepulcre, T. Talukdar et al., "Abnormally high degree connectivity of the orbitofrontal cortex in obsessive-compulsive disorder," *JAMA Psychiatry*, vol. 70, no. 6, pp. 619–629, 2013.

[25] S. Mueller, D. Wang, M. D. Fox et al., "Individual variability in functional connectivity architecture of the human brain," *Neuron*, vol. 77, no. 3, pp. 586–595, 2013.

[26] B. M. Bekele, M. Luijendijk, S. B. Schagen, M. de Ruiter, and L. Douw, "Fatigue and resting-state functional brain networks in breast cancer patients treated with chemotherapy," *Breast Cancer Research and Treatment*, vol. 189, no. 3, pp. 787–796, 2021.

[27] C. C. Lim, M. K. Devi, and E. Ang, "Anxiety in women with breast cancer undergoing treatment: a systematic review," *International Journal of Evidence-Based Healthcare*, vol. 9, no. 3, pp. 215–235, 2011.

[28] S. M. Baqutayan, "The effect of anxiety on breast cancer patients," *Indian Journal of Psychological Medicine*, vol. 34, no. 2, pp. 119–123, 2012.

[29] E. Voogt, A. van der Heide, A. F. van Leeuwen et al., "Positive and negative affect after diagnosis of advanced cancer," *Psychooncology*, vol. 14, no. 4, pp. 262–273, 2005.

[30] C. G. Ng, S. Mohamed, K. Kaur et al., "Perceived distress and its association with depression and anxiety in breast cancer patients," *PLoS One*, vol. 12, no. 3, article e0172975, 2017.

[31] A. Chintamani, R. Gogne, M. Khandelwal et al., "the correlation of anxiety and depression levels with response to neoadjuvant chemotherapy in patients with breast cancer," *JRSM Short Reports*, vol. 2, no. 3, p. 15, 2011.

[32] Z. Orszaghova, M. Mego, and M. Chovanec, "Long-term cognitive dysfunction in cancer survivors," *Frontiers in Molecular Biosciences*, vol. 8, p. 770413, 2021.

[33] D. Von Ah, B. Habermann, J. S. Carpenter, and B. L. Schneider, "Impact of perceived cognitive impairment in breast cancer survivors," *European Journal of Oncology Nursing*, vol. 17, no. 2, pp. 236–241, 2013.

[34] K. Hermelink, M. Buhner, P. Sckopke et al., "Chemotherapy and post-Traumatic stress in the causation of cognitive dysfunction in breast cancer patients," *Journal of the National Cancer Institute*, vol. 109, no. 10, 2017.

[35] A. Ardila, B. Bernal, and M. Rosselli, "Connectivity of BA46 involvement in the executive control of language," *Psicothema*, vol. 28, no. 1, pp. 26–31, 2016.

[36] J. N. de Souza-Talarico, P. Caramelli, R. Nitrini, and E. C. Chaves, "The influence of schooling on working memory performance in elderly individuals without cognitive decline," *Dement Neuropsychol*, vol. 1, no. 3, pp. 276–281, 2007.

[37] D. Zanchi, M. L. Montandon, I. Sinanaj et al., "Decreased fronto-parietal and increased default mode network activation is associated with subtle cognitive deficits in elderly controls," *Neurosignals*, vol. 25, no. 1, pp. 127–138, 2018.

[38] C. M. Kaplan, A. Schrepf, I. Mawla et al., "Neurobiological antecedents of multisite pain in children," *Pain*, vol. 163, no. 4, pp. e596–e603, 2022.

[39] H. Radhakrishnan, M. F. Ubele, S. M. Krumholz et al., "Tacrolimus protects against age-associated microstructural changes in the beagle brain," *The Journal of Neuroscience*, vol. 41, no. 23, pp. 5124–5133, 2021.

[40] S. P. Kong, Q. W. Tan, Y. Liu et al., "Specific correlation between the Hegu point (LI4) and the orofacial part: evidence from an fMRI study," *Evidence-based Complementary and Alternative Medicine*, vol. 2015, Article ID 585493, 7 pages, 2015.

[41] S. Y. Zhou, M. Suzuki, H. Hagino et al., "Volumetric analysis of sulci/gyri-defined in vivo frontal lobe regions in schizophrenia: precentral gyrus, cingulate gyrus, and prefrontal region," *Psychiatry Research*, vol. 139, no. 2, pp. 127–139, 2005.

[42] M. A. Bertolero, B. T. T. Yeo, D. S. Bassett, and M. D'Esposito, "A mechanistic model of connector hubs, modularity and cognition," *Nature Human Behaviour*, vol. 2, no. 10, pp. 765–777, 2018.

[43] M. E. Raichle, "The brain's default mode network," *Annual Review of Neuroscience*, vol. 38, no. 1, pp. 433–447, 2015.

[44] P. M. Lind, S. Salihovic, J. Stubleski, A. Karrman, and L. Lind, "Changes in plasma levels of perfluoroalkyl substances (PFASs) are related to increase in carotid intima-media thickness over 10 years - a longitudinal study," *Environmental Health*, vol. 17, no. 1, p. 59, 2018.

[45] D. Zaremba, K. Dohm, R. Redlich et al., "Association of brain cortical changes with relapse in patients with major depressive disorder," *JAMA Psychiatry*, vol. 75, no. 5, pp. 484–492, 2018.

Hindawi
Disease Markers
Volume 2022, Article ID 1853002, 7 pages
https://doi.org/10.1155/2022/1853002

*Research Article*

# Graph-Theory-Based Degree Centrality Combined with Machine Learning Algorithms Can Predict Response to Treatment with Antipsychotic Medications in Patients with First-Episode Schizophrenia

**Wenming Liu,[1] Peng Fang,[2] Fan Guo,[3] Yuting Qiao,[1] Yuanqiang Zhu,[3] and Huaning Wang[1]**

[1]*Department of Psychiatry, Xijing Hospital, Air Force Medical University, Xi'an, Shaanxi, China*
[2]*Department of Military Medical Psychology, Air Force Medical University, Xi'an, Shaanxi, China*
[3]*Department of Radiology, Xijing Hospital, Air Force Medical University, Xi'an, Shaanxi, China*

Correspondence should be addressed to Yuanqiang Zhu; zhu_yq_fmmu@163.com and Huaning Wang; xskzhu@fmmu.edu.cn

Received 7 March 2022; Revised 26 July 2022; Accepted 16 August 2022; Published 13 October 2022

Academic Editor: Dai Xi-jian



*Objectives*. Schizophrenia (SCZ) is associated with disrupted functional brain connectivity, and antipsychotic medications are the primary and most commonly used treatment for schizophrenia. However, not all patients respond to antipsychotic medications. *Methods*. The study is aimed at investigating whether the graph-theory-based degree centrality (DC), derived from resting-state functional MRI (rs-fMRI), can predict the treatment outcomes. rs-fMRI data from 38 SCZ patients were collected and compared with findings from 38 age- and gender-matched healthy controls (HCs). The patients were treated with antipsychotic medications for 16 weeks before undergoing a second rs-fMRI scan. DC data were processed using DPABI and SPM12 software. *Results*. SCZ patients at baseline showed increased DC in the frontal and temporal gyrus, anterior cingulate cortex, and precuneus and reduced DC in bilateral subcortical gray matter structures. However, those abnormalities showed a clear renormalization after antipsychotic medication treatments. Support vector machine analysis using leave-one-out cross-validation achieved a correct classification rate of 84.2% (sensitivity 78.9%, specificity 89.5%, and area under the receiver operating characteristic curve (AUC) 0.925) for differentiating effective subjects from ineffective subjects. Brain areas that contributed most to the classification model were mainly located within the bilateral putamen, left inferior frontal gyrus, left middle occipital cortex, bilateral middle frontal gyrus, left cerebellum, left medial frontal gyrus, left inferior temporal gyrus, and left angular. Furthermore, the DC change within the bilateral putamen is negatively correlated with the symptom improvements after treatment. *Conclusions*. Our study confirmed that graph-theory-based measures, combined with machine-learning algorithms, can provide crucial insights into pathophysiological mechanisms and the effectiveness of antipsychotic medications.

## 1. Introduction

Schizophrenia (SCZ) is viewed as a disease that involves the dysconnectivity of multiple neuronal circuits [1]. Evidence from resting-state functional magnetic resonance imaging (rs-fMRI) studies has revealed impairments in the interaction within and between large-scale brain networks for SCZ patients [2]. In the context of graph theory [3], disrupted topological organization of the whole-brain network such as reduced functional segregation and enhanced functional integration has been extensively reported in schizophrenia studies, both for functional network and white matter network [4, 5]. Furthermore, reduced degree centrality (DC) of hub regions (brain regions that are connected to

a remarkably large number of other regions) is also observed in SCZ [6].

Antipsychotic medications are the primary and most commonly used treatment for schizophrenia. Unfortunately, not all patients respond to antipsychotic medications [7]. Overall estimates suggest that more than 30% of patients have treatment-resistant schizophrenia (TRS) [8]. TRS patients have persistent positive, negative, and cognitive symptoms that lead to poorer outcomes. Previous studies have found functional connectivity impairments within default mode network (DMN) in TRS patients, subcortical networks, and frontal lobes compared with treatment-responsive patients [9]. However, those results are based on average estimates of differences at the group level, and the translational applicability of such data to clinical practice should be based on inferences at the individual rather than group level.

With the recent advancements in the field of machine learning, measurements derived from rs-fMRI combined with artificial intelligence algorithms have led to the improvements in the diagnosis, classification, and treatment outcome prediction for a range of diseases, in particular, for schizophrenia [10]. Our pervious study has indicated that functional connectivity can be a sensitive marker to differentiate SCZ from healthy controls (HCs) [11]; baseline spontaneous regional activities were also found to be predictive of early response to treatment for SCZ [12]. Because SCZ is associated with widespread changes in functional networks, graph-based measurements of network organization, such as degree centrality, might have potential in predicting treatment effects.

The purpose of this study was firstly to determine the dynamic changes of DC measures before and after antipsychotic medication treatment in a group of first-episode SCZ patients. Secondly, we adopt supervised machine learning-based algorithms to investigate whether the baseline DC measures can predict the treatment outcomes. We hypothesized that abnormal DC might reorganize with antipsychotic medication treatment in first-episode SCZ patients and the baseline DC in hub regions of DMN, striatum network, and cerebellum network can accurately classify treatment outcomes.

## 2. Methods

*2.1. Subjects.* Thirty-eight SCZ patients were recruited from the department of Psychiatry, Xijing Hospital affiliated to Air Force Medical University. Clinical diagnosis was according to the Diagnostic and Statistical Manual of Mental Disorders, Fifth Edition (DSM-5). The Positive and Negative Syndrome Scale (PANSS) was assessed by two senior clinical psychiatrists. Subjects were excluded if they have other psychiatric and neurological diseases or any structural abnormalities detected by routine MRI examination. At 16 weeks after first fMRI recording, we performed follow-up assessments of all patients and gathered information about antipsychotic medications and prognosis. In addition, 38 age- and gender-matched healthy controls were recruited by advertisement. This study was approved by the clinical trial ethics committee of Xijing Hospital at the Air Force Medical University. Written informed consent was obtained from each subject prior to the study.

*2.2. Image Acquisition.* The imaging data were collected using a GE 3.0 Tesla Discovery MR scanner with eight–channel phased array head coil (EXCITE, General Electric, Milwaukee, Wisconsin). Subjects were asked to keep their eyes open and to stay awake during the entire session. Using the gradient-echo planar imaging sequence, the resting-state functional images were obtained with the following parameters: echo time = 30 ms, repetition time = 2000 ms, field of view = 240 mm × 240 mm, data matrix = 64 × 64, slices = 33, and total 210 volumes. High-resolution T1-weighted image was also acquired using a volumetric three-dimensional spoiled gradient recall sequence with the following parameters: repetition time = 8.2 ms, echo time = 3.2 ms, field of view = 256 × 256 $mm^2$, matrix = 128 × 128, slice thickness = 1 mm, and 196 slices. The same parameters were used for scans of follow-up assessment of SCZ patients and for healthy controls.

*2.3. fMRI Data Preprocessing.* The Data Processing & Analysis for Brain imaging (DPABI, http://rfmri.org/dpabi) was used to preprocess the fMRI data. The first 10 images were removed for magnetization equilibrium; the remaining 200 images were subjected to slice time correction and motion realignment during which the mean frame-wise displacement (FD) was calculated. Data with head motion that exceeded 2 mm and 2° were excluded. Friston-24 model (the 24 parameters include 6 head motion parameters, 6 head motion parameters one time point before, and the 12 corresponding squared items) was used to regress out the effects of nuisance signals and head motions, as suggested by a previous study; global signal averaged over the whole brain was also regressed [13]. Then, the diffeomorphic anatomical registration through the exponentiated Lie algebra (DARTEL) tool was used for normalization (voxel size, 3 × 3 × 3 $mm^3$), the normalized data was finally band-pass filtered (0.01–0.08 Hz).

*2.4. Degree Centrality.* A correlation matrix was firstly obtained by computing Pearson correlation coefficients between time courses of each pair of voxels. A threshold of $r > 0.25$ was used to obtain the undirected adjacency matrix in order to remove the weak correlations that might be induced by noise [14]. Then, for each voxel, the degree centrality was calculated as the sum the connections between this voxel with other voxels. DC can be computed as in the following equation:

$$\mathrm{DC}(i) = \sum_{j=1}^{N} a_{ij}, \tag{1}$$

where $N$ is the number of voxels and $a_{ij}$ represents the connection or edge from node $i$ to node $j$, which is 0 if no edge exists and 1 for an edge with a weight greater than 0.25. For further statistical analysis, the weighted DC was converted

into a $z$-score map. Finally, the DC map was smoothed with 6 mm FWHM Gaussian kernel.

*2.5. Statistical Analysis.* Group differences between SCZ patients and HCs in demographic characteristics were compared using the chi-square test and Student's $t$-test with SPSS (IBM SPSS Statistics for Windows, version 19.0, IBM Corp.). For detection of between-group differences in DC, general linear model (GLM) with two-sample $t$-tests (HCs vs. SCZ at baseline; HCs vs. SCZ patients at follow-up) or paired $t$-test (baseline vs. follow-up) was used to identify regional DC changes. The threshold for significance was $P < 0.05$, corrected with the FDR criterion. Age, gender, education, and the mean FD calculated during preprocessing step were accounted by including this term as a covariate. The differences between baseline and follow-up were binarized as a mask for the further machine learning analysis.

*2.6. Support Vector Machine Analysis.* As described in our previous study, SCZ patients were classified as responders or nonresponders according to whether they achieved a reduction in PANSS over 50% [5, 15]. SVM was applied by using the Pattern Recognition for Neuroimaging Toolbox (PRoNTo) (http://www.mlnl.cs.ucl.ac.uk/pronto) to investigate whether the baseline DC can classify antipsychotic medication treatment effects [16]. The SVM soft margin parameter $C$ was fixed to its default value 1. Generally, the SVM method includes four steps: (1) feature extraction and feature selection, (2) discriminative region selection, (3) using the training data to train the classifier model, and (4) evaluating the SVM model. In the current study, feature selection consisted of identifying brain regions that differ between the two groups. The above procedure was automatically processed in PRoNTo's "Prepare feature set" programs.

Leave-one-out cross-validation (LOOCV) was used to evaluate the performance of the classifier. In this study, it involved the exclusion of a single subject from each group and training the classifier using the remaining subjects. The above procedures were automatically processed in PRoNTo's "Specify model" programs. Permutation test (1000 times) was used to evaluate the performance of the SVM model; the corresponding accuracy, sensitivity, specificity, and AUC (the area under the receiver operating characteristic curve) were obtained. Then, the weight map was built at voxel level; thus, the region contributions can be ranked and presented for illustration. Finally, the DC changes (baseline vs. follow-up) within these discriminative regions were extracted and Pearson correlation was used to examine the associations between the changes in DC and clinical scores using SPSS. Correction for multiple correlations was accomplished with the FDR criterion.

## 3. Results

*3.1. Demographic Characteristics.* During the follow-up, all patients received second-generation antipsychotic drugs, including paliperidone (10 patients), risperidone (15 patients), olanzapine (9 patients), amisulpride (3 patients), and aripiprazole (1 patient). According to the previous study, drug dose across patients was calculated as olanzapine equivalence. No significant differences were found between patients and HCs on age and gender; detailed demographic characteristics are shown in Table 1.

*3.2. DC Differences across Groups.* Compared with healthy controls, significant DC differences were found in SCZ patients at baseline. As shown in Figure 1(a), SCZ patients showed reduced DC in the bilateral cerebellum, putamen, hippocampus, thalamus, and caudate, which are mainly subcortical gray matter structures; SCZ patients showed increased DC in the bilateral inferior frontal gyrus, medial frontal gyrus, superior frontal gyrus, middle temporal gyrus, anterior cingulate cortex, and precuneus. After antipsychotic medication treatment, as shown in Figures 1(b), a restoration of DC within these regions was found. No significant differences were found between SCZ patients at follow-up and healthy controls.

*3.3. SVM Classification Model.* We obtained an accuracy of 84.2% with a sensitivity of 78.9% and specificity of 89.5% for classification of the two groups. As shown in Figure 2(a) and Table 2, the brain regions that contributed most to the classification are listed below; the top 10 regions are the right putamen (discriminative weight 4.51%), left inferior frontal gyrus (discriminative weight 4.21%), left putamen (discriminative weight 4.19%), left middle occipital cortex (discriminative weight 4.13%), left middle frontal gyrus (discriminative weight 3.92%), left cerebellum (discriminative weight 3.81%), left medial frontal gyrus (discriminative weight 3.78%), right middle frontal gyrus (discriminative weight 3.74%), left inferior temporal gyrus (discriminative weight 3.41%), and left angular (discriminative weight 3.41%). As shown in Figure 3(a), the area under the curve for the classification model was 0.925. Finally, to demonstrate the reliability of our results, we also conducted a validation test in a separate sample (10 subjects collected by Siemens MRI). Classification results for the independent validation cohorts were also high (accuracies 0.80), further emphasizing the feasibility of using models trained exclusively on data collected using a different MRI scanner.

*3.4. Correlation Results.* The changes of DC values after antipsychotic medication treatment (baseline-follow-up) were extracted to correlate with the PANSS changes in SCZ patients. Significant negative correlation was found between changes of positive scores and DC value changes in the left putamen ($r = -0.51$, $P < 0.001$) and right putamen ($r = -0.52$, $P < 0.001$). The correlation results are shown in Figure 3(b).

## 4. Discussion

This study explores the abnormalities of DC and antipsychotic medication effect on SCZ patients using resting-state fMRI. Compared with healthy controls, significant DC changes were found for SCZ patients at baseline, but those abnormalities were renormalized after antipsychotic medication administration. Using a multivariate pattern classification method, the present study demonstrates that degree centrality derived from fMRI data collected at baseline can

Table 1: Demographic characteristics and clinical measures of schizophrenia patients and healthy controls.

| | SZ ($n = 38$) | HCs ($n = 38$) | $t/\chi^2$ | $P$ value |
|---|---|---|---|---|
| Demographic characteristics | | | | |
| Age (y) | 16-59 (24.1 ± 8.6) | 17-58 (24.5 ± 8.3) | -0.2 | 0.82 |
| Gender (male/female) | 21/17 | 21/17 | 0 | 1[b] |
| Education (y) | 4-19 (12.2 ± 3.1) | 7-20 (14.1 ± 3.0) | -2.7 | 0.01* |
| Clinical measurements | | | | |
| Family history (y/n) | 5/33 | — | — | — |
| Duration (y) | 0.02-8 (1.29 ± 1.93) | — | — | — |
| Treatment before (d) | 0-13 (4.62 ± 3.95) | — | — | — |
| Interscan interval (m) | 1-12 (4.6 ± 1.9) | — | — | — |
| Olanzapine (mg/d) | 3.7-27.3 (15.71 ± 4.91) | | | |
| PANSS baseline | | | | |
| Positive score | 7-31 (22.7 ± 4.7) | — | — | — |
| Negative score | 7-34 (21.3 ± 6.4) | — | — | — |
| General score | 30-64 (44.5 ± 8.4) | — | — | — |
| Total score | 63-124 (88.9 ± 13.1) | — | — | — |
| PANSS follow-up | | | | |
| Positive score | 7-21 (9.7 ± 3.7) | — | — | — |
| Negative score | 7-28 (14.9 ± 5.2) | — | — | — |
| General score | 11-42 (25.3 ± 5.8) | — | — | — |
| Total score | 30-110 (53.6 ± 14.1) | — | — | — |

Data were presented as mean ± SD. Abbreviation: SD: standard deviation; PANSS: positive and negative syndrome scale; *$P$: $T$-test with $P < 0.05$.

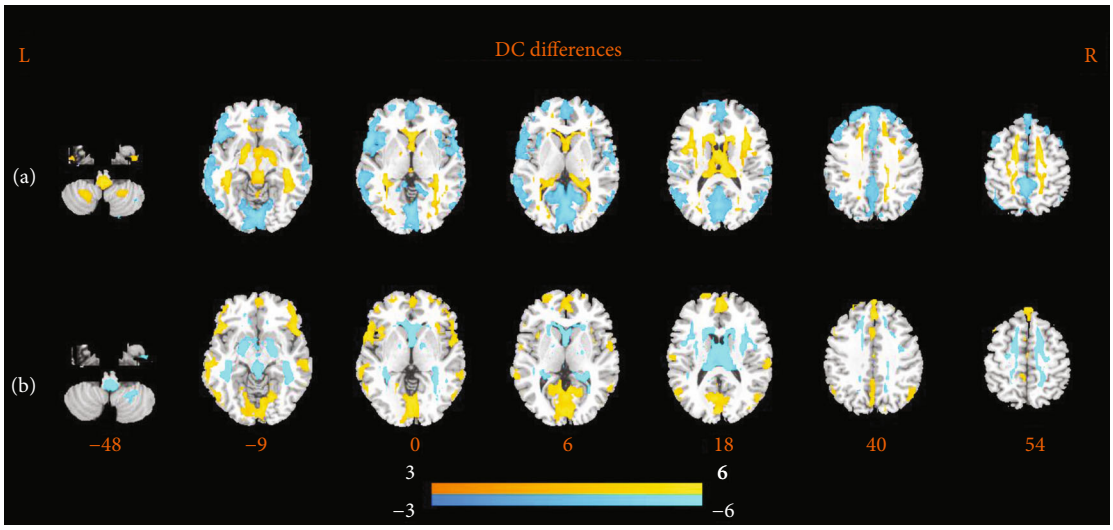


Figure 1: Axial views of significant differences of DC. (a) Regions of increased (warm) and reduced (cool) DC in healthy controls compared with SCZ patients at baseline using two-sample $t$ test. (b) Regions of increased (warm) and reduced (cool) DC in children with SCZ patients from baseline to follow-up using paired $t$ test.

be used to classify subjects on the basis of whether they were effective or ineffective to the antipsychotic medications. With excellent accuracy, the brain regions that showed the most discriminatory power were mainly located within the striatum network, default mode network, and frontal-parietal network. Furthermore, we found a significant negative correlation between the changes of PANSS and DC in the bilateral putamen after treatment. These findings suggest that graph-theory-based measures, such as DC, combined with machine-learning algorithms, can help to predict the effectiveness of antipsychotic medications.

The application of graph theory in neuroimaging allows us to view the human brain as a network at the system level; previous studies have found that patients with first-episode schizophrenia have obvious abnormal network connections [17, 18]. According to a recent study by Jiang et.al, although

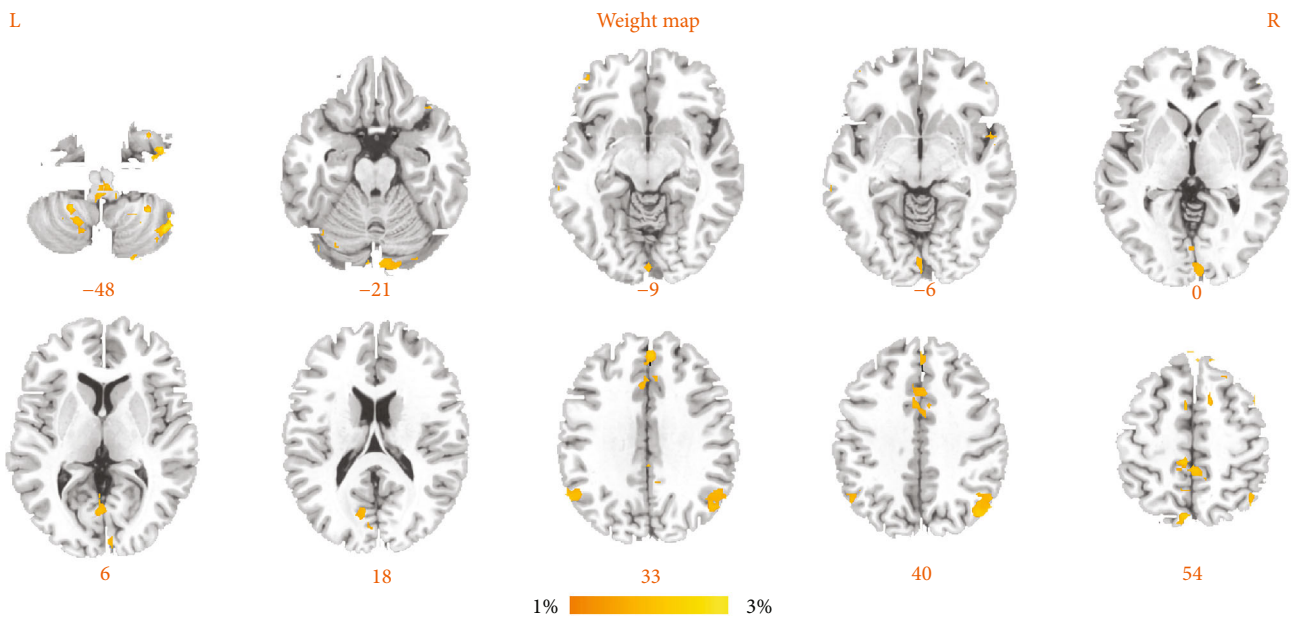


Figure 2: Brain regions of interest that contributed mostly to the accurate classification.

the cortical thickness was further reduced after antipsychotic medication administration, stronger interregional covariance was found in SCZ patients who showed treatment response. This indicated that the increased network integration induced by second-generation antipsychotic drugs might compensate the disrupted brain structure, which highlights a potential network-level regulatory mechanism of antipsychotics on symptom abnormalities [5]. As a very important indicator of network characteristics, degree centrality should also have obvious abnormalities. Consistent with our hypothesis, we found that under strict FDR test standards, there is a significant difference in the degree centrality between SCZ patients and healthy controls.

Those abnormalities involve almost the entire gray matter area, indicating that there are obvious global and local connection abnormalities in patients with schizophrenia. Compared with task-based functional magnetic resonance imaging studies, resting-state magnetic resonance reduces the deviation caused by the task [19]. This is an important advantage for patients with schizophrenia, as they often have impaired perception and cognitive functions. In addition, functional magnetic resonance data analysis can select regions of interest from a predefined map, which allows the method to be cross-validated between independent populations of subjects. The sensitivity and specificity obtained in this study are equivalent to the classification effect obtained based on structural image magnetic resonance.

We found that the top regions in the classification contribution include the bilateral putamen, which is an important part of the striatum [20]. Molecular imaging studies have found that patients with schizophrenia who respond to drugs have a greater ability to synthesize dopamine in the striatum than patients who do not respond to drugs [21]. Using fMRI [20], White et al. found that the frontal lobe striatum network showed extensive connection damage. More importantly, Sarpal et al. found that the functional connection of the striatum can even predict the response of patients with schizophrenia to drugs [22], which is also consistent with our findings in this study. The abnormality of the striatal network has been extensively confirmed in autopsy reports, structural studies, and functional studies. The frontal-striatal network involves a wide range of functions, including behavioral motivation to cognitive control functions. Dopamine signaling in the striatum also affects the advanced cognitive functions of the prefrontal lobe. Because the negative symptoms of schizophrenia include disorders of cognition, motivation, and social incompatibility, the disordered frontal-striatal connection may be the main cause of negative symptoms. In addition, the frontal-striatal network is also responsible for adaptive behavior, reward learning, and social functions. Disordered function of the striatum, especially the connection between the striatum and the frontal area, may be the main pathway that affects the social perception, decision-making, and emotional performance of patients with schizophrenia.

The top contributing regions also include the left medial frontal lobe, the left inferior temporal gyrus, and the left angular gyrus, which are important areas of the default mode network [23], as well as the left middle frontal gyrus, right middle frontal gyrus, and left occipital middle which are important areas of the frontal-parietal network [24]. The findings in these areas confirm the "triple-network hypothesis" in schizophrenia. This theory has recently been proposed to explain various mental disorders [25]; that is, impaired interactions between these networks may be related to specific psychopathological processes. The default mode network is responsible for self-supervision and is in a negative activation state when performing cognitive tasks; the frontal-parietal network is mainly composed of bilateral dorsolateral prefrontal lobe and the posterior parietal lobe,

Table 2: The top ten brain regions that contributed mostly to the accurate classification.

| Brain regions | Cluster size | Peak coordinates (MNI) | | | Discriminative weight (%) |
|---|---|---|---|---|---|
| | | *X* | *Y* | *Z* | |
| Right putamen | 354 | 12 | 0 | 6 | 4.51 |
| Left inferior frontal gyrus | 68 | -48 | 27 | 18 | 4.21 |
| Left putamen | 190 | -21 | -6 | -9 | 4.19 |
| Left middle occipital gyrus | 79 | -24 | -99 | -6 | 4.13 |
| Left middle frontal gyrus | 114 | -21 | 6 | 54 | 3.92 |
| Left cerebellum | 179 | -51 | -57 | -48 | 3.81 |
| Left medial frontal gyrus | 91 | -6 | 63 | 6 | 3.78 |
| Right middle frontal gyrus | 61 | 33 | 9 | 54 | 3.74 |
| Left inferior temporal gyrus | 54 | -63 | -21 | -21 | 3.41 |
| Left angular | 73 | -39 | -51 | 33 | 3.41 |

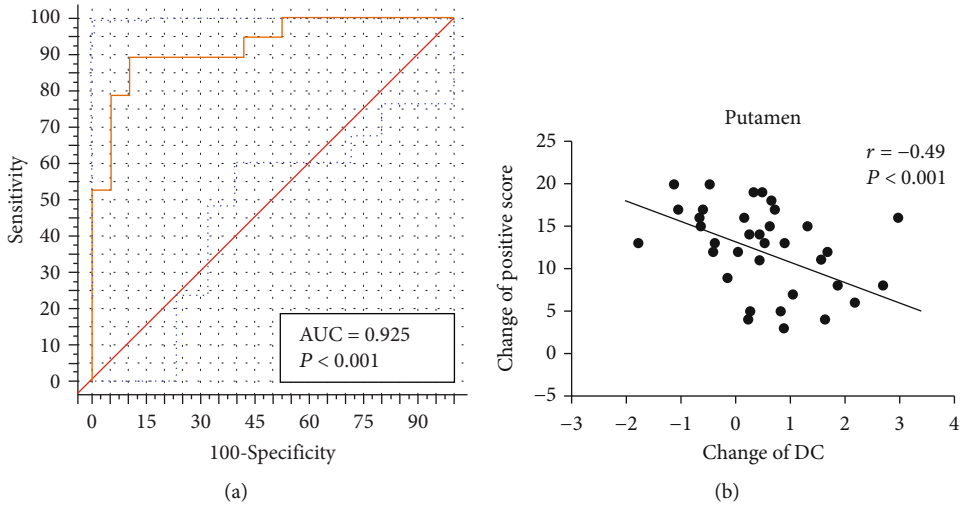


Figure 3: (a) ROC curve of the classifier. (b) Correlation between the clinical symptom improvements and the change of DC values in the bilateral putamen in SCZ patients.

and it is responsible for attention and working memory functions. The impairment of self-monitoring function often found in patients with schizophrenia may be related to the decline in the internal communication of the default mode network. The disordered activities of the default mode network may also be related to the weakening of the frontal-parietal network.

Our research has the following limitations. First of all, in the baseline state, the patient population received antipsychotic treatment. Although the patients were only exposed to antipsychotics within 2 weeks, the potential impact of the drug's contribution to the results cannot be ignored; another limitation is that all patients received second-generation antipsychotic drugs, but each patient's sensitivity to the drug is heterogeneous, and such heterogeneity will also have an impact on the current research results; finally, our study only recruited 38 cases of SZ patients and 38 healthy controls, the sample size of the validation cohorts was also too small, the statistical power may be limited, and further study should increase the sample size to guarantee the statistical power.

## 5. Conclusion

We showed a normalization of the degree centrality in patients with SCZ after antipsychotic medication treatments. With the help of magnetic resonance imaging and machine learning algorithms, the characteristics of brain networks in schizophrenia can be used as sensitive biomarkers for treatment prediction of SZ.

## Data Availability

The patient data used to support the findings of this study are restricted by the Institutional Review Board of the Xijing Hospital in order to protect patient privacy.

## Conflicts of Interest

There are no conflicts of interest.

## Authors' Contributions

Wenming Liu, Peng Fang, and Fan Guo contributed equally to this work.

## Acknowledgments

This study was supported by the Key R&D Program Projects of Shaanxi, China (Nos. 2021SF-287 and 2022JM-575); Boost Program of Xijing Hospital (XJZT19ML56); National Natural Science Foundation of China under Grant No. 81974215; China Postdoctoral Science Foundation (2019M653963); and Military Medical Science and Technology Youth Training Program (20QNPY049).

## References

[1] W. Pettersson-Yeo, P. Allen, S. Benetti, P. McGuire, and A. Mechelli, "Dysconnectivity in schizophrenia: where are we now?," *Neuroscience and Biobehavioral Reviews*, vol. 35, no. 5, pp. 1110–1124, 2011.

[2] M.-E. Lynall, D. S. Bassett, R. Kerwin et al., "Functional connectivity and brain networks in schizophrenia," *The Journal of Neuroscience*, vol. 30, no. 28, pp. 9477–9487, 2010.

[3] K. Song, J. Li, Y. Zhu, F. Ren, L. Cao, and Z. G. Huang, "Altered small-world functional network topology in patients with optic neuritis: a resting-state fMRI study," *Disease Markers*, vol. 2021, Article ID 9948751, 9 pages, 2021.

[4] Y. Liu, M. Liang, Y. Zhou et al., "Disrupted small-world networks in schizophrenia," *Brain*, vol. 131, no. 4, pp. 945–961, 2008.

[5] Y. Jiang, D. Yao, J. Zhou et al., "Characteristics of disrupted topological organization in white matter functional connectome in schizophrenia," *Psychological Medicine*, vol. 52, no. 7, pp. 1333–1343, 2022.

[6] H. Cheng, S. Newman, J. Goñi et al., "Nodal centrality of functional network in the differentiation of schizophrenia," *Schizophrenia Research*, vol. 168, no. 1-2, pp. 345–352, 2015.

[7] N. K. Chan, J. Kim, P. Shah et al., "Resting-state functional connectivity in treatment response and resistance in schizophrenia: a systematic review," *Schizophrenia Research*, vol. 211, pp. 10–20, 2019.

[8] E. P. Ganella, C. F. Bartholomeusz, C. Seguin et al., "Functional brain networks in treatment-resistant schizophrenia," *Schizophrenia Research*, vol. 184, pp. 73–81, 2017.

[9] L. Palaniyappan, T. R. Marques, H. Taylor et al., "Globally efficient brain organization and treatment response in psychosis: a connectomic study of gyrification," *Schizophrenia Bulletin*, vol. 42, no. 6, pp. 1446–1456, 2016.

[10] E. Veronese, U. Castellani, D. Peruzzo, M. Bellani, and P. Brambilla, "Machine learning approaches: from theory to application in schizophrenia," *Computational and Mathematical Methods in Medicine*, vol. 2013, Article ID 867924, 12 pages, 2013.

[11] W. Liu, X. Zhang, Y. Qiao et al., "Functional connectivity combined with a machine learning algorithm can classify high-risk first-degree relatives of patients with schizophrenia and identify correlates of cognitive impairments," *Frontiers in Neuroscience*, vol. 14, 2020.

[12] L. B. Cui, Y. F. Fu, L. Liu et al., "Baseline structural and functional magnetic resonance imaging predicts early treatment response in schizophrenia with radiomics strategy," *The European Journal of Neuroscience*, vol. 53, no. 6, pp. 1961–1975, 2021.

[13] X.-J. Dai, B.-X. Liu, S. Ai et al., "Altered inter-hemispheric communication of default-mode and visual networks underlie etiology of primary insomnia," *Brain Imaging and Behavior*, vol. 14, no. 5, pp. 1430–1444, 2020.

[14] H. Takeuchi, Y. Taki, R. Nouchi et al., "Degree centrality and fractional amplitude of low-frequency oscillations associated with Stroop interference," *NeuroImage*, vol. 119, pp. 197–209, 2015.

[15] F. Guo, Y. Q. Zhu, C. Li et al., "Gray matter volume changes following antipsychotic therapy in first-episode schizophrenia patients: a longitudinal voxel-based morphometric study," *Journal of Psychiatric Research*, vol. 116, pp. 126–132, 2019.

[16] J. Schrouff, M. J. Rosa, J. M. Rondina et al., "PRoNTo: pattern recognition for neuroimaging toolbox," *Neuroinformatics*, vol. 11, no. 3, pp. 319–337, 2013.

[17] J. A. Hadley, N. V. Kraguljac, D. M. White, L. Ver Hoef, J. Tabora, and A. C. Lahti, "Change in brain network topology as a function of treatment response in schizophrenia: a longitudinal resting-state fMRI study using graph theory," *NPJ Schizophrenia*, vol. 2, no. 1, pp. 1–7, 2016.

[18] M. P. van den Heuvel, R. C. Mandl, C. J. Stam, R. S. Kahn, and H. E. H. Pol, "Aberrant frontal and temporal complex network structure in schizophrenia: a graph theoretical analysis," *The Journal of Neuroscience*, vol. 30, no. 47, pp. 15915–15926, 2010.

[19] J. Kim, V. D. Calhoun, E. Shim, and J.-H. Lee, "Deep neural network with weight sparsity control and pre-training extracts hierarchical features and enhances classification performance: evidence from whole-brain resting-state functional connectivity patterns of schizophrenia," *NeuroImage*, vol. 124, no. Part A, pp. 127–146, 2016.

[20] T. P. White, R. Wigton, D. W. Joyce, T. Collier, A. Fornito, and S. S. Shergill, "Dysfunctional striatal systems in treatment-resistant schizophrenia," *Neuropsychopharmacology*, vol. 41, no. 5, pp. 1274–1285, 2016.

[21] L. D. Vanes, E. Mouchlianitis, T. Collier, B. B. Averbeck, and S. S. Shergill, "Differential neural reward mechanisms in treatment responsive and treatment resistant schizophrenia," *Psychological Medicine*, vol. 48, no. 14, pp. 2418–2427, 2018.

[22] D. K. Sarpal, M. Argyelan, D. G. Robinson et al., "Baseline striatal functional connectivity as a predictor of response to antipsychotic drug treatment," *The American Journal of Psychiatry*, vol. 173, no. 1, pp. 69–77, 2016.

[23] F. Sambataro, G. Blasi, L. Fazio et al., "Treatment with olanzapine is associated with modulation of the default mode network in patients with schizophrenia," *Neuropsychopharmacology*, vol. 35, no. 4, pp. 904–912, 2010.

[24] Y. Zhu, Y. Xi, N. Fei et al., "Dynamics of cerebral responses to sustained attention performance during one night of sleep deprivation," *Journal of Sleep Research*, vol. 27, no. 2, pp. 184–196, 2018.

[25] V. Menon, "Large-scale brain networks and psychopathology: a unifying triple network model," *Trends in Cognitive Sciences*, vol. 15, no. 10, pp. 483–506, 2011.

Hindawi
Disease Markers
Volume 2022, Article ID 7071877, 11 pages
https://doi.org/10.1155/2022/7071877

*Research Article*

# Exosomes Derived from Adipose Mesenchymal Stem Cells Carrying miRNA-22-3p Promote Schwann Cells Proliferation and Migration through Downregulation of PTEN

**Jianqiang Yang, Baoxin Wang, Yating Wang, Chen Feng, Lixiao Chen, Yuying Liu, Xinwei Chen, and Pin Dong**

*Department of Otorhinolaryngology and Head and Neck Surgery, Shanghai General Hospital, School of Medicine, Shanghai Jiaotong University, Shanghai, China*

Correspondence should be addressed to Pin Dong; dongpin64@aliyun.com

Received 17 May 2022; Accepted 15 July 2022; Published 13 September 2022

Academic Editor: Dai Xi-jian



Peripheral nerve injury (PNI) is often resulting from trauma, which leads to severe and permanently disability. Schwann cells are critical for facilitating the regeneration process after PNI. Adipose-derived mesenchymal stem cells (ADSCs) exosomes have been used as a novel treatment for peripheral nerve injury. However, the underlying mechanism remains unclear. In this study, we isolated ADSCs and extracted exosomes, which were verified by transmission electron microscopy (TEM), nanoparticle tracking analysis (NTA), and western blot (WB). Cocultured with Dorsal Root Ganglion (DRG) and Schwann cells (SCs) to evaluate the effect of exosomes on the growth of DRG axons by immunofluorescence, and the proliferation and migration of SCs by CCK8 and Transwell assays, respectively. Through exosomal miRNA sequencing and bioinformatic analysis, the related miRNAs and target gene were predicted and identified by dual luciferase assay. Related miRNAs were overexpressed and inhibited, respectively, to clarify their effects; the downstream pathway through the target gene was determined by real-time fluorescence quantitative polymerase chain reaction (RT-qPCR) and WB. Results found that ADSC-exosomes could promote the proliferation and migration of SCs and the growth of DRG axons, respectively. Exosomal miRNA-22-3p from ADSCs directly inhibited the expression of Phosphatase and Tensin Homolog deleted on Chromosome 10 (PTEN), activated phosphorylation of the AKT/mTOR axis, and enhanced SCs proliferation and migration. In conclusion, our findings suggest that ADSC-exosomes could promote SCs function through exosomal miRNA-22-3p, which could be used as a therapeutic target for peripheral nerve injury.

## 1. Introduction

The peripheral nerve connects the central nerve to the muscles, bones, and visceral organs. Peripheral nerve injuries (PNIs) often result in persistent dysfunction of innervated tissues. PNIs occur secondary to trauma, tumors or inflammation, with an annual incidence of approximately 13–23 per 100,000 individuals [1]. Trauma is the primary cause, and approximately 3% of trauma events are accompanied by PNIs [2]. Because of inflammation and scar formation, recovery from PNIs is often limited by the type and severity of injury. Currently, autologous nerve transplantation is the standard treatment for complete amputation, a type of severe injury. However, this method requires sacrificing the normal donor nerves, and simple end-to-end nerve suturing may result in the wrong direction of sensory and motor nerve regeneration [3]. This results in an unsatisfactory outcome; therefore, new treatments for PNIs are needed.

With the development of regenerative medicine, mesenchymal stem cells (MSCs) have increasingly been used to treat various diseases and injuries. MSCs can promote the repair of nerve injuries [4], which may occur by two mechanisms. First, MSCs can differentiate into Schwann-like cells or promote the massive proliferation of Schwann cells (SCs),

thus providing physical support for the regeneration and extension of nerve axons [5]. In addition, MSCs can secrete neurotrophic factors such as BDNF, GDNF, and NGF, which promote nerve repair [6]. Nevertheless, there are still some limitations to the direct use of MSCs to treat PNIs, such as unavoidable immunogenicity and ethical issues that limit their clinical application.

Exosomes are a class of membranous vesicles that are approximately 30–150 nm in size. They are produced by most cells, including MSCs, tumor cells, immune cells, and nerve cells [7–9]. Exosomes play an important role in intercellular communication. They can transport a variety of bioactive substances, including lipids, proteins, and nucleic acids, to recipient cells for transmission of biological information. Studies have shown that miRNAs in exosomes can bind to target genes associated with various cellular pathways, including angiogenesis, cell transport, apoptosis, and protein cleavage [10, 11]. In the nervous system, MSC-derived exosomes also play an important role in nerve regeneration [12]. A study showed that adipose-derived MSCs (ADSCs) exosomes can promote the proliferation and migration of Schwann cells [13]; however the mechanism is not clear. Moreover, the role of miRNAs in ADSC-exosomes (ADSC-Exos) remains unknown.

In the present study, exosomes were extracted from ADSCs and cocultured with SCs for exosomal miRNA sequencing to identify relevant miRNAs, as well as the downstream signaling pathways and mechanisms associated with their effects.

## 2. Materials and Methods

*2.1. Isolation of ADSCs.* Sprague-Dawley rats were purchased from Shanghai SLAC Animal Company. All animal experiments were approved by the Ethics Committee of Shanghai General Hospital and conducted strictly in accordance with the institutional guidelines for the care and use of laboratory animals. Four-week-old SD rats were anesthetized, and adipose biopsies were obtained from inguinal subcutaneous tissue and cut into small pieces using microscissors. Added 0.1% collagenase I (SCR103; Sigma-Aldrich) to digest at a shaker (37°C for 1 hour). Digested adipose tissue was centrifuged at $2000 \times$ rpm for 10 min. After filtering through a 70 $\mu$m mesh filter, cells were cultured at 37°C in 5% $CO_2$ humidified conditions in DMEM medium (11965092; Gibco) with 10% fetal bovine serum (FBS) (10082147; Gibco), and 1% penicillin/streptomycin (15070063; Gibco) [14]. The medium was replaced every two days and passaged when 90% fusion was reached.

*2.2. Multipotent Differentiation of ADSCs.* When the ADSCs reached 70% confluence, the medium was replaced with osteogenic induction medium supplemented with L-glutamine, dexamethasone, ascorbic acid, and $\beta$-glycerophosphate. The medium was changed every 3 days according to the growth conditions. After 4 weeks, the cells were stained with Alizarin Red S stain [15]. When ADSCs reached 100% confluence, the medium was replaced with adipogenic induction culture medium consisting of DMEM with insulin, dexamethasone, indomethacin, and 3-isobutyl-1-methylxanthine. The medium was replaced every three days for 14 days. Oil Red O staining was performed to detect intracellular lipid vacuoles characteristic of adipocytes [16].

*2.3. Flow Cytometric Analysis.* Cells were incubated with a specific monoclonal antibody conjugated with phycoerythrin (PE) in 200 $\mu$l PBS for 30 min in the dark at 4°C and then analyzed by flow cytometry. Antibodies against PE anti-CD11b/c (201807; BioLegend), PE anti-CD29 (102207; BioLegend), PE anti-CD45 (202207; BioLegend), and PE anti-CD90 (202523; BioLegend) were used. PE anti-mouse IgG1 (4066607; BioLegend) was used as the control.

*2.4. Extraction of Exosomes and miRNA.* ADSCs were cultured in DMEM containing 10% exosomes-free FBS (180625; SBI) for 48 h. The medium was then collected and centrifuged at $3000 \times g$ for 10 min at 4°C. The supernatant was collected, transferred to a new tube, and placed on ice. Exosomes and miRNAs were extracted using an exoRNeasy Midi Kit (77144; QIAGEN), according to the manufacturer's protocol.

*2.5. Identification of Exosomes.* The morphology of exosomes was examined by transmission electron microscopy (TEM). Exosomes were fixed in 2% paraformaldehyde (PFA)-cacodylate buffer and loaded onto copper grids covered with formvar for 30 min. Grids were washed and contrasted in 4% uranyl acetate for 5 min before being examined by TEM (FEI TECNAI G2 spititi FEI, 120 KV). The particle size of the exosomes was determined using nanoparticle tracking analysis (NTA) with Zeta View PMX 110 (Particle Metrix, Meerbusch) and the corresponding software Zeta View 8.04.02. The exosomal characteristic markers rabbit pAb CD9 (A1703; ABclonal), rabbit mAb ALIX (ab275377; Abcam), and mouse mAb GAPDH (ab8245; Abcam) were analyzed by western blotting [17].

*2.6. Internalization Assays of Exosomes.* ADSC-Exos were labeled with PKH67 (MINI67-1KT; Sigma-Aldrich) according to the manufacturer's instructions. Schwann cells were seeded in confocal dishes and coculture with PKH67 labeled ADSC-Exos. After 24 h, Schwann cells were fixed with 4% formaldehyde and stained with Actin-Tracker Red-594 (C2205S; Beyotime) and DAPI (C1005; Beyotime). Finally, cells were visualized using a laser scanning confocal microscope.

*2.7. Isolation and Culture of DRG.* Three-week-old SD rats were sacrificed by decapitation with guillotine after anesthesia. The body trunk of the rat was isolated between the forelimb and femur, and the bilateral lumbar DRGs were collected in a 35-mm culture dish with 2 ml of iced Leibovitz's L-15 medium (11415064; Gibco) [18]. Added 2 ml of prewarmed digestive system (DNase 0.1 mg/ml; Trypsin 0.4 mg/ml; Collagenase I 1 mg/ml) and digested the DRGs for 40 minutes in an incubator (37°C, 5%$CO_2$). After digestion was stopped, the cell suspension was filtered through a 100 $\mu$m membrane filter and plated onto a poly D-lysine-coated confocal dish with DMEM complete medium.

Approximately 1 d later, the Neurobasal complete medium with the addition of 10 $\mu$m cytarabine (Ara-C) was replaced. After 3 days, ADSC-Exos were added to the DRGs. The control group contained no exosomes.

*2.8. Immunofluorescence Staining.* The cells were then fixed with 4% paraformaldehyde for 30 min. After permeability and closure, the samples were incubated with primary antibodies (1 : 300, Cell Signaling Technology) overnight at 4°C and then treated with the corresponding fluorescence labeled secondary antibodies (1 : 300; Invitrogen). The results were observed using a laser scanning confocal microscope.

*2.9. Cell Counting Kit-8 (CCK-8) Assays.* Cell proliferation was detected using a Cell Counting Kit-8 kit (HY-K0301; MCE). After coculture with ADSC-Exos for 48 h, cells were seeded in 96-well plates and incubated for 24-72 h after treatment. Each well received a 10 $\mu$l CCK-8 reagent and was cultured in a cell incubator for 1 h. Optical density (OD) at 450 nm was measured using a microplate reader.

*2.10. Transwell Assays.* Migration was evaluated using a 24-well Transwell system (3422; Corning). The cells were then paved in the apical chamber in serum-free medium. The basolateral chamber was filled with a medium supplemented with 10% exosomes-free FBS as a chemical attractant. After 48 h of incubation, the membrane was stained with 0.1% crystal violet. The cells were observed under an inverted microscope.

*2.11. miRNA Sequencing of Exosomes and Bioinformatic Analysis.* Total RNA from ADSC-Exos and SC-Exos was isolated for miRNA analysis using the mirVana™ miRNA Isolation Kit (AM1560; Ambion) according to the manufacturer's protocol. Reverse transcription, library construction, miRNA sequencing, and analysis were conducted by OBIO Biotech Company. Criteria applied to select differentially expressed miRNAs were $p < 0.05$ and fold-change ≥2 or ≤0.5. The potential binding sites of the miRNAs were predicted using the online software TargetScan (http://www.Targetscan.org/vert_72/).

*2.12. Dual-Luciferase Reporter Assays.* The 3′-UTR of the PTEN fragment containing wild-type or mutant binding sites for miR-22-3p was cloned into the pmirGlO luciferase reporter vector (Asia Vector Biotech) to generate the wild-type or mutant plasmids, respectively. miRNA-NC or miR-22-3p was transfected with luciferase reporter plasmids into Schwann cells. After 72 h, luciferase activity was evaluated using a dual-luciferase assay kit (E1910; Promega). All primers used are presented in Supplementary S1.

*2.13. Quantitative Real-Time Polymerase Chain Reaction.* Total RNA was isolated using the miRNeasy Mini Kit (217004, QIAGEN), according to the manufacturer's protocol. The HyperScript® RT Supermix Reagent Kit (R202, NovaBio) and HyperScript™ miRNA 1st Strand cDNA synthesis kit (R601, NovaBio) were used to reverse transcribe mRNA and miRNA into cDNA. Real-time qPCR was performed on the StepOnePlus™ platform (Applied Biosystems) using a SYBR® qPCR Mix kit (Q204, NovaBio). Primers and reaction conditions are provided in Supplementary S2. The relative expression levels of the target genes were calculated using the $2^{-\Delta\Delta Ct}$ method and normalized to GAPDH or U6.

*2.14. Western Blot.* RIPA lysis buffer (89900, Thermo Fisher) was used to lyse the samples, which were then centrifuged at 12000 g for 20 min at 4°C. The protein concentration in the supernatant was calculated using a BCA protein assay kit (P0012; Beyotime). The samples were loaded onto an SDS-PAGE gel, electrophoresed, and transferred to the PVDF membrane. The membranes were incubated with primary antibodies (1 : 1000; CST and ABclonal) overnight at 4°C and with the corresponding secondary antibodies (1 : 20000; Proteintech) at room temperature for 1 h. Immunoblots were observed with an enhanced chemiluminescence reagent kit (P2300; NCM).

*2.15. Statistical Analysis.* All data are expressed as the mean ± SD. Comparisons between two groups were evaluated using an unpaired Student's $t$-test. One-way ANOVA with a Bonferroni posthoc test was used for groups ≥3. Statistical significance was set at $p < 0.05$. Statistical analysis was performed using the GraphPad Prism 8.0.2 software.

## 3. Results

*3.1. Identification of ADSCs.* ADSCs were isolated from SD rats and passaged to the 3rd generation. Flow cytometry analysis revealed that the ADSCs were positive for MSC markers, including CD29 (99.71%) and CD90 (98.64%), and negative for CD45 (0.43%) and CD11b/c (0.37%) (Figure 1(a)). To verify the multipotent differentiation ability, we conducted adipogenic and osteogenic experiments, and the results indicated that they exhibited significant differentiation potential (Figure 1(b)).

*3.2. Characterization and Internalization of ADSC-Exos.* Next, we characterized ADSC-Exos by isolating exosomes from the conditioned medium of the ADSCs. First, exosomes were resuspended in PBS and characterized using transmission electron microscopy (TEM). ADSC-Exos exhibited the characteristic structure of exosomes (Figure 2(a)). Second, we used NTA to confirm the size and concentration of released exosomes. The mean particle diameter was 110.2 nm, with a concentration of $1.5 \times 10^{10}$ particles/ml (Figure 2(b)). Finally, western blot analysis of the purified exosomes revealed the expression of exosomal markers CD9 and ALIX, as well as the negative marker GAPDH (Figure 2(c)). Exosomes were labeled with PKH67 to determine whether ADSC-Exos were taken up by Schwann cells. We cocultured different concentrations (5, 10, and 20 $\mu$g/ml) of ADSC-Exos with Schwann cells. After 24 h, confocal imaging revealed the presence of PKH67 spots in the recipient cells, indicating that the labeled exosomes released by ADSCs could be delivered to Schwann cells, and the uptake efficiency was concentration-dependent (Figure 2(d)).

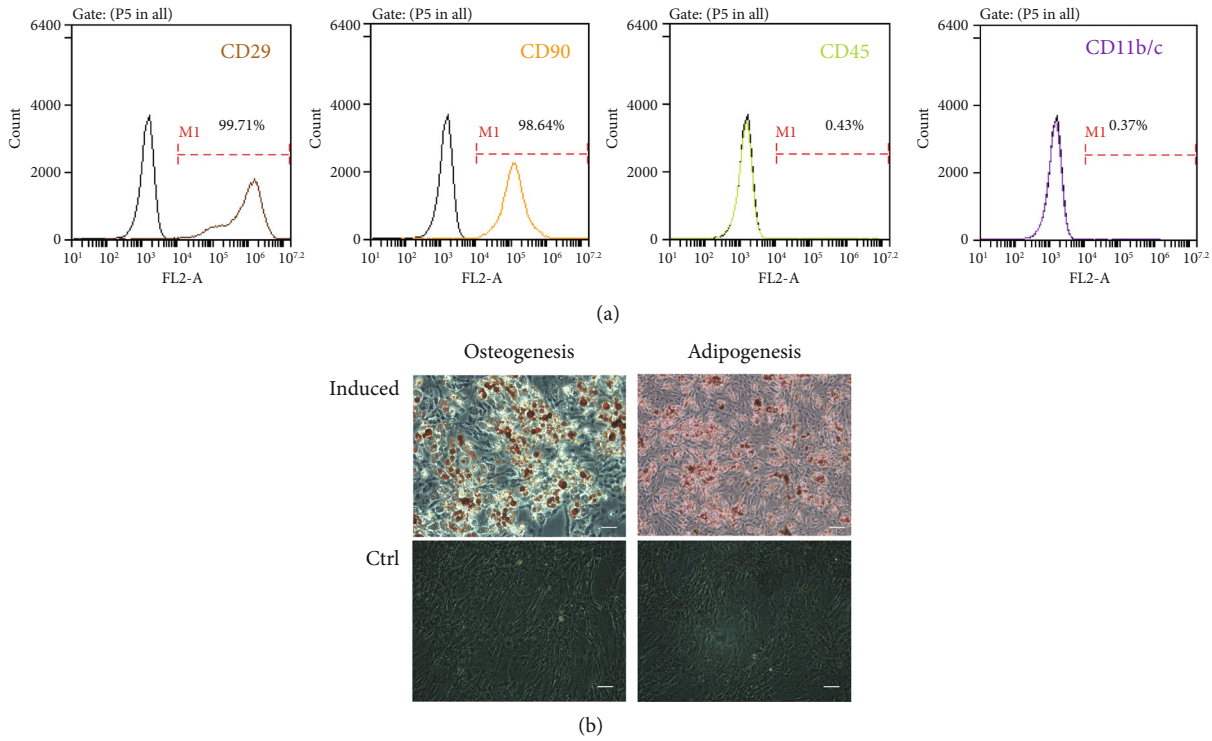


Figure 1: Characterization of ADSCs. (a) Flow cytometric analysis of surface markers of ADSCs. ADSCs were positive for MSC markers including CD29 (99.71%) and CD90 (98.64%) and were negative for CD45 (0.43%) and CD11b/c (0.37%). (b) Representative images of adipogenic differentiation and osteogenic differentiation. The visual field was filled with red lipid droplets stained with Oil Red O solution in images of adipogenic differentiation. Calcium nodules with burrs were formed in images of osteogenic differentiation, which were stained red by Alizarin Red S solution (scale bar: 100 $\mu$m). CTRL, Control group; osteogenesis, osteogenic induction group; adipogenesis, adipogenic induction group; ADSCs, Adipose-derived mesenchymal stem cells.

*3.3. Effects of ADSC-Exos on DRG Neurite Growth and SCs Proliferation and Migration.* We isolated rat primary DRGs to determine the effects of ADSC-Exos on neurite growth. After coculturing with ADSC-Exos for 3 days, immunofluorescence staining was performed to evaluate the effect of ADSC-Exos on DRG neurite growth compared with the PBS-treated control group (Figure 3(a)). The DRGs clearly developed neurites in the ADSC-Exos group, and the length of the longest neurite was significantly increased compared with that of the control group (Figure 3(b)). Next, we determined whether ADSC-Exos affected the migration and proliferation of Schwann cells. The migration assay revealed that ADSC-Exos markedly enhanced cells migration at 48 h (Figures 3(c) and 3(d)). In addition, the CCK-8 assay indicated that ADSC-Exos promoted the proliferation of Schwann cells, and there was a statistical difference between the two groups at 72 h (Figure 3(e) and 3(f)).

*3.4. Exosomal miRNA Sequencing.* miRNA sequencing results revealed that 124 miRNAs were upregulated in ADSC-Exos compared to SC-Exos ($p < 0.05$) (Supplementary S3). The distribution of the differentially expressed miRNAs of ADSC-Exos compared to SC-Exos is shown in a volcano plot, as shown in Figure 4(a). Using the KEGG database, the target genes were found to be enriched in several signaling pathways, in particular, 143 miRNAs were enriched in the mTOR signaling pathway (Figure 4(b)). We selected ten miRNAs with high different expression ($p < 0.05$) in sequencing and high score in the TargetScan software as candidates (Figure 4(c)). The results indicated that miR-22-3p has significant potential, and Pten (tensin homolog deleted on chromosome 10) was predicted to be its target gene (Figure 4(d)).

*3.5. miR-22-3p Directly Targets Pten in SCs.* To explore the mechanism of miR-22-3p regulation, a bioinformatic analysis was performed, which revealed that the target site was located at 674-681 bp in the 3′UTR of Pten. Therefore, we designed a luciferase vector containing a wild-type or mutant Pten 3′-UTR (Figure 5(a)). To verify whether miR-22-3p directly targets the 3′ UTR of Pten directly, a dual luciferase reporter assay was conducted. The results showed that the luciferase activity of the Pten WT 3′UTR was significantly reduced after cotransfection with miR-22-3p compared to that in the NC group. In contrast, no significant direct interaction was observed between miR-22-3p and the vector containing the Pten MUT 3′UTR (Figure 5(b)).

*3.6. ADSC-Exos Promote SC Proliferation and Migration via miRNA-22-3p.* To reveal the downstream regulatory effects of miR-22-3p, we synthesized a mimic and an inhibitor of miR-22-3p, as well as a negative control, which were

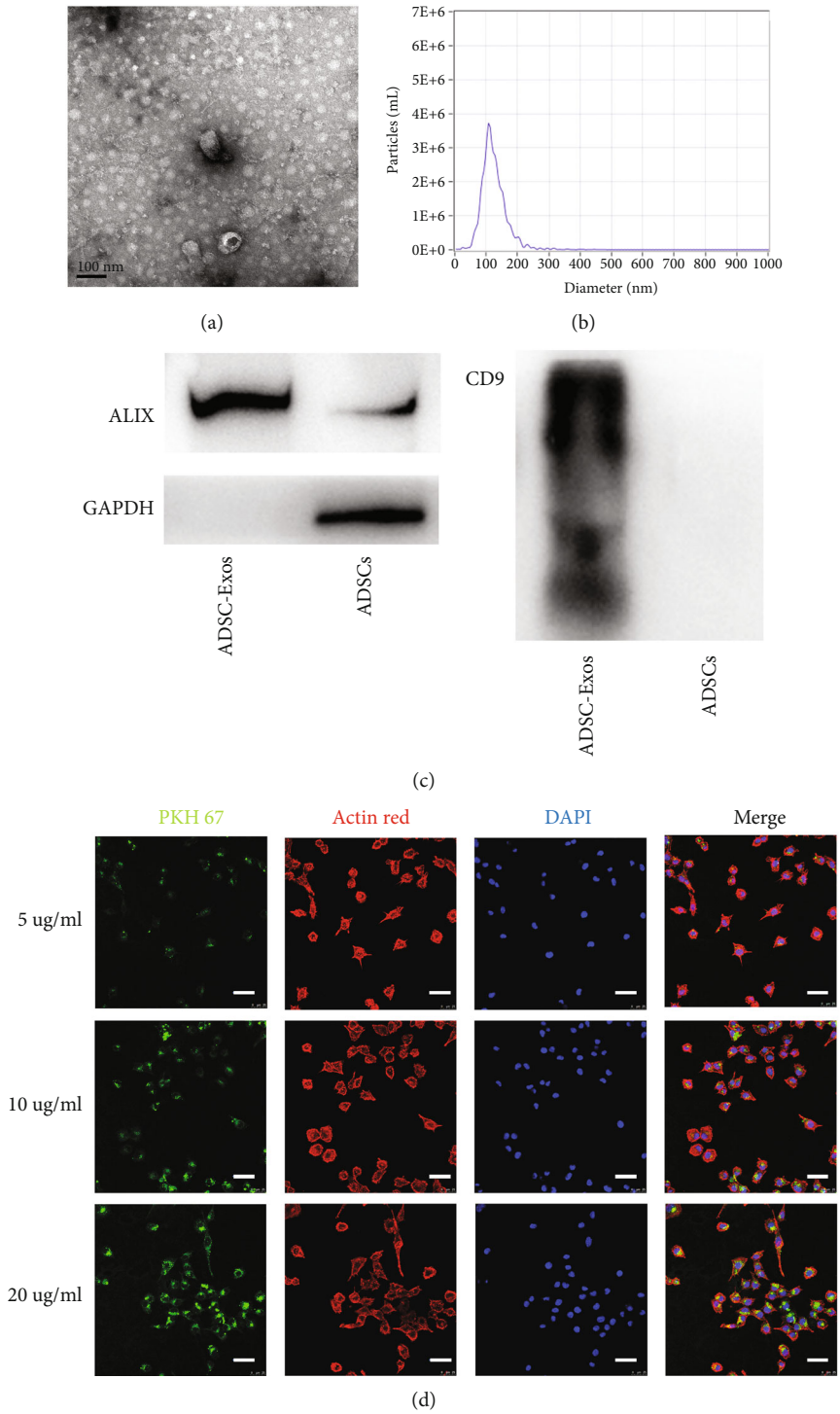


Figure 2: Characterization of exosomes from ADSCs. (a) Representative ultrastructure of ADSC-Exos by TEM. (b) The size distribution profile of ADSC-Exos by NTA. (c) Detection of exosomal markers (ALIX and CD9) and GAPDH by western blot.(d) The internalization of ADSC-Exos by SCs. Confocal images showing the SCs incubated with 5, 10, and 20 $\mu$g/ml PKH67-labeled ADSC-Exos for 24 hour (scale bar : 100 $\mu$m). TEM, Transmission Electron Microscope; NTA, Nanoparticle Tracking Analysis; DAPI, 4′-6-diamidino-2-phenylindole; PKH67, Green Fluorescent Cell Linker; Actin Red, phalloidin-Alexa Fluor 594; ADSCs, Adipose-derived mesenchymal stem cells; ADSC-Exos, the exosomes extracted from Adipose-derived mesenchymal stem cells.

transfected into Schwann cells to determine the relationship between miR-22-3p and Pten whether it regulates Schwann cells proliferation and migration. The results demonstrated that the Pten mRNA levels were unchanged in each group (Figure 5(c)); however, the expression of PTEN protein was downregulated by the miR-22-3p mimic but

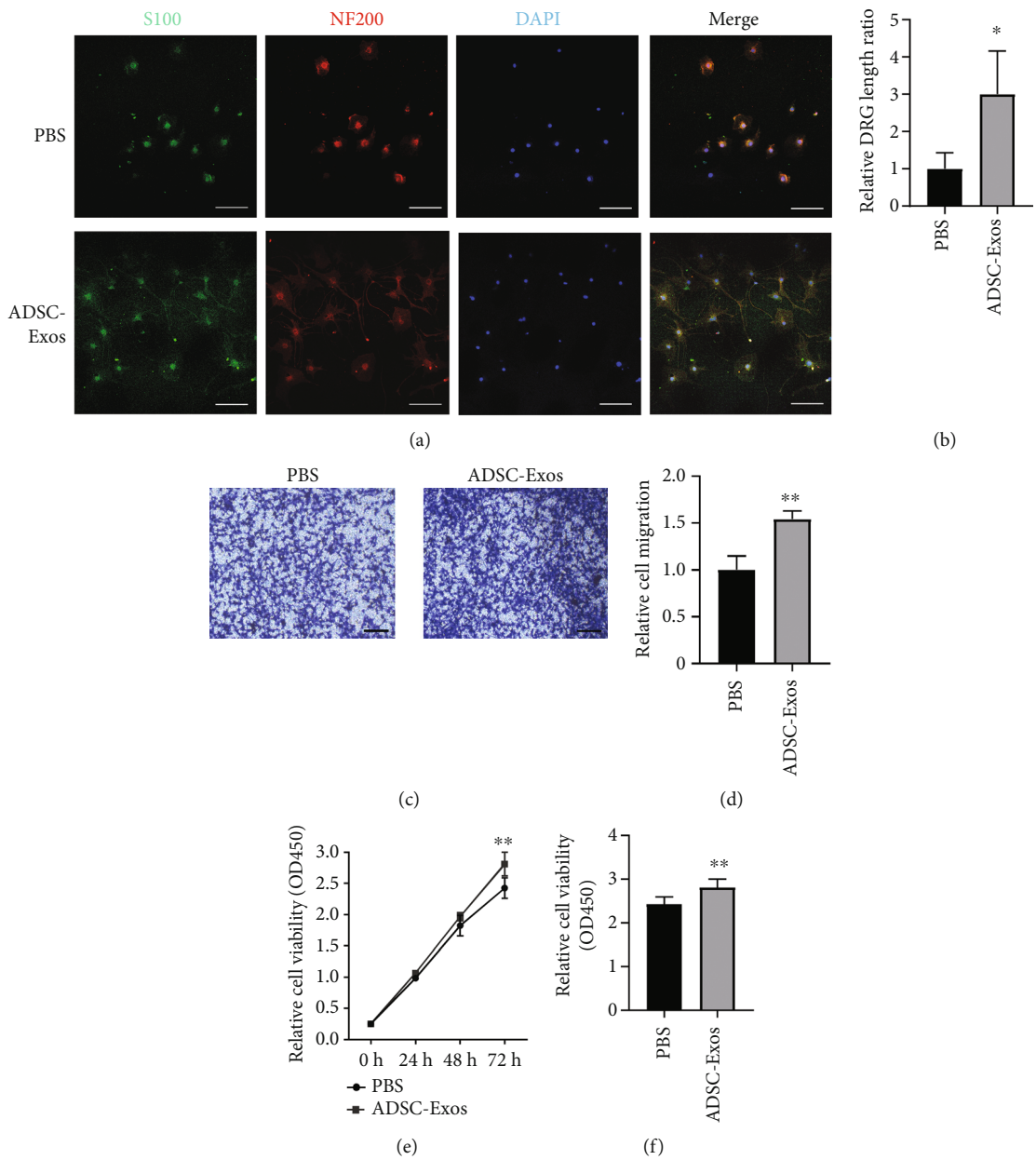


Figure 3: ADSC-Exos can enhance DRG neurite outgrowth and proliferation and migration of SCs. (a) DRG were stained with S100 antibody (green) and NF200 antibody (red). (b) Statistical analysis of length of DRG neurite. (c–d) SCs migration after cocultured with ADSC-Exos were measured by the Transwell assays. (e–f) SCs proliferation after cocultured with ADSC-Exos were measured by the CCK-8 assays. Scale bar : 100 $\mu$m. Data are expressed as means ± SD. Statistical significance was obtained with Student's $t$-test, * means $p < 0.05$; ** means $p < 0.01$. Control group added PBS; ADSC-Exos, the exosomes extracted from Adipose-derived mesenchymal stem cells.

upregulated by the inhibitor compared to the NC group. The activity of the AKT/mTOR pathway was evaluated based on exosomal miRNA sequencing results. The miR-22-3p mimic reduced the expression of PTEN and positively regulated the AKT/mTOR pathway, where the miR-22-3p inhibitor had a negative effect on this pathway (Figure 5(d)). Accordingly, we performed transwell and CCK-8 assays. Upregulation of miR-22-3p significantly increased cell migration, whereas the miR-22-3p inhibitor decreased cell motility in Schwann cells (Figure 6(a) and 6(b)). The CCK-8 assay revealed that the mimic also promoted the proliferation of Schwann cells, whereas the inhibitor had a negative effect (Figure 6(c)). Overall, these results indicate that exosomal miR-22-3p promotes proliferation and migration of Schwann cells by activating the AKT/mTOR signaling pathway.

## 4. Discussion

Although the vast majority of PNIs do not threaten the lives of patients, persistent damage brings not only long-term

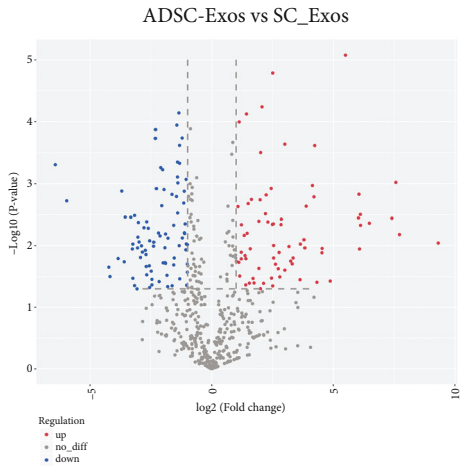


(a)

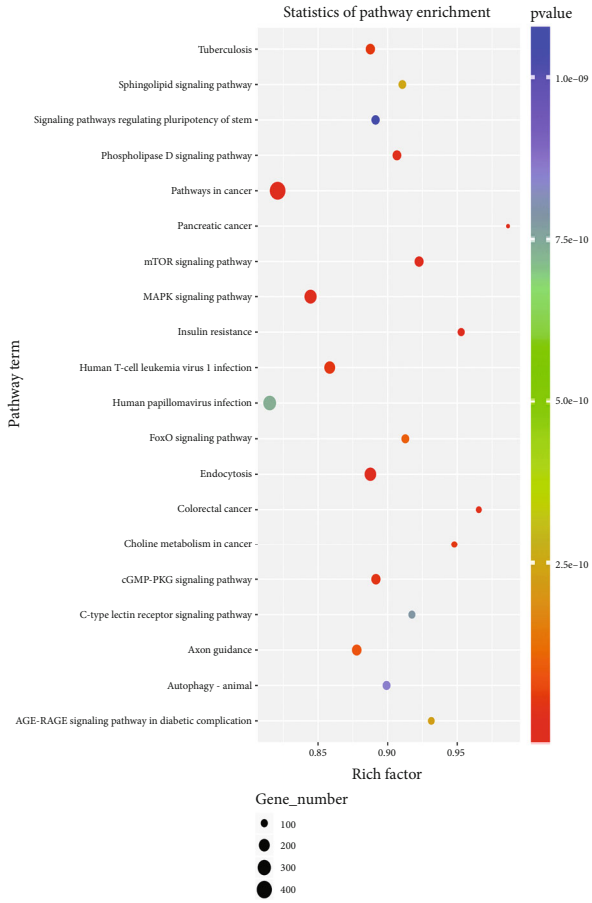


(b)

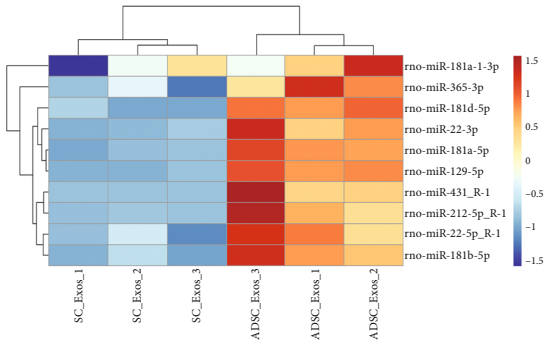


(c)

| | Predicted consequential pairing of target region (top) and miRNA (bottom) | Site | Context++ score | Context++ score percentile | Weighted context++ score | Conserved branch length | $P_{CT}$ |
|---|---|---|---|---|---|---|---|
| Position 677-684 of Pten 3' UTR<br>rno-miR-22-3p | 5' ...AUUGGUGCUAGAAAAGGCAGCUA...<br>\|\|\|\|\|\|\|<br>3' UGUCAAGAAGUUGACCGUCGA A | 8mer | −0.45 | 99 | −0.22 | 4.768 | 0.89 |

(d)

Figure 4: The miRNA expression profile between ADSC-Exos and SC-Exos. (a) The distribution of the differentially expressed miRNAs of ADSC-Exos and SC-Exos in a volcano plot. (b) The top 20 significant KEGG pathway terms sorted by rich factor. (c) Heatmap of 10 miRNAs with high expression in mTOR signaling pathway predicted by sequencing and TargetScan sofeware. (d) Binding sites of miR-22-3p and Pten predicted by TargetScan software. ADSC-Exos, the exosomes extracted from Adipose-derived mesenchymal stem cells; SC-Exos, the exosomes extracted from Schwann cells; miR, miRNA.

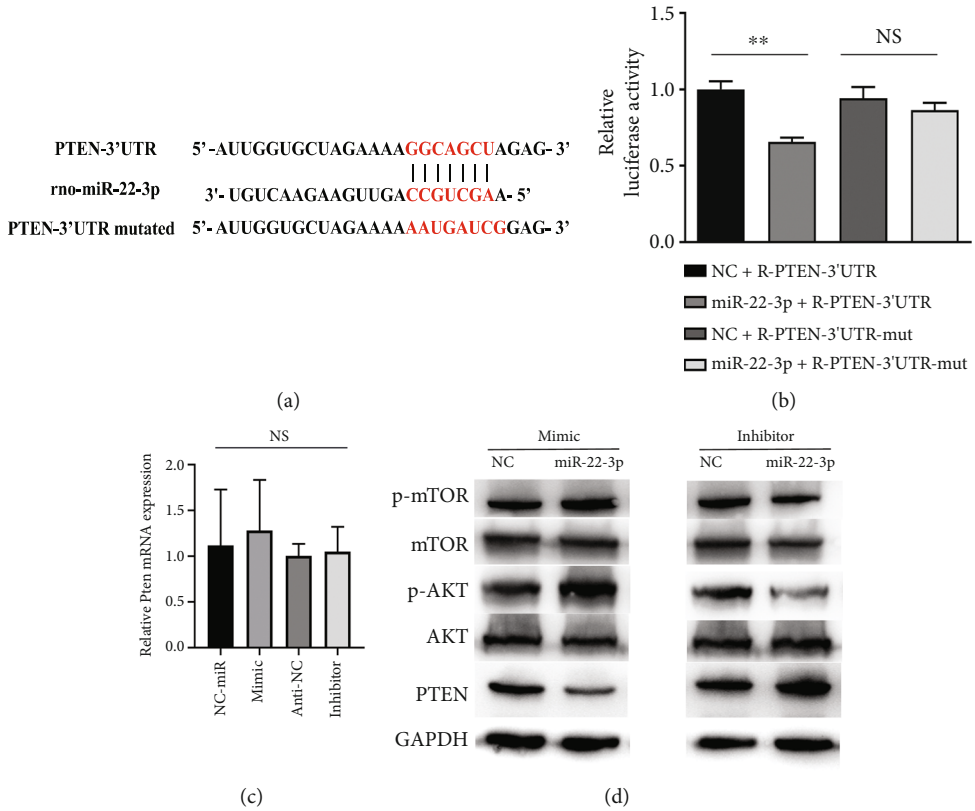


Figure 5: miR-22-3p targets PTEN and activates the AKT/mTOR signaling pathway. (a) The predicted binding sites of miR-22-3p within the 3′-UTR of Pten. (b) Dual-luciferase reporter assays showed miRNA-22-3p cotransfected with wild-type or mutation Pten 3′-UTR in SCs. (c) Pten mRNA expression in SCs after the treatment with miR-22-3p mimic, miR-22-3p inhibitor, and NC. (d) Effects of miR-22-3p mimic and miR-22-3p inhibitor on the protein expressions of AKT/mTOR pathway compare with control group. Data are expressed as means ± SD. Statistical significance was obtained with unpaired Student's $t$ test or one way ANOVA. ** means $p < 0.01$; NS means no significant. ADSC-Exos, the exosomes extracted from Adipose-derived mesenchymal stem cells; SCs, Schwann cells; miR, miRNA.

physical and mental harm to patients but also a heavy burden on families and society [19]. Following PNI, massive proliferation of SCs is triggered to form Bungner bands, which provide a large number of nutritional substrates for axon growth, including a considerable amount of extracellular matrix proteins and a variety of neurotrophic factors [20]. Additionally, SCs form a "myelin scaffold" to support axons extending distally at an average speed of 1 mm/day [21, 22]. These findings demonstrate that changes in the proliferative and migratory abilities of SCs during the repair of PNIs can influence the regeneration of nerve axons.

In the present study, we selected ADSCs as subjects because they have the advantage of minimal tissue damage after sampling, mass availability, repeatability, and high clinical value [23]. We successfully isolated primary ADSCs, identified the surface antigens using flow cytometry, and confirmed their adipogenic and osteogenic abilities through direction-induced differentiation. ADSCs promote the repair of PNIs; however, it has been reported that a paracrine mechanism is involved in MSC-mediated tissue repair, whereas direct differentiation of stem cells is weak [24, 25]. Considering the limitations of stem cell applications and the fact that the paracrine function of stem cells can be mediated by exosomes, the use of exosomes to replace stem cells for direct treatment has become a feasible alternative method.

By coculturing rat ADSC-Exos with SCs, we found that ADSC-Exos not only promoted SC proliferation but also enhanced their migratory ability, which was demonstrated for the first time. As mentioned above, SC proliferation results in the formation of new myelin channels that promote axonal regeneration. The results of our DRGs' experiment confirmed this hypothesis. Some researchers cocultured conditioned medium from mouse ADSCs with SCs and DRGs and found that the proliferation of SCs were enhanced as well as the growth of DRG axons [26]; the underlying reason may be that exosomes in the conditioned medium are responsible for the above effects. Another study reported that human ADSC-Exos significantly promoted SC proliferation, migration, and myelination [13], which are consistent with the results of this study.

However, the mechanism by which ADSC-Exos promote SC proliferation and migration remains unclear. Exosomes can carry a variety of bioactive substances and mediate intercellular signal transduction in MSC-derived exosomes mediate intercellular signal transduction [12, 27]. In the

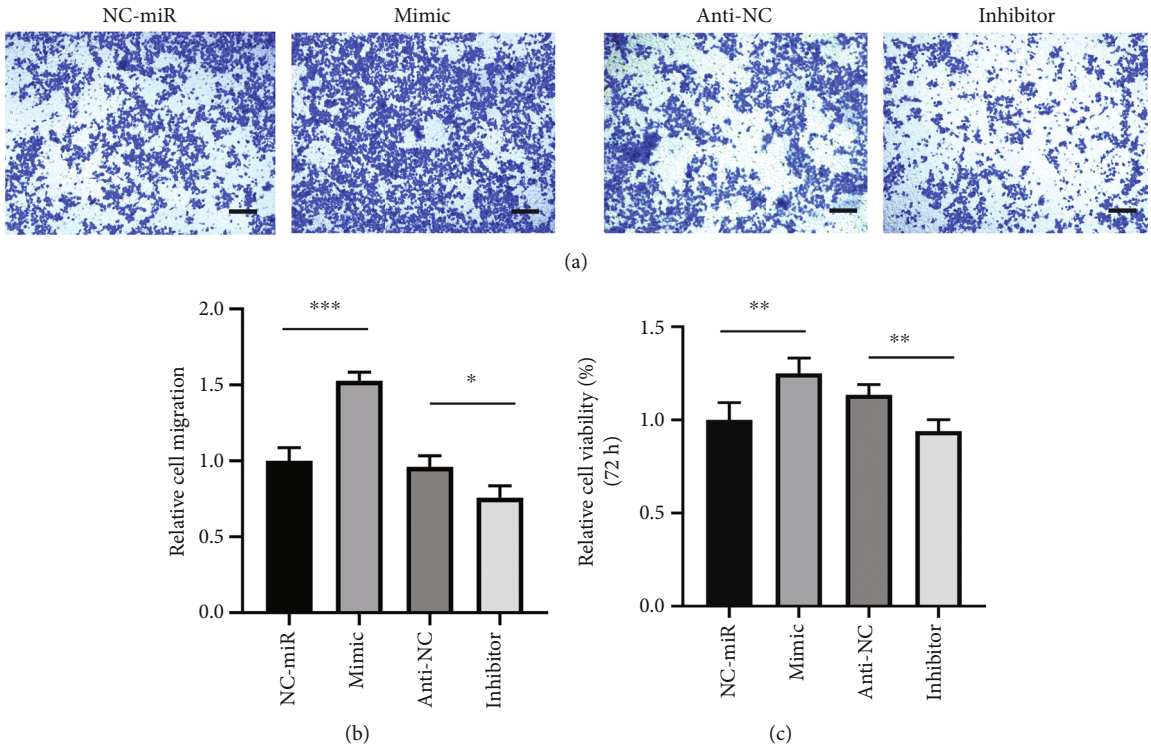


Figure 6: miR-22-3p promotes Schwann cells migration and proliferation in vitro. (a–b) The effect of miR-22-3p on the migration of Schwann cells was assessed by a Transwell assays, scale bars : 100 um. (c) Statistical analysis of CCK-8 assays at 72 h. Results from 3 independent experiments with duplicates. Data are expressed as means ± SD. Statistical significance was obtained with unpaired Student's $t$ test. * means $p < 0.05$; ** means $p < 0.01$; *** means $p < 0.001$. ADSC-Exos, the exosomes extracted from Adipose-derived mesenchymal stem cells; SCs, Schwann cells; miR, miRNA.

peripheral nervous system, exosomes can transport miRNAs to axons [28]. Therefore, exosomal miRNAs may be key elements in the effects of exosomes, and identifying the relevant miRNAs in exosomes is a prerequisite to clarify the role of exosomes in promoting peripheral nerve regeneration and postinjury repair. We speculated that miRNAs in rat ADSC-Exos may play an important role in promoting the proliferation and migration of SCs. To further explore the role of miRNAs, we performed exosomal miRNA sequencing and subsequent bioinformatic analysis.

Sequencing results revealed that 124 miRNAs were highly expressed in ADSCs. Based on KEGG pathway analysis, 143 miRNAs were enriched in the mTOR pathway. To identify the miRNAs associated with SC proliferation and migration, miR-181a-3p, miR-365-3p, miR-22-3p, miR-22-5p, miR-181a-5p, miR-181b-5p, miR-129-5p, miR-431, miR-212-5p, and miR-365-3p were selected for further bioinformatic analysis. TargetScan database search revealed that miR-22-3p is very likely to bind directly to phosphatase and tensin homolog deleted on chromosome 10 (PTEN). In addition, overexpression of miR-22-3p in HK-2 cells can directly inhibit PTEN [29]. Consequently, we focused on miR-22-3p and examined the target gene, Pten, of miR-22-3p in the Akt/mTOR pathway. PTEN is an inhibitor of the Akt/mTOR signaling pathway. Following PTEN downregulation, Akt is activated and phosphorylated to promote the activation of downstream mTOR. As an important signal transduction pathway, the PI3K/Akt/mTOR pathway plays an important biological role in cell growth, survival, proliferation, apoptosis, angiogenesis, and autophagy [30]. Conditional knockout of PTEN gene can promote regeneration of corticospinal tract (CST) axons and recovery of motor function in mice [31]. Another study also showed that PTEN knockout promotes CST regeneration, and the mechanism may involve increased mTOR activity, thus enhancing the regeneration ability of cortical neurons [32]. This indicates that repair of the central nervous system can be promoted by enhancing Akt/mTOR signaling activity. In our previous study, we found that negative regulation of PTEN activates the PI3K/Akt signaling pathway and promotes repair of the recurrent laryngeal nerve [33]. Moreover, the results of this study further confirmed that miR-22-3p directly binds to PTEN and promotes the phosphorylation of the downstream Akt/mTOR axis by inhibiting PTEN expression, thus promoting the proliferation and migration of SCs. Regarding future clinical translation for the treatment of PNIs, ADSCs may be extracted from the adipose tissue of patients and exosomes overexpressing miR-22-3p may be obtained after rapid amplification. Alternatively, exosomes may be obtained by overexpression of miR-22-3p and transplanted into the site of PNIs combined with nerve conduits.

## 5. Conclusion

In this study, we confirmed that ADSC-Exos promoted the proliferation and migration of SCs and the growth of DRG axons. Through exosomal sequencing and bioinformatic analysis, miR-22-3p was identified and its role in activating the Akt/mTOR axis by inhibiting PTEN was confirmed. These results provide a new strategy for the treatment of PNIs with stem cell-derived exosomes as a novel treatment method for PNIs.

## Data Availability

All data used to support the findings of this study are available from the corresponding author upon request.

## Ethical Approval

Animal experiments were approved by the Experimental Animal Care and Ethics Committee of the Institute of Shanghai General Hospital, Shanghai Jiao Tong University, School of Medicine.

## Conflicts of Interest

The authors declare that there is no conflict of interests.

## Authors' Contributions

J.Y. performed the experiments, analyzed the data, and wrote the first draft of the manuscript. J. Y, B.W., and P.D. designed the study and edited the final manuscript draft. Y.W., C.F., L.C., Y.L., and X.C. helped in performing the experiments and interpreting the data, and all authors approved the final version to be published. Jianqiang Yang and Baoxin Wang contributed equally to this work.

## Acknowledgments

This study was supported by grants from the National Natural Science Foundation of China (Nos. 81800893 and 81603678) and the Emerging Advanced Technology Joint Research Project of SHDC (No. SHDC 12020120). We thank the other partners of our laboratory for their kindness. Particularly, we thank Libo Sun and Xiaojie Cai for guidance on the isolation and culture of the primary DRG.

## Supplementary Materials

Supplementary S1 Primers used in Dual-Luciferase Reporter Assays. Supplementary S2: Reaction conditions and primers used in reverse transcription and RT-qPCR. Supplementary S3: The miRNA different expression between ADSC-Exos and SC-Exos, heat map showing the dominant cluster pattern of miRNAs under $p < 0.05$. Red signals and blue signals represent upregulated and downregulated expression, respectively. *(Supplementary Materials)*

## References

[1] M. J. Sabatier and A. W. English, "Pathways mediating activity-induced enhancement of recovery from peripheral nerve," *Exercise and Sport Sciences Reviews*, vol. 43, no. 3, pp. 163–171, 2015.

[2] M. Modrak, M. A. H. Talukder, K. Gurgenashvili, M. Noble, and J. C. Elfar, "Peripheral nerve injury and myelination: potential therapeutic strategies," *Journal of Neuroscience Research*, vol. 98, no. 5, pp. 780–795, 2020.

[3] C. A. Taylor, D. Braza, J. B. Rice, and T. Dillingham, "The incidence of peripheral nerve injury in extremity trauma," *American Journal of Physical Medicine & Rehabilitation*, vol. 87, no. 5, pp. 381–385, 2008.

[4] L. Jiang, Y. Zheng, O. Chen, T. Chu, J. Ding, and Q. Yu, "Nerve defect repair by differentiated adipose-derived stem cells and chondroitinase ABC-treated acellular nerves," *The International Journal of Neuroscience*, vol. 126, no. 6, pp. 568–576, 2016.

[5] A. J. Reid, M. Sun, M. Wiberg, S. Downes, G. Terenghi, and P. J. Kingham, "Nerve repair with adipose-derived stem cells protects dorsal root ganglia neurons from apoptosis," *Neuroscience*, vol. 199, pp. 515–522, 2011.

[6] X. M. Fu, Y. Wang, W. L. Fu et al., "The combination of adipose-derived Schwann-like cells and acellular nerve allografts promotes sciatic nerve regeneration and repair through the JAK2/STAT3 signaling pathway in rats," *Neuroscience*, vol. 422, pp. 134–145, 2019.

[7] L. Zheng and H. F. Cui, "Use of chitosan conduit combined with bone marrow mesenchymal stem cells for promoting peripheral nerve regeneration," *Journal of Materials Science. Materials in Medicine*, vol. 21, no. 5, pp. 1713–1720, 2010.

[8] A. F. Hill, "Extracellular vesicles and neurodegenerative diseases," *The Journal of Neuroscience*, vol. 39, no. 47, pp. 9269–9273, 2019.

[9] P. Hong, H. Yang, Y. Wu, K. Li, and Z. Tang, "The functions and clinical application potential of exosomes derived from adipose mesenchymal stem cells: a comprehensive review," *Stem Cell Research & Therapy*, vol. 10, no. 1, p. 242, 2019.

[10] B. Zhang, L. Shen, H. Shi et al., "Exosomes from human umbilical cord mesenchymal stem cells: identification, purification, and biological characteristics," *Stem Cells International*, vol. 2016, Article ID 1929536, 11 pages, 2016.

[11] A. Eirin, C. M. Ferguson, X. Y. Zhu et al., "Extracellular vesicles released by adipose tissue-derived mesenchymal stromal/stem cells from obese pigs fail to repair the injured kidney," *Stem Cell Research*, vol. 47, article 101877, 2020.

[12] B. Zhang, X. Wu, X. Zhang et al., "Human umbilical cord mesenchymal stem cell exosomes enhance angiogenesis through the Wnt4/$\beta$-catenin pathway," *Stem Cells Translational Medicine*, vol. 4, no. 5, pp. 513–522, 2015.

[13] J. Chen, S. Ren, D. Duscher et al., "Exosomes from human adipose-derived stem cells promote sciatic nerve regeneration via optimizing Schwann cell function," *Journal of Cellular Physiology*, vol. 234, no. 12, pp. 23097–23110, 2019.

[14] E. González-Cubero, M. L. González-Fernández, L. Gutiérrez-Velasco, E. Navarro-Ramírez, and V. Villar-Suárez, "Isolation and characterization of exosomes from adipose tissue-derived," *Journal of Anatomy*, vol. 238, no. 5, pp. 1203–1217, 2021.

[15] W. L. You and Z. L. Xu, "Curculigoside promotes osteogenic differentiation of ADSCs to prevent," *Journal of Orthopaedic Surgery and Research*, vol. 16, no. 1, 2021.

[16] P. Priyadarshini, S. Samuel, B. G. Kurkalli et al., "In vitro comparison of adipogenic differentiation in human adipose-derived stem," *Indian Journal of Plastic Surgery*, vol. 54, no. 3, pp. 278–283, 2021.

[17] X. Wu, S. A. A. Showiheen, A. R. Sun et al., "Exosomes extraction and identification," *Methods in Molecular Biology*, vol. 2054, pp. 81–91, 2019.

[18] M. Shekarabi, J. A. Robinson, and T. H. Burdo, "Isolation and culture of dorsal root ganglia (DRG) from rodents," *Methods in Molecular Biology*, vol. 2311, pp. 177–184, 2021.

[19] B. Rosén, P. Vikström, S. Turner et al., "Enhanced early sensory outcome after nerve repair as a result of immediate post-operative re-learning: a randomized controlled trial," *Journal of Hand Surgery*, vol. 40, no. 6, pp. 598–606, 2015.

[20] K. R. Jessen, R. Mirsky, and A. C. Lloyd, "Schwann cells: development and role in nerve repair," *Cold Spring Harbor Perspectives in Biology*, vol. 7, no. 7, article a020487, 2015.

[21] B. García-Medrano, N. Mesuro Domínguez, C. Simón Pérez et al., "Reparacion de lesiones en nervios mediante el implante de protesis obtenidas de segmentos acelulares de nervio isogenico," *Journal of Orthopaedics Surgery and Traumatology*, vol. 61, no. 5, pp. 359–366, 2017.

[22] J. P. Sand, A. M. Park, N. Bhatt et al., "Comparison of conventional, revascularized, and bioengineered methods of recurrent laryngeal nerve reconstruction," *JAMA Otolaryngology–Head & Neck Surgery*, vol. 142, no. 6, pp. 526–532, 2016.

[23] Y. An, S. Lin, X. Tan et al., "Exosomes from adipose-derived stem cells and application to skin wound healing," *Cell Proliferation*, vol. 54, no. 3, article e12993, 2021.

[24] S. Razavi, M. Jahromi, E. Vatankhah, and R. Seyedebrahimi, "Differential effects of rat ADSCs encapsulation in fibrin matrix and combination delivery of BDNF and gold nanoparticles on peripheral nerve regeneration," *BMC Neuroscience*, vol. 22, no. 1, p. 50, 2021.

[25] T. Nakajima, K. Tada, M. Nakada, M. Matsuta, and H. Tsuchiya, "Facilitatory effects of artificial nerve filled with adipose-derived stem cell sheets on peripheral nerve regeneration: an experimental study," *Journal of Orthopaedic Science*, vol. 26, no. 6, pp. 1113–1118, 2021.

[26] Y. Sowa, T. Imura, T. Numajiri, K. Nishino, and S. Fushiki, "Adipose-derived stem cells produce factors enhancing peripheral nerve regeneration: influence of age and anatomic site of origin," *Stem Cells and Development*, vol. 21, no. 11, pp. 1852–1862, 2012.

[27] S. Zhou, F. Ding, and X. Gu, "Non-coding RNAs as emerging regulators of neural injury responses and regeneration," *Neuroscience Bulletin*, vol. 32, no. 3, pp. 253–264, 2016.

[28] H. R. Hofer and R. S. Tuan, "Secreted trophic factors of mesenchymal stem cells support neurovascular and musculoskeletal therapies," *Stem Cell Research & Therapy*, vol. 7, no. 1, 2016.

[29] X. Wang, Y. Wang, M. Kong, and J. Yang, "MiR-22-3p suppresses sepsis-induced acute kidney injury by targeting PTEN," *Bioscience Reports*, vol. 40, no. 6, 2020.

[30] H. L. Yang, Y. C. Tsai, M. Korivi, C. T. Chang, and Y. C. Hseu, "Lucidone promotes the cutaneous wound healing process *via* activation of the $PI_3K$/AKT, Wnt/ $\beta$-catenin and NF-$\kappa$B signaling pathways," *Biochim Biophys Acta Mol Cell Res*, vol. 1864, no. 1, pp. 151–168, 2017.

[31] C. A. Danilov and O. Steward, "Conditional genetic deletion of PTEN after a spinal cord injury enhances regenerative growth of CST axons and motor function recovery in mice," *Experimental Neurology*, vol. 266, pp. 147–160, 2015.

[32] K. Liu, Y. Lu, J. K. Lee et al., "PTEN deletion enhances the regenerative ability of adult corticospinal neurons," *Nature Neuroscience*, vol. 13, no. 9, pp. 1075–1081, 2010.

[33] J. Xie, B. Jin, D. W. Li et al., "Effect of laminin-binding BDNF on induction of recurrent laryngeal nerve regeneration by miR-222 activation of mTOR signal pathway," *American Journal of Translational Research*, vol. 7, no. 6, pp. 1071–1080, 2015.

Hindawi
Disease Markers
Volume 2022, Article ID 1479246, 12 pages
https://doi.org/10.1155/2022/1479246

*Research Article*

# Construction of a Humanized PBMC-PDX Model to Study the Efficacy of a Bacterial Marker in Lung Cancer Immunotherapy

**Chengwei Wu, Xinning Wang, Haitao Shang, and Hong Wei**

*Precision Medicine Institute, The First Affiliated Hospital, Sun Yat-sen University, Guangzhou 510080, China*

Correspondence should be addressed to Hong Wei; weihong63528@163.com

Received 6 April 2022; Accepted 22 June 2022; Published 28 August 2022

Academic Editor: Pei-Wen Zhu



Commensal microbiome is a key factor of lung cancer immunotherapy efficacy. Elucidating the role of specific strains as bacterial markers in immunotherapy has drawn great attention from the academia. At present, most preclinical studies about the relationship between bacterial markers and immunotherapy rely on the syngeneic mouse models. However, mice differ greatly from humans in immune system and tumor characteristics. In this study, humanized mouse models based on peripheral blood mononuclear cells (PBMCs) immune reconstitution and lung cancer cell line-derived xenograft (CDX) or patient-derived xenograft (PDX) were constructed. The PBMC-PDX model was shown to be superior to the PBMC-CDX model in preserving tumor heterogeneity and construction time-saving. Through optimizing the experimental process, the time it took for humanized models to evaluate the effect of cancer treatment was reduced to 42 days. Next, by utilizing PBMC-PDX mice treated with antibiotics (ATB), the role of *Bifidobacterium longum* in lung cancer immunotherapy was studied. It was found that although both *Bifidobacterium longum* and immunotherapy drug pembrolizumab alone showed suppressing tumor growth, the efficacy of pembrolizumab was attenuated when administrated to mice colonized with *Bifidobacterium longum*. Further exploration revealed that *Bifidobacterium longum* caused significant changes in the proportion of human $CD45^+$ cells in the PBMC-PDX model. The PBMC-PDX model has the potential to be applied as an efficient platform to support evaluation of bacterial markers in immunotherapy research and facilitate development of precision medicine targeting human commensal bacteria.

## 1. Introduction

Worldwide, lung cancer remains the highest cause of cancer-related mortality [1]. And, 80% of lung cancer deaths are from non-small cell lung cancer (NSCLC) [2]. Immunotherapy has been shown to have good survival benefits with advanced NSCLC [3]. Pembrolizumab showed superior efficacy, when patients express PD-L1 in at least 50% of tumor cells, and was better tolerated as first-line therapy compared to platinum doublet chemotherapy [4]. Although breaking the PD-1/PD-L1 axis has significant therapeutic effect and contributes to prolongation of patient survival, the response rate of NSCLC patients is only about 20% [5]. It may be related to intestinal microbiota.

The growing evidence support that the microbiome has a regulatory role in cancer immunotherapy responses [6–8]. The latest research shows that intestinal symbiotic bacteria influence the efficacy of anti-PD-1 antibodies in melanoma and lung cancer and *Bifidobacterium longum* is enriched in responders [9, 10]. A large number of mouse experiments have been carried out to study the regulatory effect of intestinal microbiota on cancer immunotherapy [11]. However, most of the current studies on bacterial markers rely on mouse immune system and mouse tumor [12–14], which cannot simulate the real situation of bacterial flora and cancer immunotherapy in human body. Therefore, it is urgent to develop suitable humanized models.

Cell line-derived xenograft (CDX) mice are often used to test the antitumor drug [15, 16]. However, CDX model constructed solely from tumor cell lines cannot simulate the complex human tumor environment [17]. Patient-derived xenograft (PDX) mice have been identified as better preclinical models [18]. The PDX model retains most of the tumor tissue components, which can be better used to predict the

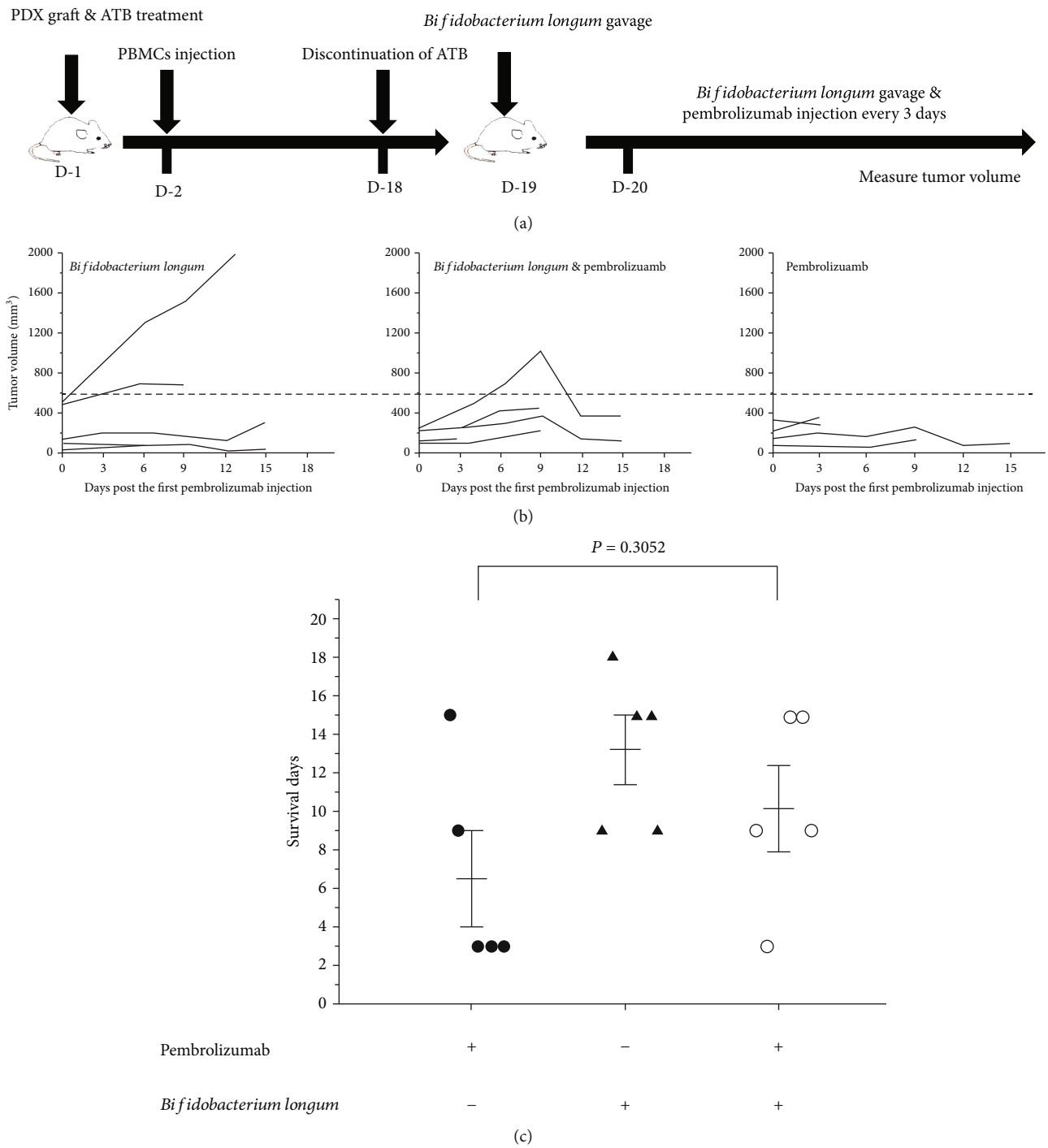


Figure 1: Establishing PBMC-PDX mice and evaluating the effect of *Bifidobacterium longum* and pembrolizumab on the models. (a) The experimental scheme about evaluating the therapeutic effect of *Bifidobacterium longum* and pembrolizumab in PBMCs immune reconstituted PDX mouse models. (b) Tumor growth curve treated with *Bifidobacterium longum* and pembrolizumab; $n = 5$. (c) Death of mice. $^{*}P < 0.05$, $^{**}P < 0.01$, and $^{***}P < 0.001$. Means ± SEM are used in graphs. (c) Two-sample $t$-test. Survival days, $P$ value was not significant.

sensitivity and resistance of drug [19, 20]. In addition, these two types are often used in humanized immune system of mice [21–24]. Compared with the humanized mice using $CD34^{+}$ hematopoietic stem cells (HSCs), the humanized model constructed by peripheral blood mononuclear cells (PBMCs) takes less time, but graft versus-host disease

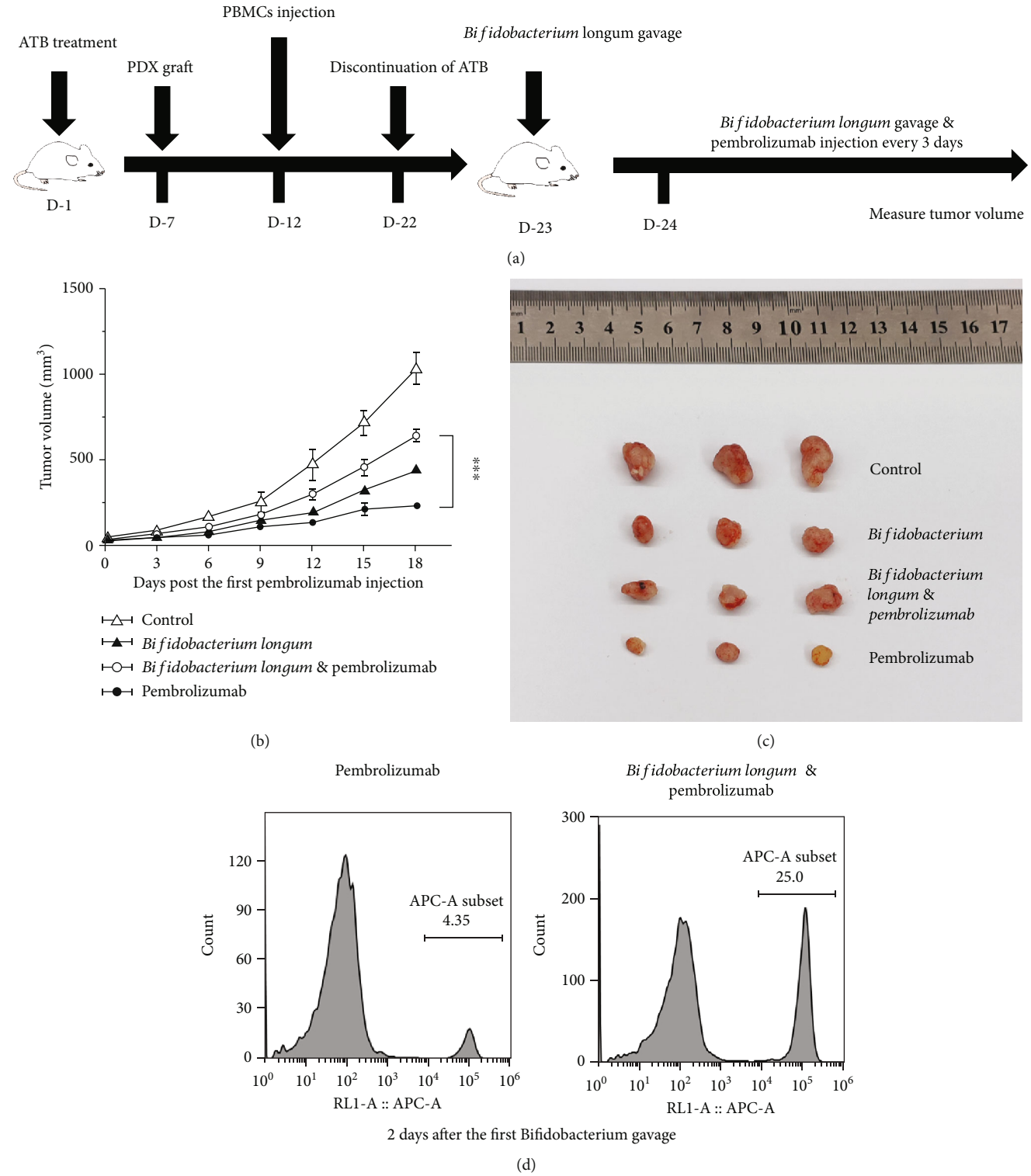


Figure 2: Continued.

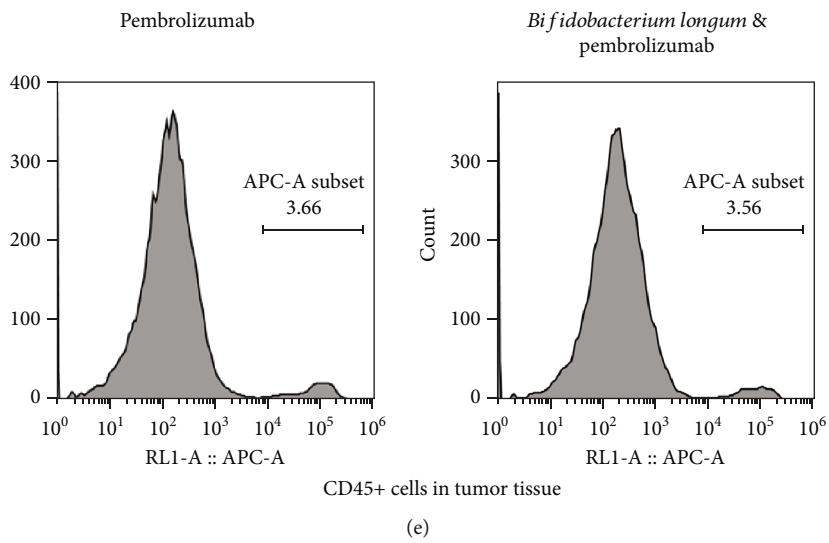


Figure 2: Optimizing the experimental scheme. (a) Optimized experimental scheme. (b) Tumor growth curve treated with *Bifidobacterium longum* and pembrolizumab; *n* for the control, *Bifidobacterium longum*, *Bifidobacterium longum*, pembrolizumab, and pembrolizumab are 5, 3, 5, and 4, respectively. The control group was treated with PBS. (c) Representative tumor pictures. (d) Human $CD45^+$ cell in peripheral blood of PBMC immune reconstituted PDX mouse model at the appointed time. (e) Human $CD45^+$ cell in tumor tissues. $^*P < 0.05$, $^{**}P < 0.01$, and $^{***}P < 0.001$. Means ± SEM are used in graphs. (b) Two-sample *t*-test. The *P* values of curve were significance.

(GvHD) occurs [25, 26]. At present, studies on bacterial markers and immunotherapy mostly adopt sterile mouse models and antibiotics (ATB) treated mice [27–29]. However, weighing the acquisition cost [30], mouse models treated with ATB are relatively more economical.

Here, we established a PBMC-PDX model that exhibited advantages over its CDX counterpart. With respect to the utilization of this model in immunotherapy research, the experimental process was optimized. The efficacy of *Bifidobacterium longum* in lung cancer immunotherapy was studied in virtue of this PBMC-PDX model, which could be further applied to elucidate the molecular mechanisms in bacterial marker-mediated immune responses.

## 2. Materials and Methods

*2.1. Mice.* In the Laboratory Animal Center of Sun Yat-sen University, all animal experiments were conducted. All executed procedures were in compliance with the Animal Welfare Committee of the Laboratory Animal Center. NOD-scid-IL2Rg−/− (NPI) mice were provided by BEIJING IDMO CO., LTD. The specific pathogen-free (SPF) cages were used to raise mice. The institutional animal care and use committee (IACUC) approves animal protocol.

*2.2. Cell Line.* A549 (non-small cell lung carcinoma cell line of human) was purchased from Procell Life Science & Technology Co., Ltd., and the RPMI-1640 Complete Medium (10%FBS; Gibco) was used for culture. When the cells reached 80% confluence, they were passed on.

*2.3. PBMCs Immune Reconstitution.* PBMCs were purchased from AllCells and processed according to the company's operating manual. Mice intravenously transplanted with $1 \times 10^7$ human PBMCs.

Pembrolizumab was purchased from Target Molecule Corp. and injected intraperitoneally into mice (250 $\mu$g/mouse) every three days.

*2.4. CDX Model.* Back injection of A549 cells ($1 \times 10^6$) to NPI mice at 6 to 8 weeks of age was conducted. Mice were injected with pembrolizumab 30 days after injection of A549 cells. Growth of tumor was monitored every three days. The formula $(\text{length} \times \text{width}^2)/2$ is used to calculate tumor volume.

*2.5. PDX Model.* The lung tumor tissues of human was provided by BEIJING IDMO CO., LTD. Tissues use were approved by the committee for the ethical review of research involving human subjects at the First Affiliated Hospital of Sun Yat-sen University. The tissue was dissected into pieces two millimeters in diameter and placed in phosphate-buffered saline (PBS) containing antibiotics. Then, these pieces were subcutaneously transplanted into 6-8-week-old NPI mice. Tumor growth was monitored when the tumor volume reached 1200 $mm^3$, and they are passed on afterwards.

*2.6. PBMC-CDX Model.* The CDX model was constructed, and then, 30 days later, mice were given PBMCs to construct the PBMC-CDX model. Mice were treated with pembrolizumab on the same day after being given PBMCs.

*2.7. PBMC-PDX Model.* The PDX model was constructed, and then PBMCs were given to construct the PBMC-PDX model at different time points according to different experimental plans, as shown in Figures 1(a) and 2(a).

*2.8. HE Staining.* Tissue blocks were collected, fixed, paraffin embedded, and sectionalized at 4 $\mu$m. The slices were dewaxed with xylene and washed with ethanol. Dye with

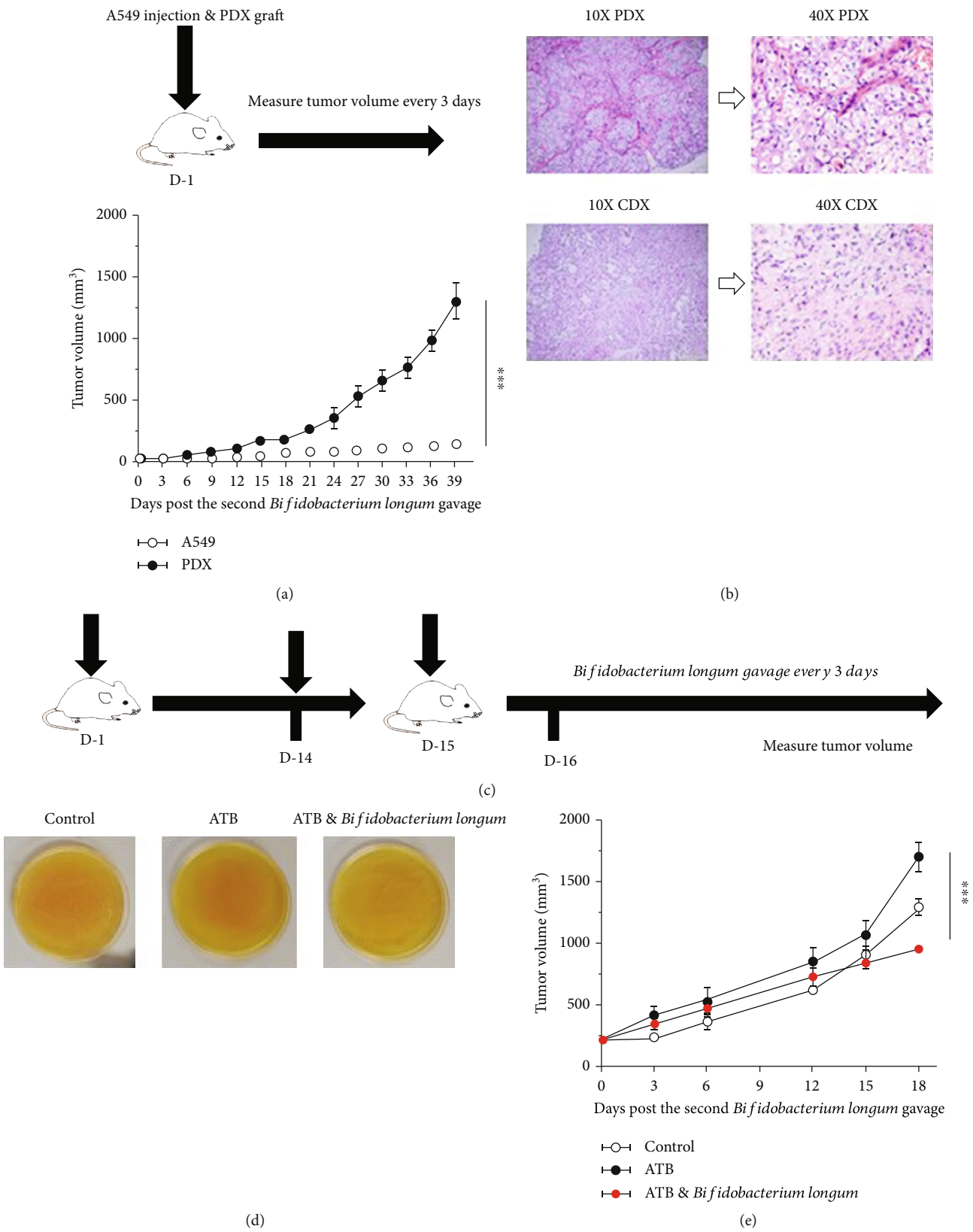


Figure 3: Continued.

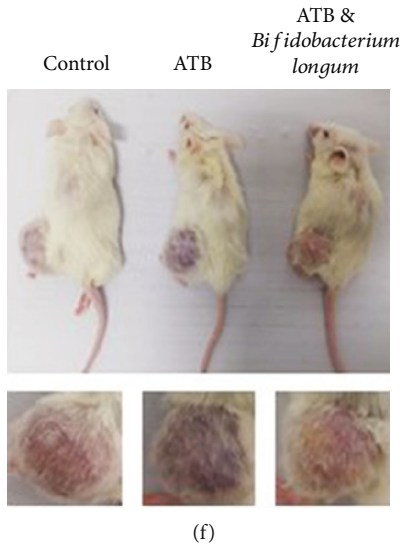


Figure 3: Establishing PDX mice and evaluating the effect of *Bifidobacterium longum* on PDX mouse models. (a) Comparison between the PDX model and CDX model. Tumor curves showed that PDX mouse model tumor growth was significantly faster than CDX mouse model; $n = 5$. (b) Histological morphology of PDX mouse model and CDX mouse model. HE staining was used. Scale bar: 2 mm. (c) Experimental design to evaluate the therapeutic effect of *Bifidobacterium longum* on PDX mouse model. (d) Anaerobic culture of mouse feces on BBL plate medium. The control group was not treated with antibiotics (ATB). (e) Effect of *Bifidobacterium longum* on PDX model. Tumor curves showed that *Bifidobacterium* longum reduced tumor growth; $n = 5$. (f) Representative mouse and tumor pictures. $^{*}P < 0.05$, $^{**}P < 0.01$, and $^{***}P < 0.001$. Means ± SEM are used in graphs. (a) Two-sample $t$-test. (e) One-way ANOVA. The $P$ values of curves (a, e) are significance.

hematoxylin for 5 minutes and rinse with running water. Differentiation with hydrochloric acid ethanol solution was done for 30 s. Soak in tap water for 15 min and eosin solution for 2 min, followed by conventional dehydration, transparent, sheet sealing. Images were acquired using the Leica optical microscope (Leica Biosystems Imaging, USA).

*2.9. Antibiotics (ATB) Treatment.* Ampicillin (1 mg/ml), colistin (1 mg/ml), streptomycin (5 mg/ml), and vancomycin (0.25 mg/ml) were configured to form ATB cocktail. ATB cocktail was added to the drinking water of mice. The ATB treatment group maintained antibiotic treatment until the end of the experiment (Figure 3(d)).

*2.10. Bacterial Administration. Bifidobacterium longum* was purchased from BeNa Culture Collection (BNCC) ORG. CN. with its number BNCC185354. BBL medium was used to continue bacterial culture in an anaerobic environment according to the operating manual provided by the company. *Bifidobacterium longum* was resuspended in PBS at $1 \times 10^9$ CFU/ml, and each mouse was given 100 $\mu$l by oral gavage.

*2.11. Fecal Culture.* 48 hours after discontinuation of antibiotic treatment, 2-3 feces of mice were collected and suspended in 1 ml PBS (Figure 3(d)). The supernatant was cultured in BBL medium in an anaerobic environment.

*2.12. Flow Cytometry.* Tumor tissues were dissected into pieces and placed in PBS including 0.2 mg/ml hyaluronidase V, 0.5 mg/ml collagenase A, and 0.02 mg/ml DNase I. The pieces were digested for 30 min at 37°C. A 70 $\mu$m cell strainer (Falcon) was used to filter the suspension. A discontinuous 40% followed by an 80% Percoll® Density Gradient Media (Solarbio) was used for isolation and purification. After collecting peripheral blood, the Red Blood Cell Lysis Buffer (Solarbio) was used to lyse the cells according to the instruction. Leukocyte was collected at 400 r.c.f. for 5 min.

All antibodies were provided by Biolegend. An Invitrogen™ Attune™ NxT device (Thermo Fisher Scientific, USA) was used to perform flow cytometric analysis. Data analysis uses the FlowJo software (v.10.8.1, FlowJo, USA). APC anti-human CD45 (HI30) and FITC anti-human CD3 (HIT3a) were used in these analyses.

*2.13. Statistical Analysis.* Statistical analysis is detailed in the figure legends. Two-sample $t$-test or one-way ANOVA was used to analyze the differences using the Origin9.0 software. Statistically significant $P$ value is <0.05.

## 3. Results

*3.1. Establishing PBMCs Humanized Mice and Evaluating the Effect of Immunotherapy on the Model.* To detect the immune reconstitution characteristics of PBMCs humanized mice, we only injected mice with PBMCs and monitored the growth of its human $CD45^+$ and $CD3^+$ cells. Flow cytometry results showed that there were two groups of $CD45^+$- and $CD3^+$-positive cells or $CD45^-$- and $CD3^-$-negative cells. Meanwhile, the proportion of double positive cells in peripheral blood gradually increased over time (Figure 4(a)). At the same time, we assessed the impact of immunotherapy on the model. Pembrolizumab was administered after injection of

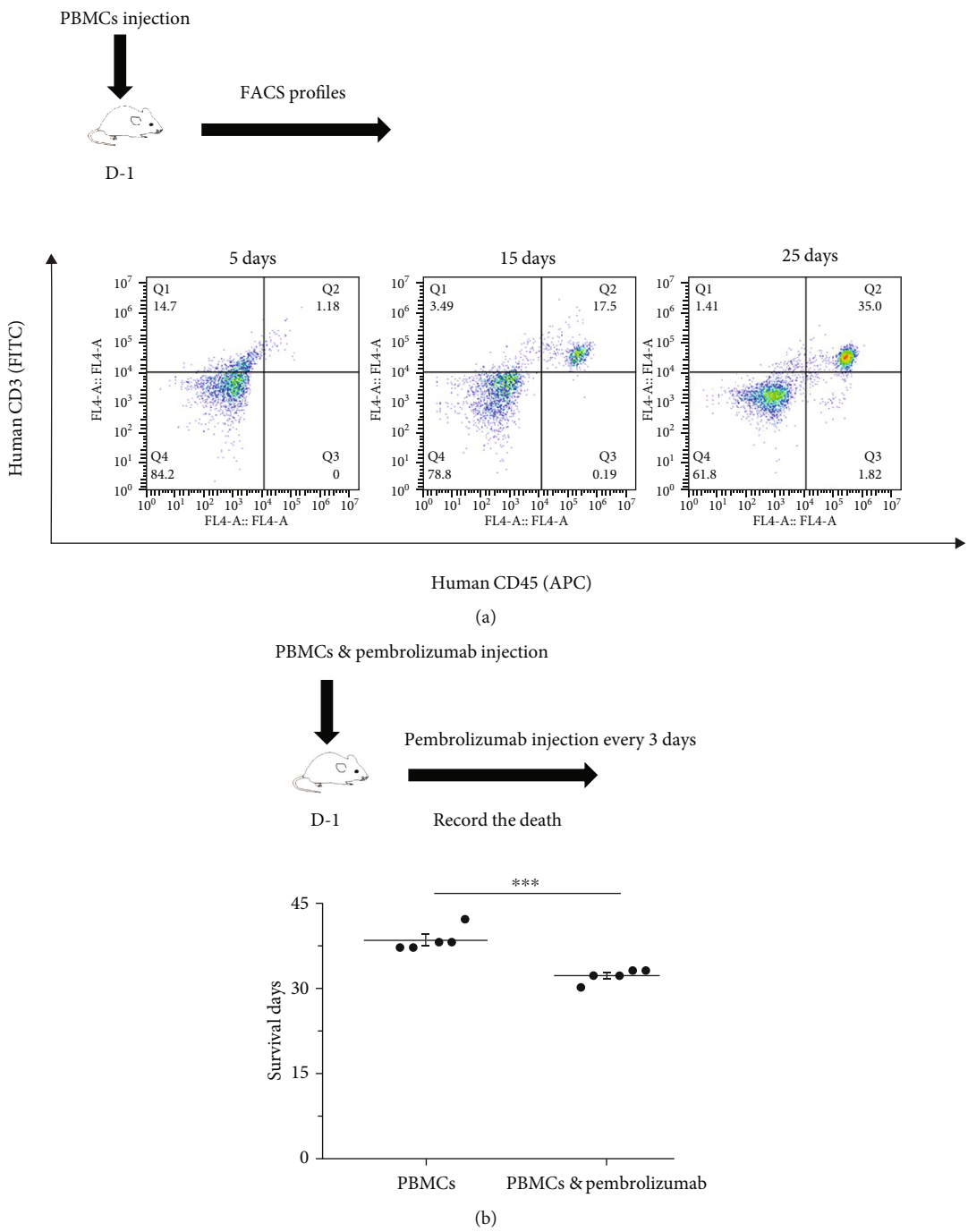


Figure 4: Establishing PBMCs humanized mice and evaluating the effect of immunotherapy on the model. (a) PBMCs humanized mice. FACS profiles of human $CD45^+$ and $CD3^+$ in NPI mice at the appointed time. (b) Effect of immunotherapy. The survival time decreased after pembrolizumab treatment; $n = 5$. $^*P < 0.05$, $^{**}P < 0.01$, and $^{***}P < 0.001$. Means ± SEM are used in graphs. Two-sample $t$-test. Statistics on survival days (b). $P$ values are significance.

PBMCs. The results showed that pembrolizumab accelerated death in mice (Figure 4(b)). These results indicated that PBMC humanized mice were successfully constructed.

*3.2. Establishing PBMC-CDX Mice and Evaluating the Effect of Immunotherapy on the Model.* Next, we constructed a CDX mouse model of A549 to evaluate the effect of immunotherapy. The results showed that pembrolizumab increased tumor growth at day 27 after 10 treatments (Figure 5(a)). Subsequently, a PBMC-CDX model was constructed to validate the antitumor efficacy of pembrolizumab (Figure 5(b)). In the presence of PBMCs, pembrolizumab slowed tumor growth after 8 treatments (Figure 5(c)). In consideration of the occurrence of GvHD in the PBMCs model (data not shown), we reduced the dose of pembrolizumab and PBMCs to extend the therapeutic time window.

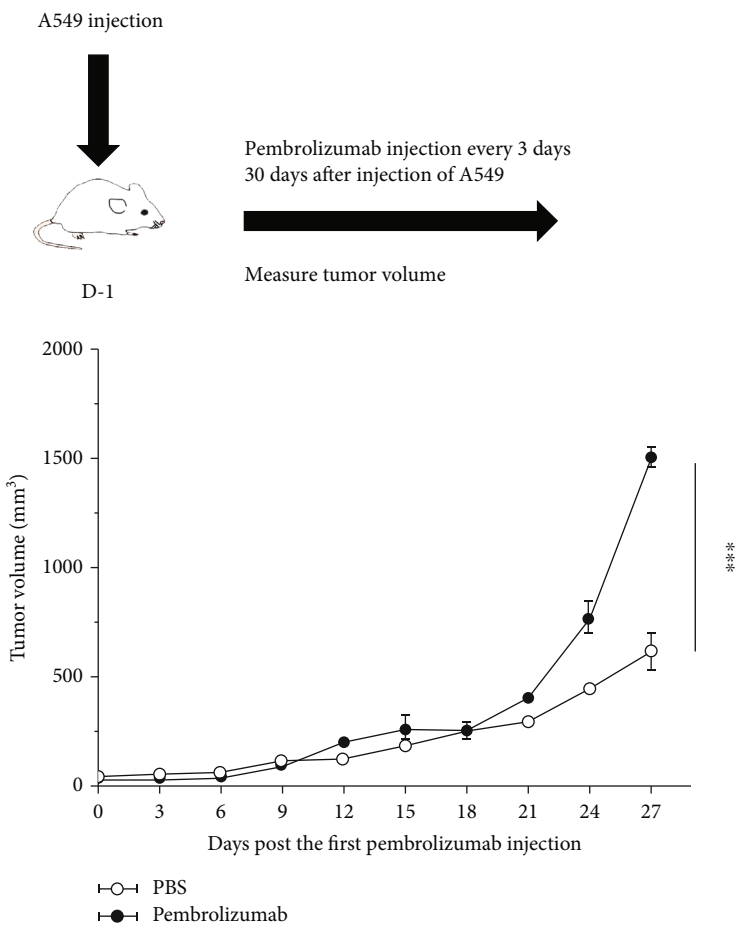


(a)

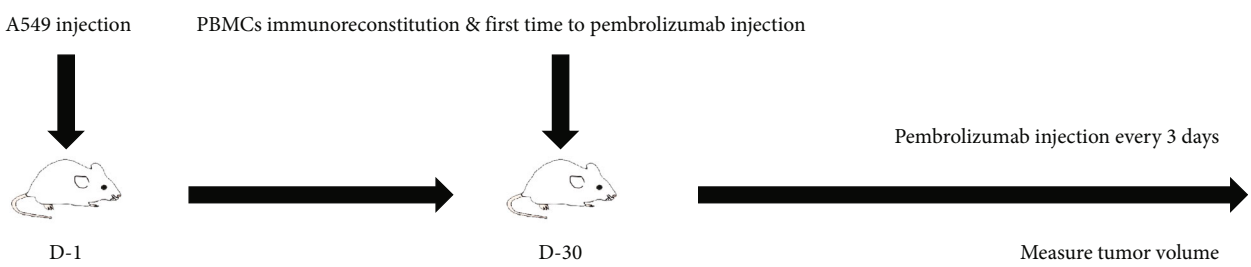


(b)

Figure 5: Continued.

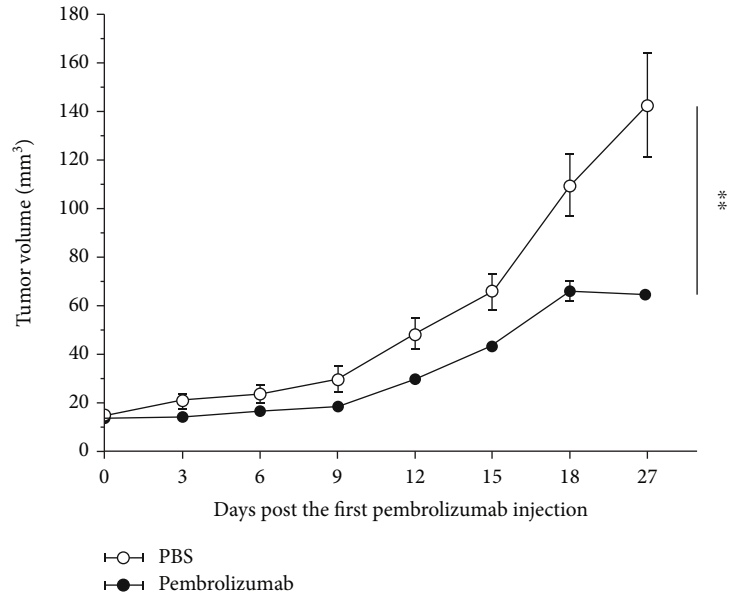


(c)

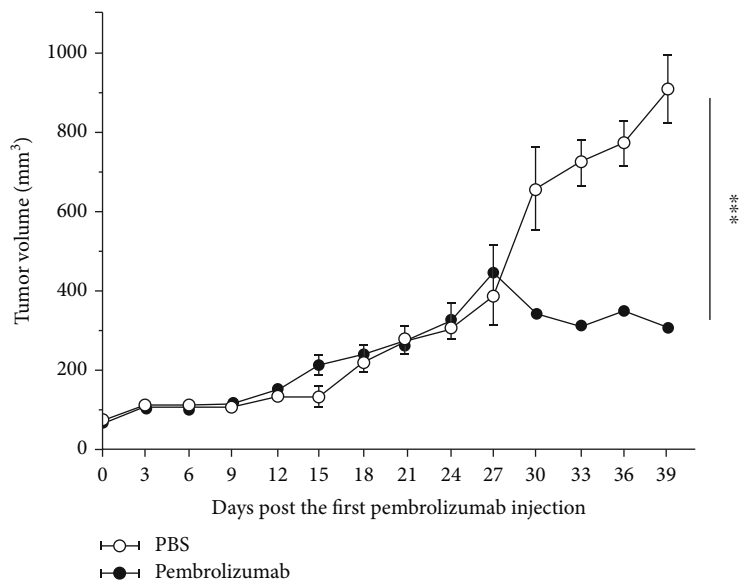


(d)

Figure 5: Establishing PBMC-CDX mice and evaluating the effect of immunotherapy on the model. (a) Effect of pembrolizumab on CDX model. Tumor curves showed that pembrolizumab promoted tumor growth in the absence of PBMCs immune reconstitution; $n = 5$. The control group was treated with PBS. (b) The experimental scheme about evaluating the therapeutic effect of pembrolizumab in PBMCs immune reconstituted CDX models. (c) Therapeutic efficacy of pembrolizumab on PBMC-CDX model. Growth curve of tumor showed that pembrolizumab has an antitumor efficacy on PBMC immune reconstituted CDX mouse models; $n = 5$. (d) The injection dose of PBMCs and pembrolizumab was halved. Tumor curves showed that tumor growth was reduced after long-term treatment in PBMCs immune reconstituted CDX mouse models; $n = 5$. $^{*}P < 0.05$, $^{**}P < 0.01$, and $^{***}P < 0.001$. Means ± SEM are used in graphs. Two-sample $t$-test was used. The $P$ values of curves (a, c, d) are significance.

The result showed that after 10 treatments with pembrolizumab, there was also a tendency to slow tumor growth (Figure 5(d)). Reducing the dose could prevent mice from dying but weaken the efficacy of tumor treatment and prolong the experimental period.

*3.3. Establishing PDX Mice and Evaluating the Effect of Bifidobacterium longum on PDX Mouse Models.* Considering the slow growth of tumor in the CDX model, we decided to replace the CDX with PDX. The tumor growth rate of PDX model was faster than CDX model (Figure 3(a)). HE staining of tumor tissue showed obvious tumor parenchyma and stroma in PDX, but not in CDX (Figure 3(b)). In order to verify the influence of *Bifidobacterium longum* on PDX model, we used antibiotics (ATB) to process PDX model, and the experimental process is shown in Figure 3(c). Fecal

culture on BBL medium showed no colony culture in ATB treatment group, but significant bacterial growth in control group and *Bifidobacterium longum* group (Figure 3(d)). At the same time, compared with the control group and ATB treatment group, after 7 times of *Bifidobacterium longum* treatment, the tumor growth rate was slowed down, and obvious inflammatory and purulent reaction occurred at the tumor site (Figures 3(e) and 3(f)). The above results showed that compared with the CDX model, the PDX model was closer to the actual growth situation of tumor in human body, and *Bifidobacterium longum* had antitumor efficacy in the PDX model.

*3.4. Establishing PBMC-PDX Mice and Evaluating the Effect of Bifidobacterium longum and Pembrolizumab on the Models.* Given the antitumor effects of *Bifidobacterium longum*, we plan to construct an ATB-treated PBMC-PDX model to evaluate the effect of *Bifidobacterium longum* on immunotherapy. On day 10 after PBMCs inoculation, the proportion of $CD45^+$ cells was 4.16% by flow cytometry (data not shown). Given that the PBMC mice were available for approximately 35 days and that immune reconstructive levels reached high levels after 15 days, we began treatment with *Bifidobacterium longum* and pembrolizumab on day 18 after PBMC transplantation, as shown in Figure 1(a). Mice that received *Bifidobacterium longum* and pembrolizumab tended to have faster tumor growth than mice that received pembrolizumab alone (Figure 1(b)). At the same time, with the progress of the experiment, mice died successively. Comparing the death of mice treated with pembrolizumab and *Bifidobacterium longum* and pembrolizumab, *Bifidobacterium longum* may slow down the role of pembrolizumab in promoting GvHD, although there is no statistical difference (Figure 1(c)). Mice died during the study, but these results suggest that *Bifidobacterium longum* and pembrolizumab alone treatment may slow tumor growth, whereas *Bifidobacterium longum* combined with pembrolizumab may not exert further antitumor efficacy.

*3.5. Optimizing the Experimental Scheme.* To avoid mouse death during the trial, PBMC administration was performed 12 days before pembrolizumab injection. Meanwhile, according to the time of tumor growth to 120-180 $mm^3$, we set the timing of tumor inoculation on the 17th day before drug administration; the experimental process is shown in Figure 2(a). The results showed that both *Bifidobacterium longum* and pembrolizumab had antitumor efficacy; however, the combination of the two attenuated the antitumor efficacy (Figures 2(b) and 2(c)). These results are basically consistent with the above experimental results.

After two days of *Bifidobacterium longum* gavage, the peripheral blood has an increased proportion of $CD45^+$ cells of the *Bifidobacterium longum* and pembrolizumab group compared with the pembrolizumab group (Figure 2(d)). Finally, tumor cells from the mice were collected for flow cytometry. The proportion of infiltrated human $CD45^+$ cells in the tumor was no significant difference (Figure 2(e)). These results indicate that the optimized experimental procedure can be used to study the interaction of *Bifidobacterium longum* and pembrolizumab.

## 4. Discussion

In this study, we constructed PBMC-CDX and PBMC-PDX models of lung cancer and analyzed the characteristics of the two. The experimental result showed that pembrolizumab promotes GvHD in the humanized mouse model of PBMCs, which is consistent with related reports [31, 32]. In general, PBMC humanized mice were able to construct human T cells to a great extent, but the presence of GvHD reduced the duration of the experiment, especially after pembrolizumab treatment. Meanwhile, we found that pembrolizumab promoted GvHD in the absence of PBMCs immune reconstitution. This is consistent with reports that anti-PD-1 antibodies promote tumor hyperprogression [33]. These results suggest that immune reconstruction is the basis for evaluating the antitumor efficacy of immunotherapy. Next, we verified that the PBMC-PDX model was closer to the human situation and had a shorter experimental period for subsequent evaluation of a bacterial marker in immunotherapy. Although a PBMC-PDX model has been identified as a model for assessing the anti-PD-1 antibody efficacy, the application of PBMC-PDX model in clarifying the role of *Bifidobacterium longum* in immunotherapy has not been reported. Our study showed that the ATB-treated PBMC-PDX model has an ability to evaluate the antitumor efficacy of *Bifidobacterium longum* and pembrolizumab.

In cancer research, CDX and PDX models are common models. Recently, it has been reported that PDX has various advantages over CDX in preserving tumor heterogeneity and microenvironment [34]. Our results show that the PDX model is more similar in characteristics of human tumor. Meanwhile, given the antitumor ability of *Bifidobacterium longum* in PDX model without immune reconstitution itself may be a potential model to evaluate the antitumor effect of bacterium.

Although it has been reported, *Bifidobacterium* is beneficial to pembrolizumab treatment in lung cancer [9]. A study based on the syngeneic mouse model reported that even if the bacterium has antitumor effect, it will not promote immunotherapy, and only specific strains are useful [35]. Our results showed that in the ATB-treated PBMC-PDX model, although *Bifidobacterium longum* played an antitumor role, it showed an antagonistic effect against pembrolizumab treatment. Flow cytometry results of peripheral blood showed that *Bifidobacterium longum* treatment induced significant changes in proportion of $CD45^+$ cell.

In summary, we have constructed a PBMC-PDX model for evaluating the role of *Bifidobacterium longum* in lung cancer immunotherapy. The establishment of the model and the optimization of the experiment process were performed. This model may provide an alternative and suitable experimental platform for the study of bacterial markers in cancer immunity and help to further discover the underlying mechanism to guide individualized immunotherapy in the foreseeable future.

## Data Availability

Data supporting the findings of this study are available on request from the corresponding author.

## Conflicts of Interest

The authors declare that there is no conflict of interest regarding the publication of this paper.

## Acknowledgments

This work was supported by grants from the National Key Research and Development Program of China (2017YFD0500503 and 2017YFD0501000), the National Program on Key Basic Research Project of China (973 Program) (2007CB513007 and 2013CB531406), and the National Natural Science Foundation of China (81770434 and 81370906).

## References

[1] H. Sung, J. Ferlay, R. L. Siegel et al., "Global cancer statistics 2020: GLOBOCAN estimates of incidence and mortality worldwide for 36 cancers in 185 countries," *CA: A Cancer Journal for Clinicians*, vol. 71, no. 3, pp. 209–249, 2021.

[2] Z. Chen, C. M. Fillmore, P. S. Hammerman, C. F. Kim, and K. K. Wong, "Non-small-cell lung cancers: a heterogeneous set of diseases," *Nature Reviews Cancer*, vol. 14, no. 8, pp. 535–546, 2014.

[3] R. S. Herbst, E. B. Garon, D. W. Kim et al., "Long-term outcomes and retreatment among patients with previously treated, programmed death-ligand 1–positive, advanced non–small-cell lung cancer in the KEYNOTE-010 study," *Journal of Clinical Oncology: Official Journal of the American Society of Clinical Oncology*, vol. 38, no. 14, pp. 1580–1590, 2020.

[4] M. Reck, D. Rodríguez-Abreu, A. G. Robinson et al., "Pembrolizumab versus chemotherapy for PD-L1-positive non-small-cell lung cancer," *The New England Journal of Medicine*, vol. 375, no. 19, pp. 1823–1833, 2016.

[5] T. Shukuya and D. P. Carbone, "Predictive markers for the efficacy of anti-PD-1/PD-L1 antibodies in lung cancer," *Journal of Thoracic Oncology*, vol. 11, no. 7, pp. 976–988, 2016.

[6] A. E. Frankel, L. A. Coughlin, J. Kim et al., "Metagenomic shotgun sequencing and unbiased metabolomic profiling identify specific human gut microbiota and metabolites associated with immune checkpoint therapy efficacy in melanoma patients," *Neoplasia*, vol. 19, no. 10, pp. 848–855, 2017.

[7] M. Vétizou, J. M. Pitt, R. Daillère et al., "Anticancer immunotherapy by CTLA-4 blockade relies on the gut microbiota," *Science*, vol. 350, no. 6264, pp. 1079–1084, 2015.

[8] N. Chaput, P. Lepage, C. Coutzac et al., "Baseline gut microbiota predicts clinical response and colitis in metastatic melanoma patients treated with ipilimumab," *Annals of Oncology*, vol. 28, no. 6, pp. 1368–1379, 2017.

[9] Y. Jin, H. Dong, L. Xia et al., "The diversity of gut microbiome is associated with favorable responses to anti-programmed death 1 immunotherapy in Chinese patients with NSCLC," *Journal of Thoracic Oncology*, vol. 14, no. 8, pp. 1378–1389, 2019.

[10] V. Matson, J. Fessler, R. Bao et al., "The commensal microbiome is associated with anti-PD-1 efficacy in metastatic melanoma patients," *Science*, vol. 359, no. 6371, pp. 104–108, 2018.

[11] J. Fessler, V. Matson, and T. F. Gajewski, "Exploring the emerging role of the microbiome in cancer immunotherapy," *Journal for Immunotherapy of Cancer*, vol. 7, no. 1, p. 108, 2019.

[12] B. Routy, E. Le Chatelier, L. Derosa et al., "Gut microbiome influences efficacy of PD-1-based immunotherapy against epithelial tumors," *Science*, vol. 359, no. 6371, pp. 91–97, 2018.

[13] Y. Li, L. Elmén, I. Segota et al., "Prebiotic-induced anti-tumor immunity attenuates tumor growth," *Cell Reports*, vol. 30, no. 6, pp. 1753–1766.e, 2020.

[14] C. W. Chang, C. Y. Liu, H. C. Lee et al., "Lactobacillus casei variety rhamnosus probiotic preventively attenuates 5-fluorouracil/oxaliplatin-induced intestinal injury in a syngeneic colorectal cancer model," *Frontiers in Microbiology*, vol. 9, p. 983, 2018.

[15] Z. Gong, H. Xu, Y. Su, W. Wu, L. Hao, and C. Han, "Establishment of a novel bladder cancer xenograft model in humanized immunodeficient mice," *Cellular Physiology and Biochemistry: International Journal of Experimental Cellular Physiology, Biochemistry, and Pharmacology*, vol. 37, no. 4, pp. 1355–1368, 2015.

[16] O. O. Oduwole, A. Poliandri, A. Okolo et al., "Follicle-stimulating hormone promotes growth of human prostate cancer cell line-derived tumor xenografts," *The FASEB Journal*, vol. 35, no. 4, article e21464, 2021.

[17] G. S. Herter-Sprie, A. L. Kung, and K. K. Wong, "New cast for a new era: preclinical cancer drug development revisited," *The Journal of Clinical Investigation*, vol. 123, no. 9, pp. 3639–3645, 2013.

[18] D. Siolas and G. J. Hannon, "Patient-derived tumor xenografts: transforming clinical samples into mouse models," *Cancer Research*, vol. 73, no. 17, pp. 5315–5319, 2013.

[19] E. Izumchenko, K. Paz, D. Ciznadija et al., "Patient-derived xenografts effectively capture responses to oncology therapy in a heterogeneous cohort of patients with solid tumors," *Annals of Oncology*, vol. 28, no. 10, pp. 2595–2605, 2017.

[20] J. Merk, J. Rolff, M. Becker, G. Leschber, and I. Fichtner, "Patient-derived xenografts of non-small-cell lung cancer: a pre-clinical model to evaluate adjuvant chemotherapy?," *European journal of cardio-thoracic surgery: official journal of the European Association for Cardio-thoracic Surgery*, vol. 36, no. 3, pp. 454–459, 2009.

[21] C. Ye, H. Yang, M. Cheng et al., "A rapid, sensitive, and reproducible in vivo PBMC humanized murine model for determining therapeutic-related cytokine release syndrome," *The FASEB Journal*, vol. 34, no. 9, pp. 12963–12975, 2020.

[22] L. Cheng, J. Ma, G. Li, and L. Su, "Humanized mice engrafted with human HSC only or HSC and thymus support comparable HIV-1 replication, immunopathology, and responses to ART and immune therapy," *Frontiers in Immunology*, vol. 9, p. 817, 2018.

[23] L. D. Shultz, M. A. Brehm, J. V. Garcia-Martinez, and D. L. Greiner, "Humanized mice for immune system investigation: progress, promise and challenges," *Nature Reviews. Immunology*, vol. 12, no. 11, pp. 786–798, 2012.

[24] T. M. Allen, M. A. Brehm, S. Bridges et al., "Humanized immune system mouse models: progress, challenges and

opportunities," *Nature Immunology*, vol. 20, no. 7, pp. 770–774, 2019.

[25] R. Sluyter and D. Watson, "Use of humanized mouse models to investigate the roles of purinergic signaling in inflammation and immunity," *Frontiers in Pharmacology*, vol. 11, article 596357, 2020.

[26] J. Courtois, C. Ritacco, S. Dubois et al., "Itacitinib prevents xenogeneic GVHD in humanized mice," *Bone Marrow Transplantation*, vol. 56, no. 11, pp. 2672–2681, 2021.

[27] N. Iida, A. Dzutsev, C. A. Stewart et al., "Commensal bacteria control cancer response to therapy by modulating the tumor microenvironment," *Science*, vol. 342, no. 6161, pp. 967–970, 2013.

[28] L. Bird, "Microbial metabolite boosts immunotherapy," *Nature Reviews. Immunology*, vol. 20, no. 11, pp. 648-649, 2020.

[29] Z. Zhu, T. Kaiser, and C. Staley, "Antibiotic conditioning and single gavage allows stable engraftment of human microbiota in mice," *Methods in Molecular Biology*, vol. 2327, pp. 281–291, 2021.

[30] M. Al-Asmakh and F. Zadjali, "Use of germ-free animal models in microbiota-related research," *Journal of Microbiology and Biotechnology*, vol. 25, no. 10, pp. 1583–1588, 2015.

[31] A. Ijaz, A. Y. Khan, S. U. Malik et al., "Significant risk of graft-versus-host disease with exposure to checkpoint inhibitors before and after allogeneic transplantation," *Biology of Blood and Marrow Transplantation*, vol. 25, no. 1, pp. 94–99, 2019.

[32] A. K. Singh, L. F. Porrata, O. Aljitawi et al., "Fatal GvHD induced by PD-1 inhibitor pembrolizumab in a patient with Hodgkin's lymphoma," *Bone Marrow Transplantation*, vol. 51, no. 9, pp. 1268–1270, 2016.

[33] S. Du, N. McCall, K. Park et al., "Blockade of tumor-expressed PD-1 promotes lung cancer growth," *Oncoimmunology*, vol. 7, no. 4, article e1408747, 2018.

[34] T. Inoue, N. Terada, T. Kobayashi, and O. Ogawa, "Patient-derived xenografts as in vivo models for research in urological malignancies," *Nature reviews Urology*, vol. 14, no. 5, pp. 267–283, 2017.

[35] S. H. Lee, S. Y. Cho, Y. Yoon et al., "Bifidobacterium bifidum strains synergize with immune checkpoint inhibitors to reduce tumour burden in mice," *Nature Microbiology*, vol. 6, no. 3, pp. 277–288, 2021.

Hindawi
Disease Markers
Volume 2022, Article ID 3044186, 9 pages
https://doi.org/10.1155/2022/3044186

*Research Article*

# Altered Functional Connectivity in Pain-Related Brain Regions and Its Correlation with Pain Duration in Bone Metastasis with Cancer Pain

**Xiaoyu Zhou, Yong Tan, Jiao Chen, Chengfang Wang, Yu Tang, Jiang Liu, Xiaosong Lan, Hong Yu, Yong Lai, Yixin Hu, Jing Zhang, Ying Cao, Daihong Liu, and Jiuquan Zhang**

*Department of Radiology, Chongqing University Cancer Hospital, School of Medicine, Chongqing University, Chongqing 400030, China*

Correspondence should be addressed to Daihong Liu; liudaihong121@163.com and Jiuquan Zhang; zhangjq_radiol@foxmail.com

Received 26 May 2022; Accepted 13 August 2022; Published 28 August 2022

Academic Editor: Pei-Wen Zhu



Bone metastatic pain is thought to be a severe type of cancer pain that has refractory characteristics and a long duration. This study is aimed at exploring the brain functional connectivity (FC) pattern in lung cancer patients with bone metastatic pain. In this study, 27 lung cancer patients with bone metastatic pain (CP+), 27 matched lung cancer patients without pain-related complaints (CP−), and 27 matched healthy controls (HC) were recruited. All participants underwent fMRI data acquisition and clinical assessments. One-way ANOVA or a Mann–Whitney *U* test was applied to compare clinical data according to data distribution. Seventeen hypothesis-driven pain-related brain regions were selected as regions of interest (ROIs). FC values among pain-related brain regions across the three groups were computed by using ROI–ROI functional connectivity analysis. ANCOVA with a post hoc test was applied to compare FC differences among the three groups. $p < 0.05$ indicated statistical significance. Correlation analysis was conducted to explore the potential relationship between the FC values and clinical characteristics. Except for years of education, no significant differences were revealed among the three groups in age, gender, or neuropsychological assessment. In the CP+ group, FC alterations were mainly concentrated in the dorsal lateral prefrontal cortex (DLPFC), anterior cingulate cortex (ACC), secondary somatosensory cortex (SII), and amygdala compared to the CP− group. Among these brain regions with statistical differences, FC between the right DLPFC and the right ACC showed a positive correlation with the duration of cancer pain in the CP+ group. In addition, in the CP− group, altered FC was found in the bilateral SII, ACC, and thalamus compared to the HC group. Altered FC in pain-related brain regions may be a brain pattern of bone metastatic pain and may be associated with the long duration of cancer pain.

## 1. Introduction

Pain is a common symptom in cancer patients. Approximately 64% of cancer patients with advanced cancer or metastases report cancer pain [1]. Bone metastatic pain is thought to be a severe type of cancer pain that has refractory characteristics with a long duration [2]. Therefore, exploring the mechanism of bone metastatic pain is of great significance for early prevention and intervention.

The pathophysiological mechanisms of bone metastatic pain have begun to be elucidated. Nociceptors are activated by bone metastasis itself or secreted pain-inducing mediators [3]. In addition, acid-sensitive ion channels of nociceptors are activated by acids produced during bone remodeling [4]. Beyond that, peripheral and central sensitization increases the sensitivity of pain [5]. The above pathological abnormalities eventually manifest as pain perceptions and unpleasant emotions, which can be generated and regulated by the brain.

Table 1: Templates of the pain-related brain regions.

| Templates | Brain region | Abbreviation | Hemisphere |
|---|---|---|---|
| Anatomical Automatic Labeling | Thalamus | THA | L |
| | | | R |
| | Insula | INS | L |
| | | | R |
| | Amygdala | AMY | L |
| | | | R |
| | Anterior cingulate cortex | ACC | L |
| | | | R |
| Juelich Histological Atlas | Primary somatosensory cortex | SI | L |
| | | | R |
| | Secondary somatosensory cortex | SII | L |
| | | | R |
| Brainnetome Atlas | Dorsolateral prefrontal cortex | DLPFC | L |
| | | | R |
| | Medial prefrontal cortex | mPFC | L |
| | | | R |
| Harvard Ascending Arousal Network Atlas | Periaqueductal gray | PAG | / |

Abbreviations: MNI: Montreal Neurological Institute; R: right; L: left.

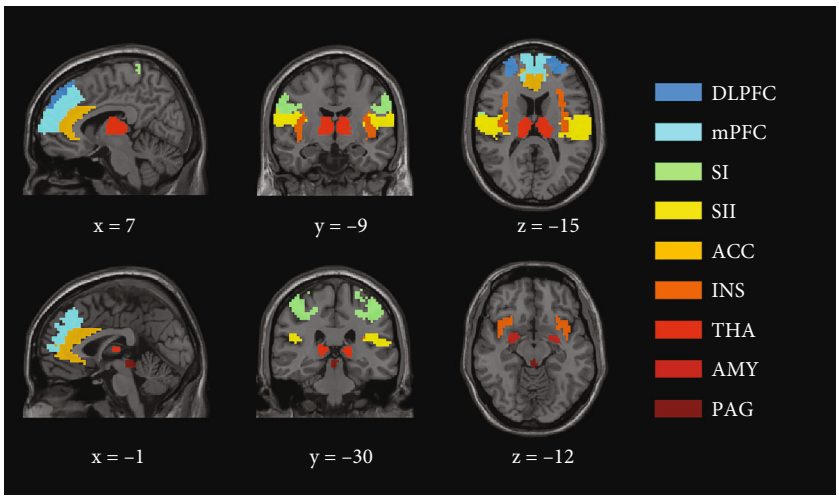


Figure 1: The pain-related brain region masks. DLPFC: dorsal lateral prefrontal cortex; mPFC: medial prefrontal cortex; SI: primary somatosensory cortex; SII; secondary somatosensory cortex; ACC: anterior cingulate cortex; INS: insula; THA: thalamus; AMY: amygdala; PAG: periaqueductal gray.

The function and structure of the brain change can accordingly be detected by magnetic resonance imaging (MRI).

Neuroimaging studies of patients with pain have suggested that pain is closely related to alterations in brain function and structure [6, 7]. Brain regions processing pain-related information were considered as a "pain matrix" as follows. The thalamus, posterior insula, and primary somatosensory cortex (SI) can receive nociceptive afferent information and then encode pain intensity. The anterior cingulate gyrus (ACC), anterior insula, and secondary somatosensory cortex (SII) can manage unpleasant pain-related emotions. Midbrain periaqueductal gray matter (PAG) is an important hub for pain regulation [8]. Moreover, the amygdala and prefrontal cortex participate in processing pain-related emotion, memory, and fear [9]. A large number of studies have explored the abnormal brain function within the pain matrix in various types of chronic pain. In general, stronger functional connectivity of the pain-related brain areas was demonstrated in patients with pain compared to controls in most instances [10–14]. Functional connectivity manifests differently in different pain conditions

Table 2: Demographic and clinical characteristics.

| | CP+ ($n = 27$) | CP− ($n = 27$) | HC ($n = 27$) | $p$ value |
|---|---|---|---|---|
| *Demographics* | | | | |
| Age (years) | 60.11 ± 8.45 (45–76) | 59.96 ± 7.05 (48–73) | 59.00 ± 8.18 (44–74) | 0.855 |
| Gender (man : female) | 18: 9 | 18: 9 | 18: 9 | 1.000 |
| Education (years) | 8.19 ± 3.60 (0–16) | 7.59 ± 2.39 (4–12) | 11.00 ± 4.24 (0–20) | 0.001 |
| Anxiety SAS | 36.15 ± 10.06 (25–62) | 31.37 ± 4.58 (25–42) | 34.15 ± 7.66 (25–47) | 0.069 |
| Depression SDS | 34.42 ± 10.93 (25–70) | 29.70 ± 4.45 (25–43) | 33.56 ± 9.40 (25–62) | 0.111 |
| *Clinical characteristics* | | | | |
| Cancer stage, No. (%) | | | | |
| I | 0 | 3 (11.11%) | NA | NA |
| II | 0 | 1 (3.70%) | NA | NA |
| III | 0 | 6 (22.22%) | NA | NA |
| IV | 27 (100%) | 17 (62.92%) | NA | NA |
| Subtype, No. (%) | | | NA | NA |
| Adenocarcinoma | 16 (59.26%) | 15 (55.56%) | NA | NA |
| Squama cancer | 9 (33.33%) | 10 (37.04%) | NA | NA |
| Sarcomatoid carcinoma | 0 | 1 (3.70%) | NA | NA |
| Small cell cancer | 2 (7.41%) | 1 (3.70%) | NA | NA |
| Therapeutic regimen, No. (%) | | | NA | NA |
| Chemotherapy | 21 (43.75%) | 16 (53.33%) | NA | NA |
| Radiotherapy | 10 (20.83%) | 4 (13.33%) | NA | NA |
| Targeted therapy | 10 (20.83%) | 5 (16.67%) | NA | NA |
| Surgery | 3 (6.25%) | 5 (16.67%) | NA | NA |
| Immunotherapy | 1 (2.08%) | 0 | NA | NA |
| Chinese medicinal therapy | 3 (6.25%) | 0 | NA | NA |
| NRS | 2.33 ± 1.66 (1–7) | 0 | 0 | NA |
| Duration of cancer pain (days) | 265.93 ± 430.36 (20–2095) | NA | NA | NA |

Note: values shown are mean ± SD (MIN–MAX) unless noted otherwise. Abbreviation: CP+: lung cancer patients with bone metastases suffering from cancer pain; CP−: lung cancer patients without pain-related complaints; HC: health controls; SD: standard deviation; MIN: minimum; MAX: maximum; BMI: body mass index; SAS: Self-Rating Anxiety Scale; SDS: Self-Rating Depression Scale; NA: not applicable.

and has a potential to assist in diagnostic classification [15]. However, neuroimaging studies on pain have mainly focused on noncancer chronic pain and have paid little attention to cancer pain.

The prevalence of chronic pain among adult cancer survivors is nearly double that of adults without a cancer diagnosis [16]. Previous studies have explored the cerebral structure [17] and functional connectivity [18] of chronic neuropathic pain after surgery in breast cancer patients with or without psychological interventions. The above studies found that higher fractional anisotropy (FA) values in the left subcortical regions [17] and greater posterior cingulate connectivity with medial prefrontal regions [18] are both associated with a reduction in pain perception after psychological interventions. Previous studies on brain function in bone metastatic pain have been carried out using animal models. In studies of a mouse model with chronic pain from bone metastasis, abnormalities in functional connectivity were found in the PAG, amygdala, thalamus, and somatosensory cortex [19]. In mice with bone metastatic pain, the prefrontal cortex, cingulate cortex, and ventral striatum are regarded as central regions participating in pain-related network remodeling [20]. To our knowledge, functional connectivity abnormalities in patients with bone metastatic pain have not yet been reported.

Due to the long duration and the special pathophysiological mechanisms of bone metastatic pain, it is necessary to explore its neuroimaging mechanism. As far as we know, functional connectivity analysis has been reported in a mouse model of metastatic bone cancer, however, not in the human population. This study provides a first attempt to explore the functional connectivity within pain-related brain regions in lung cancer patients with bone metastasis suffering from cancer pain by using region of interest- (ROI-) ROI functional connectivity analyses. We hypothesized that abnormalities in functional connectivity within pain-related brain regions may occur in lung cancer patients with bone metastatic pain and that altered functional connectivity may correlate with pain-related clinical characteristics.

## 2. Methods

*2.1. Participants.* Participants were lung cancer patients with bone metastases suffering from cancer pain (CP+), lung cancer patients without pain-related complaints (CP−), and healthy

controls (HC). The above three groups were matched by age and gender. All participants were recruited at Chongqing University Cancer Hospital from August 2020 to January 2022. All patients (both CP+ and CP−) were pathologically confirmed to have lung cancer. On the basis of pathologically diagnosed lung cancer, patients with bone metastasis were diagnosed when meeting one of two conditions: (a) the results of bone lesion biopsy showed lung cancer metastasis and (b) typical imaging manifestations of bone metastasis. Pain perception was assessed by the Numeric Rating Scale (NRS) for all participants. The CP+ group should meet NRS ≥ 1, while the CP− and HC group need to meet NRS = 0. All CP+ patients received regular analgesic therapy. Exclusion criteria were as follows: (a) intracranial metastases, encephalatrophy, trauma, or a history of brain surgery; (b) a history of psychiatric disorders; (c) extensive head motion (a maximum rotation greater than 3° or a maximum displacement greater than 3 mm); and (d) claustrophobia. This study was approved by the Research Ethical Committee of Chongqing University Cancer Hospital (IRB: CZLS2021042). Signed informed consent was obtained from all participants.

Of the 40 lung cancer patients with bone metastatic pain who were initially recruited for this study, seven patients had brain metastasis, four patients were diagnosed with encephalatrophy, and two patients had head motion displacement greater than 3 mm. Of the 35 recruited lung cancer patients without cancer pain, four patients had brain metastases, one patient had a history of cerebral hemorrhage, and three patients had head motion displacement greater than 3 mm. Of the recruited healthy volunteers, 27 matched volunteers were selected for this study. Therefore, 27 lung cancer patients with bone metastatic pain, 27 lung cancer patients without cancer pain, and 27 healthy volunteers were included in this study.

*2.2. Clinical Assessments.* Clinical pain, depression, and anxiety assessments and MRI scans for each participant were acquired on the same day. NRS was adopted to evaluate pain intensity. The NRS includes 11 numbers, and 0 represents "no pain" to 10 represents "the worst pain imaginable." The participants scored the pain intensity under the guidance of an experienced physician. The duration of cancer pain in the CP+ group was calculated according to the medical record. Anxiety and depression statuses were assessed by the Self-Rating Anxiety Scale (SAS) and Self-Rating Depression Scale (SDS), respectively. Demographic information of all participants was obtained by the self-report questionnaire.

*2.3. Resting-State Functional MR Data Acquisition.* Acquisition MRI scans were examined on a 3.0 T scanner (Magnetom Prisma; Siemens Healthcare, Erlangen, Germany) equipped with a 64-channel head-neck coil. Participants were instructed to remain motionless, close their eyes, stay awake, and avoid thinking about any topics. Earplugs were used to alleviate the influence of noise, and cushions were used to restrict head motion. Three sequences were collected as follows. First, the structural information was acquired to guide subsequent functional imaging with a T1-weighted three-dimensional magnetization prepared rapid gradient echo (MPRAGE) sequence: repetition time (TR) = 2100 milliseconds (ms), echo time (TE) = 2.26 ms, flip angle = 8°, field of view (FOV) = 256 × 256 $mm^2$, matrix = 256 × 256, slice thickness = 1 mm with no slice gap, and slices = 192. The total scanning time was 4 minutes and 53 seconds. Second, rapid gradient echo-planar pulse imaging (EPI) was used to acquire the resting-state blood oxygenation level-dependent (BOLD) signal: TR = 2000 ms, TE = 30 ms, flip angle = 70°, FOV = 240 × 240 $mm^2$, slices = 36 (interleaved), matrix = 80 × 80, and voxel size = 3 × 3 × 3 $mm^3$. From each participant, 240 volumes were acquired over 8 minutes and 8 seconds. Additionally, routine axial T2-weighted images were obtained to exclude subjects with intracranial metastases or other lesions, as demonstrated by the exclusion criteria above.

*2.4. Brain Region Masks.* Based on functional connectivity analysis results from previous pain-related studies, 17 hypothesis-driven pain-related brain regions were selected as ROIs in the current fMRI study. The selected brain regions included the bilateral thalamus, bilateral insula, bilateral amygdala, bilateral ACC, bilateral SI, bilateral SII, bilateral dorsal lateral prefrontal cortex (DLPFC), bilateral medial prefrontal cortex (mPFC), and PAG. Detailed information on these pain-related brain regions is shown in Table 1. Masks for most pain-related regions were selected from the Anatomical Automatic Labeling (AAL) Atlas, including the bilateral thalamus, insula, amygdala, and ACC. In addition, the masks for bilateral SI and SII were chosen from the Juelich Histological Atlas [21], which was distributed with the FMRIB Software Library (FSL) tool. In addition, the bilateral DLPFC and mPFC were selected from the Brainnetome Atlas [22]. Finally, the PAG mask was chosen from the Harvard Ascending Arousal Network Atlas [23]. The selected brain region masks are shown in Figure 1.

*2.5. Processing of Resting-State fMRI Data.* The preprocessing of the BOLD data was carried out using the Data Processing Assistant for Resting-State fMRI (DPARSF, http://rfmri.org/DPARSF) based on MATLAB R2020a. All process followed a standard procedure as described in previous studies [24]. Briefly, we first converted all DICOM files into NifTI files. Then, the first 10 volumes of each participant were removed to reach signal equilibration. A correction was made for time differences between slices, and then, the scans were realigned to the middle point to account for head motion. The head motion parameters of all participants were then assessed, and participants with a maximum rotation greater than 3° or a maximum displacement greater than 3 mm were excluded. The head motion parameter, mean framewise displacement by Jenkinson, of the remaining subjects was extracted for the subsequent step. We performed nuisance regression separately on white matter and cerebrospinal fluid. The motion-corrected BOLD images were spatially normalized and then resampled with a voxel size of 3 × 3 × 3 $mm^3$. To reduce spatial noise, the images were spatially smoothed with a Gaussian kernel of 6 mm full width at half maximum (FWHM). A bandpass filter was set as 0.01 Hz < $f$ < 0.10 Hz to remove the influence of low-frequency physiological drift and high-frequency noise. After these steps, a 4-dimensional residual time series dataset

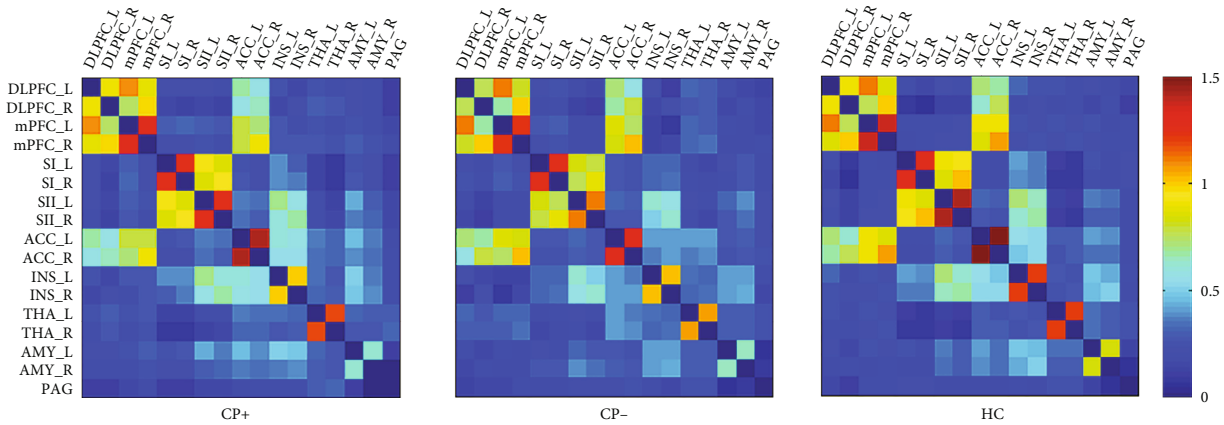


Figure 2: Functional connectivity matrices of the three groups. Colormap shows $z$ values of functional connectivity. CP+: lung cancer patients with bone metastases suffering from cancer pain; CP−: lung cancer patients without pain-related complaints; HC: health controls; DLPFC: dorsal lateral prefrontal cortex; mPFC: medial prefrontal cortex; SI: primary somatosensory cortex; SII: secondary somatosensory cortex; ACC: anterior cingulate cortex; INS: insula; THA: thalamus; AMY: amygdala; PAG: periaqueductal gray; R: right; L: left.

Table 3: Functional connectivity differences of the pain-related brain regions in three groups.

| Brain region | ANCOVA $F$ ($H$) value | ANCOVA $p$ value | Post hoc test $t$ ($\mu$) value | Post hoc test $p$ value |
|---|---|---|---|---|
| DLPFC (R)—ACC (R) | 3.297 | 0.043 | −2.400[a] | 0.019[a] |
| ACC (L)—AMY (L) | 7.394* | 0.025* | 2.661*[b] | 0.023*[b] |
| SII (L)—SII (R) | 5.769 | 0.005 | 2.003[b] | 0.049[b] |
| | | | −3.377[c] | 0.001[c] |
| ACC (L)—ACC (R) | 6.446 | 0.003 | −3.594[c] | 0.001[c] |
| THA (L)—THA (R) | 4.493 | 0.014 | −2.980[c] | 0.004[c] |

* means results of nonparametric test; [a]CP + <CP − ; [b]CP + >CP − ; [c]CP − <HC. Abbreviations: CP+: lung cancer patients with bone metastases suffering from cancer pain; CP−: lung cancer patients without pain-related complaints; HC: health controls; ANCOVA: analysis of covariance; DLPFC: dorsolateral prefrontal cortex; ACC: anterior cingulate gyrus; AMY: amygdala; SII: secondary somatosensory cortex; THA: thalamus; R: right; L: left.

was created in the standard MNI space. Intragroup functional connectivity ROI-ROI analysis was conducted among the 17 pain-related brain regions using RESTplus V1.22 (http://www.restfmri.net). For each ROI, the mean time series was calculated and then correlated with the other ROIs for each subject. By using Fisher's $r$-to-$z$ transformation, Pearson correlation coefficients were converted to normally distributed scores.

*2.6. Statistical Analysis.* All data were analyzed using the statistical program SPSS 25.0. For intergroup comparisons of demographic data and neuropsychological test scores, the Shapiro–Wilk test was used to verify the normality of the data. Subject characteristics were compared among three groups using ANOVA or the Mann–Whitney $U$ test depending on their distributions. The gender proportion was examined using the chi–square test. $p < 0.05$ indicated statistical significance.

For intergroup comparisons of functional connectivity, the normally distributed $z$ scores of functional connectivity between two ROIs were analyzed using one-way ANCOVA among the three groups. Age [25, 26] and gender [24, 27] were regarded as important factors in pain perception. Education in years was different among three groups in this study. And diversity in fMRI results was thought to covary with subject movements [28]. Because of the above reasons, age, gender, education in years, and head motion parameters were set as covariates. The post hoc LSD test was used to identify the relationship between each group pairing. The Kruskal–Wallis ANCOVA (with covariates controlled) and a post hoc Manne–Whitney $U$ tests were used to analyze $z$ scores with nonnormal distributions. The above ANCOVA tests were also controlled for multiple comparisons with a Bonferroni correction of $p < 0.003$ (resulting from $p = 0.05/17$ functional connectivity measures).

A partial correlation was conducted on the CP+ group to evaluate the association between the transformed $z$ scores of functional connectivity and clinical characteristics (pain intensity, duration of cancer pain, and scores on the SAS and SDS). Age, gender, education in years, and head motion parameters were set as covariates. $p < 0.05$ was considered as statistically significant.

## 3. Results

*3.1. Demographic Data.* The demographic and clinical characteristics of the participants are detailed in Table 2. No significant differences were revealed among the three groups in regard to age, gender, or neuropsychological assessment. Years of education among the three groups showed statistical significance.

*3.2. Functional Connectivity in the Three Groups.* Functional connectivity matrices of the three groups are shown in

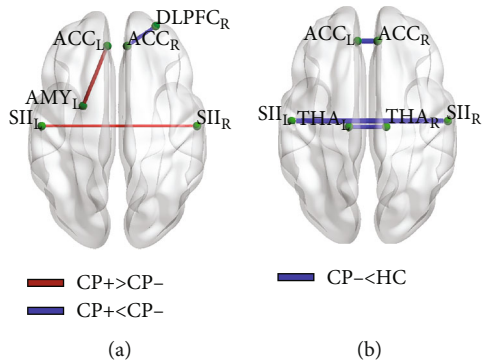


Figure 3: Statistical differences of functional connectivity in intergroup comparisons. (a) Shows the comparison between CP+ and CP−. (b) Shows comparison between CP− and HC. CP+: lung cancer patients with bone metastases suffering from cancer pain; CP−: lung cancer patients without pain-related complaints; HC: health controls; DLPFC: dorsal lateral prefrontal cortex; SII: secondary somatosensory cortex; ACC: anterior cingulate cortex; THA: thalamus; AMY: amygdala; L: left; R: right.

Figure 2. Statistically differences in functional connectivity are shown in this exploratory study of pain-related brain regions among the three groups (Table 3 and Figure 3). Compared to the CP− group, the CP+ group showed significantly decreased FC between the right DLPFC and the right ACC. Moreover, the CP+ group showed significantly increased FC between the left ACC and the left amygdala, as well as between the bilateral SII. Compared to the HC group, the CP− group showed significantly decreased FC between the bilateral SII, between the bilateral ACC, and between the bilateral thalamus. No significant differences were found between the CP+ and HC groups. Unfortunately, the ANCOVA results of functional connectivity could not bear the multiple comparisons correction ($p > 0.05/17$).

*3.3. Correlations in the CP+ Group.* As shown in Figure 4, in the CP+ group, FC between the right DLPFC and the right ACC was positively correlated with the duration of cancer pain ($r = 0.451$, $p = 0.035$). No significant correlations were found between the FC values and pain intensity.

## 4. Discussion

We report alterations in functional connectivity in pain-related brain regions in lung cancer patients with bone metastasis suffering from cancer pain compared to the control groups and correlations between altered functional connectivity and the duration of cancer pain. The results showed that the altered functional connectivity was mainly concentrated in the DLPFC, ACC, SII, and amygdala in the CP+ group compared to the CP− group. Among these brain regions that showed statistical differences, functional connectivity between the right DLPFC and the right ACC showed a positive correlation with the duration of cancer pain in the CP+ group. In addition, altered functional connectivity was found in the bilateral SII, ACC, and thalamus between the CP− group and the HC group.

We found weaker functional connectivity between the right DLPFC and the right ACC in the CP+ group compared to the CP− group, and this functional connectivity showed a positive correlation with the duration of cancer pain. The DLPFC and ACC are two major cognitive-emotional modulation areas that are known to receive nociceptive input from the periphery and control pain perception by top-down modulation [29]. A previous study demonstrated that after taking analgesics, patients with chronic radicular neuropathic pain were relieved with a reduction in network connectivity between the DLPFC and ACC [11]. Similarly, we found weaker functional connectivity between the right DLPFC and the right ACC in the CP+ group (all CP+ patients had experienced analgesics). With the long duration of cancer pain that had not been cured, this functional connectivity gradually recovered. We speculate that the DLPFC and ACC may be critical brain regions that cause cancer pain to be refractory. Moreover, DLPFC stimulation by repetitive transcranial magnetic stimulation (rTMS) has a potential analgesic effect on chronic pain [30, 31]. This provides a possibility for future studies on the analgesia of cancer pain.

In addition, we found stronger functional connectivity between the left ACC and the left amygdala in the CP+ group compared to the CP− group. The amygdala is a crucial subcortical region thought to contribute to emotional components of pain [32]. Hyperexcitability of the pathway between the basolateral amygdala and the ACC was found in mouse models with neuropathic pain, and inhibiting basolateral amygdala inputs can elicit pain-related aversion [33]. Effective connections were found between the ACC and amygdala in adults during the experience of pain while also experiencing sadness [34]. It is plausible to suggest that stronger functional connectivity between the ACC and amygdala in patients with cancer pain may result from a cerebral response to pain-related aversion.

Moreover, we found stronger functional connectivity between the left SII and the right SII in the CP+ group compared to the CP− group. To our knowledge, SII generally presented stronger functional connectivity with the other pain-related brain regions in patients under pain conditions [12, 35]. Surprisingly, in lung cancer patients with bone metastatic pain, stronger functional connectivity between the SII in both cerebral hemispheres was found. SII is responsible for spatial, tactile, and motor memory associated with sensory experiences [36]. Our finding suggests that somatosensory

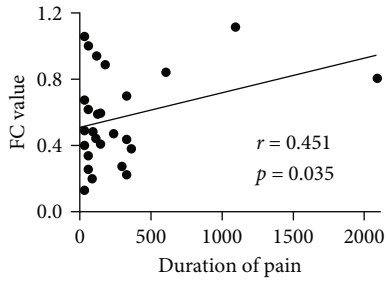


Figure 4: Positive correlation between the functional connectivity of the right DLPFC and the right ACC with the duration of cancer pain in the CP+ group. CP+: lung cancer patients with bone metastases suffering from cancer pain; DLPFC: dorsal lateral prefrontal cortex; ACC: anterior cingulate cortex; FC: functional connectivity.

perception coding between the two hemispheres increased during bone metastatic pain.

In addition, in the CP− group, weaker functional connectivity was found in bilateral SII, ACC, and thalamus compared to the HC group, due to the complexity of lung cancer, brain function susceptible to cancer treatment, psychological factors, and the lung cancer itself [37]. Researchers found that lung cancer patients both with and without chemotherapy had cognitive impairment [38]. Connectivity differences in the default mode network, predominantly in the anterior temporal network and cerebellum network, were found in lung cancer patients versus healthy controls. According to these studies, to eliminate the physiological and psychological effects of lung cancer on brain function in the present study, we used lung cancer patients without pain-related complaints as a control group. Finally, we found no significant differences between the CP+ group and HC group. We supposed that too many confounding factors were present to directly compare the results. The results suggest that the different effects on the brain function may not have simply appeared successively but rather mutually influenced one another, leading to countermeasures. Actually, these results need to be interpreted with caution. Another possible reason is the bias caused by the small sample size.

The limitations of this study should be mentioned. First, our results could not bear the multiple comparisons correction in this exploratory study. However, a previous study found a high false-positive rate when using a stringent threshold for multiple comparison correction and revealed that small $p$ values may not yield robust findings [39]. Because of the exploratory nature of this study, multiple comparison correction was not used in the comparisons within the $17 \times 17$ correlation matrix. Second, we also did not use seed-based global functional connectivity analysis. Instead, we restricted our analysis to a priori selected ROIs. Third, the relatively small sample size of this study may limit its generalizability. However, the sample size here was larger than that reported in previous neuroimaging studies of cancer pain (ranging between 10 and 13 participants) [17, 18]. Last, due to the cross-sectional design of the present study, the direction of causality underlying the observed associations remains unknown. Thus, longitudinal studies will be important in the future.

## 5. Conclusion

These data were the first to show altered brain functional connectivity within pain-related brain regions in lung cancer patients with bone metastatic pain and to reveal its correlation with pain duration. This study may provide a better understanding of bone metastatic pain.

## Data Availability

The study data presented may be made available from the corresponding authors upon reasonable request.

## Conflicts of Interest

The authors declare that they have no conflicts of interests.

## Authors' Contributions

Xiaoyu Zhou and Yong Tan contributed equally to this work.

## Acknowledgments

This work was supported by the National Natural Science Foundation of China (grant number 82071883); the Graduate Research and Innovation Foundation of Chongqing, China (grant number CYS21071); the Chongqing Medical Research Project of Combination of Science and Medicine (grant number 2021MSXM035); the 2020 SKY Imaging Research Fund of the China International Medical Foundation (grant number Z-2014-07-2003-24); and the Natural Science Foundation of Chongqing (grant numbers cstc2021jcyj-msxmX0319, cstc2021jcyj-msxmX0313).

## References

[1] M. H. van den Beuken-van Everdingen, J. M. de Rijke, A. G. Kessels, H. C. Schouten, M. van Kleef, and J. Patijn, "Prevalence of pain in patients with cancer: a systematic review of the past 40 years," *Annals of Oncology*, vol. 18, no. 9, pp. 1437–1449, 2007.

[2] B. M. Scarborough and C. B. Smith, "Optimal pain management for patients with cancer in the modern era," *CA: a Cancer Journal for Clinicians*, vol. 68, no. 3, pp. 182–196, 2018.

[3] N. Renema, B. Navet, M. F. Heymann, F. Lezot, and D. Heymann, "RANK-RANKL signalling in cancer," *Bioscience Reports*, vol. 36, no. 4, 2016.

[4] S. H. Park, M. R. Eber, D. B. Widner, and Y. Shiozawa, "Role of the bone microenvironment in the development of painful complications of skeletal metastases," *Cancers (Basel)*, vol. 10, no. 5, p. 141, 2018.

[5] P. Mantyh, "Bone cancer pain: causes, consequences, and therapeutic opportunities," *Pain*, vol. 154, Supplement 1, pp. S54–s62, 2013.

[6] T. D. Wager, L. Y. Atlas, M. A. Lindquist, M. Roy, C. W. Woo, and E. Kross, "An fMRI-based neurologic signature of physical

pain," *The New England Journal of Medicine*, vol. 368, no. 15, pp. 1388–1397, 2013.

[7] H. C. Fritz, J. H. McAuley, K. Wittfeld et al., "Chronic back pain is associated with decreased prefrontal and anterior insular gray matter: results from a population-based cohort study," *The Journal of Pain*, vol. 17, no. 1, pp. 111–118, 2016.

[8] A. Mouraux and G. D. Iannetti, "The search for pain biomarkers in the human brain," *Brain*, vol. 141, no. 12, pp. 3290–3307, 2018.

[9] K. T. Martucci and S. C. Mackey, "Neuroimaging of pain," *Anesthesiology*, vol. 128, no. 6, pp. 1241–1254, 2018.

[10] F. Cauda, K. Sacco, S. Duca et al., "Altered resting state in diabetic neuropathic pain," *PLoS One*, vol. 4, no. 2, article e4542, 2009.

[11] L. Weizman, L. Dayan, S. Brill et al., "Cannabis analgesia in chronic neuropathic pain is associated with altered brain connectivity," *Neurology*, vol. 91, no. 14, pp. e1285–e1294, 2018.

[12] M. N. Baliki, A. T. Baria, and A. V. Apkarian, "The cortical rhythms of chronic back pain," *The Journal of Neuroscience*, vol. 31, no. 39, pp. 13981–13990, 2011.

[13] R. Yu, R. L. Gollub, R. Spaeth, V. Napadow, A. Wasan, and J. Kong, "Disrupted functional connectivity of the periaqueductal gray in chronic low back pain," *Neuroimage Clin*, vol. 6, pp. 100–108, 2014.

[14] Y. Jiang, D. Oathes, J. Hush et al., "Perturbed connectivity of the amygdala and its subregions with the central executive and default mode networks in chronic pain," *Pain*, vol. 157, no. 9, pp. 1970–1978, 2016.

[15] S. L. Thorp, T. Suchy, and N. Vadivelu, "Functional connectivity alterations: novel therapy and future implications in chronic pain management," *Pain Physician*, vol. 21, no. 3, pp. E207–e214, 2018.

[16] M. Fillon, "Exploring the causes of chronic cancer pain and possible remedies," *CA: a Cancer Journal for Clinicians*, vol. 70, no. 2, pp. 75-76, 2020.

[17] O. Mioduszewski, T. Hatchard, Z. Fang et al., "Breast cancer survivors living with chronic neuropathic pain show improved brain health following mindfulness-based stress reduction: a preliminary diffusion tensor imaging study," *Journal of Cancer Survivorship*, vol. 14, no. 6, pp. 915–922, 2020.

[18] A. M. Smith, A. Leeming, Z. Fang et al., "Mindfulness-based stress reduction alters brain activity for breast cancer survivors with chronic neuropathic pain: preliminary evidence from resting-state fMRI," *Journal of Cancer Survivorship*, vol. 15, no. 4, pp. 518–525, 2021.

[19] D. Buehlmann, G. D. Ielacqua, J. Xandry, and M. Rudin, "Prospective administration of anti-nerve growth factor treatment effectively suppresses functional connectivity alterations after cancer-induced bone pain in mice," *Pain*, vol. 160, no. 1, pp. 151–159, 2019.

[20] D. Buehlmann, J. Grandjean, J. Xandry, and M. Rudin, "Longitudinal resting-state functional magnetic resonance imaging in a mouse model of metastatic bone cancer reveals distinct functional reorganizations along a developing chronic pain state," *Pain*, vol. 159, no. 4, pp. 719–727, 2018.

[21] C. Grefkes, S. Geyer, T. Schormann, P. Roland, and K. Zilles, "Human somatosensory area 2: observer-independent cytoarchitectonic mapping, interindividual variability, and population map," *NeuroImage*, vol. 14, no. 3, pp. 617–631, 2001.

[22] L. Fan, H. Li, J. Zhuo et al., "The human Brainnetome Atlas: a new brain Atlas based on connectional architecture," *Cerebral Cortex*, vol. 26, no. 8, pp. 3508–3526, 2016.

[23] B. L. Edlow, E. Takahashi, O. Wu et al., "Neuroanatomic connectivity of the human ascending arousal system critical to consciousness and its disorders," *Journal of Neuropathology and Experimental Neurology*, vol. 71, no. 6, pp. 531–546, 2012.

[24] Y. J. Dai, X. Zhang, Y. Yang et al., "Gender differences in functional connectivities between insular subdivisions and selective pain-related brain structures," *The Journal of Headache and Pain*, vol. 19, no. 1, p. 24, 2018.

[25] A. M. González-Roldán, J. L. Terrasa, C. Sitges, M. van der Meulen, F. Anton, and P. Montoya, "Age-related changes in pain perception are associated with altered functional connectivity during resting state," *Frontiers in Aging Neuroscience*, vol. 12, p. 116, 2020.

[26] S. Lautenbacher, "Experimental approaches in the study of pain in the elderly," *Pain Medicine*, vol. 13, Suppl 2, pp. S44–S50, 2012.

[27] C. Linnman, J. C. Beucke, K. B. Jensen, R. L. Gollub, and J. Kong, "Sex similarities and differences in pain-related periaqueductal gray connectivity," *Pain*, vol. 153, no. 2, pp. 444–454, 2012.

[28] J. L. Andersson, C. Hutton, J. Ashburner, R. Turner, and K. Friston, "Modeling geometric deformations in EPI time series," *NeuroImage*, vol. 13, no. 5, pp. 903–919, 2001.

[29] J. Lorenz, S. Minoshima, and K. L. Casey, "Keeping pain out of mind: the role of the dorsolateral prefrontal cortex in pain modulation," *Brain*, vol. 126, no. 5, pp. 1079–1091, 2003.

[30] E. B. Plow, A. Pascual-Leone, and A. Machado, "Brain stimulation in the treatment of chronic neuropathic and non-cancerous pain," *The Journal of Pain*, vol. 13, no. 5, pp. 411–424, 2012.

[31] F. Brighina, M. De Tommaso, F. Giglia et al., "Modulation of pain perception by transcranial magnetic stimulation of left prefrontal cortex," *The Journal of Headache and Pain*, vol. 12, no. 2, pp. 185–191, 2011.

[32] C. Strobel, S. Hunt, R. Sullivan, J. Y. Sun, and P. Sah, "Emotional regulation of pain: the role of noradrenaline in the amygdala," *Science China. Life Sciences*, vol. 57, no. 4, pp. 384–390, 2014.

[33] K. S. Meda, T. Patel, J. M. Braz et al., "Microcircuit mechanisms through which mediodorsal thalamic input to anterior cingulate cortex exacerbates pain-related aversion," *Neuron*, vol. 102, no. 5, pp. 944–959.e3, 2019.

[34] A. Yoshino, Y. Okamoto, K. Onoda et al., "Sadness enhances the experience of pain via neural activation in the anterior cingulate cortex and amygdala: an fMRI study," *NeuroImage*, vol. 50, no. 3, pp. 1194–1201, 2010.

[35] M. S. Prüß, A. Bayer, K. E. Bayer et al., "Functional brain changes due to chronic abdominal pain in inflammatory bowel disease: a case-control magnetic resonance imaging study," *Clinical and Translational Gastroenterology*, vol. 13, no. 2, article e00453, 2022.

[36] N. Kumar, T. F. Manning, and D. J. Ostry, "Somatosensory cortex participates in the consolidation of human motor memory," *PLoS Biology*, vol. 17, no. 10, article e3000469, 2019.

[37] A. Mentzelopoulos, K. Gkiatis, I. Karanasiou et al., "Chemotherapy-induced brain effects in small-cell lung cancer patients: a multimodal MRI study," *Brain Topography*, vol. 34, no. 2, pp. 167–181, 2021.

[38] M. Simó, X. Rifà-Ros, L. Vaquero et al., "Brain functional connectivity in lung cancer population: an exploratory study," *Brain Imaging and Behavior*, vol. 12, no. 2, pp. 369–382, 2018.

[39] X.-Z. Jia, N. Zhao, H.-M. Dong et al., "Small _P_ values may not yield robust findings: an example using REST-meta-PD," *Science Bulletin*, vol. 66, no. 21, pp. 2148–2152, 2021.

Hindawi
Disease Markers
Volume 2022, Article ID 5838104, 6 pages
https://doi.org/10.1155/2022/5838104

*Research Article*

# A Novel Mutation in the FYCO1 Gene Causing Congenital Cataract: Case Study of a Chinese Family

**Shuping Mei,[1,2] Jingwei Lin,[1,2] Zhen Liu,[1] and Cheng Li[1,2]**

[1]*Department of Ophthalmology, Xiang'an Hospital of Xiamen University, Eye Institute & Affiliated Xiamen Eye Center, School of Medicine, Xiamen University, Xiamen 361102, China*
[2]*Fujian Provincial Key Laboratory of Ophthalmology and Visual Science, School of Medicine, Xiamen University, Xiamen 361102, China*

Correspondence should be addressed to Zhen Liu; liuzhen3394@163.com and Cheng Li; cheng-li@xmu.edu.cn

Received 31 May 2022; Accepted 14 August 2022; Published 26 August 2022

Academic Editor: Pei-Wen Zhu



Congenital cataract is the most important global cause of visual impairment in children. Autosomal dominant and autosomal recessive inheritance account for the majority of the hereditary nonsyndromic congenital cataract. The function of FYCO1 gene is to guide the transport of the microtubule-directed vesicles. Mutations in the FYCO1 gene may cause cataracts. We reported a novel nonsense mutation in FYCO1 (c.1411C > T, P. R471 ∗), which could cause nonsyndrome autosomal recessive congenital cataract. We underwent an ophthalmology examination of all participants and collected blood samples from all participants and extracted genomic DNAs. By whole exome sequencing, we found that this family carried an unreported mutation in the FYCO1 gene: c.1411C > T, P. R471 ∗. Sanger sequencing was performed to verify the mutation. We used ITASSER and PYMOL to predict and compare the structure and function of the mutated proteins. Using SIFT software and referring to the relevant guidelines of ACMG, the mutation was determined to be pathogenic. The models suggested that the nonsense mutation p.R471∗ resulted in a profound disruption of the FYCO1 protein structure. This report expands the locus information of the FYCO1 mutations.

## 1. Introduction

Lens is one of the important refractive stroma in the eyeball [1]. The newborn lens fiber cells express the key proteins needed to realize the structure and transparency of the mature lens and completely eliminate the nucleus and all organelles, in order to ensure the normal function of the lens [2, 3]. Cataract is characterized by an opacity and protein degeneration of the lens. Human crystallin has three major protein components, including $\alpha$-crystallin, $\beta$-crystallin, and $\gamma$-crystallin. Among them, the most important crystallin is $\alpha$-crystallin, which is composed of A and B subunits [4–6]. A common feature of several cataracts is the misfolding of crystallin [7]. Thus, misfolding of crystallin can be an important cause of cataract [8].

Congenital cataract (CC) is the most important global cause of visual impairment in children. According to statistical analysis, about 1/4$^{th}$ of CCs are caused by genetic defects [9]. In the early stage of the fetal development, the disorder of protein metabolism in the lens affects the transparency of the embryonic lens and leads to the occurrence of CC. The increase of protein content in the lens worsens the microstructure of the lens and leads to the opacity of the lens [10]. To date, more than 50 different sites of CC have been identified [11]. Autosomal dominant and autosomal recessive inheritance account for the majority of the hereditary nonsyndromic CCs. X-linked recessive inheritance accounts for only a small fraction [12]. Nonsyndromic CC occurs in 1 to 6 out of every 10000 live births [13], of which about 1/3$^{rd}$ of the CC cases are familial [14]. In addition, about 70% of the cases are nonsyndromic and can only lead to lens damage [15]. The gene associated with nonsyndrome autosomal recessive CC (ARCC) includes EphA2 (gene ID1969, OMIM 176946) [16], GJA8 (gene ID2703, OMIM 600897) [17], FOXE3 (gene ID2301, OMIM 601094) [18], FYCO1 (gene ID 79443, OMIM 607182) [11, 19–21], GCNT2 (gene

ID2651, OMIM 600429) [22], AGK (gene ID 55750, OMIM 610345) [23], DNMBP (gene ID 23268, OMIM 611282) [24], and CRYBB1 (gene ID 1414, OMIM 600929) [25]. Numerous mutations have been reported in the FYCO1 gene, which result in loss of function of FYCO1, resulting in ARCC [19, 26].

In the present study, we report a novel mutation in the FYCO1 gene leading to congenital cataract in a Chinese family, using whole exon sequencing. Furthermore, the clinical features and treatment process of the case are described in detail.

## 2. Subjects and Methods

*2.1. Subjects.* The subject for the present study included a Chinese family with CC. The family consisted of two children with CC and their parents whose ocular presentations were normal (Figure 1(a)). The daughter was 18 years old. When she was 1 year old, she underwent a "binocular cataract extraction" because of "binocular congenital cataract." She was regularly reviewed after the operation, and she had not been implanted with intraocular lens and wore glasses for a long time. In 2021, after detailed ophthalmological examination and evaluation in the Xiang'an Hospital affiliated to Xiamen University, secondary intraocular lens implantation was performed in the left eye and right eye, respectively. The son was 10 years old, and his symptoms were the same as his sister. At the age of 1, he underwent a "binocular cataract extraction" because of "binocular congenital cataract." He was regularly reviewed after the operation, but had not been implanted with intraocular lens and wore glasses for a long time. In 2021, after detailed ophthalmological examination and evaluation in Xiang'an Hospital affiliated to Xiamen University, secondary intraocular lens implantation was performed in the left eye and right eye, respectively. The results of clinical examination and evaluation of the two patients are detailed in the table below (Table 1). The vitreous bodies of the two children presented a mild opacity (Figure 2). The parents' eye manifestations were normal, and there was no cataract or any other disease. Prior to the genetic testing, all participants voluntarily signed an informed consent form. This study was permitted by the Ethics Committee of Xiang'an Hospital of Xiamen University and was in line with the Helsinki Declaration.

*2.2. Methods*

*2.2.1. Extraction of DNA.* Blood samples were collected from the subjects after obtaining their informed consent. Total DNA extraction from blood was performed using the TIANamp Blood DNA kit (Tiangen Biotech Co., Ltd., China). The integrity of 2% agarose gel electrophoresis showed that the main band of DNA was obvious, and there was no degradation. Using NanoDrop1000 spectrophotometer (Thermo Fisher, USA) to detect the purity and concentration, the concentration of OD260/280 was 18-20, the concentration was greater than 20 ng/ul, and the total amount was greater than 500 ng.

*2.2.2. FYCO1 Mutation Detection.* In order to study the cause of the disease, we performed a whole exome sequencing (WES) on the daughter, son, and the father. Hieff NGS OnePot DNA Library Prep Kit (Yeasen Biotech Co., Ltd., Shanghai, China) was used for DNA enzyme fragmentation and whole genome library construction. The whole exon group library of the parents and their parents was constructed by hybridizing and capturing the whole exon group library with the Human Comprehensive Exome Panel (Twist Bioscience Co., Ltd., USA). The PE100 mode was used for double-terminal sequencing on the MGISEQ-T7 sequencing platform.

The BWA software was used to compare the hg19 version of the human genome reference sequence provided by UCSC, and the SNV and InDel mutations were found through the HaplotypeCaller of GATK. The pathogenicity was evaluated using the SIFT software (http://siftdna.org), and the variation was determined to be a pathogenic variation by referring to the relevant guidelines of the ACMG.

Sanger sequencing was performed on the sample obtained from the mother to confirm the pathogenic variant in the patients. Two primers (forward primer: GCCTCT TGCAGACTGGAGTT; reverse primer: ATGCAGGAGCT AGGGGAGAA) were used to verify the region of the gene mutation. Sanger sequencing was performed according to the standard protocol. PCR was performed by placing each 20 ng of human DNA in standard PCR buffer (50 $\mu$l). The PCR product was then purified using the Cwbio gel extraction kit (Cwbio, Beijing, China). Finally, an ABI 3500 Genetic Analyzer (Applied Biosystems, Foster City, CA) was used to sequence the DNA.

## 3. Results

*3.1. Mutational Analysis.* By WES, we found that this family carried an unreported mutation in the FYCO1 gene: c.1411 C > T, P. R471 ∗. The daughter and the son with CC exhibited homozygous mutations, while the normal parents exhibited heterozygous mutations. We also verified this mutation in FYCO1 by Sanger sequencing of the mother's DNA (c.1411C > T, p. R471∗) (Figure 1(c)). In addition, the aforesaid mutation was not found in the 1000Genome Project database and the GnomAD exon database.

The original amino acid (p.Arg471) of the mutated region was found to be well conserved. Using SIFT software (http://sift-dna.org) and referring to the relevant guidelines of ACMG, the mutation was determined to be pathogenic. From this point of view, the observed FYCO1 mutation (c.1411C > T, p. R471 ∗) is highly likely to be a pathogenic mutation.

*3.2. Protein Structures.* To investigate the potential harm of this FYCO1 protein mutation, we modeled this variant using some software. We use ITASSER (https://zhanggroup.org/I-TASSER/) [27–29] and PYMOL (https://pymol.org/2/) to predict and compare the structure and function of the mutated proteins. The models suggested that the nonsense mutation p.R471∗ resulted in a profound disruption of the protein structure (Figure 3).

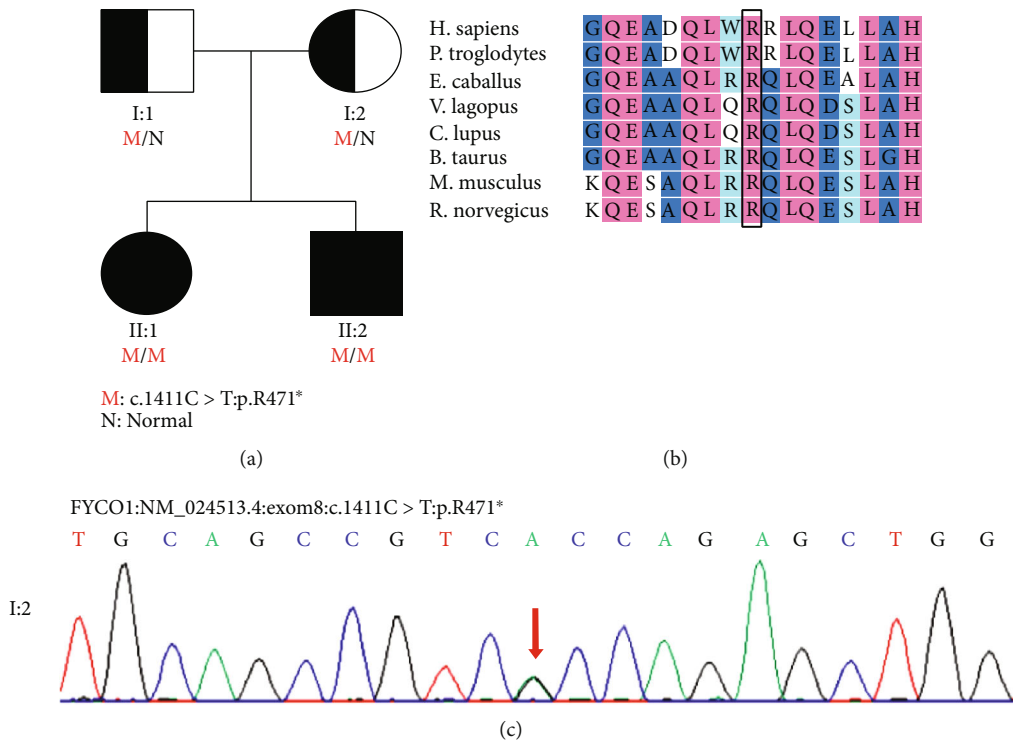


Figure 1: Family history and genomic analysis. (a) Detailed family history. The daughter and son with congenital cataracts were homozygous mutations (c.1411C > T: p.R471∗). The parents carried heterozygous mutations without any symptoms. (b) Evolutionary conservation of the altered amino acid residues. (c) Sanger sequencing of the mother's DNA. Mutation validation results showed that the sequence on the template chain: G was replaced by A. This is equivalent to C on the coding chain being replaced by T.

Table 1: Specialist examination of two patients.

| Patient | Daughter | | Son | |
|---|---|---|---|---|
| | OD | OS | OD | OS |
| Age (years) | 18 | | 11 | |
| Age when the lens removed (years) | 1 | | 1 | |
| Correct vision | 0.3 | 0.8 | 0.15 | 0.5 |
| Intraocular pressure (mmHg) | 17 | 17 | 15 | 18 |
| Pupil position | Up | Centre | Centre | Centre |
| Pupil shape | Not round | Round | Round | Round |
| Pupillary diameter (mm) | 2 | 3 | 3 | 3 |
| Reflection on light | Dullness | Dullness | Dullness | Dullness |
| Corneal endothelial cells (/mm$^2$) | 3984 | 3471 | 3056 | 3156 |
| Lens | Lacking | Lacking | Lacking | Lacking |
| Retina | Normal | Normal | Normal | Normal |
| Vitreous body | Mild opacity | Mild opacity | Mild opacity | Mild opacity |
| Eyeball | Normal | Normal | Horizontal tremor | Horizontal tremor |
| Eye axis (mm) | 25.05 | 22.88 | 23.52 | 22.86 |

*3.3. Clinical Treatment.* The daughter was 18 years old in the course of this study. When she was 1 years old, she underwent a "binocular cataract extraction" because of "binocular congenital cataract." She was regularly reviewed after the operation, and she had not been implanted with intraocular lens and wore glasses for a long time. In 2021, after detailed ophthalmological examination and evaluation at the Xiang'an Hospital affiliated to the Xiamen University, secondary intraocular lens implantation was performed in the left eye and the right eye, respectively, and the postoperative visual acuity recovered well. Her brother was 10 years old in course of the study, and his symptoms were the same as his sister. At the age of 1, he underwent a "binocular cataract extraction" because of "binocular congenital cataract." After

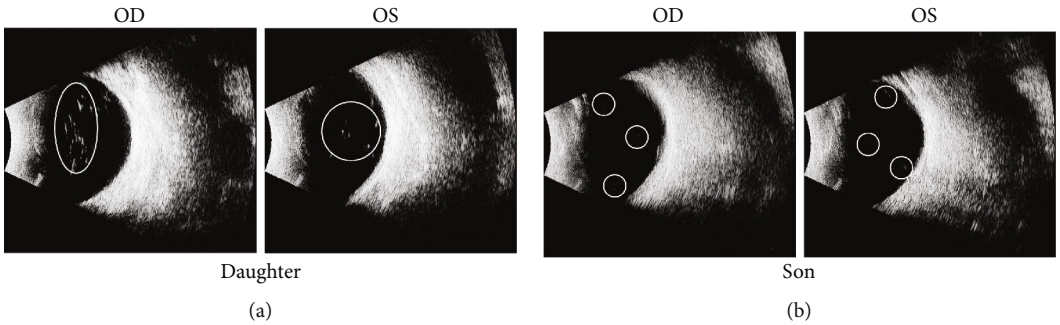


Figure 2: Ocular ultrasound images. (a) Vitreous bodies with mild opacity of the daughter. (b) Vitreous bodies with mild opacity of the son. The daughter's vitreous opacity was more pronounced and none of them found the lens.

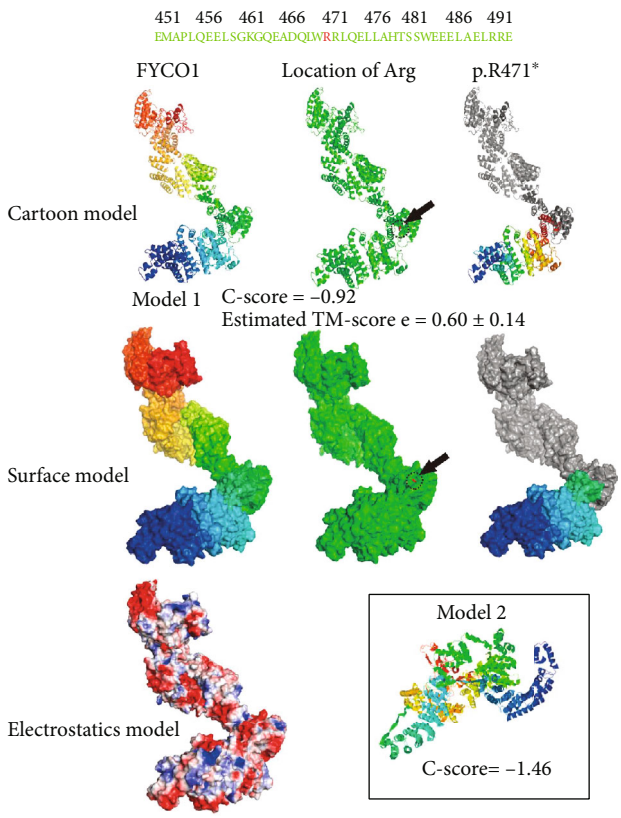


Figure 3: 3D-structure model of the variant (The FYCO1 protein structure is shown in different color. The location of the mutation p.R471∗ is marked in red in the green color scheme. The protein structure disruption caused by the nonsense mutation p.R471∗ is shown in gray. The models are predicted by I-TASSER (include model 1 and model 2). C-score is typically in the range of [-5, 2], where a C-score of a higher value signifies a model with a higher confidence. A $TM-score > 0.5$ indicates a model of correct topology (model 1 $C-score = -0.92$; model 2 $C-score = -1.46$; model 1 $TM-score = 0.60 \pm 0.14$)).

regular follow-up, he was not implanted with an intraocular lens and wore glasses for a long time. In 2021, after detailed ophthalmological examination and evaluation at the Xian-g'an Hospital, secondary intraocular lens implantation was performed in the left eye and the right eye, respectively, and the postoperative visual acuity recovered well.

## 4. Conclusions

FYCO1 has a PI (3) P-binding protein and a Rab7 effector protein. Studies have shown that its function is to guide the transport of the microtubule-directed vesicles. And immunofluorescence staining shows that FYCO1 is localized to autophagosomes [30]. The longest region in the structure of FYCO1 is the coiled-coil region, where most of the mutations occur. In one side of the coiled-coil region lies the RUN domain and three regions in the other side, including FYVE, LIR, and GOLD [31].

After the formation of autophagosome, the adventitia of autophagosome fuses immediately with the lysosome to form autolysosome. Rab7 plays an important role in this process [32, 33]. Rab7 recruits FYCO1 in the formation of the autophagosome [34]. As Rab7 is bound to GTP, FYCO1 preferentially interacts with it [19]. FYCO1 has also been shown to bind to the outer membrane of the autophagosome through its FYVE domain. Some studies have proposed that autophagosomes are connected to the microtubule motor proteins through FYCO1, enabling a smooth autophagosome transport. Deletion of the FYCO1 leads to autophagosome aggregation [26].

Some other researchers believe that FYCO1 directly interacts with $\alpha$ A-and $\alpha$ B-crystallin, which are the main components of the lens. Using FYCO1 knockout mice, it was found that increased $\alpha$A- and $\alpha$B-crystallin precipitates in the lenses. The findings suggest that normal FYCO1 function may be linked to the autolysosomes, wherein the damaged $\alpha$ crystal proteins are transported and degraded. Therefore, when FYCO1 is mutated, it cannot perform its normal function, and the damaged $\alpha$-crystallin cannot be degraded, which eventually leads to the cataract [21]. From this point of view, the function of FYCO1 is very important, as its mutation causes cataract, thereby affecting people's lives.

In this study, both the daughter and son of this family suffered from CC and underwent "binocular cataract extraction" at the age of one year. They were reexamined regularly after operation, but no intraocular lens was implanted and wore glasses for a long time. Later, a two-stage intraocular lens implantation was performed in the left eye and the right eye, and the postoperative visual acuity was improved. The lens and other eye tissue functions of their parents were

normal. Therefore, we speculate that the CC in this family may be a nonsyndromic autosomal recessive disease. After sequencing the whole exon group of the family, we found a new FYCO1 gene mutation (c.1411C > T, p. R471 ∗). It resulted in the mutation of the arginine in the coiled-coil domain to a stop codon, resulting in a disturbing change in the protein structure of FYCO1. The parents of the patients carried heterozygous mutations without any symptoms, while the two children with CCs were homozygous mutations. This result is consistent with our conjecture.

Our study proves that FYCO1 is closely related to the occurrence of CC. This report expands the locus information of the FYCO1 mutations and can be helpful in an accurate diagnosis of CC, so as to better prevent and treat it.

## Data Availability

The data that support the findings of this study are available on request from the corresponding author, C.L.

## Conflicts of Interest

The authors declare no conflicts of interest.

## Authors' Contributions

C.L. performed the study conceptualization; resources; data curation; and writing the original manuscript draft, review, and editing. Z.L. contributed to the study design, resources, and visualization. S.M. performed the data acquisition and curation. J.L. performed the data analysis and writing the original manuscript draft. Shuping Mei and Jingwei Lin contributed equally to this work.

## Acknowledgments

We thank all subjects for their involvement and cooperation. This study was supported in part by grants from The National Key R&D Program of China (nos. 2020YFA0908100 and 2018YFA0107301), the National Natural Science Foundation of China (nos. 82070931, 81770891, and 82000936), and the Huaxia Translational Medicine Fund for Young Scholars (no. 2017-A-001).

## References

[1] A. Tardieu, "α -Crystallin quaternary structure and interactive properties control eye lens transparency," *International Journal of Biological Macromolecules*, vol. 22, no. 3-4, pp. 211–217, 1998.

[2] S. Bassnett, Y. Shi, and G. F. Vrensen, "Biological glass: structural determinants of eye lens transparency," *Philosophical Transactions of the Royal Society of London. Series B, Biological Sciences*, vol. 366, no. 1568, pp. 1250–1264, 2011.

[3] A. Sue Menko, "Lens epithelial cell differentiation," *Experimental Eye Research*, vol. 75, no. 5, pp. 485–490, 2002.

[4] U. P. Andley, "The lens epithelium: focus on the expression and function of the α-crystallin chaperones," *The International Journal of Biochemistry & Cell Biology*, vol. 40, no. 3, pp. 317–323, 2008.

[5] U. P. Andley, "Crystallins in the eye: function and pathology," *Progress in Retinal and Eye Research*, vol. 26, no. 1, pp. 78–98, 2007.

[6] X. Wang, C. M. Garcia, Y. B. Shui, and D. C. Beebe, "Expression and regulation of alpha-, beta-, and gamma-crystallins in mammalian lens epithelial cells," *Investigative Ophthalmology & Visual Science*, vol. 45, no. 10, pp. 3608–3619, 2004.

[7] K. L. Moreau and J. A. King, "Protein misfolding and aggregation in cataract disease and prospects for prevention," *Trends in Molecular Medicine*, vol. 18, no. 5, pp. 273–282, 2012.

[8] X. J. Chen, L. D. Hu, K. Yao, and Y. B. Yan, "Lanosterol and 25-hydroxycholesterol dissociate crystallin aggregates isolated from cataractous human lens via different mechanisms," *Biochemical and Biophysical Research Communications*, vol. 506, no. 4, pp. 868–873, 2018.

[9] X. Wu, E. Long, H. Lin, and Y. Liu, "Prevalence and epidemiological characteristics of congenital cataract: a systematic review and meta-analysis," *Scientific Reports*, vol. 6, no. 1, p. 28564, 2016.

[10] J. Yi, J. Yun, Z. K. Li, C. T. Xu, and B. R. Pan, "Epidemiology and molecular genetics of congenital cataracts," *International Journal of Ophthalmology*, vol. 4, no. 4, pp. 422–432, 2011.

[11] N. A. Barashkov, F. A. Konovalov, T. V. Borisova et al., "Autosomal recessive cataract (CTRCT18) in the Yakut population isolate of Eastern Siberia: a novel founder variant in the *FYCO1* gene," *European Journal of Human Genetics*, vol. 29, no. 6, pp. 965–976, 2021.

[12] A. Shiels, T. M. Bennett, and J. F. Hejtmancik, "Cat-map: putting cataract on the map," *Molecular Vision*, vol. 16, pp. 2007–2015, 2010.

[13] S. R. Lambert and A. V. Drack, "Infantile cataracts," *Survey of Ophthalmology*, vol. 40, no. 6, pp. 427–458, 1996.

[14] A. Foster, "Cataract–a global perspective: output, outcome and outlay," *Eye*, vol. 13, no. 3, pp. 449–453, 1999.

[15] J. F. Hejtmancik, "Congenital cataracts and their molecular genetics," *Seminars in Cell & Developmental Biology*, vol. 19, no. 2, pp. 134–149, 2008.

[16] H. Kaul, S. A. Riazuddin, M. Shahid et al., "Autosomal recessive congenital cataract linked to EPHA2 in a consanguineous Pakistani family," *Molecular Vision*, vol. 16, pp. 511–517, 2010.

[17] S. P. Ponnam, K. Ramesha, S. Tejwani, B. Ramamurthy, and C. Kannabiran, "Mutation of the gap junction protein alpha 8 (GJA8) gene causes autosomal recessive cataract," *Journal of Medical Genetics*, vol. 44, no. 7, article e85, 2007.

[18] S. Y. Khan, S. Vasanth, F. Kabir et al., "*FOXE3* contributes to Peters anomaly through transcriptional regulation of an autophagy-associated protein termed DNAJB1," *Nature Communications*, vol. 7, no. 1, p. 10953, 2016.

[19] J. Chen, Z. Ma, X. Jiao et al., "Mutations in *FYCO1* cause autosomal-recessive congenital cataracts," *American Journal of Human Genetics*, vol. 88, no. 6, pp. 827–838, 2011.

[20] H. Iqbal, S. Y. Khan, L. Zhou et al., "Mutations in *FYCO1* identified in families with congenital cataracts," *Molecular Vision*, vol. 26, pp. 334–344, 2020.

[21] K. Satoh, Y. Takemura, M. Satoh, K. Ozaki, and S. Kubota, "Loss of FYCO1 leads to cataract formation," *Scientific Reports*, vol. 11, no. 1, p. 13771, 2021.

[22] E. Pras, J. Raz, V. Yahalom et al., "A nonsense mutation in the glucosaminyl (N-acetyl) transferase 2 gene (GCNT2): association with autosomal recessive congenital cataracts,"

*Investigative Ophthalmology & Visual Science*, vol. 45, no. 6, pp. 1940–1945, 2004.

[23] M. A. Aldahmesh, A. O. Khan, J. Y. Mohamed, M. H. Alghamdi, and F. S. Alkuraya, "Identification of a truncation mutation of acylglycerol kinase (AGK) gene in a novel autosomal recessive cataract locus," *Human Mutation*, vol. 33, no. 6, pp. 960–962, 2012.

[24] M. Ansar, H. L. Chung, R. L. Taylor et al., "Bi-allelic loss-of-function variants in *DNMBP* cause infantile cataracts," *American Journal of Human Genetics*, vol. 103, no. 4, pp. 568–578, 2018.

[25] D. Cohen, U. Bar-Yosef, J. Levy et al., "Homozygous CRYBB1 deletion mutation underlies autosomal recessive congenital cataract," *Investigative Ophthalmology & Visual Science*, vol. 48, no. 5, pp. 2208–2213, 2007.

[26] S. Pankiv, E. A. Alemu, A. Brech et al., "FYCO1 is a Rab7 effector that binds to LC3 and PI3P to mediate microtubule plus end-directed vesicle transport," *The Journal of Cell Biology*, vol. 188, no. 2, pp. 253–269, 2010.

[27] W. Zheng, C. Zhang, Y. Li, R. Pearce, E. W. Bell, and Y. Zhang, "Folding non-homologous proteins by coupling deep-learning contact maps with I-TASSER assembly simulations," *Methods*, vol. 1, no. 3, p. 100014, 2021.

[28] C. Zhang, P. L. Freddolino, and Y. Zhang, "COFACTOR: improved protein function prediction by combining structure, sequence and protein-protein interaction information," *Nucleic Acids Research*, vol. 45, no. W1, pp. W291–w299, 2017.

[29] J. Yang and Y. Zhang, "I-TASSER server: new development for protein structure and function predictions," *Nucleic Acids Research*, vol. 43, no. W1, pp. W174–W181, 2015.

[30] J. Ma, C. Becker, C. Reyes, and D. M. Underhill, "Cutting edge: FYCO1 recruitment to dectin-1 phagosomes is accelerated by light chain 3 protein and regulates phagosome maturation and reactive oxygen production," *Journal of Immunology*, vol. 192, no. 4, pp. 1356–1360, 2014.

[31] A. Rose, S. J. Schraegle, E. A. Stahlberg, and I. Meier, "Coiled-coil protein composition of 22 proteomes–differences and common themes in subcellular infrastructure and traffic control," *BMC Evolutionary Biology*, vol. 5, no. 1, p. 66, 2005.

[32] M. G. Gutierrez, D. B. Munafó, W. Berón, and M:. I. Colombo, "Rab7 is required for the normal progression of the autophagic pathway in mammalian cells," *Journal of Cell Science*, vol. 117, no. 13, pp. 2687–2697, 2004.

[33] S. Jäger, C. Bucci, I. Tanida et al., "Role for Rab7 in maturation of late autophagic vacuoles," *Journal of Cell Science*, vol. 117, no. 20, pp. 4837–4848, 2004.

[34] S. Pankiv and T. Johansen, "FYCO1: linking autophagosomes to microtubule plus end-directing molecular motors," *Autophagy*, vol. 6, no. 4, pp. 550–552, 2010.

Hindawi
Disease Markers
Volume 2022, Article ID 9701047, 14 pages
https://doi.org/10.1155/2022/9701047

*Research Article*

# miR-33a-5p Targets RAP2A to Mediate the Sensitivity of Gastric Cancer Cells to 5-FU

**Gang Ti,[1] Zongliang Guo,[2] Lili Li,[3] Yongqiang Lv,[4] Bin Yang,[5] Jian Wang,[5] Rui Guo,[5] Yunqing Chen,[5] Debin Meng,[2] and Feng Li[6]**

[1]*Department of medical record, Shanxi Bethune Hospital, Shanxi Academy of Medical Sciences, Tongji Shanxi Hospital, Third Hospital of Shanxi Medical University, Taiyuan, 030032 Shanxi, China*
[2]*Department of General Surgery, Shanxi Province Cancer Hospital/Shanxi Hospital Affiliated to Cancer Hospital, Chinese Academy of Medical Sciences/Cancer Hospital Affiliated to Shanxi Medical University, Taiyuan 030012, China*
[3]*Department of Radiotherapy Abdominopelvic, Shanxi Province Cancer Hospital/Shanxi Hospital Affiliated to Cancer Hospital, Chinese Academy of Medical Sciences/Cancer Hospital Affiliated to Shanxi Medical University, Taiyuan 030012, China*
[4]*Department of Quality Control, Shanxi Province Cancer Hospital/Shanxi Hospital Affiliated to Cancer Hospital, Chinese Academy of Medical Sciences/Cancer Hospital Affiliated to Shanxi Medical University, Taiyuan 030012, China*
[5]*Surgical VIP, Shanxi Cancer Hospital, Affiliated Cancer Hospital of Shanxi Medical University, Taiyuan 030012, China*
[6]*Department of Cell Biology, Shanxi Province Cancer Hospital/Shanxi Hospital Affiliated to Cancer Hospital, Chinese Academy of Medical Sciences/Cancer Hospital Affiliated to Shanxi Medical University, Taiyuan 030012, China*

Correspondence should be addressed to Yunqing Chen; chenmao1965@sina.com, Debin Meng; sophie1019@163.com, and Feng Li; lifenglover@sina.com

Received 27 May 2022; Accepted 27 July 2022; Published 22 August 2022

Academic Editor: Yi Shao



*Objective*. The objective of this study is to explore the effects of microRNA-33a-5p (miR-33a-5p)-ras-related protein Rap-2a (RAP2A) on biological functions of gastric cancer (GC) and to find the potential functional mechanism. *Methods*. We measured the miR-33a-5p expression in 30 GC tissues and cellular level and 30 adjacent normal tissues as control. Besides, the expression of miR-33a-5p was checked at cell level as well. To screen the possible targets of miR-33a-5p, prediction software was used and gene RAP2A attracted our attention. Through a series of experiments including real-time polymerase chain reaction (qRT-PCR), luciferase assay, and western blotting (WB), we verified RAP2A as a potential target of miR-33a-5p. The impacts of miR-33a-5p and RAP2A on biological functions of GC cell lines (BGC-823 and MGC-803) were analyzed by subsequent experiments. Cell invasion was tested by invasion assays. Cell proliferation was measured by cell counting kit-8 (CCK-8) assay. Cell clone was measured by clone formation assays. Finally, the expression of RAP2A protein was analyzed by WB assay. *Results*. We found miR-33a-5p was expressed lowly in GC tissues and cells. Overexpression of miR-33a-5p in BGC-823 and MGC-803 cells greatly inhibited the cell invasion and colony number. Furthermore, compared to sh-control (shControl), RAP2A knockdown (sh-RAP2A/shRAP2A) raised the sensitivity of GC cells to 5-FU significantly, characterized as reducing cell apoptosis. *Conclusions*. The expression of miR-33a-5p was lower in GC cell lines and tissues obviously, indicating that miR-33a-5p served as the antitumor gene in GC. The expression of RAP2A regulated negatively the sensitivity of GC cells to 5-FU. According to our in vitro experiments, miR-33a-5p/RAP2A was likely to become a new therapeutic target for GC.

## 1. Introduction

Gastric cancer (GC) is one of the most common malignant tumors in the world and the third leading cause of cancer-associated mortality worldwide [1]. The early diagnosis and treatment rate of GC are not high, both less than 10% in China [2]. However, the incidence and mortality of GC remain high. The 5-year survival rate is not optimistic [3]. Previous studies showed that GC development was relevant to many other factors, including familial inheritance, living

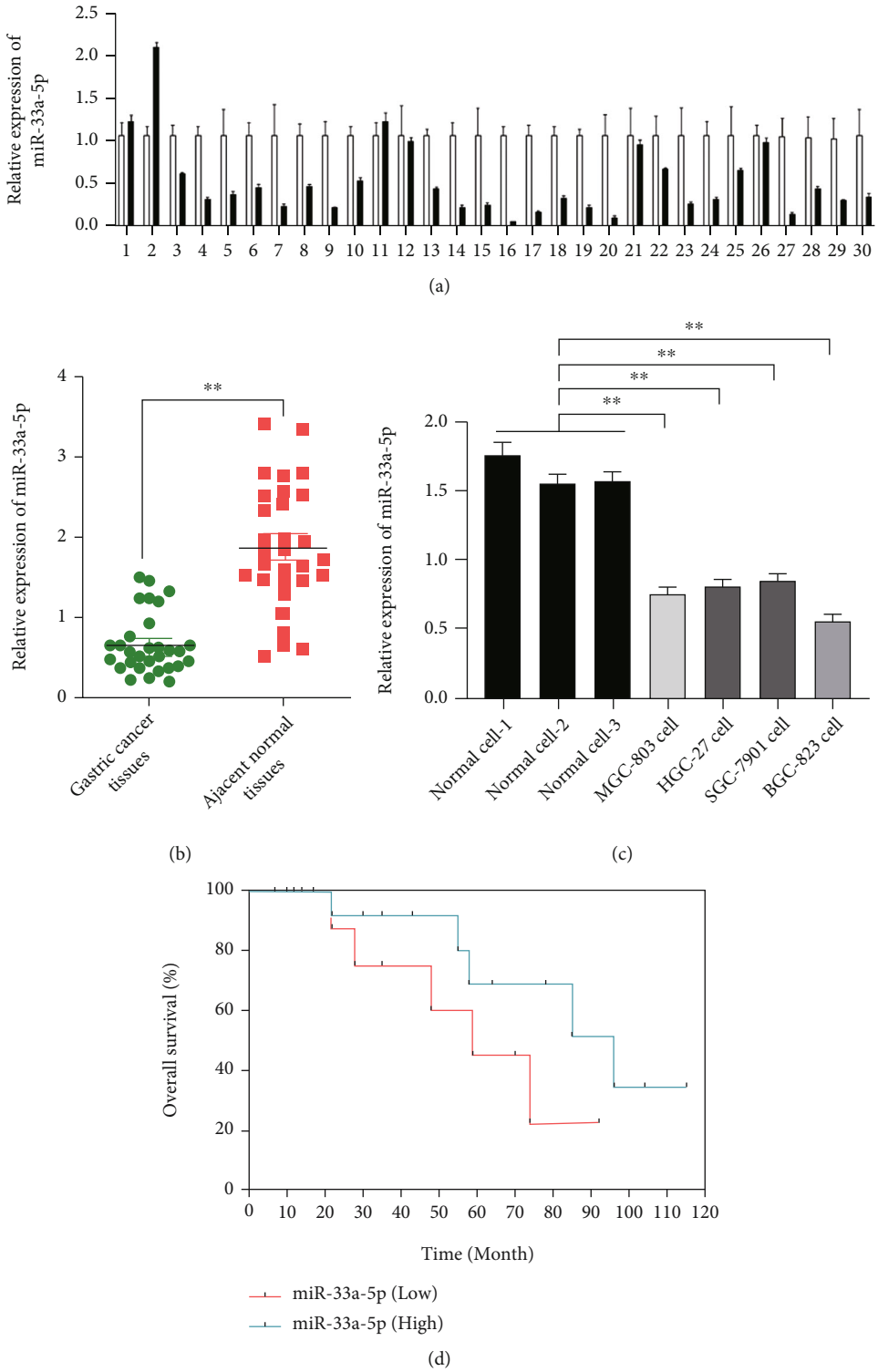


Figure 1: Decreased expression of miR-33a-5p in GC Samples. (a) Relative expression of miR-33a-5p in GC tissues and adjacent normal tissues pairs. (b) Mean relative expression level of miR-33a-5p in GC tissues with respect to adjacent normal tissues. (c) Endogenous relative expression level of miR-33a-5p in GC cell lines (MGC-803, BGC-823, HGC-27, and SGC-7901) and normal cells. (d) Survival analysis for miR-33a-5p in a clinical data set. miRNA levels were normalized, mean + / – SEM is shown for (a)–(c). $^{*}p < 0.05$, $^{**}p < 0.01$, *t*-test.

habits, Helicobacter pylori infection, and other pathogenic reasons such as chronic atrophic gastritis and environmental factor [4, 5]. Due to the lack of specific symptoms in the early stage of GC, it has already advanced to the middle and late stages when detected, which is the main reason for the poor prognosis of most patients [6]. Therefore, there is

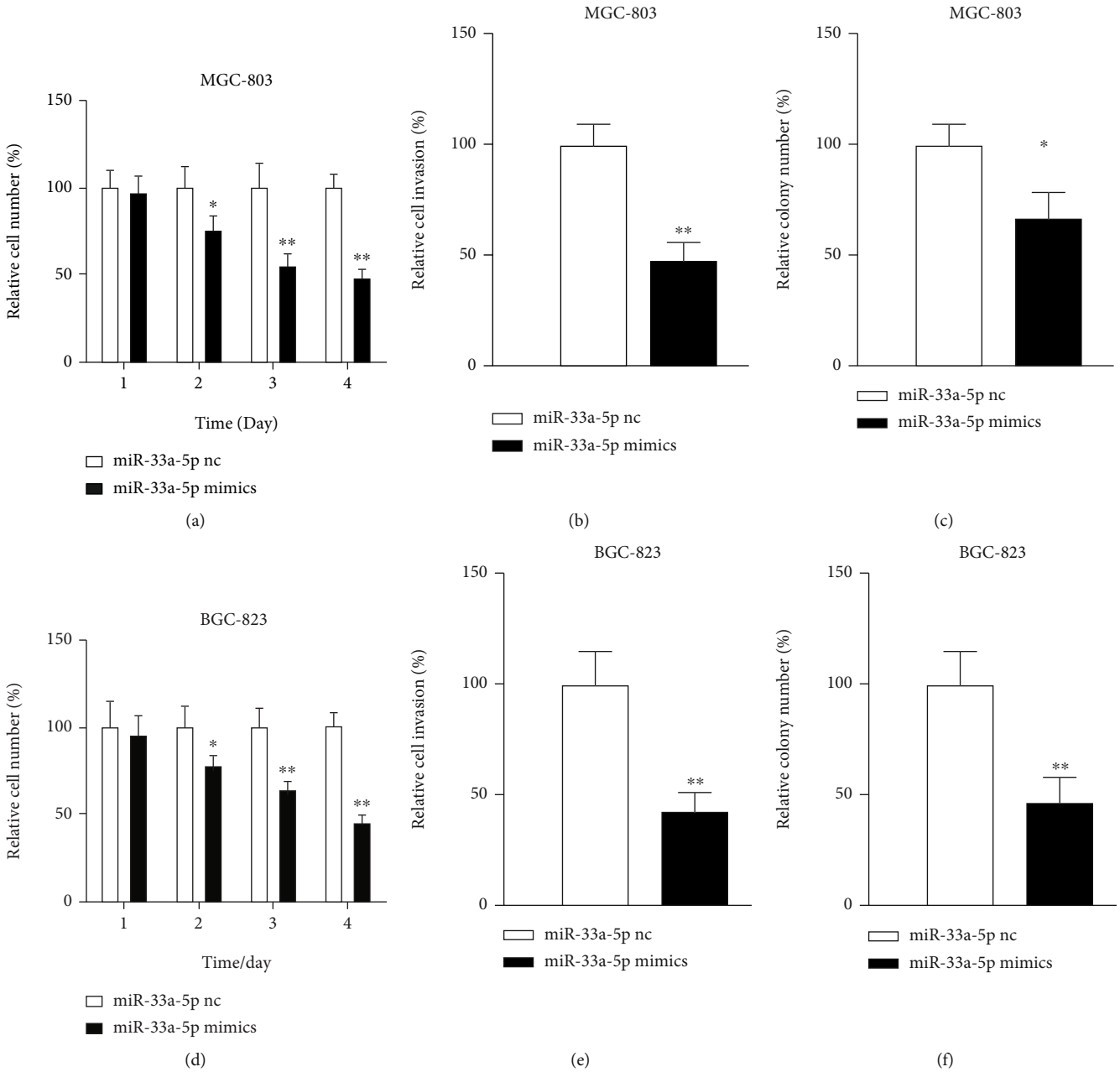


Figure 2: Functional impact of miR-33a-5p mimics. (a) Proliferation, (b) invasion, and (c) anchorage independent growth of MGC-803 cells transfected with miR-33a-5p mimic. (d) Proliferation, (e) invasion, and (f) anchorage independent growth of BGC-823 cells transfected with miR-33a-5p mimic. Mean + / – SEM is shown. $^{*}p < 0.05$, $^{**}p < 0.01$; $t$-test.

an urgent need to find new diagnostic and therapeutic approaches to reduce GC-related mortality and improve patient clinical outcomes.

microRNAs (miRNAs) have 18-22 nucleotides and not encode RNA. But they can regulate the expression through the 3′UTR region of complementary mRNA [7, 8]. Many studies have found that miRNAs are involved in regulating many biological processes such as cell growth and apoptosis [9, 10]. In particular, differential expression of miRNA is involved in the development of some tumors [11]. For example, miR-33a-5p blocks the progression of esophageal cancer by KK1-Wnt/$\beta$-catenin axis [12]. PD-L1 inhibitor can regulate the miR-33a-5p/PTEN axis and increase the sensitivity of glioblastoma to radiation [13]. Meanwhile, Yanfen Lian et al. found that miR-33a-5p-RAP2A inhibited pancreatic duct adenocarcinoma cell growth. Furthermore, Dan Lin et al. and Qiong Wu et al. explored that the expression of miR-33a-5p was descending in GC. However, how it regulates drug resistance of target genes was rarely studied [14, 15].

Rap2A is a member of the RAS oncogene family. RAP2A gene, located at 13Q34, contains a 549 bp open reading frame with a molecular weight of 20,434 and can encode 183 amino acids [4]. Studies have revealed that RAP2A can

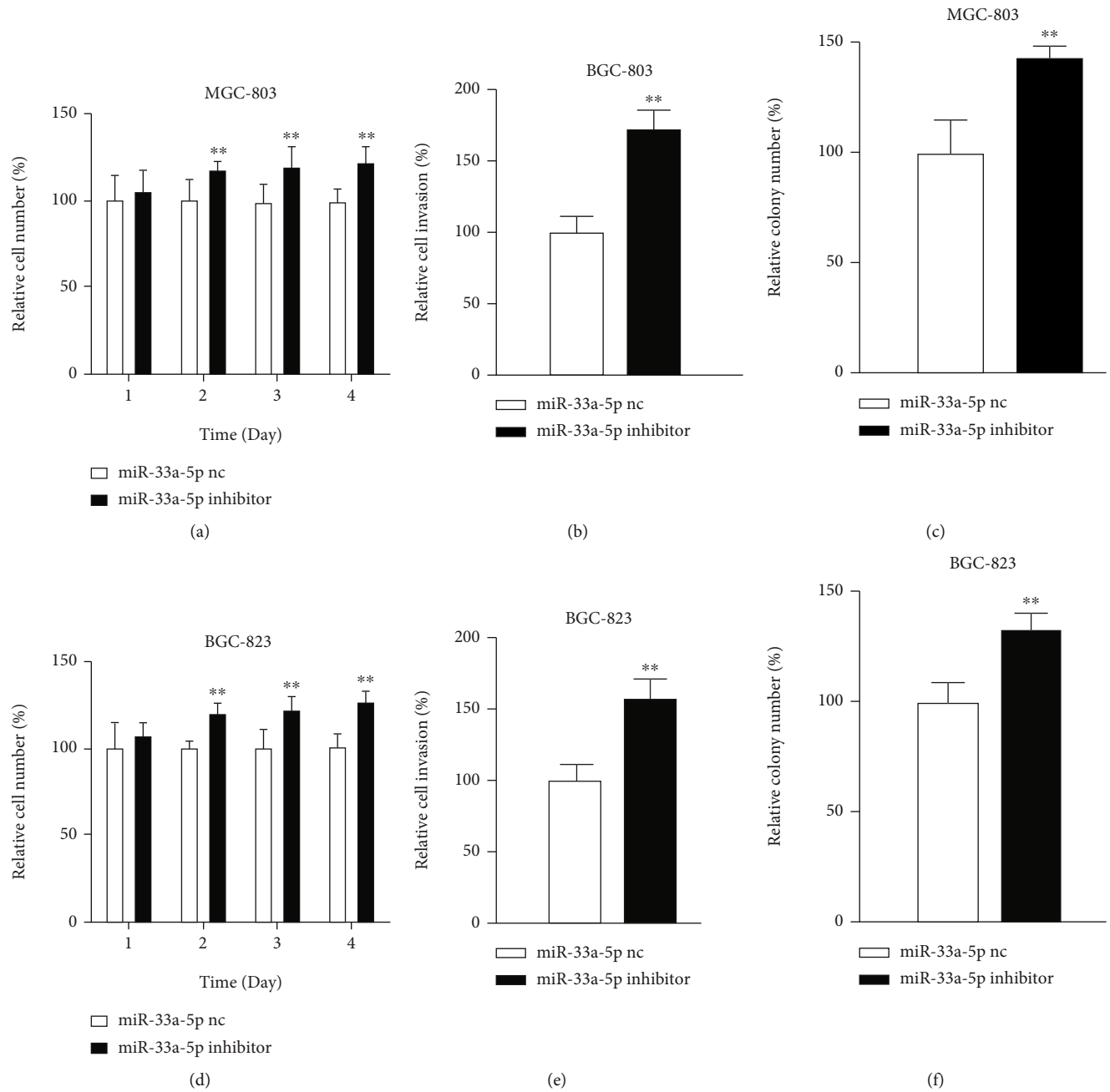


Figure 3: Functional impact of miR-33a-5p inhibition. (a) Proliferation, (b) invasion, and (c) anchorage independent growth of MGC-803 cells transfected with miR-33a-5p inhibitor. (d) Proliferation, (e) invasion, and (f) anchorage independent growth of BGC-823 cells transfected with miR-33a-5p inhibitor. Mean + / – SEM is shown. $^{*}p < 0.05$, $^{**}p < 0.01$; $t$-test.

regulate cell migration, cytoskeletal recombination, and other cellular processes [5–7]. In addition, it has been reported that RAP2A is upregulated in prostate cancer, thyroid cancer, nasopharyngeal cancer, and other human cancers [8–10]. However, the expression of RAP2A in GC has not been reported, except for one study that detected high expression of Rap2A in human hepatoblastoma HepG2 cells.

The relationship between GC and ncRNA has been proved by many studies, but the function and mechanism still needs to further explore. MiR-33a-5p has a regulatory role in many tumors, including GC. Thus, our study speculated the occurrence and development of GC by regulating miR-33a-5p/RAP2A and verify it through relevant experiments. The flow cytometry and CCK8 assay confirmed that miR-33a-5p can inhibit GC cell apoptosis and proliferation. Furthermore, dual luciferase reporter assay confirmed that RAP2A may target miR-33a-5p. RAP2A was upregulated in GC and modulated GC cells proliferation and apoptosis through p-JAK and p-STAT3 proteins. Therefore, we suspected whether miR-33a-5p would also impact on the prognosis of GC patients and the sensitivity to 5-FU through the RAP2A/JAK/STAT3 pathway.

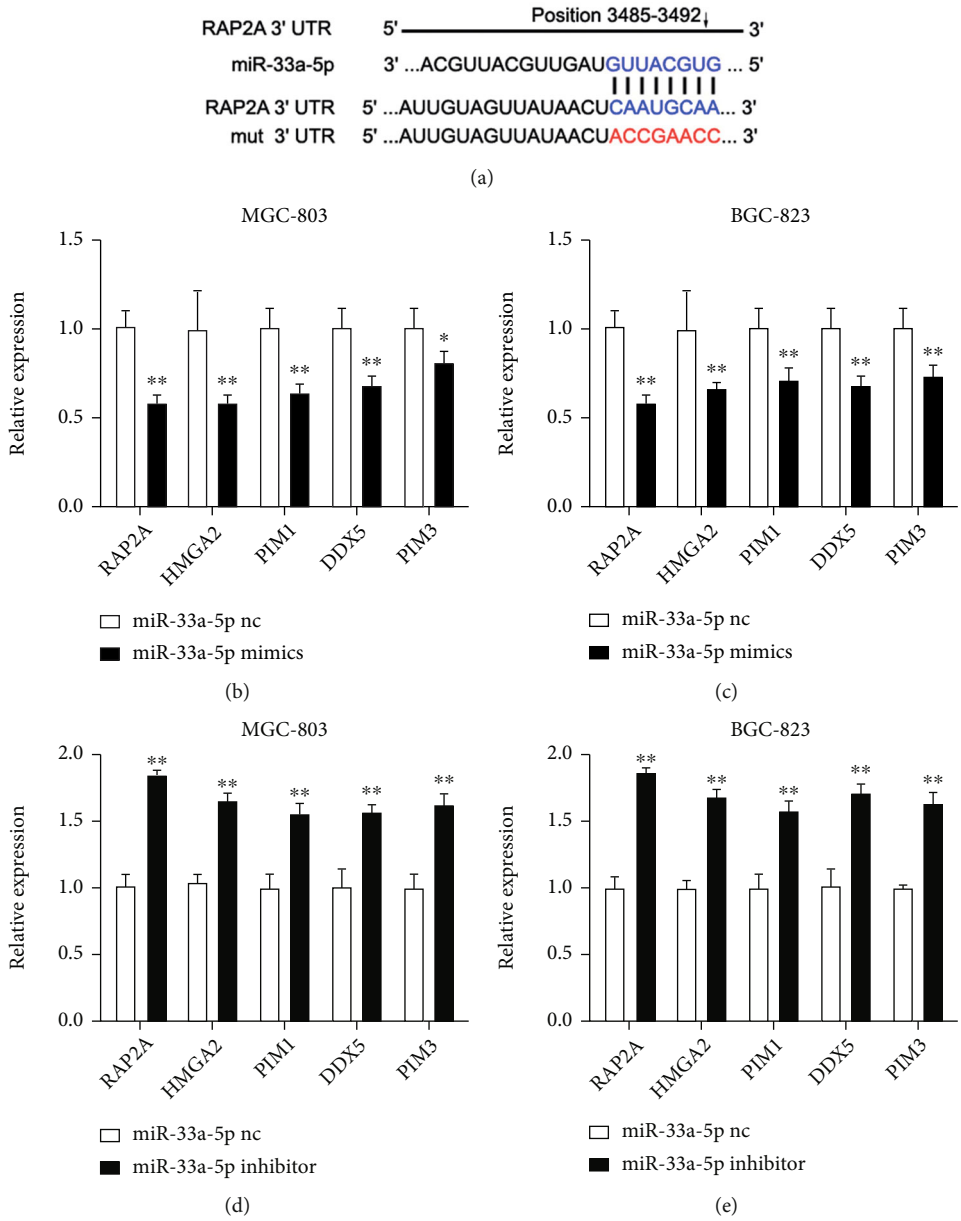


Figure 4: MiR-33a-5p target genes. (a) The target-map representation of relationship between in miR-33a-5p and RAP2A. (b) QRT-PCR validation of selected potential miR-33a-5p target genes in miR-33a-5p mimics transfected (b) MGC-803 and (c) BGC-823 cells and in miR-33a-5p inhibitor transfected (d) MGC-803 and (e) BGC-823 cells compared to the control cells. mRNA levels were normalized to GAPDH. Mean + / – SEM is shown for (b)–(e). $^{*}p < 0.05$, $^{**}p < 0.01$; $t$-test.

## 2. Materials and Methods

*2.1. Clinical Samples and Cell Lines.* GC tissues and adjacent normal tissues from 30 patients were acquired at the Shanxi Cancer Hospital from 2019 to 2020. All patients signed informed consent, and the correlation sample experiments were consented by the Ethics Committee of the Shanxi Cancer Hospital.

The human SGC-7901, HGC-27, BGC-823, and MGC-803 cell lines were obtained from ATCC. They were cultured in complete medium (DMEM with 10% fetal bovine serum; Hyclone). All cells need to be replaced periodically, expand culture and cell cryopreservation, and screened for mycoplasma.

*2.2. RNA Extraction and qQT-PCR.* Total RNA was extracted by TRIZOL method (Invitrogen, NY) and converted to cDNA using the TaqMan Reverse Transcription kit (Applied Biosystems, CA) in a thermal cycler at 16°C for 25~30 minutes, 41°C for 25~30 minutes, and 85°C for 10 minutes. qRT-PCR was using the SYBR Green PCR Mix (Life Technologies, CA) at 95°C for 13 minutes, 40 cycles at 95°C for 17 seconds, and 60°C for 2 minutes. These reference genes (GAPDH) were used as control expression.

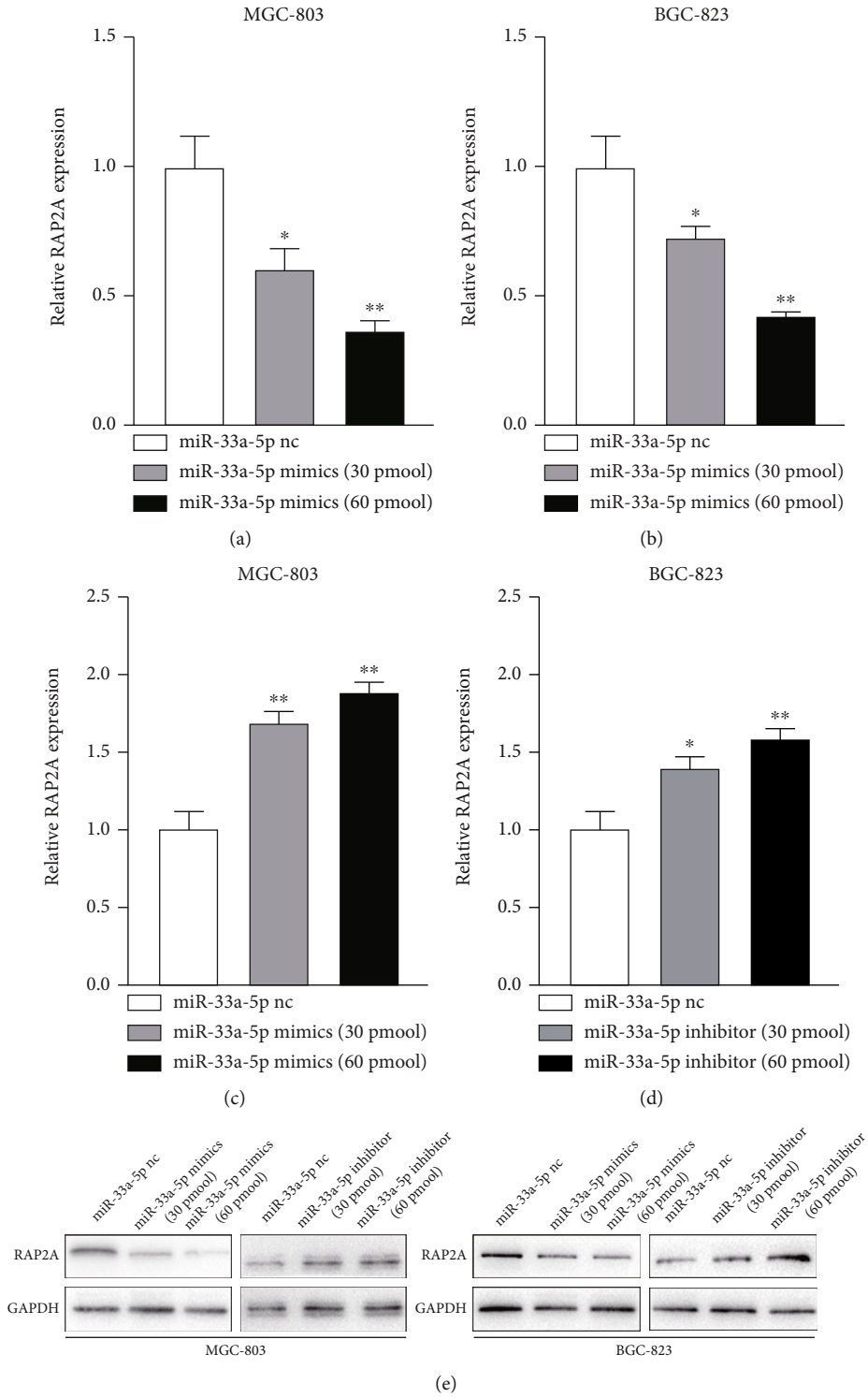


Figure 5: Continued.

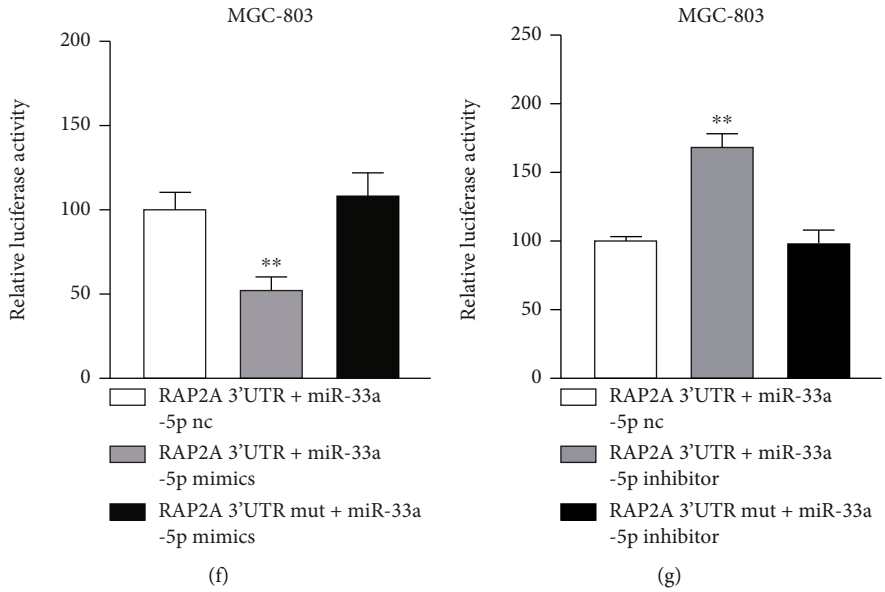


Figure 5: RAP2A expression is repressed by 3′UTR binding of miR-33a-5p. Relative mRNA level of RAP2A in MGC-803 cells transfected with either 30 pmol or 60 pmol (a) mimic miR-33a-5p or (c) miR-33a-5p inhibitor. Relative mRNA level of RAP2A in BGC-823 cells transfected with either 30 pmol or 60 pmol (b) miR-33a-5p mimic or (d) miR-33a-5p inhibitor. (e) Relative protein level of RAP2A in MGC-803 cells and BGC-823 transfected with either 30 pmol or 60 pmol miR-33a-5p mimics or miR-33a-5p inhibitor. Relative luciferase activity of wild-type and mutated RAP2A 3′UTR in MGC-803 cells transfected with (f) miR-33a-5p mimic or (g) miR-33a-5p inhibitor. mRNA levels were normalized to GAPDH and protein levels were normalized to GAPDH, Mean + / – SEM is shown. $^{*}p < 0.05$, $^{**}p < 0.01$.

The experimental data were calculated using $2^{-\Delta\Delta Ct}$ method. Sequence of primers: miR-33a-5p Forward: 5′-GATCCT CAGTGCATTGTAGTTGC-3′, Reverse: 5′-CTCTGTCTC TCGTCTTGTTGGTAT-3′. U6 Forward: 5′-CTCGCTTCG GCAGCACA-3′, Reverse: 5′-AACGCTTCACGAATTT GCGT-3′. RAP2A Forward: 5′-ACAATGGTGGACGAAC TCTTT-3′, Reverse: 5′-CAGAACAGCATGGGTCATCTT-3′. GAPDH Forward: 5′-GGCTGTTGTCATACTTCTCAT GG-3′; Reverse: 5′-AGGAAAAGCATCACCCGGAG-3′.

*2.3. Transfection.* miR-33a-5p were synthesized and transfected to GC cell lines to analyze biological function. QRT-PCR was used to determine whether the transfection efficiency was successful. Cells were divided into three group based on their specific treatment: NC group (negative control), miR-33a-5p mimics, and miR-33a-5p inhibitor. Lipofectamine 3000 (Invitrogen, USA) was used for cell transfection by the manufacturer's instructions.

*2.4. Cell Proliferation.* The cell activity was detected using the cell counting kit-8 (CCK-8) assay (Dojindo, Japan) as follows. The cells in different groups after transfection were inoculated into a 24-well plate. At 0, 1, 2, 3, and 4 days after transfection, an equal amount of GC cells were cultured into a 96-well plate. 10 $\mu$L CCK-8 was then added, followed by incubation with 5% $CO_2$ at 37°C for 1.5~2 h. The absorbance value (A value) at 450 nm was detected using the multifunctional microplate reader, and 630 nm was used as the reference wavelength. Cells were counted 3 times in each group, and the above assays were repeated 3 times.

*2.5. Cell Clone Formation.* In colony formation assay, the transfected cells were growing in a 6-well plate at $2 \sim 3 \times 10^3$ cells per well for 10~12 days. Then, it was fixed with formaldehyde, washed with phosphate-buffered saline (PBS), stained with methyl violet, and counted the cell number using microscope (Olympus, Japan). The colony − inhibition rate = [(1 − number of experimental group)/control group] × 100% ; and colony − forming rate = 1 − colony − inhibition rate.

*2.6. Cell Invasion Assay.* In the invasion assay, $2 \sim 3 \times 10^5$ MGC-803 or HGC-27 cells were cultured onto the transwell chambers (Millipore, Switzerland) in serum-free medium. The Matrigel (Sigma-Aldrich, USA) was coated in the upper chamber, and the 20% FBS was added to the lower chamber. After 24 h, the cells on the surface of the chamber were removed with cotton wool. Invasive cells of the lower surface were stained with Giemsa stain (Sigma, USA) and counted with microscope (Olympus, Japan).

*2.7. Western Blot Assay.* In western blot assay, the extraction protein was separated by 10% SDS-PAGE and transferred onto PVDF membranes (Millipore, USA). Membranes were sealed with 5% nonfat dried milk and incubated with anti-RAP2A antibody (Millipore) at 1: 1500 dilution; anti-pJAK and anti-JAK antibody (Cell Signaling) at 1 : 700 dilution; anti-pSTAT3 and anti-STAT3 antibody (Cell Signaling) at 1 : 600 dilution; and anti-GAPDH antibody (Cell Signaling) at 1 : 45,000 dilution. The membranes were washed with TBST and incubated at 37°C for 2 h with second antibody (Cell Signaling) at 1 : 20,000.

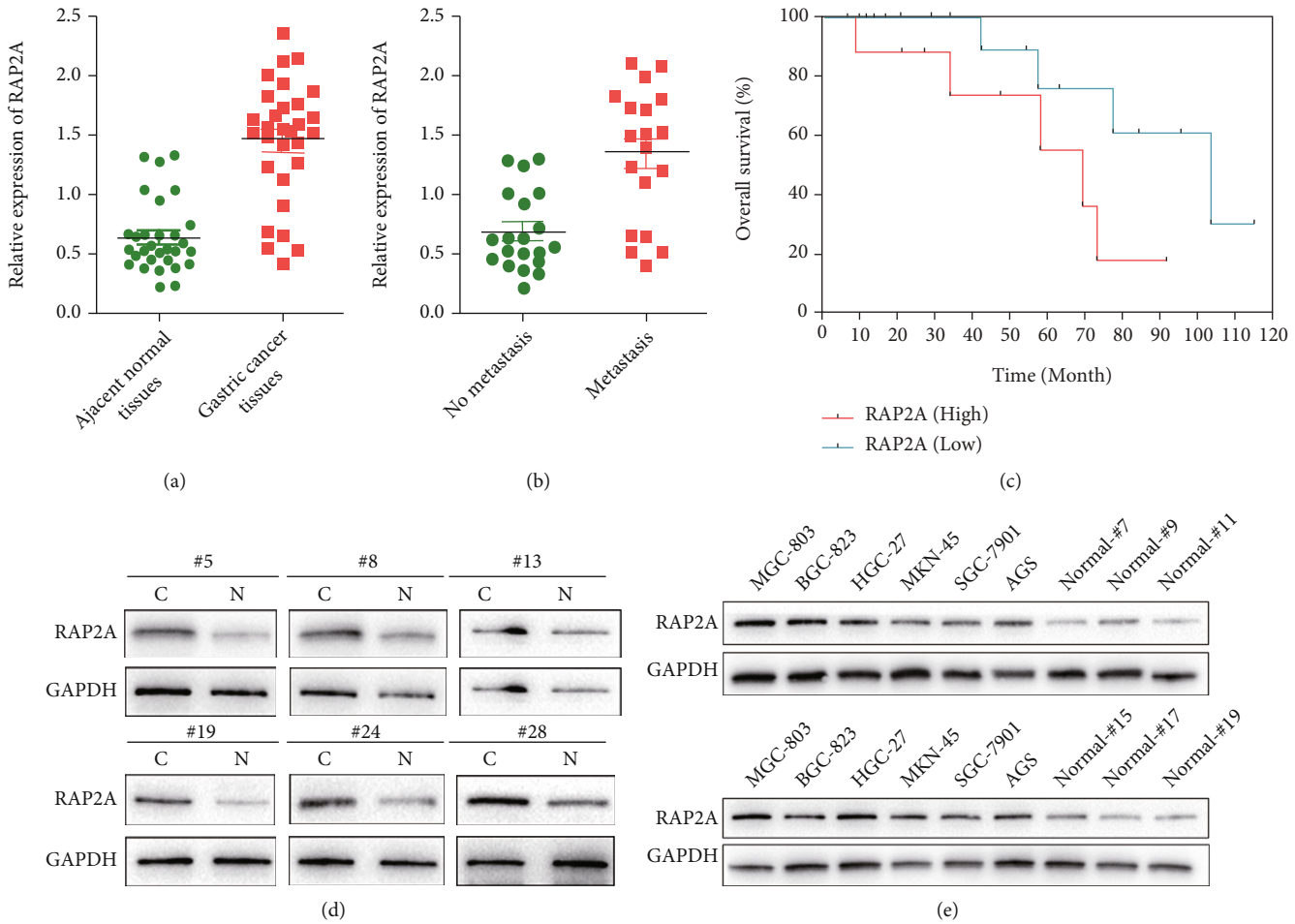


Figure 6: Decreased expression of RAP2A in GC Samples. (a) Relative expression of RAP2A in GC tissues and adjacent normal tissues pairs. (b) Relative expression of RAP2A in no metastasis and metastasis pairs. (c) Survival analysis for RAP2A in a clinical data set. Relative protein level of RAP2A in different samples (d) and cells (MGC-803, BGC-823, HGC-27, MKN-45, AGS, and SGC-7901and normal cells) (e). mRNA levels were normalized, Mean + / – SEM is shown for (a) and (b). $^{*}p < 0.05$, $^{**}p < 0.01$, $t$-test.

*2.8. Luciferase Reporter Assays.* In luciferase reporter assays, the transfection cells were washed with PBS three times. 100 $\mu$L passive lysis buffer (PLB) was added to each cell hole and collected the cell lysate. Then, add 100 $\mu$L LAR II working fluid, mix it quickly, and read the first value. Add 100 $\mu$L Stop & Glo® Reagent and put it into the luminescent detector to read the second value. Finally, the relative fluorescence intensity was calculated.

*2.9. Statistical Analysis.* Statistical analysis was performed with a Student's $F$-test or $t$-test. $p < 0.05$ (two-sided) was supposed significant. Data were analyzed by Prism7.02 software (La Jolla, CA, USA).

## 3. Results

*3.1. miR-33a-5p Expression Reduced in GC Samples and Cells.* QRT-PCR results indicated that the expression of miR-33a-5p was lower significantly in GC tissues (Figure 1(a)). Evaluation of miR-33a-5p expression in all adjacent normal tissues showed 2.6-fold descent in GC tissues ($p < 0.01$, Figure 1(b)). The same results were got in the in vitro determination; the miR-33a-5p level was declined in GC cells (especially in BGC-823 and MGC-803cells) comparing with in normal cells (Figure 1(c)). Then, we analyzed a clinical data set with overall survival in GC tissues and showed that reduced miR-33a-5p is correlated with poor survival (Figure 1(d)).

*3.2. MiR-33a-5p Acts as Tumor Suppressor in GC.* To analyze what impact miR-33a-5p plays in GC cells, we transfected MGC-803 and BGC-823 cells with miR-33a-5p nc or miR-33a-5p mimics/inhibitor and evaluated the alterations in cell functions. In cell assays, miR-33a-5p mimics transfected in MGC-803 cells proliferation descended by up to 51%, invasion by 52%, and clone formation by up to 33% (Figures 2(a)–2(c)). The result was the same in BGC-823 cells, and miR-33a-5p overexpression decreased the proliferation by 55%, invasion by 58%, and clone formation by 53% (Figures 2(d)–2(f)). Then, we further analyzed the effectiveness of miR-33a-5p inhibitor transfection in cells. MiR-33a-5p inhibitor heightened proliferation by 22%, invasion by 72%, and clone formation by 43% (Figures 3(a)–3(c)). In BGC-823 cells, miR-33a-5p inhibitor ascended the proliferation by

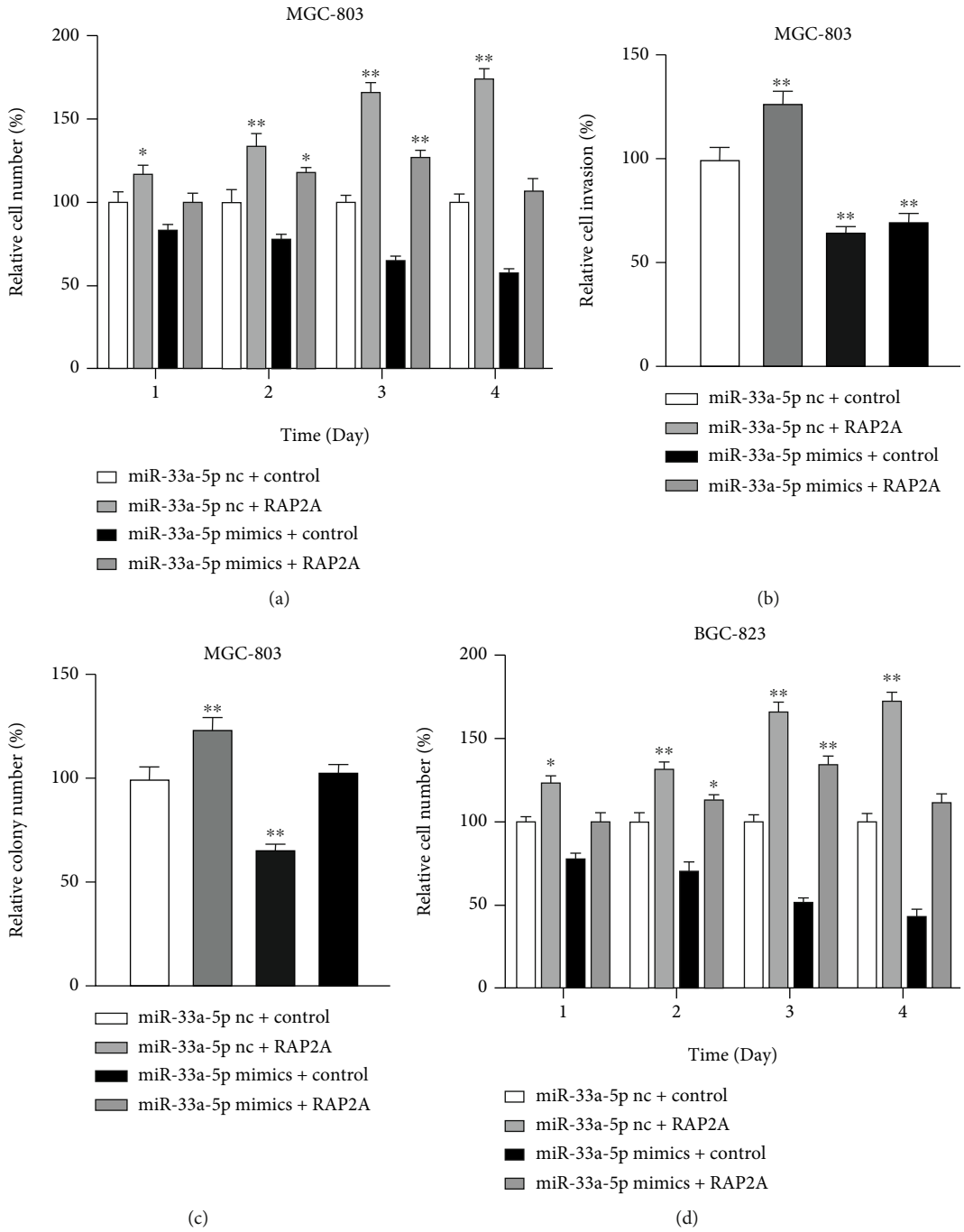


Figure 7: Continued.

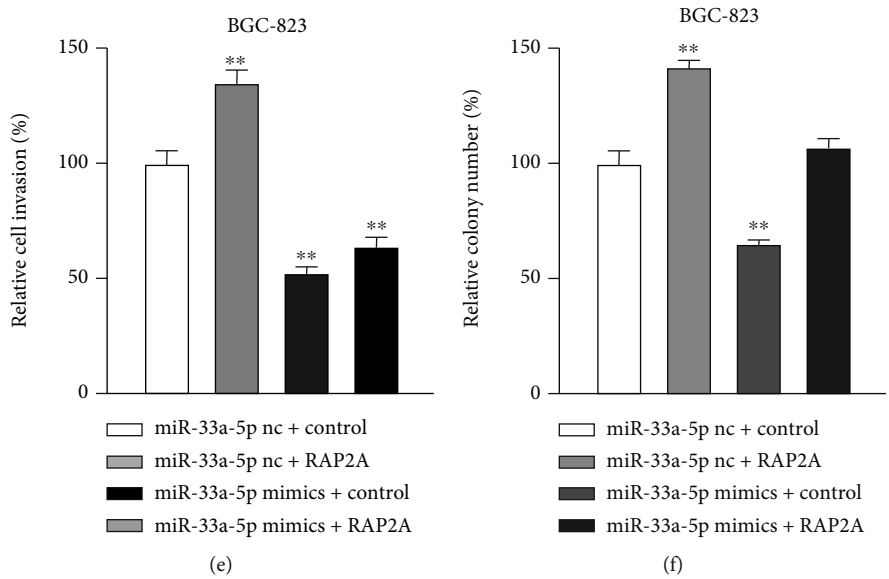


Figure 7: RAP2A expression increases proliferation and anchorage independent growth. (a) Proliferation, (b) invasion, and (c) colony number and RAP2A overexpressing MGC-803 cells transfected with miR-33a-5p mimic. (d) Proliferation, (e) invasion, and (f) colony number and RAP2A overexpressing BGC-823 cells transfected with miR-33a-5p inhibitor. Mean + / – SEM is shown. $^{*}p < 0.05$, $^{**}p < 0.01$; *t*-test.

27%, invasion by 58%, and clone formation by 33% (Figures 3(d)–3(f)). Taken together, these experiments reveal that miR-33a-5p has tumor suppression functions in GC cells.

*3.3. Identification of miR-33a-5p Targets in GC.* To explore potential miR-33a-5p targets in GC cells, we chose the website (https://www.targetscan.org/vert_80/) to identify possible binding sites (Figure 4(a)). The analysis revealed a conserved sequence between positions 3485-3492 of RAP2A 3′UTR as a potential target for miR-33a-5p. We prioritized these potential target genes and screened 5 candidate genes of miR-33a-5p. Then, we selected those genes to further validation: RAP2A, HMGA2, PIM1, DDX5, and PIM3. In BGC-823 and MGC-803 cells, the increased expression of miR-33a-5p reduced these genes significantly, especially RAP2A (Figures 4(b) and 4(c)). However, miR-33a-5p downregulation confirmed RAP2A, HMGA2, PIM1, DDX5, and PIM3 as potential targets in BGC-823 and MGC-803 cells (Figures 4(d) and 4(e)). According to the results of qRT-PCR, RAP2A was selected for further analysis, because it declined significantly after changes in the miR-33a-5p expression.

*3.4. MiR-33a-5p Downregulates RAP2A through Targeting RAP2A.* To validate the targets RAP2A, we initially selected 2 different concentrations of mature miR-33a-5p inhibitor or mimics to analyze RAP2A mRNA and protein levels. QRT-PCR and western blot results showed that the RAP2A expression decreased significantly with the higher concentrations of miR-33a-5p mimics (Figures 5(a), 5(b), and 5(e)). On the contrary, the higher miR-33a-5p inhibitor resulted in RAP2A expression increased obviously (Figures 5(c)–5(e)).

Cotransfecting with miR-33a-5p mimics/inhibitor and either the wild-type RAP2A 3′UTR or the mutation RAP2A 3′UTR (same region in the predicted seed sequence) containing luciferase reporter in MGC-803 cells revealed that miR-33a-5p blocked the luciferase activity of the wild-type RAP2A 3′UTR, however, not that of the RAP2A 3′UTR mut compared to miR-33a-5p nc control (Figure 5(f)). Furthermore, cotransfection with miR-33a-5p inhibitor led to increase in the luciferase activity of the wild-type RAP2A 3′UTR obviously, but no alter was founded in the mutant reporter construct activity (Figure 5(g)). According to the results, RAP2A targets miR-33a-5p directly in MGC-803 cell lines.

*3.5. Aberrant Expression of RAP2A in GC Tissues and Cell Lines.* We performed qPCR analysis in 30 pairs of clinical GC tissues to detect RAP2A expression. The results showed that RAP2A mRNA levels were elevated in 26 cases (87%) of GC tissues (C) compared with their adjacent normal tissues (N), but only 4 tissues (13%) showed downregulated RAP2A mRNA levels (Figure 6(a)). To further explore the correlation between RAP2A and clinicopathological factors, we analyzed the relative RAP2A levels in GC tissues at different stages of progression (nonparametric test). Obviously, we got that a high RAP2A level accompanied with GC pM stage (Figure 6(b), nonmetastasis vs. metastasis, $p < 0.001$) in GC patients. In addition, GC patients with high RAP2A expression had worse disease-free survival and overall survival (Figure 6(c)).

To further confirm these results, we detected the RAP2A protein levels in 6 pairs of GC tissues (C and N) randomly. The protein level of RAP2A was significantly elevated (>2-fold) in GC tissues (Figure 6(d)). Moreover, The RAP2A

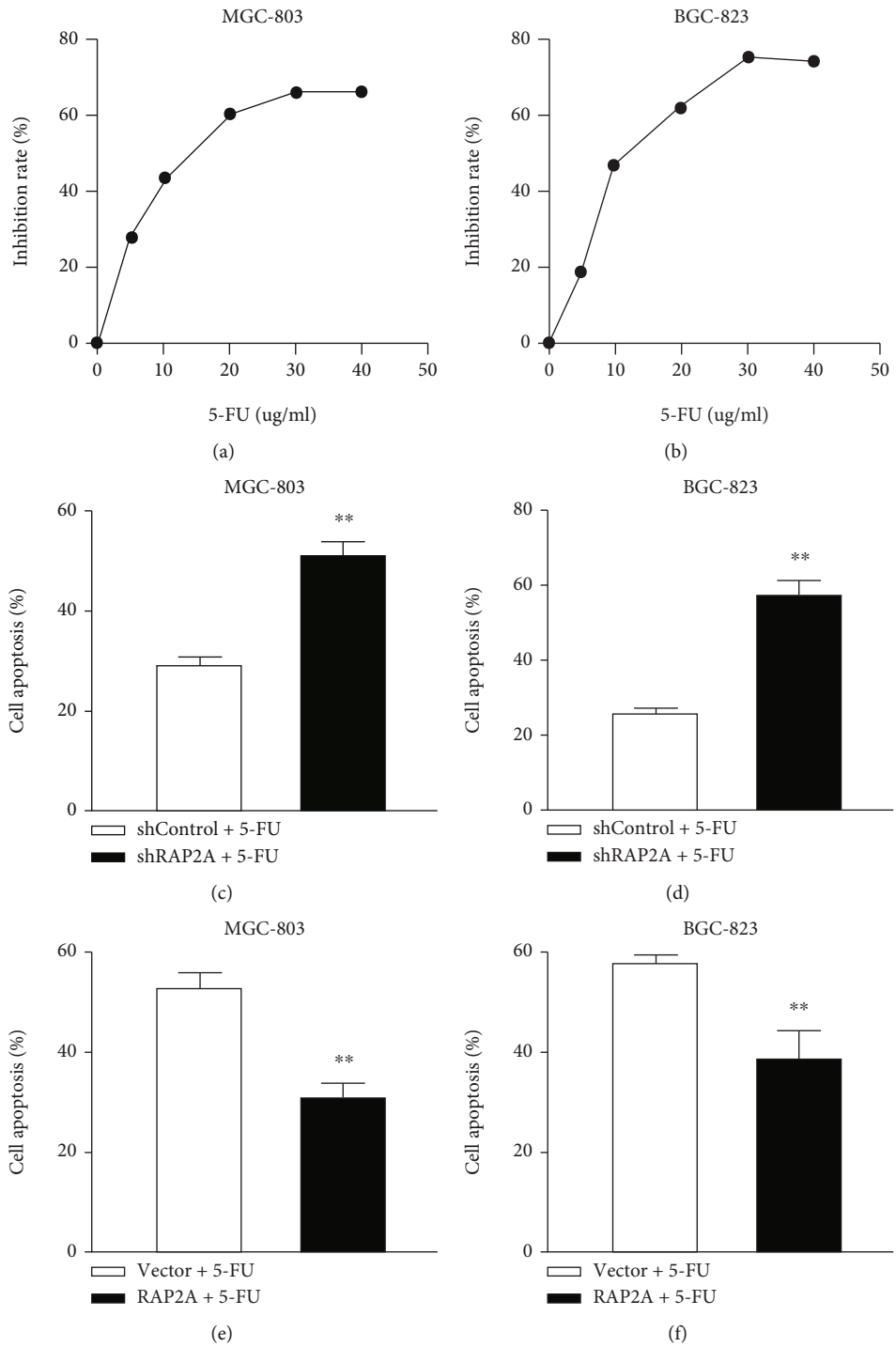


Figure 8: Continued.

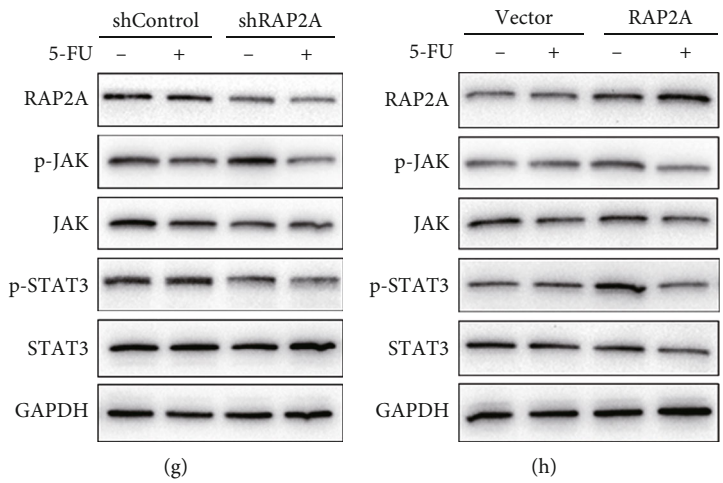


Figure 8: Knockdown or overexpression of RAP2A affects the sensitivity of GC cancer cells to 5-FU. 24 h after drug administration, CCK-8 was added, the IC50 of MGC-803 cells was 11.134 $\mu$g/mL (a), and that of BGC-823 cells was 10.634 $\mu$g/mL (b). Cell viability was detected by CCK-8. (c) MGC-803 shControl and shRAP2A were treated with 11 $\mu$g/mL 5-FU, and (d) BGC-823 shControl and shRAP2A were treated with 10 $\mu$g/mL 5-FU. (e) MGC-803 vector and RAP2A were treated with 11 $\mu$g/mL 5-FU, and (f) BGC-823 vector and RAP2A were treated with 10 $\mu$g/mL 5-FU. (g) Representative western blot image shows the expression of RAP2P, pJAK, JAK, pSTAT3, and STAT3 in MGC-803 shControl and MGC-803 shRAP2P cells treated with 11 $\mu$g/mL 5-FU for 24 h. (h) Representative western blot image shows the expression of RAP2P, pJAK, JAK, pSTAT3, and STAT3 in BGC-823 vector and BGC-823 RAP2P cells treated with 10 $\mu$g/mL 5-FU for 24 h.

protein was sharply rose in GC cell lines (MKN-45, MGC-803, HGC-27, BGC-823, AGS, and SGC-7901) in contrast with normal cells (Figure 6(e)). The results showed that the upregulation of RAP2A may play a potential driving role in GC tumorigenesis.

*3.6. MiR-33a-5p Reverses the Effects of RAP2A Associated with GC Progression.* RAP2A is a member of the small GTPase protein superfamily, which is involved in many cellular functions including cell adhesion and proliferation. In our studies, miR-33a-5p mimics led to a decline in RAP2A mRNA and protein levels (Figures 5(a) and 5(e)). In MGC-803 cells, RAP2A overexpression promoted proliferation by 74% and cell invasion by 25% (Figures 7(a) and 7(b)). However, the proliferation induction rate of RAP2A was reduced to 6%, and the clone formation rate was reduced to 4% after the introduction of miR-33a-5p into MGC-803 cells (Figures 7(a) and 7(c)). In BGC-823 cells, the cell proliferation decreased from 72% to 8%, and the clone formation rate decreased from 34% to 7% after the introduction of miR-33a-5p (Figures 7(d)–7(f)).

*3.7. RAP2A Reduces the Sensitivity of GC Cells to 5-FU through the JAK/STAT3 Signaling Axis.* MGC-803 cells and BGC-823 cells of wild-type cells were treated with different concentrations of 5-FU. 24 h after drug administration, CCK-8 was added, and OD value was detected by a microplate reader. The IC50 of MGC-803 cells was 11.134 $\mu$g/mL (Figure 8(a)) and that of BGC-823 cells was 10.634 $\mu$g/mL (Figure 8(b)). To explore whether RAP2A affects on 5-FU-induced apoptosis of GC cells, cells were collected after 5-FU treatment for 24 h, and cell apoptosis ratio was detected by flow cytometry. The results showed that the apoptosis rate of MGC-803 shControl was 29.06% and that of MGC-803 shRAP2A was 51.13% (Figure 8(c)). Low RAP2A expression significantly increased the 5-FU-induced apoptosis rate ($p < 0.01$). The apoptosis rate of MGC-803 no-load cells was 53.42% and that of MGC-803 RAP2A was 31.45% (Figure 8(e)). The high expression of RAP2A significantly reduced the 5-FU-induced apoptosis rate ($p < 0.01$). The results showed that the apoptosis rate of BGC-823 shControl was 25.13% and that of BGC-823 shRAP2A was 57.04% (Figure 8(d)). Low RAP2A expression significantly increased the 5-FU-induced apoptosis rate ($p < 0.01$). The apoptosis rate of BGC-823 no-load cells was 57.12% and that of BGC-823 RAP2A was 38.24% (Figure 8(f)). The high expression of RAP2A significantly reduced the 5-FU-induced apoptosis rate ($p < 0.01$).

Studies have shown that RAP2A promotes the proliferation of GC cells by activating the JAK/STAT3 signaling pathway. To investigate the mechanism of RAP2A affecting the sensitivity of GC cells to 5-FU, we detected the phosphorylation level of JAK and the STAT3. The results indicated that the expression levels of p-JAK and p-STAT3 in MGC-803 shRAP2A cells were significantly decreased 24 h after 5-FU treatment compared with MGC-803 shControl cells ($p = 0.023$; $p = 0.005$) (Figure 8(g)). Compared with BGC-823 no-load cells, the levels of p-JAK and p-STAT3 in BGC-823 RAP2A cells were significantly increased ($p = 0.004$; $p = 0.006$) (Figure 8(h)). These results suggest that RAP2A plays a role in reducing the sensitivity of GC cells to 5-FU by upregulating the JAK/STAT3 pathway.

## 4. Discussion

In our conclusion, we determined that the expression of miR-33a-5p was decreased in GC tissues compared with adjacent normal tissues. In addition, miR-33a-5p overexpression increased the proliferation, invasion, and clone growth of GC cells in vitro, while reduction of miR-33a-5p

had the inverse effect. Therefore, our results suggest that miR-33a-5p plays a tumor suppressor role in GC. Moreover, we induced significant changes in miR-33a-5p levels through enhancing or silencing in cell experiments. However, as the dose response of miR-33a-5p deletion in GC is not clear, it is difficult to determine its corresponding biological response in GC.

Many studies have found that miR-33a-5p plays a regulatory role in variety of tumors [12, 16]. To explore the miR-33a-5p effect in GC cells, we confirmed the expression, potential targets by QRT-PCR, western blot, and luciferase assay. Analysis indicated that HMGA2, PIM1, DDX5, PIM3, and RAP2A were potential targets of miR-33a-5p. Since RAP2A is an obvious oncogene in GC cells, we selected it for further experimental [4].

As we mentioned above, miR-33a-5p could regulate multiple genes in GC cell lines; in this study, upregulation of RAP2A almost promotes cell proliferation and invasion in GCs, suggesting that RAP2A is the dominant target of miR-33a-5p effect in the GC cells. The relationship between RAP2A and prognosis and progression of GC was further investigated. To further explore the correlation between RAP2A and clinicopathological factors, we analyzed the relative RAP2A levels in GC tissues at different stages of progression (nonparametric test). Obviously, we got that a high RAP2A level accompanied with GC pM stage (Figure 6(b), nonmetastasis vs. metastasis, $p < 0.001$) in GC patients. In addition, GC patients with high RAP2A expression had worse disease-free survival and overall survival.

Drug resistance based on 5-FU is a major problem in the clinical treatment of advanced GC. It has not been reported whether the high expression of RAP2A in GC will affect the sensitivity of GC cells to 5-FU. Studies have shown that RAP2A promotes the proliferation of GC cells by activating the JAK/STAT3 signaling pathway. To investigate the mechanism of RAP2A affecting the sensitivity of GC cells to 5-FU, we detected the phosphorylation level of JAK and STAT3. The results indicated that the expression levels of p-JAK and p-STAT3 in MGC-803 shRAP2A cells were significantly decreased 24 h after 5-FU treatment compared with MGC-803 shControl cells ($p = 0.023$; $p = 0.005$). The results of this study showed that RAP2A negatively regulated the sensitivity of GC cells to 5-FU. This suggests that RAP2A may be a biomarker for predicting the effectiveness of 5-FU-based treatment decisions.

In summary, our results indicate that miR-33a-5p is underexpressed in GC cells, and miR-33a-5p negatively regulates RAP2A. However, the high expression of RAP2A was negatively correlated with the survival of GC patients, and the high expression of RAP2A could reduce the sensitivity of GC cells to 5-FU. RAP2A is expected to be a marker of prognosis and chemotherapy resistance in patients with GC.

## Abbreviations

GC: Gastric cancer
RAP2A: Ras-related protein rap-2a
HMGA2: High mobility group AT-hook 2
PIM1: Pim-1 proto-oncogene
DDX5: DEAD-box helicase 5
PIM3: Pim-3 proto-oncogene
miRNA: microRNA.

## Data Availability

The underlying data supporting the results of your study can be found by lifenglover@sina.com.

## Ethical Approval

All experiments were repeated at least three times. Statistical analyses were evaluated by the two-tailed t-test and one-way ANOVA. Statistically significance was set at $p < 0.05$ using SPSS program (SPSS 15.0, USA).

## Conflicts of Interest

The authors disclose no potential conflicts of interest.

## Authors' Contributions

Feng Li designed and performed the experiments, interpreted data, and wrote the manuscript; Gang Ti and Zongliang Guo performed bioinformatics analysis; Lili Li provided the experimental material of gastric cancer patients and healthy donors; Yongqiang Lv helped collect the samples and performed the partial experiments. Bin Yang, Jian Wang, and Rui Guo performed the partial experiments. Yunqing Chen and Debin Meng designed the study, directed the experiments, and wrote the manuscript. All authors read and approved the manuscript. Gang Ti, Zongliang Guo, and Lili Li contributed equally to this work.

## Acknowledgments

This work was supported by grants from the Scientific Research of Health Commission of Shanxi Province (2019062 to Yunqing Chen) and the Scientific Research and Innovation Team Construction Project of Shanxi Cancer Hospital (2020 to Feng Li).

## References

[1] B. W. Stewart and C. P. Wild, Eds., *World Cancer Report 2014*, IARC, Lyon, France, 2014.

[2] Z. Zhu, H. Huiqin, and X. Wang, "Advances in the application of tumor autoantibodies in early diagnosis and screening of gastric cancer," *Guangdong Medical Journal*, vol. 37, no. 15, pp. 2358–2360, 2016.

[3] J. Cui, N. Cao, G. Wang et al., "HuR promotes the progression of gastric cancer through mediating CDC5L expression," *Disease Markers*, vol. 2022, Article ID 5141927, 12 pages, 2022.

[4] J. Zhang, Y. Wei, J. Min et al., "Knockdown of RAP2A gene expression suppresses cisplatin resistance in gastric cancer cells," *Oncology Letters*, vol. 19, no. 1, pp. 350–358, 2020.

[5] Y. Y. Lee and M. H. Derakhshan, "Environmental and lifestyle risk factors of gastric cancer," *Archives of Iranian Medicine*, vol. 16, no. 6, pp. 358–365, 2013.

[6] H. Yoon and N. Kim, "Diagnosis and management of high risk group for gastric cancer," *Gut and Liver*, vol. 9, no. 1, pp. 5–17, 2015.

[7] Z. R. Zhang and N. Yang, "MiR-33a-5p inhibits the growth and metastasis of melanoma cells by targeting SNAI 2," *Neoplasma*, vol. 67, no. 4, pp. 813–824, 2020.

[8] R. Gupta, T. Arkatkar, J. Keck et al., "Antigen specific immune response in *Chlamydia muridarum* genital infection is dependent on murine microRNAs-155 and -182," *Oncotarget*, vol. 7, no. 40, pp. 64726–64742, 2016.

[9] L. Alessandrini, M. Manchi, V. de Re, R. Dolcetti, and V. Canzonieri, "Proposed molecular and miRNA classification of gastric cancer," *International Journal of Molecular Sciences*, vol. 19, no. 6, p. 1683, 2018.

[10] J. Ouyang, Z. Xie, X. Lei, G. Tang, R. Gan, and X. Yang, "Clinical crosstalk between microRNAs and gastric cancer (review)," *International Journal of Oncology*, vol. 58, no. 4, p. 7, 2021.

[11] H. Mollaei, R. Safaralizadeh, and Z. Rostami, "MicroRNA replacement therapy in cancer," *Journal of Cellular Physiology*, vol. 234, no. 8, pp. 12369–12384, 2019.

[12] Q. Song, H. Liu, C. Li, and H. Liang, "miR-33a-5p inhibits the progression of esophageal cancer through the DKK1-mediated Wnt/$\beta$-catenin pathway," *Aging*, vol. 13, no. 16, pp. 20481–20494, 2021.

[13] W. Xia, J. Zhu, Y. Tang et al., "PD-L1 inhibitor regulates the miR-33a-5p/PTEN signaling pathway and can be targeted to sensitize glioblastomas to radiation," *Frontiers in Oncology*, vol. 10, p. 821, 2020.

[14] D. Lin, X. Lin, T. He, and G. Xie, "Gambogic acid inhibits the progression of gastric cancer via circ RNA_ASAP2/mi R-33a-5p/CDK7 Axis," *Cancer Management and Research*, vol. 12, pp. 9221–9233, 2020.

[15] Q. Wu, S. Xiang, J. Ma et al., "Long non-coding RNA CASC15 regulates gastric cancer cell proliferation, migration and epithelial mesenchymal transition by targeting CDKN1A and ZEB1," *Molecular Oncology*, vol. 12, no. 6, pp. 799–813, 2018.

[16] D. Liao, X. Liu, X. Yuan et al., "Long non-coding RNA tumor protein 53 target gene 1 promotes cervical cancer development via regulating microRNA-33a-5p to target forkhead box K2," *Cell Cycle*, vol. 21, no. 6, pp. 572–584, 2022.

Hindawi
Disease Markers
Volume 2022, Article ID 3372217, 15 pages
https://doi.org/10.1155/2022/3372217

*Research Article*

# Systematic Bibliometric and Visualized Analysis of Research Hotspots and Trends on Autism Spectrum Disorder Neuroimaging

**Yi Lu**,[1] **Li Zhang**,[2] **Xing-yang Wu**,[3] **Fang-rong Fei**,[4] **and Hui Han**[5]

[1]*Department of Nursing, Xinxiang Medical University, Xinxiang, China*
[2]*Department of Rehabilitation, Children's Hospital of Nanjing Medical University, Nanjing, China*
[3]*Department of Medical Engineering, Xinxiang Medical University, Xinxiang, Henan, China*
[4]*Zhejiang Provincial Center for Disease Control and Prevention, Hangzhou, China*
[5]*Department of Nursing, First Affiliated Hospital of Huzhou University, Huzhou, China*

Correspondence should be addressed to Fang-rong Fei; frfei@cdc.zj.cn and Hui Han; hanhui30@126.com

Received 28 May 2022; Revised 26 June 2022; Accepted 30 June 2022; Published 18 July 2022

Academic Editor: Yi Shao



*Background*. Autism spectrum disorder (ASD) is a chronic developmental disability caused by differences in the brain. The gold standard for the diagnosis of this condition is based on behavioral science, but research on the application of neurological detection to diagnose the atypical nervous system of ASD is ongoing. ASD neuroimaging research involves the examination of the brain's structure, functional connections, and neurometabolic. However, limited medical resource and the unique heterogeneity of ASD have resulted in many challenges when neuroimaging is utilized. *Objective*. This bibliometric study is aimed at summarizing themes and trends in research on autism spectrum disorder neuroimaging and at proposing potential directions for future inquiry. *Methods*. Citations were downloaded from the Web of Science Core Collection database on neuroimaging published from January 1, 2012, to December 31, 2021. The retrieved information was analyzed using Bibliometric.com, CiteSpace.5.8. R3, and VOS viewer. *Results*. A total of 1,363 papers were published across 58 regions. The United States was the leading source of publications. The League of European Research Universities published the largest number of articles (171). Burst keywords from 2018 to 2021 include identification and network. The clusters of references that continued into 2020 included graph theory, functional connectivity, and classification, which represent key research topics. *Conclusions*. Imaging data is being used to identify neuro-network models with higher accuracy for ASD discrimination. Functional near-infrared imaging is advantageous compared to other neuroimaging. In the future, research on systematic and accurate computer-aided diagnosis technology should be encouraged. Moreover, the study of neuroimaging of ASD in different psychological and behavioral states can inspire new ideas about the diagnosis and intervention training of ASD and should be explored.

## 1. Introduction

Autism spectrum disorder (ASD) is a neurodevelopmental disorder that manifests itself in infancy. Its primary symptoms are social communication and communication disorders, as well as repetitive stereotyped behavior [1]. Owing to the limited availability of accurate prenatal screening tools, early diagnostic biomarkers, and effective treatment methods, the prevalence of ASD has been increasing annually [2]. The results of the survey and monitoring points of the American Autism and Developmental Disorder Monitoring Network (ADMN) published in 2020 and 2021 revealed that in 2016, the overall prevalence of ASD in four-year-old children was approximately one in 64, and there was one ASD child in every 59 for this age group in the United States in 2018 [3, 4]. Standardized assessment and diagnostic methods are the gold standard for clinical diagnosis of ASD [5–7]. Although there is no complete

description of the etiology and pathogenesis of ASD, research on the application of neurological detection to describe the atypical nervous system of ASD is ongoing.

ASD neuroimaging research examines the brain from a variety of perspectives including brain structure, functional connections, and neurometabolic [8–10]. Structural magnetic resonance imaging (sMRI) is a technique for examining the anatomical structure of the brain. Several sMRI studies have proved that there are structural abnormalities in the frontal lobe, temporal lobe, hippocampus, amygdala, and striatum of ASD subjects [11–16]. Functional neuroimaging of ASD brains mainly includes functional magnetic resonance imaging (fMRI), magnetic resonance spectroscopy (MRS), positron emission tomography (PET), single positron emission computed tomography (SPECT), diffusion tensor imaging (DTI), and functional near-infrared spectroscopy (fNIRS). These techniques are frequently used to investigate brain functional connectivity, metabolite content, nerve receptor distribution, and brain activation. fMRI studies involve the measurement and analysis of the changes in the degree of oxygenation in the local cerebral blood flow of subjects during a task state or resting state [17–19]. fNIRS measures the hemodynamic characteristics of the cerebral cortex via near-infrared spectroscopy to detect neural activity, which is a promising method for the early identification of quantitative biomarkers in autism sites [20, 21]. MRS can detect molecular behavior abnormalities associated with ASD [22]. As a molecular nuclear medicine imaging technology, SPECT and PET facilitate the study of cerebral blood perfusion, glucose metabolism, and protein metabolism by detecting the distribution of different radioactive tracers [23, 24]. DTI is a magnetic resonance imaging (MRI) technique that can reflect the burden of nervous system diseases [25].

Neuroimaging studies of ASD involve a variety of imaging methods and subgroups. However, a bibliometric analysis of this field has not been performed. The purpose of this study is to summarize themes and trends in research on autism spectrum disorder neuroimaging and to propose potential directions for future inquiry. We used bibliometric methods to analyze scientific citation index (SCI) papers in the field. The data included the references of countries, regions, institutions, journals, research categories, keywords, and references. In addition, as the core of this study, we established a visual and unbiased method for exploring the areas of high research activity and the frontiers of ASD neuroimaging research. The research methods, distribution, and influence of these published works are discussed. The future development space and potential challenges of ASD neuroimaging are also discussed. This report can serve as a reference for doctors, neuroimaging experts, and researchers in this field.

## 2. Data Sources and Research Methods

*2.1. Data Sources.* The Web of Science Core Collection (WoSCC) database was chosen as the literature source for this study. Two authors (YL and WY) independently verified this work. The search formula was TS = ("structural magnetic resonance imaging" or sMRI or "functional magnetic resonance imaging" or fMRI or "magnetic resonance spectroscopy" or MRS or "diffusion-tensor imaging" or DTI or "functional near-infrared spectroscopy" or fNIRS or "single-photon emission computed tomography" or SPECT or "positron emission tomography" or PET) and (autism∗ or ASD or autistic or "Kanner Syndrome" or Asperger∗). The period was 2012–202, the language was English, and the document was published articles. We excluded book chapters, data papers, early access papers, and proceedings. The retrieval time was April 24, 2022. A total of 1956 English literatures were obtained. In addition, we manually screened the retrieved literature to avoid biased analysis results. Inclusion criteria are as follows: (1) research on ASD neuroimaging and (2) the research object can be human or animal. Exclusion criteria are as follows: (1) the study disease did not include ASD, (2) no imaging technology was used, and (3) the study sites were nonbrain body parts. Finally, the Web of Science (WoS) literature output function and the CiteSpace deduplication algorithm yielded 1363 effective literature. The detailed search and analysis processes are depicted in Figure 1.

## 3. Research Methods

Using the WoS data analysis module in CiteSpace5.R3 to visually analyze the collected data, the number of articles published each year, the country of origin, publishing organization, study categories, keywords, and references were all used to objectively assess the research status of ASD neuroimaging. The materials and methods section should contain sufficient detail so that all procedures can be repeated. It may be divided into headed subsections if several methods are described. https://bibliometric.com/app was used to show the volume of documents and the cooperation between countries.

## 4. Results and Discussion

*4.1. Distribution of Articles by Publication Year.* To some extent, the number of articles published in academic journals on a particular topic reflects the level of interest in the research area. The annual publishing data, as well as their growth rate, can show the evolution of the field over time and the change in its level of importance. Figure 2 depicts an overall increasing trend for the number of papers published from 2012 to 2021, with an average annual increase of approximately 14 articles. The popularity of ASD neuroimaging research is increasing. COVID-19 may have an impact on the number of papers published in 2021 compared to 2020. In addition, at present, some articles published in 2021 have not been included in the database.

*4.2. Countries or Regions.* The 1363 publications on ASD neuroimaging included in the analysis originated from 58 nations or regions. Figure 3 uses https://bibliometric.com/app to describe the number of documents submitted by each country and the cooperation between countries. The size of the areas with different colors indicates the number of documents submitted by the country represented by the

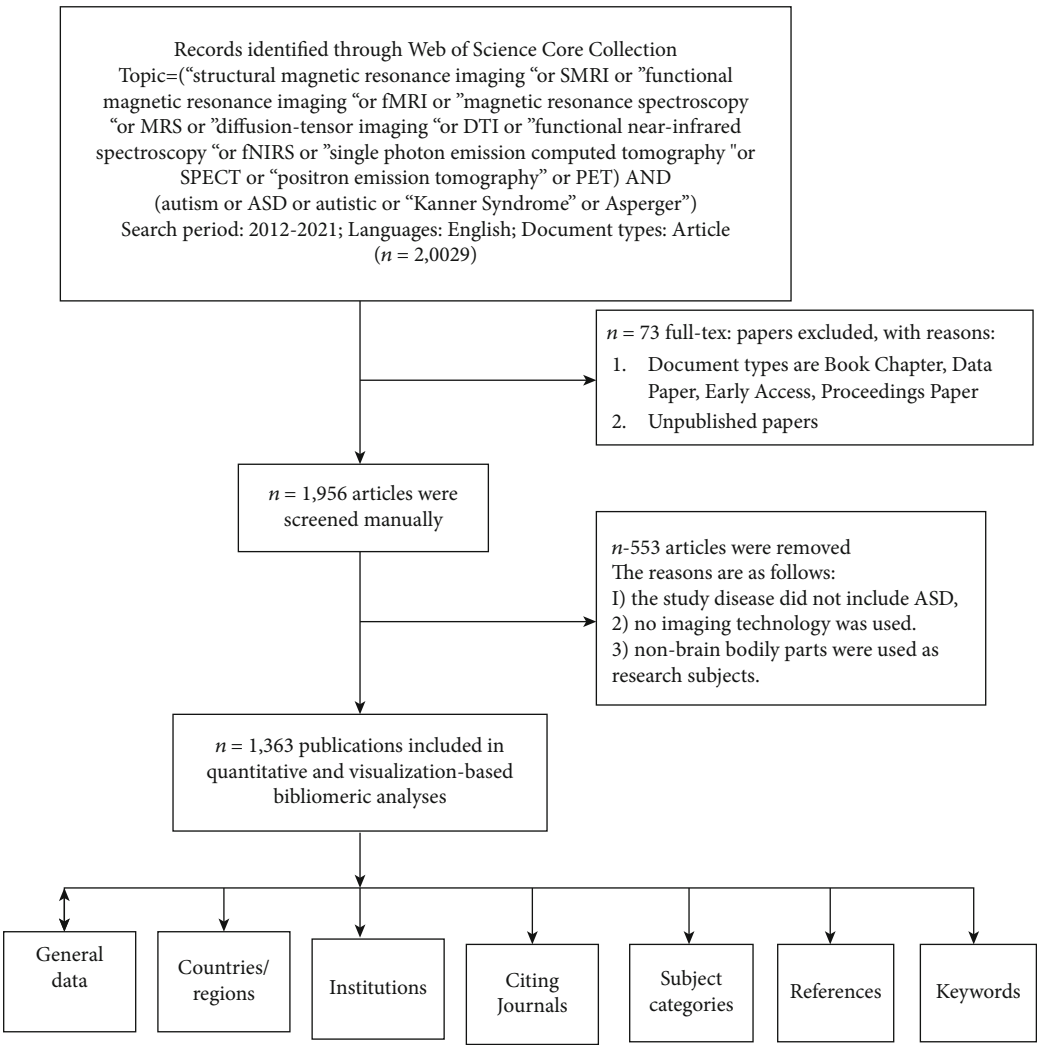


Figure 1: A frame flow diagram showing the detailed selection criteria and bibliometric analysis steps of neuroimaging of ASD.

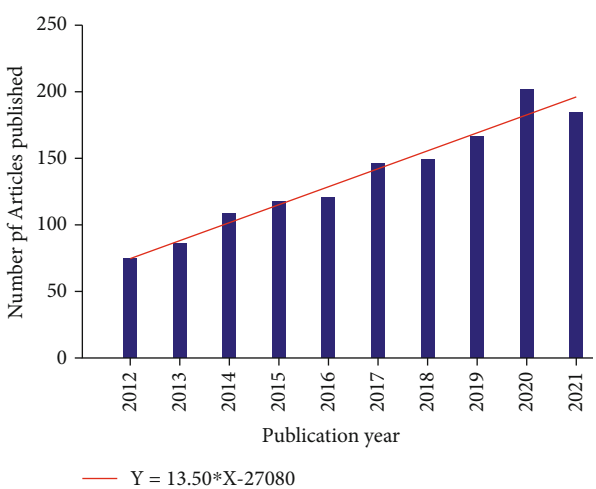


Figure 2: Trends in the number of publications on neuroimaging of ASD from 2012 to 2021.

label. The connection between regions indicates the existence of cooperative relationships among connected countries. For example, it is evident that the United States has the largest number of documents. Research that originated in the United States and the United Kingdom cooperates more closely with other countries. Figure 4 shows the national cooperation network using the VOSviewer, which shows that the primary country in this field is the United States. Table 1 quantifies the main findings. The default parameters of the CiteSpace program were used to generate centrality among them. The higher the centrality value, especially if it is larger than 0.1, the more essential the role. The United States (0.41), England (0.19), Germany (0.19), New Zealand (0.17), and the Netherlands (0.17) are the countries with the highest centrality among the top ten countries in terms of document volume (0.11). The *h*-index was derived from the WoS database search report and shows the article's influence. The two countries with the highest *h*-index are the United States (73) and the England (40). China has a large number of publications, but the centrality and *h*-index are small.

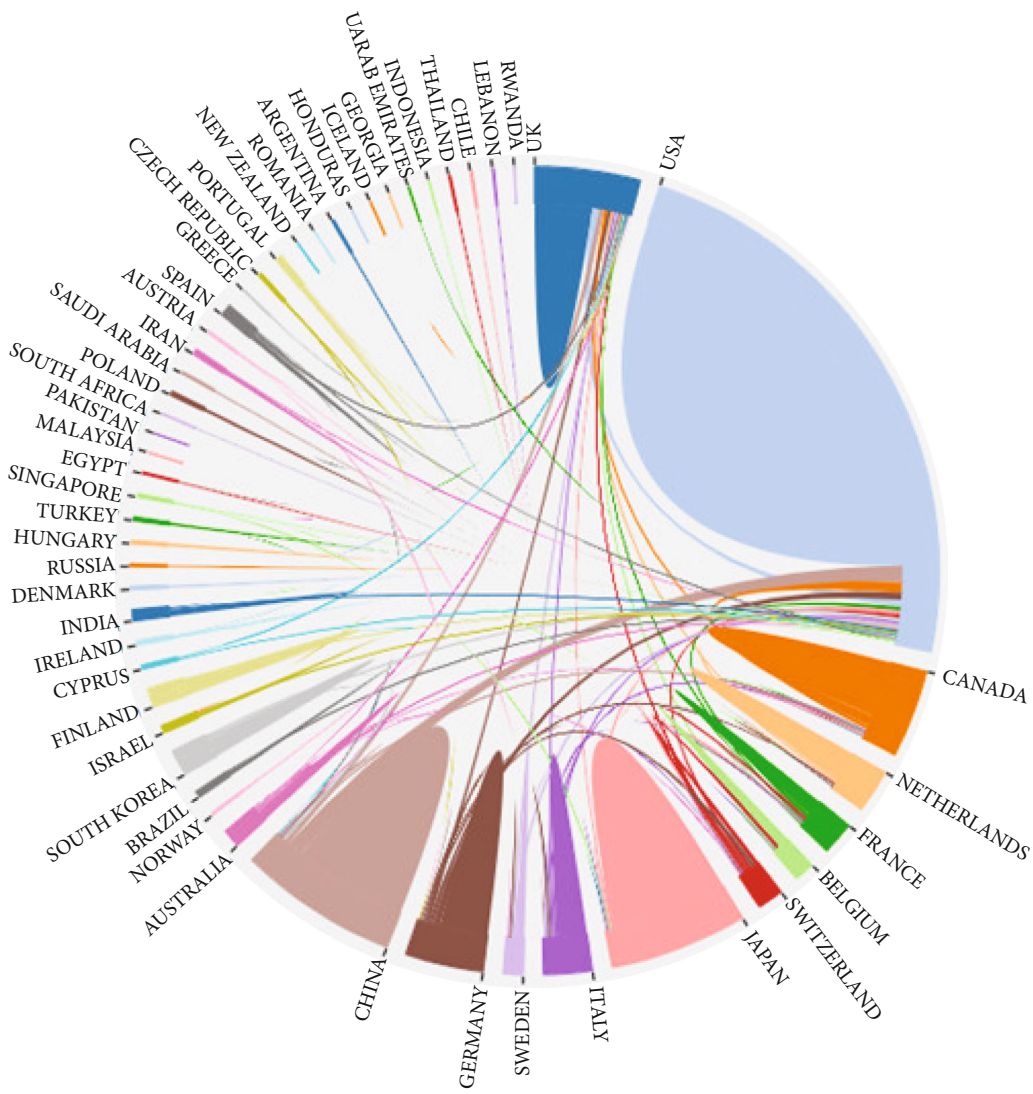


Figure 3: The cooperation of countries or regions that contributed to publications on neuroimaging of ASD from 2012 to 2021.

*4.3. Institutions.* The number and location of the top ten institutions are shown in Table 2. Their total number of documents accounts for 59.5% of all documents. Six American institutions are represented among these organizations: the University of California system (126 articles), Harvard University (86 articles), the University of North Carolina (55 articles), the University of Cambridge (53 articles), the University of North Carolina Chapel Hill (53 articles), and Yale University (51 articles). The number of documents issued by these institutions accounts for 52.28% of all documents issued by the top ten institutions. Furthermore, all of the top ten institutions are from developed countries.

*4.4. Journals and Research Categories.* We used CiteSpace to analyze citing journals and cited journals. Figure 5 shows the citing and cited journals in different research fields. On the left is the research field of citing journals, which represents the research frontier. On the right is the research field of cited journals, which represents the knowledge base. The colored lines represent a research discipline for which research in a specific field is often cited. It is evident from the lines shown in Figure 5 that articles published in journals in the research field of molecular/biology/genetics are probably cited by journals in the research field of molecular/biology/immunology/psychology/education/health. Articles published in journals in the research field of psychology/education/social are usually cited by journals in the research field of molecular/biology/immunology/neurology/sports/ophthalmology. Tables 3 and 4 list the top ten citing journals and cited journals, respectively. It was determined that the knowledge base of ASD neuroimaging research is mostly neuroscience articles. Based on the research field of the citing journals, it is evident that genetics in neuroimaging of ASD has become a research frontier.

Figure 6 shows the top ten research categories with citations analyzed using the CiteSpace software. Each circular node represents a research category. The area generation size of the node table shows the number of research categories. The purple ring represents centrality, which identifies and measures the publication's importance. A node with a high

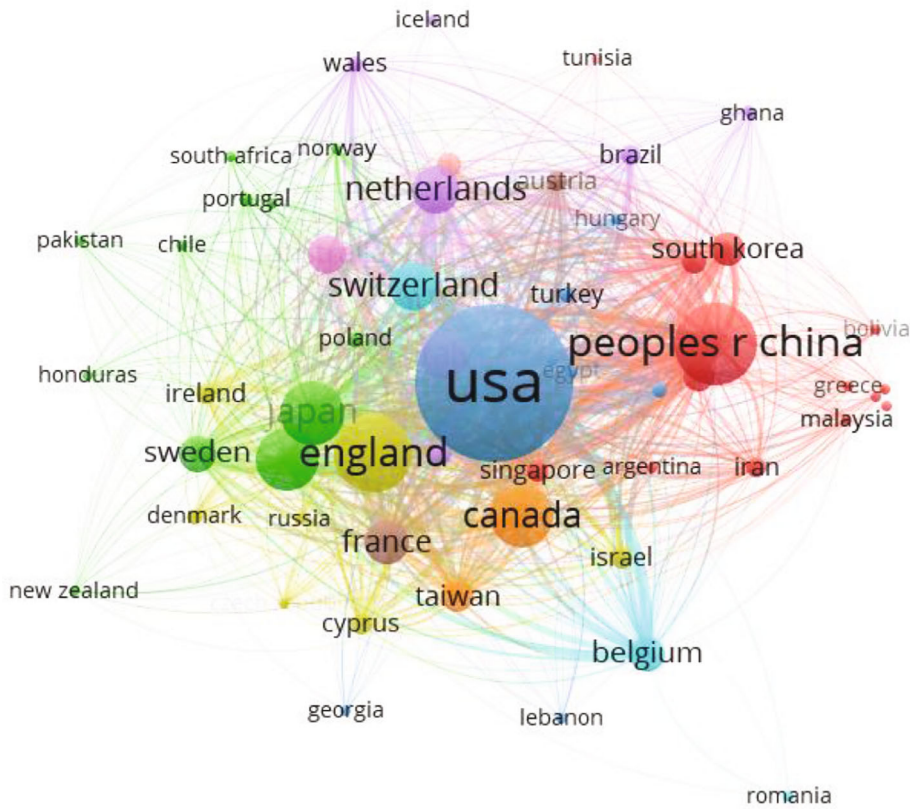


Figure 4: The cooperation of countries or regions that contributed to publications on neuroimaging of ASD from 2012 to 2021.

Table 1: The top 10 countries or regions with publications on neuroimaging of ASD from 2012 to 2021.

| Rank | Countries or regions | Count | Centrality | *h*-index |
|---|---|---|---|---|
| 1 | USA | 718 | 0.41 | 73 |
| 2 | People's Republic of China | 202 | 0.05 | 28 |
| 3 | England | 177 | 0.19 | 40 |
| 4 | Japan | 122 | 0.01 | 30 |
| 5 | Canada | 115 | 0.05 | 28 |
| 6 | Germany | 115 | 0.19 | 29 |
| 7 | Italy | 66 | 0.01 | 26 |
| 8 | Netherlands | 65 | 0.11 | 20 |
| 9 | Switzerland | 65 | 0.17 | 26 |
| 10 | France | 59 | 0.04 | 21 |

centrality was considered to be a pivotal point in the publication [26]. The number of each study category was derived using the WoS citation analysis function and is shown in Table 5. Both Figure 6 and Table 5 show that neuroscience has the largest number of studies, whereas psychology is the most influential research category.

*4.5. Keywords.* CiteSpace was used to analyze the keywords that emerged over time, which is depicted in Figure 7. The red block represents the period of emerging keywords. Year per slice was set to 2. In order to extract the top 10% keywords in each time period, we set the top *n*% to 10%. And the minimum duration was set to 2. The keywords that emerged during the period from 2012 to 2015 were Asperger syndrome, diffusion, corpus callosum, white matter, sentence comprehension, connectivity MRI, hippocampus, diagnostic interview, and high functioning autism. The keywords that emerged from 2012 to 2017 were sense comprehension and task. From 2018 to 2020, the emergent keywords were event-related fMRI, resting-state fMRI, and pattern, whereas the emerging keywords from 2018 to 2021 included identification and network.

*4.6. Citing Articles and References.* Table 6 lists the 10 most frequently cited studies in the literature. fMRI was used in all these studies. The main challenges and limitations of these studies include the lack of description of the changes in global brain functional connectivity in ASD patients with age. The subjects were not representative, and there were instances of limited age groups and high-function autism. In addition, the selection of a control group is a challenging problem.

The frequently cited literature had an important influence on their respective fields. We use the default setting of CiteSpace and a pruning algorithm to cluster the references. Indexing terms were used as the display of the clustering labels. Figure 8 shows the active topics over time. The influence of the cluster to which the references belong is arranged from top to bottom. The cluster tags are "#0 graph theory," "#1 functional connectivity," "#2 coherence," "#3 diffusion tensor imaging," "#4 classification," and "#5 infant." The

Table 2: The top 10 institutions with publications on neuroimaging of ASD from 2012 to 2021.

| Rank | Institutions | Country | Count | % of 1,363 |
|---|---|---|---|---|
| 1 | League of European Research Universities | Britain, Ireland, France, German, Italy, Sweden, Switzerland, Spain, Belgium, Finland, Denmark, Netherlands | 171 | 12.546 |
| 2 | University of California system | America | 126 | 9.244 |
| 3 | University of London | England | 93 | 6.823 |
| 4 | Harvard University | America | 86 | 6.31 |
| 5 | King's College London | England | 68 | 4.989 |
| 6 | University of North Carolina | America | 55 | 4.035 |
| 7 | University of Toronto | Canada | 55 | 4.035 |
| 8 | University of Cambridge | America | 53 | 3.888 |
| 9 | University of North Carolina Chapel Hill | America | 53 | 3.888 |
| 10 | Yale University | America | 51 | 3.742 |

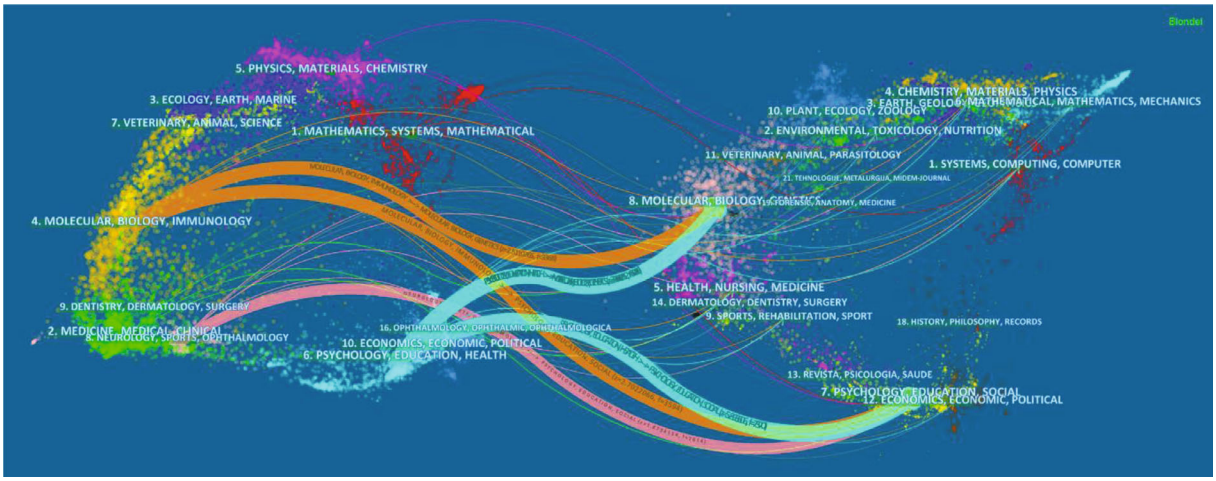


Figure 5: The dual map overlay of journals that contributed to publications on neuroimaging of ASD from 2012 to 2021.

Table 3: The top 10 citing journals of publications on neuroimaging of ASD from 2012 to 2021.

| Rank | Citing journals | Research fields | Count | 2020 journal impact factor |
|---|---|---|---|---|
| 1 | Autism Research | Medicine/behavioural science | 73 | 5.216 |
| 2 | NeuroImage: Clinical | Medicine/neuroimaging | 64 | 4.881 |
| 3 | Frontiers in Human Neuroscience | Medicine/neuroscience | 51 | 3.169 |
| 4 | Human Brain Mapping | Medicine/neuroimaging | 47 | 5.038 |
| 5 | Journal of Autism and Developmental Disorders | Psychology, developmental | 47 | 4.291 |
| 6 | Cerebral Cortex | Medicine/neuroscience | 44 | 5.357 |
| 7 | Translational Psychiatry | Medicine/psychiatry | 42 | 6.222 |
| 8 | Molecular Autism | Medicine/genetics | 40 | 7.509 |
| 9 | Frontiers in Neuroscience | Medicine/neuroscience | 39 | 3.59 |
| 10 | PLOS One | Multidisciplinary science | 37 | 3.24 |

bold timeline in Figure 8 indicates the active topic. The popular reference clusters that lasted until 2015 include coherence and diffusion tensor imaging. The active topic from 2013 to 2019 is infant, and the actively investigated fields that remained popular until 2020 include graph theory and functional connectivity.

Table 4: The top 10 cited journals of publications on neuroimaging of ASD from 2012 to 2021.

| Rank | Cited journals | Research fields | Count | 2020 journal impact factor |
|---|---|---|---|---|
| 1 | NeuroImage | Medicine/neuroscience | 1203 | 6.556 |
| 2 | Journal of Autism and Developmental Disorders | Psychology, developmental | 1005 | 4.291 |
| 3 | Biological Psychiatry | Medicine/neuroscience | 902 | 13.382 |
| 4 | Brain | Medicine/clinical neurology | 892 | 13.501 |
| 5 | Human Brain Mapping | Medicine/neuroimaging | 892 | 5.038 |
| 6 | Cerebral Cortex | Medicine/neuroscience | 872 | 5.357 |
| 7 | Journal of Neuroscience | Medicine/neuroscience | 845 | 6.167 |
| 8 | Proceedings of the National Academy of Sciences of the United States of America | Multidisciplinary sciences | 835 | 11.2048 |
| 9 | PLOS One | Multidisciplinary sciences | 766 | 3.24 |
| 10 | Neuron | Medicine/neuroscience | 697 | 17.173 |


Figure 6: The network map of research categories for publications on neuroimaging of ASD from 2012 to 2021.

## 5. Discussion

*5.1. Overall Results.* It is evident from the above results that the number of documents exhibited an overall stable rising trend from 2012 to 2021. As shown in Figure 2, the average annual growth is 13.5 articles. The number of literature in 2021 was lower compared to 2020, probably because of the challenges introduced due to COVID-19 in terms of research on ASD [37].

In terms of the number of national documents, the United States ranks first in the number and centrality of the documents and has the highest *h*-index. This shows that this country is in a leading position in this research field. In addition, the research of developed countries such as England, Germany, Switzerland, and the Netherlands has a strong central position and influence. In terms of the distribution of documents, the top ten research institutions are concentrated in the United States, the United Kingdom, Canada, and several developed countries in Europe, which corresponds to the analysis results of national distribution. The number of articles published by the League of European Research Universities (LERU) ranks first and accounts for approximately 12.5% of the total number of studies. LERU is a University Alliance of 23 research universities located in 12 countries in Europe [38]. Based on its strong academic potential and professional knowledge, it has an important impact on European research, innovation, and higher education policies [39]. It is evident that the number of documents issued is related to the strength of interagency contacts. Further, when the institutions are more closely linked, researchers can obtain more research resources and more integration between various professional disciplines, promoting the growth of the field.

In addition to neuroimaging, it is evident from the research direction of the top ten cited journals that most of the articles involve behavioral science, neuroscience, psychiatry, psychology, and genetics. The top three research directions include neuroscience, psychiatry, and psychological development, which account for approximately 81% of the total. Therefore, we can see that ASD neuroimaging combines the research on psychological and behavioral development. In addition, the change in research hotspots can be estimated from the emerging keywords over time. From 2012 to 2017, the research focused on a certain brain region of high-function autism and the relationship between brain function and psychological and behavioral development.

Table 5: The top 10 research categories for publications on neuroimaging of ASD from 2012 to 2021.

| Rank | Research categories | Count | % of 1,363 | Centrality |
|---|---|---|---|---|
| 1 | Neurosciences | 1203 | 46.809 | 0.17 |
| 2 | Psychiatry | 1005 | 19.369 | 0.08 |
| 3 | Psychology developmental | 902 | 14.6 | 0.25 |
| 4 | Neuroimaging | 892 | 13.94 | 0.00 |
| 5 | Behavioural sciences | 892 | 9.244 | 0.01 |
| 6 | Clinical neurology | 872 | 8.437 | 0.04 |
| 7 | Psychology | 845 | 8.217 | 0.25 |
| 8 | Radiology nuclear medicine medical imaging | 835 | 7.924 | 0.03 |
| 9 | Multidisciplinary science | 766 | 6.163 | 0.00 |
| 10 | Psychology experimental | 697 | 6.016 | 0.00 |

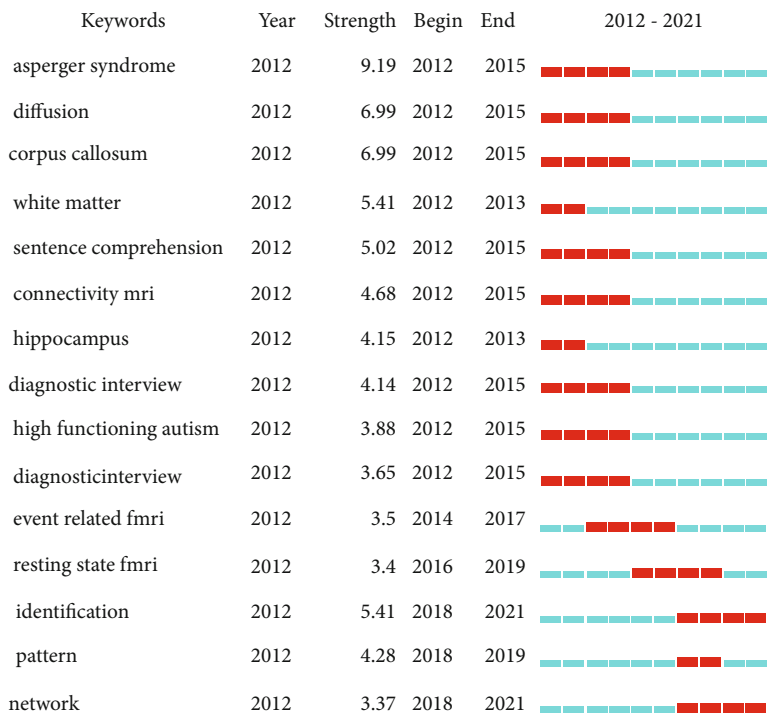


Figure 7: The keywords with the strongest citation bursts of publications on neuroimaging of ASD from 2012 to 2021.

From 2018 to 2020, functional magnetic resonance imaging was used to perform brain imaging of autism in different states. From 2018 until recently, research on autism recognition and brain networks has been a research hotspot. The importance of magnetic resonance imaging in neuroimaging research of autism is evident based on the emerging keywords and top 10 citing articles. From the analysis of the cited literature, it is evident that the knowledge base of current research is also focused on the classification and brain function connection of ASD patients. From the research limitations and challenges of the top ten cited literatures, it can be concluded that the research still has limitations. The more prominent limitations are that the subjects are not representative enough, and the image signal is likely to be disturbed. Future studies need to include subjects of different ages and disease grades. Imaging techniques that are less susceptible to interference and appropriate for ASD subjects must be prioritized.

In general, research institutions should strengthen contacts and promote new research. Functional magnetic resonance imaging had a significant influence in the field of neuroimaging of ASD. In recent years, the research has focused on the identification of diseases and the functional connectivity of brain networks.

### 5.2. Research Hotspots

*5.2.1. Identification.* At present, the gold standard for the diagnosis of ASD is based on behavioral science [40]. Research on the pathogenesis of ASD based on neuroimaging has been conducted, but this has not yet produced practical clinical applications [41].

Table 6: The top 10 citing articles on neuroimaging of ASD from 2012 to 2021.

| Rank | Title of citing documents | DOI | Times cited | Imaging technology | Interpretation of the findings | Research limitations or challenges |
|---|---|---|---|---|---|---|
| 1 | "The Autism Brain Imaging Data Exchange: Towards a Large-Scale Evaluation of the Intrinsic Brain Architecture in Autism" [27] | 10.1038/mp.2013.78 | 782 | fMRI | This study found that the internal functional connectivity of the whole brain of ASD exhibited the coexistence of high connectivity and low connectivity. The dysfunction sites of ASD lie in the middle and rear of the insula, the posterior cingulate gyrus, the cortex, and the thalamus. | (1) It is necessary to study the dynamic changes in brain function and age development of autism (2) Researchers should focus on standardized phenotypes, including an extended diagnostic assessment, and comprehensively describe the brain-behavior relationship of dimensions (3) Physiological measurements that can index ASD related brain dysfunction should be considered |
| 2 | "Differences in White Matter Fiber Tract Development Present from 6 to 24 Months in Infants with Autism" [28] | 10.1176/appi.ajp.2011.11091447 | 415 | MRI | This research established that longitudinal data are essential for categorizing the dynamic age-related brain and behavior changes at the core of this neurodevelopmental disorder. In the first year of life, abnormal development of white matter pathways may precede the manifestation of autistic symptoms. | (1) In this study, only high-risk ASD siblings were included, and the absence of a low-risk control group limited the interpretation of results beyond ASD family background (2) Follow-up evaluation provides a positive guarantee for the diagnostic results |
| 3 | "Single Subject Prediction of Brain Disorders in Neuroimaging: Promises and Pitfalls" [29] | 10.1016/j.neuroimage.2016.02.079 | 375 | MRI | This study shows that neuroimaging data have great potential in predicting various diseases in a single subject. At present, the limited sample size is a problem, which can be solved by the modern data sharing model discussed in this paper. | (1) This review examined limited diseases (2) Some potential problems in the research were covered in this review, such as experimental design, the influence of head movement, and other factors on fMRI research |
| 4 | "Brain Hyperconnectivity in Children with Autism and Its Links to Social Deficits" [30] | 10.1016/j.celrep.2013.10.001 | 293 | fMRI | This study found that the brains of autistic patients are highly connected in function, leading to their social dysfunction. | ASD subjects do not fully represent the characteristics of this group |
| 5 | "Identification of Autism Spectrum Disorder Using Deep Learning and the ABIDE Dataset" [31] | 10.1016/j.nicl.2017.08.017 | 253 | fMRI | This study objectively identified the functional connection patterns of ASD participants from fMRI data. | This study failed to provide an overall assessment of autism classification. The use of resting-state fMRI data does not meet the biomarker criteria |

Table 6: Continued.

| Rank | Title of citing documents | DOI | Times cited | Imaging technology | Interpretation of the findings | Research limitations or challenges |
|---|---|---|---|---|---|---|
| 6 | "Deriving Reproducible Biomarkers from Multi-site Resting-State Data: An Autism-Based Example" [32] | 10.1016/ j.neuroimage.2016.09.038 | 241 | fMRI | This study proved the feasibility of using fMRI to classify the neuropsychiatric states of autism. | (1) There is a deviation in the representativeness of the study samples (2) The predictive indicators of the classification model only use accuracy and do not use additional criteria, such as sensitivity and specificity (3) Limitations of data sets included in the study |
| 7 | "Altered Functional and Structural Brain Network Organization in Autism" [33] | 10.1016/ j.neuroimage.2016.10.045 | 240 | fMRI | Children and adolescents with ASD demonstrated typical age-related modifications in the balance of local and global efficiency between structural and functional networks. And this imbalance was related to the severity of ASD individuals' socio-communicative deficiencies. | (1) This study was limited to ASD high functioning children and adolescents (2) More imaging acquisition, more adaptable modeling methods, and large-scale collaborative mechanism research will be encouraged (3) The comparison with other neurological diseases and the study of potential mechanisms such as genetic risk factors are very important for the description of brain network abnormalities in autism |
| 8 | "Fractionation of Social Brain Circuits in Autism Spectrum Disorders" [34] | 10.1016/ j.nicl.2012.11.006 | 213 | fMRI | This study found reduced connectivity between social brain regions. In addition, the connections between the regions supporting language and sensory-motor processes and limbic-related brain regions were also selective. | (1) The subjects' ASD symptoms were underrepresented (2) Selecting an appropriate control group was a challenging task |
| 9 | "Impaired Thalamocortical Connectivity in Autism Spectrum Disorder: A Study of Functional and Anatomical Connectivity" [35] | 10.1093/brain/aws160 | 200 | fMRI and DTI | Compared with matched participants with normal development, the anatomical connectivity and functional connectivity of ASD children and adolescents were generally reduced. | (1) The subjects included in this study are underrepresented (2) The correlation between ASD thalamic connectivity index and the neuropsychological score is affected by variability (3) The specificity of the connection between the narrower specialized region and the thalamus, and any abnormality may not be found |

Table 6: Continued.

| Rank | Title of citing documents | DOI | Times cited | Imaging technology | Interpretation of the findings | Research limitations or challenges |
|---|---|---|---|---|---|---|
| 10 | "Default Mode Network in Childhood Autism: Posteromedial Cortex Heterogeneity and Relationship with Social Deficits" [36] | 10.1016/ j.biopsych.2012.12.013 | 197 | fMRI | The precuneus showed hypoconnectivity with the visual cortex, basal ganglia, and locally within the posteromedial cortex in ASD children. The severity of social impairments in ASD was linked to abnormal posterior cingulate cortex hyperconnectivity, but precuneus hypoconnectivity was unrelated to social deficits. | (1) The age of the subjects selected in the study of the coordinate definition reference of the region of interest is different from that in this study (2) Potential impact of uncontrolled drugs and comorbid diseases on study results |

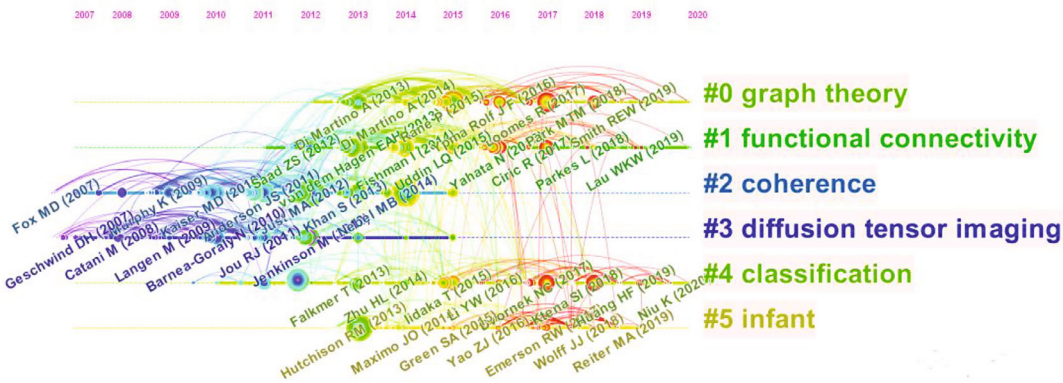


Figure 8: Cocited reference timeline map of publications on neuroimaging of ASD from 2012 to 2021.

One possible reason is that the recruited subjects are not fully representative of the ASD population in terms of symptoms and number [33, 35]. The complexity of brain connections and the heterogeneity of ASD hinder efforts to identify abnormal neurobiological signals [42, 43]. The combination of Autism Brain Imaging Data Exchange I (ABTDE I) and Autism Brain Imaging Data Exchange II (ABIDE II) provides researchers with a cross-sectional data set that allows for the selection of samples for scientific research [44]. Bi et al. proposed a cluster classifier with 100% accuracy to classify ASD patients and typical controls in the ABIDE database [45]. Dominic et al. used the four-dimensional resting-state fMRI obtained from ABIDE I to prove the detectability of ASD neuroimaging markers [46]. Eslami et al. designed a data enhancement strategy and used brain imaging data from 17 different brain imaging centers to generate the synthetic data set required to train a machine learning model to distinguish between the fMRI data of ASD. Finally, 82% classification accuracy was obtained [47]. Li et al. used ABIDE data set to evaluate a functional diagram discrimination network for ASD classification, which proved that this method can effectively distinguish between ASD patients and healthy controls [48].

In addition to the existing neuroimaging database, task state and resting-state ASD neuroimaging data can also identify atypical neurophysiological signals. Pretzsch et al. used fMRI analysis to determine that individuals with autism spectrum disorders have low functional connectivity (FC) between the ventral striatum and the frontal and pericentral regions (related to emotional, motor, and visual processing). In addition, they had higher striatum FC and higher putamen FC, and the temporal region involved speech and language [49]. A study conducted in Japan using fNIRS and a fragrance pulse injection system found that ASD participants with lower odor sensitivity presented reduced activity of the right dorsolateral prefrontal cortex in response to odor stimuli compared to a TD control group [50]. Several studies have also demonstrated that ASD has atypical features of FA and FC when performing language judgment, facial difference recognition, and memory tasks [51–53]. Neuroscience research on early identification of ASD or people at high risk for ASD has been emphasized [54, 55]. Earlier studies have established that the atypical development of ASD is related to the abnormal whole-brain connection, which may be congenital [56]. Padilla et al. studied the relationship between the MRI of infants

with a gestational age of less than 27 weeks and preterm infants at full term and the future diagnosis of ASD (at the age of 6.5 years). It was determined that the MRI scan of ASD in infancy showed that the brain structure was different from that of typical development (TD) infants [57]. An fNIRS study found that compared to low-risk siblings of ASD subjects, high-risk siblings of ASD infants had reduced functional activity (FA) and FC during social interaction at 6 to 9 months, and hyperlinks were present between hemispheres at rest [58]. Many studies have shown that fNIRS is a promising tool to explore the neural development of ASD [59–61].

There are usually two ways to use neuroimaging for specific signal discrimination of ASD. One is to use public data sets, such as ABIDE, and the other is to analyze neural signal data under various task stimuli or resting states. A rigorous scientific evaluation of all task paradigms must be considered. Several studies have determined that fNIRS is a good choice for neural network connectivity analysis of ASD infants and young children compared to functional magnetic resonance imaging, because it has relatively high time resolution and is more tolerant to head motion [62, 63].

*5.2.2. Network.* Neuroimaging technology can describe the neurophysiological patterns of different brain regions, which helps individuals to identify the abnormal brain structure and functional connections between TD individuals and nontypical development people.

Due to the heterogeneity of ASD, the description of atypical functional activation and functional connection of different brain regions in various states of ASD for a given period involves a variety of sensory organs or behavioral responses. For example, the theory-of-mental (ToM) network, including the medial prefrontal cortex, temporoparietal junction, inferior frontal gyrus, superior temporal sulcus, and posterior cingulate cortex, which is related to the development of key skills for effective social interaction, reflects the atypical ability of ASD subjects to emphasize and attribute views and intentions. Kana et al. demonstrated that when ASD individuals watched an animation of geometry, both FA and FC in the ToM network decreased [64]. Cao et al. found that the atypical development of the right temporoparietal junction may be a crucial aspect regarding the social defects of autistic patients from childhood to adolescence [65]. Farrant and Uddin found a hyperconnectivity of regions of interest in ASD children's attention network [66]. He et al. used MRI and discovered that the morphological connectivity of the cortical-striatum-thalamus-cortical network of ASD increased and the morphological connectivity of the cortical-cortical network decreased [16]. In addition, several studies have shown that the working memory neural network and visual-motor neural network of ASD exhibit different FC patterns compared to a TD group [67, 68].

In the field of medical imaging, artificial intelligence computer-aided diagnosis technology, including machine learning and deep learning algorithms, plays an important role [69]. The current research indicates that the development of new feature selection methods is an important direction of classification between ASD individuals and TD subjects, which can promote the application of machine learning methods to determine the most discriminative features [70]. A convolutional neural network (CNN) is an example of a deep learning algorithm, which can probably serve as a classifier for ASD recognition [71]. Wang et al. proposed a CCN architecture for fMRI analysis, which can effectively capture the FC characteristics of related applications in fMRI analysis [72]. A deep learning algorithm (deep belief network (DBN)) was used to combine the data from an Autism Brain Imaging Data Exchange I and II (ABIDE I and ABIDE II) to diagnose childhood ASD [73]. He et al. found that when the artificial neural network model is applied to the FC group data of very preterm infants, it can predict the cognitive results for 2 years old [74].

In general, the development of artificial intelligence-based models combined with neuroimaging datasets or task-based neurobiological signal data as a tool for diagnosing ASD has recently become an active area of research.

*5.3. Study Limitations.* The current research has some potential limitations. First, the downloaded citation only contains research in the WoSCC database for approximately a decade (2012-2021) and does not include earlier literature or that of other databases, which may cause a bias. Secondly, although the two authors manually removed irrelevant literature and participated in data analysis, this does not exclude subjective judgment. Third, some recent studies are in progress and have not been published, which will also bias the research results.

## 6. Conclusion

In conclusion, combining fMRI data to identify computer-aided diagnosis technology with higher accuracy for ASD discrimination and for determining the difference between FA and FC of neural networks that describe different states of ASD has become an area of active research. Among the countries involved in this research, the United States is the most influential in the field of ASD neuroimaging. Close cooperation between countries has positively impacted research progress. There are more fMRI-related studies than other neuroimaging studies. However, several studies are limited by their inadequate sample representation. To better address this problem, the strengthening of interagency contacts and the establishment of an ASD imaging database are recommended to promote scientific inquiry. In addition, fNIRS is proposed as a more suitable imaging research tool for the study of ASD neural FC and FA. In the future, research on systematic and accurate AI algorithms for ASD imaging data discrimination should be encouraged. This could serve as the basis for studies on neuroimaging of ASD in different psychological and behavioral states, which can inspire new ideas about the diagnosis and intervention training of ASD and should be explored. These findings can potentially inspire new ideas about the diagnosis and intervention training of ASD and serve as a reference for clinicians, rehabilitation trainers, and the staff of special education institutions.

## Data Availability

The underlying data used to support the findings of this study are available from the corresponding author upon request.

## Conflicts of Interest

The authors declare that the research was conducted in the absence of any commercial or financial relationships that could be construed as a potential conflict of interest.

## Authors' Contributions

Yi Lu and Li Zhang contributed to the work equally and should be regarded as co-first authors.

## Acknowledgments

The research was funded by the Science and Technology Development Fund of Nanjing Medical University (NMUB20210079).

## References

[1] C. Rachel, *Diagnosing the diagnostic and statistical manual of mental disorders:fifth edition*, Taylor and Francis, 2013.

[2] L. Rylaarsdam and A. Guemez-Gamboa, "Genetic causes and modifiers of autism spectrum disorder," *Frontiers in Cellular Neuroscience*, vol. 13, p. 385, 2019.

[3] K. A. Shaw, M. J. Maenner, A. V. Bakian et al., "Early identification of autism spectrum disorder among children aged 4 years - autism and developmental disabilities monitoring network, 11 sites, united states, 2018," *MMWR Surveillance Summaries*, vol. 70, pp. 1–14, 2021.

[4] K. A. Shaw, M. J. Maenner, J. Baio et al., "Early identification of autism spectrum disorder among children aged 4 years - early autism and developmental disabilities monitoring network, six sites, united states, 2016," *Mmwr Surveillance Summaries*, vol. 69, pp. 1–11, 2020.

[5] K. L. Coulter, M. L. Barton, H. Boorstein et al., "The toddler autism symptom inventory: use in diagnostic evaluations of toddlers," *Autism*, vol. 25, pp. 2386–2399, 2021.

[6] A. B. Hinojosa, L. L. Garcia, O. P. Navarro, E. V. Bondelle, and R. C. Escalona, "Sensitivity and specificity of dsm-5 diagnostic criteria for autism spectrum disorder in a child and adolescent sample," *Revista de Psiquiatría y Salud Mental (English Edition)*, vol. 14, pp. 202–211, 2021.

[7] F. Craig, A. Crippa, A. De Giacomo et al., "Differences in developmental functioning profiles between male and female preschoolers children with autism spectrum disorder," *Autism Research*, vol. 13, pp. 1537–1547, 2020.

[8] M. Astorkia, H. M. Lachman, and D. Y. Zheng, "Characterization of cell-cell communication in autistic brains with single-cell transcriptomes," *Journal of Neurodevelopmental Disorders*, vol. 14, p. 20, 2022.

[9] C. P. Santana, E. A. de Carvalho, I. D. Rodrigues, G. S. Bastos, A. D. de Souza, and L. L. de Brito, "rs-fMRI and machine learning for ASD diagnosis: a systematic review and meta-analysis," *Scientific Reports*, vol. 12, p. 20, 2022.

[10] L. Xu, X. X. Zheng, S. X. Yao et al., "The mirror neuron system compensates for amygdala dysfunction- associated social deficits in individuals with higher autistic traits," *Neuroimage*, vol. 251, p. 11, 2022.

[11] S. Uono, W. Sato, T. Kochiyama et al., "Neural substrates of the ability to recognize facial expressions: a voxel-based morphometry study," *Social Cognitive and Affective Neuroscience*, vol. 12, pp. 487–495, 2017.

[12] S. Vigneshwaran, S. Suresh, B. S. Mahanand, N. Sundararajan, and IEEE, "ASD detection in males using MRI- an age-group based study," in *Presented at International Joint Conference on Neural Networks (IJCNN), Killarney, IRELAND, 2015. IEEE International Joint Conference on Neural Networks (IJCNN)*, New York, 2015.

[13] G. J. Cardon, S. Hepburn, and D. C. Rojas, "Structural covariance of sensory networks, the cerebellum, and amygdala in autism spectrum disorder," *Frontiers in Neurology*, vol. 8, p. 10, 2017.

[14] V. P. Reinhardt, A. M. Iosif, L. Libero et al., "Understanding hippocampal development in young children with autism spectrum disorder," *Journal of the American Academy of Child and Adolescent Psychiatry*, vol. 59, pp. 1069–1079, 2020.

[15] D. A. Baribeau, A. Dupuis, T. A. Paton et al., "Structural neuroimaging correlates of social deficits are similar in autism spectrum disorder and attention-deficit/hyperactivity disorder: analysis from the pond network," *Translational Psychiatry*, vol. 9, p. 14, 2019.

[16] C. C. He, J. M. Cortes, X. D. Kang et al., "Individual-based morphological brain network organization and its association with autistic symptoms in young children with autism spectrum disorder," *Human Brain Mapping*, vol. 42, pp. 3282–3294, 2021.

[17] E. D. Bigler, "Magnetic resonance imaging in the evaluation of cognitive function," *Pediatric Blood & Cancer*, vol. 61, pp. 1724–1728, 2014.

[18] M. Khodatars, A. Shoeibi, D. Sadeghi et al., "Deep learning for neuroimaging-based diagnosis and rehabilitation of autism spectrum disorder: a review," *Computers in Biology and Medicine*, vol. 139, p. 25, 2021.

[19] S. X. Yao, B. Becker, and K. M. Kendrick, "Reduced inter-hemispheric resting state functional connectivity and its association with social deficits in autism," *Frontiers in Psychiatry*, vol. 12, p. 12, 2021.

[20] E. Conti, E. Scaffei, C. Bosetti et al., "Looking for "fNIRS signature" in autism spectrum: a systematic review starting from preschoolers," *Frontiers in Neuroscience*, vol. 16, p. 13, 2022.

[21] S. Lloyd-Fox, A. Blasi, and C. E. Elwell, "Illuminating the developing brain: the past, present and future of functional near infrared spectroscopy," *Neuroscience and Biobehavioral Reviews*, vol. 34, pp. 269–284, 2010.

[22] T. C. Ford and D. P. Crewther, "A comprehensive review of the h-1-mrs metabolite spectrum in autism spectrum disorder," *Frontiers in Molecular Neuroscience*, vol. 9, p. 27, 2016.

[23] B. J. Hwang, M. A. Mohamed, and J. R. Brasic, "Molecular imaging of autism spectrum disorder," *International Review of Psychiatry*, vol. 29, pp. 530–554, 2017.

[24] N. R. Zurcher, A. Bhanot, C. J. McDougle, and J. M. Hooker, "A systematic review of molecular imaging (pet and spect) in autism spectrum disorder: current state and future research opportunities," *Neuroscience and Biobehavioral Reviews*, vol. 52, pp. 56–73, 2015.

[25] K. H. Taber and R. A. Hurley, "The role for diffusion tensor imaging in neuropsychiatry," *Current Opinion in Psychiatry*, vol. 16, pp. 341–347, 2003.

[26] K. Y. Zheng and X. Q. Wang, "Publications on the association between cognitive function and pain from 2000 to 2018: a bibliometric analysis using citespace," *Medical Science Monitor*, vol. 25, pp. 8940–8951, 2019.

[27] A. Di Martino, C. G. Yan, Q. Li et al., "The autism brain imaging data exchange: towards a large-scale evaluation of the intrinsic brain architecture in autism," *Molecular Psychiatry*, vol. 19, pp. 659–667, 2014.

[28] J. J. Wolff, H. B. Gu, G. Gerig et al., "Differences in white matter fiber tract development present from 6 to 24 months in infants with autism," *American Journal of Psychiatry*, vol. 169, pp. 589–600, 2012.

[29] M. R. Arbabshirani, S. Plis, J. Sui, and V. D. Calhoun, "Single subject prediction of brain disorders in neuroimaging: promises and pitfalls," *Neuroimage*, vol. 145, pp. 137–165, 2017.

[30] K. Supekar, L. Q. Uddin, A. Khouzam et al., "Brain hyperconnectivity in children with autism and its links to social deficits," *Cell Reports*, vol. 5, pp. 738–747, 2013.

[31] A. S. Heinsfeld, A. R. Franco, R. C. Craddock, A. Buchweitz, and F. Meneguzzi, "Identification of autism spectrum disorder using deep learning and the abide dataset," *Neuroimage-Clinical*, vol. 17, pp. 16–23, 2018.

[32] A. Abraham, M. P. Milham, A. Di Martino et al., "Deriving reproducible biomarkers from multi-site resting-state data: an autism-based example," *Neuroimage*, vol. 147, pp. 736–745, 2017.

[33] J. D. Rudie, J. A. Brown, D. Beck-Pancer et al., "Altered functional and structural brain network organization in autism," *Neuroimage-Clinical*, vol. 2, pp. 79–94, 2013.

[34] S. J. Gotts, W. K. Simmons, L. A. Milbury, G. L. Wallace, R. W. Cox, and A. Martin, "Fractionation of social brain circuits in autism spectrum disorders," *Brain*, vol. 135, pp. 2711–2725, 2012.

[35] A. Nair, J. M. Treiber, D. K. Shukla, P. Shih, and R. A. Muller, "Impaired thalamocortical connectivity in autism spectrum disorder: a study of functional and anatomical connectivity," *Brain*, vol. 136, pp. 1942–1955, 2013.

[36] C. J. Lynch, L. Q. Uddin, K. Supekar, A. Khouzam, J. Phillips, and V. Menon, "Default mode network in childhood autism: posteromedial cortex heterogeneity and relationship with social deficits," *Biological Psychiatry*, vol. 74, pp. 212–219, 2013.

[37] D. Rudd and S. K. Hwang, "Participatory research in a pandemic: the impact of covid-19 on co-designing research with autistic people," *Qualitative Social Work*, vol. 11, 2021.

[38] https://www.leru.org/members.

[39] https://www.leru.org/mission.

[40] American Psychiatric Association, *Diagnostic and statistical manual of mental disorders: Dsm-5*, American Psychiatric Association, Washington, DC, 2013.

[41] D. Baribeau and E. Anagnostou, *Neuroimaging in Autism Spectrum Disorders*, Springer, New York, 2015.

[42] C. Kelly, B. B. Biswal, C. Craddock, F. X. Castellanos, and M. P. Milham, "Characterizing variation in the functional connectome: promise and pitfalls," *Trends in Cognitive Sciences*, vol. 16, pp. 181–188, 2012.

[43] R. Grzadzinski, M. Huerta, and C. Lord, "DSM-5 and autism spectrum disorders (ASDs): an opportunity for identifying ASD subtypes," *Molecular Autism*, vol. 4, p. 6, 2013.

[44] A. Di Martino, D. O'Connor, B. Chen et al., "Data descriptor: enhancing studies of the connectome in autism using the autism brain imaging data exchange II," *Scientific Data*, vol. 4, p. 15, 2017.

[45] X. A. Bi, Y. C. Liu, Q. Jiang, Q. Shu, Q. Sun, and J. H. Dai, "The diagnosis of autism spectrum disorder based on the random neural network cluster," *Frontiers in Human Neuroscience*, vol. 12, 2018.

[46] N. Dominic, T. W. Daniel, A. Cenggoro, A. Budiarto, and B. Pardamean, "Transfer learning using inception-ResNet-v2 model to the augmented neuroimages data for autism spectrum disorder classification," *Communications in Mathematical Biology and Neuroscience*, vol. 21, 2021.

[47] T. Eslami, V. Mirjalili, A. Fong, A. R. Laird, and F. Saeed, "ASD-DiagNet: a hybrid learning approach for detection of autism spectrum disorder using fMRI data," *Frontiers in Neuroinformatics*, vol. 13, p. 11, 2019.

[48] J. C. Li, F. Wang, J. H. Pan, and Z. F. Wen, "Identification of autism spectrum disorder with functional graph discriminative network," *Frontiers in Neuroscience*, vol. 15, p. 11, 2021.

[49] C. M. Pretzsch, D. L. Floris, B. Voinescu et al., "Modulation of striatal functional connectivity differences in adults with and without autism spectrum disorder in a single-dose randomized trial of cannabidivarin," *Molecular Autism*, vol. 12, p. 14, 2021.

[50] M. D. Xu, Y. Minagawa, H. Kumazaki, K. Okada, and N. Naoi, "Prefrontal responses to odors in individuals with autism spectrum disorders: functional nirs measurement combined with a fragrance pulse ejection system," *Frontiers in Human Neuroscience*, vol. 14, p. 17, 2020.

[51] A. Bernas, E. M. Barendse, A. P. Aldenkamp et al., "Brain resting-state networks in adolescents with high-functioning autism: analysis of spatial connectivity and temporal neurodynamics," *Brain and Behavior*, vol. 8, p. 10, 2018.

[52] L. Y. Fan, J. R. Booth, M. Liu, T. L. Chou, and S. S. F. Gau, "Developmental differences in neural connectivity for semantic processing in youths with autism," *Journal of Child Psychology and Psychiatry*, vol. 62, pp. 1090–1099, 2021.

[53] J. Bathelt, P. C. M. Koolschijn, and H. M. Geurts, "Atypically slow processing of faces and non-faces in older autistic adults," *Autism*, vol. 15, 2021.

[54] L. K. Koegel, R. L. Koegel, K. Ashbaugh, and J. Bradshaw, "The importance of early identification and intervention for children with or at risk for autism spectrum disorders," *International Journal of Speech-Language Pathology*, vol. 16, pp. 50–56, 2014.

[55] M. Steele, M. Uljarevic, G. Rached et al., "Psychiatric characteristics across individuals with PTEN mutations," *Frontiers in Psychiatry*, vol. 12, p. 7, 2021.

[56] M. L. Bauman and T. L. Kemper, "Neuroanatomic observations of the brain in autism: a review and future directions," *International Journal of Developmental Neuroscience*, vol. 23, pp. 183–187, 2005.

[57] N. Padilla, E. Eklof, G. E. Martensson, S. Bolte, H. Lagercrantz, and U. Aden, "Poor brain growth in extremely preterm neonates long before the onset of autism spectrum disorder symptoms," *Cerebral Cortex*, vol. 27, pp. 1245–1252, 2017.

[58] A. N. Bhat, N. M. McDonald, J. E. Eilbott, and K. A. Pelphrey, "Exploring cortical activation and connectivity in infants with and without familial risk for autism during naturalistic social interactions: a preliminary study," *Infant Behavior & Development*, vol. 57, p. 15, 2019.

[59] T. Liu, X. C. Liu, L. Yi, C. Z. Zhu, P. S. Markey, and M. Pelowski, "Assessing autism at its social and developmental roots: a review of autism spectrum disorder studies using functional near-infrared spectroscopy," *Neuroimage*, vol. 185, pp. 955–967, 2019.

[60] A. Mazzoni, R. Grove, V. Eapen, R. K. Lenroot, and J. Bruggemann, "The promise of functional near-infrared spectroscopy in autism research: what do we know and where do we go?," *Social Neuroscience*, vol. 14, pp. 505–518, 2019.

[61] F. Zhang and H. Roeyers, "Exploring brain functions in autism spectrum disorder: a systematic review on functional near-infrared spectroscopy (fNIRS) studies," *International Journal of Psychophysiology*, vol. 137, pp. 41–53, 2019.

[62] H. J. Niu, Z. Li, X. H. Liao et al., "Test-retest reliability of graph metrics in functional brain networks: a resting-state fnirs study," *Plos One*, vol. 8, p. 18, 2013.

[63] F. Irani, S. M. Platek, S. Bunce, A. C. Ruocco, and D. Chute, "Functional near infrared spectroscopy (fnirs): an emerging neuroimaging technology with important applications for the study of brain disorders," *The Clinical Neuropsychologist*, vol. 21, no. 1, pp. 9–37, 2007.

[64] R. K. Kana, J. O. Maximo, D. L. Williams et al., "Aberrant functioning of the theory-of-mind network in children and adolescents with autism," *Molecular Autism*, vol. 6, p. 12, 2015.

[65] W. Cao, H. L. Zhu, Y. Li et al., "The development of brain network in males with autism spectrum disorders from childhood to adolescence: evidence from fnirs study," *Brain Sciences*, vol. 11, p. 13, 2021.

[66] K. Farrant and L. Q. Uddin, "Atypical developmental of dorsal and ventral attention networks in autism," *Developmental Science*, vol. 19, pp. 550–563, 2016.

[67] E. M. Barendse, L. J. Schreuder, G. Thoonen et al., "Working memory network alterations in high-functioning adolescents with an autism spectrum disorder," *Psychiatry and Clinical Neurosciences*, vol. 72, pp. 73–83, 2018.

[68] R. J. Lepping, W. S. McKinney, G. C. Magnon et al., "Visuomotor brain network activation and functional connectivity among individuals with autism spectrum disorder," *Human Brain Mapping*, vol. 43, pp. 844–859, 2022.

[69] P. B. Bhattad and V. Jain, "Artificial intelligence in modern medicine - the evolving necessity of the present and role in transforming the future of medical care," *Cureus*, vol. 12, p. 5, 2020.

[70] M. J. Liu, B. J. Li, and D. W. Hu, "Autism spectrum disorder studies using fmri data and machine learning: a review," *Frontiers in Neuroscience*, vol. 15, p. 17, 2021.

[71] M. R. Ahmed, Y. Zhang, Y. Liu, and H. E. Liao, "Single volume image generator and deep learning-based asd classification," *IEEE Journal of Biomedical and Health Informatics*, vol. 24, pp. 3044–3054, 2020.

[72] L. B. Wang, K. M. Li, and X. P. P. Hu, "Graph convolutional network for fMRI analysis based on connectivity neighborhood," *Network Neuroscience*, vol. 5, pp. 83–95, 2021.

[73] M. A. Aghdam, A. Sharifi, and M. M. Pedram, "Combination of rs-fMRI and sMRI data to discriminate autism spectrum disorders in young children using deep belief network," *Journal of Digital Imaging*, vol. 31, pp. 895–903, 2018.

[74] L. L. He, H. L. Li, S. K. Holland, W. H. Yuan, M. Altaye, and N. A. Parikh, "Early prediction of cognitive deficits in very preterm infants using functional connectome data in an artificial neural network framework," *Neuroimage-Clinical*, vol. 18, pp. 290–297, 2018.

Hindawi
Disease Markers
Volume 2022, Article ID 3406890, 10 pages
https://doi.org/10.1155/2022/3406890

*Review Article*

# Research Progress of Artificial Intelligence Image Analysis in Systemic Disease-Related Ophthalmopathy

**Yuke Ji**,[1] **Nan Chen**,[1] **Sha Liu**,[1] **Zhipeng Yan**,[1] **Hui Qian**,[1] **Shaojun Zhu**,[2] **Jie Zhang**,[3] **Minli Wang**,[4] **Qin Jiang**,[1] **and Weihua Yang**[1]

[1]*The Laboratory of Artificial Intelligence and Bigdata in Ophthalmology, Affiliated Eye Hospital, Nanjing Medical University, Nanjing, China*
[2]*School of Information Engineering, Huzhou University, Huzhou, China*
[3]*Advanced Ophthalmology Laboratory (AOL), Robotrak Technologies, Nanjing, China*
[4]*First Affiliated Hospital of Huzhou University, Huzhou, China*

Correspondence should be addressed to Qin Jiang; jqin710@vip.sina.com and Weihua Yang; benben0606@139.com

Received 20 April 2022; Accepted 9 June 2022; Published 24 June 2022

Academic Editor: Yi Shao



The eye is one of the most important organs of the human body. Eye diseases are closely related to other systemic diseases, both of which influence each other. Numerous systemic diseases lead to special clinical manifestations and complications in the eyes. Typical diseases include diabetic retinopathy, hypertensive retinopathy, thyroid associated ophthalmopathy, optic neuromyelitis, and Behcet's disease. Systemic disease-related ophthalmopathy is usually a chronic disease, and the analysis of imaging markers is helpful for a comprehensive diagnosis of these diseases. Recently, artificial intelligence (AI) technology based on deep learning has rapidly developed, leading to numerous achievements and arousing widespread concern. Presently, AI technology has made significant progress in research on imaging markers of systemic disease-related ophthalmopathy; however, there are also many limitations and challenges. This article reviews the research achievements, limitations, and future prospects of AI image analysis technology in systemic disease-related ophthalmopathy.

## 1. Introduction

The term artificial intelligence (AI) was proposed by John McCarthy in 1956. It is a new technical science that studies and develops theories, methods, technologies, and application systems used to simulate, extend, and expand human intelligence. Since it was proposed in 1956, AI has played a significant role in image recognition, data mining, and language processing, showing infinite potential. In recent years, AI technology has developed rapidly and has been widely employed in numerous fields. Among them, AI image analysis technology has made great progress and has played a significant role in research and application in the medical field, particularly in ophthalmology [1]. Because the development and anatomy of the eye are closely related to the whole body, systemic diseases such as diabetes, hypertension, hyperthyroidism, and autoimmune diseases can cause eye diseases. Some eye manifestations are characteristic. By examining the ocular structures such as the fundus and orbit, not only can various ophthalmic diseases be diagnosed but also the condition of systemic diseases involving the eyes can be judged. Recently, the main research and application direction of AI technology in ophthalmology is the use of deep learning to study and analyze eye images to assist in the diagnosis of ophthalmopathy. Applying AI image analysis based on deep learning to the automatic analysis of eye images is crucial to diagnose the corresponding ophthalmopathy and judge the condition of related systemic diseases (such as diabetes, hypertension, and hyperthyroidism). Presently, AI image analysis technology has led to significant achievements in research on systemic disease-related ophthalmopathy. This paper mainly reviews the research

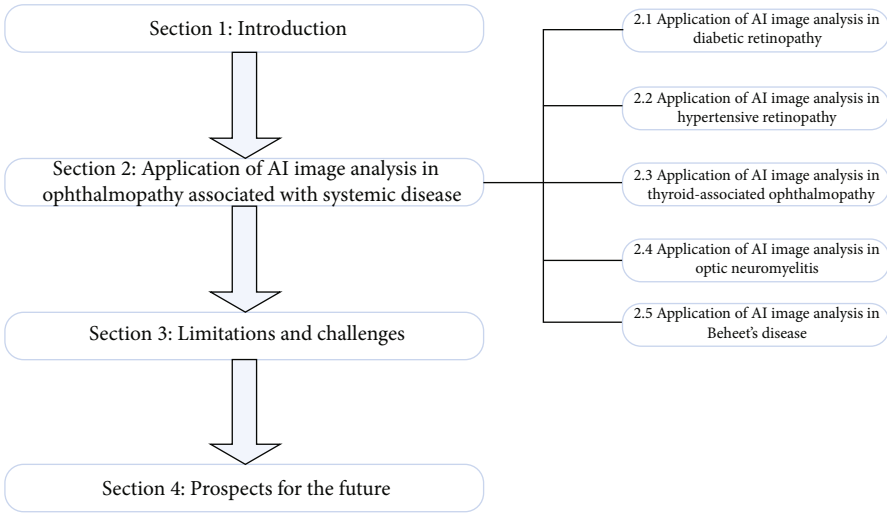


Figure 1: The basic framework of this review paper.

progress of AI image analysis technology in systemic disease-related ophthalmopathy in recent years.

This review paper is divided into four parts. Firstly, the first part introduces the basic research status of AI technology in systemic disease-related ophthalmopathy. Secondly, the second part introduces the research progress of AI technology in systemic disease-related ophthalmopathy, such as diabetic retinopathy, hypertensive retinopathy, thyroid-associated ophthalmopathy, neuromyelitis optica, and Behcet's disease. Thirdly, the third section discusses the limitations and challenges of medical application of AI technology. Finally, the fourth section discusses the prospect of medical application of AI technology, as shown in Figure 1.

## 2. Application of AI Image Analysis in Ophthalmopathy Associated with Systemic Disease

*2.1. Application of AI Image Analysis in Diabetic Retinopathy.* Diabetic retinopathy (DR) is one of the main complications of diabetic microangiopathy. It is a chronic, progressive, and potentially harmful retinal microvascular disease that is associated with persistent hyperglycemia. DR is the most common retinal vascular disease [2] and is also the retinal vascular disease with the highest blindness rate [3]. In people with diabetes, the main factors affecting the occurrence and development of DR are the course of the disease and the level of blood glucose control [4]. Patients with DR may not have any symptoms in the early stages of the disease and may experience varying degrees of vision loss when the lesions involve the macula. According to disease severity, DR is divided into nonproliferative diabetic retinopathy (NPDR) and proliferative diabetic retinopathy (proliferative diabetic retinopathy, PDR) [5]. The main fundus lesions in patients with DR include retinal microhemangioma, retinal hemorrhage, rigid exudation, cotton velvet spot, retinal edema, retinal neovascularization, and serious complications such as vitreous hemorrhage, traction retinal detachment, neovascular glaucoma, and macular edema. These complications seriously threaten the vision of patients and even lead to blindness. PDR and macular edema are the main causes of severe visual loss in patients with DR [6]. Presently, the main treatment modalities for patients with DR include drug therapy, anti-VEGF drug therapy, laser photocoagulation, and vitrectomy. For DR patients with macular edema, vitreous injection of anti-VEGF drugs can significantly improve visual acuity [7]; for patients with PDR, panretinal laser photocoagulation can effectively alleviate the decline in visual acuity [8]. At present, DR has become one of the main causes of blindness in the world [9], seriously affecting the quality of life of patients. Studies have shown that approximately 90.0% patients with DR can avoid severe vision loss through early diagnosis of DR and timely and effective treatment [10]. Therefore, early detection and treatment of DR can control the condition in most patients and reduce and avoid the occurrence of blindness, which is of great significance.

Gulshan et al. [11] developed a deep convolution neural network based on deep learning to assist in the clinical diagnosis and grading of diabetic retinopathy and diabetic macular edema. In this study, the neural network was trained using a dataset containing 128,175 retinal images, and the neural network was tested and verified using the EyePACS-1 dataset (including 9963 retinal images) and Messidor-2 dataset (including 1748 retinal images). The results indicated that on the EyePACS-1 dataset, the area under the curve (AUC) value was 0.991, the sensitivity was 90.3%, and the specificity was 98.1%; on the Messidor-2 dataset, the corresponding values were 0.990, 87.0%, and 98.5%. Ai et al. [12] constructed an algorithm based on the deep ensemble learning and attention mechanism that could detect HR. Simultaneously, to improve the accuracy of the algorithm, the author created a complete detection model DR-IIXRN (composed of Inception V3, Xception, ResNeXt101, and NASNetLarge). In this study, a total of 945 fundus images were collected, of which 133 were randomly selected for testing, and the remaining were used for training. The

Table 1: Summary of DR diagnosis model based on deep learning method.

| Study | Task | Sample size | AI model | Output |
|---|---|---|---|---|
| Gulshan et al. [11] | Identification and detection | EyePACS-1 dataset and Messidor-2 dataset | Deep learning-trained algorithm | On the EyePACS-1 dataset, the AUC value was 0.991, the sensitivity was 90.3%, and the specificity was 98.1%; on the Messidor-2 dataset, the corresponding values were 0.990, 87.0%, and 98.5%. |
| Ai et al. [12] | Detection | 35,126 images | DR-IIXRN | The AUC value and accuracy were 0.95 and 92%. |
| Bhardwaj et al. [13] | Identification and detection | The DRIVE, STARE, and DIARETDB1 datasets | InceptionResnet-V2 | The accuracy was 93.33%. |
| Li et al. [14] | Detection | 35201 images | Deep learning algorithm | The AUC value, sensitivity, and specificity were 0.989, 97.0%, and 91.4%, respectively |
| Li et al. [15] | Identification | 120002 images | The retinal artificial intelligence diagnosis system | The accuracy was 98.1%. |

experimental results show that, compared with the traditional detection algorithm, the AUC value and accuracy of this algorithm were as high as 95% and 92%, respectively. Bhardwaj et al. [13] constructed a quadrant ensemble-automated DR grading model based on the InceptionResnet-V2 depth neural network. The accuracy of the model was improved through methods such as histogram equalization, optic disk location, and quadrant segmentation. They used the open fundus datasets DRIVE, STARE, and DIARETDB1 to train and test the model. The final results show that the accuracy of the model is as high as 93.33%, which is 13.58% higher than that of the classical Inception-V3 CNN model. Based on Inception-V3, Li et al. [14] proposed a deep learning algorithm based on AI, which was used to detect DR. In this study, 71,043 fundus image photos were used for training and testing of the algorithm, and 35,201 fundus image photos were used for external verification. The results showed that the AUC value, sensitivity, and specificity of the algorithm were 0.989, 97.0%, and 91.4%, respectively. Table 1 summarizes the DR diagnosis model based on deep learning method in the above research.

Based on the above research results, AI image analysis technology shows great potential in clinical detection, auxiliary diagnosis, staging, and other aspects of DR. At present, for diabetic patients, the timeliness of DR screening, the quality of screening, and medical affordability are important factors to prevent blindness. Therefore, if AI technology can be fully applied to clinical work, it will greatly alleviate the work pressure of doctors, improve work efficiency, and reduce the burden of medical treatment of DR patients; at the same time, it is of great significance for early screening and diagnosis of DR in patients with diabetes, which can greatly reduce the blindness rate of patients with DR.

*2.2. Application of AI Image Analysis in Hypertensive Retinopathy.* According to the international standard for hypertension, hypertension is diagnosed when the systolic blood pressure is greater than or equal to 140 mmHg and diastolic blood pressure is greater than or equal to 90 mmHg [16]. At present, hypertension is a serious epidemiological problem, and approximately 10 million people die from hypertension every year [17]. Hypertensive retinopathy (HR) is a type of retinal angiopathy caused by hypertension. Hypertensive patients experience continuous contraction and tension of systemic arterioles. Long-term hypertension can cause arterial lumen stenosis, subsequently leading to hypertensive arteriosclerosis, resulting in retinal vascular stenosis thinning [18, 19]. In the early stages, the fundus of patients with hypertension may not show any pathological changes. When the systemic arterial pressure increases, the fundus of patients with HR may show pathological changes such as decreased retinal arteriovenous diameter ratio, hypertensive retinal arteriosclerosis, retinal edema and hemorrhage, cotton velvet spot, and optic disk edema [20]. At present, the main treatment modality of HR patients is to control systemic blood pressure within the normal range by oral antihypertensive drugs [21]. If HR patients are complicated with macular edema, vitreous injection of anti-VEGF drugs can significantly improve the visual acuity of patients [22]. The study found that, compared with the more serious fundus lesions in patients with HR, if the early fundus changes can be diagnosed and treated in time, then the fundus changes may be reversible. Because HR is a process of gradual change caused by hypertension, early screening and diagnosis of HR can not only effectively prevent its further development but also lead to the best treatment to obtain the best treatment effect.

Based on the framework of DenseNet, Abbas et al. [23] developed a HYPER-RETINO system by segmenting HR-related lesions to assist in the clinical staging diagnosis of HR. After ten times cross-verification, the sensitivity of the system was 90.5%, the specificity was 91.5%, the accuracy was 92.6%, the $\boldsymbol{F1}$ score was 92%, and the AUC was 0.915. The experimental results show that the system has good

Table 2: Summary of HR diagnosis model based on deep learning method.

| Study | Task | Sample size | AI model | Output |
|---|---|---|---|---|
| Abbas et al. [23] | Clinical staging diagnosis | 1400 images | DenseNet | The sensitivity was 90.5%, the specificity was 91.5%, the accuracy was 92.6%, the $F1$ score was 92%, and the AUC value was 0.915. |
| Akbar et al. [24] | Detection and classification | The INSPIRE-AVR and VICAVR datasets and a local dataset | Support vector machine and radial basis function | The average accuracies of the first part were 95.10%, 95.64%, and 98.09%, respectively, and the average accuracies of the second part were 95.93% and 97.50%, respectively. |
| Arsalan et al. [25] | Detection | The DRIVE, CHASE-DB1, and STARE datasets | A dual-residual-stream-based vessel segmentation network | The sensitivity, specificity, AUC value, and accuracy were as follows: DRIVE: 80.22%, 98.1%, 98.2%, and 96.55%, respectively; CHASE-DB1: 82.06%, 98.41%, 98.0%, and 97.26%, respectively; and STARE: 85.26%, 97.91%, 98.83%, and 96.97%, respectively. |
| Li et al. [15] | Identification | 120002 images | The retinal artificial intelligence diagnosis system | The accuracy was 83.7%. |

applicability for the clinical staging diagnosis of HR. Akbar et al. [24] constructed an intelligent system that can realize automatic detection and classification of HR based on support vector machine and a radial basis function. The system comprises two parts: the first part is used to calculate and analyze the arteriovenous ratio, while the second part is used to analyze the optic disk region. The data verification results showed that the average accuracies of the first part on the INSPIRE-AVR and VICAVR datasets and a local dataset were 95.10%, 95.64%, and 98.09%, respectively, and the average accuracies of the second part on the START and local datasets were 95.93% and 97.50%, respectively. The system can be used as a novel method for automatic detection and grading of HR, which is helpful for clinical diagnosis. Arsalan et al. [25] proposed a dual-residual-stream-based vessel segmentation network (Vess-Net) to segment retinal vessels intelligently to assist in the diagnosis of HR. They used three open vascular segmentation datasets (DRIVE, CHASE-DB1, and STARE) to validate and evaluate the Vess-Net method. The results showed that the sensitivity, specificity, AUC value, and accuracy of Vess-Net on the three datasets were as follows: DRIVE: 80.22%, 98.1%, 98.2%, and 96.55%, respectively; CHASE-DB1: 82.06%, 98.41%, 98.0%, and 97.26%, respectively; and STARE: 85.26%, 97.91%, 98.83%, and 96.97%, respectively. This method can be used to assist in the clinical diagnosis of HR. Table 2 summarizes the HR diagnosis model based on deep learning method in the above research.

Thus, the above AI image analysis model exhibited good performance for clinical diagnosis and grading of HR and can be used in clinical practice in the future to achieve early detection, diagnosis, and treatment of HR patients.

*2.3. Application of AI Image Analysis in Thyroid-Associated Ophthalmopathy.* Thyroid-associated ophthalmopathy (TAO) is a chronic, multisystem damage disease caused by autoimmune response, which is closely related to thyroid disease. Among adult orbital diseases, the incidence of TAO is the highest [26]. At present, the etiology of the disease is not completely clear, but it has been recognized as an autoimmune or organ immune disease and is closely related to the functional state of the systemic endocrine system. The main clinical manifestations of TAO patients are eyelid sign, exophthalmos, diplopia, eye movement disorder, conjunctival and keratopathy, and optic neuropathy. In severe cases, it can affect the patient's appearance and vision and even lead to blindness [27]. The histopathological changes of TAO are early inflammatory cell infiltration, edema leading to obvious inflammatory reaction, tissue degeneration, and dysfunction caused by fibrosis in the later stages. Early anti-inflammatory therapy using glucocorticoids and radiotherapy can help achieve a good therapeutic effect. After the occurrence of extraocular muscle fibrosis in the later stage, the effect of anti-inflammatory treatment becomes poor, and exophthalmos and strabismus can only be improved by surgical treatment [28].

Lin et al. [29] constructed a deep learning system based on a deep convolution neural network (composed of a convolution layer, pooled layer, and fully connected layer) to distinguish between inactive and active patients of TAO. They also added a nonlinear activation function to optimize the learning system. They collected MRI images of the eyes of 160 patients with TAO. Eighty percent of the images were randomly selected for deep learning system training and verification, and 20% of the images were used for the final test. The experimental results showed that the accuracy,

Table 3: Summary of TAO diagnosis model based on deep learning method.

| Study | Task | Sample size | AI model | Output |
|---|---|---|---|---|
| Lin et al. [29] | Detection | 160 MRI images of the eyes | A deep learning system based on a deep convolution neural network | The accuracy, sensitivity, specificity, and $F1$ scores of network A were $0.863 \pm 0.055$, $0.750 \pm 0.136$, $0.896 \pm 0.042$, and $0.712 \pm 0.121$, respectively; the accuracy, sensitivity, specificity, and $F1$ scores of network B were $0.855 \pm 0.018$, $0.821 \pm 0.071$, $0.865 \pm 0.021$, and $0.719 \pm 0.040$, and the AUC values of the two networks were 0.922. |
| Song et al. [30] | Detection and identification | 1135 orbital CT images | A ResNet-18 derived network | The accuracy, sensitivity, and specificity were 0.87, 0.88, and 0.85, respectively, and the AUC value was 0.919. |
| Salvi et al. [31] | Classification and progression prediction | 242 patients' ophthalmic examination results | A back propagation neural network model with 17 input parameters | The classification accuracy of the model was 78.3%, and the accuracy of predicting progress was 69.2%. |

sensitivity, specificity and $\boldsymbol{F1}$ scores of network A were $0.863 \pm 0.055$, $0.750 \pm 0.136$, $0.896 \pm 0.042$, and $0.712 \pm 0.121$, respectively; the accuracy, sensitivity, specificity, and $\boldsymbol{F1}$ scores of network B were $0.855 \pm 0.018$, $0.821 \pm 0.071$, $0.865 \pm 0.021$, and $0.719 \pm 0.040$, and the AUC values of the two networks were 0.922. This system can be used to assist in the clinical diagnosis of TAO in the future. Song et al. [30] constructed an AI image analysis model for screening and testing TAO patients based on a ResNet-18 derived network (using 3D-ResNet instead of 2D-ResNet). The orbital CT images of 193 patients with TAO and 715 healthy subjects were used for model training and testing, and the orbital CT images of 49 patients with TAO and 178 healthy persons were used for external verification. The results indicated that in the external verification of the AI image analysis model, the accuracy, sensitivity, and specificity were 0.87, 0.88, and 0.85, respectively, and the AUC value was 0.919. The AI image analysis model may become a new TAO screening tool. Salvi et al. [31] constructed a back propagation neural network model with 17 input parameters for clinical classification and progression prediction of TAO. In this study, the ophthalmic examination results of 242 patients were collected, of which 87 patients were selected to test the clinical classification ability of the model for TAO, and 28 patients were selected to test the ability of the model to predict the progression of TAO. The results indicated that the classification accuracy of the model was 78.3%, and the accuracy of predicting progress was 69.2%. In the authors' view, this model can be used to assist in the clinical classification of TAO and to predict disease progression beginning from the first clinical examination. Table 3 summarizes the TAO diagnosis model based on deep learning method in the above research.

The above studies confirm that AI technology has achieved some research results in assisting in the clinical diagnosis of TAO. The clinical application of AI image analysis technology will help improve the accuracy of clinical diagnosis of TAO, thereby helping doctors to provide accurate treatment methods for patients.

*2.4. Application of AI Image Analysis in Optic Neuromyelitis.* Optic neuritis (ON) generally refers to various inflammatory lesions involving the optic nerve. Neuromyelitis optica (NMO) and multiple sclerosis (MS) are demyelinating diseases of the central nervous system and are the most common causes of neurological dysfunction in young and middle-aged people [32]. The pathogenesis of MS and NMO is mainly related to various immune-related molecules and immune pathways [33]. NMO mainly selectively involves the optic nerve and spinal cord, and the main clinical manifestations are rapid and severe visual loss in both eyes at the same time or in succession, such as optic disk edema, tortuous dilatation of retinal veins, perioptic exudation, and other fundus changes; recovery of visual function is poor, and most patients suffer from serious visual impairment in both eyes or at least one eye. Treatment is mainly to prevent further disease development; it is particularly important to note that visual dysfunction may only be one of the symptoms of potential systemic diseases, so it is necessary to be referred to the relevant specialties for systemic treatment in time. The clinical manifestations and imaging features of MS and NMO have many similarities. In terms of clinical diagnosis, differentiating between the two diseases is challenging [34, 35]. Approximately 30% of patients with MS are misdiagnosed as having NMO, thus delaying the treatment of the disease and leading to aggravation of the disease [36]. Therefore, it is particularly important to improve the diagnostic accuracy for the two diseases.

Huang et al. [37] collected magnetic resonance images of 116 patients with demyelinating diseases of the central nervous system (including 38 cases of NMO and 78 cases of MS). Based on radiological and clinical features, a

Table 4: Summary of NMO diagnosis model based on deep learning method.

| Study | Task | Sample size | AI model | Output |
|---|---|---|---|---|
| Huang et al. [37] | Detection and identification | 116 images of magnetic resonance | A multi-parameter multivariate random forest model | In training, the accuracy of the MM-RF model was 0.849, and the AUC value was 0.826; for testing, the accuracy of the MM-RF model was 0.871, and the AUC value was 0.902. |
| Hagiwara et al. [38] | Detection and identification | 53 patients' examination results | SqueezeNet | The AUC value of the model is 0.859, and the accuracies of NMO and MS are 81.1% and 83.3%, respectively. |
| Kim et al. [39] | Detection and identification | 338 patients' images of magnetic resonance | ResNeXt | The AUC value of the model was 0.82, and the accuracy was 71.1%. |
| Khoury et al. [40] | Identification | 202 serum samples | A random forest classification machine learning algorithm | The sensitivity and specificity were 1.00 and 1.00. |

multiparameter multivariate random forest (MM-RF) model was developed to assist in the differential diagnosis of NMO and MS. The magnetic resonance images of 86 patients were randomly selected for training the model, and the remaining were used for independent testing of the model. After 10 times cross-validation and independent testing, the results showed that in training, the accuracy of the MM-RF model was 0.849, and the AUC value was 0.826; for testing, the accuracy of the MM-RF model was 0.871, and the AUC value was 0.902. Hagiwara et al. [38] constructed a convolution neural network model based on SqueezeNet to distinguish between NMO and MS. In this study, 35 patients with MS and 18 patients with NMO were enrolled, and left-over cross-validation (leave-one-out cross validation) was used to evaluate the performance of the model. The results showed that the AUC value of the model is 0.859, and the diagnostic accuracies of NMO and MS are 81.1% and 83.3%, respectively. Kim et al. [39] created a 3D convolution neural network model based on ResNeXt to assist in the diagnosis of NMO and MS. In this study, magnetic resonance images of 338 patients (including 213,125 patients with MS and 125 patients with NMO) were collected, and images of 152, 51, and 135 patients were randomly selected for training, verification, and testing of the model, respectively. The final experimental results are as follows: the AUC value of the model was 0.82, and the diagnostic accuracy of MS and NMO was 71.1%. Table 4 summarizes the NMO diagnosis model based on deep learning method in the above research.

In summary, AI image analysis technology shows satisfactory accuracy in clinical differential diagnosis of NMO and MS. If AI image analysis technology can be fully applied to the process of clinical diagnosis, it will greatly improve the accuracy of differential diagnosis of NMO and MS.

*2.5. Application of AI Image Analysis in Behcet's Disease.* Behcet's disease, first reported by Hulusi Behcet in 1937, is a chronic, persistent, multisystem disease that affects numerous organs [41]. The main pathological change of Behcet's disease is occlusive vasculitis. Simultaneously, the disease is characterized by uveitis, oral ulcer, skin lesions, and pudendal ulcer, among which oral ulcers are the most common [42, 43]. At present, the cause of the disease is not clear because patients with the disease often possess a variety of autoantibodies; therefore, it may be an autoimmune disease. Simultaneously, the disease has an obvious genetic background and is significantly related to HLA-B5 [44]. Studies have found that untreated uveitis in Behcet's disease has a poor prognosis, resulting in a high rate of blindness in patients [45]. At present, the treatment of Behcet's disease complicated with uveitis follows the general principles of uveitis: dilating pupils, antagonizing inflammation, and eliminating etiology.

The Standardization of Uveitis Nomenclature (SUN) Working Group [46] collected the medical records of 248 patients with Behcet's disease complicated with uveitis and 718 patients with other types of uveitis and randomly divided them into training and test sets. Using the machine learning method of multinomial logistic regression for the training set, a standard of uveitis in Behcet's disease was developed to distinguish uveitis from other types of uveitis in Behcet's disease. The standard they developed was verified on the test set, and the results showed that the accuracy was 96.3% on the test set and 94.0% on the training set. The error rate of the differentiation criteria of Behcet's disease complicated with uveitis established in this study was very low, and the standard can be used to assist in clinical diagnosis in the future. Based on the delta-bar-delta training algorithm, Guler and Ubeyli [47] constructed a multilayer perceptron neural network (MLPNN) model for the detection of ocular Behcet's disease. In this study, the Doppler signals of ophthalmic artery were collected from 106 subjects, including 54 patients with ocular Behcet's disease, and the remaining were normal. Fifty-four cases were randomly divided into the training set, the remaining were used as the test set, and 10 cases were randomly selected from the training set as the cross-validation set. The MLPNN model was evaluated by performance indicators and statistical methods, and its accuracy was 96.43% and 93.75%, respectively. Based on the above results, the model is feasible for the detection of ocular Behcet's disease. Table 5 summarizes the Behcet's disease diagnosis model based on deep learning method in the above research.

Table 5: Summary of Behcet's disease diagnosis model based on deep learning method.

| Study | Task | Sample size | AI model | Output |
|---|---|---|---|---|
| The Standardization of Uveitis Nomenclature Working Group [46] | Detection and identification | 966 patients | The machine learning method of multinomial logistic regression | The accuracy was 96.3% on the test set and 94.0% on the training set. |
| Guler and Ubeyli [47] | Detection | The Doppler signals of 106 subjects | A multilayer perceptron neural network model | The accuracy was 96.43% and 93.75%, respectively. |

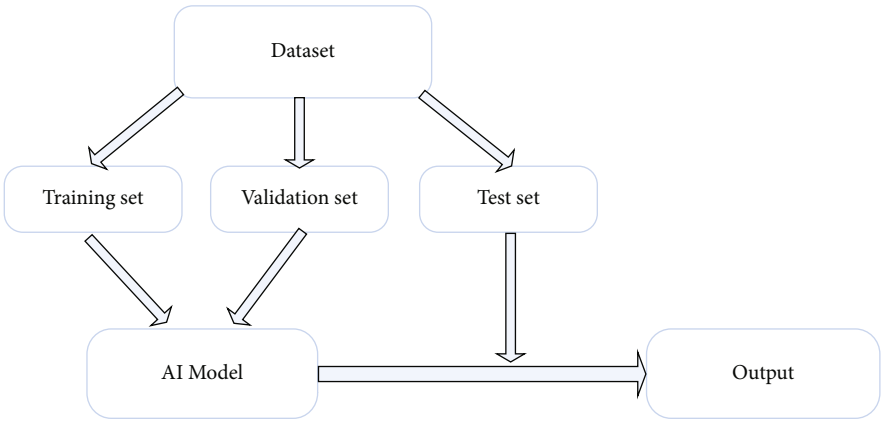


Figure 2: AI model research flow chart.

To sum up, the AI image analysis model based on the deep learning algorithm showed good performance and practicability for the auxiliary diagnosis of Behcet's disease complicated with uveitis and can be used in clinical diagnosis and treatment in the future.

The flow chart of all the above AI model studies is as follows: firstly, the dataset used for research is randomly divided into training set, validation set, and testing set; then, the training set and validation set are used to train and verify the AI model, and the corresponding improvements and optimizations are made according to the results; finally, the optimized AI model is externally verified with the testing set, and the results are compared with the expert results, so as to obtain the diagnostic performance of the AI model, as shown in Figure 2.

## 3. Limitations and Challenges

At present, in many published studies on AI-aided diagnosis of systemic disease-related ophthalmopathy, although the accuracy and specificity of the AI image analysis model based on deep learning have achieved satisfactory results, there are still some limitations and challenges. The following are the main results: (1) there is a deviation in the datasets of systemic disease-related ophthalmopathy. The training and test datasets used by many AI image analysis models are public datasets, and there are some deviations in these datasets, which lead to a decline in the external applicability of the AI image analysis model and may even magnify these deviations [48]. (2) Deep learning algorithms lack interpretability in clinical applications. Many clinicians do not fully learn and understand the deep learning algorithm, resulting in the "black box phenomenon." This leads to reduced acceptance of the AI image analysis model, and clinicians may even resist the model [49]. (3) Some patients have prejudice to AI model diagnosis and treatment. Research shows that numerous patients are unwilling or do not accept computer-aided diagnosis but prefer to see a doctor face-to-face, which hinders the clinical application of AI intelligent models because of the lack of trust of patients [50]. After all, medicine is a life science, and it does not rule out that some patients do not trust and do not accept the diagnosis and treatment of artificial intelligence from the very beginning, which is a major obstacle to the development of artificial intelligence in the medical field. (4) Errors in AI models can lead to many medical legal problems. False-positive results may occur in the clinical application of AI image analysis models. If the mistakes of AI image analysis models lead to medical malpractice, then it is unclear who would bear the responsibility and legal consequences of these medical accidents [51]. No one is perfect, and the AI model cannot be perfect, can go wrong, or even cause bigger problems. With the continuous progress of artificial intelligence technology, the AI model may produce results that exceed the designer's design intention. How to determine its behavior? How to strengthen legal monitoring and establish clear ethical norms and legal and regulatory requirements. These are some complex and difficult medical legal problems. (5) Privacy and security of patients: when using patients' clinical data for experiments, clinical data may affect patients' privacy or even cause new social problems, which is a challenge in terms of applying AI image analysis technology [52]. Medical data focus on patients' health, disease status, biological genes, and other information; once

leaked, the consequences are unimaginable. Therefore, the health information and privacy protection of patients are also major challenges for artificial intelligence. (6) Legal guarantee of medical application of artificial intelligence technology. In recent years, the rapid development of artificial intelligence technology has brought convenience to all aspects of our life. However, the legislative process of artificial intelligence is relatively slow. The current law does not provide for the rights and obligations of artificial intelligence and the treatment of social hazards, nor does it stipulate the legal provisions, responsibility attribution, and development direction of all aspects of artificial intelligence research and development and development and production process. All these will affect the development and application of artificial intelligence. (7) The social supervision and management system of artificial intelligence technology is not perfect. Artificial intelligence technology involves surpassing human potential, and its development needs to be strictly managed and monitored. At present, the necessary supervision direction and supervision and management system cannot keep up with the development of artificial intelligence technology, which may lead to a large number of ethical and social problems, thus affecting the application of artificial intelligence technology in the medical field. The social supervision and management system of artificial intelligence technology is not perfect. Artificial intelligence technology involves surpassing human potential, and its development needs to be strictly managed and monitored. At present, the necessary supervision direction and supervision and management system cannot keep up with the development of artificial intelligence technology, which may lead to a large number of ethical and social problems, thus affecting the application of artificial intelligence technology in the medical field.

## 4. Prospects for the Future

Although AI technology based on deep learning faces many challenges and numerous unsolved problems exist in the research of systemic disease-related ophthalmopathy, its application prospect is bright. With the assistance of AI technology, assistance in clinical diagnosis can be achieved by identifying the unique image markers of each systemic disease-related ophthalmopathy. In addition, the AI image analysis model can also assist in the screening and diagnosis of systemic disease-related ophthalmopathy and may provide clinical screening and medical opportunities for more patients, thus reducing medical costs and medical investment and alleviating the pressure of seeking medical treatment in backward areas.

With the advancement of research, the results of AI application in the field of systemic disease-related ophthalmopathy will greatly improve the level of diagnosis and treatment of systemic disease-related ophthalmopathy to achieve early detection, diagnosis, and treatment of systemic disease-related ophthalmopathy. The application of AI technology in the field of ophthalmology has begun, but on the whole, it is only beginning. As we are entering the era of AI, we should fully utilize AI technology to advance ophthalmology research and make full use of this opportunity and technology to bring about fundamental changes in modern ophthalmology and make AI technology produce more fruitful results in ophthalmology research. This will help in assisting clinicians in the diagnosis and treatment of ophthalmic diseases.

## Data Availability

The datasets used and/or analyzed during the present study are available from the corresponding author on reasonable request.

## Conflicts of Interest

The authors declare that the research was conducted in the absence of any commercial or financial relationships that could be construed as a potential conflict of interest.

## Authors' Contributions

Yuke Ji, Nan Chen, and Sha Liu contributed equally to this work.

## Acknowledgments

This study was supported by the Nanjing Enterprise Expert Team Project, the Medical Science and Technology Development Project Fund of Nanjing (grant no. YKK21262) and National Computer Basic Education Research Association project (2021-AFCEC-566).

## References

[1] E. J. Topol, "High-performance medicine: the convergence of human and artificial intelligence," *Nature Medicine*, vol. 25, no. 1, pp. 44–56, 2019.

[2] P. Song, Y. Xu, M. Zha, Y. Zhang, and I. Rudan, "Global epidemiology of retinal vein occlusion: a systematic review and meta-analysis of prevalence, incidence, and risk factors," *Journal of Global Health*, vol. 9, no. 1, article 010427, 2019.

[3] Z. Tang, X. Zhang, G. Yang et al., "Automated segmentation of retinal nonperfusion area in fluorescein angiography in retinal vein occlusion using convolutional neural networks," *Medical Physics*, vol. 48, no. 2, pp. 648–658, 2021.

[4] N. Kumari, M. Bhargava, D. Q. Nguyen et al., "Six-year incidence and progression of diabetic retinopathy in Indian adults: the Singapore Indian Eye study," *The British Journal of Ophthalmology*, vol. 103, no. 12, pp. 1732–1739, 2019.

[5] A. G. Palis, K. C. Golnik, E. P. Mayorga, H. P. Filipe, and P. Garg, "The International Council of Ophthalmology 360-degree assessment tool: development and validation," *Canadian Journal of Ophthalmology*, vol. 53, no. 2, pp. 145–149, 2018.

[6] R. Lee, T. Y. Wong, and C. Sabanayagam, "Epidemiology of diabetic retinopathy, diabetic macular edema and related vision loss," *Eye and Vision*, vol. 2, no. 1, p. 17, 2015.

[7] T. Y. Wong, J. Sun, R. Kawasaki et al., "Guidelines on diabetic eye care: the international council of ophthalmology recommendations for screening, follow-up, referral, and treatment based on resource settings," *Ophthalmology*, vol. 125, no. 10, pp. 1608–1622, 2018.

[8] L. A. Everett and Y. M. Paulus, "Laser therapy in the treatment of diabetic retinopathy and diabetic macular edema," *Current Diabetes Reports*, vol. 21, no. 9, p. 35, 2021.

[9] S. J. Song, K. Han, K. S. Choi et al., "Trends in diabetic retinopathy and related medical practices among type 2 diabetes patients: results from the National Insurance Service Survey 2006–2013," *Journal of Diabetes Investigation*, vol. 9, no. 1, pp. 173–178, 2018.

[10] N. Relhan and H. W. Flynn Jr., "The Early Treatment Diabetic Retinopathy Study historical review and relevance to today's management of diabetic macular edema," *Current Opinion in Ophthalmology*, vol. 28, no. 3, pp. 205–212, 2017.

[11] V. Gulshan, L. Peng, M. Coram et al., "Development and validation of a deep learning algorithm for detection of diabetic retinopathy in retinal fundus photographs," *JAMA*, vol. 316, no. 22, pp. 2402–2410, 2016.

[12] Z. Ai, X. Huang, Y. Fan, J. Feng, F. Zeng, and Y. Lu, "DR-IIXRN: detection algorithm of diabetic retinopathy based on deep ensemble learning and attention mechanism," *Frontiers in Neuroinformatics*, vol. 15, article 778552, 2021.

[13] C. Bhardwaj, S. Jain, and M. Sood, "Deep learning-based diabetic retinopathy severity grading system employing quadrant ensemble model," *Journal of Digital Imaging*, vol. 34, no. 2, pp. 440–457, 2021.

[14] Z. Li, S. Keel, C. Liu et al., "An automated grading system for detection of vision-threatening referable diabetic retinopathy on the basis of color fundus photographs," *Diabetes Care*, vol. 41, no. 12, pp. 2509–2516, 2018.

[15] L. Dong, W. He, R. Zhang et al., "Artificial intelligence for screening of multiple retinal and optic nerve diseases," *JAMA Network Open*, vol. 5, no. 5, article e229960, 2022.

[16] T. Unger, C. Borghi, F. Charchar et al., "2020 International Society of Hypertension global hypertension practice guidelines," *Hypertension*, vol. 75, no. 6, pp. 1334–1357, 2020.

[17] P. K. Whelton, R. M. Carey, W. S. Aronow et al., "2017 ACC/AHA/AAPA/ABC/ACPM/AGS/APhA/ASH/ASPC/NMA/PCNA guideline for the prevention, detection, evaluation, and management of high blood pressure in adults: executive summary: a report of the American College of Cardiology/American Heart Association task force on clinical practice guidelines," *Hypertension*, vol. 71, no. 6, pp. 1269–1324, 2018.

[18] C. Y. Cheung, Y. Zheng, W. Hsu et al., "Retinal vascular tortuosity, blood pressure, and cardiovascular risk factors," *Ophthalmology*, vol. 118, no. 5, pp. 812–818, 2011.

[19] C. Y. Cheung, V. Biousse, P. A. Keane, E. L. Schiffrin, and T. Y. Wong, "Hypertensive eye disease," *Nature Reviews. Disease Primers*, vol. 8, no. 1, 2022.

[20] J. Dziedziak, A. Zaleska-Zmijewska, J. P. Szaflik, and A. Cudnoch-Jedrzejewska, "Impact of arterial hypertension on the eye: a review of the pathogenesis, diagnostic methods, and treatment of hypertensive retinopathy," *Medical Science Monitor*, vol. 28, article e935135, 2022.

[21] J. E. Klig, "Ophthalmologic complications of systemic disease," *Emergency Medicine Clinics of North America*, vol. 26, pp. 217–231, 2008.

[22] S. Padhy and V. Kumar, "Dramatic response to intravitreal bevacizumab in hypertensive retinopathy," *Indian Journal of Ophthalmology*, vol. 66, no. 10, pp. 1494-1495, 2018.

[23] Q. Abbas, I. Qureshi, and M. E. A. Ibrahim, "An automatic detection and classification system of five stages for hypertensive retinopathy using semantic and instance segmentation in DenseNet architecture," *Sensors (Basel)*, vol. 21, no. 20, p. 6936, 2021.

[24] S. Akbar, M. U. Akram, M. Sharif, A. Tariq, and U. U. Yasin, "Arteriovenous ratio and papilledema based hybrid decision support system for detection and grading of hypertensive retinopathy," *Computer Methods and Programs in Biomedicine*, vol. 154, pp. 123–141, 2018.

[25] M. Arsalan, M. Owais, T. Mahmood, S. W. Cho, and K. R. Park, "Aiding the diagnosis of diabetic and hypertensive retinopathy using artificial intelligence-based semantic segmentation," *Journal of Clinical Medicine*, vol. 8, no. 9, p. 1446, 2019.

[26] J. D. Stein, D. Childers, S. Gupta et al., "Risk factors for developing thyroid-associated ophthalmopathy among individuals with Graves disease," *JAMA Ophthalmol*, vol. 133, no. 3, pp. 290–296, 2015.

[27] T. J. Smith, "TSHR as a therapeutic target in Graves' disease," *Expert Opinion on Therapeutic Targets*, vol. 21, no. 4, pp. 427–432, 2017.

[28] L. Bartalena, L. Baldeschi, K. Boboridis et al., "The 2016 European Thyroid Association/European Group on Graves' orbitopathy guidelines for the management of Graves' orbitopathy," *European Thyroid Journal*, vol. 5, no. 1, pp. 9–26, 2016.

[29] C. Lin, X. Song, L. Li et al., "Detection of active and inactive phases of thyroid-associated ophthalmopathy using deep convolutional neural network," *BMC Ophthalmology*, vol. 21, no. 1, p. 39, 2021.

[30] X. Song, Z. Liu, L. Li et al., "Artificial intelligence CT screening model for thyroid-associated ophthalmopathy and tests under clinical conditions," *International Journal of Computer Assisted Radiology and Surgery*, vol. 16, no. 2, pp. 323–330, 2021.

[31] M. Salvi, D. Dazzi, I. Pellistri, F. Neri, and J. R. Wall, "Classification and prediction of the progression of thyroid-associated ophthalmopathy by an artificial neural network," *Ophthalmology*, vol. 109, no. 9, pp. 1703–1708, 2002.

[32] A. Compston and A. Coles, "Multiple sclerosis," *Lancet*, vol. 359, no. 9313, pp. 1221–1231, 2002.

[33] Z. Li, Y. Liu, A. Jia, Y. Cui, and J. Feng, "Cerebrospinal fluid cells immune landscape in multiple sclerosis," *Journal of Translational Medicine*, vol. 19, no. 1, p. 125, 2021.

[34] J. F. Rosenthal, B. M. Hoffman, and W. R. Tyor, "CNS inflammatory demyelinating disorders: MS, NMOSD and MOG antibody associated disease," *Journal of Investigative Medicine*, vol. 68, no. 2, pp. 321–330, 2020.

[35] H. Tatekawa, S. Sakamoto, M. Hori et al., "Imaging differences between neuromyelitis optica spectrum disorders and multiple sclerosis: a multi-institutional study in Japan," *AJNR. American Journal of Neuroradiology*, vol. 39, no. 7, pp. 1239–1247, 2018.

[36] A. J. Solomon, R. T. Naismith, and A. H. Cross, "Misdiagnosis of multiple sclerosis: impact of the 2017 McDonald criteria on clinical practice," *Neurology*, vol. 92, no. 1, pp. 26–33, 2019.

[37] J. Huang, B. Xin, X. Wang et al., "Multi-parametric MRI phenotype with trustworthy machine learning for differentiating CNS demyelinating diseases," *Journal of Translational Medicine*, vol. 19, no. 1, p. 377, 2021.

[38] A. Hagiwara, Y. Otsuka, C. Andica et al., "Differentiation between multiple sclerosis and neuromyelitis optica spectrum disorders by multiparametric quantitative MRI using convolutional neural network," *Journal of Clinical Neuroscience*, vol. 87, pp. 55–58, 2021.

[39] H. Kim, Y. Lee, Y. H. Kim et al., "Deep learning-based method to differentiate neuromyelitis optica spectrum disorder from multiple sclerosis," *Frontiers in Neurology*, vol. 11, article 599042, 2020.

[40] Y. El Khoury, M. Gebelin, J. de Sèze et al., "Rapid discrimination of neuromyelitis optica spectrum disorder and multiple sclerosis using machine learning on infrared spectra of sera," *International Journal of Molecular Sciences*, vol. 23, no. 5, 2022.

[41] I. Ksiaa, N. Abroug, M. Kechida et al., "Eye and Behçet's disease," *Journal Français d'Ophtalmologie*, vol. 42, no. 6, pp. 626–641, 2019.

[42] T. Sakane, M. Takeno, N. Suzuki, and G. Inaba, "Behçet's disease," *The New England Journal of Medicine*, vol. 341, no. 17, pp. 1284–1291, 1999.

[43] C. Evereklioglu, "Current concepts in the etiology and treatment of Behçet disease," *Survey of Ophthalmology*, vol. 50, no. 4, pp. 297–350, 2005.

[44] N. Mizuki, H. Inoko, H. Ando et al., "Behçet's disease associated with one of the HLA-B51 subantigens, HLA- $B^*$ 5101," *American Journal of Ophthalmology*, vol. 116, no. 4, pp. 406–409, 1993.

[45] R. O. Kacmaz, J. H. Kempen, and C. Newcomb, "Ocular inflammation in Behçet disease: incidence of ocular complications and of loss of visual acuity," *American Journal of Ophthalmology*, vol. 146, no. 6, pp. 828–836, 2008.

[46] "Classification criteria for Behçet disease uveitis," *American Journal of Ophthalmology*, vol. 228, pp. 80–88, 2021.

[47] I. Guler and E. D. Ubeyli, "Detection of ophthalmic arterial Doppler signals with Behcet disease using multilayer perceptron neural network," *Computers in Biology and Medicine*, vol. 35, no. 2, pp. 121–132, 2005.

[48] T. Y. A. Liu and N. M. Bressler, "Controversies in artificial intelligence," *Current Opinion in Ophthalmology*, vol. 31, no. 5, pp. 324–328, 2020.

[49] T. M. Maddox, J. S. Rumsfeld, and P. R. O. Payne, "Questions for artificial intelligence in health care," *JAMA*, vol. 321, no. 1, pp. 31-32, 2019.

[50] S. Keel, P. Y. Lee, J. Scheetz et al., "Feasibility and patient acceptability of a novel artificial intelligence- based screening model for diabetic retinopathy at endocrinology outpatient services: a pilot study," *Scientific Reports*, vol. 8, no. 1, p. 4330, 2018.

[51] H. R. Sullivan and S. J. Schweikart, "Are current tort liability doctrines adequate for addressing injury caused by AI?," *AMA Journal of Ethics*, vol. 21, no. 2, pp. E160–E166, 2019.

[52] B. Murdoch, "Privacy and artificial intelligence: challenges for protecting health information in a new era," *BMC Medical Ethics*, vol. 22, no. 1, p. 122, 2021.

Hindawi
Disease Markers
Volume 2022, Article ID 2501886, 9 pages
https://doi.org/10.1155/2022/2501886

*Research Article*

# Aberrant Spontaneous Brain Activity in Coronary Heart Disease Using Fractional Amplitude of Low-Frequency Fluctuations: A Preliminary Resting-State Functional MRI Study

**Simin Lin,[1] Yi Han,[2] Shaoyin Duan,[3] PuYeh Wu,[4] Naiming Wu,[1] Ting Xie,[1] Qin Li,[1] Qing Lu,[1] and Hengyu Zhao[1]**

[1]*Department of Radiology, Xiamen Cardiovascular Hospital of Xiamen University, School of Medicine, Xiamen University, Xiamen 361006, China*
[2]*Fujian Provincial Key Laboratory of Ophthalmology and Visual Science, Eye Institute of Xiamen University, School of Medicine, Xiamen University, Xiamen 361100, China*
[3]*Department of Radiology, Zhongshan Hospital of Xiamen University, School of Medicine, Xiamen University, Xiamen 361001, China*
[4]*GE Healthcare, Beijing 100020, China*

Correspondence should be addressed to Hengyu Zhao; xzzx_paper@163.com

Received 27 February 2022; Revised 14 April 2022; Accepted 17 May 2022; Published 3 June 2022

Academic Editor: Dai Xi-jian



*Objective*. This study is aimed at exploring the spontaneous brain activity changes by measuring the fractional amplitude of low-frequency fluctuations (fALFF) and their relationship with clinical characteristics in patients with coronary heart disease (CHD). *Methods*. Coronary heart disease patients ($n = 25$) and age, gender, and education level-matched control subjects (controls, $n = 35$) were included. The grey matter volume (GMV) and fALFF values were calculated to assess the difference in brain structure and function between the two groups, respectively. Correlation analyses between the fALFF values and clinical characteristics were further assessed in CHD patients. In addition, receiver operating characteristic (ROC) curves were conducted to access the diagnostic ability of the fALFF method. *Results*. There was no significant difference in GMV between the CHD and control groups. Compared with the control group, patients with CHD showed significantly decreased fALFF in the left precentral/postcentral gyrus and increased fALFF in the right inferior cerebellum. Patients with a history of myocardial infarction (MI) showed significantly decreased fALFF values of the right inferior cerebellum than patients without MI. There was no significant correlation between the fALFF values in specific brain regions and disease duration. Furthermore, the ROC curves of abnormal brain regions showed the perfect accuracy of the fALFF value in distinguishing between CHD patients and controls. *Conclusion*. CHD demonstrated aberrant neural activity in specific brain regions mainly related to sensorimotor networks and pain processing, which may contribute to understanding the underlying neurological mechanism of CHD.

## 1. Introduction

Coronary heart disease (CHD), one of the primary causes of death, poses serious threats to physical health [1]. Angina pectoris is the most common symptom of CHD. Over the past decade, due to timely and effective clinical interventions, the mortality rate of CHD declined by 14.6% in the United States [2]. Although CHD survival rates have improved in recent years, it is an urgent requirement to cope with the effects of CHD "successful aging." Increasing cases of CHD-related brain function decline were reported in recent years [3, 4]. van de Vorst et al. indicated that people with CHD had an increased risk of cognitive decline and higher rates of depression and anxiety compared with normal controls [5]. Hence, recent research focus turned to the brain function disorder caused by CHD. Neuroimaging has proved to be an effective tool for assessing brain function. Many previous MRI studies demonstrated that patients

with CHD have white matter lesion, grey matter atrophy, and cerebral blood flow change [6–10]. Nevertheless, little is known about the changes of CHD in brain activity. Measurement of neural activity is a suitable method for researching the potential impacts of CHD on brain function [10].

Resting-state functional MRI (rs-fMRI), a useful and noninvasive method for neural activity assessment, has attracted substantial attention in recent years [11]. Resting-state fMRI detects spontaneous neural activity independent of stimulation or task design constraints via detecting blood oxygen level-dependent (BOLD) signals [12, 13]. In the field of cardiovascular, Bernard et al. used resting-state fMRI to study alterations of functional connectivity in acute coronary syndrome and showed evidence of abnormal neural networks [14]. This research only concentrated on the alteration of functional connectivity between two aberrant brain areas. Based on previous reports [4, 15], we speculate that the influence of CHD on the brain might be global; thus, it is of certain significance to analyze the whole brain activity in patients with CHD.

The fractional amplitude of low-frequency fluctuations (fALFF) is regarded as a novel method to assess global spontaneous brain activity. The fALFF is used to measure the amplitude of a spontaneous, low-frequency (0.01~0.08 Hz) BOLD signal, which reflects the aberrant brain activity at baseline and offers valuable information about brain activity [16]. In contrast with the amplitude of low-frequency fluctuations (ALFF), fALFF can effectively suppress physiological noise, decrease interference with cerebrospinal fluid, and show high sensitivity to detect spontaneous neural activity [16]. In recent years, ALFF and fALFF analyses have been widely applied in a series of neuropsychiatric disorders and have been used in the research on pain mechanisms, showing abnormalities of neural activity in pain-related diseases such as Crohn's disease, irritable bowel syndrome, and chronic low back pain [17–19].

In this study, we mainly explored the alterations in spontaneous neural activity by measuring fALFF in patients with CHD and their relationship with clinical features. We hypothesized that (1) patients might have abnormal fALFF values in specific brain areas and (2) the alterations of spontaneous neural activity may provide new insight into the neurological mechanism of CHD.

## 2. Materials and Methods

*2.1. Subjects.* The experiment was authorized by the Ethics Committee of Xiamen Cardiovascular Hospital of Xiamen University. All participants in the current research obtained written informed consent. Twenty-six patients with CHD were enrolled from the Xiamen Cardiovascular Hospital of Xiamen University from May 2020 to May 2021. Thirty-six volunteers matched in age, gender, and education level were enrolled from the local community as control subjects (controls).

According to the current guidelines, the diagnostic criteria for CHD are either provocable myocardial ischemia or at least one coronary artery stenosis of 50% or greater [20, 21]. Inclusion criteria for CHD patients were (1) duration of disease of at least 7 days, (2) left ventricular ejection fraction (LVEF) greater than 50%, and (3) age range between 40 and 70. To reduce the insidious effects of neurodegeneration on cognitive status, elderly patients older than 70 years were not recruited. Inclusion criteria for control subjects were (1) no symptoms or biochemical evidence of cardiovascular disease and (2) no obvious abnormalities in transthoracic echocardiography and ECG. Exclusion criteria for all participants were (1) history of brain lesions and neurological or psychiatric disorders, (2) aphasia and severe visual or hearing deficiency, (3) cardiomyopathy/severe or complex arrhythmias/congestive heart failure, (4) history of trauma or surgery in the last three months (excluding percutaneous coronary intervention), (5) history of alcohol and toxicology abuse, (6) left-hander, and (7) MRI contraindications.

*2.2. MRI Parameters.* All MRI data were obtained using a 3-Tesla MRI scanner (SIGNA Pioneer, GE Healthcare, Milwaukee, WI, USA) at the Xiamen Cardiovascular Hospital of Xiamen University. All participants were reminded to close their eyes but stay awake and keep silent during the whole scanning. We used earplugs to diminish the acoustic noise and used foam pads to minimize motion-related artifacts during scanning.

High-resolution structural images were acquired using a 3D T1-weighted inversion recovery prepared fast spoiled gradient-recalled echo (IR FSPGR) pulse sequence. The parameters of structural images are as follows: echo time (TE) = 3.2 ms, repetition time (TR) = 8.3 ms, inversion time (TI) = 450 ms, flip angle (FA) = 12°, field of view (FOV) = 240 mm × 240 mm, thickness = 1.0 mm, matrix = 240 × 240, gap = 0 mm, voxel size = 1.0 mm × 1.0 mm × 1.0 mm, and number of slices = 168 or 184.

Resting-state fMRI images, including 185 volumes, were acquired by a 2D gradient-recalled echo echo-planar imaging (GRE-EPI) pulse sequence in the axial plane. The parameters of functional images are as follows: TE = 30 ms, TR = 2000 ms, FA = 90°, FOV = 240 mm × 240 mm, thickness = 4.0 mm, matrix = 64 × 64, gap = 0 mm, voxel size = 3.75 mm × 3.75 mm × 4.0 mm, and number of slices = 36.

*2.3. Voxel-Based Morphometry Analysis.* The 3D T1-weighted images were analyzed using the VBM8 toolbox (http://dbm.neuro.uni-jena.de/vbm) based on SPM8 (http://www.fil.ion.ucl.ac.uk./spm/). First of all, all structural images were visually screened to exclude poor-quality images and subsequently segmented into white matter (WM), grey matter (GM), and cerebrospinal fluid (CSF) with default parameters by the standard segmentation model. After an affine-registered map of GM concentrations to Montreal Neurological Institute (MNI) space, the images of GM concentrations were nonlinear deformations using the DARTEL algorithm and then resampled to 1.5 $mm^3$ isotropic voxel size. The normalized and modulated tissue probability map of GM volume was acquired by multiplying the GM concentration map by the nonlinear determinant. Finally, the images of GM were smoothed with a full-width at half-maximum (FWHM) of 8 mm.

*2.4. Functional Data Preprocessing and Analysis.* Firstly, all images were examined by MRIcro (https://www.MRIcro.com), and images with severe artifacts were removed. Then, the fMRI data were preprocessed and analyzed by CONN (https://www.nitrc.org/projects/conn) implemented in MATLAB 2013b (https://www.mathworks.com/products/matlab). Specifically, the data were preprocessed by the following procedures: (1) removal of the initial time point: the initial five scan volumes were removed for each participant to reach a signal equilibrium and reduce the deviation; (2) slicing timing correction: the collected layers of each scan volume were calibrated to a correct time point; (3) motion correction: all scan volumes were realigned to correct head movements, and participants with head motion more than 2.5 mm of maximal translation or rotation more than 2.5° were excluded; (4) normalization: all functional images were spatially standardized to the MNI standard space after registration with the structural images to minimize differences between individuals and resampled to 3 mm voxels; (5) smoothing: all functional images were smoothed with a FWHM of 6 mm. The purposes of smoothing were (a) to make the data follow a Gaussian distribution, (b) to increase the signal-to-noise ratio, and (c) to compensate for the registration error in the spatial normalization step; (6) linear detrending; and (7) linear regression of confounding effects: realignment (including six head motion parameters and six head motion parameters one time point before), scrubbing, average BOLD signal of WM, and CSF were regressed out.

After preprocessing, the time series were transformed to the frequency domain utilizing fast Fourier transform (FFT). Subsequently, the square root of the power spectrum was calculated, and then, the averaged square root was acquired across 0.01-0.08 Hz to obtain the ALFF. fALFF was subsequently calculated by dividing the power spectrum of the low-frequency range of 0.01-0.08 Hz by the power spectrum of the entire frequency range of 0-0.25 Hz [16]. Finally, to minimize the global influence, the fALFF values were divided by the global mean fALFF values for standardization, which was taken as the mean fALFF.

*2.5. Statistical Analysis.* Differences in demographics and clinical characteristics between CHD and control groups were calculated using SPSS 26.0. The two-sample $t$-test was utilized for continuous variables, and the chi-squared test was used for proportions. The significance threshold of the statistical test was 0.05.

Regarding the fMRI data, differences in GVM and fALFF values of each voxel between CHD and control groups were compared by an independent two-sample $t$-test using SPM8 software implemented in MATLAB. Age, gender, and education levels were imported as covariates to eliminate the impact of confounding covariates on fALFF values. In the meantime, cardiovascular risks (hypertension, diabetes, and smoking) can affect brain structure and function and further interfere with the reliability of the results [10, 22, 23]. Therefore, hypertension, diabetes, and smoking were matched in the CHD and control groups to reduce potential confounding impacts. The cluster-level family-wise error (FWE) method was applied for multiple comparison correction, and a cluster-defined threshold was set to 0.001, and a corrected cluster significance was $p < 0.05$.

The course of disease does not conform to the normal distribution, so the Spearman correlation was applied to identify the association between the mean fALFF in altered brain areas and disease duration. The independent two-sample $t$-test was applied to analyze the association between the fALFF and the history of myocardial infarction (MI). The statistical threshold was set at $p < 0.05$. Additionally, we utilized the receiver operating characteristic (ROC) curve analysis to access the diagnostic ability of the fALFF method in altered brain regions in distinguishing CHD patients from controls. The area under the curve [24] was calculated to represent the degree of accuracy. Accuracy was considered perfect when the AUC was more than 0.9.

## 3. Results

*3.1. Demographics and Clinical Characteristics.* A total of 62 participants (26 patients and 36 control subjects) were recruited for the current study, and one patient and one control were eliminated due to excessive movement of the head. Sixty subjects (25 patients and 35 control subjects) were included for the following analysis, and no significant differences were observed in gender ($p = 0.757$), age ($p = 0.064$), years of education ($p = 0.513$), BMI ($p = 0.942$), history of smoking ($p = 0.775$), hypertension ($p = 0.895$), diabetes ($p = 0.898$), and LVEF ($p = 0.784$) between the CHD patients and control subjects. Details are summarized in Table 1.

*3.2. Comparison of GMV.* For the VBM analysis, no statistical difference was observed in GMV between the CHD and control groups ($p > 0.05$, cluster-level FWE-corrected). Overall, however, the GMV of patients with CHD was lower than that of the control group. Details about total grey and white matter volume are shown in Table 2.

*3.3. Differences in fALFF.* Compared with the control group, patients with CHD showed decreased fALFF values in the left precentral/postcentral gyrus and increased fALFF values in the right inferior cerebellum (Table 3 and Figure 1).

*3.4. Correlation Analysis between fALFF and Clinical Characteristics.* Patients of CHD were divided into the ischemic group and the infarction group, without a history of myocardial infarction (MI) and with a history of MI, respectively. The fALFF values of the right inferior cerebellum were significantly lower in the infarction group ($p = 0.0026$). No statistical difference was discovered in fALFF values of the left precentral/postcentral gyrus between the ischemic and infarction groups ($p = 0.9145$) (Figure 2). There was also no significant correlation between the aberrant fALFF values and disease duration ($p > 0.05$).

*3.5. Receiver Operating Characteristic Curve.* We speculated that the significant differences in fALFF values might be helpful imaging biomarkers to differentiate CHD patients from controls; thus, we further performed ROC curve analysis with the averaged fALFF values in these altered brain regions. The AUC results of fALFF values in the left

Table 1: Demographic and clinical characteristics.

| | Control subjects ($n = 35$) | CHD patients ($n = 25$) | Statistics | $p$ value |
|---|---|---|---|---|
| Demographic characteristics | | | | |
| Gender: men (%) | 21 (60%) | 14 (56%) | $\chi^2 = 0.096$ | 0.757[b] |
| Age (year) | 53.74 ± 7.66 | 57.44 ± 7.18 | $t = -1.892$ | 0.064[a] |
| Education (year) | 10.03 ± 3.51 | 9.32 ± 4.77 | $t = 0.659$ | 0.513[a] |
| BMI (kg/m$^2$) | 23.66 ± 2.70 | 23.71 ± 2.62 | $t = -0.073$ | 0.942[a] |
| Clinical characteristics | | | | |
| Hypertension, $n$ (%) | 19 (54%) | 14 (56%) | $\chi^2 = 0.017$ | 0.895[b] |
| Diabetes, $n$ (%) | 4 (11%) | 4 (16%) | $\chi^2 = 0.016$ | 0.898[b] |
| Smoking, $n$ (%) | 11 (31%) | 7 (28%) | $\chi^2 = 0.082$ | 0.775[b] |
| LVEF (%) | 65.46 ± 6.80 | 65.96 ± 5.93 | $t = -0.276$ | 0.784[a] |
| Disease duration (month) | N/A | 37.99 ± 43.13 | N/A | N/A |
| History of MI, $n$ (%) | N/A | 6 (24%) | N/A | N/A |

The data are shown as the mean values ± standard deviations. N/A = not applicable; BMI = body mass index; LVEF = left ventricular ejection fraction; MI = myocardial infarction. [a]The $p$ value was obtained by a two-sample $t$-test. [b]The $p$ value was obtained by the chi-squared test.

Table 2: Total brain volume between control subjects and CHD patients.

| | Control subjects ($n = 35$) | CHD patients ($n = 25$) | Statistics | $p$ value |
|---|---|---|---|---|
| Total grey matter volume | 634.47 ± 51.99 | 621.33 ± 47.07 | $t = 1.003$ | 0.320[a] |
| Total white matter volume | 533.36 ± 69.60 | 515.40 ± 49.30 | $t = 1.106$ | 0.273[a] |

The data are shown as the mean values ± standard deviations. [a]The $p$ value was obtained by a two-sample $t$-test.

Table 3: Differences in fALFF values between control subjects and CHD patients.

| Brain regions | Peak MNI coordinates | | | Cluster size | $t$ value |
|---|---|---|---|---|---|
| | $x$ | $y$ | $z$ | | |
| CHD < controls | | | | | |
| Left precentral/postcentral gyrus | -39 | -15 | 60 | 83 | 4.4716 |
| CHD > controls | | | | | |
| Right inferior cerebellum | 30 | -51 | -57 | 25 | -5.2498 |

*$x$, $y$, and $z$ are the locations of the peak voxels in standard MNI coordinates. FWE correction, cluster-level: $p < 0.05$. MNI = Montreal Neurological Institute.

precentral/postcentral gyrus and right inferior cerebellum were 0.9326 and 0.9017, respectively, indicating the accuracy was perfect (Figure 3).

## 4. Discussion

We designed this study to determine whether patients with CHD display abnormal brain activity compared with the control group. Coronary heart disease is an urgent, rapidly developing critical disease with high disability and mortality, which seriously endangers human health [1, 25]. Previous studies have indicated that patients with CHD exhibited an increased risk of mild cognitive and emotional dysfunction [4, 5]. Therefore, our study is aimed at preliminarily exploring the underlying neural mechanisms by measuring spontaneous brain activity changes of CHD via resting-state fMRI. To the best of our knowledge, it is the first time to investigate the spontaneous brain activity alterations in patients with CHD.

The present results demonstrated no significant difference was discovered in GMV between the two groups and revealed the aberrant neural activity in CHD patients by measuring fALFF using rs-fMRI. The fALFF reflects the spontaneous neural activity by measuring changes in the BOLD signal. The fALFF can effectively suppress physiological noise and improve the specificity and sensitivity of spontaneous neuronal activity compared with ALFF [16]. Compared with controls, the CHD patients showed lower fALFF values in the left precentral/postcentral gyrus and higher fALFF values in the right inferior cerebellum. Compared with patients without a history of MI, MI patients showed lower fALFF values in the right inferior cerebellum. However, there was no statistical correlation between the fALFF values in brain areas and the course of the disease.

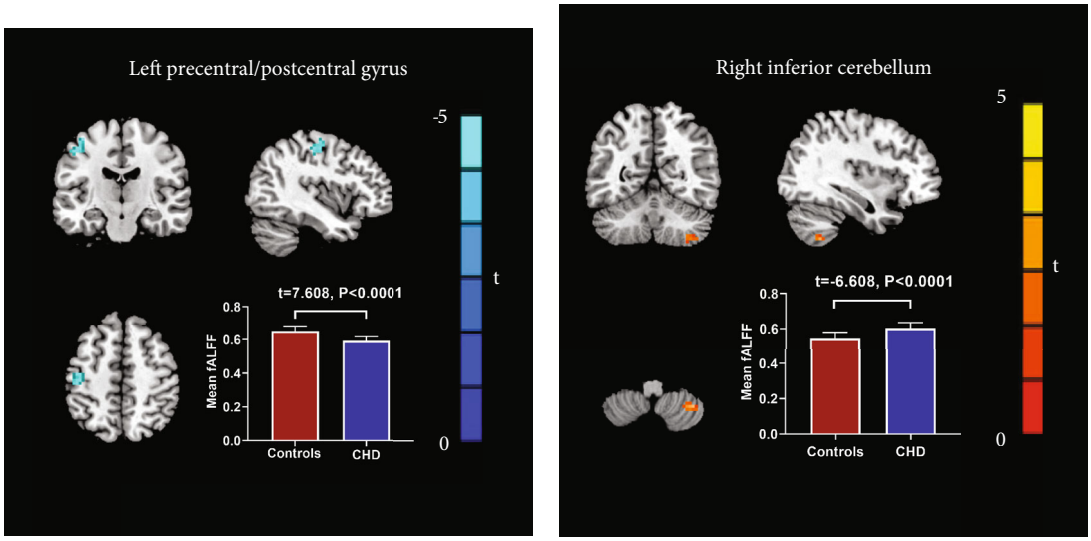


(a) (b)

Figure 1: Mean fALFF differences between the control subjects and CHD patients. Compared to control subjects, (a) shows decreased fALFF values of the left precentral/postcentral gyrus in CHD patients. (b) Shows increased fALFF values of the right inferior cerebellum in CHD patients. Error bars indicate the standard deviation. fALFF = fractional amplitude of low-frequency fluctuations; CHD = coronary heart disease.

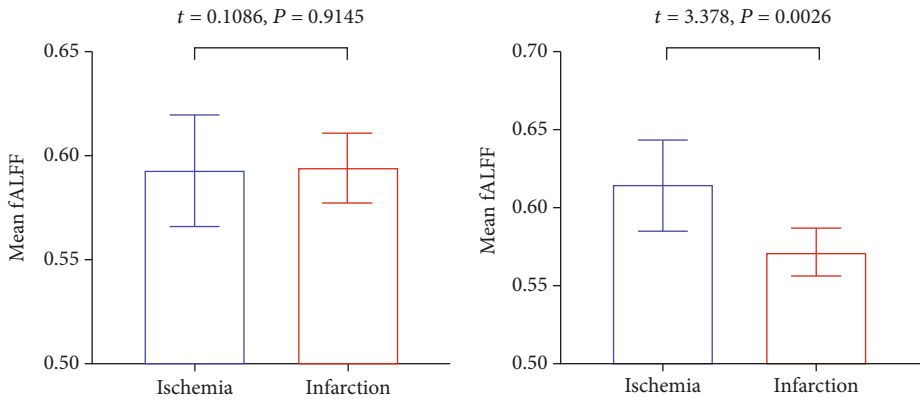


(a) (b)

Figure 2: Mean fALFF differences between the ischemia and infarction groups. (a) Shows fALFF values in the left precentral/postcentral gyrus. (b) Shows fALFF values in the right inferior cerebellum.

In addition, no significant difference was discovered in GMV between the two groups.

Our current research demonstrated no evidence of a statistical difference in GMV between patients with CHD and matched controls, which is inconsistent with previous studies. Koschack and Irle demonstrated smaller GMV in the hippocampus, which may be a biomarker to predict later cognitive decline or dementia [26]. Almeida et al. revealed that CHD was related to grey matter atrophy in a series of brain regions, including the precentral and postcentral cortex, the left medial frontal lobe, and right temporal lobe, some of which were of great significance in cognitive function and behavior [27]. A case-control study found that the cerebral cortex volume of the left pars triangularis, left fusiform, and left superior temporal gyrus decreased significantly in patients with CHD combined with cognitive impairment [8]. GMV abnormalities in the brain regions were also inconsistent in the above studies. Shorter exposure time to vascular risk factors in relatively young CHD patients in this study may be contributing to explaining these results. Different inclusion criteria between the CHD and control groups are also one of the reasons that account for the inconsistent results. Other potential reasons include differences in structural MRI data processing methods (VBM vs. CURRUY) and statistical analysis approaches.

Previous neuroimaging reports showed the atrophy of grey matter and reduction of cerebral blood flow in precentral and postcentral gyri in patients with CHD [6, 9]. The current study showed lower fALFF values in the left precentral/postcentral gyrus in patients with CHD. Therefore, we

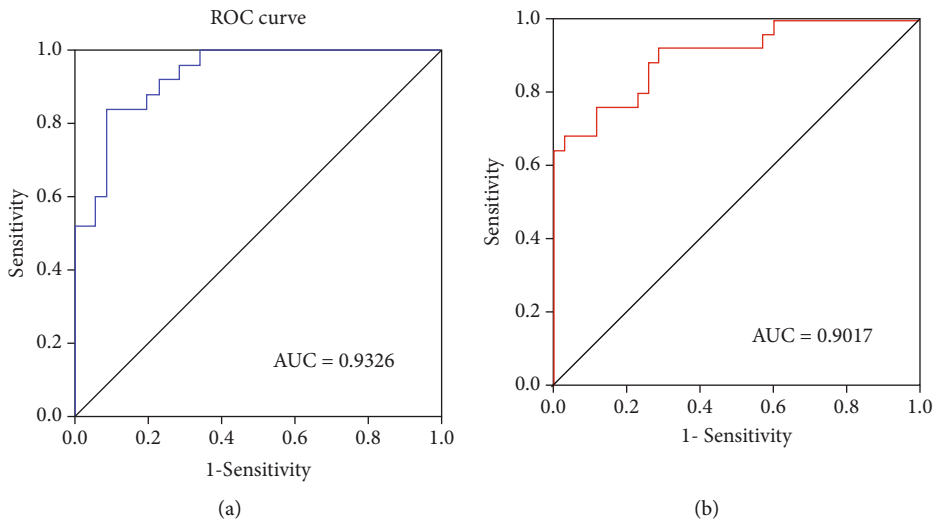


Figure 3: ROC curve analysis of fALFF values for altered brain regions. (a) Left precentral/postcentral gyrus. AUC were 0.9326 ($p < 0.0001$; 95% CI: 0.8740-0.9911); (b) right inferior cerebellum. AUC were 0.9017 ($p < 0.0001$; 95% CI: 0.8233-0.9801). ROC = receiver operating characteristic; AUC = area under the curve; CI = confidence interval.

speculated that the precentral and postcentral gyri may be the vital brain regions closely associated with CHD. It is well known that the postcentral gyrus is the primary somatosensory cortex (S1) and the precentral gyrus is the primary motor cortex (M1), which play important roles in primary sensory and motor control functions, respectively. The decreased neural activity of the postcentral and precentral gyri, the crucial components of the sensorimotor network, is associated with the modulation dysfunction of the sensorimotor network [28, 29]. Both postcentral and precentral gyri are involved in pain processing, which is a multidimensional experience involving sensory discrimination, cognition evaluation, and affective motivation [30]. A large number of researches have proven the essential roles of the postcentral and precentral gyri in chronic pain-related [17, 18, 31]. Therefore, we hold the opinion that the decreased neural activity in the postcentral and precentral gyri may be associated with angina pectoris. The postcentral gyrus is a component of the homeostatic-afferent network that participates in the central processing of visceral pain [32] and plays a vital role in the discrimination and localization of pain [33]. Kong et al. reported that S1 was involved in the pathological pain state of chronic low back pain [34]. Liu et al. demonstrated that regional cerebral blood flow in S1 was highly correlated with pain intensity in patients with postherpetic neuralgia [35]. Some neuroimaging studies had confirmed that chronic pain patients were also associated with abnormal excitability in the cortical motor area [19, 36]. Motor cortex stimulation can relieve plenty of chronic pain syndromes [37]. Bernard et al. suggested that the precentral gyrus may be a vital brain area as a target for chronic pain treatment in somatoform pain disorders [14]. Meanwhile, the precentral gyrus is located in the frontal lobe, which is associated with the regulation of emotion and plays an important part in emotional memory storage [17]. Zhang et al. indicated that decreased volume of grey matter in the precentral gyrus may be associated with an increased risk of depressive disorder [38]. Xiong et al. pointed out that the altered cortical thickness of the left precentral gyrus may stand for state-independent abnormalities in major depressive disorder [39]. Plenty of studies demonstrated that patients with CHD have an increased incidence of depression, but the exact neural mechanism is unclear [40, 41]. The decreased fALFF in the precentral gyrus may contribute to explaining the underlying neural mechanism of increased risk of depression in CHD. Previous neuroimaging studies also demonstrated that the motor cortex may be involved in cognitive functions, including implicit motor learning ability [42] and working memory [43]. Bush et al. demonstrated that the precentral gyrus participates in the executive control of response inhibition [24]. Many neuropsychological tests have shown that CHD is associated with an increased risk for cognitive decline, especially executive function, which we suspect may be associated with lower neural activity in the precentral gyrus [14]. These pieces of evidence from neuroimaging research may indicate that the precentral gyrus is not only involved in motor control but also in pain modulation and emotional and cognitive processing. The significantly lower fALFF values in the left precentral/postcentral gyrus in patients with CHD may be involved in the dysfunction of the sensorimotor network and pain coding and even associated with emotional and cognitive processing.

Compared with the control group, the CHD patients exhibited higher fALFF values in the right inferior cerebellum. The cerebellum is regarded as a major motor control region [44]. Several studies have proved that the cerebellum also participates in the processing of emotion and cognition [29, 45]. The low ReHo value of the cerebellum in patients with major depressive disorder suggested that the cerebellum was involved in mood regulation [46]. The cerebellum has recently been proven to play a part in somatosensory processing, including nociception [47]. Moulton et al. confirmed that the cerebellum participated in pain processing

[30]. We supposed that the increased brain activity in the right cerebellum may have part of compensatory effects with regard to both motor and nonmotor dysfunctions due to brain activity reduction in the precentral and postcentral gyri. We indicated that the fALFF values of the right inferior cerebellum in patients with MI were lower than those in patients without MI, which may indicate that the compensatory effects of MI patients are lower than that of patients without MI. Therefore, patients with MI may show a greater possibility of brain function decline.

We acknowledged that several limitations still exist. First, the deficiency of objective psychological or cognitive evaluation restricted our interpretation of the outcomes, and the exact mechanism of altered neural fALFF activity in CHD remains unclear. Second, the sample size was relatively small, especially the number of patients with a history of MI, which could limit the statistical capacity to detect tiny changes in the brain. Third, part of patients with CHD was receiving multiple drugs that might have possible impacts on brain activity. Medication-naive groups should be considered to exclude this potential bias in further research.

## 5. Conclusions

Our investigation demonstrated that there were significant changes in spontaneous brain activity prior to structural changes in patients with CHD. These abnormal brain activities were mainly located in the left precentral/postcentral gyrus and the right inferior cerebellum. Spontaneous brain activity abnormalities may provide useful hints regarding underlying neural mechanisms of abnormal brain function in CHD.

## Data Availability

The data used to support the findings of this study are available from the corresponding author upon request.

## Conflicts of Interest

The authors declare that they have no conflict of interest.

## Authors' Contributions

SL designed the study and analyzed the data. YH and SD undertook the statistical analysis. WM, QL, TX, and QL selected the patients and performed written agreement and scanning. SL, YH, and HZ wrote the manuscript. All authors approved the final manuscript.

## Acknowledgments

We thank all participants in this study, and this work was supported by grants from the Natural Science Foundation of Fujian Province, China (Grant No. 2015J01535).

## References

[1] H. D. Wang, M. Naghavi, C. Allen et al., "Global, regional, and national life expectancy, all-cause mortality, and cause-specific mortality for 249 causes of death, 1980-2015: a systematic analysis for the Global Burden of Disease Study 2015," *Lancet*, vol. 388, no. 10053, pp. 1459–1544, 2016.

[2] E. J. Benjamin, P. Muntner, A. Alonso et al., "Heart disease and stroke statistics-2019 update a report from the American Heart Association," *Circulation*, vol. 139, no. 10, pp. E56–E528, 2019.

[3] L. Zheng, W. Mack, H. Chui et al., "Coronary artery disease is associated with cognitive decline independent of Changes on Magnetic Resonance Imaging in cognitively normal elderly Adults," *Neurology*, vol. 60, no. 3, pp. 499–504, 2012.

[4] S. P. Rovio, K. Pahkala, and O. T. Raitakari, "Cognitive decline before and after incident coronary heart disease opportunity to intervene cognitive function trajectories," *Journal of the American College of Cardiology*, vol. 73, no. 24, pp. 3051–3053, 2019.

[5] I. E. van de Vorst, H. L. Koek, R. de Vries, M. L. Bots, J. B. Reitsma, and I. Vaartjes, "Effect of vascular risk factors and diseases on mortality in individuals with dementia: a systematic review and meta-analysis," *Journal of the American Geriatrics Society*, vol. 64, no. 1, pp. 37–46, 2016.

[6] U. C. Anazodo, J. K. Shoemaker, N. Suskin, T. Ssali, D. J. J. Wang, and K. S. St Lawrence, "Impaired cerebrovascular function in coronary artery disease patients and recovery following cardiac rehabilitation," *Frontiers in Aging Neuroscience*, vol. 7, 2016.

[7] C. Santiago, N. Herrmann, W. Swardfager et al., "White matter microstructural integrity is associated with executive function and processing speed in older adults with coronary artery disease," *American Journal of Geriatric Psychiatry*, vol. 23, no. 7, pp. 754–763, 2015.

[8] M. Barekatain, H. Askarpour, F. Zahedian et al., "The relationship between regional brain volumes and the extent of coronary artery disease in mild cognitive impairment," *Journal of Research in Medical Sciences*, vol. 19, no. 8, pp. 739–745, 2014.

[9] O. P. Almeida, G. J. Garrido, C. Beer, N. T. Lautenschlager, L. Arnolda, and L. Flicker, "Cognitive and brain changes associated with ischaemic heart disease and heart failure," *European Heart Journal*, vol. 33, no. 14, pp. 1769–1776, 2012.

[10] Y. Cui, Y. Jiao, Y. C. Chen et al., "Altered spontaneous brain activity in type 2 diabetes: a resting-state functional MRI study," *Diabetes*, vol. 63, no. 2, pp. 749–760, 2014.

[11] A. Peterson, J. Thome, P. Frewen, and R. A. Lanius, "Resting-state neuroimaging studies: a new way of identifying differences and similarities among the anxiety disorders?," *Canadian Journal of Psychiatry-Revue Canadienne De Psychiatrie*, vol. 59, no. 6, pp. 294–300, 2014.

[12] K. Tillisch and J. S. Labus, "Advances in imaging the brain-gut axis: functional gastrointestinal disorders," *Gastroenterology*, vol. 140, no. 2, pp. 407–411.e1, 2011.

[13] S. Ogawa, D. W. Tank, R. Menon et al., "Intrinsic signal changes accompanying sensory stimulation-functional brain mapping with magnetic-resonance-imaging," *Proceedings of the National Academy of Sciences of the United States of America*, vol. 89, no. 13, pp. 5951–5955, 1992.

[14] C. Bernard, G. Catheline, B. Dilharreguy et al., "Cerebral changes and cognitive impairment after an ischemic heart disease: a multimodal MRI study," *Brain Imaging and Behavior*, vol. 10, no. 3, pp. 893–900, 2016.

[15] K. Deckers, S. H. J. Schievink, M. M. F. Rodriquez et al., "Coronary heart disease and risk for cognitive impairment or

dementia: systematic review and meta-analysis," *PLoS One*, vol. 12, no. 9, article e0184244, 2017.

[16] Q. H. Zou, C. Z. Zhu, Y. Yang et al., "An improved approach to detection of amplitude of low-frequency fluctuation (ALFF) for resting-state fMRI: fractional ALFF," *Journal of Neuroscience Methods*, vol. 172, no. 1, pp. 137–141, 2008.

[17] L. Li, J. Ma, J. G. Xu et al., "Brain functional changes in patients with Crohn's disease: a resting-state fMRI study," *Brain and Behavior: A Cognitive Neuroscience Perspective*, vol. 11, no. 8, article e2243, 2021.

[18] W. Q. Ao, Y. G. Cheng, M. X. Chen et al., "Intrinsic brain abnormalities of irritable bowel syndrome with diarrhea: a preliminary resting-state functional magnetic resonance imaging study," *BMC Medical Imaging*, vol. 21, no. 1, p. 4, 2021.

[19] B. L. Zhang, M. Jung, Y. H. Tu et al., "Identifying brain regions associated with the neuropathology of chronic low back pain: a resting-state amplitude of low-frequency fluctuation study," *British Journal of Anaesthesia*, vol. 123, no. 2, pp. E303–e311, 2019.

[20] T. F. Members, G. Montalescot, U. Sechtem et al., "2013 ESC guidelines on the management of stable coronary artery disease: the Task Force on the management of stable coronary artery disease of the European Society of Cardiology," *European Heart Journal*, vol. 34, no. 38, pp. 2949–3003, 2013.

[21] A. Arbab-Zadeh and V. Fuster, "The risk continuum of atherosclerosis and its implications for defining CHD by coronary angiography," *Journal of the American College of Cardiology*, vol. 68, no. 22, pp. 2467–2478, 2016.

[22] T. C. Durazzo, A. Mon, D. Pennington, C. Abe, S. Gazdzinski, and D. J. Meyerhoff, "Interactive effects of chronic cigarette smoking and age on brain volumes in controls and alcohol-dependent individuals in early abstinence," *Addiction Biology*, vol. 19, no. 1, pp. 132–143, 2014.

[23] D. Newby, L. Winchester, W. Sproviero et al., "Associations between brain volumes and cognitive tests with hypertensive burden in UK Biobank," *Journal of Alzheimers Disease*, vol. 84, no. 3, pp. 1373–1389, 2021.

[24] G. Bush, P. J. Whalen, B. R. Rosen, M. A. Jenike, S. C. McInerney, and S. L. Rauch, "The counting stroop: an interference task specialized for functional neuroimaging - Validation study with functional MRI," *Human Brain Mapping*, vol. 6, no. 4, pp. 270–282, 1998.

[25] Authors/Task Force Members, "Guidelines on the management of stable angina pectoris: executive summary," *European Heart Journal*, vol. 27, no. 11, pp. 1341–1381, 2006.

[26] J. Koschack and E. Irle, "Small hippocampal size in cognitively normal subjects with coronary artery disease," *Neurobiology of Aging*, vol. 26, no. 6, pp. 865–871, 2005.

[27] O. P. Almeida, G. J. Garrido, C. Beer et al., "Coronary heart disease is associated with regional grey matter volume loss: implications for cognitive function and behaviour," *Internal Medicine Journal*, vol. 38, no. 7, pp. 599–606, 2008.

[28] F. Y. Zhang, B. Hua, T. F. Wang, M. Wang, Z. X. Ding, and J. R. Ding, "Abnormal amplitude of spontaneous low-frequency fluctuation in children with growth hormone deficiency: a resting-state functional magnetic resonance imaging study," *Neuroscience Letters*, vol. 742, p. 135546, 2021.

[29] Y. Yu, L. H. Chen, Q. H. Wang et al., "Altered amplitude of low-frequency fluctuations in inactive patients with nonneuropsychiatric systemic lupus erythematosus," *Neural Plasticity*, vol. 2019, 10 pages, 2019.

[30] E. A. Moulton, J. D. Schmahmann, L. Becerra, and D. Borsook, "The cerebellum and pain: passive integrator or active participator?," *Brain Research Reviews*, vol. 65, no. 1, pp. 14–27, 2010.

[31] J. Yang, B. Li, Q. Y. Yu et al., "Altered intrinsic brain activity in patients with toothaches using the amplitude of low-frequency fluctuations: a resting-state fMRI study," *Neuropsychiatric Disease and Treatment*, vol. Volume 15, pp. 283–291, 2019.

[32] Y. Al Omran and Q. Aziz, "Functional brain imaging in gastroenterology: to new beginnings," *Nature Reviews Gastroenterology & Hepatology*, vol. 11, no. 9, pp. 565–576, 2014.

[33] W. Kim, S. K. Kim, and J. Nabekura, "Functional and structural plasticity in the primary somatosensory cortex associated with chronic pain," *Journal of Neurochemistry*, vol. 141, no. 4, pp. 499–506, 2017.

[34] J. Kong, R. B. Spaeth, H. Y. Wey et al., "S1 is associated with chronic low back pain: a functional and structural MRI study," *Molecular Pain*, vol. 9, 2013.

[35] J. Liu, Y. Hao, M. Du et al., "Quantitative cerebral blood flow mapping and functional connectivity of postherpetic neuralgia pain: a perfusion fMRI study," *Pain*, vol. 154, no. 1, pp. 110–118, 2013.

[36] J. Kregel, M. Meeus, A. Malfliet et al., "Structural and functional brain abnormalities in chronic low back pain: A systematic review$A'$," *Seminars in Arthritis and Rheumatism*, vol. 45, no. 2, pp. 229–237, 2015.

[37] T. Ostergard, C. Munyon, and J. P. Miller, "Motor Cortex Stimulation for Chronic Pain," *Neurosurgery Clinics of North America*, vol. 25, no. 4, pp. 693–698, 2014.

[38] X. C. Zhang, S. Q. Yao, X. Z. Zhu, X. Wang, X. L. Zhu, and M. T. Zhong, "Gray matter volume abnormalities in individuals with cognitive vulnerability to depression: a voxel-based morphometry study," *Journal of Affective Disorders*, vol. 136, no. 3, pp. 443–452, 2012.

[39] G. Xiong, D. F. Dong, C. Cheng et al., "State-independent and -dependent structural alterations in limbic-cortical regions in patients with current and remitted depression," *Journal of Affective Disorders*, vol. 258, pp. 1–10, 2019.

[40] J. H. Lichtman, J. T. Bigger, J. A. Blumenthal et al., "Depression and coronary heart disease: recommendations for screening, referral, and treatment: a science advisory from the American Heart Association Prevention Committee of the Council on Cardiovascular Nursing, Council on Clinical Cardiology, Council on Epidemiology and Prevention, and Interdisciplinary Council on Quality of Care and Outcomes Research endorsed by the American Psychiatric Association," *Circulation*, vol. 118, no. 17, pp. 1768–1775, 2008.

[41] B. D. Thombs, E. B. Bass, D. E. Ford et al., "Prevalence of depression in survivors of acute myocardial infarction - review of the evidence," *Journal of General Internal Medicine*, vol. 21, no. 1, pp. 30–38, 2006.

[42] M. A. Nitsche, A. Schauenburg, N. Lang et al., "Facilitation of implicit motor learning by weak transcranial direct current stimulation of the primary motor cortex in the human," *Journal of Cognitive Neuroscience*, vol. 15, no. 4, pp. 619–626, 2003.

[43] T. D. Wager and E. E. Smith, "Neuroimaging studies of working memory:," *Cognitive, Affective, & Behavioral Neuroscience*, vol. 3, no. 4, pp. 255–274, 2003.

[44] Q. Zhu, W. Chen, Y. Y. Cui et al., "Structural and functional changes in the cerebellum and brainstem in patients with benign paroxysmal positional vertigo," *The Cerebellum*, vol. 20, no. 5, pp. 804–809, 2021.

[45] D. Timmann, J. Drepper, M. Frings et al., "The human cerebellum contributes to motor, emotional and cognitive associative learning. A review," *Cortex*, vol. 46, no. 7, pp. 845–857, 2010.

[46] Z. F. Liu, C. Xu, Y. Xu et al., "Decreased regional homogeneity in insula and cerebellum: a resting-state fMRI study in patients with major depression and subjects at high risk for major depression," *Psychiatry Research: Neuroimaging*, vol. 182, no. 3, pp. 211–215, 2010.

[47] C. Y. Saab and W. D. Willis, "The cerebellum: organization, functions and its role in nociception," *Brain Research Reviews*, vol. 42, no. 1, pp. 85–95, 2003.

Hindawi
Disease Markers
Volume 2022, Article ID 3361172, 5 pages
https://doi.org/10.1155/2022/3361172

*Research Article*

# Post-Ortho-K Corneal Epithelium Changes in Myopic Eyes

**Dongyi Qu**[1] **and Yuehua Zhou**[2,3]

[1]*Beijing AIER Fukang Eye Hospital, China*
[2]*Ming Vision Eye Clinic, Beijing, China*
[3]*Ineye Hospital of Chengdu University of TCM, China*

Correspondence should be addressed to Dongyi Qu; dongyiqu@outlook.com

Received 7 March 2022; Accepted 8 May 2022; Published 29 May 2022

Academic Editor: Pei-Wen Zhu



The study is aimed at evaluating corneal epithelial thickness changes associated with overnight orthokeratology (ortho-K). In this retrospective study, epithelial thickness was measured using optical coherence tomography (OCT) before and after 1 day, 1 week, 1 month, and 3 months ortho-K nightly lens wear. Compared with pre-orthokeratology measurements, central (2 mm) corneal epithelium thickness was significantly reduced at 1 day, 1 week, 1 month, and 3 months with ortho-K ($P < 0.05$). Paracentral (2 mm~5 mm annular ring) epithelial thickness was also significantly reduced at superior temporal, inferior temporal, temporal, and inferior locations after ortho-K ($P < 0.05$), while midperipheral (5 mm~6 mm annular ring) epithelial thickness was greater post- than pre-ortho-K at superior, superior temporal, inferior temporal, inferior, and inferior nasal locations ($P < 0.05$). In other zones, superior, superior nasal, nasal, and inferior nasal in paracentral annular ring and temporal and superior nasal in midperipheral ring, epithelial thickness underwent no significant change. Ortho-K lens wear caused the central corneal epitheliums to thin. The temporal half zones become thinner in paracentral zones and thicker in midperipheral zones.

## 1. Introduction

Orthokeratology, also referred as ortho-K or Ok, involves reverse-geometry design breathable and rigid contact lenses. Overnight ortho-K lens wearing results in reduced central cornea thickness temporally, reduced refractive error, and 20/20 or better unaided vision during the subsequent daytime with continuing wearing. Cho and Cheung [1] confirmed that ortho-K had the effect of slowing axial length progression and controlling myopia development in myopic children via myopic defocus. The central corneal curvature is flattened corresponding to relatively flat fitting base curve of ortho-K lens. And midperipheral cornea is steepened corresponding to relatively steep fitting reverse curve of ortho-K lens. Data display that central refractive power decreases and peripheral refractive power increases. Corneal topography shows a classic bull's eye because central cornea flattens and midperipheral cornea steepens after a well-centered ortho-K lens wear. The present study was designed to retrospectively research corneal epithelial changes post-ortho-K lens wear, which helps to explain corneal morphological changes.

Previous studies have reported central epithelial thinning and midperipheral epithelial thickening, measured by a modified optical pachymeter after 90 days of ortho-K lens wear [2]. Tao et al. measured the topographic thickness of the cornea and epithelium using spectral-domain OCT with ultrahigh resolution (~3 $\mu$m) and concluded that the corneal epithelial thickness between the nasal side and temporal side had no significant differences [3]. In a further study, Du et al. used the same OCT as Tao's to measure the corneal epithelial

thickness M at 10:00 AM and again at 6 and 8 hours later and confirm thinning of the superior midperipheral epithelium in the vertical meridian and thickening of the temporal and nasal midperipheries in the horizontal meridian [4]. Kim confirmed thinning of the central corneal epithelium and thickening of the midperipheral epithelium following ortho-K lens wear [5]. Zhang et al. [6] assessed the epithelial thickness in corneal zones before and after ortho-K lens wear using the RTVue OCT (Optovue Inc., Fremont, CA, United States) and found insignificant change in paracentral (2–5 mm) and midperipheral (5–6 mm) annular ring corneal epithelial thickness. There is a lack of consensus to date on corneal epithelium redistribution after ortho-K lenses wear. Swarbrick et al. [7] found that the epithelium measured using OCT was significantly thinner in ortho-K wearers than in nonlens wearers, not evolving paracentral and peripheral corneal epithelium. Interventions to control myopia take effect over time, so it is important to understand corneal changes that occur in prolonged ortho-K lens wear. The present study is the first to investigate central and zonal corneal epithelial changes over a period of up to three months of ortho-K lens wear.

## 2. Materials and Methods

*2.1. Participants.* Records of 78 children (146 eyes) aged between 8 and 13 years were reviewed in this study. The children had worn ortho-K lenses for 8 to 10 hours per night. The inclusion criteria were a spherical refractive error of less than 5.00 diopters (D) with astigmatism of 1.50 D or less, best-corrected distance visual acuity of 20/20 or better before treatment. And ortho-K lens centered or decentered by less than 1.0 mm radially determined by slit lamp examination. The exclusion criterion was any current ocular or systemic disease. All subjects were treated according to the tenets of the Declaration of Helsinki. A consent form was signed by the parent of each child.

*2.2. Ortho-K Lens Fitting.* Ortho-K lenses from Paragon CRT (Paragon Vision Sciences, Mesa, AZ, United States) were used for all subjects. Lens fitting was evaluated using fluorescein. The typical bull's eye pattern in the corneal topography confirmed an adequate fit after an overnight trial. At each visit after the beginning of ortho-K lens wear, a complete contact lens follow-up examination was performed, including slit lamp examination, visual acuity, corneal topography (Medmont, Arlington, WA, United States), and OCT to investigate the response to ortho-K lens wear.

*2.3. Measurement of Corneal Epithelial Thickness.* The corneal epithelial thickness data were obtained at baseline examination and during the follow-up visits. Unaided distance visual acuity of 20/20 or better and satisfactory topographic change were achieved in all patients and at all visits. We scanned the cornea in eight meridians using a Pachymetry+Cpwr scan over a 6 mm diameter zone centered at the corneal apex using the RTVue OCT system with a corneal anterior module set at a wavelength of 830 nm. The corneal epithelial thickness maps were divided into a total of 17 sectors using an automatic algorithm, including one central 2 mm diameter zone, eight paracentral zones within an annulus between 2 and 5 mm diameters, and eight midperipheral annuli between the 5 and 6 mm diameter ring zones. The mean measurements at the central zone and in each of eight measurements in the paracentral and midperipheral zones were analyzed statistically. All of the OCT images were performed by the same examiners. OCT was conducted after one day, one week, one month, and three months of ortho-K wear in 42, 40, 60, and 34 eyes, respectively (Table 1).

*2.4. Data Analysis.* SPSS version 21.0 for Windows (IBM Corp., Armonk, NY, United States) was applied to analyze statistically. Corneal epithelial thickness values were compared using the ANOVA test before and after OK lens wear. Data were recorded according to follow-up time (baseline, 1 day, 1 week, 1 month, and 3 months) to monitor the difference in refractive error and corneal thickness. One-way analysis of variance (ANOVA) was performed to compare differences among these 5 subgroups. All statistical significance was defined as $P < 0.05$.

## 3. Results

The study included 146 eyes of 30 male and 48 female subjects successfully treated with ortho-K lenses to control myopia progression. The mean age of the subjects was $10.2 \pm 1.67$ years (range: 7 to 14). Spherical equivalent refractive error reduced after treatment, as summarized in Table 1.

OCT was carried out after one day, one week, one month, and three months of ortho-K lens wear in 42 eyes, 40 eyes, 60 eyes, and 34 eyes, respectively. Not each subject attend all the routine aftercare visit due to personal reasons. At each of these time points, the flat and steep keratometry ($k$) readings were significantly reduced compared with pre-ortho-K readings. Compared with the one-day time point, flat and steep $k$ readings were significantly reduced at one week, one month, and three months. However, the $k$ readings at one week, one month, and three months were statistically similar (Table 2).

Flat $k$ and steep $k$ decreased at different time points significantly post-Ok compared with pre-Ok. Compared with 1-day post-Ok, flat $k$ and steep $k$ also decreased significantly at 1 week, 1 month, and 3 months post-Ok. Compared with 1-week post-Ok, flat $k$ and steep $k$ at 1 month and 3 months decreased not significantly. Flat $k$ and steep $k$ have no difference between 1-month and 3-month curvature.

*3.1. Corneal Epithelial Thickness Changes.* Compared with pre-ortho-K thickness, the central corneal epithelial thickness decreased significantly at each of the four time points ($P < 0.05$) (Table 3). Paracentral corneal thickness in the temporal zone was significantly decreased at day one; in the superior temporal, temporal, inferior temporal, and

Table 1: Eye number at different follow-up time points.

| Follow-up time | 1 day | 1 week | 1 month | 3 months |
|---|---|---|---|---|
| Eye number | 42 | 40 | 60 | 34 |

inferior zones at one week; in the temporal, inferior temporal, and inferior zones at one month; and in the superior temporal, temporal, and inferior temporal zones at three months ($P < 0.05$) (Table 3). In contrast, the midperipheral epithelial thickness was increased compared with pre-ortho-K levels in the inferior zone at one week; in the superior, superior temporal, and inferior temporal zones at one month; and in the inferior and inferior nasal zones at three months ($P < 0.05$) with no significant change in other zones at each of these time points (Table 3).

There was a trend that overnight ortho-K remains stable at temporal direction. It was suggested that corneal epithelial redistribution occurred in the central and paracentral temporal, superior and inferior temporal, and inferior zones with migration to midperipheral temporal half-sectors within 6 mm zones surrounding the corneal apex, while the nasal zones did not change statistically (Figure 1).

## 4. Discussions

Designed with four to five curves, modern ortho-K lenses as a reverse-geometry contact lens have an enhanced centration and predictability of myopia control [8]. Ortho-K lenses are made of breathable materials, which are safe for overnight wear and allow subsequent daytime visual acuity to reach 20/20 or better. Orthokeratology has therefore become a common treatment to control myopia, arresting or slowing myopia progression [9–13] based on myopic defocus theory [14, 15]. The ortho-K lens central base curve is flatter than the cornea, and pressure is placed on the cornea from the lens eyelids and tear fluid. The reverse curve is steeper than the cornea providing space for central corneal epithelial migration. Corneal epithelial thickening in the reverse curve zones converts peripheral retinal hyperopic defocus into myopic defocus which may stop or slow axial length progression [14, 15].

Kim et al. [5] showed corneal epithelial thinning centrally and thickening in the midperiphery. The 5~6 mm annular ring showed no significant thickening compared to baseline values. Changes in epithelial thickness showed a nonuniform pattern with more thinning of the temporal and inferior zones compared with the nasal and superior zones of the paracentral region, with further thickening in the nasal zone compared with the temporal zone in the midperiphery [5]. In the present study, all of the thinning and thickening occurred at temporal half-zones in the 2~5 and 5~6 mm annuli. Thinning of the temporal 2~5 mm annular ring resulted in thickening of the temporal 5~6 mm annulus due to epithelial migration from the paracentral region to the midperiphery.

Morphological analysis performed using a confocal microscope showed significant structural changes particularly in the central epithelium after 15 days, one month, and one year after ortho-K wear [16, 17]. Our study confirmed that central corneal epitheliums were stably thinning till 3 months after ortho-K lens wear.

Wang et al. found thinning of the central epithelium and thickening in the midperiphery [18]. Several other studies have also found central corneal epithelial thinning [5–7, 19, 20] and flattening, with corneal curvature and myopia reduced and unaided visual acuity at 20/20 or better. In contrast with these findings, the present study found that thinning of the paracentral epithelium and thickening in the midperiphery happened at temporal half-meridian.

Zhang et al. [6] commented central epithelial thinning but no change in thickness at the 2–5 mm and 5–6 mm annular zones over time. The thickness at each time point after lens wear was significant compared with the thickness before lens wear. The present study demonstrated that epithelial thinning at the central 2 mm zone postlens wear reached the thinnest peak at one week post-ortho-K. The epithelium concordant with reverse curve area thickened after one day of lens wear and became stable at one week.

The reverse geometry of ortho-K lenses results in corneal epithelial morphological changes and redistribution. The base curve diameter of the lenses used in the present study is 6 mm. OCT images showed epithelial thinning in the central 2 mm, thinning in some paracentral zones in an annulus 2~5 mm from the corneal apex, and thickening in zones of the midperipheral annulus 5~6 mm from the apex. OCT measures the corneal central 6 mm zones and 5~6 mm annular ring area coincidence with the transition area from ortho-K lens' base curve to reverse curve. Additionally, 5~6 mm temporal half-annular area thickening is the anatomy basic of forming red myopic defocus ring displayed on the tangential corneal topography. Myopic defocus is a central theory in the control of myopia, and the present study provides a morphological basis for this theory.

The current research showed that thickness of the corneal epithelium was stable after one week of ortho-K lens wear in the 2 mm~5 mm paracentral annular ring and by one month in the 5-6 mm midperipheral annulus. Paracentral superior temporal, temporal, inferior temporal, and inferior corneal epithelium thinned significantly while other sectors thickened insignificantly. In the midperiphery, significant thickening was found in the superior, superior temporal, inferior temporal, inferior, and inferior nasal zones while changes in the nasal, temporal, and superior nasal zones were insignificant. As explained earlier, the findings are not in complete agreement with previous findings in this field.

The changes in corneal epithelial thickness all occurred in the temporal quadrants, both superior and inferior. It is known that human cornea is usually prolate ellipse and the nasal and temporal meridian eccentricity values are different [21, 22]. The cornea becomes flattening from center to periphery [23], and the flattening degree along the nasal meridians is greater than that along the temporal

Table 2: Corneal curvature changes pre- and post-Ok lens wear.

| | Pre-Ok | 1 day post-Ok | 1 week post-Ok | 1 month post-Ok | 3 months post-Ok |
|---|---|---|---|---|---|
| Steep *k* | 43.86 ± 1.41 | 42.47 ± 1.60 | 41.43 ± 1.56 | 41.25 ± 1.56 | 41.22 ± 1.38 |
| Flat *k* | 42.74 ± 1.26 | 41.48 ± 1.44 | 40.59 ± 1.53 | 40.42 ± 1.63 | 40.46 ± 1.47 |

Table 3: Corneal epithelium thickness changes (average differences = thickness pre-Ok − thickness post-Ok).

| | C | M S | M ST | M T | M IT | M I | M IN | M N | M SN | P S | P ST | P T | P IT | P I | P IN | P N | P SN |
|---|---|---|---|---|---|---|---|---|---|---|---|---|---|---|---|---|---|
| 1 d | 4.69* | -0.27 | 0.99 | 2.23* | 1.83 | 0.96 | -0.12 | -0.61 | -0.69 | -0.72 | -1.10 | -0.32 | -1.30 | -1.33 | -1.43 | -0.10 | -0.48 |
| 1 w | 9.22* | 0.12 | 2.70* | 5.00* | 4.64* | 2.56* | 0.49 | -0.46 | -1.11 | -2.30 | -2.20 | -0.53 | -1.38 | -3.10* | -3.03 | -1.65 | -2.04 |
| 1 m | 8.42* | -1.44 | 1.94 | 4.50* | 3.97* | 2.13* | 0.09 | -1.13 | -1.56 | -3.14* | -2.86* | -2.51 | -4.18* | -4.39* | -3.04* | -2.13 | -2.31 |
| 3 m | 7.41* | -0.27 | 3.32* | 5.49* | 4.45* | 1.72 | -0.55 | -1.04 | -1.63 | -1.20 | -0.59 | 0.89 | -0.55 | -3.86* | -3.30* | -1.32 | -0.26 |

S = superior; ST = superior temporal; T = temporal; IT = inferior temporal; I = inferior; IN = inferior nasal; N = nasal; SN = superior nasal; C = central; M = midperipheral; P = peripheral. $^*P < 0.05$.

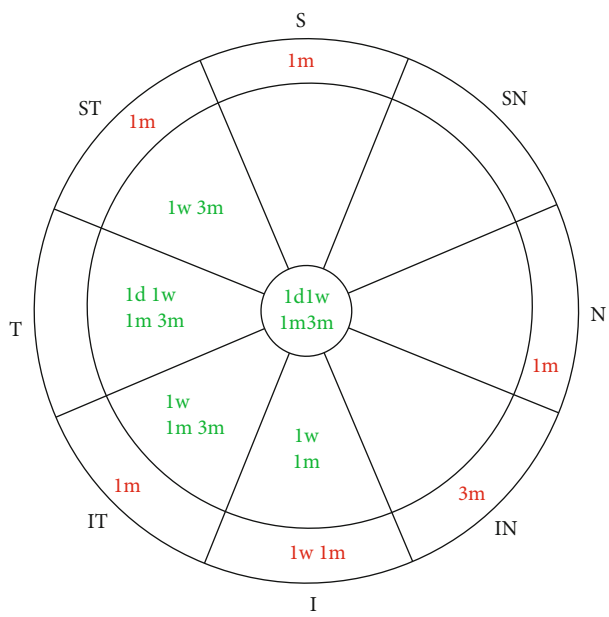


Figure 1: Corneal epithelium thickness changes after overnight ortho-K wearing. Green characters mean thickness decreases; red characters mean thickness increases.

meridians from the center to the periphery [24]. After two weeks of ortho-K wearing, in the central circular zone, the temporal quadrant curvature is significantly flattened, and in the paracentral annular zone, the temporal curvature significantly steepened [25]. The current study included ortho-K lenses centered or decentered by no more than 1 mm as determined by slit lamp microscopy, yet all of the epithelial changes after ortho-K occurred in the temporal quadrants mainly. These results suggest that ortho-K had a trend to be stable at temporal quadrant not central zone and not nasal sector although nasal meridian becomes flatter than temporal one after ortho-K, which needs further researches. There is a limitation that the study is a retrospective one, which meant that some subjects were not followed up regularly and data collected were missed partly. Caution also needs to be taken; the current research subjects are children while the cornea shape during ortho-K may vary among adults or the elderly.

## Data Availability

The data used to support the findings of this study are included within the article.

## Conflicts of Interest

The authors declare that they have no conflicts of interest.

## References

[1] P. Cho and S. W. Cheung, "Retardation of myopia in orthokeratology (ROMIO) study: a 2-year randomized clinical trial," *Investigative Ophthalmology & Visual Science*, vol. 53, no. 11, pp. 7077–7085, 2012.

[2] A. Alharbi and H. A. Swarbrick, "The effects of overnight orthokeratology lens wear on corneal thickness," *Investigative Ophthalmology & Visual Science*, vol. 44, no. 6, pp. 2518–2523, 2003.

[3] A. Tao, J. Wang, Q. Chen et al., "Topographic thickness of Bowman's layer determined by ultra-high resolution spectral domain-optical coherence tomography," *Investigative Ophthalmology & Visual Science*, vol. 52, no. 6, pp. 3901–3907, 2011.

[4] C. Du, J. Wang, L. Cui, M. Shen, and Y. Yuan, "Vertical and horizontal corneal epithelial thickness profiles determined by ultrahigh resolution optical coherence tomography," *Cornea*, vol. 31, no. 9, pp. 1036–1043, 2012.

[5] W. K. Kim, B. J. Kim, I. H. Ryu, J. K. Kim, and S. W. Kim, "Corneal epithelial and stromal thickness changes in myopic orthokeratology and their relationship with refractive change," *PLoS One*, vol. 13, no. 9, p. e0203652, 2018.

[6] J. Zhang, J. Li, X. Li, F. Li, and T. Wang, "Redistribution of the corneal epithelium after overnight wear of orthokeratology

contact lenses for myopia reduction," *Contact Lens & Anterior Eye*, vol. 43, no. 3, pp. 232–237, 2020.

[7] H. A. Swarbrick, P. Kang, and R. Peguda, "Corneal total and epithelial thickness measured by Sonogage ultrasound pachometry and high-resolution optical coherence tomography," *Optometry and Vision Science*, vol. 97, no. 5, pp. 346–350, 2020.

[8] P. Cho and Q. Tan, "Myopia and orthokeratology for myopia control," *Clinical & Experimental Optometry*, vol. 102, no. 4, pp. 364–377, 2019.

[9] J. Charm and P. Cho, "High myopia-partial reduction orthokeratology (HM-PRO): study design," *Contact Lens & Anterior Eye*, vol. 36, no. 4, pp. 164–170, 2013.

[10] C. Chen, S. W. Cheung, and P. Cho, "Myopia control using toric orthokeratology (TO-SEE study)," *Investigative Ophthalmology & Visual Science*, vol. 54, no. 10, pp. 6510–6517, 2013.

[11] P. Cho, S. W. Cheung, and M. Edwards, "The longitudinal orthokeratology research in children (LORIC) in Hong Kong: a pilot study on refractive changes and myopic control," *Current Eye Research*, vol. 30, no. 1, pp. 71–80, 2005.

[12] J. Santodomingo-Rubido, C. Villa-Collar, B. Gilmartin, and R. Gutiérrez-Ortega, "Myopia control with orthokeratology contact lenses in Spain: refractive and biometric changes," *Investigative Ophthalmology & Visual Science*, vol. 53, no. 8, pp. 5060–5065, 2012.

[13] J. J. Walline, L. A. Jones, and L. T. Sinnott, "Corneal reshaping and myopia progression," *The British Journal of Ophthalmology*, vol. 93, no. 9, pp. 1181–1185, 2009.

[14] P. Kang and H. Swarbrick, "Peripheral refraction in myopic children wearing orthokeratology and gas-permeable lenses," *Optometry and Vision Science*, vol. 88, no. 4, pp. 476–482, 2011.

[15] A. Queirós, J. M. González-Méijome, J. Jorge, C. Villa-Collar, and A. R. Gutiérrez, "Peripheral refraction in myopic patients after orthokeratology," *Optometry and Vision Science*, vol. 87, no. 5, pp. 323–329, 2010.

[16] A. Nieto-Bona, A. González-Mesa, M. P. Nieto-Bona, C. Villa-Collar, and A. Lorente-Velázquez, "Short-term effects of overnight orthokeratology on corneal cell morphology and corneal thickness," *Cornea*, vol. 30, no. 6, pp. 646–654, 2011.

[17] A. Nieto-Bona, A. González-Mesa, M. P. Nieto-Bona, C. Villa-Collar, and A. Lorente-Velázquez, "Long-term changes in corneal morphology induced by overnight orthokeratology," *Current Eye Research*, vol. 36, no. 10, pp. 895–904, 2011.

[18] J. Wang, D. Fonn, T. L. Simpson, L. Sorbara, R. Kort, and L. Jones, "Topographical thickness of the epithelium and total cornea after overnight wear of reverse-geometry rigid contact lenses for myopia reduction," *Investigative Ophthalmology & Visual Science*, vol. 44, no. 11, pp. 4742–4746, 2003.

[19] Y. Lian, M. Shen, J. Jiang et al., "Vertical and horizontal thickness profiles of the corneal epithelium and Bowman's layer after orthokeratology," *Investigative Ophthalmology & Visual Science*, vol. 54, no. 1, pp. 691–696, 2013.

[20] J. Zhou, F. Xue, X. Zhou, R. K. Naidu, and Y. Qian, "Thickness profiles of the corneal epithelium along the steep and flat meridians of astigmatic corneas after orthokeratology," *BMC Ophthalmology*, vol. 20, no. 1, p. 240, 2020.

[21] P. R. Preussner, J. Wahl, C. Kramann, and K. C. Wahl, "Corneal model," *Journal of Cataract and Refractive Surgery*, vol. 29, no. 3, pp. 471–477, 2003.

[22] S. Serrao, G. Lombardo, and M. Lombardo, "Differences in nasal and temporal responses of the cornea after photorefractive keratectomy," *Journal of Cataract and Refractive Surgery*, vol. 31, no. 1, pp. 30–38, 2005.

[23] F. Eghbali, K. K. Yeung, and R. K. Maloney, "Topographic determination of corneal asphericity and its lack of effect on the refractive outcome of radial keratotomy," *American Journal of Ophthalmology*, vol. 119, no. 3, pp. 275–280, 1995.

[24] J. J. Rowsey, H. D. Balyeat, R. Monlux et al., "Prospective evaluation of radial keratotomy: photokeratoscope corneal topography," *Ophthalmology*, vol. 95, no. 3, pp. 322–334, 1988.

[25] V. Maseedupally, P. Gifford, E. Lum, and H. Swarbrick, "Central and paracentral corneal curvature changes during orthokeratology," *Optometry and Vision Science*, vol. 90, no. 11, pp. 1249–1258, 2013.

Hindawi
Disease Markers
Volume 2022, Article ID 9108129, 8 pages
https://doi.org/10.1155/2022/9108129

*Research Article*

# Predictive Value of CT-Based Radiomics in Distinguishing Renal Angiomyolipomas with Minimal Fat from Other Renal Tumors

**Zhiwei Han,[1] Yuanqiang Zhu,[1] Jingji Xu,[1] Didi Wen,[1] Yuwei Xia,[2] Minwen Zheng,[1] Tao Yan,[3] and Mengqi Wei[1]**

[1]*Department of Radiology, Xijing Hospital, Air Force Medical University, Xi'an, Shaanxi, China*
[2]*Huiying Medical Technology Co., Ltd., Room A206, B2, Dongsheng Science and Technology Park, Haidian District, Beijing 100192, China*
[3]*Department of Radiology, Xi'an XD Group Hospital, Xi'an, Shaanxi, China*

Correspondence should be addressed to Mengqi Wei; weimengqi2008@163.com

Received 6 March 2022; Accepted 3 May 2022; Published 28 May 2022

Academic Editor: Pei-Wen Zhu



*Objectives*. This study is aimed at determining whether CT-based radiomics models can help differentiate renal angiomyolipomas with minimal fat (AMLmf) from other solid renal tumors. *Methods*. This retrospective study included 58 patients with a postoperative pathologically confirmed AMLmf (observation group) and 140 patients with other common renal tumors (control group). Non-contrast-enhanced CT and contrast-enhanced CT data were evaluated. Radiomics features were extracted from manually delineated volume of interest (VOIs). The least absolute shrinkage and selection operator (LASSO) regression was used for feature screening. Five classifiers, including logistic regression, multilayer perceptron (MLP), support vector machine (SVM), *k*-nearest neighbor (KNN), and logistic regression (LR), were used, with leave-out validation (128 training, 60 testing). The diagnostic performance of the classifier was evaluated and compared by receiver operating characteristic curve (ROC) analysis. *Results*. Among the 1029 extracted features, prediction models of AMLmf were composed, by 2, 10, 4, and 9 selected features for precontrast phase (PCP), corticomedullary phase (CMP), nephrographic phase (NP), and excretory phase (EP), respectively. Models of CMP and NP achieved adequate performance after using MLP classifier, with prediction accuracy of 0.767 (AUC 0.85, sensitivity 0.76, and specificity 0.78) and 0.783 (AUC 0.83, sensitivity 0.79, and specificity 0.78), respectively. MLP model of features selected from the combination of the all features had the best diagnostic performance (accuracy 0.8500, sensitivity 0.8095, specificity 0.9444, and AUC 0.9193). *Conclusions*. Radiomics features may help to distinguish benign AMLmf from common malignant kidney masses, which may contribute to the selection of interventions for renal tumors.

## 1. Introduction

Most renal tumors are asymptomatic and are found incidentally (1). Among them, renal cell carcinomas (RCCs) are the most common, and 85% of renal masses smaller than 4 cm are reported to be RCCs (2, 3). Most malignant renal masses require active intervention of surgical resection or radiofrequency ablation. Angiomyolipoma (AML) is the most common benign solid renal neoplasm which can be diagnosed accurately by identifying the intratumoral fat component. However, for AML with minimal fat (AMLmf), the diagnosis is challenging as it does not contain any fat cells nor contain an insufficient amount of fat cells to provide a computed tomography (CT) image-based diagnosis (4–6). Therefore, AMLmf are often misdiagnosed as RCC and these patients often have surgeries, which would not only increase their economic and psychological burden but also increase the workload of hospitals and waste the cost of medical insurance (7, 8).

Using morphological and enhancement features, Sung found the predictive values were around 80%, which is not very satisfactory (9). Using logistic regression analysis, Zhang et al. found several parameters are valuable in differentiating AMLmf from RCCs, such as unenhanced

attenuation characteristic and intratumoral vessels (10). A comparable study using multidetector computed tomography (MDCT) found the long-to-short axis ratio, attenuation and enhancement degree precontrast phase (PCP), corticomedullary phase (CMP), nephrographic phase (NP), and excretory phase (EP) showed significant differences between AMLmf from RCCs (11). Although many studies and efforts have been made on the differential diagnosis of AMLmf and other malignant masses (12), it is still difficult in practice.

In recent years, artificial intelligence and radiomics analysis techniques have provided new methods for image analysis. By extracting and analyzing the radiomics features of renal lesions on routine CT images, it is possible to distinguish between benign and malignant tumors of the kidney (13–16). However, the accuracy and specificity of texture analysis are inconsistent in various reports, and the sample size is too small to get convincing outcomes. In the current study, we included large sample size patients of AML with minimal fat (AMLmf) and other various pathological types of renal tumors, who had been operated in our hospital in the past ten years. The CT images of tumors were retrospectively analyzed and modeled using radiomics techniques for differential diagnosis. We hypothesized that radiomics strategy combined with large dataset will guarantee fine differentiation of the two renal tumors.

## 2. Materials and Methods

The study was approved by the ethics committee of the hospital. Because this was a retrospective study based only on medical records and all data were analyzed in our hospital, patient consent was waived.

*2.1. Patient Selection.* The patients were selected from the pathological and radiological databases of our hospital from January 2010 to October 2018. We searched for any CT investigations for renal masses performed before surgery or biopsy. The CT examinations included four phases of precontrast phase (PCP), corticomedullary phase (CMP), nephrographic phase (NP), and excretory phase (EP) and were performed within two weeks before surgery. Pathological examination was available for each patient and included both histology (hematoxylin-eosin-safran staining) and immunohistochemistry. Patients with renal lesions containing radiologically visible fat or inadequate CT image quality were excluded.

Between January 2010 and October 2018, 318 patients underwent surgical removal of renal masses with preoperative CT scanning and with minimal fat on CT images were included (Figure 1). We excluded patients with inadequate image quality and incomplete scanning phases ($n = 120$). Fifty-eight patients with AMLs with minimal fat and 140 patients with other renal tumors were finally included.

*2.2. CT Technique.* All patients underwent CT scans on multislice spiral CT devices (SOMATOM, TOSHIBA, GE, UNITED IMAGING) using a 4-stage protocol: precontrast phase and then the CMP (30 to 40 s after beginning the iodine contrast injection), NP (70 to 120 s), and excretory phase (3 to 6 min). The contrast medium was injected intravenously into the brachial vein (100 ml, not exceeding 2 ml/kg patient body weight; injection rate: 2.5 to 3.5 ml/s).

*2.3. Segmentation of the Volume of Interests from Images.* The DICOM images of the 198 patients were transferred into the radiomics platform (Big Data Intelligent Analysis Cloud Platform, Huiying Medical Technology Co., Ltd., Beijing, https://mics.radcloud.cn/).

One reader within eight years of experience in urological imaging delineated the lesion boundaries at all slices of each phase as volumes of interest (VOIs) based on the difference in attenuation and enhancement pattern between the lesion and normal renal parenchyma. Lesions on the PCP usually have lower or equal attenuation and have various patterns of enhancement, compared with renal parenchyma. The outer margin of an exophytic lesion could be easily distinguished from the surrounding fat. If the lesion contour in the PCP was unclear, the PCP phases were referred. Another reader reviewed the VOIs, and if he disagreed with the first reader, a senior radiologist was consulted for the final decision. First, the images of 20 patients were randomly selected for training contour drawing, and then, the interested areas of all patients were drawn (Figure 2). To minimize the CT intensity variations, before feature extraction for VOIs, we normalized by standard deviation $[\mu - 3\sigma, \mu + 3\sigma]$, and the platform then automatically analyzed all delineated VOIs and put out data of 1029 features.

*2.4. Feature Extraction and Screening.* First-order statistics, shape-based features, and texture features deriving from gray-level cooccurrence matrix (GLCM), gray-level run-length matrix (GLRLM), gray-level size zone matrix (GLSZM), and neighborhood gray-tone difference matrix (NGTDM) were extracted for each VOI. Also, we applied Laplacian, logarithmic, exponential, and wavelet filters to images and then extracted features based on the filtered image. A total of 1029 radiomics features were extracted. The features were consistent with the imaging biomarker standardization initiative (IBSI) (17). In this study, the least absolute shrinkage and selection operator (LASSO) was used for feature screening and dimension reduction. In high-dimensional data, the LASSO regression method has been proved to be effective and efficient (18, 19). The model coefficients were compressed by selecting the optimal harmonic parameter $\lambda$ in the model by 10-fold cross-validation, and the coefficients of the unrelated variables were reduced to zero while retaining the variables of nonzero coefficients. Finally, several or a dozen significant highly correlated features were retained for further analysis.

*2.5. Machine Learning for Model Building.* As the value range of feature may vary greatly, for example, the value of feature 1 is 1000~2000, and the value of feature 2 is 0.1~0.2, which may affect the contribution of feature to the model. To ensure the convergence of the training model, the value range of features should be within the same scale, so we standardized the value of features (range, 0-1). The selected features were constructed into a prediction model,

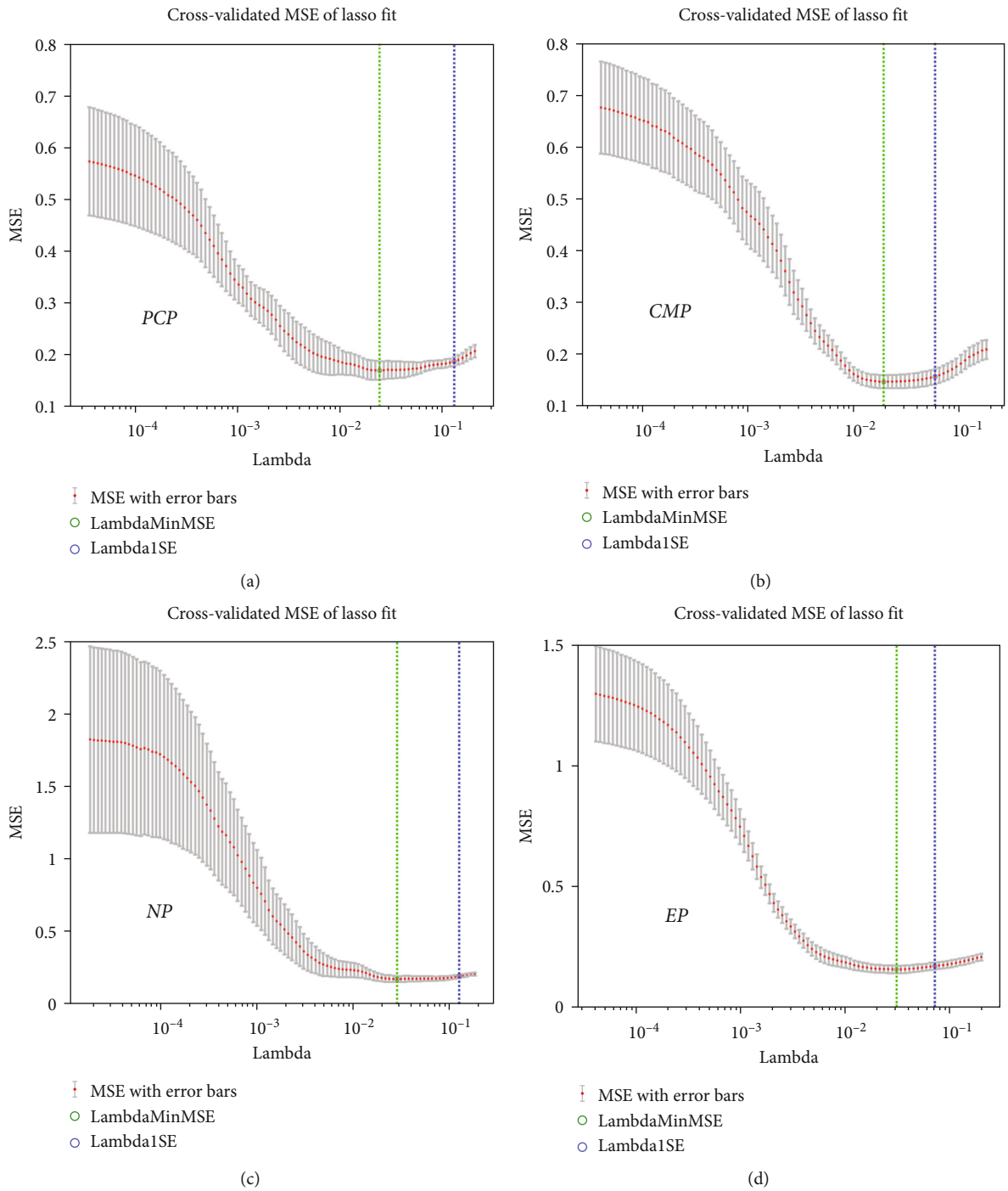


Figure 1: Least absolute shrinkage and selection operator (LASSO) was used for feature screening and dimension reduction. PCP: precontrast phase; CMP: corticomedullary phase; NP: nephrographic phase; EP: excretory phase.

using leave-out validation (128 training and 60 testing). Five models including logistic regression, multilayer perceptron (MLP), support vector machine (SVM), $k$-nearest neighbor (KNN), and logistic regression (LR) were used to select the classifier with the best diagnostic performance. Model predictive capability is assessed using the receiver operating characteristic curve (ROC) analysis and area under the curve (AUC) as well as accuracy, sensitivity, and specificity.

## 3. Results

*3.1. Patient Characteristics.* The study included 198 patients (111 males and 87 females) aged 22~84 years (mean age, 54.84 ± 12.46 years), of which 58 were AMLs with minimal fat and 140 were other common types of renal tumors, including clear cell RCCs ($n = 63$), chromophobe RCCs ($n = 32$), papillary RCCs ($n = 31$), and oncocytomas ($n = 14$).

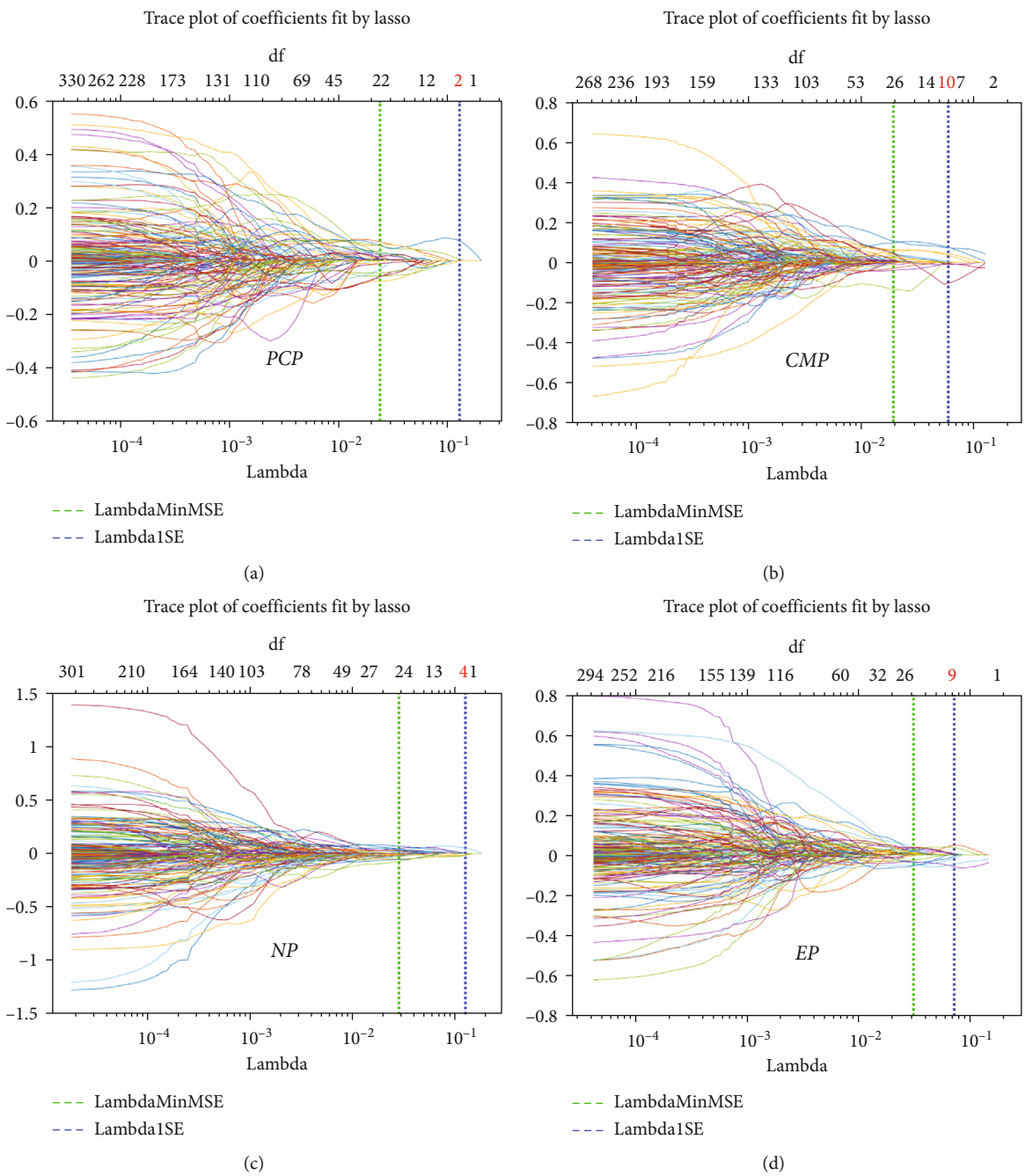


Figure 2: The number of features selected for each phase: 2, 10, 4, and 9 features were selected, for PCP, CMP, NP, and EP, respectively. PCP: precontrast phase; CMP: corticomedullary phase; NP: nephrographic phase; EP: excretory phase.

*3.2. Selected Radiomics Features and Machine Learning Models.* A total of 1029 radiological features, including 19 first-order statistics, 15 shape-based features, 59 texture features, and features extracted from filtered data, were extracted from each VOI. The texture features included features of GLRLM ($n = 16$), GLCM ($n = 27$), and GLSZM ($n = 16$).

The LASSO regression was used to reduce the data dimension. From the extracted features of PCP, CMP, NP, and EP, 2, 10, 4, and 9 features were selected, respectively (Figures 1 and 2). Thirteen features were selected from the combination of the all features (Figures 3(a) and 3(b)).

The classification performance of the models was explored by ROC. The optimal model was MLP, as shown in Figure 3(c). MLP model of features selected from the combination of the all features had the best diagnostic performance (accuracy 0.8500, sensitivity 0.8095, specificity 0.9444, and AUC 0.9193) (Table 1).

## 4. Discussion

The detection rate of renal masses has increased in the last decades owing to the widespread use of abdominal imaging. Although RCC accounts for the majority of renal masses (20,

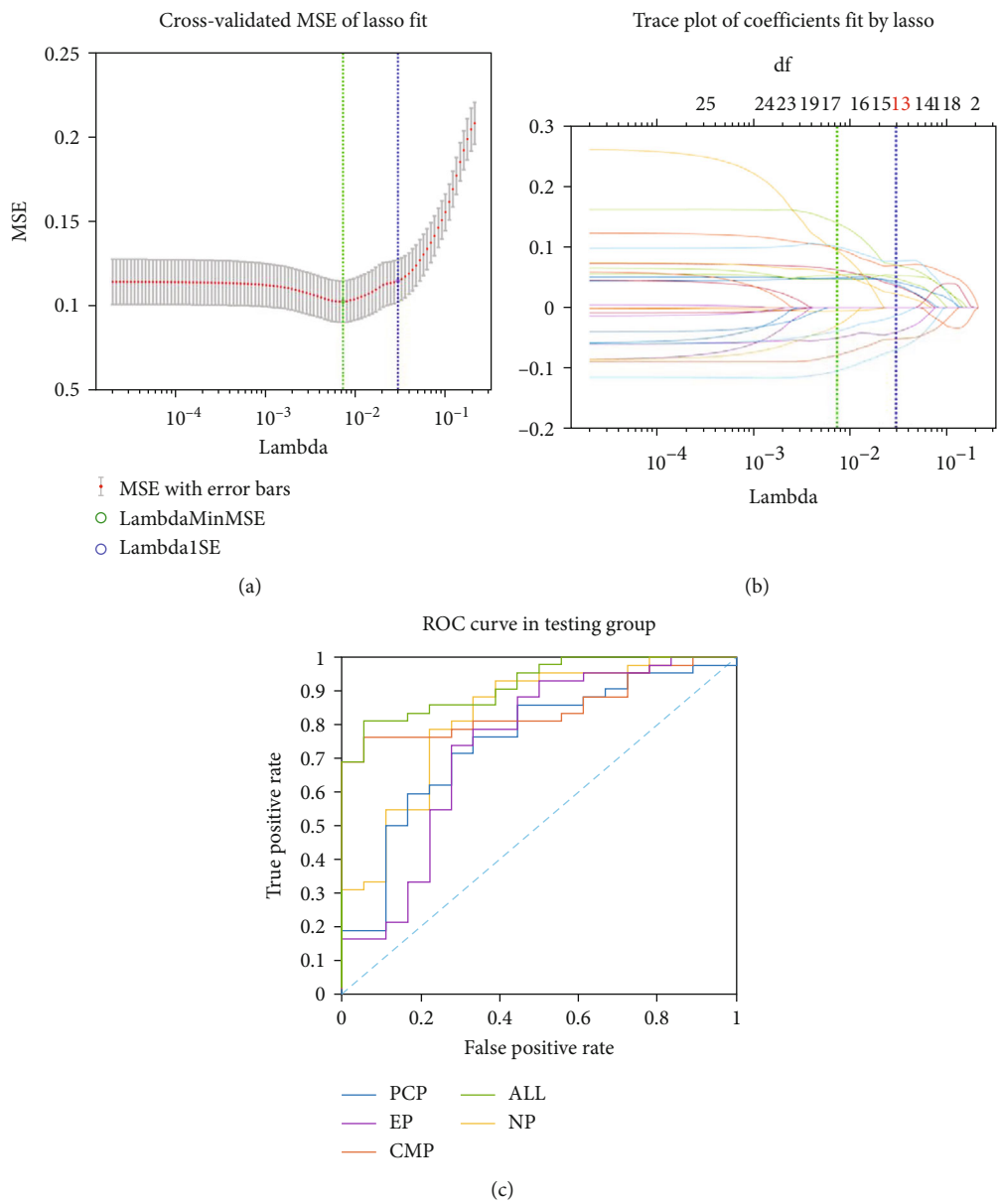


Figure 3: (a) Least absolute shrinkage and selection operator for the combination of the four phases. (b) Thirteen features were selected from the combination of the all features. (c) ROC for each phase and the combination of the four phases using MLP model. MLP: multilayer perceptron.

21), 20% of all surgically treated cases are benign, and half of these are AMLs with minimal fat, resulting in unnecessary invasive treatment (22–24). AML is pathologically composed of fat, smooth muscle, and vascular components in different proportions (25). AMLs with minimal fat are mainly composed of smooth muscle and vascular components, and there is no visible fat.

At present, CT is the primary method for diagnosing renal masses, and CT diagnosis of renal angiomyolipoma mainly depends on the intramass visible fat. However, this is not available in cases of AMLs with minimal fat. Current imaging methods have not yet been sufficient to identify AMLs with minimal fat. Radiomics may provide new diagnostic pathways by obtaining and analyzing a large number of features from images. Recent studies have shown that radiomics is important in identifying tumor heterogeneity in several kinds of tumors. Because AMLs with minimal fat is relatively rare compared to renal clear cell and renal papillary cell carcinoma, radiomics studies of renal tumors are

Table 1: The classification performance of the models using features from different phases.

| Phase | AUC | Sensitivity | Specificity | Accuracy |
|---|---|---|---|---|
| PCP | 0.7500 | 0.7143 | 0.7222 | 0.7167 |
| CMP | 0.8492 | 0.7619 | 0.7778 | 0.7667 |
| NP | 0.8254 | 0.7857 | 0.7778 | 0.7833 |
| EP | 0.7394 | 0.7381 | 0.7222 | 0.7333 |
| ALL | **0.9193** | **0.8095** | **0.9444** | **0.8500** |

focused on relatively common renal tumors. Studies on the most frequently occurring are in (2, 3, 5, 9).

A total of 1029 features for each CT imaging phase were extracted from each manually delineated VOI, and 2 to 10 valid features were selected using the LASSO method. We also combined the extracted features of all phase and ultimately selected thirteen optimal features using the LASSO method. We found that in the five data groups of MSCT phases (PCP, three postcontrast phases, and combined), the ultimately selected features contained first-order statistics and GLCM features, suggesting variations in the gray scale distribution of each entity. First-order statistics describe the distribution of voxel intensities of preset VOI regions through commonly used and basic metrics. The statistics used in this study were mean (mean of image intensity values), median (median of image intensity values), skewness (asymmetry of intensity distribution), and 10 percentile. By calculating the correlation of gray scale between two points of a certain distance and a certain direction in the image, GLCM reflects the comprehensive information of the image in direction, interval, and change. Maximum probability was included in the effective GLCM features of all the five groups, indicating that the distribution of gray value between adjacent pixels of different types of lesions was different.

Among the five classifiers of logistic regression, KNN, LR, MLP, and SVW, the classifier with the best performance was MLP, whose AUC were above 0.73 to 0.85 in the dataset of the four phases. The AUC of combined all phases reached 0.9193, with an accuracy of 0.8500. At present, there were many studies on the use of machine learning to assist in the identification of renal tumors (14, 26, 27), and there were also many studies focused on the differential diagnosis of AMLs with minimal fat (13, 28, 29). Among them, the accuracy of the SVM classifier for identifying AMLs with minimal fat and clear cell carcinoma was 72.3% and 72.1%, respectively. Our study had similar results. In our study, multiphase data were analyzed, and the regions of interest were obtained by volumetric delineation, which was more reflective of the spatial characteristics of tumors than some single-layer delineation, making the extracted features more valuable for differential diagnosis. In the process of VOI delineation, two abdominal radiologists with ten years of experience were present at the same time. When there was inconsistency, a senior abdominal radiologist was consulted. We applied five classifiers, adopted leave-out cross-validation (128 training and 60 testing), for the feature selection of multiphase and combined phase data, making the selected features more valuable for differential diagnosis.

Our study was retrospective and had a large time span; there was some variance in CT scanner, scanning protocol, and contrast agents. The data was not completely unified. Although our results were not the best, they were more consistent with the actual clinical situation, and the results were more suitable for popularization. Among the patients who underwent surgery for renal masses within eight years, a total of 75 cases of AMLs with minimal fat with preoperative misjudgment were found. All these patients underwent unnecessary surgical treatment, which was caused by the limitations of diagnosis. Only 58 cases were included in the study, and the remaining cases were excluded from the study due to incomplete data. The disease accounts for a lower proportion of patients undergoing surgery for renal masses, which may lead to misclassification. Some studies adopted data amplification method to solve this problem (28, 30, 31). In the absence of data amplification, we found little difference between the predicted results and the actual results.

Unlike some literatures (13, 20, 28, 32), we did not separately compare AMLs with minimal fat with a distinct pathological type of renal tumors. We compared AMLs with minimal fat with common renal tumors as a whole, which was consistent with the real diagnostic situation. When we found a small renal mass with minimal fat, clear cell carcinoma was the most likely diagnosis. However, it was difficult to determine the diagnosis; when the mass was located superficially, the attenuation of the unenhanced scan was relatively high, the enhanced scan had no typical enhancement pattern of wash-in and washout, and there were no surrounding fat stranding sign, increased vessels, or lymph nodes. Although relatively rare, we need to consider the possibility of benign lesions, especially AMLmf, with the highest proportion of benign lesions, and thus, the identification of AMLmf with renal carcinoma is consistent with the diagnostic procedure. Finally, we included 198 patients with renal tumors (63 cases of renal clear cell carcinoma, 31 cases of papillary renal cell carcinoma, 32 cases of chromophobe cell carcinoma, 58 cases of AMLmf, and 14 cases of oncocytoma), who underwent surgical resection in our hospital during the same period. Benign tumors accounted for 22.73% in our study, of which AMLmf accounted for approximately 64.44% of benign tumors, which is roughly the same as reported in the literature (20, 23).

The study had some limitations. First of all, the total sample size was not very large, mainly because of the low incidence of AMLmf, and we had only chosen patients who had surgery in our hospital without multicenter cooperation, which may increase the risk of overfitting. Working with more medical centers to obtain more cases will lead to better models. Second, we did not select all the clear cell carcinomas operated in our hospital at the same period, but only selected the cases with radiographic manifestations similar to those of AMLmf in this group of patients, which were not particularly typical clear cell carcinomas on CT images. Third, the cases included in this study had a large time span, and different CT machines and scanning technologies were used, which was consistent with the clinical practice. However, the early scanning equipment and technologies may have reduced the overall diagnostic accuracy. Third, the cases included in this study had a large time span, and different CT machines and scanning technologies were used, which was consistent with the clinical practice. However, the early scanning equipment and technologies may have reduced the overall diagnostic accuracy.

In conclusion, the machine learning model established by radiomics features extracted from multiphase MSCT images can be used to identify AMLmf from other renal masses. These models are expected to assist manual diagnosis and improve work efficiency and accuracy, which is a noninvasive and effective method for differential diagnosis.

## Data Availability

The patient data used to support the findings of this study are restricted by the Institutional Review Board of Xijing Hospital in order to protect patient privacy.

## Conflicts of Interest

YX was employed by Huiying Medical Technology Company. The remaining authors declare that the research was conducted in the absence of any commercial or financial relationships that could be construed as a potential conflict of interest.

## Authors' Contributions

Zhiwei Hana and Yuanqiang Zhu contributed equally to this work.

## Acknowledgments

This work was supported by the Key Research and Development Plan of Shaanxi Province (grant number 2019SF-182), the National Science Foundation of Shaanxi Province (grant number 2020JQ-461), and the Discipline Promotion Project of Xijing Hospital (grant number XJZT18MJ52).

## References

[1] S. Mazziotti, G. Cicero, T. D'Angelo et al., "Imaging and management of incidental renal lesions," *BioMed Research International*, vol. 2017, 1854015 pages, 2017.

[2] E. Jonasch, J. Gao, and W. K. Rathmell, "Renal cell carcinoma," *BMJ*, vol. 349, no. nov10 11, article g4797, 2014.

[3] H. Lee, H. Hong, J. Kim, and D. C. Jung, "Deep feature classification of angiomyolipoma without visible fat and renal cell carcinoma in abdominal contrast-enhanced CT images with texture image patches and hand-crafted feature concatenation," *Medical Physics*, vol. 45, no. 4, pp. 1550–1561, 2018.

[4] M. Jinzaki, H. Akita, and M. Oya, "Imaging features of renal cell carcinoma differential diagnosis, staging, and posttreatment evaluation," in *Renal Cell Carcinoma*, pp. 139–176, Springer, Tokyo, 2017.

[5] M. G. Harisinghani, M. M. Maher, D. A. Gervais et al., "Incidence of malignancy in complex cystic renal masses (Bosniak category III): should imaging-guided biopsy precede surgery?," *AJR. American Journal of Roentgenology*, vol. 180, no. 3, pp. 755–758, 2003.

[6] R. Wang, J. S. Wolf Jr., D. P. Wood Jr., E. J. Higgins, and K. S. Hafez, "Accuracy of percutaneous core biopsy in management of small renal masses," *Urology*, vol. 73, no. 3, pp. 586–590, 2009.

[7] A. C. Mues and J. Landman, "Small renal masses: current concepts regarding the natural history and reflections on the American Urological Association guidelines," *Current Opinion in Urology*, vol. 20, no. 2, pp. 105–110, 2010.

[8] R. Heuer, I. S. Gill, G. Guazzoni et al., "A critical analysis of the actual role of minimally invasive surgery and active surveillance for kidney cancer," *European Urology*, vol. 57, no. 2, pp. 223–232, 2010.

[9] Y. Y. Zhang, S. Luo, Y. Liu, and R. T. Xu, "Angiomyolipoma with minimal fat: differentiation from papillary renal cell carcinoma by helical CT," *Clinical Radiology*, vol. 68, no. 4, pp. 365–370, 2013.

[10] M. H. Kim, J. Lee, G. Cho, K. S. Cho, J. Kim, and J. K. Kim, "MDCT-based scoring system for differentiating angiomyolipoma with minimal fat from renal cell carcinoma," *Acta Radiologica*, vol. 54, no. 10, pp. 1201–1209, 2013.

[11] C. K. Sung, S. H. Kim, S. Woo et al., "Angiomyolipoma with minimal fat: differentiation of morphological and enhancement features from renal cell carcinoma at CT imaging," *Acta Radiologica*, vol. 57, no. 9, pp. 1114–1122, 2016.

[12] K. Ishigami, M. G. Pakalniskis, L. V. Leite, D. K. Lee, D. G. Holanda, and M. Rajput, "Characterization of renal cell carcinoma, oncocytoma, and lipid-poor angiomyolipoma by unenhanced, nephrographic, and delayed phase contrast- enhanced computed tomography," *Clinical Imaging*, vol. 39, no. 1, pp. 76–84, 2015.

[13] B. A. Varghese, F. Chen, D. H. Hwang et al., "Differentiation of predominantly solid enhancing lipid-poor renal cell masses by use of contrast-enhanced CT: evaluating the role of texture in tumor sub-typing," *AJR. American Journal of Roentgenology*, vol. 211, no. 6, pp. W288–W296, 2018.

[14] H. S. Yu, J. Scalera, M. Khalid et al., "Texture analysis as a radiomic marker for differentiating renal tumors," *Abdom Radiol.*, vol. 42, no. 10, pp. 2470–2478, 2017.

[15] S. Leng, N. Takahashi, D. Gomez Cardona et al., "Subjective and objective heterogeneity scores for differentiating small renal masses using contrast-enhanced CT," *Abdom Radiol.*, vol. 42, no. 5, pp. 1485–1492, 2017.

[16] L. Yan, Z. Liu, G. Wang et al., "Angiomyolipoma with minimal fat: differentiation from clear cell renal cell carcinoma and papillary renal cell carcinoma by texture analysis on CT images," *Academic Radiology*, vol. 22, no. 9, pp. 1115–1121, 2015.

[17] A. Zwanenburg, M. Vallières, M. A. Abdalah et al., "The image biomarker standardization initiative: standardized quantitative radiomics for high-throughput image-based phenotyping," *Radiology*, vol. 295, no. 2, pp. 328–338, 2020.

[18] Y. Huang, C. Liang, L. He et al., "Development and validation of a radiomics nomogram for preoperative prediction of lymph node metastasis in colorectal cancer," *Journal of Clinical Oncology*, vol. 34, no. 18, pp. 2157–2164, 2016.

[19] Z. Ma, M. Fang, Y. Huang et al., "CT-based radiomics signature for differentiating Borrmann type IV gastric cancer from primary gastric lymphoma," *European Journal of Radiology*, vol. 91, pp. 142–147, 2017.

[20] C. W. Yang, S. H. Shen, Y. H. Chang et al., "Are there useful CT features to differentiate renal cell carcinoma from lipid-poor renal angiomyolipoma?," *AJR. American Journal of Roentgenology*, vol. 201, no. 5, pp. 1017–1028, 2013.

[21] S. C. Campbell, A. C. Novick, A. Belldegrun et al., "Guideline for management of the clinical T1 renal mass," *The Journal of Urology*, vol. 182, no. 4, pp. 1271–1279, 2009.

[22] Y. Fujii, Y. Komai, K. Saito et al., "Incidence of benign pathologic lesions at partial nephrectomy for presumed RCC renal masses: Japanese dual-center experience with 176 consecutive patients," *Urology*, vol. 72, no. 3, pp. 598–602, 2008.

[23] M. E. Snyder, A. Bach, M. W. Kattan, G. V. Raj, V. E. Reuter, and P. Russo, "Incidence of benign lesions for clinically localized renal masses smaller than 7 cm in radiological diameter:

influence of sex," *The Journal of Urology*, vol. 176, no. 6, pp. 2391–2396, 2006.

[24] H. G. Jeon, S. R. Lee, K. H. Kim et al., "Benign lesions after partial nephrectomy for presumed renal cell carcinoma in masses 4 cm or less: prevalence and predictors in Korean patients," *Urology*, vol. 76, no. 3, pp. 574–579, 2010.

[25] M. A. Bosniak, A. J. Megibow, D. H. Hulnick, S. Horii, and B. N. Raghavendra, "CT diagnosis of renal angiomyolipoma: the importance of detecting small amounts of fat," *AJR. American Journal of Roentgenology*, vol. 151, no. 3, pp. 497–501, 1988.

[26] H. Chandarana, A. B. Rosenkrantz, T. C. Mussi et al., "Histogram analysis of whole-lesion enhancement in differentiating clear cell from papillary subtype of renal cell cancer," *Radiology*, vol. 265, no. 3, pp. 790–798, 2012.

[27] S. P. Raman, Y. Chen, J. L. Schroeder, P. Huang, and E. K. Fishman, "CT texture analysis of renal masses: pilot study using random forest classification for prediction of pathology," *Academic Radiology*, vol. 21, no. 12, pp. 1587–1596, 2014.

[28] Z. Feng, P. Rong, P. Cao et al., "Machine learning-based quantitative texture analysis of CT images of small renal masses: differentiation of angiomyolipoma without visible fat from renal cell carcinoma," *European Radiology*, vol. 28, no. 4, pp. 1625–1633, 2018.

[29] H. S. Lee, H. Hong, D. C. Jung, S. Park, and J. Kim, "Differentiation of fat-poor angiomyolipoma from clear cell renal cell carcinoma in contrast-enhanced MDCT images using quantitative feature classification," *Medical Physics*, vol. 44, no. 7, pp. 3604–3614, 2017.

[30] D. Fehr, H. Veeraraghavan, A. Wibmer et al., "Automatic classification of prostate cancer Gleason scores from multiparametric magnetic resonance images," *Proc Natl Acad Sci USA.*, vol. 112, no. 46, pp. E6265–E6273, 2015.

[31] X. Xu, Y. Liu, X. Zhang et al., "Preoperative prediction of muscular invasiveness of bladder cancer with radiomic features on conventional MRI and its high-order derivative maps," *Abdom Radiol.*, vol. 42, no. 7, pp. 1896–1905, 2017.

[32] E. M. Cui, F. Lin, Q. Li et al., "Differentiation of renal angiomyolipoma without visible fat from renal cell carcinoma by machine learning based on whole-tumor computed tomography texture features," *Acta Radiologica*, vol. 60, no. 11, pp. 1543–1552, 2019.

Hindawi
Disease Markers
Volume 2022, Article ID 7588084, 9 pages
https://doi.org/10.1155/2022/7588084

*Research Article*

# Identification of Hub Genes Associated with Nonspecific Orbital Inflammation by Weighted Gene Coexpression Network Analysis

**Hanhan Liu,[1] Lu Chen,[2] Xiang Lei,[1] Hong Ren,[1] Gaoyang Li,[1] and Zhihong Deng[1]**

[1]*Department of Ophthalmology, The Third Xiangya Hospital, Central South University, Changsha, Hunan, China*
[2]*Department of Ophthalmology, Xiangya Hospital, Central South University, Changsha, Hunan, China*

Correspondence should be addressed to Zhihong Deng; dzhxy3yy@126.com

Received 1 April 2022; Accepted 3 May 2022; Published 27 May 2022

Academic Editor: Pei-Wen Zhu



*Background*. Nonspecific orbital inflammation is a common ophthalmopathy with a high prevalence among adult females. Yet, its molecular mechanisms behind are poorly understood. Regulation of gene expression probably plays an important role in this disease. Thus, we utilized gene coexpression networks to identify key modules and hub genes involved in nonspecific orbital inflammation. *Methods*. Data of gene expression in nonspecific orbital inflammation samples ($n = 61$) and healthy samples ($n = 28$) were obtained from the public Gene Expression Omnibus database. Afterward, differentially expressed genes were performed. Then, weighted correlation network analysis was done to define the key modules. Next, functional enrichment analysis was conducted by Gene Ontology and Kyoto Encyclopedia of Genes and Genomes pathway in key modules. Finally, a protein-protein interaction network and Cytohubba plugin were used to screen hub genes. *Results*. Differential expression of 716 genes was identified, among which 169 genes were upregulated and 547 genes were downregulated in the nonspecific orbital inflammation group. In weighted correlation network analysis, we clarified 2 key modules (MEturquoise and MEblue) that are likely to play key roles in nonspecific orbital inflammation. Functional enrichment analysis indicated that these genes are predominately involved in immune response and matrix homeostasis. In addition, among 2 key modules, there are 20 hub genes identified. *Conclusion*. With this new approach, we identified several genes that could be critical to pathologies of nonspecific orbital inflammation. These findings may contribute to further therapeutic target development.

## 1. Introduction

Nonspecific orbital inflammation (NSOI), an idiopathic chronic proliferative inflammatory disease, was first described in 1905 by Birch-Hirschfield [1]. It is also known as "idiopathic orbital inflammatory syndrome" or "orbital pseudotumor." NSOI accounts for approximately 6%–16% of all orbital lesions and 11% of orbital tumors [2–4]. It is prevalent among middle-aged adults, especially females [5, 6]. The detailed pathophysiological cause for NSOI remains unknown. Some studies suggest it might be correlated with Streptococcal pharyngitis, viral upper respiratory infection, or other autoimmune disorders, such as rheumatologic disease, multifocal fibrosclerosis, and Crohn disease [7, 8]. The typical clinical feature of NSOI is an acute onset of orbital ache and headache, lid swelling, and proptosis with unilateral polymorphous lymphoid infiltration [5, 9]. For treatment, steroids are the standard therapeutics [10]. The recurrence rate is still higher than 50% even with proper corticosteroid treatment [11]. Thus, further understanding of the molecular mechanism of NSOI is essential for the development of novel therapeutic approaches to prevent recurrence as well as improve the outcomes of patients.

With the support of bioinformatic tools, high-throughput data analysis was widely used to systematically identify the functional networks of genes in different disease models, thus providing important clues for molecular mechanism studies [12, 13]. In NSOI-related studies, by using microarrays, Rosenbaum et al. have identified the gene expression profile NSOI [14]; moreover, they found there is no significant difference between granulomatosis with polyangiitis (GPA) and

NSOI [15]. However, little is known about the hub genes which are closely related to the pathogenesis of NSOI. Herein, we used a novel tool, weighted gene coexpression network analysis (WGCNA), to identify the potential molecular interaction and correlation networks in this disease. WGCNA is an effective bioinformatic method to clarify synergetic expressed modules and to identify the relationship of gene networks at the transcriptome level [16]. It can provide high sensitivity to genes with low abundance or marginal fold changes [17]. In recent years, WGCNA has been successfully applied in different disease models to generate correlation networks, further identifying candidate biomarkers or therapeutic targets [18–21].

In our study, WGCNA was used to analyze the differentially expressed genes (DEGs) from 89 samples from a public dataset. Then, key gene modules related to DEGs were defined. We also examined the biological functions and pathways of genes in the key modules. These informative genes identified in our study may provide a novel insight into the understanding of the pathogenesis of NSOI. Moreover, the findings may be significant to new therapeutic target development for the treatment of NSOI patients.

## 2. Methods

*2.1. Data Preparation and Preprocessing.* The WGCNA dataset related to NSOI was downloaded from NCBI GEO (http://www.ncbi.nlm.nih.gov/geo) with accession number GSE58331, which consists of 89 samples (28 samples of normal control, 61 samples of NSOI). The (HG-U133_Plus_2) Affymetrix Human Genome U133 Plus 2.0 Array platform was used. Prior to WGCNA analysis, DEGs from the candidate genes were identified using the limma package in R from the Bioconductor website: (http://www.bioconductor.org/packages/release/bioc/html/limma.html). $P < 0.05$ and $|\log2\,(\text{fold change})| > 1$ were considered the cut-off criteria.

*2.2. Screening NSOI-Related Key Modules Based on WGCNA.* WGCNA [16] is a typical biologic algorithm for constructing gene coexpression networks. We used the WGCNA to analyze the expression values of the DEGs obtained in the previous screening in each group and screened the modules and genes associated with NSOI. Firstly, to calculate the adjacency matrix, the trait-based node significance measure was calculated with the following formula:

$$S_{ij} = \left|\text{cor}_{(i,j)}\right|, \tag{1}$$

where $i$ and $j$ stand for the expression gene $i$ and $j$, respectively. The Pearson coefficient of these two vectors was defined as cor. To improve the robustness of the coexpression network, this transition was designed to give more weight to the strong connections. Meanwhile, we decreased the value of weak connections in the predicted coexpression network.

Subsequently, a *power function* was then applied to correlate the adjacency of genes:

$$a_{ij} = \text{power}_{(S_{ij},\beta)}. \tag{2}$$

Afterward, the adjacency matrix was converted to a topological matrix using the following formula:

$$w_{ij} = \frac{l_{ij} + a_{ij}}{\min\left\{k_i, k_j\right\} + 1 - a_{ij}}. \tag{3}$$

The topological properties were also confirmed. Then, the dynamic tree cut method was used to accomplish module identification. Highly similar modules were identified by cluster analysis and then merged with a height cut-off of 0.95. Furthermore, the $p$ value of gene expression difference between the NSOI group and control was evaluated with a Student $t$-test. The significant gene was defined by the log $P$ value. The mean value of gene significance (GS) derived from modules comprising gene was defined as module significance (MS).

*2.3. Functional Enrichment Analysis in Key Modules.* To understand the functional significance of DEGs in NSOI-related key modules, the Gene Ontology (GO) enrichment analysis and Kyoto Encyclopedia of Genes and Genomes (KEGG) pathway enrichment analysis were performed by using the R package. We used DAVID 6.7 (https://david-d.ncifcrf.gov/) online tools to conduct the GO analysis. GO enrichment analysis consists of cellular component (CC), molecular function (MF), and biological process (BP). The cut-off of $P$ value < 0.05 was regarded as significant.

*2.4. Protein-Protein Interaction (PPI) Network Analysis.* The PPI network of DEGs was established using the Search Tool called TRING [22] (Version: 10.0, http://www.string-db.org/) to predict and analyze the interactions between proteins encoded by DEGs. In the network, nodes represent genes and edges represent the interactions between the nodes. Then, the software Cytoscape (Cytohubba plugin) [23] (Version: 3.2.0, http://www.cytoscape.org/) was used to perform the network analysis.

*2.5. Identification of Hub Genes.* Based on the PPI network, the software Cytoscape (Cytohubba plugin) [23] (Version: 3.2.0, http://www.cytoscape.org/) was used to perform the network analysis. The molecular Complex Detection algorithm was used within Cytoscape to detect crucial gene clusters based on the DEG coexpression network. The top 10 of the high degree genes in each module were identified based on the MCC method.

## 3. Results

*3.1. Identification of DEGs between NSOI and Healthy Controls.* To identify the DEGs, the gene microarray data of 89 samples (28 samples of normal control and 61 samples of NSOI) were downloaded from the GEO database. After normalization, batch correction, and gene annotation, gene

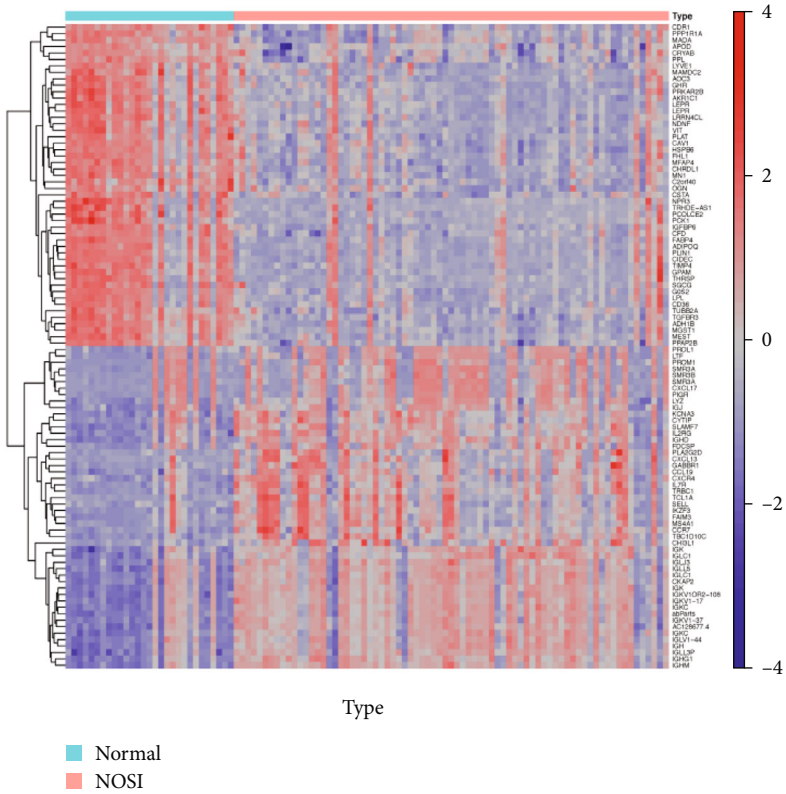


(a)

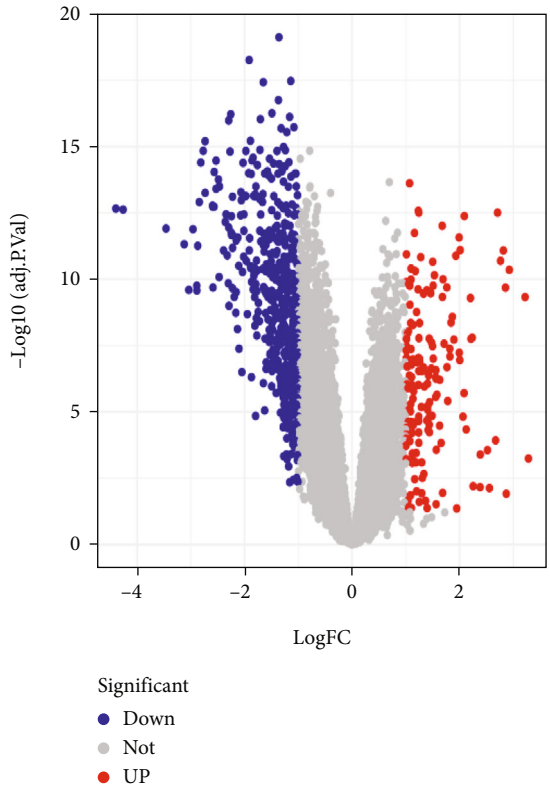


(b)

Figure 1: The heatmap (a) and volcano plot (b) of DEGs between NSOI and healthy controls.

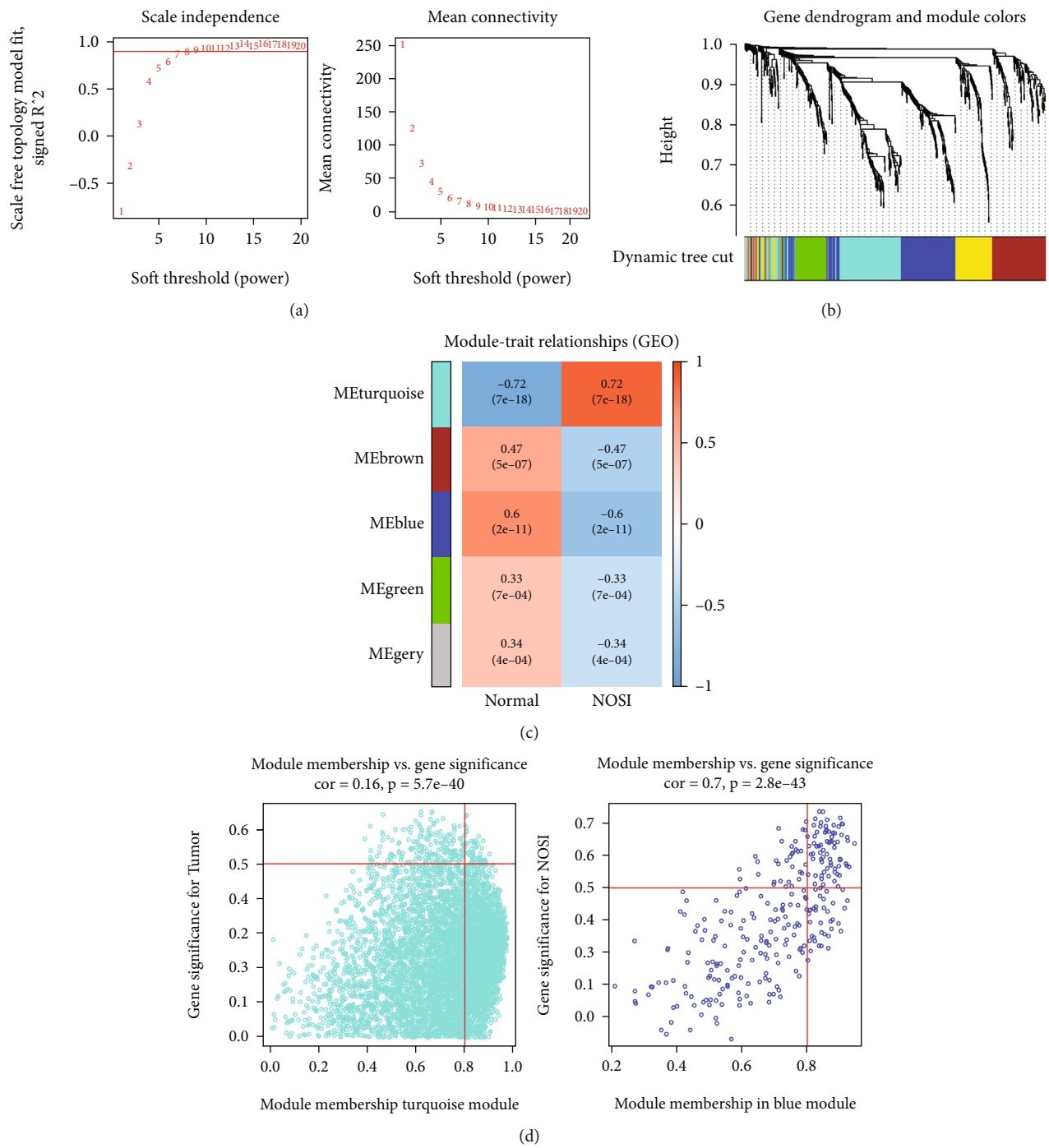


Figure 2: Identification of key modules based on WGCNA: (a) analysis of the scale-free topology model fit index for soft threshold powers ($\beta$) and the mean connectivity for soft threshold powers. (A) Displays the influence of soft-thresholding power ($x$-axis) on a scale-free fit index ($y$-axis). (B) Shows the influence of soft-thresholding power ($x$-axis) on mean connectivity (degree, $y$-axis). The approximate scale-free topology can be attained at the soft-thresholding power of 8. (b) A cluster dendrogram was built based on the dissimilarity of the topological overlap, together with assigned module colors. (c) Heatmaps of the plot of the adjacencies in the hub gene network include the trait weight. (d) The scatter plots of gene significance (GS) versus Module Membership (MM) of MEturquoise and MEblue.

expression distribution of each sample was depicted. Subsequently, a total number of 716 DEGs were identified, of which 169 genes were upregulated and 547 genes were downregulated in the NSOI group. The gene expression heatmap and volcano plot are shown in Figures 1(a) and 1(b), respectively.

For bars on the top, the light blue bar indicates a normal sample, while the light red bar indicates the NSOI sample.

*3.2. Identification of Key Modules Based on WGCNA.* To better understand the gene expression network of NSOI, WGCNA was performed on the obtained 716 DEGs. Firstly,

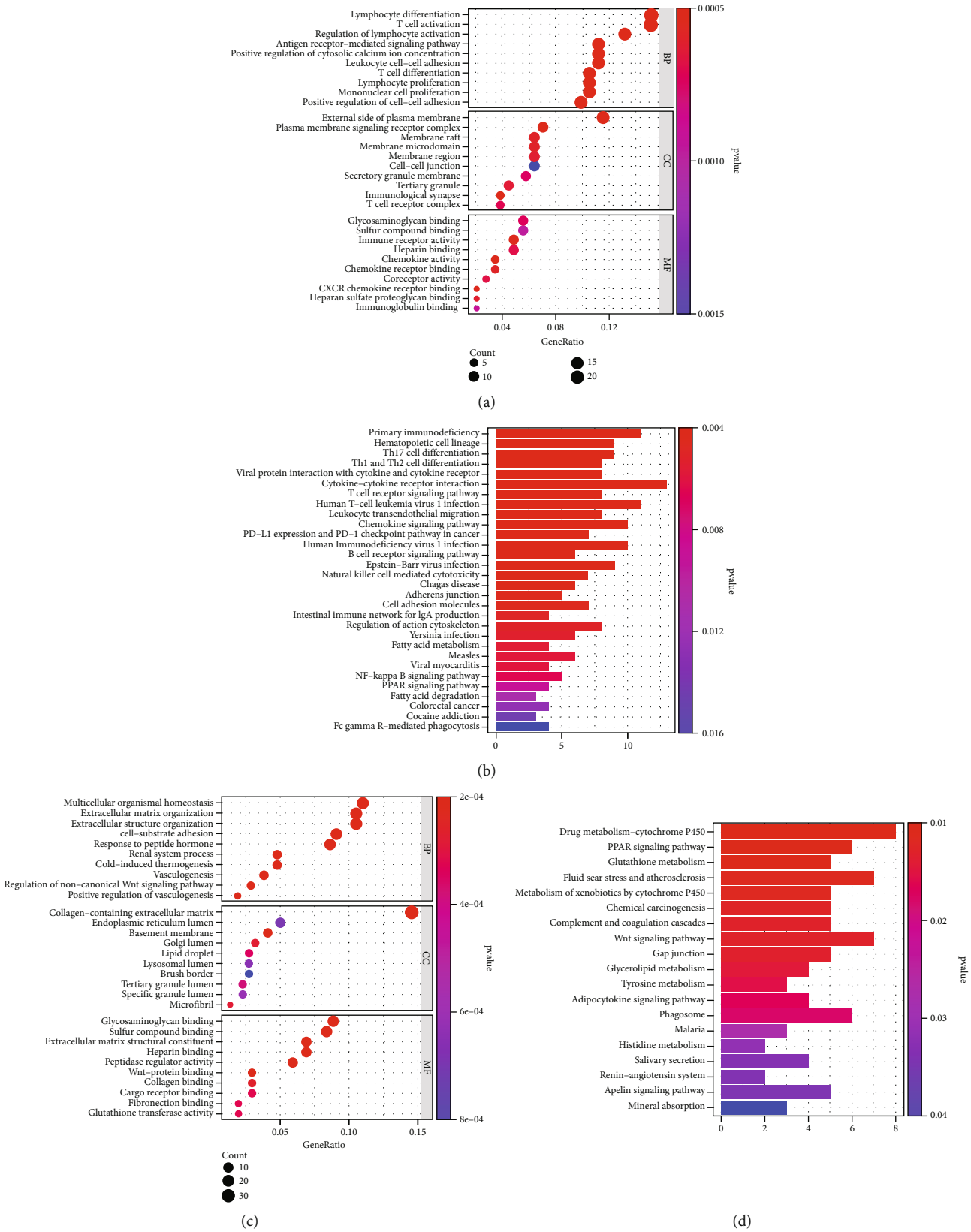


Figure 3: Functional enrichment analysis of genes in MEturquoise and MEblue by GO and KEGG analyses. (a) Bubble plot showed results of GO analysis (BP, CC, and MF) in MEturquoise module. (b) Barplot showed KEGG analysis of genes in MEturquoise module. (c) GO analysis (BP, CC, and MF) of genes in MEblue. (d) KEGG analysis of genes in MEblue.

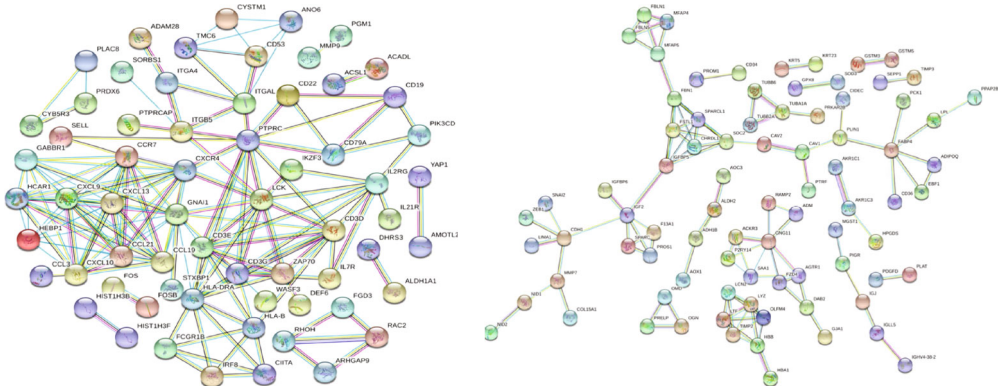


(a) (b)

Figure 4: PPI network analysis in MEbrown (a) and MEblue (b).

network topology analysis was performed to obtain relatively balanced scale independence and mean connectivity of the WGCNA. As shown in Figure 2(a), the $X$-axis shows matrix weighting power while the $Y$-axis shows a quadratic correlation index derived from log $(k)$ and log $(P(k))$ of the corresponding network. In this figure, when the correlation index reached 0.90, we took power as 8. Subsequently, a hierarchical clustering tree (dendrogram) of the 716 genes was analyzed (Figure 2(b)). Then, five modules (MEturquoise, MEbrown, MEblue, MEgreen, and MEgrey) were generated with the setting of MEDissThres as 0.25 (Figure 2(c)), of which MEturquoise was identified as the key module which has the strongest positive correlation with trait weight of NSOI, while MEblue has the strongest negatively correlation with trait weight of NSOI. The scatter plots of gene significance (GS) versus Module Membership (MM) of MEturquoise and MEblue are shown in Figure 2(d). Taken together, MEturquoise and MEblue were considered to be the key modules in the NSOI. Both of them were taken into further study.

*3.3. Functional Enrichment Analysis of Genes in MEturquoise and MEblue.* To clarify the biological functions associated with NSOI in the MEturquoise, functional enrichment analyses including GO and KEGG pathway enrichment analyses were performed. For GO biological processes, genes in MEturquoise were significantly enriched in "lymphocyte differentiation," "T cell activation," and "lymphocyte activation" (Figure 3(a)). For KEGG pathway analysis, the genes were mainly enriched in "cytokine–cytokine receptor interaction" and "primary immunodeficiency" (Figure 3(b)). In genes of MEblue, the GO analysis revealed that the most significant GO terms were "organismal homeostasis," "extracellular matrix," and "cell–substrate adhesion" (Figure 3(c)). The KEGG pathway analysis showed that the most significantly enriched pathways were "drug metabolism–cytochrome P450," "fluid shear stress and atherosclerosis," and "Wnt signaling pathway." (Figure 3(d)) Pathway analysis suggested that local inflammation was involved in the development of NSOI.

Table 1: Top 10 in network string ranked by MCC method in MEturquoise and MEblue.

| Ranked by MCC | MEturquoise | | MEblue | |
|---|---|---|---|---|
| | Gene name | Score | Gene name | Score |
| 1 | GNAI1 | 3628923.0 | SDC2 | 121.0 |
| 2 | CXCR4 | 3628804.0 | IGFBP5 | 121.0 |
| 3 | CCR7 | 3628801.0 | FBN1 | 121.0 |
| 4 | CXCL10 | 3628801.0 | FSTL1 | 120.0 |
| 5 | CCL21 | 3628800.0 | CHRDL1 | 120.0 |
| 6 | CCL19 | 3628800.0 | SPARCL1 | 120.0 |
| 7 | CXCL13 | 3628800.0 | LYZ | 48.0 |
| 8 | CXCL9 | 3628800.0 | LTF | 48.0 |
| 9 | HEBP1 | 3628800.0 | OLFM4 | 48.0 |
| 10 | HCAR1 | 3628800.0 | TIMP2 | 48.0 |

*3.4. PPI and Coexpression Networks to Identify Hub Genes Associated with NSOI.* Subsequently, PPI network analysis was used to predict and analyze the interactions between proteins encoded by DEGs in MEturquoise and MEblue. As shown in Figures 4(a) and 4(b), for the whole network, there were 152 nodes in the MEturquoise and 105 nodes in the MEblue. As highly connected genes in the key modules (MEturquoise and MEblue), they play significant parts in the biological processes of NSOI. We chose the top 10 genes ranked by degree of the protein-protein interaction nodes as candidate hub genes (Table 1). In MEturquoise, identified hub genes were GNAI1, CXCR4, CCR7, CXCL10, CCL21, CCL19, CXCL13, CXCL9, HEBP1, and HCAR1 (Figures 5(a) and 5(b)), and in MEblue, hub genes include SDC2, IGFBP5, FBN1, FSTL1, CHRDL1, SPARCL1, LYZ, LTF, OLFM4, and TIMP2 (Figures 5(c) and 5(d)).

The node size is based on the PPI degree value.

## 4. Discussion

In recent years, the high-throughput sequencing technique generates huge data for biological studies. Until now, the

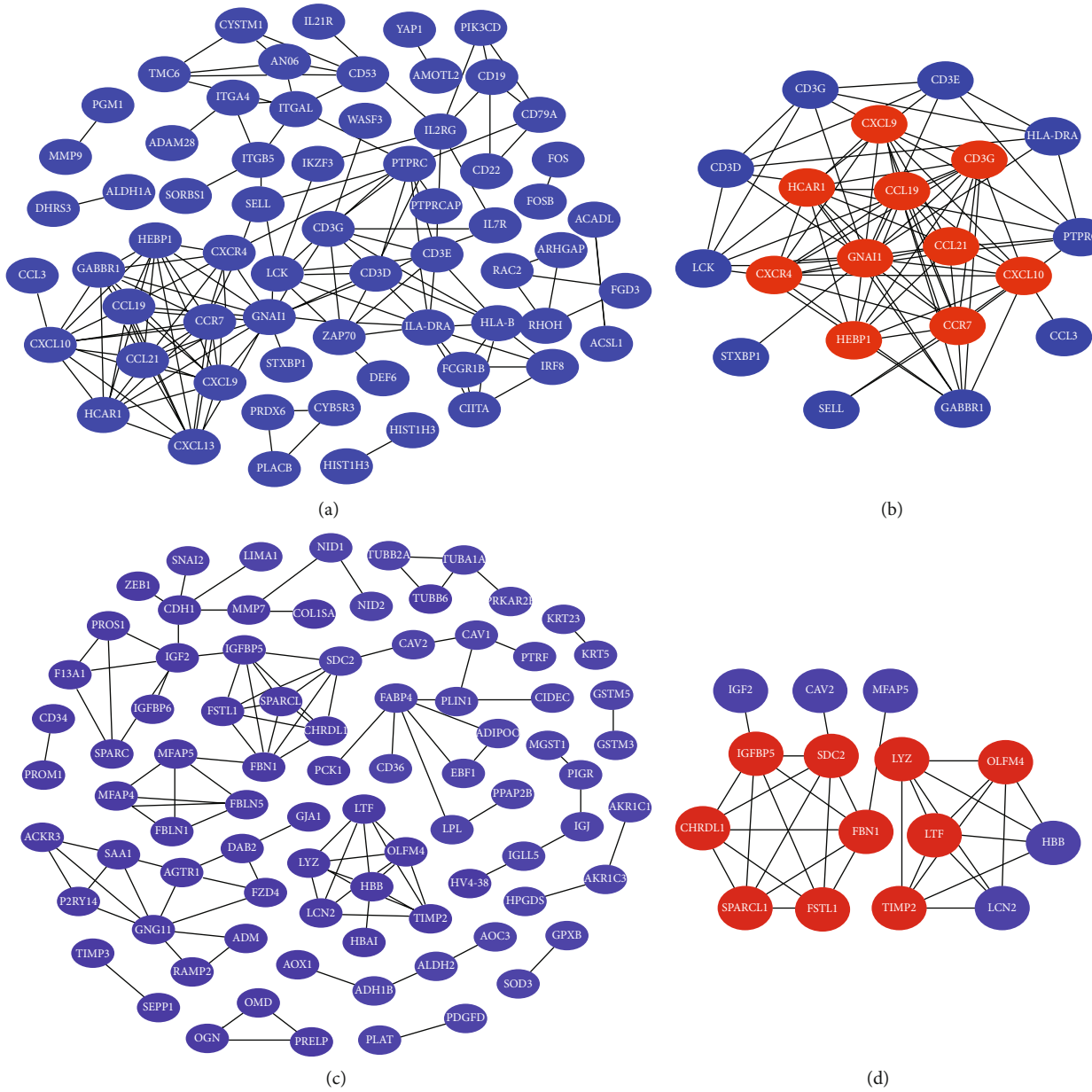


Figure 5: Hub gene identification in MEturquoise and MEblue. Genes labeled with red were considered hub genes.

majority of the existing bioinformatic tools concentrate only on unweighted networks [14]. However, WGCNA is a comprehensive novel statistical approach that can be used for both weighted and unweighted correlation networks and to further explore the module (cluster) structure in a network. Moreover, it also can be used to rank genes or modules in independent datasets to identify the hub genes [16]. In our study, 2 modules including the turquoise module (MEturquoise) and the blue module (MEblue) were considered to be the key modules in NSOI by using WGCNA. GO and KEGG pathway enrichment analyses were performed on genes in these two modules and identify that inflammation and immune-related pathways are broadly involved in NSOI.

The development of NSOI is a complex, heterogeneous, and multifactorial process [24]. In the present study, the results from GO and KEGG pathway analyses suggested that immune cells, including lymphocyte and T cells, were closely associated with the pathogenesis of NSOI. Moreover, the imbalance of cellular homeostasis and dysfunction of the extracellular matrix could be the other molecular mechanism of NSOI development. Previous studies suggested that aberrant immune-mediated production of fibrogenic cytokines leads to the progression of NSOI [25, 26]. Followed studies have focused on NSOI-related immunophenotypic features. Lowen et al's [27] study enrolled 55 cases for exploring the histopathologic and immunohistochemical pattern of NSOI; they found

that NSOI displayed a predominance of T cells, which coordinates with our results. Despite the immune alteration, variable degrees of collagen deposition also are considered an essential pathologic change of NSOI as previously reported [28, 29]. However, the cellular mechanism remains not fully understood.

PPI networks are useful in cell functions and disease mechanism prediction, especially for relationships between the species through conserved pathways and protein complexes, and discover new therapeutic targets [30, 31]. In this study, based on the DEGs in MEturquoise and MEblue, we identified 152 nodes in the MEturquoise and 105 nodes in the MEblue in the whole PPI network. Then, hub genes in each module were identified based on the Cytohubba degree. The hub genes include GNAI1, CXCR4, CCR7, CXCL10, CCL21, CCL19, CXCL13, CXCL9, HEBP1, HCAR1, SDC2, IGFBP5, FBN1, FSTL1, CHRDL1, SPARCL1, LYZ, LTF, OLFM4, and TIMP2. Among them, GNAI1, which is known as G protein subunit alpha i1, has the highest connection degree. GNAI1 is a member of the GNA family which is abundantly expressed in immune cells; it mainly participates in G protein-coupled receptor (GPCR) and non-GPCR signaling pathways [32, 33]. Studies reported that GNAI1 may have effects on angiogenesis by regulating VEGF-induced Akt-mTOR and Erk-MAPK activation [34]. Moreover, GNAI1 could act as a tumor suppressor in colon cancer by regulating the IL6 signaling pathway [35]. The genes of chemokines and chemokine receptors, such as CXCR4, CCR7, CXCL10, CCL21, CCL19, CXCL13, and CXCL9, were enriched in NSOI tissue, suggesting that chemokine-related factors may play important roles in the pathologic process of NSOI. Recently, studies demonstrated that chemokine-related pathways, e.g., IGF-1R and PPAR$\gamma$ signaling pathways, were involved in NSOI [36, 37]. However, the mechanism of GNAI1 and chemokines in NSOI is insufficient and needs further investigation.

In summary, with WGCNA network analysis, our study identifies a coexpression module in genes of patients with NSOI. Two modules (MEturquoise and MEblue) were found highly enriched in multiple pathways. Furthermore, the identified 20 hub genes have the potential to be biomarkers for the diagnosis and treatment of NSOI.

## Data Availability

The data that support the findings of this study are openly available in GEO (http://www.ncbi.nlm.nih.gov/geo), GSE58331.

## Conflicts of Interest

The authors declare that they have no financial or other conflicts of interest.

## Authors' Contributions

Hanhan Liu and Lu Chen are co-first authors.

## Acknowledgments

This work was supported by the Changsha Municipal Natural Science Foundation (Grant No. KQ2014253) and National Natural Science Foundation of China (Grant No. 82071002).

## References

[1] A. Birch-Hirschfeld, *Zur Diagnostic and Pathologic der Orbital Tumoren. Bericht uber die Zusammenkunft der Deutschen Ophthalmologischen Gesellschaft*, vol. 32, Ophthalmologischen Gesellschaft, 1905.

[2] I. A. Chaudhry, F. A. Shamsi, Y. O. Arat, and F. C. Riley, "Orbital pseudotumor: distinct diagnostic features and management," *Middle East African Journal of Ophthalmology*, vol. 15, no. 1, pp. 17–27, 2008.

[3] B. N. Swamy, P. McCluskey, A. Nemet et al., "Idiopathic orbital inflammatory syndrome: clinical features and treatment outcomes," *The British Journal of Ophthalmology*, vol. 91, no. 12, pp. 1667–1670, 2007.

[4] J. Spindle, S. X. Tang, B. Davies et al., "Pediatric idiopathic orbital inflammation: clinical features of 30 cases," *Ophthalmic Plastic and Reconstructive Surgery*, vol. 32, no. 4, pp. 270–274, 2016.

[5] S. J. Yuen and P. A. Rubin, "Idiopathic orbital inflammation: ocular mechanisms and clinicopathology," *Ophthalmology Clinics of North America*, vol. 15, no. 1, pp. 121–126, 2002.

[6] B. Eshraghi, S. A. Sonbolestan, M. A. Abtahi, and A. Mirmohammadsadeghi, "Clinical characteristics, histopathology, and treatment outcomes in adult and pediatric patients with nonspecific orbital inflammation," *Journal of current ophthalmology*, vol. 31, no. 3, pp. 327–334, 2019.

[7] G. M. Espinoza, "Orbital inflammatory pseudotumors: etiology, differential diagnosis, and management," *Current Rheumatology Reports*, vol. 12, no. 6, pp. 443–447, 2010.

[8] F. A. Jakobiec, Z. A. Syed, A. M. Stagner et al., "Orbital inflammation in pregnant women," *American Journal of Ophthalmology*, vol. 166, pp. 91–102, 2016.

[9] M. N. Pakdaman, A. R. Sepahdari, and S. M. Elkhamary, "Orbital inflammatory disease: pictorial review and differential diagnosis," *World Journal of Radiology*, vol. 6, no. 4, pp. 106–115, 2014.

[10] W. M. Mendenhall and A. M. Lessner, "Orbital pseudotumor," *American Journal of Clinical Oncology*, vol. 33, no. 3, pp. 304–306, 2010.

[11] S. Reggie, M. Neimkin, and J. Holds, "Intralesional corticosteroid injections as treatment for non-infectious orbital inflammation," *Orbit*, vol. 37, no. 1, pp. 41–47, 2018.

[12] H. J. Nam, J. Jeon, and S. Kim, "Bioinformatic approaches for the structure and function of membrane proteins," *BMB Reports*, vol. 42, no. 11, pp. 697–704, 2009.

[13] D. Chasman, A. Fotuhi Siahpirani, and S. Roy, "Network-based approaches for analysis of complex biological systems," *Current Opinion in Biotechnology*, vol. 39, pp. 157–166, 2016.

[14] J. T. Rosenbaum, D. Choi, C. A. Harrington et al., "Gene expression profiling and heterogeneity of nonspecific orbital inflammation affecting the lacrimal gland," *JAMA ophthalmology*, vol. 135, no. 11, pp. 1156–1162, 2017.

[15] J. T. Rosenbaum, D. Choi, D. J. Wilson et al., "Orbital pseudotumor can be a localized form of granulomatosis with

polyangiitis as revealed by gene expression profiling," *Experimental and Molecular Pathology*, vol. 99, no. 2, pp. 271–278, 2015.

[16] P. Langfelder and S. Horvath, "WGCNA: an R package for weighted correlation network analysis," *BMC Bioinformatics*, vol. 9, no. 1, p. ???, 2008.

[17] G. Pei, L. Chen, and W. Zhang, "WGCNA application to proteomic and metabolomic data analysis," *Methods in Enzymology*, vol. 585, pp. 135–158, 2017.

[18] Q. Yang, R. Wang, B. Wei et al., "Candidate biomarkers and molecular mechanism investigation for glioblastoma multiforme utilizing WGCNA," *BioMed Research International*, vol. 2018, Article ID 4246703, 10 pages, 2018.

[19] S. Chen, D. Yang, C. Lei et al., "Identification of crucial genes in abdominal aortic aneurysm by WGCNA," *PeerJ*, vol. 7, article e7873, 2019.

[20] H. Tian, D. Guan, and J. Li, "Identifying osteosarcoma metastasis associated genes by weighted gene co-expression network analysis (WGCNA)," *Medicine*, vol. 97, no. 24, article e10781, 2018.

[21] Y. Luo, J. Wang, W. Lu, Y. Liu, Y. Huang, and D. Luo, "Identifification of a disease-specifific gene expression profifile of children with acute asthma by weighted gene co-expression network analysis," *Genes & Genetic Systems*, vol. 95, no. 6, pp. 315–321, 2021.

[22] D. Szklarczyk, A. Franceschini, S. Wyder et al., "STRING v10: protein-protein interaction networks, integrated over the tree of life," *Nucleic Acids Research*, vol. 43, no. 1, pp. 447–452, 2015.

[23] P. Shannon, A. Markiel, O. Ozier et al., "Cytoscape: a software environment for integrated models of biomolecular interaction networks," *Genome Research*, vol. 13, no. 11, pp. 2498–2504, 2003.

[24] K. P. Cockerham, S. H. Hong, and E. E. Browne, "Orbital inflammation," *Current Neurology and Neuroscience Reports*, vol. 3, no. 5, pp. 401–409, 2003.

[25] I. Mombaerts, R. Goldschmeding, R. O. Schlingemann, and L. Koornneef, "What is orbital pseudotumor?," *Survey of Ophthalmology*, vol. 41, no. 1, pp. 66–78, 1996.

[26] C. Atabay, A. Tyutyunikov, D. Scalise et al., "Serum antibodies reactive with eye muscle membrane antigens are detected in patients with nonspecific orbital inflammation," *Ophthalmology*, vol. 102, no. 1, pp. 145–153, 1995.

[27] M. S. Lowen, V. S. Saraiva, M. C. Martins, and M. N. Burnier Jr., "Immunohistochemical profile of lymphoid lesions of the orbit," *Canadian journal of ophthalmology Journal canadien d'ophtalmologie*, vol. 40, no. 5, pp. 634–639, 2005.

[28] A. A. Cruz, E. V. Alves-Ferreira, G. Milbratz-Moré et al., "Sclerosing orbital inflammation caused by Leishmania braziliensis," *The American Journal of Tropical Medicine and Hygiene*, vol. 96, no. 1, pp. 197–199, 2017.

[29] I. Mombaerts, G. E. Rose, and J. A. Garrity, "Orbital inflammation: biopsy first," *Survey of Ophthalmology*, vol. 61, no. 5, pp. 664–669, 2016.

[30] A. Athanasios, V. Charalampos, T. Vasileios, and G. M. Ashraf, "Protein-protein interaction (PPI) network: recent advances in drug discovery," *Current Drug Metabolism*, vol. 18, no. 1, pp. 5–10, 2017.

[31] S. K. Miryala, A. Anbarasu, and S. Ramaiah, "Discerning molecular interactions: a comprehensive review on biomolecular interaction databases and network analysis tools," *Gene*, vol. 642, pp. 84–94, 2018.

[32] C. Cao, X. Huang, Y. Han et al., "Gαi1and Gαi3Are required for epidermal growth factor-mediated activation of the Akt-mTORC1 pathway," *Science Signaling*, vol. 2, no. 68, 2009.

[33] Z. Wang, R. Dela Cruz, F. Ji et al., "G(i)α proteins exhibit functional differences in the activation of ERK1/2, Akt and mTORC1 by growth factors in normal and breast cancer cells," *Cell Communication and Signaling*, vol. 12, no. 1, pp. 1–12, 2014.

[34] J. Sun, W. Huang, S. F. Yang et al., "Gαi1 and Gαi3mediate VEGF-induced VEGFR2 endocytosis, signaling and angiogenesis," *Theranostics*, vol. 8, no. 17, pp. 4695–4709, 2018.

[35] Z. W. Li, B. Sun, T. Gong et al., "GNAI1 and GNAI3 reduce colitis-associated tumorigenesis in mice by blocking IL6 signaling and down-regulating expression of GNAI2," *Gastroenterology*, vol. 156, no. 8, pp. 2297–2312, 2019.

[36] T. J. Smith, "Challenges in orphan drug development: identification of effective therapy for thyroid-associated ophthalmopathy," *Annual Review of Pharmacology and Toxicology*, vol. 59, no. 1, pp. 129–148, 2019.

[37] M. J. Lee, S. R. Planck, D. Choi et al., "Non-specific orbital inflammation: current understanding and unmet needs," *Progress in Retinal and Eye Research*, vol. 81, article 100885, 2021.

Hindawi
Disease Markers
Volume 2022, Article ID 5338725, 12 pages
https://doi.org/10.1155/2022/5338725

*Research Article*

# Corneal Endothelial Characteristics in Normal Chinese Han Children and Youngsters: A Study from the Specular Microscopy Descriptions

**Lilian Xie,[1] Huilong Fang,[2] Yuyu Xie,[3] Haiyan Wang,[4] Ru Liu,[1] Zhiyuan Li,[1,5] and Jundong Zhu[6]**

[1]*The Ophthalmology Department of the Affiliated Chenzhou Hospital, Hengyan Medical School, University of South China, Chenzhou, Hunan, China 423000*
[2]*Department of Pathogenic Biology and Immunology, Xiangnan University, Chenzhou, Hunan, China 423000*
[3]*Graduate School of Medical School of Shanghai Jiaotong University, Shanghai, China 200025*
[4]*The Operation Department of the Affiliated Chenzhou Hospital, Hengyan Medical School, University of South China, Chenzhou, Hunan, China 423000*
[5]*The Diagnosis and Treatment Technology Research and Development Centre for Dry Eye and Ocular Surface Disease of Chenzhou, Chenzhou, Hunan, China 423000*
[6]*Changsha Aier Eye Hospital, Changsha Hunan, China 410000*

Correspondence should be addressed to Zhiyuan Li; tolizhiyuan01@163.com and Jundong Zhu; zhujundong73@sina.com

Lilian Xie and Huilong Fang contributed equally to this work.

Received 27 March 2022; Accepted 22 April 2022; Published 20 May 2022

Academic Editor: Pei-Wen Zhu



*Objective.* To observe the morphological changes of corneal endothelial cells in healthy Chinese children and youngsters and analyze the sensitive and specificity of the endothelial assessments. *Methods.* 14,670 Chinese healthy volunteers enrolled were examined by specular microscopy, and the endothelial descriptive indexes: the central corneal thickness (CCT), endothelial cell density (ECD), coefficient of variation in average cell size (CV), the percentage of regular hexagonal cells (hexagonality, HEX), cell size of minimal cell ($S_{min}$), cell size of maximal cell ($S_{max}$), average cell size ($S_{avg}$), and size of standard deviation of cell area ($S_{sd}$) as well as sex and age were analyzed. *Results.* The average age of this study is $17.36 \pm 7.58$ (4–30) years. There is no sex predominance: 7,260 male (49.5%) and 7,410 female (50.5%). The mean CCT, ECD, CV, HEX, $S_{min/max}$, $S_{avg}$, and $S_{sd}$ are $529.94 \pm 31.53$ (437–644) $\mu$m, $3{,}051.28 \pm 375.49$ (2,031–4,074) cells/mm$^2$, $28.34 \pm 4.36$ (18–40) %, $61.21 \pm 10.29$ (17–89) %, ($147.79 \pm 21.94$ to $678.29 \pm 120.96$) $\mu$m$^2$, $332.74 \pm 44.62$ $\mu$m$^2$, and $95.02 \pm 23.17$ $\mu$m$^2$, respectively. The CCTs keep consistency. The ECD decreased rate is 1.02%/year. The curve of ECD and hexagonality expresses the same linear tender. The CCT and endothelial evaluation indexes have no sex predominant ($p > 0.05$); the quantitative indicators: CCT, ECD, and HEX are significant negative associated with age ($p = 0.001$ or $p < 0.001$); the variability indexes: the CV, $S_{min}$, $S_{max}$, $S_{avg}$, and $S_{sd}$ are positive correlation ($p < 0.001$). The coefficients of CCT, HE, and $S_{min}$ are -0.35, -0.59, and 1.17, respectively. *Conclusions.* The ECD decrease rate is 1.02%/year of the normal Chinese Han childhood to the earlier adulthood. The ages 4 to 12, 13 to 20, and 21 to 30 can be named as the childhood, puberty and adulthood from endothelial biologic identity. The HEX is the sensitivity marks for the polymorphisms while the $S_{min}$ is the specificity indicator CVs upon the Topcon Noncon Specular microscopy results.

## 1. Introduction

Human corneal endothelial cells (hCECs), originated from the neural crest, fulfill the posterior surface of the cornea and are construct of a monolayer of overlapping cells arranged in a mosaic pattern of mostly hexagonal appearance [1]. These metabolically lively cells are responsible for adjusting fluid and solute conveying between the aqueous humor and corneal stoma so as to preserve normal corneal thickness and transparency [2]. Not as the epithelia, the hCECs cannot regenerate and the density declining throughout the entire human life [2, 3]. Other factors that contribute to alteration of CEC morphology and quantity include injury [2], contact lens wearing [4], dry eye [5], intraocular surgery [6], and systemic diseases such as diabetes mellitus [7].

As a result, in cases when the age grows, the endothelial cell density (ECD) and the percentage of hexagonality (HEX) of these cells have decreased, with a corresponding proportional increase in the average cell area (polymorphism) [8]. Repair of hurts to corneal endothelial cells occurs by extension, migration, and amitotic nucleus cleavage of the residual endothelial cells. Therefore, parameters such as the amount, pleomorphism, and hexagonality of these cells are used to evaluate the capacity of endothelial cells [9].

Overall analysis of the corneal endothelial can be executed with a specular microscopy that distracts a slim light onto the corneal tissue surface and gathers the reflected light through a film plane. The central corneal thickness (CCT, $\mu$m), mean endothelial cell density (ECD, cell/mm$^2$), coefficient of variation of cell area (CV), percentage of hexagonality cell (HEX), and mean cell area (AVG, $\mu$m$^2$) are measured by the specular microscopy [10] so as to delusive these distinctive features.

Anyway, there is still lack of evidence to clarify the human endothelial cell transmutation of normal Chinese Han childhood, puberty, or adulthood. There are routine eight evaluation indicators by Noncon Specular microscopy (SP-1P, Topcon Corporation), and the sensitive and specificity of each symbols should be clarified.

## 2. Materials and Methods

*2.1. General Data and Schedule.* After obtaining informed consent, 14,670 volunteers (14,670 eyes, right eye) were performed with Snellen VA, autorefraction, slit-lamp biomicroscopy, conjunctival and corneal fluorescein staining, fundus examination, and IOP assessment. Amount and sharp of endothelial were examined using a noncontact specular microscopy (Topcon Noncon Specular microscopy, SP-1P; Topcon Corporation, Tokyo, Japan) at the Changsha Aier Eye Hospital (Group), Central South University and the First People's Hospital of Chenzhou, Hengyang Medicine School, South China University from January 2021 to December 2021. Each age group included the following: 4-8, 9-12, 13-16, 17-20, 21-25, and 26-30 years old. Endothelial cell measurements were performed with the autofocusing model at the central cornea point with 4 mm diameter area and autocell selection, and analysis was applied in the examination.

The main corneal parameters were as follows: the central corneal thickness (CCT), endothelial cell density (ECD), coefficient of variation in average cell size (CV), the percentage of regular hexagonal cells (hexagonality, HEX), cell size of minimal cell ($S_{min}$), cell size of maximal cell ($S_{max}$), average cell size ($S_{avg}$), and size of standard deviation of cell area ($S_{sd}$).These eight parameters of endothelial layer were analyzed by the SP-1P machine built-in software (Figure 1).

*2.2. Inclusion and Exclusion Criteria.* Patients' age and sex were also noted. All the patients were Chinese Han nationality. The patients were examined by routine slit lamp and ophthalmoscope.

The exclusion criteria were as follows: diabetes mellitus, corneal, and intraocular diseases including keratitis, glaucoma, or using antiglaucoma medications, corneal disorders (i.e., ectasia, scar, dystrophy, and dry eye with ocular surface fluorescein staining), congenital cornea diseases, congenital iris disorder and congenital cataract, pterygium that margin into cornea > 2 mm, recent ocular infection, previous ocular surgery or ocular trauma, history of contact lens wear within 14 days, and refractive errors with spherical equivalent beyond ±6 diopters.

*2.3. Project Design.* The age of all subjects ranged from 4 to 30 years, and subjects were allocated into six groups stratified by age. The volunteers' distribution is as follows: 4–8 years (2,080 eyes, 2,080 patients), 9–12 years (3,010 eyes, 3,010 patients), 13–16 years (2,040 eyes, 2,040 patients), 17–20 years (1,930 eyes, 1,930 patients), 21–25 years (2,720 eyes, 2,720 patients), and 26–30 years (2,890 eyes, 2,890 patients). The number of men and women in each group was nearly matched. Only the data of the right eye was used for demonstrating the relationship between age, corneal CCT, and endothelial parameters. This model was chosen because the ECD of each volunteer's eye was repeatedly measured for the eligible data.

The main corneal parameters were calculated, and results were compared among these groups. Correlations between the main corneal parameters (CCT, ECD, CV, HEX, $S_{min}$, $S_{max}$, $S_{avg}$, and $S_{sd}$) and age were found.

*2.4. Medical Ethics.* This study followed the principium of the Declaration of Helsinki, and this protocol was approved by the institutional review board of the ethnic committee of the Changsha Aier Eye Hospital (group) (ID: 2021KYYJ002).

*2.5. Statistical Analysis.* The majority of data did not have a normal distribution; thus, nonparametric tests were adopted. Statistical analyses were performed using SPSS for Windows IBM SPSS® 23.0 (SPSS Inc., Chicago, IL, USA). Student's pair $t$-test and Pearson's correlation coefficient ($r$) values were calculated. ANOVA test was used to compare the eight parameters of endothelial cells among study groups. The categorical variables use Fisher exact or chi-square test. Multiply linear regressions modeling analysis was used to

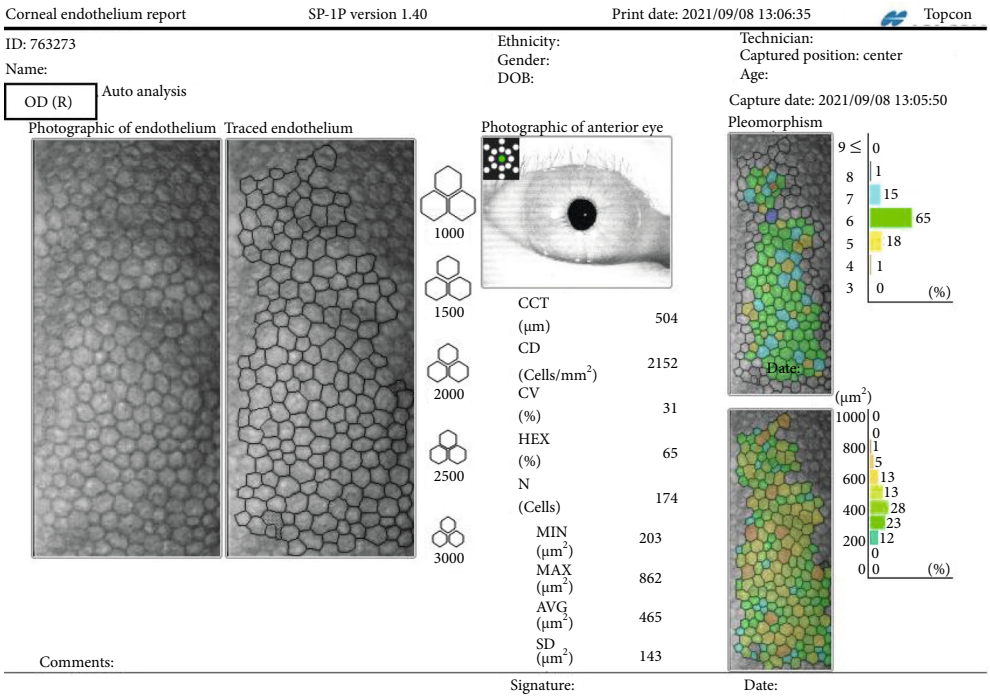


Figure 1: The schematic diagram for human corneal endothelial capture by SP-1P.

estimate the corneal ECD over time and between each stage. Both vicariate and multivariate analyses were performed to estimate unadjusted and adjusted effects. All predictors with $p < 0.25$ in the vicariate models were considered sufficiently important for consideration. The exception to this rule was ECD, the study effect, which was forced into the multivariable model regardless. A value of $p < 0.05$ was considered as statistically significant.

## 3. Results

The mean age of participants in this study was 17.36 ± 7.58 (range, 4–30) years. There was no sex predominance: 7,260 male (49.5%) and 7,410 female (50.5%).The measurements of all parameters in all studied eyes were shown in Table 1. The mean CCT was 529.94 ± 31.53 (range, 437–644) $\mu$m. Mean ECD was 3,051.28 ± 375.49 (range, 2,031–4,074) cells/mm$^2$. Mean CV was 28.34 ± 4.36 (range, 18–40) %. Mean HEX (%) was 61.21 ± 10.29 (range, 17–89) %. $S_{min}$ was 147.79 ± 21.94 $\mu$m$^2$. $S_{max}$ was 678.29 ± 120.96 $\mu$m$^2$. $S_{avg}$ was 332.74 ± 44.62 $\mu$m$^2$. $S_{sd}$ was 95.02 ± 23.17 $\mu$m$^2$.

Table 2 and Figure 2 the parameters of corneal endothelial in different age groups of normal Chinese children, 221 youngsters and adults were shown in Table 2 and Figure 2.

The ranges of the eight parameters in 6 groups were demonstrated in Figure 3. CCT in different groups has no difference ($p = 0.061$), but the ECD quantity index combined with those endothelial morphology descriptive index such as HEX, CV, $S_{min}$, $S_{max}$, $S_{avg}$, and $S_{sd}$ for endothelial demonstrates these obvious difference according to age criterions ($p < 0.001$).

Table 1: Parameters of corneal thickness and endothelial characteristics in normal Chinese Han children and youngsters.

| Parameters | Minimal value | Maximal value | Average (mean ± SD) |
|---|---|---|---|
| Counted cells (cells) | 86 | 394 | 221.71 ± 63.21 |
| CCT ($\mu$m) | 437 | 644 | 529.94 ± 31.53 |
| ECD (cells/mm$^2$) | 2031 | 4074 | 3051.28 ± 375.49 |
| CV (%) | 18 | 40 | 28.34 ± 4.36 |
| HEX (%) | 17 | 89 | 61.21 ± 10.29 |
| $S_{min}$ (S/$\mu$m$^2$) | 37 | 316 | 147.79 ± 21.94 |
| $S_{max}$ (S/$\mu$m$^2$) | 428 | 997 | 678.29 ± 120.96 |
| $S_{avg}$ (S/$\mu$m$^2$) | 231 | 678 | 332.74 ± 44.62 |
| $S_{sd}$ (S/$\mu$m$^2$) | 52 | 223 | 95.02 ± 23.17 |

Note: CCT: central corneal thickness; ECD: endothelial cell density; CV: coefficient of variability; HEX: hexagonality; $S_{min}$: size of minimal cell; $S_{max}$: size of maximal cell; $S_{avg}$: average cell size; $S_{sd}$: size standard deviation.

The CCT at the same level is upon the aged groups; the ECD has the decreased rate as 1.02%/year. Our data also show that the ECD decrease rate is different according to those childhood and youngster observers, and the childhood stage figure as 1.26%/year shows the fierce stage of endothelial declined so that this stage should keep stable without outside spur or noxious; meanwhile, the youngsters' yearly ECD decrease is 0.298% which is the most sluggish stage of our targeted volunteers. The curve of ECD and HEX manifested the same crests and troughs tender.

Table 2: Parameters of corneal thickness and endothelial characteristics in different age groups of normal Chinese Han children and youngsters.

| Parameters | Ages 4-8 | Ages 9-12 | Ages 13-16 | Ages 17-20 | Ages 21-25 | Ages 26-30 | Hc/F | $p$ |
|---|---|---|---|---|---|---|---|---|
| Counted cells ($n$) | 258.45 ± 61.97 | 246.09 ± 60.84 | 218.73 ± 56.53 | 211.27 ± 58.63 | 200.21 ± 59.41 | 199.15 ± 56.86 | 43.262 | <0.001 |
| CCT ($\mu$m) | 532.76 ± 28.46 | 532.96 ± 31.00 | 531.44 ± 33.08 | 529.48 ± 32.36 | 527.63 ± 32.40 | 526.16 ± 31.35 | 2.117 | 0.061 |
| ECD (cells/mm$^2$) | 3,407.40 ± 279.84 | 3,246.36 ± 271.53 | 3,129.45 ± 269.88 | 3,031.46 ± 315.56 | 2,838.22 ± 286.72 | 2,750.39 ± 346.17 | 175.896 | <0.001 |
| CV (%) | 25.28 ± 3.12 | 25.87 ± 3.10 | 27.70 ± 3.53 | 28.34 ± 3.75 | 30.88 ± 4.20 | 31.14 ± 4.19 | 115.119 | <0.001 |
| HEX (%) | 258.45 ± 61.97 | 246.09 ± 60.84 | 218.73 ± 56.53 | 211.27 ± 58.63 | 200.21 ± 59.41 | 199.15 ± 56.86 | 79.334 | <0.001 |
| $S_{min}$ (S/$\mu$m$^2$) | 134.95 ± 14.05 | 139.14 ± 15.30 | 143.50 ± 15.12 | 149.58 ± 18.05 | 156.62 ± 26.65 | 159.55 ± 24.36 | 61.226 | <0.001 |
| $S_{max}$ (S/$\mu$m$^2$) | 590.41 ± 80.17 | 616.72 ± 83.27 | 646.13 ± 92.69 | 680.44 ± 106.65 | 746.06 ± 119.64 | 763.14 ± 116.97 | 121.240 | <0.001 |
| $S_{avg}$ (S/$\mu$m$^2$) | 295.00 ± 23.99 | 310.24 ± 26.41 | 321.90 ± 28.31 | 340.34 ± 44.35 | 355.73 ± 44.72 | 364.28 ± 45.37 | 133.426 | <0.001 |
| $S_{sd}$ (S/$\mu$m$^2$) | 74.83 ± 9.93 | 80.24 ± 10.94 | 89.19 ± 13.27 | 97.04 ± 19.04 | 109.60 ± 21.99 | 114.01 ± 24.56 | 200.588 | <0.001 |

Note: CCT: central corneal thickness; ECD: endothelial cell density; CV: coefficient of variability; HEX: hexagonality; $S_{min}$: size of minimal cell; $S_{max}$: size of maximal cell; $S_{avg}$: average cell size; $S_{sd}$: size standard deviation.

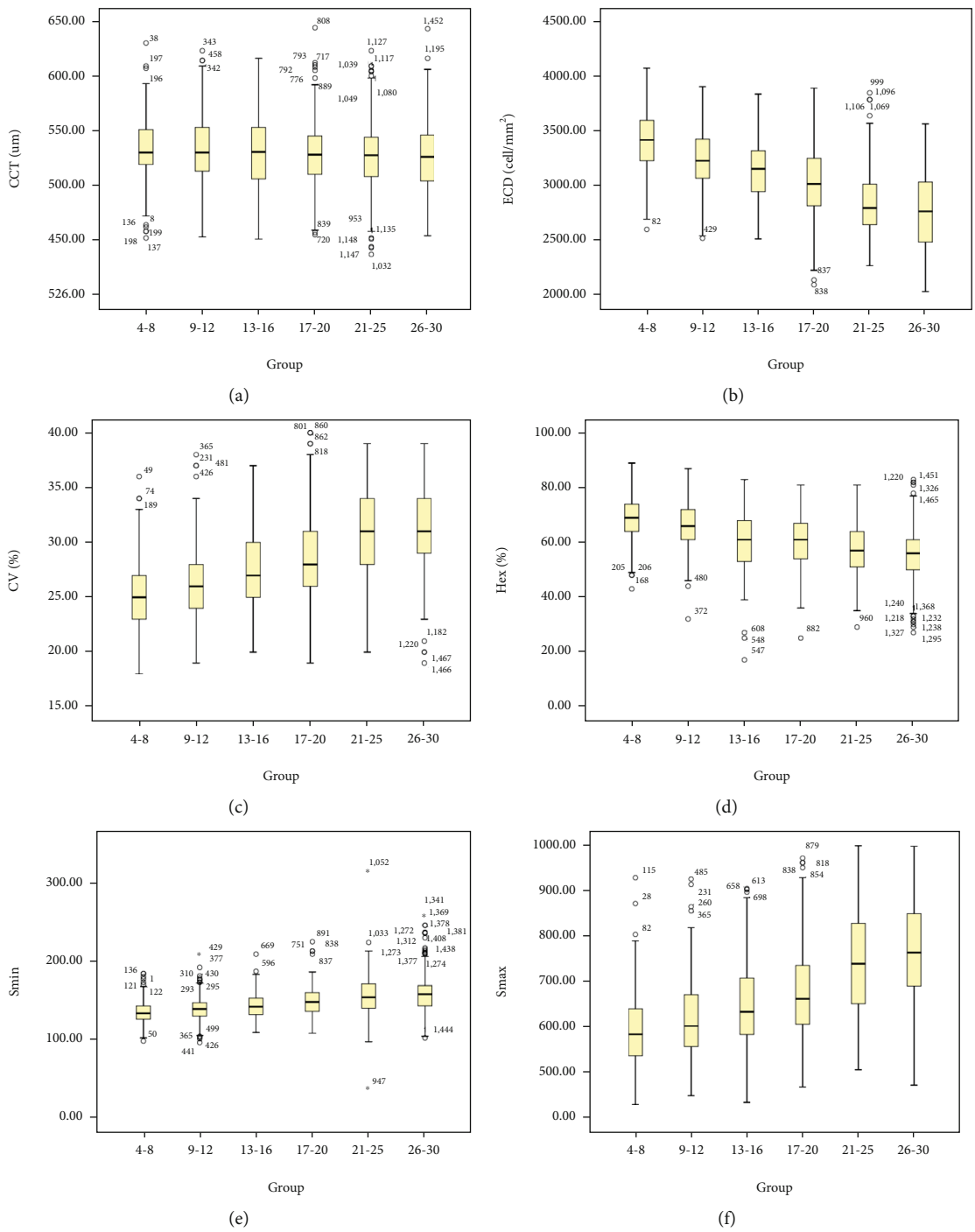


Figure 2: Continued.

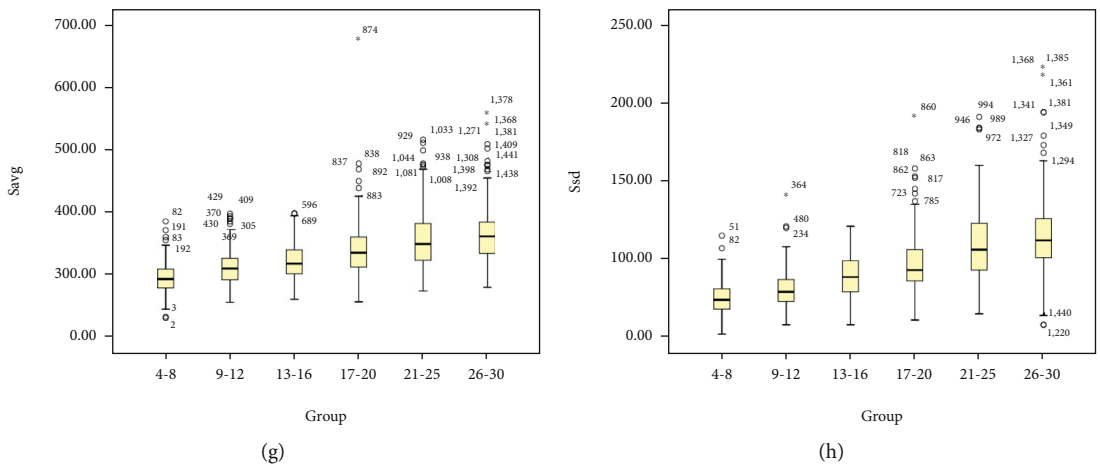


Figure 2: Eight parameters in different study groups. (a) Central corneal thickness. (b) Endothelial cell density. (c) Coefficient of variability. (d) Hexagonality. (e) Size of minimal cell. (g) Average cell size. (h) Size standard deviation.

The CCT and endothelial characteristics from both qualitative and quantitative evaluation index between male and female in normal Chinese Han children and youngsters in different groups have no difference ($p > 0.05$) (Table 3).

All the data analyzed by ANOVA test indicated that eight parameters of corneal thickness and endothelial characteristics were significantly different among different age groups (Table 4). The quantitative indicators such as the CCT, ECD, and HEX had the significant negative association with age by multivariate analysis ($p = 0.001$ or $p < 0.001$). Meanwhile, the corneal endothelial variability index such as the CV, $S_{min}$, $S_{max}$, $S_{avg}$, and $S_{sd}$ showed positive correlation ($p < 0.001$).

*3.1. The Multivariate Regression Equation Analysis between Age and Different Parameters Was Shown in Figure 4.* The coefficient of variation (CV) of CCT is -0.35, slight negative association; the coefficient of variation (CV) of ECD is -30.31 which is the obvious negative correlation index; the coefficient of variation (CV) of CV is 0.29 which is a normal index; the coefficient of variation (CV) of HE is -0.59 which is a bit exaggerated indication upon this regress line equation.

## 4. Discussion

*4.1. The Physiology of Corneal Endothelial Cells.* On the corneal posterior surface, a single film of corneal endothelial cells (CECs) is constructed in a tightly packed tessellated pattern on its basement membrane, the Descemet membrane (DM), which forms a baffle between the corneal stroma and anterior aqueous chamber [11], depending on the species, the corneal epithelium, the corneal endothelium, or both have a major role in regulating corneal hydration [12]. CECs are metabolically active and accelerate a continuous drawing action with a fluid-coupled active efflux of ions from the corneal stroma into the aqueous humor by ionic channel active transport [13].

*4.2. The Fundamental Process of Endothelial Variations.* In vivo, postpartum human CECs are terminally differentiated (TD), nonmitotic organs, which are static in the G1 phase of the cell cycle [14]. A plurality of factors, including cell-cell contact inhibition, the exits of cell cycle negative regulators (e.g., cell cyclin-dependent kinase inhibitors, p15INK4b, and p27kip1), growth inhibitors (e.g., transforming growth factor-$\beta$ and TGF-$\beta$) immersing in the aqueous humor, and stress-induced precocious senescence, contribute to the retention of CECs in their nonregenerative conformation [15, 16]. The mean CEC density is the highest of the neonates (at 3,000-4,000 cells/mm$^2$), decreases gently at the promised rate of about 0.3-0.6% per annum, and comes to ~2,800 cells/mm$^2$ in adolescence and~2,000 cells/mm$^2$ in elder [17, 18]. Previous literatures have the conclusion that with the age growth, the human corneal endothelial becomes hexagonal morphologically irregular and may become easier permeability to fluorescein staining [19].

*4.3. The Characteristic of 4-30 Years Chinese's Endothelial Count.* According to our 4-30 years period of Chinese volunteers' cell biological measurements, these data also show that the ECD has the decreased rate as 1.02%/year which is higher than previous studies [20–22]. Ought to the targeted observes from the childhood to the earlier adults' popular selection or statistical sample size bias, the ECD decrease rate of childhood stage figure is 1.26%/year which states that this is the fierce stage of endothelial declined so that this 4-12 years childhood phase should be shielded from outsider spurs or noxious as least as possible; meanwhile, the youngsters' (13-20 years old) yearly ECD decrease is 0.298% which is the steadiest stage of our participants. The graph of both ECD and hexagonality has nearly the same curve; anyway, the percentage of hexagonality has the decreased rate as 1.08%/year which is resemblance to the rate of ECD reduction. Those data affirm that the different endothelial qualifications such as ECD and hexagonality reach the evaluation dimensions consistency which coincide with Joo et al.'s publications [23].

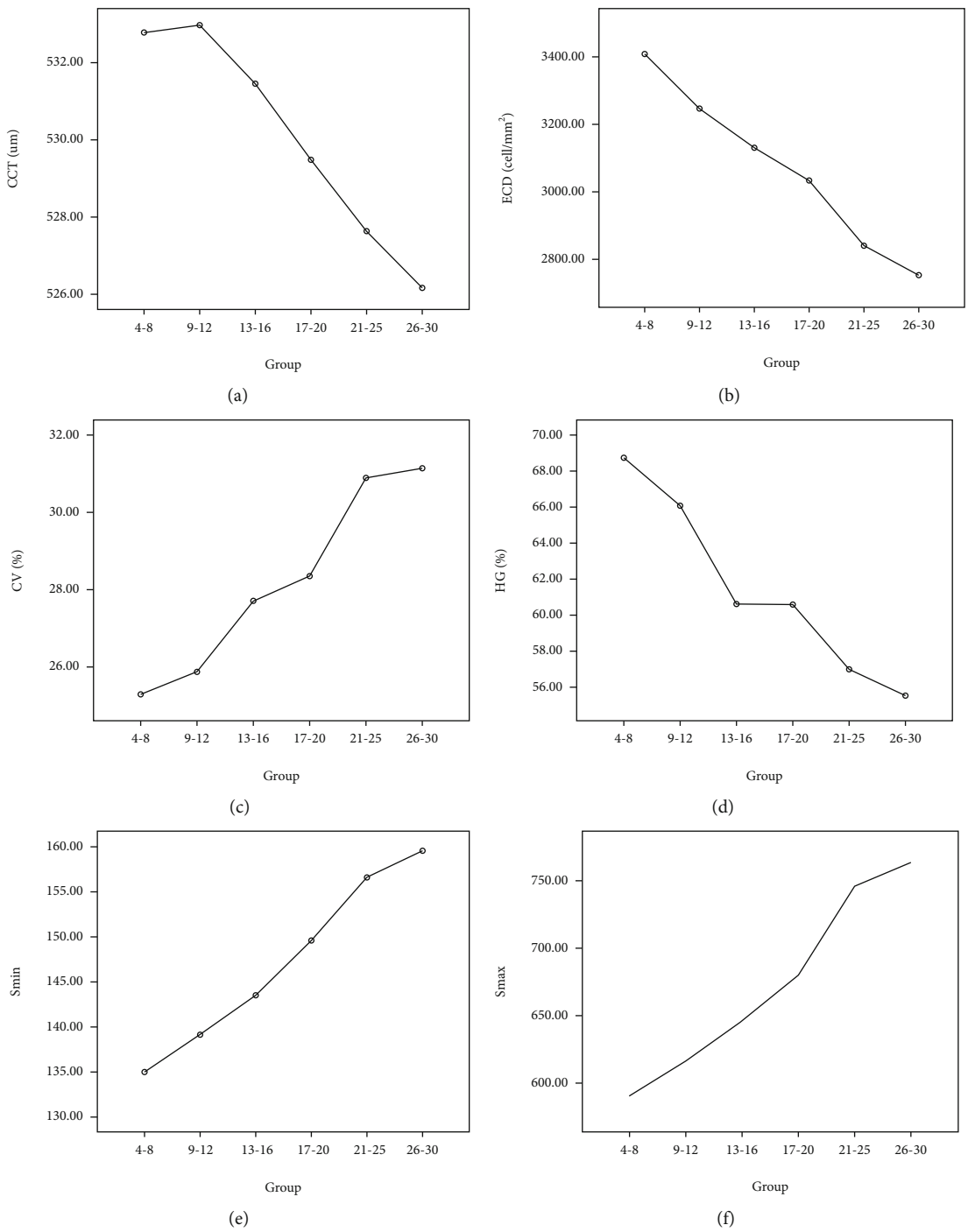


Figure 3: Continued.

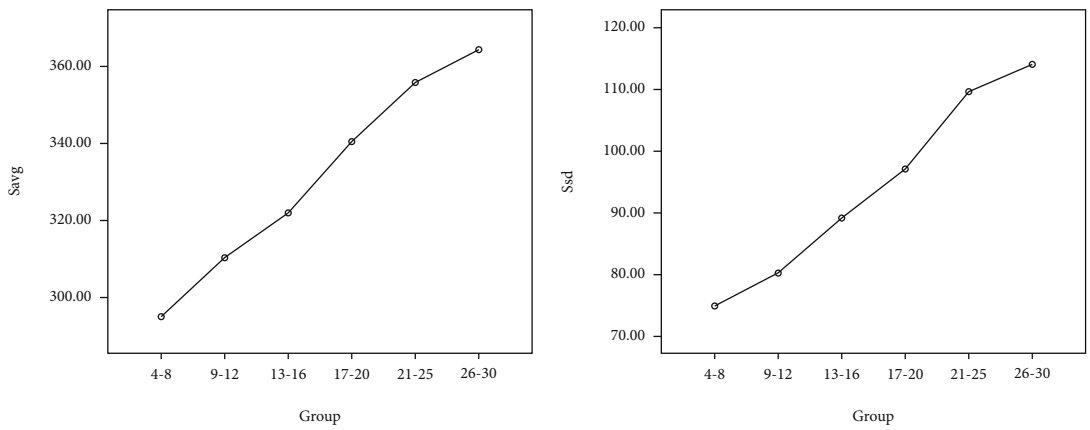


(g) (h)

Figure 3: Eight parameters in different study groups. (a) Central corneal thickness. (b) Endothelial cell density. (c) Coefficient of variability. (d) Hexagonality. (e) Size of minimal cell. (g) Average cell size. (h) Size standard deviation.

Table 3: Comparison of variables pertaining to the corneal thickness and endothelial characteristics between male and female in normal Chinese children and youngsters.

| Parameters | Male (mean ± SD) | Female (mean ± SD) | $t$-test | $p$ value |
|---|---|---|---|---|
| CCT ($\mu$m) | 529.52 ± 31.89 | 530.34 ± 31.19 | 0.248 | 0.618 |
| ECD (cells/mm$^2$) | 3060.42 ± 383.64 | 3042.33 ± 367.36 | 0.851 | 0.356 |
| CV (%) | 28.14 ± 4.12 | 28.53 ± 4.58 | 2.891 | 0.089 |
| HEX (%) | 61.48 ± 10.11 | 60.95 ± 10.47 | 0.990 | 0.320 |
| $S_{min}$ (S/$\mu$m$^2$) | 147.39 ± 23.63 | 148.19 ± 20.16 | 0.481 | 0.488 |
| $S_{max}$ (S/$\mu$m$^2$) | 681.53 ± 128.06 | 675.11 ± 113.57 | 1.032 | 0.310 |
| $S_{avg}$ (S/$\mu$m$^2$) | 330.64 ± 45.27 | 334.80 ± 43.90 | 3.188 | 0.074 |
| $S_{sd}$ (S/$\mu$m$^2$) | 95.11 ± 24.43 | 94.94 ± 21.87 | 0.019 | 0.891 |

Note: SD: standard deviation; CCT: central corneal thickness; ECD: endothelial cell density; CV: coefficient of variation in cell area; HEX: hexagonal cells; $S_{min}$: size of minimal cell; $S_{max}$: size of maximal cell; $S_{avg}$: average cell size; $S_{sd}$: size standard deviation.

Table 4: Correlation between age and variables pertaining to the corneal thickness and endothelial characteristics in normal Chinese Han children and youngsters.

| Parameters | Pearson's correlation coefficient ($r$) | $p$ value |
|---|---|---|
| CCT ($\mu$m) | −0.084 | 0.001 |
| ECD (cells/mm$^2$) | −0.612 | <0.001 |
| CV (%) | 0.502 | <0.001 |
| HEX (%) | −0.436 | <0.001 |
| $S_{min}$ (S/$\mu$m$^2$) | 0.406 | <0.001 |
| $S_{max}$ (S/$\mu$m$^2$) | 0.518 | <0.001 |
| $S_{avg}$ (S/$\mu$m$^2$) | 0.547 | <0.001 |
| $S_{sd}$ (S/$\mu$m$^2$) | 0.618 | <0.001 |

Note: SD: standard deviation; CCT: central corneal thickness; ECD: endothelial cell density; CV: coefficient of variation in cell area; HEX: hexagonal cells; $S_{min}$: size of minimal cell; $S_{max}$: size of maximal cell; $S_{avg}$: average cell size; $S_{sd}$: size standard deviation.

*4.4. The Cell Size and Morphology Changes upon Stages of Human Development.* The size and hexagon of endothelial cell area can be the unique property for the human development [24]. Meanwhile, Radman et al.'s literatures have reported that the sharp of the human endothelial be associated with the age growth stage, even that so-called childhood obesity criterion can be realized fiercely different with adolescence and earlier adulthood [25]. From our obtained data of the age correlative cell size criterions, the 4-8 and 9-12 age groups are the same level (childhood); the 13-16 and the 17-20 age group (puberty) have the same tender; meanwhile, the 21-25 and the 26-30 age group (adulthood) presses the consistency curve. From the data of human corneal endothelial variations within the dimension that manifests that the 4-12 year phrase should name as the childhood, the 13-20 year group can be treat as the puberty, and the age more than 21 year could be attributed as the adulthood.

*4.5. The Standard Approved Proposal for Endothelial Estimation.* Endothelial cell density (ECD) is an important parameter for assessing the endothelial function and health. Polymegathism, marked by the coefficient of variation in cell surface (CV), and pleomorphism, determinate by the ratio of Hexagonal cells (HEX), are other vital parameters that dispose stress to the endothelial [26]. The Food and Drug

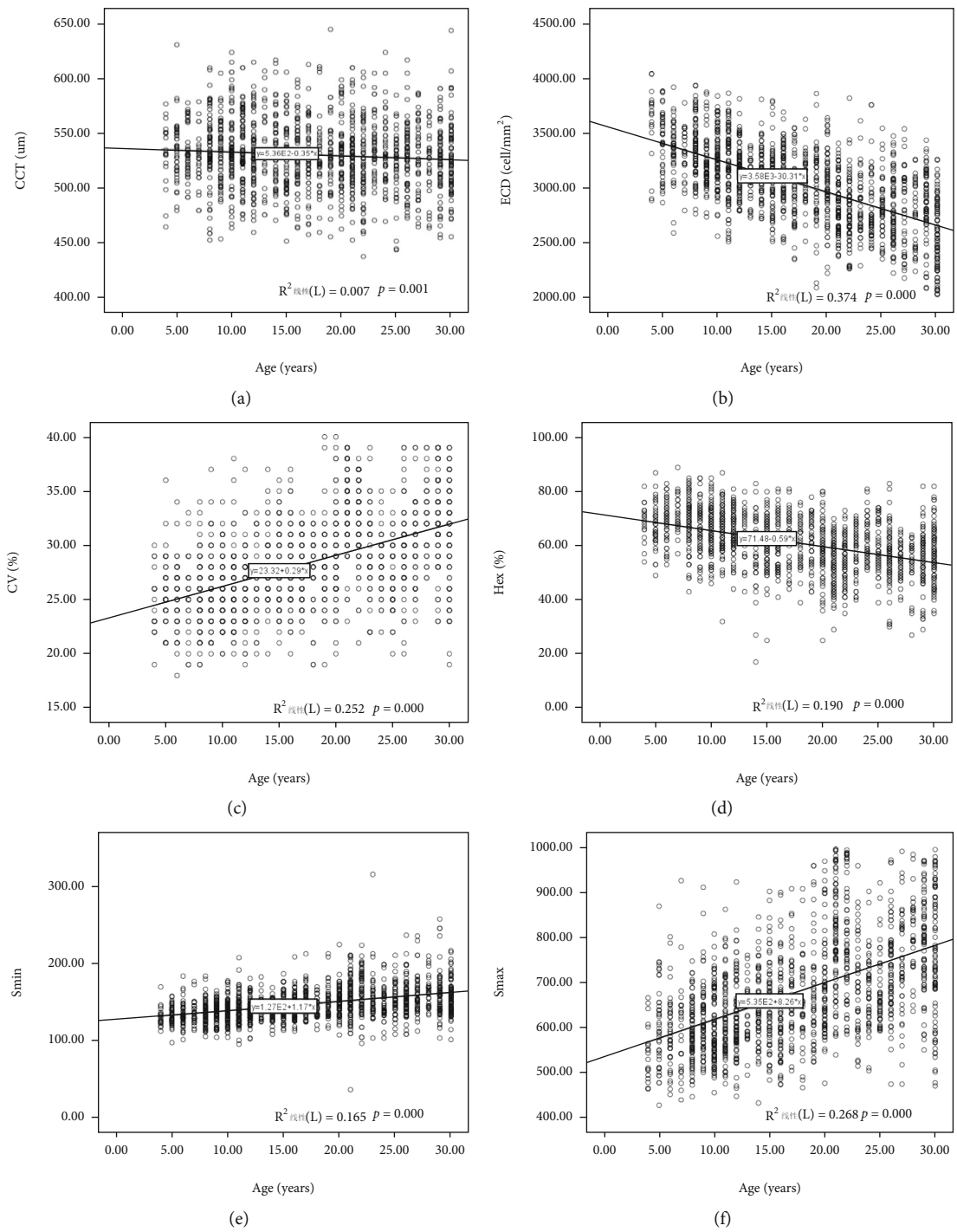


Figure 4: Continued.

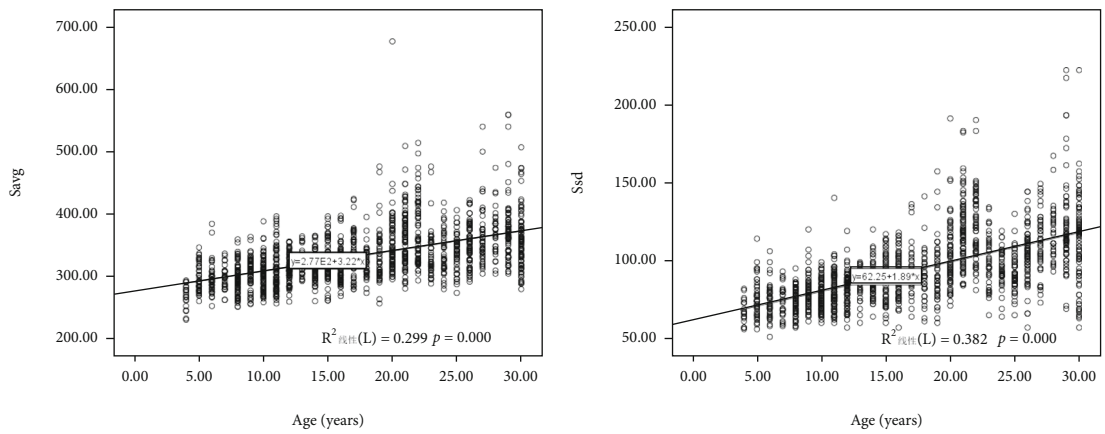


(g) (h)

Figure 4: Eight parameters in different study groups. (a) Central corneal thickness. (b) Endothelial cell density. (c) Coefficient of variability. (d) Hexagonality. (e) Size of minimal cell. (g) Average cell size. (h) Size standard deviation.

Administration of USA recommends the key method of specular microscopy as the "gold standard;" meanwhile, it is used by essentially each technical reading center [27, 28]. The multiply-center method allows the inclusion of the superficial cells and increases the NUM (the number of analyzed cells) and should be recommended for cases with least unambiguously cell numbers [29], and our eye hospital groups make up of more than thousands bunch of hospitals that assure the random assigned center method reliable and homogenization which requires the handle-automatic boundary tracing of the contiguous cell fulfills the cell-center dotting and should be more time consuming than the traditional center method. Actuality, the least contiguous countable cells in an image of our study are 86 which are more trustworthy than previous literatures [30, 31].

*4.6. The Valuable of HEX and $S_{min}$ Index.* Our observe trial has enrolled more than 10 thousand age-appropriated volunteers (14,670, 6 age groups) and massive information collection ensuring the accurate and reliable of those inferred conclusions. The quantitative indicators such as the CCT, ECD, and HEX had the significant negative association with age by multivariate regressive analysis ($p = 0.001$ or $p < 0.001$) which confirmed with Jha's literature [32]. Meanwhile, the corneal endothelial variability quotas such as the CV, $S_{min}$, $S_{max}$, $S_{avg}$, and $S_{sd}$ express the opposite correlation ($p < 0.001$). Anyway, the age relative CCT data can be the least statistic valuable influence compared with all other aspects. The CV of HE is -0.59 which is a bit more exaggerated index for the intention curve, so that from the regression equation index dimension, the HEX can be the most sensitive index for the morphology of single endothelial the same as Abdellah's commends [10]. The CV of the size of minimal cell is 1.17 which is the least among all these polymegathism assessment quotas; from the cell size index dimension, the minimal cell size should be the most specific index for the variation of endothelial.

*4.7. Limitations.* Our study focuses on the normal Chinese Han endothelial biology development of the childhood to early adults. Although the enrollment volunteer number is large and the gender bias is under control, the distinctive ECD seems higher than those all-periods' human beings' ECD decrease rate. Meanwhile, this characteristic should be test and verified on other ethnicities or/and age groups' population for further considerations.

## 5. Conclusion

In conclusion, this study provides the first characterization of specular microscopy-based CCT and CEC in 4 to 30 years healthy Chinese Hans' corneal endothelial subjects.

The CCT was decreased during this period but without statistic significant. The ECD decrease rate is 1.02%/year from the childhood to the earlier adulthood of Chinese Han nationality. The corneal endothelial variations within the scope that manifests that the aged 4-12, 13-20, and more than 21 year old can be redefine as the childhood, puberty, and adulthood.

Although the Topcon Noncon Specular microscopy can provide the eight evaluation indexes, quality, and quantity, the percentage of regular hexagonal cells (HEX) can be the most sensitive one for the endothelial polymorphisms. The cell size of minimal cell ($S_{min}$) should be the most specificity assessment indicators for the variability.

## Data Availability

The datasets used and/or analyzed during the present study are available from the corresponding author on reasonable request.

## Consent

There was an oral consent from the patient before the formal check-up enrollments.

## Conflicts of Interest

The authors declare that they have no competing interests.

## Authors' Contributions

Zhiyuan Li and Jundong Zhu participated in the project design, sample size calculation, and revision of the manuscript. Huilong Fang and Lilian Xie were responsible for the enrolment and follow-up of patients. Yuyu Xie, Ru Liu, and Haiyan Wang performed the clinic treatment and participated in performing the statistical analysis. All the authors confirm the authenticity of the raw data and read and approved the final manuscript. Lilian Xie and Huilong Fang contributed equally to this work.

## Acknowledgments

We thank the participants of the study. The authors acknowledge the guidance and support provided by Prof. Xiaohe Lu from the Ophthalmology Department, Zhujiang Hosptial of Southern Medical University. The present study was sponsored by the Outstanding Youth Fund of the First People's Hospital of Chenzhou City (grant No. N2019-006), the Hospital Management Fund by University of South China (grant No. 2019YJGL04), and the Chenzhou Science and Technology Bureau Fund (grant No. ZDYF-20200092).

## References

[1] G. O. Waring 3rd, W. M. Bourne, H. F. Edelhauser, and K. R. Kenyon, "The corneal endothelium: normal and pathologic structure and function," *Ophthalmology*, vol. 89, no. 6, pp. 531–590, 1982.

[2] S. Mishima, "Clinical investigations on the corneal endothelium: XXXVIII Edward Jackson Memorial Lecture," *American Journal of Ophthalmology*, vol. 93, no. 1, pp. 1–29, 1982.

[3] H. S. Ong, M. Ang, and J. Mehta, "Evolution of therapies for the corneal endothelium: past, present and future approaches," *British Journal of Ophthalmology*, vol. 105, no. 4, pp. 454–467, 2021.

[4] Y. Wang, X. Zhang, X. Yang, Y. Xu, B. Luo, and Y. Qian, "Effects of long-term soft contact lens wear on corneal epithelial thickness after small incision lenticule extraction," *Experimental and Therapeutic Medicine*, vol. 23, no. 1, p. 8, 2022.

[5] A. Kheirkhah, V. Satitpitakul, P. Hamrah, and R. Dana, "Patients with dry eye disease and low subbasal nerve density are at high risk for accelerated corneal endothelial cell loss," *Cornea*, vol. 36, no. 2, pp. 196–201, 2017.

[6] Y. Oka, N. Sasaki, and V. P. Injev, "Comparison of femtosecond laser-assisted cataract surgery and conventional phacoemulsification on endothelial cell density when using torsional modality," *Clinical Ophthalmology*, vol. 15, no. 15, pp. 4227–4237, 2021.

[7] C. Pont, F. J. Ascaso, A. Grzybowski, and V. Huerva, "Densite des cellules endotheliales corneennes au cours du traitement du diabete mellitus et du diabete oculaire," *Journal Français d'Ophtalmologie*, vol. 43, no. 8, pp. 794–798, 2020.

[8] K. Zhang, L. Zhao, C. Zhu et al., "The effect of diabetes on corneal endothelium: a meta-analysis," *BMC Ophthalmology*, vol. 21, no. 1, p. 78, 2021.

[9] L. J. Jeang, C. E. Margo, and E. M. Espana, "Diseases of the corneal endothelium," *Experimental Eye Research*, vol. 205, p. 108495, 2021.

[10] M. M. Abdellah, H. G. Ammar, M. Anbar et al., "Corneal endothelial cell density and morphology in healthy Egyptian eyes," *Journal of Ophthalmology*, vol. 2019, Article ID 6370241, 8 pages, 2019.

[11] N. M. Sie, G. H. Yam, Y. Q. Soh et al., "Regenerative capacity of the corneal transition zone for endothelial cell therapy," *Stem Cell Research & Therapy*, vol. 11, no. 1, p. 523, 2020.

[12] R. Afzal and H. B. Hwang, "Persimmon leaves (Diospyros kaki) extract enhances the viability of human corneal endothelial cells by improving $Na^+$-$K^+$-ATPase activity," *Pharmaceuticals*, vol. 15, no. 1, p. 72, 2022.

[13] X. Wang, Y. Zhong, M. Liang, Z. Lin, H. Wu, and C. Li, "Cross-linking-induced corneal endothelium dysfunction and its protection by topical ripasudil treatment," *Disease Markers*, vol. 2022, Article ID 5179247, 12 pages, 2022.

[14] Z. Li, H. Duan, Y. Jia et al., "Long-term corneal recovery by simultaneous delivery of hPSC-derived corneal endothelial precursors and nicotinamide," *The Journal of Clinical Investigation*, vol. 132, no. 1, article e146658, 2022.

[15] T. Yamaguchi, K. Higa, Y. Yagi-Yaguchi et al., "Pathological processes in aqueous humor due to iris atrophy predispose to early corneal graft failure in humans and mice," *Science Advances*, vol. 6, no. 20, article eaaz5195, 2020.

[16] L. Y. Ying, W. Y. Qiu, B. H. Wang, P. Zhou, B. Zhang, and Y. F. Yao, "Corneal endothelial regeneration in human eyes using endothelium-free grafts," *BMC Ophthalmology*, vol. 22, no. 1, p. 32, 2022.

[17] S. Chaurasia and M. Vanathi, "Specular microscopy in clinical practice," *Indian Journal of Ophthalmology*, vol. 69, no. 3, pp. 517–524, 2021.

[18] J. V. Forrester, D. Forrester, and R. McMenamin, *The eye (5th edition) basic sciences in practice*, Elsevier Ltd, Amsterdam, 2020.

[19] S. Erdem, M. Karahan, S. Ava, M. E. Dursun, L. Hazar, and U. Keklikci, "Examination of the effects of COVID 19 on corneal endothelium," *Graefe's Archive for Clinical and Experimental Ophthalmology*, vol. 259, no. 8, pp. 2295–2300, 2021.

[20] S. Yunliang, H. Yuqiang, L. Ying-Peng, Z. Ming-Zhi, D. S. Lam, and S. K. Rao, "Corneal endothelial cell density and morphology in healthy Chinese eyes," *Cornea*, vol. 26, no. 2, pp. 130–132, 2007.

[21] M. Wang, W. Sun, L. Ying, and X. G. Dong, "Corneal endothelial cell density and morphology in Chinese patients with pseudoexfoliation syndrome," *International Journal of Ophthalmology*, vol. 5, no. 2, pp. 186–189, 2012.

[22] M. Wu, D. X. Kuang, Y. Q. Huang, Y. R. Miao, X. C. Liu, and J. J. Dai, "Age-related changes of corneal endothelial cell in healthy Chinese tree shrew measured by non-contact specular microscope," *International Journal of Ophthalmology*, vol. 10, no. 12, pp. 1798–1804, 2017.

[23] J. H. Joo and T. G. Kim, "Comparison of corneal endothelial cell changes after phacoemulsification between type 2 diabetic and nondiabetic patients," *Medicine (Baltimore)*, vol. 100, no. 35, article e27141, 2021.

[24] I. Chaban, E. Baranova, N. Kononenko, M. Khaliluev, and E. Smirnova, "Distinct differentiation characteristics of Endothelium determine its ability to form pseudo-embryos in tomato ovules," *International Journal of Molecular Sciences*, vol. 21, no. 1, p. 12, 2020.

[25] M. Radman, J. McGuire, and J. Zimmerman, "Childhood obesity, endothelial cell activation, and critical illness," *Frontiers in Pediatrics*, vol. 8, p. 441, 2020.

[26] M. J. Mannis and E. J. Holland, *Cornea 2 volume Set*, Elsevier, Rotterdam, 5th edition, 2021.

[27] B. E. McCarey, H. F. Edelhauser, and M. J. Lynn, "Review of corneal endothelial specular microscopy for FDA clinical trials of refractive procedures, surgical devices, and new intraocular drugs and solutions," *Cornea*, vol. 27, no. 1, pp. 1–16, 2008.

[28] F. S. Sorrentino, "Qualitative alterations on corneal endothelial cell morphometry and HEXagonality after cataract surgery," *Clinical Ophthalmology*, vol. 15, pp. 4847–4853, 2021.

[29] Konan Inc, "KONAN MEDICAL [CellCheck Overview Video]," (2020), https://konanmedical.com/cellchek.

[30] Y. Shi, J. Huang, E. Baghdasaryan et al., "Representation of central endothelial cell density by analysis of single best specular microscopy image regardless of cell size variance," *Translational Vision Science & Technology*, vol. 8, no. 3, p. 23, 2019.

[31] M. Minami and E. Chihara, "Overestimation of corneal endothelial cell density by automated method in glaucomatous eyes with impaired corneal endothelial cells," *International Ophthalmology*, vol. 42, no. 1, pp. 133–145, 2022.

[32] A. Jha, A. Verma, and A. R. Alagorie, "Association of severity of diabetic retinopathy with corneal endothelial and thickness changes in patients with diabetes mellitus," *Eye (London, England)*, 2021.

Hindawi
Disease Markers
Volume 2022, Article ID 7475704, 11 pages
https://doi.org/10.1155/2022/7475704

*Research Article*

# Expression, Purification, and In Silico Characterization of *Mycobacterium smegmatis* Alternative Sigma Factor SigB

**Rakesh Kumar Singh,[1] Lav Kumar Jaiswal,[1] Tanmayee Nayak,[1] Ravindra Singh Rawat,[2] Sanjit Kumar,[2] Sachchida Nand Rai,[3] and Ankush Gupta[1]**

[1]*Molecular Microbiology Laboratory, Department of Biochemistry, Institute of Science, Banaras Hindu University, Varanasi-221005, Uttar Pradesh, India*
[2]*Centre for Bioseparation Technology, Vellore Instiute of Technology, Vellore-632014, Tamil Nadu, India*
[3]*Centre for Biotechnology, University of Allahabad, Prayagraj-211002, Uttar Pradesh, India*

Correspondence should be addressed to Ankush Gupta; ankushgupta@bhu.ac.in

Received 28 February 2022; Accepted 5 May 2022; Published 20 May 2022

Academic Editor: Pei-Wen Zhu



Sigma factor B (SigB), an alternative sigma factor (ASF), is very similar to primary sigma factor SigA ($\sigma^{70}$) but dispensable for growth in both *Mycobacterium smegmatis* (Msmeg) and *Mycobacterium tuberculosis* (Mtb). It is involved in general stress responses including heat, oxidative, surface, starvation stress, and macrophage infections. Despite having an extremely short half-life, SigB tends to operate downstream of at least three stress-responsive extra cytoplasmic function (ECF) sigma factors (SigH, SigE, SigL) and SigF involved in multiple signaling pathways. There is very little information available regarding the regulation of SigB sigma factor and its interacting protein partners. Hence, we cloned the SigB gene into pET28a vector and optimized its expression in three different strains of *E. coli*, viz., (BL21 (DE3), C41 (DE3), and CodonPlus (DE3)). We also optimized several other parameters for the expression of recombinant SigB including IPTG concentration, temperature, and time duration. We achieved the maximum expression of SigB at 25°C in the soluble fraction of the cell which was purified by affinity chromatography using Ni-NTA and further confirmed by Western blotting. Further, structural characterization demonstrates the instability of SigB in comparison to SigA that is carried out using homology modeling and structure function relationship. We have done protein-protein docking of RNA polymerase (RNAP) of Msmeg and SigB. This effort provides a platform for pulldown assay, structural, and other studies with the recombinant protein to deduce the SigB interacting proteins, which might pave the way to study its signaling networks along with its regulation.

## 1. Introduction

Prokaryotic transcription is mediated by RNA polymerase (RNAP) which is made up of five core subunits ($\alpha_2\beta\beta'\omega$) that binds with the sigma factor ($\sigma$), also known as transcription initiation factor that provides specificity during transcription initiation. Based on the structure and function, $\sigma$ factors are classified into two major groups, viz., (i) sigma 70 ($\sigma^{70}$), i.e., primary sigma and (ii) sigma 54 ($\sigma^{54}$) which is involved in nitrogen fixation and found mostly in plant growth promoting rhizobacteria. Further, $\sigma^{70}$ is classified into four major groups based on the domain organization, viz., groups 1, 2, 3, and 4. Group 1 (SigA) has an extended N-terminal region and four highly conserved regions, namely, regions 1, 2, 3, and 4. The group 2 (SigB) does not have the N-terminus extended region, but all the four conserved regions are present. The group 3 (SigF) has only three regions, viz., 2, 3, and 4 while the group 4 (also known as the Extra Cytoplasmic Function (ECF) sigma factor) contains only regions 2 and 4. The regions 2 and 4 are extremely important in promoter recognition and binds at -10 and -35 regions of the promoter, respectively [1, 2].

$\sigma^{70}$ being the principle $\sigma$ factor contributes in the expression of all housekeeping genes under normal conditions [3, 4]. However, under various stressful conditions, alternative sigma factors (ASF) redirect the transcription machinery

towards the expression of a wide range of genes, which help the organism to respond to the internal or environmental stresses [5, 6]. Due to unequal division of tasks, $\sigma^{70}$ has broad range promoter recognition efficiency but ASF deal with very high promoter recognition stringency. By these mechanisms that regulate transcription initiation, the organism ensures its survival and adaptability [7–9]. SigB responds to different stresses like heat shock, surface, oxidative, starvation stresses, and macrophage infections [3, 10, 11]. It is also expressed while transition to stationary phase during bacterial growth to cope with the environmental stresses [12–15].

In contrast to SigA, the half-life of Msmeg SigB is very short (less than 8 mins.) and in *E. coli*, it is only 2 minutes [12, 16–18]. This indicates towards the nature and role of SigB as a protein with a short half-life and involved in regulatory functions. The transcription of SigB was shown to occur from two distinct types of promoters: one, recognized by the stress-inducible sigma factors, viz., SigE, SigH, and SigL and the other recognized by SigF [19–22]. This infers that multiple sigma factor signaling networks converge at the SigB promoter. On the other hand, this observation is also supported by the deletion analysis of SigC, SigE, SigF, SigH, and SigL sigma factors resulting in the reduced expression of SigB, demonstrated in the mice model [19, 23–26]. The regulatory network and structure of the primary sigma factor SigA are already deduced. However, very little information about the regulatory network of SigB and other stress-responsive ECF sigma is available in the literature. Although recombinant and purified SigB is essential for the study of protein interactions/elucidation of its regulatory network as well as crystallization studies, detailed and optimized expression and purification of this short-lived protein in higher quantities and highly soluble form are not available in the literature. Here, we optimize and demonstrate the expression and purification of highly soluble Msmeg SigB.

## 2. Material and Methods

*2.1. Bacterial Strains, Chemicals, and Reagents. E.coli* DH5$\alpha$ (Zymo Research, USA) was used as cloning host, and BL21 (DE3), C41 (DE3) (Millipore Sigma (Novagen)), and CodonPlus (DE3) (Agilent Technologies) cells were used as expression host strains. The pET28a expression vector (Thermo Scientific, USA), Taq DNA polymerase (G-Biosciences, USA), restriction enzymes (New England Bio Labs Ltd., UK), T4 DNA ligase (New England Bio Labs Ltd., UK), and molecular biology grade reagents were obtained from Sigma-Aldrich (USA). His-Tag monoclonal antibody and secondary anti-mouse IgG (H + L) (peroxidase/HRP conjugated) were from Puregene: Genetix Biotech Asia Pvt. Ltd., respectively.

*2.2. Plasmid Construction.* The nondirectional cloning strategy was employed for the cloning of *SigB* (MSMEG_2752) gene of *M. smegmatis* mc$^2$155. The primer pair used to amplify the *SigB* gene from the genomic DNA of *M. smegmatis* mc$^2$155 was forward primer SigB_2752_EcoRI 5′-CGGAATTCATGGCAAATGCCACCACAAGCC-3′ and reverse primer SigB_2752_EcoRI 5′-CGGAATTCGGAGG CGTAGGAGCGGAGGCGG-3′ respectively, where underline sequences are showing the EcoRI restriction site. The condition for PCR amplification was initial denaturation at 95°C for 5 minutes, 35 cycles (denaturation 95°C for 30 sec, annealing 60°C for 45 sec, elongation 72°C for 1 minute), and final elongation 72°C for 5 minutes. The amplified PCR product was ligated into the EcoRI digested and dephosphorylated pET28a expression vector. The ligation product was transformed into DH5$\alpha$ cells, and the recombinant positive clones (His-SigB) were confirmed by EcoRI restriction digestion and sequencing.

### 2.3. The Expression of Recombinant His-SigB Protein

*2.3.1. Expression Host Strain Optimization.* The clones containing His-SigB in positive orientation were transformed into three expression host strains of *E.coli*, viz., BL21 (DE3), C41 (DE3), and CodonPlus (DE3) [27]. These expression strains possess $\lambda$DE3 lysogen that carries the gene T7 RNA polymerase under the control of lacUV5 promoter. So, IPTG (isopropyl $\beta$-D-1-thiogalatopyranoside) induction for the protein expression was performed to obtain maximum expression. The selected clone was inoculated from a single colony and cultured overnight in 5 ml Luria Bertani (LB) containing 50 $\mu$g/ml kanamycin at 37°C in a shaking incubator at 150 rpm. Next day, 1% (v/v) of secondary culture was incubated at 37°C until the $OD_{600}$ of the culture reached ~0.4 O.D., and the culture was induced with 0.1 mM IPTG and grown for 3 hrs at 37°C at 150 rpm. For analysis of the His-SigB protein expression, sodium dodecyl sulphate polyacrylamide gel electrophoresis (SDS-PAGE) was performed as described by [28]. For SDS-PAGE, 0.1 $OD_{600}$ equivalent cell lysate prepared in 4× sample loading buffer (10% SDS, 40% glycerol, 0.25 M Tris–Cl (pH 6.8), 200 mM DTT, and 0.05% bromophenol blue) after heat denaturation at 100°C was loaded onto the gel. For visualization, the gel was stained by Coomassie brilliant blue (R-250) followed by destaining.

*2.3.2. IPTG Optimization.* Commonly, IPTG was used to achieve high level of expression for recombinant proteins. To optimize the concentration of IPTG on *E. coli* strains and the optimum protein expression, we selected best expressing host strain for a range of IPTG concentrations, viz., 0.05, 0.1, 0.25, and 0.5 mM and induced at approximately <0.4 $OD_{600}$ at 37°C 150 rpm for 3 hrs. To determine the solubility of protein at various IPTG concentrations, the pellet/supernatant fractionation of the lysate was performed. The harvested cell cultures were washed and resuspended in 1× phosphate buffer saline (PBS, pH 8.0) and thereafter sonicated at 15% amplitude (ultrasonic homogenizer) for 2-3 min. The lysate was clarified by centrifugation at 13,000 rpm for 20 min at 4°C containing soluble His-SigB in the supernatant fraction while the pellet fraction was resuspended in equal volume of lysis buffer (1× PBS). The protein bands were visualized by electrophoresis in denaturing SDS-PAGE after staining with Coomassie R-250 as

mentioned above. Semiquantitative analysis of the gels was performed with Quantity One software (Bio-Rad).

*2.3.3. Temperature Optimization.* To optimize suitable temperature for protein expression, the best expressing host strain cultured at different temperatures, viz., 37°C, 25°C, and 16°C. The cells were induced with 0.1 mM IPTG at 37°C and 25°C for 3 hours, while at 16°C for 12 hours with shaking at 150 rpm. The protein bands were visualized by SDS-PAGE, and solubility fractionation analysis was done as above.

*2.3.4. Time Point Optimization.* To check the best time point for the expression of His-SigB in the best expressing host strain, it was induced with 0.1 mM IPTG at 25°C/150 rpm for different time intervals, viz., 0, 15, 30, 60, 120, and 180 min. The expression profile was visualized in 10% SDS PAGE.

*2.4. His-SigB Purification and Immunoblotting.* The recombinant His-SigB was purified by affinity using Ni-NTA beads as per manufacturer's instructions. Briefly, the cells were lysed by sonication at 15% amplitude in buffer A (Tris.Cl 50 mM (pH 8.0), NaCl 300 mM, imidazole 10 mM, Triton X-100 1% (v/v), PMSF 2 mM, lysozyme 1 mg/ml), and the soluble lysate was clarified by centrifugation at 13,000 rpm (RCF 14,926 × g) for 15 min. at 4°C. The preequilibrated Ni-NTA beads (Qiagen) in buffer A were incubated with the lysate at 4°C for 30 mins., washed thrice with buffer B (Tris.Cl 50 mM (pH 8.0), NaCl 300 mM, Imidazole 50 mM, Triton X-100 0.5% (v/v)), and eluted thrice with buffer C (Tris.Cl 50 mM (pH 8.0), NaCl 300 mM, imidazole 400 mM, Triton X-100 0.5% (v/v)).

The purified His-SigB was resolved by SDS-PAGE and transferred to the PVDF membrane followed by blocking in 5% (w/v) skimmed milk powder (HiMedia laboratories) in 1× PBST (phosphate saline buffer containing 0.1% Tween-20). The blot was washed thrice by 1× PBST and incubated with anti-His antibody (0.5 $\mu$g/$\mu$l, 1 : 1000 in 1% PBST; Puregene) for 1 hr., washed with PBST, and further incubated with secondary antibody anti-Mouse IgG (H + L peroxidase/HRP conjugated, 1 : 5000 Pure gene Genetix Biotech) in PBST. Finally, the blot was washed thrice by PBST, developed in Clarity$^{Tm}$ ECL Bio-Rad, and analyzed by the ChemiDoc Imaging System (Bio-Rad).

*2.5. Homology Modeling and Structural Comparison of SigA and SigB.* The protein sequences of *M. smegmatis* sigma factors SigA and SigB were retrieved from the National Center for Biotechnology Information (NCBI) database [29]. To construct the homology models, the amino acid sequences of both the proteins were submitted to Phyre$^2$ server [30]. Phyre$^2$ server utilizes multiple templates to produce the accurate model of the protein. In case of *M. smegmatis* SigA, three templates were used, namely, 5TW1 (RNA polymerase sigma factor) [31], 6C05 (crystal structure of RNA polymerase sigma factor from *M. tuberculosis*) [32], and 4YG2 (X-ray crystal structure of sigma 70 holoenzyme from *E. coli*) [33] with percent identities of 99%, 97%, and 55%, respectively. Similarly, the *M. smegmatis* SigB model was build using two templates 5TW1 (RNA polymerase sigma factor) [31] and 6C05 (crystal structure of RNA polymerase sigma factor from *M. tuberculosis*) [32] with percent identities of 65% and 64%, respectively. Both the models were validated on SAVES server using PROCHECK tool [34].

*2.6. Protein-Protein Docking of Core RNA Polymerase (RNAP) and SigB.* The protein-protein docking utilizes a multistage method for generating poses followed by their rankings. Here, we have used MOE platform [35] for the protein-protein docking experiment of core RNA polymerase (RNAP) and SigB upon importing RNAP (PDB ID: 6EYD [36]) to MOE (https://www.chemcomp.com/Products.htm), workbench. Structure issues such as missing atoms and missing chains were automatically corrected using quick prep module. Optimal hydrogen positions and charges were optimized using protonated 3D module using the MOE software recommended settings. We have used here core enzyme of 6YED [36] PDB without sigma factor A (SigA). Before commencement of docking, bad crystallographic contacts or other imperfect geometries were overcome by the energy minimization method using Amber EHT 10 force field recommended by the MOE platform. Energy minimize application itself can be used to adjust hydrogens and lone pairs and to calculate partial charges. Similarly, SigB protein was prepared before docking. The SigB model was considered as ligand, and PDB ID: 6YED [36] was considered as a receptor. After the docking run, the appropriate protein-protein fingerprints were generated for each pose which can be viewed using the PLIF visualization panel. Approximately, 100 coordinates were developed according to the binding energy. The best twenty dock complexes were considered for analysis.

## 3. Results

*3.1. Expression Host Strain Optimization for the Expression of Recombinant His-SigB.* The pET28a vector belongs to the pET series of vectors that contain a T7 promoter with *lac* operator for the IPTG inducible expression of downstream recombinant genes. However, these genes can only be expressed when T7 RNA polymerase is made available in expression hosts containing a DE3 lysogen under the control of IPTG inducible lacUV5 promoter in their genomic DNA [27]. Hence, we utilized three expression host strains of *E. coli* containing the DE3 lysogen, viz., BL21 (DE3), C41 (DE3), and CodonPlus (DE3) for the optimization of the expression of recombinant His-SigB. Empty pET28a vector and uninduced recombinant His-SigB clones were used as negative control for the expression host strains BL21 (DE3), C41 (DE3), and CodonPlus (DE3) in Figure 1 (lanes: V.O. and U), respectively. These negative controls did not show any expression of the recombinant His-SigB as depicted in Figure 1. However, the maximum expression of the recombinant His-SigB (~42 kDa) is observed in the expression host CodonPlus (DE3) followed by C41 (DE3) and BL21 (DE3), respectively (lane I for each cell type in Figure 1).

*3.2. Optimization of IPTG Concentration for Recombinant His-SigB.* CodonPlus (DE3) depicted the maximum

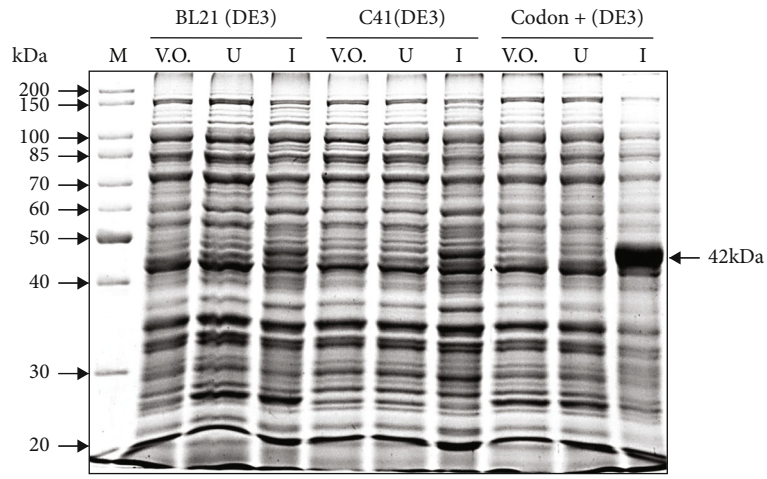


Figure 1: Expression host strain optimization for the expression of recombinant His-SigB. 10% SDS PAGE depicting recombinant His-SigB protein expression profile from three expression host strains, namely, BL21(DE3), C41 (DE3), and CodonPlus (DE3) expressed with 0.1 mM IPTG grown for 3 hrs at 37°C with shaking at 150 rpm. The highest protein expression is observed in the host strain CodonPlus (DE3). M: molecular size marker; V.O.: pET28a vector only control; U: uninduced His-SigB clone; I: induced His-SigB clone.

expression of the recombinant His-SigB protein; hence, it was decided to optimize the maximum protein expression at different IPTG concentrations (0.05-0.5 mM). The expression of His-SigB at IPTG concentrations: 0.05, 0.1, and 0.25 mM was comparable which was approximately 30% higher than the expression at 0.5 mM concentration (as depicted in Figures 2(a) and 2(c)). Amongst the three concentrations, the best expression was found in 0.1 mM IPTG. When the pellet and supernatant fractions of the induced CodonPlus (DE3) cells were observed, comparable distribution of the soluble His-SigB protein was observed in the supernatant fractions at different IPTG concentrations as depicted in Figures 2(b) and 2(d). However, total expression and relative solubility of the recombinant His-SigB were optimum at 0.1 mM IPTG concentration which was selected further studies.

*3.3. Temperature Optimization for the Expression of Recombinant His-SigB Protein.* At the optimized IPTG concentration of 0.1 mM, His-SigB was induced at 37°C as well as lower temperatures, viz., 25°C and 16°C for increasing the relative solubility of His-SigB. The maximum expression of His-SigB was obtained at 37°C and the expression decreased drastically to approximately 62% and 54% at temperatures: 25°C and 16°C, respectively (Figures 3(a) and 3(c) as compared to that at 37°C. However, when the distribution of the soluble His-SigB protein was observed in the supernatant fractions at different temperatures, it was observed that almost 31%, 55%, and 54% of the total induced proteins fractionated to supernatant at temperatures: 37°C, 25°C, and 16°C, respectively (Figure 3(b) and 3(d)). Thus, higher total expression and maximum relative solubility of the recombinant His-SigB were observed at 25°C temperature.

*3.4. Time Course Experiments, Ni-NTA Affinity Purification, and Immunoblotting of Purified His-SigB.* The time course experiment was carried out with for determining the maximum expression of soluble His-SigB protein at the optimized conditions of 25°C with 0.1 mM IPTG for different time points, viz., 0, 15, 30, 60, 120, and 180 minutes. The maximum expression was observed at 180 minutes after the IPTG induction as depicted in Figure 4(a).

His-SigB protein was purified using Ni-NTA affinity chromatography. The affinity purified His-SigB protein was found to have minimal proteolytic degradation as depicted by the Coomassie stained gel in Figure 4(b). In spite of the short half-life of His-SigB, approximately 2 mg-2.2 mg/l culture of the protein was purified. To further rule out the possibility of proteolytic degradation of the recombinant protein, immunoblotting was performed using a monoclonal anti-6XHis antibody. It was observed that a highly purified His-SigB protein without any proteolytic degradation was obtained under the conditions optimized in this article as depicted in Figure 4(c).

*3.5. Structural Characterization of SigA and SigB.* The Ramachandran plots for *M. smegmatis* SigA and SigB proteins demonstrate 98.1% and 98.7% residues falling in the allowed regions, respectively (Supplementary Figure 1). The models of SigA and SigB, however, also exhibited few structural differences. *M. smegmatis* SigA differs from SigB in possessing an N-terminal extended domain. It has been observed that the presence of N-terminal extended domain provides stability to the molecule and consequently, and SigA is comparatively more stable than SigB.

The C-terminal domains of SigA and SigB are composed of four $\alpha$-helices. The first and the fourth $\alpha$-helices of the domain lie adjacent to one another in a parallel fashion and run in opposite directions. The second and fourth helices are shorter than the first and third helices. Furthermore, second and fourth helices are connected to the ends of third helix in perpendicular manner through short loops (Figures 5(a) and 5(b)). The region connecting the first and second helix could not be modeled precisely.

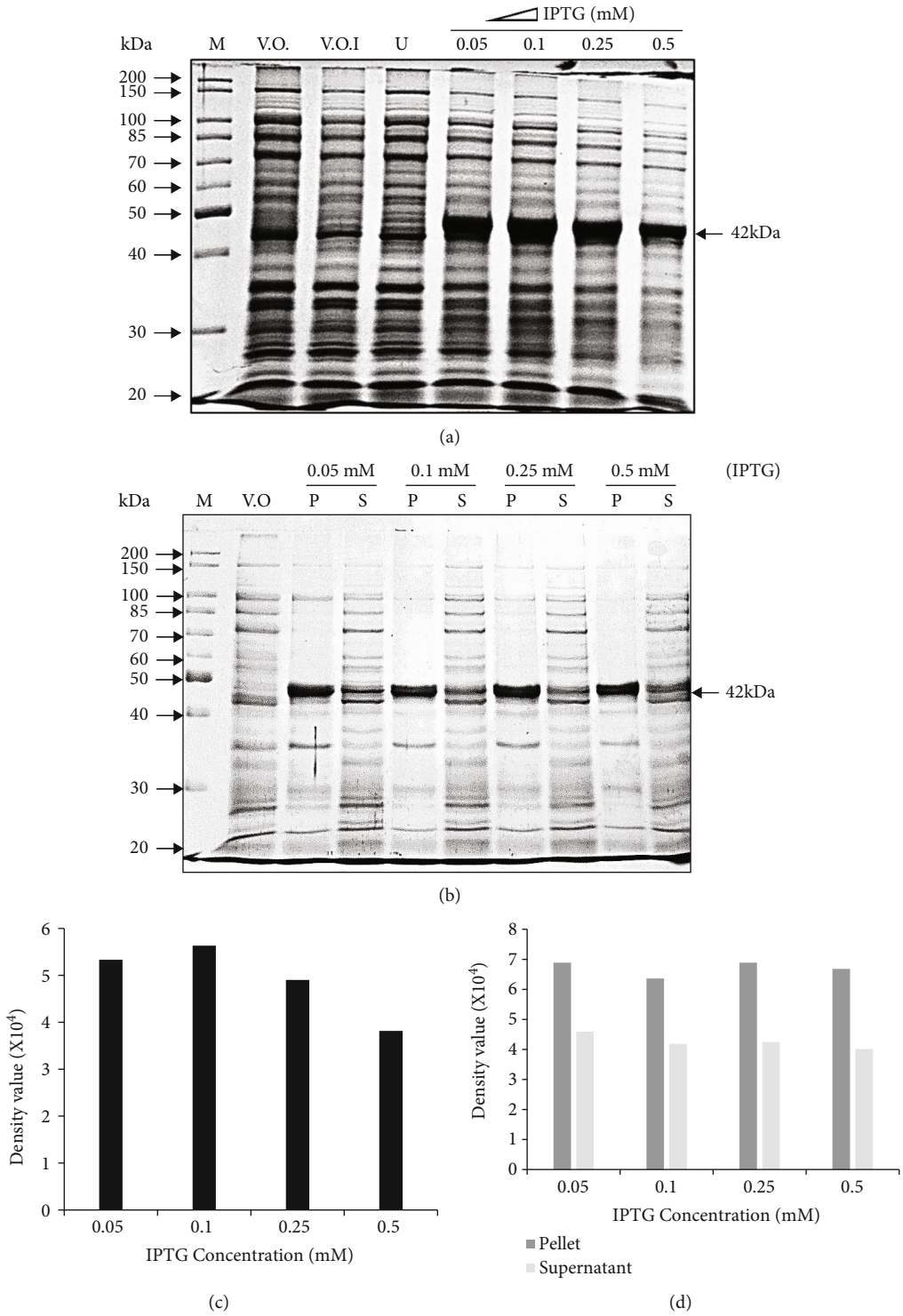


Figure 2: IPTG concentration optimization for the expression of recombinant His-SigB. (a) 10% SDS PAGE depicting recombinant His-SigB protein expression profile in CodonPlus (DE3) host strain. The highest protein expression is observed in 0.1 mM IPTG. (b) Solubility of the recombinant His-SigB in different IPTG concentrations at 37°C. 10% SDS PAGE depicting recombinant His-SigB protein distribution in cell pellet and supernatant in CodonPlus (DE3) induced with IPTG concentration from 0.05 to 0.5 mM IPTG. The highest protein solubility observed in the supernatant fraction at 0.1 mM IPTG. M: molecular size marker; V.O.: pET28a vector only control; V.O.I: pET28a vector only induced; U: uninduced His-SigB clone; P: pellet; S: supernatant. (c) Gel-based semiquantitative analysis from (a) also depicts the highest expression of His-SigB at 0.1 mM IPTG concentration. (d) Semiquantitative analysis from (b) depicts higher relative protein solubility observed in the supernatant fraction at 0.1 mM IPTG. Semiquantitative analysis of the gels was performed with Quantity One software (BIO-RAD).

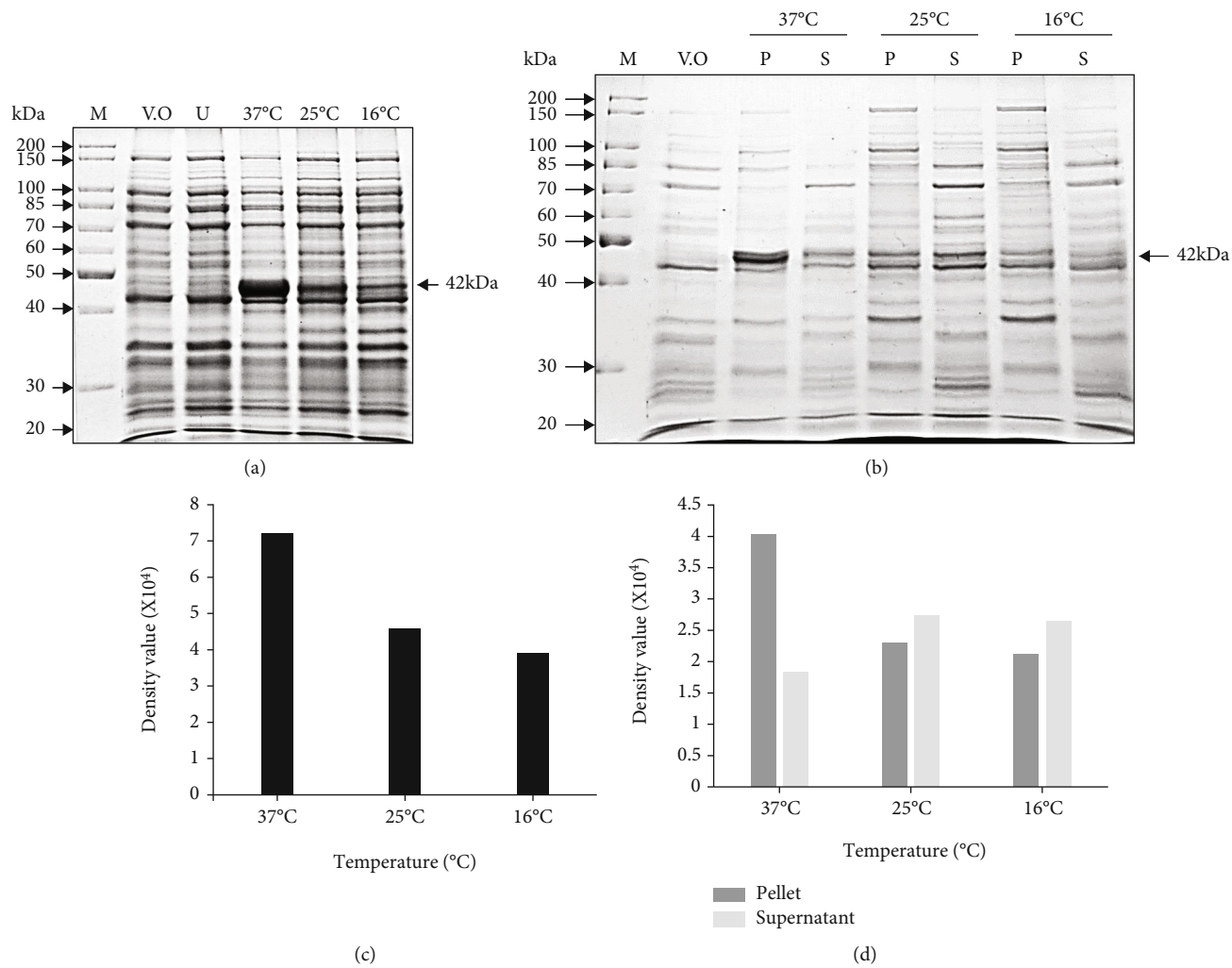


Figure 3: Temperature optimization for the expression of recombinant His-SigB protein. (a) 10% SDS PAGE depicting recombinant His-SigB protein expression profile in CodonPlus (DE3) cells at temperatures: 37°C, 25°C, and 16°C with 0.1 mM IPTG. The highest protein expression was observed at 37°C. (b) 10% SDS PAGE depicting distribution of recombinant His-SigB protein in cell pellet and supernatant fractions at different temperatures. The highest protein solubility was observed at 25°C supernatant fraction. M: marker; V.O.: pET28a vector only control; U: uninduced His-SigB clone; P: pellet; S: supernatant. (c) Gel-based semiquantitative analysis from (a) depicts the highest expression of His-SigB at 37°C with 0.1 mM IPTG concentration. (d) Semiquantitative analysis from (b) depicts higher relative protein solubility observed in the supernatant fraction at 25°C with 0.1 mM IPTG. Semiquantitative analysis of the gels was performed with Quantity One software (BIO-RAD).

*3.6. Molecular Interactions of RNAP and SigB.* Conformational changes of RNAP are required to initiate the transcription process. To investigate the interactions of SigB with RNAP, protein-protein docking experiment was performed. The protein-protein docking experiment revealed SigB bound to RNAP with binding energy of -70.39 (sixteen dock complexes). The *M. smegmatis* RNAP is composed of five subunits including $\alpha$ (two copies of chains A and B), $\beta$ (chain C), $\beta'$ (chain D), and $\omega$ (chain E) (Figure 5(c). These five chains together formed the core enzyme and help to synthesize the RNA using DNA as template and ribonucleotides as the substrate. To start this process, the core enzyme has to bind to a sigma factor. In RNAP of *M. smegmatis*, chains C and D mainly interact with SigB (Figure 5(d)). Arg846 and Leu408 of chain C and Arg67, Thr38, Lys64, Thr150, Arg345, Glu250, and Glu275 of chain D play a major role in the molecular interactions with SigB which are in contrast with the molecular interactions of SigA.

## 4. Discussion

Although, SigB is dispensable for growth in both Msmeg and Mtb [15, 37], nevertheless, SigB acts as a general stress responsive transcription factor. The importance of SigB protein is elucidated by the fact that it occurs downstream in the signaling pathways of several stress responsive ECF and other sigma factors [13, 14, 22]. The expression of recombinant SigB has been mentioned in reference to the in vitro transcription assay experiment in BL21 (DE3) strain which is deficient of lon and omp-t proteases and is therefore suitable for expression of nontoxic genes but the SigB protein is very poorly expressed in this strain as demonstrated from

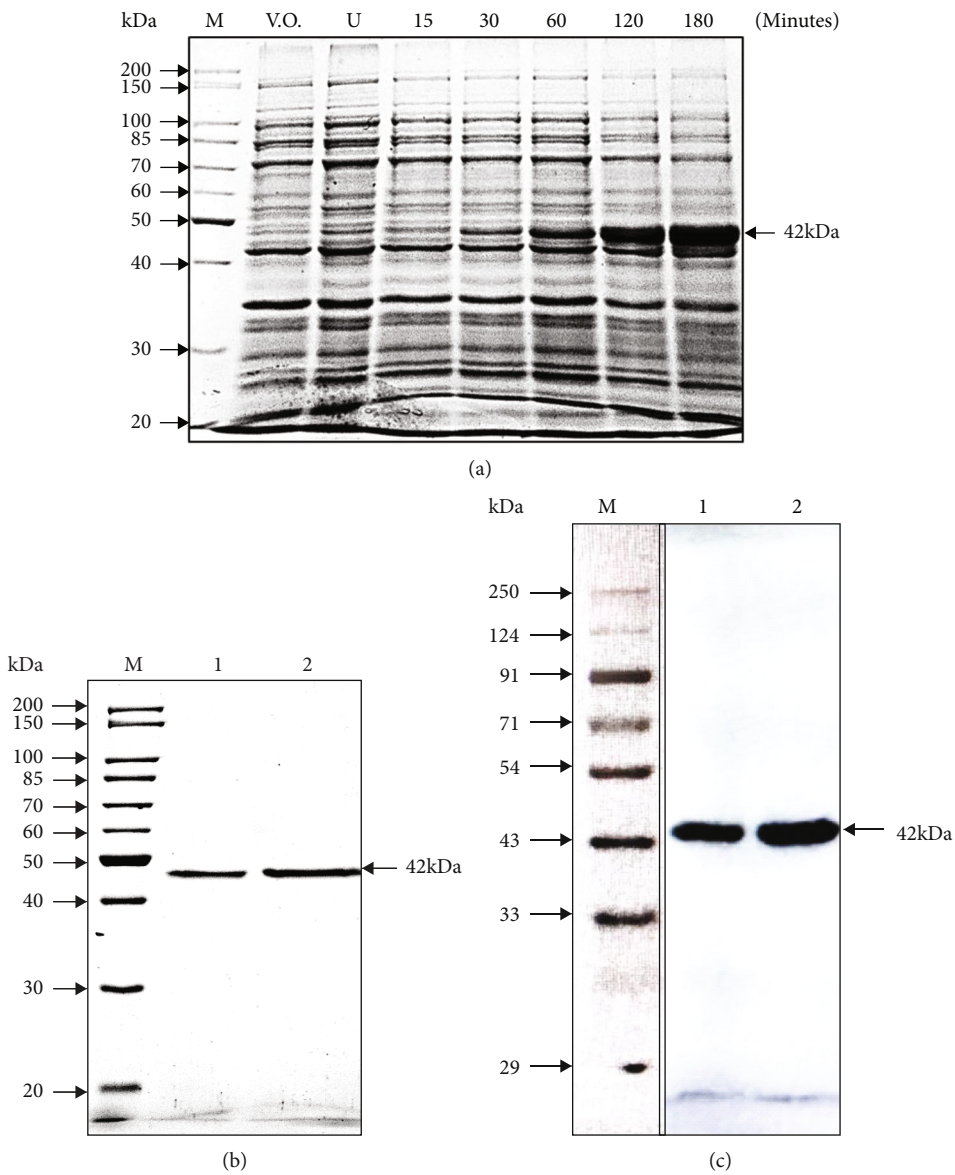


Figure 4: (a) The expression of recombinant His-SigB protein at different time points. 10% SDS PAGE depicting recombinant His-SigB protein expression profile collected at time points 15, 30, 60, 120, and 180 minutes. The highest protein expression was observed at 180 minutes after induction with 0.1 mM IPTG. (b) Ni-NTA affinity purification of His-SigB: lanes denoting M: molecular size marker; 1: 5 $\mu$g; 2: 7.5 $\mu$g His-SigB purified protein stained with Coomassie R-250. (c) Western blotting with purified recombinant His-SigB. Mouse anti-His monoclonal antibody (Genetix) was used to probe purified His-SigB. M: marker; V.O.: pET28a vector only control; U: uninduced His-SigB clone; lane 1: 5 $\mu$g; lane 2: 10 $\mu$g purified His-SigB protein.

our results (Figure 1) [14]. This leads us to express SigB in other alternative strains like C41 (DE3) and CodonPlus (DE3). C41 (DE3), derived from BL21 (DE3), contains an uncharacterized mutation that prevents cell death due to the expression of many toxic recombinant proteins. Hence, it is often utilized for the expression of toxic and membrane proteins from all classes of organisms [38]. However, in our case, it leads to only a marginal increase in the expression of recombinant SigB (Figure 1). CodonPlus (DE3) improves the protein expression by preventing codon bias and by providing additional copies of specific tRNA genes, viz., argU, ileY, leuW, and proL genes that recognize AGA/AGG, AUA, CUA, and CCC codons, respectively, that are rare in *E. coli* and occur commonly in GC-rich genomes like Mycobacterium [39, 40]. SigB of Msmeg in our case contains at least 8 prolines out of which 2 are encoded by CCC codons which might be an important reason for the lower expression in other strains utilized.

During the optimization with different IPTG concentrations, it was clearly observed that the total protein expression was higher at 0.1 mM IPTG concentration (Figures 2(a) and 2(c) with comparable relative expression of soluble SigB at IPTG concentrations like 0.05-0.25 mM (Figures 2(b) and 2(d). Since, the total expression was higher at 0.1 mM with comparable solubility; hence, 0.1 mM was finally selected for final expressions. Greater IPTG often leads to faster

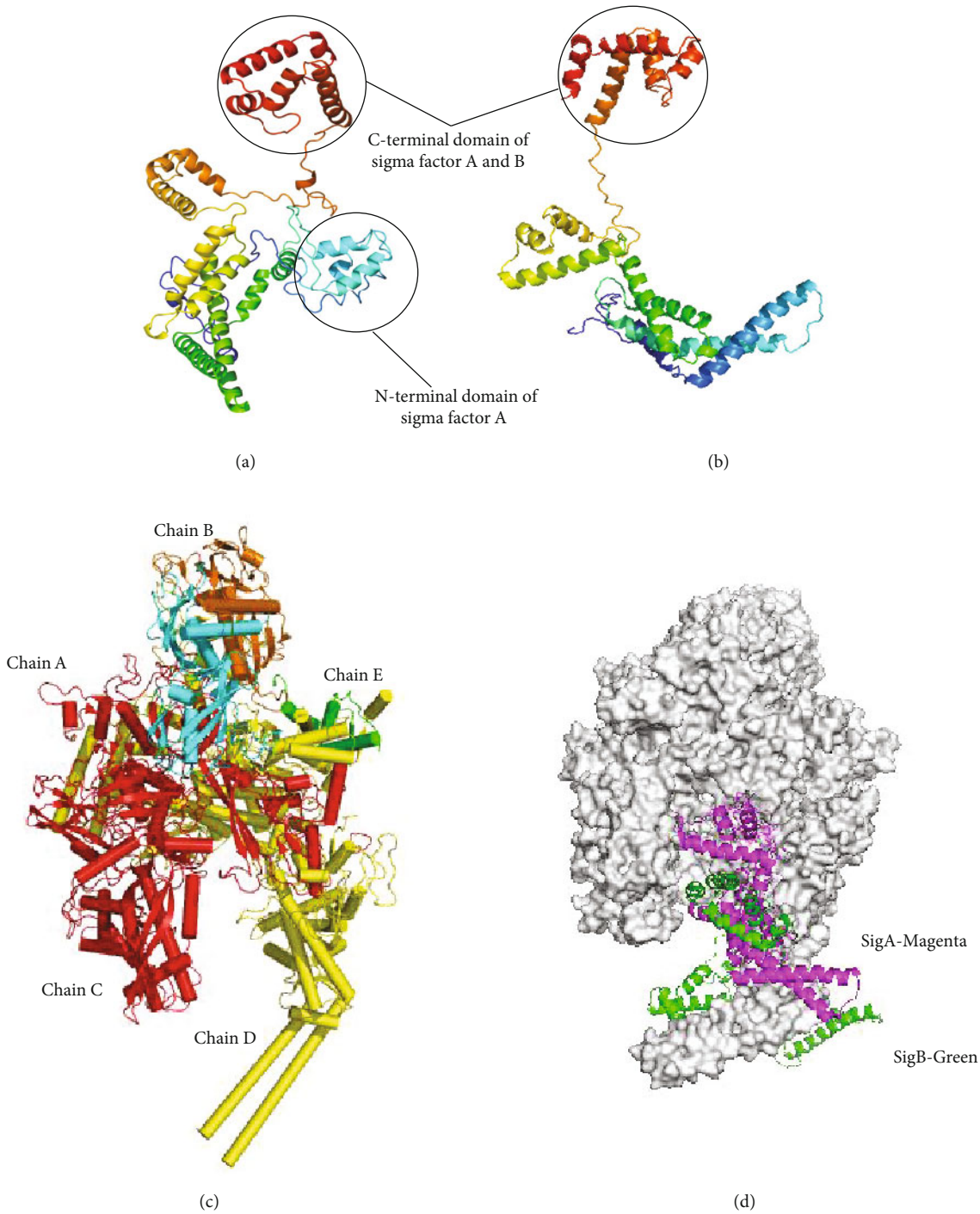


Figure 5: Homology models of (a) *M. smegmatis* sigma factor SigA, (b) *M. smegmatis* sigma factor SigB, (c) structure of the core RNA polymerase of *M. smegmatis*, and (d) comparative surface topology of SigA and SigB interactions with core RNA polymerase of *M. smegmatis*.

protein expression resulting in increased formation of inclusion bodies; hence, higher IPTG concentrations were not included for final expressions. Similarly, when three different temperatures were utilized for the SigB expression, there was a drastic decrease in the expression from 38% to 46% at 25°C and 16°C, respectively, as compared to that at 37°C. However, the relative fraction of total protein expressed as soluble fraction in the supernatant was much greater at lower temperatures like 25°C and 16°C. The intermediate temperature of 25°C was best suited for our experimental work (Figure 3). The IPTG induction of recombinant proteins like human RNase L, human growth hormone (hGH), and several other proteins at lower temperatures in bacteria favors relatively higher yield of the expressed protein in the soluble fraction of the cell [41–47]. The experimental conditions optimized above for the recombinant SigB expression provided a high

yield of soluble and proteolytically undergraded protein which can be visualized by the immunoblotting of purified SigB using a monoclonal anti-6XHis antibody, since no degradation products could be visualized at higher concentrations of the purified protein (Figure 5).

However, the highly unstable nature of this protein can be further improved by using various stabilizers and (or) another cofactor so that future experiments like protein-protein interactions and crystallization of SigB can be carried out smoothly. *M. smegmatis* RNA polymerases SigA and Sig B showed 60% sequence identity. Sigma factor A differs from sigma factor B in possessing N-terminal domain, which may provide stability. Our docking studies demonstrated that SigB binds to RNAP where chain C and chain D of RNAP play a significant role in molecular interactions. In silico comparative binding studies of SigA and SigB demonstrated that they both bind to similar regions of RNAP. In future, our aim will be to cocrystallize SigB-RNAP together to better understand the mechanism of their molecular interactions.

## 5. Conclusion

SigB has significant similarities with house-keeping sigma factor SigA with regards to the domain organization; however, it has drastically short half-life as compared to SigA. Despite its short half-life, it is also involved in multiple stress response regulatory pathways of *Mycobacterium* in coordination with ECF and other sigma factors. Higher quantities of soluble and purified recombinant SigB are essential for the study of its structure, function, and regulation but there is dearth of literature that depicts it. In this report, we demonstrate an efficient method for the production of soluble and purified recombinant His-SigB protein that can be used as a tool to unravel the structure, function, and regulation of its signaling cascade.

## Data Availability

The data used in this study to support the findings are available from the corresponding author upon request.

## Disclosure

This manuscript has been presented as a preprint in research square (https://new.bhu.ac.in/Site/FacultyProfile/1_149?FA000066/).

## Conflicts of Interest

The authors declare no conflict of interest.

## Acknowledgments

We acknowledge the financial assistance in the form of Senior Research Fellowships (SRF) to RKS and LKJ from the Indian Council of Medical Research (ICMR) and to TN from University Grants Commission (UGC), New Delhi, and Dr. SNR as UGC D.S. Kothari Postdoctoral Fellowship (Ref. no. F.4/2006 (BSR)/BL/20/0032) and the Inter Disciplinary School of Life Sciences (ISLS), BHU, Varanasi, for providing the instrumentation facility.

## Supplementary Materials

Supplementary Figure 1: Ramachandran plots for the homology models of (a) *M. smegmatis* SigA and (b) *M. smegmatis* SigB. *(Supplementary Materials)*

## References

[1] K. S. Murakami, S. Masuda, and S. Darst, "Structural basis of transcription initiation: RNA polymerase holoenzyme at 4 Å resolution," *Science*, vol. 296, no. 5571, pp. 1280–1284, 2002.

[2] D. G. Vassylyev, S. I. Sekine, O. Laptenko et al., "Crystal structure of a bacterial RNA polymerase holoenzyme at 2.6 Å resolution," *Nature*, vol. 417, no. 6890, pp. 712–719, 2002.

[3] R. Manganelli, E. Dubnau, S. Tyagi, F. R. Kramer, and I. Smith, "Differential expression of 10 sigma factor genes in Mycobacterium tuberculosis," *Molecular Microbiology*, vol. 31, no. 2, pp. 715–724, 1999.

[4] S. Wu, S. T. Howard, D. L. Lakey et al., "The principal sigma factor sigA mediates enhanced growth of Mycobacterium tuberculosis in vivo," *Molecular Microbiology*, vol. 51, no. 6, pp. 1551–1562, 2004.

[5] M. S. B. Paget and J. D. Helmann, "The $\sigma$70 family of sigma factors," *Genome Biology*, vol. 4, no. 1, pp. 203–206, 2003.

[6] D. F. Browning and S. J. W. Busby, "The regulation of bacterial transcription initiation," *Nature Reviews. Microbiology*, vol. 2, no. 1, pp. 57–65, 2004.

[7] T. M. Gruber and C. A. Gross, "Multiple sigma subunits and the partitioning of bacterial transcription space," *Annual Review of Microbiology*, vol. 57, no. 1, pp. 441–466, 2003.

[8] B. M. Koo, V. A. Rhodius, G. Nonaka, P. L. DeHaseth, and C. A. Gross, "Reduced capacity of alternative $\sigma$s to melt promoters ensures stringent promoter recognition," *Genes & Development*, vol. 23, no. 20, pp. 2426–2436, 2009.

[9] A. Feklistov and S. A. Darst, "Promoter recognition by bacterial alternative $\sigma$ factors: the price of high selectivity?: figure 1," *Genes & Development*, vol. 23, no. 20, pp. 2371–2375, 2009.

[10] J. C. Betts, P. T. Lukey, L. C. Robb, R. A. McAdam, and K. Duncan, "Evaluation of a nutrient starvation model of Mycobacterium tuberculosis persistence by gene and protein expression profiling," *Molecular Microbiology*, vol. 43, no. 3, pp. 717–731, 2002.

[11] D. Schnappinger, S. Ehrt, M. I. Voskuil et al., "Transcriptional adaptation of Mycobacterium tuberculosis within macrophages: insights into the phagosomal environment," *The Journal of Experimental Medicine*, vol. 198, no. 5, pp. 693–704, 2003.

[12] Y. Hu and A. R. M. Coates, "Transcription of two sigma 70 homologue genes, sigA and sigB, in stationary-phase Mycobacterium tuberculosis," *Journal of Bacteriology*, vol. 181, no. 2, pp. 469–476, 1999.

[13] P. Sachdeva, R. Misra, A. K. Tyagi, and Y. Singh, "The sigma factors of mycobacterium tuberculosis: regulation of the regulators," *The FEBS Journal*, vol. 277, no. 3, pp. 605–626, 2010.

[14] J. H. Lee, P. C. Karakousis, and W. R. Bishai, "Roles of SigB and SigF in the Mycobacterium tuberculosis sigma factor network," *Journal of Bacteriology*, vol. 190, no. 2, pp. 699–707, 2008.

[15] P. A. Fontan, M. I. Voskuil, M. Gomez et al., "TheMycobacterium tuberculosissigma factor σBIs required for full response to cell envelope stress and hypoxia in vitro, but it is dispensable for in vivo growth," *Journal of Bacteriology*, vol. 191, no. 18, pp. 5628–5633, 2009.

[16] T. R. Rustad, K. J. Minch, W. Brabant et al., "Global analysis of mRNA stability in Mycobacterium tuberculosis," *Nucleic Acids Research*, vol. 41, no. 1, pp. 509–517, 2013.

[17] J. A. Bernstein, A. B. Khodursky, P. H. Lin, S. Lin-Chao, and S. N. Cohen, "Global analysis of mRNA decay and abundance inEscherichia coliat single-gene resolution using two-color fluorescent DNA microarrays," *Proceedings of the National Academy of Sciences of the United States of America*, vol. 99, no. 15, pp. 9697–9702, 2002.

[18] H. I. Zgurskaya, M. Keyhan, and A. Matin, "The σS level in starving Escherichia coli cells increases solely as a result of its increased stability, despite decreased synthesis," *Molecular Microbiology*, vol. 24, no. 3, pp. 643–651, 1997.

[19] E. Dainese, S. Rodrigue, G. Delogu et al., "Posttranslational regulation ofMycobacterium tuberculosisextracytoplasmic-function sigma factor σland roles in virulence and in global regulation of gene expression," *Infection and Immunity*, vol. 74, no. 4, pp. 2457–2461, 2006.

[20] M. Riccardo, I. V. Martin, K. S. Gary, and S. Issar, "The Mycobacterium tuberculosis ECF sigma factor σE: role in global gene expression and survival in macrophages†," *Molecular Microbiology*, vol. 41, no. 2, pp. 423–437, 2001.

[21] S. Raman, T. Song, X. Puyang, S. Bardarov, J. Jacobs, and R. N. Husson, "The alternative sigma factor sigh regulates major components of oxidative and heat stress responses in mycobacterium tuberculosis," *Journal of Bacteriology*, vol. 183, no. 20, pp. 6119–6125, 2001.

[22] R. Chauhan, J. Ravi, P. Datta et al., "Reconstruction and topological characterization of the sigma factor regulatory network of Mycobacterium tuberculosis," *Nature Communications*, vol. 7, no. 1, p. 12, 2016.

[23] M. Ando, T. Yoshimatsu, C. Ko, P. J. Converse, and W. R. Bishai, "Deletion of mycobacterium tuberculosis sigma factor E results in delayed time to death with bacterial persistence in the lungs of aerosol-infected mice," *Infection and Immunity*, vol. 71, no. 12, pp. 7170–7172, 2003.

[24] D. E. Geiman, D. Kaushal, C. Ko et al., "Attenuation of late-stage disease in mice infected by the mycobacterium tuberculosis mutant lacking the SigF alternate sigma factor and identification of SigF-dependent genes by microarray analysis," *Infection and Immunity*, vol. 72, no. 3, pp. 1733–1745, 2004.

[25] M. Y. Hahn, S. Raman, M. Anaya, and R. N. Husson, "The mycobacterium tuberculosis extracytoplasmic-function sigma factor SigL regulates polyketide synthases and secreted or membrane proteins and is required for virulence," *Journal of Bacteriology*, vol. 187, no. 20, pp. 7062–7071, 2005.

[26] D. Kaushal, B. G. Schroeder, S. Tyagi et al., "Reduced immunopathology and mortality despite tissue persistence in aMycobacterium tuberculosismutant lacking alternative σ factor, SigH," *Proceedings of the National Academy of Sciences of the United States of America*, vol. 99, no. 12, pp. 8330–8335, 2002.

[27] J. Sambrook, E. Fritsch, and T. Maniatis, *Molecular Cloning: A Laboratory Manual*, Cold spring Harbor laboratory, 1989.

[28] W. C. Tsai, T. C. Wu, B. L. Chiang, and H. W. Wen, "Cloning, expression, and purification of recombinant major mango allergen Man i 1 in Escherichia coli," *Protein Expression and Purification*, vol. 130, pp. 35–43, 2017.

[29] E. W. Sayers, R. Agarwala, E. E. Bolton et al., "Database resources of the National Center for biotechnology information," *Nucleic Acids Research*, vol. 47, p. 13, 2019.

[30] L. A. Kelley, S. Mezulis, C. M. Yates, M. N. Wass, and M. J. E. Sternberg, "The Phyre2 web portal for protein modeling, prediction and analysis," *Nature Protocols*, vol. 10, no. 6, pp. 845–858, 2015.

[31] E. A. Hubin, A. Fay, C. Xu et al., "Structure and function of the mycobacterial transcription initiation complex with the essential regulator RbpA," *eLife*, vol. 6, no. 1, p. 40, 2017.

[32] H. Boyaci, J. Chen, M. Lilic et al., "Fidaxomicin jams Mycobacterium tuberculosis RNA polymerase motions needed for initiation via RBPA contacts," *eLife*, vol. 7, no. 1, p. 19, 2018.

[33] K. S. Murakami, "X-ray crystal structure of Escherichia coli RNA polymerase σ70 holoenzyme," *The Journal of Biological Chemistry*, vol. 288, no. 13, pp. 9126–9134, 2013.

[34] R. A. Laskowski, M. W. MacArthur, D. S. Moss, and J. M. Thornton, "PROCHECK: a program to check the stereochemical quality of protein structures," *Journal of Applied Crystallography*, vol. 26, no. 2, pp. 283–291, 1993.

[35] *Molecular Operating Environment (MOE)*, Chemical Computing Group Inc., 1010 Sherbooke St. West, Suite #910, Montreal, QC, Canada, H3A 2R7, 2012.

[36] T. Kouba, J. Pospíšil, J. Hnilicová, H. Šanderová, I. Barvík, and L. Krásný, "The core and holoenzyme forms of RNA polymerase fromMycobacterium smegmatis," *Journal of Bacteriology*, vol. 201, no. 4, p. e00583, 2019.

[37] R. Mukherjee, M. Gomez, N. Jayaraman, I. Smith, and D. Chatterji, "Hyperglycosylation of glycopeptidolipid of Mycobacterium smegmatis under nutrient starvation: structural studies," *Microbiology*, vol. 151, no. 7, pp. 2385–2392, 2005.

[38] L. Dumon-Seignovert, G. Cariot, and L. Vuillard, "The toxicity of recombinant proteins in Escherichia coli : a comparison of overexpression in BL21(DE3), C41(DE3), and C43DE3," *Protein Expression and Purification*, vol. 37, no. 1, pp. 203–206, 2004.

[39] C.-P. Carstens and A. Waesche, "Codon bias-adjusted BL21 derivatives for protein expression," *Strategies*, vol. 12, no. 2, pp. 49–51, 1999.

[40] X. Hu, Q. Shi, T. Yang, and G. Jackowski, "Specific Replacement of Consecutive AGG Codons Results in High-Level Expression of Human Cardiac Troponin T in Escherichia coli," *Protein Expression and Purification*, vol. 7, no. 3, pp. 289–293, 1996.

[41] A. Gupta and P. C. Rath, "Expression, purification and characterization of the interferon-inducible, antiviral and tumour-suppressor protein, human RNase L," *Journal of Biosciences*, vol. 37, no. 1, pp. 103–113, 2012.

[42] M. J. Kim, H. S. Park, K. H. Seo, H. J. Yang, S. K. Kim, and J. H. Choi, "Complete solubilization and purification of recombinant human growth hormone produced in Escherichia coli," *PLoS One*, vol. 8, no. 2, pp. 1–8, 2013.

[43] M. Li, W. Cui, C. Mo, J. Wang, Z. Zhao, and M. Cai, "Cloning, expression, purification, antiserum preparation and its characteristics of the truncated UL6 protein of herpes simplex virus 1," *Molecular Biology Reports*, vol. 41, no. 9, pp. 5997–6002, 2014.

[44] K. M. Santosh, K. Nitish, K. Gautam, K. Tara, and P. Krishna, "Recombinant human interferon regulatory factor-1 (IRF-1)

protein expression and solubilisation study in Escherichia coli," *Molecular Biology Reports*, vol. 45, no. 5, pp. 1367–1374, 2018.

[45] J. Kaur, A. Kumar, and J. Kaur, "Strategies for optimization of heterologous protein expression in _E. coli_ : Roadblocks and reinforcements," *International Journal of Biological Macromolecules*, vol. 106, pp. 803–822, 2018.

[46] X. Zou, Z. Xu, Y. Wang et al., "Expression, purification, and antiserum production of the truncated UL31 protein of herpes simplex virus 1," *Iranian Journal of Biotechnology*, vol. 17, no. 1, pp. 74–79, 2019.

[47] H. P. Sørensen and K. K. Mortensen, "Soluble expression of recombinant proteins in the cytoplasm of Escherichia coli," *Microbial Cell Factories*, vol. 4, no. 1, pp. 1–8, 2005.

Hindawi
Disease Markers
Volume 2022, Article ID 8762936, 11 pages
https://doi.org/10.1155/2022/8762936

*Research Article*

# Effects of Yellow Light on Airborne Microbial Composition and on the Transcriptome of Typical Marker Strain in Ward

**Xuanqi Zhao,[1,2] Jing Wei,[2] Wenjie Chen,[3] Xuan Xu,[4] Ruizhe Zhu,[2] Puyuan Tian,[5] and Tingtao Chen[1,2]**

[1]*School of Life Science, Nanchang University, Nanchang, China*
[2]*National Engineering Research Center for Bioengineering Drugs And The Technologies, Institute of Translational Medicine, Nanchang University, Nanchang, China*
[3]*Queen Mary School, Nanchang University, Nanchang, China*
[4]*Huankui Academy, Nanchang University, Nanchang, China*
[5]*Precision Medicine Institute, The First Affiliated Hospital, Sun Yat-Sen University, Guangdong, China*

Correspondence should be addressed to Puyuan Tian; 461580012@qq.com and Tingtao Chen; chentingtao1984@163.com

Received 1 April 2022; Accepted 27 April 2022; Published 18 May 2022

Academic Editor: Shih-Ping Hsu



Airborne diseases are transmitted by pathogens in the air. The complex microbial environment in wards is usually considered a major cause of nosocomial infection of various diseases which greatly influences the health of patients with chronic diseases, whereas the illuminant of wards impacts on the microbe especially the disease marker strain is seldom studied. In the present study, high-throughput sequencing was used to study the effect of yellow light on airborne microbial composition, and changes of transcriptome of marker strains *Escherichia coli*, *Staphylococcus aureus* and *Pseudomonas aeruginosa*, which were isolated from wards, were further studied after the irradiation by yellow light. High-throughput sequencing results indicated that yellow light significantly decreased $\alpha$-diversity. The relative abundance of Firmicutes at the phylum level, and *Clostridium sensu stricto 1*, *Paraclostridium* at the genus level were significantly reduced. RNA sequencing results declared that yellow light significantly downregulated the genes associated with flagella, heme transport system and carbohydrate, amino acid metabolism in *E. coli*, and the genes related to arginine biosynthesis and the biosynthesis of isoleucine, leucine, and valine in *S. aureus*. Meanwhile, yellow light significantly upregulated the genes relating to porphyrin metabolism *in P. aeruginosa*. In conclusion, our work reveals the impacts of yellow light on the microbe in wards, pointing out the application value of yellow light in the prevention of infectious diseases in clinical practice.

## 1. Introduction

Hospital environment including hospital and healthcare settings [1] has a pivotal impact on patients to meet them with a variety of needs, such as medical care and spiritual comfort [2, 3]. Within the hospital, the indoor air contains suspended particles of multifarious properties and mediates the short-distance and long-distance transmission of microbes made up of bacteria and fungi [4]. Studies have shown that the spreading of microbes is connected with microbial pollution and diseases [5–7]. Thereinto, Proteobacteria, Phylum Firmicutes are wildly distributed in hospital wards and *Escherichia coli*, *Pseudomonas aeruginosa*, and *Staphylococcus aureus* are the most common pathogenetic bacteria in nosocomial acquired infections which mainly transmits in the manner of hospital air [8–13]. The spreading of these bacteria widely in the air causes hospital-acquired infections and occupational diseases [14, 15], affecting children, aged people, chronic patients with a weak immune system, and healthcare workers [16]. Obviously, the increasing in the number or diversity of pathogens will certainly raise the risk of disease. Thus, the risk of infection from airborne

pathogens is an important consideration that must be taken into account on hospital wards for individuals or groups [17].

In recent years, visible light has been shown to have multifarious effects on bacteria [18]. There were significant differences in the composition, abundance, and viability of microbial communities associated with household dust when exposed to sunlight [19]. For these three representative vital pathogenic bacteria of nosocomial infection, many studies have revealed the inactivation effect of visible light. For example, McClary and Boehm irradiated *S. aureus* with full spectrum light 6 hours and measured transcript abundance by RNA sequencing to find out that *S. aureus* was inhibited by full spectrum sunlight [20]. Exposing *S. aureus*, *P. aeruginosa*, and *E. coli* strains to a single blue laser irradiation (450 nm) and counting the number of living bacteria, De Sousa et al. concluded that blue light significantly inhibited the growth of bacteria under low-intensity conditions [21]. Additionally, the effect of yellow light on bacteria has been preliminarily explored. Among them, Weng et al. injected *S. aureus* to construct infected wounds in mice then treat it with yellow light and a ZnO composite, thereby achieving effective sterilization [22]. Zhao et al. utilized yellow light LED and MG1363-pMG36e-mCXCL12 in the treatment of the burn wounds in mice and found that skin pathogens were significantly reduced, excessive inflammatory response was inhibited, and the wound healing was promoted [23].

Currently, there is still no research to evaluate the effect of yellow light on wards microorganisms. There are also few studies on the effect of yellow light on *E. coli*, *S. aureus*, and *P. aeruginosa* at transcriptome level. Hence, in the present study, we first performed high-throughput sequencing method to preliminarily identify the distribution and composition of common microorganisms on the yellow light-treated wards. In order to explore the effect of yellow light on specific pathogenic bacteria in wards, we selected 3 bacteria (including Gram-positive and Gram-negative bacteria) that were highly related with nosocomial infection. These pathogenic bacteria were detected by a viable count method. Meanwhile, we explored the effects of yellow light on *E. coli*, *S. aureus*, and *P. aeruginosa* by conducting the transcriptome analysis of these pathogens. These studies will help to reveal the effect of yellow light on the microorganism in the air of hospital wards and the transcription level of related pathogenic bacteria. This study provides a theoretical basis for the effective control methods of the common pathogenic microorganisms, guiding the prevention of ward infectious diseases, which is of great significance to reduce the nosocomial infection and transmission.

## 2. Materials and Methods

*2.1. Air Sample Collection and Processing.* The study was performed in June 2019 (summer; $T = 30.1^{\circ}$C; RH = 43.8%) in the second affiliated hospital of Nanchang University, Nanchang, China. Analyses were conducted in general ward of gastrointestinal surgery department. The wards are located on the eighth floor of the hospital. Each ward has a door for regular entrance, and the rooms are equipped with natural ventilation with windows. The light treatment of wards consisted of a light-emitting diode (LED) yellow light (570–600 nm, 16 W) or light-emitting diode (LED) white light (all-spectrum, 16 W) for 15 hours a day for 2 months.

Air sampling of each ward was done by impaction using a small flow TSP air sampler (MAS100, Merck KGaA, Darmstadt, Germany) with a flow rate of 10 L/min. Air samples were collected using glass fiber filter sampling membrane with 0.22 $\mu$m pore size, and the sampling time is 72 h. Air sampling was performed at a height of 1.0 m above the floor to simulate the breathing zone. After removing the sampling membrane, we wrap it with tin foil and store at -80°C.

*2.2. Acquisition and Treatment of Bacterial Strains.* Strains of *E. coli* ATCC 25922, *S. aureus* ATCC 25923, and *P. aeruginosa* ATCC 27853 were obtained from the American Type Culture Collection (ATCC) and were provided by the clinical laboratory of the second affiliated hospital of Nanchang University.

The above strains were grown in LB overnight and then subcultured into fresh medium and grown at 37°C with aeration to an $OD_{600}$ of 1.0. 100 $\mu$L bacterial cultures were kept on Petri plates containing Luria-Bertani culture medium (BD, New Jersey, PA) and irradiating with LED yellow light or white light for different durations (8 h, 12 h, 20 h, and 24 h for each group, respectively). After irradiation, the bacteria were incubated at a temperature of 37°C until stable growth period. Then, the standard plate count method was used to determine the total number of viable cells of *E. coli*, *S. aureus*, and *P. aeruginosa* as the colony-forming units (CFU) on nutrient agar media after incubation at 37°C for 24 h.

Each bacterial cultures were irradiating with LED yellow light or white light for different durations (4 h for *E. coli* and *S. aureus*, 8 h for *P. aeruginosa*). All the strains were collected in Eppendorf tube (Trypticase Soy Broth, BD, New Jersey, PA), placed in liquid nitrogen (30 min) for quick freezing, and then stored at -80°C.

*2.3. High-Throughput Sequencing and Data Analysis.* Bioaerosol total genomic DNA was extracted from about the glass fiber filters using TIANamp Bacteria DNA Kit (QIAGEN) following the manufacturer's instructions. Extracted DNA was conducted whole genome sequencing in Shanghai Personal Biotechnology Cp. Ltd.

The concentration and quality of extracted genomic DNA were tested prior to sequencing using the NanoDrop spectrophotometer (Thermo, United States). Primers of 338F/806R were used to amplify the V3-V4 region of 16S rRNA genes of the extracted genomic DNA. FLASH was applied to merge overlapped reads, and sequence analysis was done using UPARSE software package. Reads with quality scores lower than 20, ambiguous bases, and improper primers were discarded before clustering. Simultaneously, chimaeras were checked and eliminated during clustering. The resultant high-quality sequences were clustered into operational taxonomic units (OTUs) at 97% similarity. According to the annotation of taxa, the relative abundance of total bacteria in each sample was categorized to different

classification levels (Kingdom, Phylum, Class, Order, Family, and Genera). The alpha diversity index (Shannon index and Chao 1 index) was calculated, and the beta diversity index (principal component analysis) was mapped in QIIME2 software (version 2019.4). The raw reads were deposited in the Sequence Read Archive (SRA) database of NCBI (PRJNA778878).

*2.4. RNA Sequencing and Data Analysis.* Total bacterial RNA was extracted from strains of *E. coli*, *S. aureus*, and *P. aeruginosa* under different light treatments using the TRIzol reagent (Thermo Fisher Scientific, USA). DNase I was added to eliminate potential contaminating genomic DNA. The quality of RNA was verified using a NanoDrop spectrometer (Thermo, United States). The $A_{260/280}$ absorbance ration was in the range of 2.0-2.2 and the $A_{260/230}$ ratio was above 1.8. Ribosomal RNA was removed using the Ribo-Zero rRNA Removal Kit (Illumina, San Diego, CA, USA). Then, the mRNA was sequenced and the enriched mRNA was broken into short fragments and reverse transcribed into cDNA afterwards. When the second strand of cDNA was synthesized, the using of dUTP improves the accuracy of the results. The DNA library was sequenced with pair-end sequencing ($2 \times 150$ bp) on the Illumina Hiseq platform by Shanghai Personal Biotechnology Cp. Ltd. The transcriptome data were deposited in the Sequence Read Archive (SRA) under the accession number: PRJNA779215.

Raw RNA-seq data was checked by FastQC software (http://www.bioinformatics.babraham.ac.uk/projects/fastqc/) to realize the data filter and quality control analysis. We used the fastx-toolkit to remove potential adapter sequences (http://hannonlab.cshl.edu/fastx_toolkit/index.html). The remaining clean reads were mapped to corresponding bacterial genome using Bowtie2 software (http://bowtie-bio.sourceforge.net/index.shtml).

The RPKM (reads per kilobase per million reads) values were used to measure the expression level of each gene in the sample. The differential expression of the transcripts was calculated using DESeq software (version 1.18.0). The differentially expressed genes (DEGs) were screened according to the differences in expression and the $p$ values. The genes with $p < 0.05$ and an absolute value of $\log_2$ fold change > 1 were defined as displaying a significant expression difference. The volcano map of differentially expressed genes were plotted using ggplots2 software package on R language.

Then, we use TopGO for GO enrichment analysis. By the calculation of the gene number in each term and the calculation of $p$ value by hypergeometric distribution method, we find the GO term with a significant enrichment of differential genes. We counted the number of differentially expressed genes at different levels of each KEGG pathway to determine the metabolic pathways and signaling pathways that differentially expressed genes were mainly involved in.

Finally, novel transcripts were predicted using the Rockhopper program (http://cs.wellesley.edu/~btjaden/Rockhopper) comparing against the NCBI nonredundant database, Swiss-Prot database, and eggNOG database.

*2.5. Statistical Analysis.* Statistical analysis was carried out using Student's $t$-test by SPSS 26.0 and GraphPad Prism 8.0 software. All data are presented as mean ± standard deviation. Statistical analysis was performed using the Student $t$-test, and all $p$ values < 0.05 were considered significant.

## 3. Results

*3.1. The Illumination of Yellow Light Influenced the Composition of the Microbiome.* High-throughput sequencing analysis was used to monitor the differences of airborne microorganism in the hospital under different light modes. All hospital airborne samples underwent sampling collection, DNA extraction, target fragment obtaining, and Illumina sequencing. In total, 2,492,655 effective original sequences were collected with an average of 276,961.67 reads per sample passing quality filtering. The valid data was filtered, and those sequences with over 97% similarity were clustered as one OTU, and a total of 851 unique OTUs were clustered with an average of 94.56 OTUs per sample.

The abundance of dominant bacteria microorganisms in the nosocomial ward bioaerosols were identified by high-throughput sequencing. The sharp reduction of Chao 1 index and Shannon index in group Y indicated that the $\alpha$-diversity in group Y had markedly reduced ($p < 0.05$) (Figures 1(a) and 1(b)). According to the results of the Venn diagram, there are 331 and 240 unique OTUs in group Y and group W, respectively, with a total of 19 core OTUs in both groups (Figure 1(c)). Beta diversity index focuses on differences between samples. Through principal component analysis (PCA), the two main components PC1 and PC2 of the genetic diversity of the microbial community structure represent 44.9% and 35% of the total variable, PCA indicated that all samples in group Y were obviously departed from group W, and all samples in group W clustered together (Figure 1(d)).

The relative abundance of the top twenty microorganism populations indicated that Proteobacteria, Firmicutes, and Bacteroidetes constituted the three most dominant phylum both in the Y and W groups. Proteobacteria and Firmicutes were the two most prevalent microbes among the hospital air microorganisms, and their total percentage accounted for approximately 85% and 82% in the W group and Y group, respectively (Figure 1(e)). Compared with group W, the relative abundance of Firmicutes was significantly decreased (Figure 1(g)). At the genus level, dominant microorganisms were *Clostridium sensu stricto 1* (relative abundance greater than 40.5%), *Paraclostridium* (relative abundance greater than 11.2%), *Acinetobacter* (relative abundance greater than 5.9%), and *Ralstonia* (relative abundance greater than 5.49%) in W group (Figure 1(f)), while *Clostridium sensu stricto* 1 and *Paraclostridium* had not detected in group Y (Figures 1(h) and 1(i)).

*3.2. The Illumination of Yellow Light Affects the Number of E. coli, P. aeruginosa, and S. aureus.* As represented in Figure 2, the concentrations of bacteria varied and ranged from $10^3$ CFU/mL to $10^{10}$ CFU/mL. After the yellow light treatment, the concentration of *E. coli* and *P. aeruginosa* was decreased, while *S. aureus* concentration was no reduced (Figure 2).

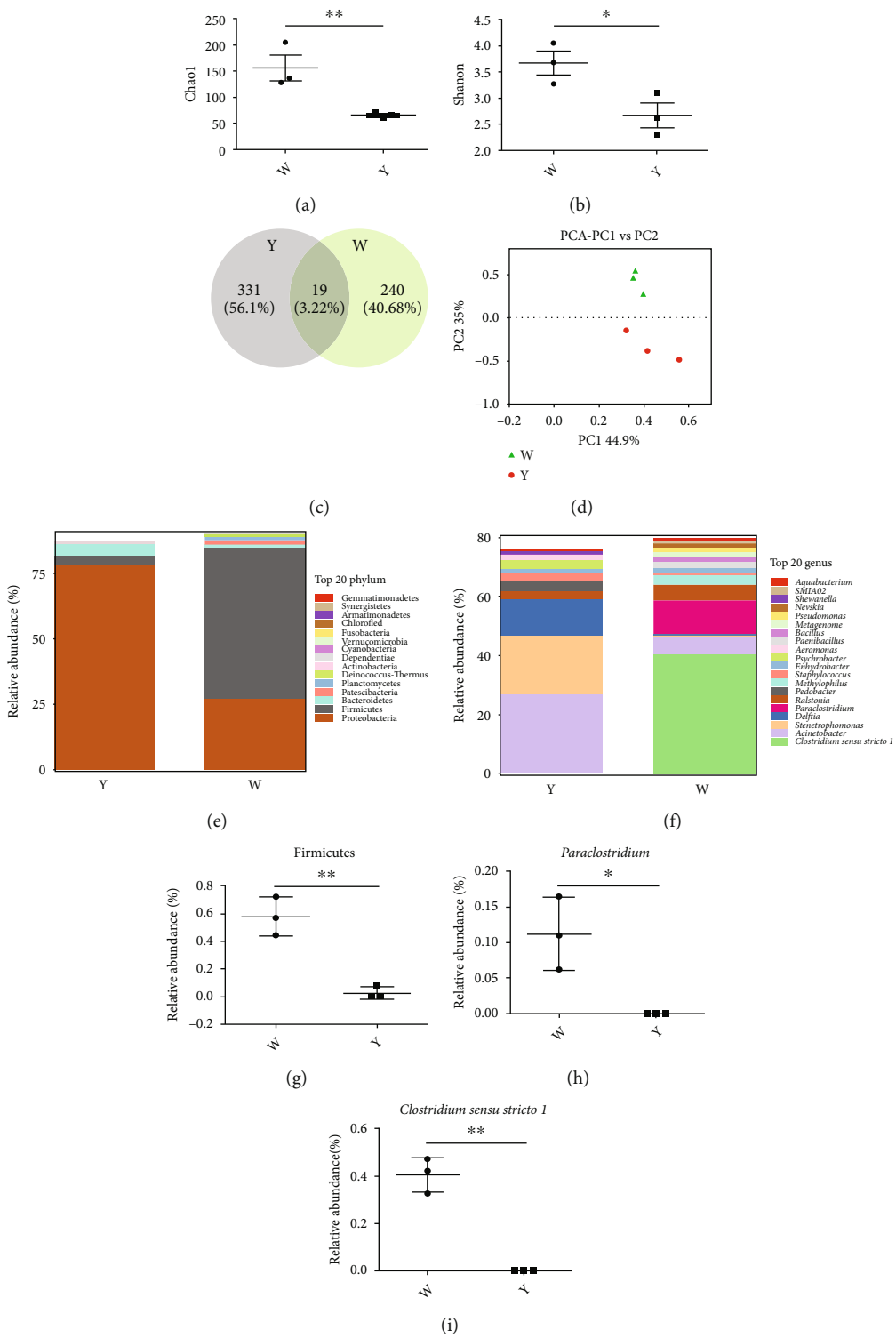


Figure 1: The effects of the irradiation of visible light (white light and yellow light) on the airborne microorganisms' diversity of medical facilities. (a, b) The Chao 1 index and Shannon index. (c) Scalar Venn representation. (d) Principal component analysis (PCA) results. (e) The relative abundance of the bacteria at phylum level. (f) The relative abundance of the bacteria at genus level. (g–i) The relative abundance of bacteria which are significantly changed. W: the airborne microorganisms under the radiation of white light; Y: the airborne microorganisms under the radiation of yellow light. $^{*}p < 0.05$, $^{**}p < 0.01$.

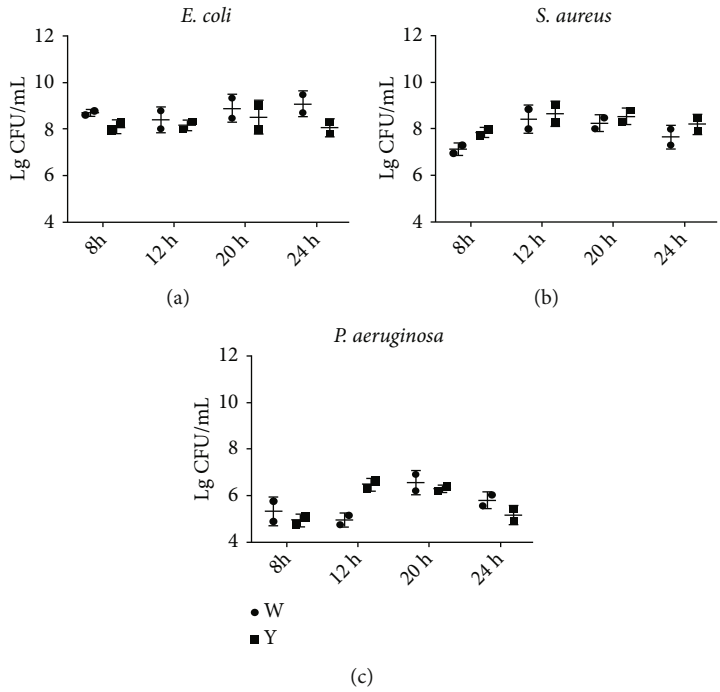


Figure 2: The effects of the irradiation of visible light (white light and yellow light) on colony forming unit of *E. coli*, *S. aureus*, and *P. aeruginosa*.

*3.3. Changes in Gene Expression of E. coli Caused by Yellow Light Irradiation.* By using the Illumina sequencing platform, 47,219,278 original sequences and 45,624,814 original sequences were harvested from *E. coli* W and *E. coli* Y, respectively, including 44,152,460 and 43,044,670 clean reads after strict filtration. After the DEG screening from the collection of mapped genes, there were 34 DEGs found, including 4 upregulated and 30 downregulated (Figure 3(a)). Hierarchical clustering of gene expression patterns was performed by analyzing the RPKM expression values (Figure 3(b)).

In the *E. coli* Y vs. *E. coli* W, 492 DEGs were annotated in biological process, 303 DEGs were annotated in molecular function, and 153 DEGs were annotated in cellular component. Then, we selected the top 10 GO term entries with the most significant enrichment for display ($p$ value < 0.05). Comparing *E. coli* Y to *E. coli* W, in BP category (bacterial-type flagellum-dependent swarming motility, locomotion, and glycogen metabolic process), CC category (bacterial-type flagellum hook, bacterial-type flagellum part, and cell projection part), and MF category (heme transporter activity, cofactor transporter activity, and transporter activity), the top 3 significantly changed subcategories were listed, respectively (Figure 3(c)).

Subsequently, KEGG metabolic pathway variance analyses were performed and the DEGs in *E. coli* Y vs. *E. coli* W were matched to 16 different KEGG pathways. The most significantly changed pathways included butanoate metabolism, alanine, aspartate and glutamate metabolism, starch and sucrose metabolism, and biofilm formation-*E. coli* and pyruvate metabolism ($p$ value < 0.05) (Figure 3(d)).

*3.4. Changes in Gene Expression of S. aureus Caused by Yellow Light Irradiation. S. aureus* W and *S. aureus* Y contained a total of 41,032,965 and 41,927,208 reads, respectively, 38,015,275 and 39,241,966 clean reads involved correspondingly. A total of 105 genes were identified differentially expressed in the comparison of *S. aureus* Y and *S. aureus* W, with 9 upregulated and 96 downregulated (Figure 4(a)). Hierarchical clustering was performed to determine the unknown function of genes (Figure 4(b)).

In the *S. aureus* Y vs. *S. aureus* W, 1519, 685 and 281 DEGs were annotated in biological process, molecular function, and cellular component, respectively. Nitrate metabolic process, reactive nitrogen species metabolic process, and response to metal ion were top 3 significantly changed subcategories in BP category; extracellular region, nitrate reductase complex, and condensed chromosome were in CC category; oxidoreductase activity, acting on other nitrogenous compounds as donors, carboxyl- or carbamoyltransferase activity, and iron-sulfur cluster binding were in MF category (Figure 4(c)).

There were 40 different KEGG pathways found in *S. aureus* Y vs. *S. aureus* W, including Staphylococcus aureus infection, nitrogen metabolism, arginine biosynthesis, valine, leucine and isoleucine biosynthesis, pyrimidine metabolism, bacterial invasion of epithelial cells, and ether lipid metabolism ($p$ value < 0.05) (Figure 4(d)).

*3.5. Changes in Gene Expression of P. aeruginosa Caused by Yellow Light Irradiation.* In *P. aeruginosa* W and *P. aeruginosa* Y, a total of 50,340,184 and 49,181,358 raw reads was detected, respectively, containing 46,444,907 and

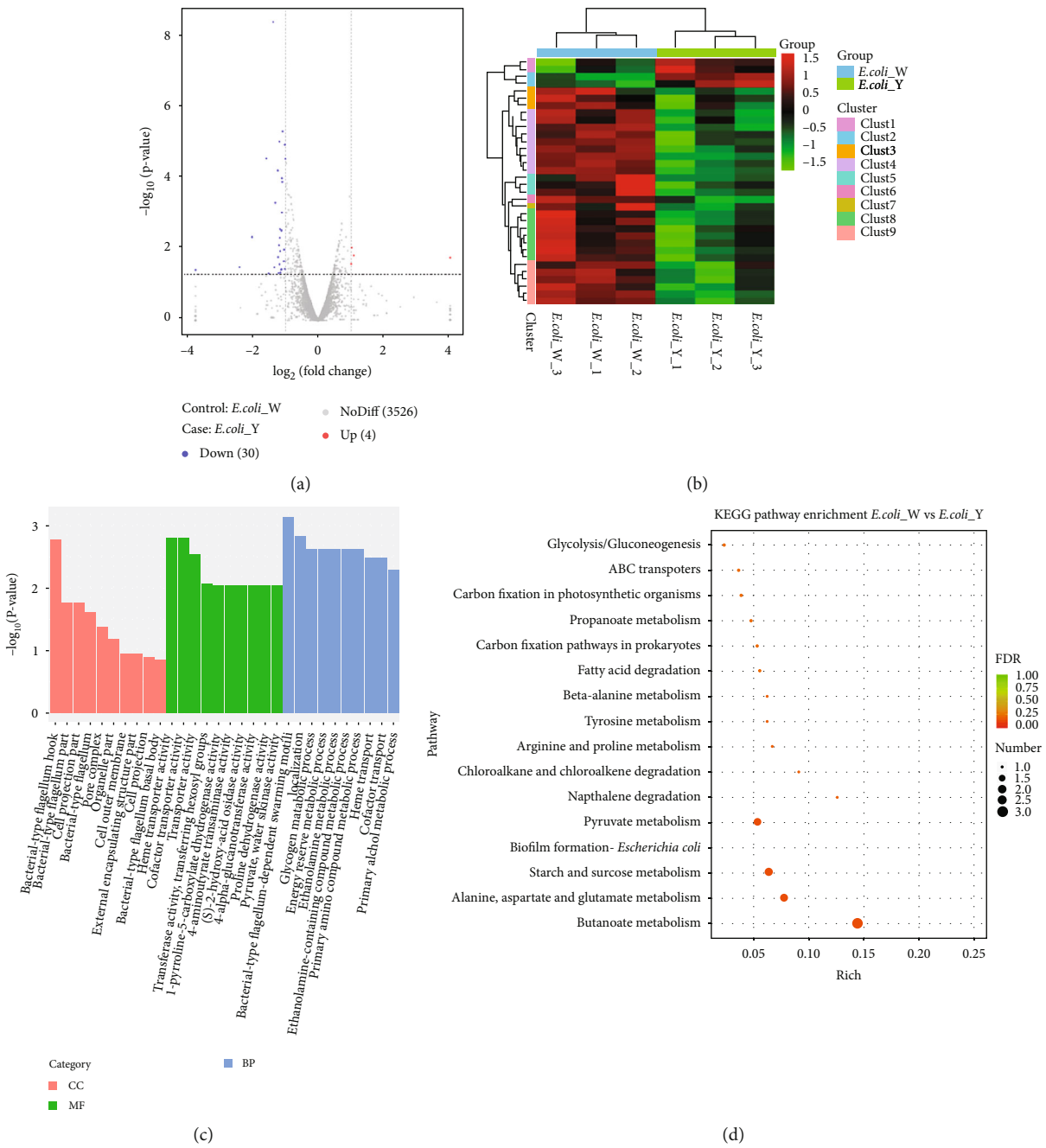


Figure 3: Global comparison of transcript profiles and DEGs in *E. coli* W vs. *E. coli* Y. (a) Volcano plots showing transcriptional differences in pairwise comparisons of transcriptomes. (b) Heat map of the hierarchical cluster analysis of gene expression. (c) GO term enrichment results. (d) KEGG pathway enrichment analysis of differentially expressed genes in response to yellow laser. *E. coli*_W: *E. coli* under the radiation of white light; *E. coli*_Y: *E. coli* under the radiation of yellow light.

46,098,015 clean reads correspondingly. 25 DEGs were detected between the comparison of *P. aeruginosa* Y and *P. aeruginosa* W; thereinto, 19 were up-regulated and 6 were repressed (Figure 5(a)). We performed a hierarchical clustering analysis, and the results are shown in Figure 5(b).

In the *P. aeruginosa* Y vs. *P. aeruginosa* W, 391 DEGs were annotated in biological process (BP) GO terms; among them, the top 3 significantly changed subcategories were oxidation-reduction process, toluene metabolic process, and toluene catabolic process. There were 41 DEGs annotated in cellular component GO terms, and cytosol, cytoplasmic part, and cytoplasm were changed significantly in CCs. 174 DEGs annotated in molecular function (MF) GO terms, precorrin-6A reductase activity, carnitine 3-dehydrogenase activity, and 3-hydroxyisobutyrate dehydrogenase activity were the top 3 significantly changed subcategories (Figure 5(c)).

The DEGs in *P. aeruginosa* Y vs. *P. aeruginosa* W were matched to 5 different KEGG pathways. The most significantly changed pathways were porphyrin and chlorophyll metabolism ($p$ value < 0.05) (Figure 5(d)).

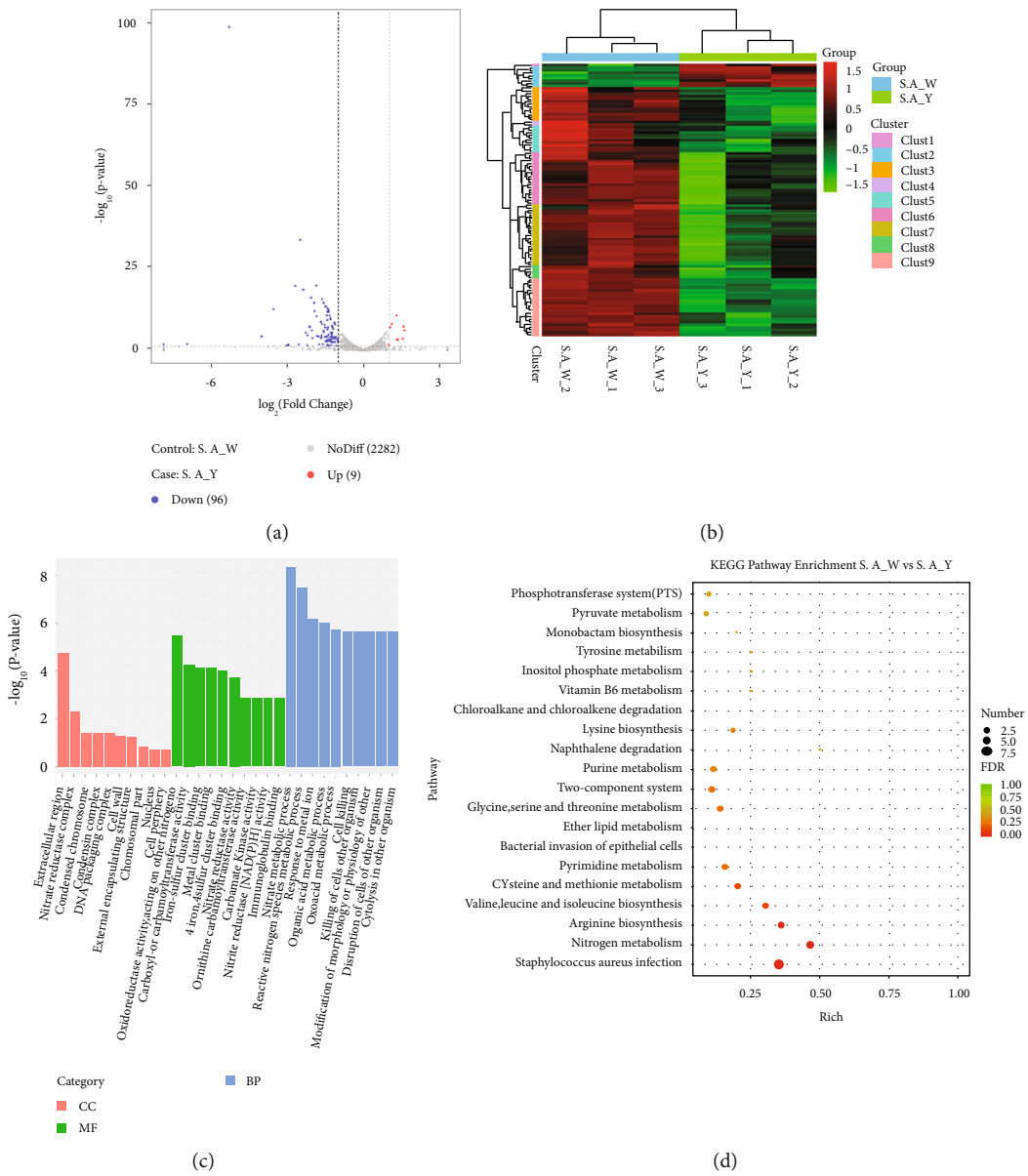


Figure 4: Global comparison of transcript profiles and DEGs in *S. aureus* W and *S. aureus* Y. (a) Volcano plots showing transcriptional differences in pairwise comparisons of transcriptomes. (b) Heat map of the hierarchical cluster analysis of gene expression. (c) GO term enrichment results. (d) KEGG pathway enrichment analysis of differentially expressed genes in response to yellow laser. *S. A*_W: *S. aureus* under the radiation of white light; *S. A*_Y: *S. aureus* under the radiation of yellow light.

## 4. Discussion

This study characterized the differences in the composition of air microflora and the differences in the transcriptomic expression of *E. coli*, *P. aeruginosa*, and *S. aureus* under yellow and white light, with the aim of determining whether the yellow light had an impact on some of common pathogenic bacteria in nosocomial acquired infections.

Our results suggested that the exposure to yellow light at 570–600 nm in hospital wards had relationships with the structure, composition, and functional pathways of atmospheric microbiota. After treatment with yellow light, the community diversity and the bacterial load in the air were decreased and the sanitation of hospital wards were improved. Among the decreased strains, Firmicutes consisted of a kind of typical pathogenic bacteria such as *Bacilli* and *Clostridia* causing nosocomial infection, including inflammation, emesis, and diarrhea [24–27]. To be specific, at the genus level, the relative abundance of *Clostridium sensu stricto 1* and *Paraclostridium* decreased significantly. *Paraclostridium*, found in the human gut, had the ability to exacerbate inflammation and has been shown to be associated with diseases such as metastatic osteomyelitis, necrotizing pneumonia, and bacteremia [28]. As obligate anaerobe, *Clostridium sensu stricto 1* formed air-tolerant, metabolically dormant spores to transmit the disease [29]. When the main cause of nosocomial infection is the presence of pathogens [7], our treatment showed a certain ability of disinfection

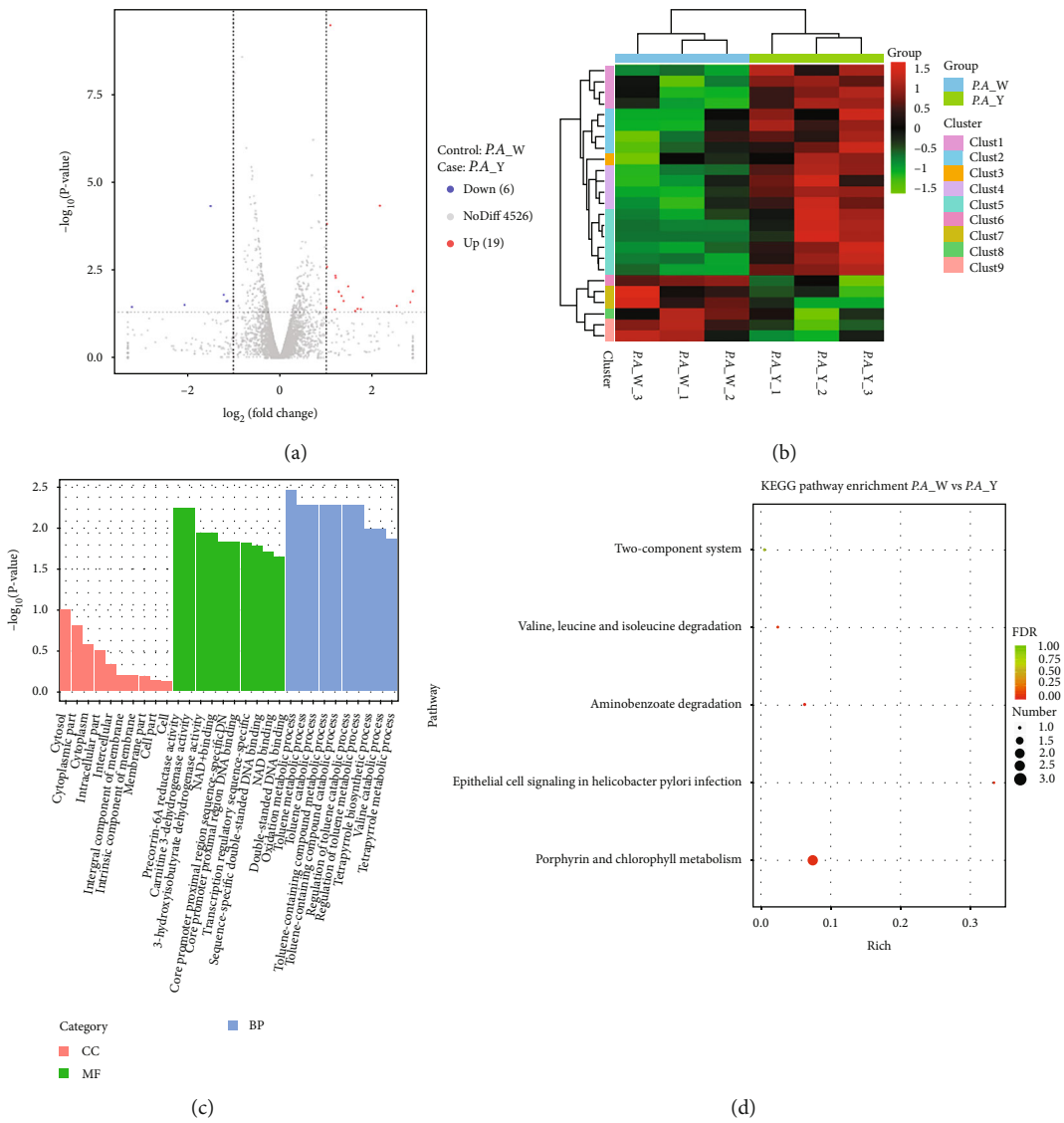


Figure 5: Global comparison of transcript profiles and DEGs in *P. aeruginosa* W vs. *P. aeruginosa* Y. (a) Volcano plots showing transcriptional differences in pairwise comparisons of transcriptomes. (b) Heat map of the hierarchical cluster analysis of gene expression. (c) GO term enrichment results. (d) KEGG pathway enrichment analysis of differentially expressed genes in response to yellow laser. *P. A*_W: *P. aeruginosa* under the radiation of white light; *P. A*_Y: *P. aeruginosa* under the radiation of yellow light.

to modulate the air quality of wards and reduce the occurrence of nosocomial infection.

Previous high-throughput sequencing results showed that yellow light decreased the relative abundance of airborne pathogens. We selected three common pathogenic bacteria from hospital. *P. aeruginosa* and *E. coli* were the most prevalent Gram-negative conditional pathogens in nosocomial infections [11]. The Gram-positive bacterium *S. aureus* was a well-known opportunistic pathogen, which was considered one of the leading causes of hospital-acquired infections [30]. We further studied the effect of yellow light on the above three pathogenic bacteria through viable count method and RNA-Seq.

After yellow LED illumination at 570–600 nm, the number of *E. coli* decreased by the viable count method, and we were surprised to find that the microbial gene associated with carbohydrate, amino acid metabolism had lower expression amount. This indicated that irradiation with yellow light had an impact on microbial (*E. coli*) nutrient metabolism. Downregulation of carbohydrate metabolism and amino acid metabolism genes closely related to microbial carbon and nitrogen source decomposition and utilization which weakened the energy harvesting and restrained the bacteria growth [31, 32]. Furthermore, the products of the above metabolisms, such as short-chain/branched-chain fatty acids and biogenic amines, might mediate the growth of *E. coli* [33]. The expression of flagella-related genes was significantly reduced after the yellow light illumination, resulting in the weakening of virulence and pathogenicity [34–36]. In addition, we found that the expression of heme transport system-related genes was reduced in *E. coli*. The decrease expression of the gene, which was closely related

to the ability of bacteria to cause diseases, led to the reduction of the virulence of *E. coli* [37, 38]. In conclusion, LED yellow light inhibits the growth of *E. coli* and reduces the pathogenicity by inhibiting the energy metabolism and the metabolic synthesis of important growth substances and downregulating genes related to flagella and heme transport system.

After yellow LED illumination, the number of *P. aeruginosa* decreased by the viable count method; afterwards, we observed that yellow light significantly upregulated the genes relating with porphyrin metabolism. One possible explanation for the phenomenon was the difference in the number of endogenous porphyrin compounds in the bacterial cells. When bacterial cells were exposed to the energy of light, photosensitizers would be excited, such as either exogenous or endogenous porphyrin molecules [39]. Once these porphyrin compounds absorbed visible light in the presence of oxygen, reactive oxygen species (ROS) were produced, consequently poisoning the bacterial [39]. The ROS such as singlet oxygen, superoxide anion, and the hydroxyl radical might damage membrane lipids, enzymes, proteins, or DNA [40]. Therefore, the upregulation of porphyrin metabolism-related genes in *P. aeruginosa* caused by yellow light can increase the production of reactive oxygen species and promoting the bacterial death.

Though the number of *S. aureus* did not decrease after yellow light irradiation, the metabolic pathways of *S. aureus* were significantly affected and the pathogenicity decreased. Arginine biosynthesis in *S. aureus* was pivotal in diseases leading. The biosynthesis of arginine, which was then metabolized to synthesize ammonia, to alleviate the influence of ROS [41]. Additionally, the downstream products of arginine production, such as ornithine and polyamines, were shown to be pivotal compound in cell metabolism [42]. Hence, downregulation of arginine biosynthesis limits the ability of *S. aureus* easing ROS killing effect, making it more vulnerable to ROS attack and reduces the content of downstream metabolically pivotal compound. Besides, genes related to the biosynthesis of isoleucine, leucine, and valine were downregulated, and these three amino acids were essential for the growth of *S. aureus*, which represented an important group of nutrients for *S. aureus* metabolism and virulence [43]. The changes in the expression of these different genes may reduce the synthesis of key substances, making *S. aureus* less resistant to ROS and less virulent.

## 5. Conclusions

In the present study, we studied the effect of yellow light on the air microbiota in hospital wards, as well as the effect of yellow light on *E. coli*, *S. aureus*, and *P. aeruginosa*, three common hospital pathogens. We found that yellow light could reduce the abundance of air microorganisms in wards. In addition, by regulating the expression level of bacterial transcriptome, yellow light reduced the expression of virulence genes or metabolism genes in bacteria and promoted the death of bacteria. Our results provide meaningful information on the mechanism by which yellow light affects ward microbes.

## Data Availability

The datasets presented in this study can be found in online repositories. The names of the repository/repositories and accession number(s) can be found in the article.

## Conflicts of Interest

The authors declare that there is no conflict of interest regarding the publication of this article.

## Authors' Contributions

Xuanqi Zhao contributed to the methodology, investigation, formal analysis, visualization, and writing—original draft. Puyuan Tian contributed to the methodology, investigation, and visualization. Jing Wei and Ruizhe Zhu contributed to the formal analysis. Wenjie Chen contributed to the methodology. Xuan Xu contributed to the investigation. Tingtao Chen contributed to the conceptualization, funding acquisition, supervision, and writing—review and editing. All authors contributed to the article and approved the submitted version.

## Acknowledgments

This study was supported by the National Natural Science Foundation of China (Grant No. 82060638), Academic and Technical Leaders of Major Disciplines in Jiangxi Province (Grant No. 20194BCJ22032), and Double Thousand Plan of Jiangxi Province (High-End Talents Project of Scientific and Technological Innovation).

## References

[1] M. C. Bottero, M. Buffoli, S. Capolongo et al., "A multidisciplinary sustainability evaluation system for operative and in-design hospitals," *Green Energy and Technology*, vol. 218, 2015.

[2] M. C. Giménez, L. M. Geerdinck, M. Versteylen et al., "Patient room lighting influences on sleep, appraisal and mood in hospitalized people," *Journal of Sleep Research*, vol. 26, no. 2, pp. 236–246, 2017.

[3] D. Gordon, J. Ward, C. J. Yao, and J. Lee, "Built environment airborne infection control strategies in pandemic alternative care sites," *Heal. Environ. Res. Des. J*, vol. 14, no. 2, pp. 38–48, 2021.

[4] R. Tignat-Perrier, A. Dommergue, A. Thollot et al., "Global airborne microbial communities controlled by surrounding landscapes and wind conditions," *Scientific Reports*, vol. 9, no. 1, pp. 1–11, 2019.

[5] Q. Zhen, Y. Deng, Y. Wang et al., "Meteorological factors had more impact on airborne bacterial communities than air pollutants," *Sci. Total Environ.*, vol. 601-602, pp. 703–712, 2017.

[6] W. Yang, M. Guo, G. Liu et al., "Detection and analysis of fine particulate matter and microbial aerosol in chicken houses in Shandong Province, China," *Poult. Sci*, vol. 97, no. 3, pp. 995–1005, 2018.

[7] P. Pati, "Review on common microbiological contamination found in hospital air," *Journal of Microbiology and Pathology*, vol. 2, 2018.

[8] M. T. El Rakaiby, S. Gamal-Eldin, M. A. Amin, and R. K. Aziz, "Hospital microbiome variations as analyzed by high-throughput sequencing," *Omi. A J. Integr. Biol.*, vol. 23, no. 9, pp. 426–438, 2019.

[9] X. L. Gao, M. F. Shao, Q. Wang et al., "Airborne microbial communities in the atmospheric environment of urban hospitals in China," *Journal of Hazardous Materials*, vol. 349, pp. 10–17, 2018.

[10] S. H. Mirhoseini, M. Nikaeen, Z. Shamsizadeh, and H. Khanahmad, "Hospital air: a potential route for transmission of infections caused by $\beta$-lactam-resistant bacteria," *American Journal of Infection Control*, vol. 44, no. 8, pp. 898–904, 2016.

[11] G. Laverty, S. P. Gorman, and B. F. Gilmore, "Biomolecular mechanisms of Pseudomonas aeruginosa and Escherichia coli biofilm formation," *Pathogens*, vol. 3, no. 3, pp. 596–632, 2014.

[12] S. Y. C. Tong, J. S. Davis, E. Eichenberger, T. L. Holland, and V. G. Fowler, "Staphylococcus aureus infections: epidemiology, pathophysiology, clinical manifestations, and management," *Clinical Microbiology Reviews*, vol. 28, no. 3, pp. 603–661, 2015.

[13] K. Qudiesat, A. Elkarmi, M. Hamad, and M. Abussaud, "Assessment of airborne pathogens in healthcare settings," *African J. Microbiol. Res*, vol. 3, pp. 66–76, 2009.

[14] S. Cabo Verde, S. M. Almeida, J. Matos et al., "Microbiological assessment of indoor air quality at different hospital sites," *Research in Microbiology*, vol. 166, no. 7, pp. 557–563, 2015.

[15] H. Liu, X. Zhang, H. Zhang et al., "Effect of air pollution on the total bacteria and pathogenic bacteria in different sizes of particulate matter," *Environmental Pollution*, vol. 233, pp. 483–493, 2018.

[16] P. Ilić, J. Božić, and S. Ilić, "Microbiological air contamination in hospital," *Int. J. Progress. Sci. Technol*, vol. 7, pp. 183–191, 2018.

[17] F. Nordsiek, E. Bodenschatz, and G. Bagheri, "Risk assessment for airborne disease transmission by poly-pathogen aerosols," *PLoS One*, vol. 16, no. 4, pp. 1–41, 2021.

[18] R. Lubart, A. Lipovski, and A. Gedanken, "The use of visible light and metal oxide nano particles for pathogen inactivation," *AIP Conference Proceedings*, vol. 1486, pp. 36–40, 2012.

[19] A. K. Fahimipour, E. M. Hartmann, A. Siemens et al., "Daylight exposure modulates bacterial communities associated with household dust," *Microbiome*, vol. 6, no. 1, pp. 1–13, 2018.

[20] J. S. McClary and A. B. Boehm, "Transcriptional response of Staphylococcus aureus to sunlight in oxic and anoxic conditions," *Frontiers in Microbiology*, vol. 9, 2018.

[21] N. T. A. de Sousa, M. F. Santos, R. C. Gomes, H. E. Brandino, R. Martinez, and R. R. de Jesus Guirro, "Blue laser inhibits bacterial growth of Staphylococcus aureus, Escherichia coli, and Pseudomonas aeruginosa," *Photomedicine and Laser Surgery*, vol. 33, no. 5, pp. 278–282, 2015.

[22] Z. Weng, F. Yu, Q. Leng et al., "Electrical and visible light dual-responsive ZnO nanocomposite with multiple wound healing capability," *Materials Science and Engineering: C*, vol. 124, article 112066, 2021.

[23] X. Zhao, S. Li, J. Ding et al., "Combination of an engineered Lactococcus lactis expressing CXCL12 with light- emitting diode yellow light as a treatment for scalded skin in mice," *Microbial Biotechnology*, vol. 14, no. 5, pp. 2090–2100, 2021.

[24] C. N. Seong, J. W. Kang, J. H. Lee et al., "Taxonomic hierarchy of the phylum Firmicutes and novel Firmicutes species originated from various environments in Korea," *Journal of Microbiology*, vol. 56, pp. 1–10, 2018.

[25] M. Otto and D. Ph, "Staphylococcus epidermidis – the "accidental" pathogen Michael," *NIH Public Access*, vol. 7, pp. 555–567, 2009.

[26] L. P. S. Arnesen, A. Fagerlund, and P. E. Granum, "From soil to gut : Bacillus cereus and its food poisoning toxins," *Fed. Eur. Microbiol. Soc*, vol. 32, pp. 579–606, 2008.

[27] A. M. Mitchell and T. J. Mitchell, "_Streptococcus pneumoniae_ : virulence factors and variation," *Eur. Soc. Clin. Infect. Dis*, vol. 16, no. 5, pp. 411–418, 2010.

[28] R. Kutsuna, J. Tomida, Y. Morita, and Y. Kawamura, "Paraclostridium bifermentans exacerbates pathosis in a mouse model of ulcerative colitis," *PLoS One*, vol. 13, no. 5, pp. 1–16, 2018.

[29] A. Shena, A. N. Edwardsb, M. R. Sarkerc, and D. Paredes-Sabjae, "Sporulation and germination in Clostridial pathogens Aimee," *Microbiol Spectr*, vol. 176, pp. 139–148, 2016.

[30] N. Bravo-Santano, J. K. Ellis, L. M. Mateos et al., "Intracellular Staphylococcus aureus modulates host central carbon metabolism to activate autophagy," *mSphere*, vol. 3, 2018.

[31] Y. Bertin, F. Chaucheyras-Durand, C. Robbe-Masselot et al., "Carbohydrate utilization by enterohaemorrhagic Escherichia coli O157:H7 in bovine intestinal content," *Environmental Microbiology*, vol. 15, no. 2, pp. 610–622, 2013.

[32] A. Maser, K. Peebo, and R. Nahku, "Avoiding amino acid depletion in a complex medium results in improved Escherichia coli BW25113 growth," *Microbiol. (United Kingdom)*, vol. 165, pp. 37–46, 2019.

[33] O. Wang, T. A. McAllister, G. Plastow, K. Stanford, B. Selinger, and L. L. Guan, "Interactions of the hindgut mucosa-associated microbiome with its host regulate shedding of Escherichia coli O157: H7 by cattle," *Applied and Environmental Microbiology*, vol. 84, no. 1, pp. 1–15, 2018.

[34] S. Wang, F. Yang, and B. Yang, "Global effect of CsrA on gene expression in enterohemorrhagic Escherichia coli O157:H7," *Research in Microbiology*, vol. 168, no. 8, pp. 700–709, 2017.

[35] G. Parthasarathy, Y. Yao, and K. S. Kim, "Flagella promote Escherichia coli K1 association with and invasion of human brain microvascular endothelial cells," *Infection and Immunity*, vol. 75, no. 6, pp. 2937–2945, 2007.

[36] A. Kakkanat, M. Totsika, K. Schaale et al., "The role of H4 flagella in _Escherichia coli_ ST131 virulence," *Scientific Reports*, vol. 5, no. 1, pp. 1–14, 2015.

[37] K. M. Holden, G. F. Browning, A. H. Noormohammadi, P. F. Markham, and M. S. Marenda, "TonB is essential for virulence in avian pathogenic _Escherichia coli_," *Comparative Immunology, Microbiology and Infectious Diseases*, vol. 35, no. 2, pp. 129–138, 2012.

[38] D. J. Morton, T. W. Seale, L. L. Madore, T. M. VanWagoner, P. W. Whitby, and T. L. Stull, "The haem-haemopexin utilization gene cluster (hxuCBA) as a virulence factor of Haemophilus influenzae," *Microbiology*, vol. 153, no. 1, pp. 215–224, 2007.

[39] M. J. Kim, M. Mikš-Krajnik, A. Kumar, and H. G. Yuk, "Inactivation by 405 ± 5 nm light emitting diode on _Escherichia coli_ O157:H7, _Salmonella_ Typhimurium, and _Shigella sonnei_ under refrigerated condition might be due to the loss

of membrane integrity," *Food Control*, vol. 59, pp. 99–107, 2016.

[40] D. K. Kim and D. H. Kang, "Efficacy of light-emitting diodes emitting 395, 405, 415, and 425 nm blue light for bacterial inactivation and the microbicidal mechanism," *Food Research International*, vol. 141, article 110105, 2021.

[41] R. Yee, P. Cui, W. Shi, J. Feng, and Y. Zhang, "Genetic screen reveals the role of purine metabolism in Staphylococcus aureus persistence to rifampicin," *Antibiotics*, vol. 4, no. 4, pp. 627–642, 2015.

[42] R. Yee, P. Cui, T. Xu et al., "Identification of a novel gene argJ involved in arginine biosynthesis critical for persister formation in Staphylococcus aureus," *Discov. Med*, vol. 29, pp. 65–77, 2017.

[43] J. C. Kaiser, S. Sen, A. Sinha, B. J. Wilkinson, and D. E. Heinrichs, "The role of two branched-chain amino acid transporters in Staphylococcus aureus growth, membrane fatty acid composition and virulence," *Molecular Microbiology*, vol. 102, no. 5, pp. 850–864, 2016.

Hindawi
Disease Markers
Volume 2022, Article ID 2141854, 6 pages
https://doi.org/10.1155/2022/2141854

*Research Article*

# Nogo-A Is a Potential Prognostic Marker for Spinal Cord Injury

**Haojun Shi,[1] Liangyu Xie,[2] Wenchang Xu,[2] Shengnan Cao,[2] and Yuanzhen Chen[2]**

[1]*Second Clinical Medical College of Henan University of Traditional Chinese Medicine, Zhengzhou, Henan, China*
[2]*Bone Biomechanics Engineering Laboratory of Shandong Province, Neck-Shoulder and Lumbocrural Pain Hospital of Shandong First Medical University, Shandong First Medical University & Shandong Academy of Medical Sciences, Jinan, Shandong, China*

Correspondence should be addressed to Shengnan Cao; csn0630@163.com and Yuanzhen Chen; chenyuanzhen2011@163.com

Received 28 March 2022; Revised 11 April 2022; Accepted 15 April 2022; Published 4 May 2022

Academic Editor: Pei-Wen Zhu



*Objective*. Spinal cord injury (SCI) has become prevalent worldwide in recent years, and its prognosis is poor and the pathological mechanism has not been fully elucidated. Nogo-A is one of the isoforms of the neurite outgrowth inhibitory protein reticulon 4. The purpose of this study was to determine whether Nogo-A could be used as a marker for predicting the prognosis of SCI. *Methods*. We screened eligible SCI patients and controls based on inclusion and exclusion criteria. We also collected baseline clinical information and peripheral venous blood of the enrolled population. Participants' baseline serum Nogo-A levels were measured by enzyme-linked immunosorbent assay (ELISA). The American Spinal Injury Association (ASIA) scale was used to evaluate the prognosis of SCI patients after 3 months. *Results*. Baseline clinical information (age; gender; smoking; drinking; SBP, systolic blood pressure; DBP, diastolic blood pressure; fasting blood glucose; WBC, white blood cells; CRP, C-reactive protein) of SCI patients and controls were not statistically significant academic differences ($p > 0.05$). The baseline serum Nogo-A levels of SCI patients and controls were $192.7 \pm 13.9$ ng/ml and $263.1 \pm 22.4$ ng/ml, respectively, and there was a statistically significant difference between the two groups ($p < 0.05$). We divided SCI patients into 4 groups according to their baseline serum Nogo-A quartile levels and analyzed their relationship with ASIA scores. The trend test results showed that with the increase of Nogo-A level, the ASIA sensation score and ASIA motor score were significantly decreased ($p < 0.001$). Multivariate regression analysis showed that serum Nogo-A levels remained a potential cause affecting the prognosis of SCI after adjusting for confounding factors in multiple models. *Conclusions*. Serum Nogo-A levels were significantly elevated in SCI patients. Moreover, elevated Nogo-A levels often indicate poor prognosis and can be used as a marker to predict the prognosis of SCI.

## 1. Introduction

The spinal cord injury (SCI) refers to damage to any part of the spinal cord or the nerve at the end of the spinal canal (cauda equina) that often results in permanent changes in strength, sensation, and other bodily functions below the injury site [1]. With the expansion of human activities in modern civilization, the incidence of SCI has gradually increased, with reported incidence ranging from 13/1 million to 220/1 million. Of these, developed countries have incidence rates of 13 to 163 per million people, while developing countries have rates ranging from 13 to 220 per million people [2]. SCI can be divided into traumatic SCI and nontraumatic SCI. A quick, traumatic impact to the spine that fractures, dislocates, pinches, or compresses one or more vertebrae can cause bleeding, edema, inflammation, and fluid buildup in and around the spinal cord, resulting in traumatic SCI [3, 4]. Arthritis, cancer, inflammation, infection, or degeneration of the spinal discs can all cause nontraumatic spinal cord injury. The socioeconomic burden of SCI is heavy. According to statistics, the annual cost of SCI in the United States is estimated to be between 5 million and 9 million US dollars, while in Australia, the figure is about 2 billion US dollars [5–7]. The pathogenic mechanism after SCI has not yet been fully elucidated, and the prognosis is poor, which affects the self-care ability of patients [8]. Therefore, finding prognostic markers for SCI and precise treatment are the top priorities.

Nogo-A, a membrane protein with a high molecular weight that is expressed on the surface of oligodendrocytes

and neurons, is a growth inhibitory, antiadhesive, and growth cone collapse factor [9]. Nogo-A also has repellent and directing effects on growing neurites throughout development, influences the migration of early neural tube cells, and is a key limiting factor for axon regeneration and plasticity in the adult central nervous system [10]. In the adult and developing central nervous systems, Nogo-A is a key axonal development inhibitor. Nogo-A has been demonstrated to block neuronal and non-neuronal cell migration and spreading in vitro, which could have crucial consequences in CNS illnesses requiring angiogenesis, such as stroke, nerve injury, and retinal diseases [11, 12]. Nogo-A belongs to RTN4 family member, and its domain can interact with several different receptors, such as Nogo receptor 1 (NgR1) and immunoglobulin-like receptor (PirB) [13]. Although Nogo-A signals through different receptors, all of which converge to the Rho GTPase pathway, Nogo-A causes different effects.

In view of the neurite outgrowth inhibitory properties of Nogo-A, functional inhibitors of Nogo-A and its receptors have received extensive attention in spinal cord injuries in which axons cannot spontaneously regenerate. The purpose of our study is to observe the expression changes of Nogo-A and its relationship with prognosis in SCI patients, aiming to provide a new direction for the prevention and treatment of SCI.

## 2. Methods

*2.1. Research Object.* SCI patients admitted to Neck-Shoulder and Lumbocrural Pain Hospital of Shandong First Medical University since 2020 were screened. The patients who met the inclusion criteria but not the exclusion criteria were included in the study. Inclusion criteria were acute patients within 24 years of onset of SCI and consent to participate in this research. Exclusion criteria are as follows: age <18 years old or >80 years old; previous history of SCI; combined with severe heart, liver, lung, and kidney disease, etc.; combined with tumor or active immune disease; refused to participate in the study or did not cooperate with follow-up; and died within 3 months. Additionally, we recruited 52 volunteers to join the study as controls. The study was approved by the hospital ethics committee, and patients or family members gave full informed and written consent to the study.

*2.2. Baseline Clinical Information.* Baseline clinical information was collected after participants were enrolled. Information on age, gender, smoking, and alcohol consumption was collected through questionnaires. Data on blood pressure, blood glucose, leukocytes, and C-reactive protein were obtained from routine clinical hematology tests. All baseline clinical information was recorded by team members.

*2.3. Serum Nogo-A Detection.* Peripheral fasting venous blood was collected from all participants within 24 days of enrollment. Peripheral venous blood was left standing at room temperature for 20 minutes and then centrifuged in a low-temperature ultracentrifuge at a centrifugal speed of 12,000 g for a total of 10 minutes. After centrifugation, serum was collected and aliquoted into a -80 °C refrigerator [14, 15]. Reagents for the detection of Nogo-A were purchased from MyBioSource (San Diego, CA, USA), and all ELISA procedures were performed according to the instructions.

*2.4. ASIA Scale Evaluation.* The ASIA scale, developed by the American Spinal Cord Injury Association, is a general classification tool for spinal cord injury based on standardized sensory and motor assessments. This impairment scale includes motor and sensory examinations to determine left and right sensory and motor levels and overall neurological levels. In the ASIA sensory test, it is a clinical examination of 28 dermatomes to test whether sensation is absent (score of 0), impaired (score of 1), or normal (score of 2), with a total score of 224, with higher scores indicating that the sensory function is better. In the ASIA motor function test, scoring is based on evaluating 10 key upper and lower extremity muscles (score: 0-5). The total score of the ASIA motor score is 100, with higher scores indicating better motor function. The ASIA scale evaluation was completed by two trained physicians.

*2.5. Statistical Analysis.* Continuous variables and non-continuous variables were expressed as mean ± standard deviation or $n$, respectively, and $t$-test or chi-square analysis was used to further analyze differences between groups. The P for trend test was used to analyze the relationship between ASIA scale scores and Nogo-A interquartile range. Multivariate regression to explore the etiology that affects the prognosis of motor and sensory function in patients with SCI. SPSS 22.0 was used for statistical analysis, and the threshold for statistical difference was set at 0.05.

## 3. Results

*3.1. Baseline Clinical Information.* Baseline clinical information of SCI patients was counted. Clinical baseline information included age, gender, smoking, alcohol, systolic blood pressure (SBP), diastolic blood pressure (DBP), fasting blood glucose, leukocytes, and C-reactive protein. The statistical results are shown in Table 1. There was no statistically significant difference in baseline clinical information between the SCI group and the control group ($p > 0.05$).

*3.2. ELISA Results.* ELISA was used to detect serum Nogo-A levels. The baseline serum Nogo-A levels of SCI patients and controls were 192.7 ± 13.9 ng/ml and 263.1 ± 22.4 ng/ml, respectively, and there was a statistically significant difference between the two groups ($p < 0.05$). The specific results are shown in Table 1 and Figure 1.

*3.3. Correlation between Serum Nogo-A and ASIA Score.* We divided SCI patients into four groups according to the quartile range of serum Nogo-A levels and analyzed the ASIA sensory and motor function scores of each group. P for trend test was used to analyze the correlation between serum Nogo-A level and ASIA score. The results showed that both the ASIA sensory function score and the ASIA motor

Table 1: The clinical information of all participants.

| | Controls ($n = 52$) | SCI ($n = 108$) | $p$ |
|---|---|---|---|
| Age, years | 53.1 ± 6.2 | 53.5 ± 6.7 | 0.718 |
| Gender, male, $n$ (%) | 35 (67.3) | 78 (72.2) | 0.523 |
| Smoking, $n$ (%) | 21 (40.4) | 45 (41.7) | 0.877 |
| Drinking, $n$ (%) | 24 (46.2) | 49 (45.4) | 0.926 |
| SBP, mmHg | 113.3 ± 9.5 | 112.9 ± 9.2 | 0.799 |
| DBP, mmHg | 77.0 ± 5.8 | 77.3 ± 6.3 | 0.773 |
| Fasting blood glucose, mmol/L | 5.4 ± 0.6 | 5.6 ± 0.8 | 0.112 |
| WBC, $10^9$/L | 6.9 ± 1.3 | 7.3 ± 1.5 | 0.101 |
| CRP, $\mu$g/ml | 4.1 ± 0.4 | 4.0 ± 0.5 | 0.209 |
| Nogo-A, ng/ml | 192.7 ± 13.9 | 263.1 ± 22.4 | <0.001 |

Abbreviations: SCI, spinal cord injury; SBP: systolic blood pressure; DBP: diastolic blood pressure; WBC, white blood cells; CRP, C-reactive protein.

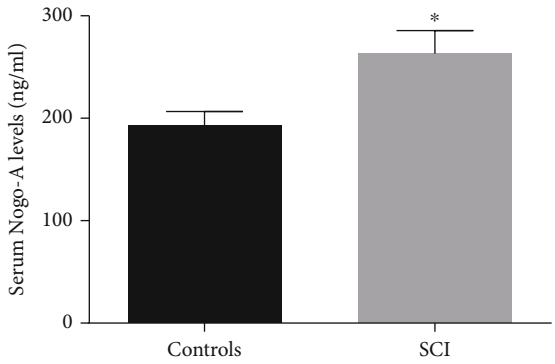


Figure 1: Comparison of serum Nogo-A levels between the two groups. $*p < 0.05$ compared to controls. SCI, spinal cord injury.

function score showed a downward trend with the increase of serum Nogo-A levels. The correlation analysis between the quartile levels of serum Nogo-A and the ASIA score is shown in Table 2.

*3.4. Multivariate Regression Analysis.* We performed multivariate regression analysis with ASIA functional function score and ASIA motor function score as dependent variables. The results showed that the serum Nogo-A score remained the etiological predictor of SCI prognosis in multiple adjusted models. The specific results of the multivariate regression analysis are shown in Table 3.

## 4. Discussions

The main finding of this study was that serum Nogo-A levels were significantly elevated in SCI patients, and elevated Nogo-A levels were associated with lower ASIA sensory and motor function scores. Through further regression analysis, it was found that the serum Nogo-A may be used as a biomarker for predicting the prognosis of SCI. Our study is the first to investigate the relationship between serum Nogo-A levels and prognosis of sensory and motor function in SCI patients.

Nogo, also known as a neurite outgrowth inhibitor or Reticulon 4, is a human protein that is mainly expressed by neurons during neural development and provides inhibitory signals for the migration and sprouting of central nervous endothelial cells. It has been identified as a CNS-specific inhibitor of neurite outgrowth [16]. RTN4 gene belongs to the reticular coding gene family and is involved in neuroendocrine secretion or membrane transport of neuroendocrine cells, and its product is a potent neurite outgrowth inhibitor [17, 18]. Additionally, three Nogo isomers have been identified: Nogo A, B, and c. Nogo-A, the most studied isoform, has two known inhibitory domains, including the N-terminal amino-Nogo and Nogo-66, which constitute extracellular loop molecules and are involved in the inhibition of nerve regeneration [19]. Among them, N-terminal amino-Nogo mainly inhibited neurite outgrowth, while Nogo-66 mainly caused growth cone destruction [20].

Nogo-A is involved in the pathogenesis of various neurological disorders. The study of Joseph et al. found that the expression of Nogo-A was significantly increased in rats with cerebral infarction; thus, its excitotoxicity and inhibitory effect on nerve regeneration may be one of the mechanisms of brain injury after cerebral infarction, and anti-Nogo-A treatment may be a potential avenue for the treatment of stroke [21]. A recent study by Rust et al. used a stroke model in mice with Nogo-A or its receptor S1PR2 gene deletion and found that it could improve the regeneration and repair of blood vessels after cerebral ischemia in mice and reduce neurological deficits, suggesting that the anti-Nogo-A treatment can improve the repair of blood vessels and nerves after ischemic central nerve injury [22]. As we all know, there is currently no effective treatment for ischemic stroke except thrombolysis [23]. In addition to the above two studies, the involvement of Nogo-A in ischemic stroke has been widely reported [24–27]. In addition to ischemic stroke, Chinese scholars have found that Nogo-A/PirB/TrkB pathway plays an inhibitory role in a rat model of intracranial hemorrhage, indicating that Nogo-A is involved in the pathogenic mechanism of secondary brain injury after intracerebral hemorrhage [28]. However, Japanese scholars

Table 2: Correlation between serum Nogo-A levels and SCI.

| Variable | Serum Nogo-A levels (ug/ml) | | | | $p$ |
|---|---|---|---|---|---|
| | Q1 | Q2 | Q3 | Q4 | |
| ASIA sensation score | 151.6 ± 17.1 | 144.9 ± 15.6 | 135.4 ± 13.2 | 124.1 ± 11.9 | <0.001 |
| ASIA motor score | 83.1 ± 7.8 | 74.6 ± 6.5 | 66.2 ± 5.6 | 57.3 ± 4.8 | <0.001 |

Abbreviations: SCI, spinal cord injury; ASIA, American Spinal Injury Association.

Table 3: Regression analysis of serum Nogo-A levels and ASIA scores.

| | ASIA sensation score | | ASIA motor score | |
|---|---|---|---|---|
| | Regression coefficient | $p$ Values | Regression coefficient | $p$ Values |
| Model 1 | 0.374 | <0.001 | 0.368 | <0.001 |
| Model 2 | 0.283 | <0.001 | 0.295 | 0.027 |
| Model 3 | 0.246 | 0.033 | 0.251 | 0.042 |

Model 1: adjusted for age and gender; Model 2: further adjusted for smoking and drinking; Model 3: further adjusted for SBP, DBP, fasting blood glucose, WBC, and CRP. Abbreviations: ASIA, American Spinal Injury Association; SBP: systolic blood pressure; DBP: diastolic blood pressure; WBC, white blood cells; CRP, C-reactive protein.

found that in the rat model of intracranial hemorrhage, exercise training did not change the expression of Nogo-A in the brain, indicating that the role of Nogo-A in the rehabilitation of intracranial hemorrhage may be controversial, and further research is needed in the future [29]. Research from Xiangya Medical University shows that $\alpha$-tocopherol has a neuroprotective effect on traumatic brain injury rats, and the mechanism may be that $\alpha$-tocopherol can reduce the expression of Nogo-A and NgR in brain tissue after traumatic brain injury and promote the Neurodegeneration [30]. Another study from Shanghai Jiao Tong University found that in traumatic brain injury, elevated serum Nogo-A levels were strongly associated with poor prognosis, suggesting that Nogo-A levels could be used as a biomarker for predicting the prognosis of traumatic brain injury [31]. In addition, the role of Nogo-A in multiple sclerosis and immune encephalomyelitis has also been reported [32–34].

The role of Nogo-A in SCI has also attracted the attention of researchers. Swedish researchers found that Nogo-A knockout rats exhibited stronger neurodegenerative and neuroplasticity responses after SCI, suggesting that anti-Nogo-A therapy may be a new target for the treatment of SCI [35]. Swedish scholars further found that intrathecal anti-Nogo-A treatment can improve the regeneration and remodeling of the damaged central nervous system without obvious side effects [36]. The study by William B. J. Cafferty's team found that the synergistic effect of Nogo-A with MAG and OMgp is an important mechanism for inhibiting axonal regrowth and neural recovery after SCI [37]. For the first time, a multinational research team has demonstrated the efficacy of intratunnel injection of anti-Nogo-A antibodies in SCI patients [38]. Nevertheless, the research on the correlation between Nogo-A and SCI prognosis is still blank.

Our study has limitations. First, our sample size was not very large; second, we did not do longer-term follow-up; and finally, we did not do intervention studies. Nonetheless, we are the first report to investigate Nogo-A and prognosis in SCI.

## 5. Conclusions

Our study found that the serum Nogo-A level in SCI patients was higher than that in the normal population and was closely related to the degree of SCI injury. The serum Nogo-A may be one of the indicators to predict the degree of sensory and motor function recovery after SCI. This conclusion needs to be further confirmed and provide a new reference for the early intervention and intervention of SCI.

## Data Availability

The study data presented may be made available from the corresponding author upon reasonable request.

## Conflicts of Interest

The authors report no conflict of interest.

## Acknowledgments

This study was supported by the TCM Technology Development Project of Shandong Province (2019-0543 and 2019-0545) and the Shandong Province Medical and Health Science and Technology Development Plan (202004070787).

## References

[1] Y. Chen, D. Wang, S. Cao, G. Hou, H. Ma, and B. Shi, "Association between serum IL-37 and spinal cord injury: a prospective observational study," *BioMed Research International*, vol. 2020, Article ID 6664313, 2020.

[2] A. Ackery, C. Tator, and A. Krassioukov, "A global perspective on spinal cord injury epidemiology," *Journal of Neurotrauma*, vol. 21, no. 10, pp. 1355–1370, 2004.

[3] R. A. Cripps, B. B. Lee, P. Wing, E. Weerts, J. Mackay, and D. Brown, "A global map for traumatic spinal cord injury epidemiology: towards a living data repository for injury prevention," *Spinal Cord*, vol. 49, no. 4, pp. 493–501, 2011.

[4] P. W. New, R. A. Cripps, and B. Bonne Lee, "Global maps of non-traumatic spinal cord injury epidemiology: towards a living data repository," *Spinal Cord*, vol. 52, no. 2, pp. 97–109, 2014.

[5] S. Yuan, Z. Shi, F. Cao, J. Li, and S. Feng, "Epidemiological features of spinal cord injury in China: a systematic review," *Frontiers in Neurology*, vol. 9, p. 683, 2018.

[6] D. McDaid, A. L. Park, A. Gall, M. Purcell, and M. Bacon, "Understanding and modelling the economic impact of spinal cord injuries in the United Kingdom," *Spinal Cord*, vol. 57, no. 9, pp. 778–788, 2019.

[7] M. Fitzharris, R. A. Cripps, and B. Lee, "Estimating the global incidence of traumatic spinal cord injury," *Spinal Cord*, vol. 52, no. 2, pp. 117–122, 2014.

[8] H. Ma, F. Lu, Y. Guo, Z. Shen, and Y. Chen, "The prognostic value of leucine-rich $\alpha$2 glycoprotein 1 in pediatric spinal cord injury," *BioMed Research International*, vol. 2021, Article ID 7365204, 2021.

[9] A. B. Huber and M. E. Schwab, "Nogo-A, a potent inhibitor of neurite outgrowth and regeneration," *Biological Chemistry*, vol. 381, no. 5-6, pp. 407–419, 2000.

[10] V. Pernet and M. E. Schwab, "The role of Nogo-A in axonal plasticity, regrowth and repair," *Cell and Tissue Research*, vol. 349, no. 1, pp. 97–104, 2012.

[11] K. T. Wright, W. el Masri, A. Osman et al., "Bone marrow stromal cells stimulate neurite outgrowth over neural proteoglycans (CSPG), myelin associated glycoprotein and Nogo-a," *Biochemical and Biophysical Research Communications*, vol. 354, no. 2, pp. 559–566, 2007.

[12] V. Pernet, "Nogo-A in the visual system development and in ocular diseases," *Biochimica et Biophysica Acta (BBA)-Molecular Basis of Disease*, vol. 1863, no. 6, pp. 1300–1311, 2017.

[13] M. Zagrebelsky and M. Korte, "Maintaining stable memory engrams: new roles for Nogo-A in the CNS," *Neuroscience*, vol. 283, pp. 17–25, 2014.

[14] Q. Wang, K. Wang, Y. Ma, S. Li, and Y. Xu, "Serum galectin-3 as a potential predictive biomarker is associated with post-stroke cognitive impairment," *Oxidative Medicine and Cellular Longevity*, vol. 2021, Article ID 5827812, 2021.

[15] Y. Xu, K. Wang, Q. Wang, Y. Ma, and X. Liu, "The antioxidant enzyme PON1: a potential prognostic predictor of acute ischemic stroke," *Oxidative Medicine and Cellular Longevity*, vol. 2021, 2021.

[16] B. L. Tang, "Nogo-A and the regulation of neurotransmitter receptors," *Neural Regeneration Research*, vol. 15, no. 11, pp. 2037-2038, 2020.

[17] A. M. Sartori, A.-S. Hofer, and M. E. Schwab, "Recovery after spinal cord injury is enhanced by anti-Nogo-A antibody therapy – from animal models to clinical trials," *Current Opinion in Physiology*, vol. 14, pp. 1–6, 2020.

[18] N. Zhang, Y. Cui, Y. Li, and Y. Mi, "A novel role of Nogo proteins: regulating macrophages in inflammatory disease," *Cellular and Molecular Neurobiology*, 2021.

[19] W. Xu, P. Xiao, S. Fan et al., "Blockade of Nogo-A/Nogo-66 receptor 1 (NgR1) inhibits autophagic activation and prevents secondary neuronal damage in the thalamus after focal cerebral infarction in hypertensive rats," *Neuroscience*, vol. 431, pp. 103–114, 2020.

[20] Y. Sekine, J. A. Lindborg, and S. M. Strittmatter, "A proteolytic C-terminal fragment of Nogo-A (reticulon-4A) is released in exosomes and potently inhibits axon regeneration," *Journal of Biological Chemistry*, vol. 295, no. 8, pp. 2175–2183, 2020.

[21] J. L. Cheatwood, A. J. Emerick, M. E. Schwab, and G. L. Kartje, "Nogo-A expression after focal ischemic stroke in the adult rat," *Stroke*, vol. 39, no. 7, pp. 2091–2098, 2008.

[22] R. Rust, L. Grönnert, C. Gantner et al., "Nogo-A targeted therapy promotes vascular repair and functional recovery following stroke," *Proceedings of the National Academy of Sciences*, vol. 116, no. 28, pp. 14270–14279, 2019.

[23] Y. Xu, Q. Wang, J. Chen, Y. Ma, and X. Liu, "Updating a strategy for histone deacetylases and its inhibitors in the potential treatment of cerebral ischemic stroke," *Disease Markers*, vol. 2020, Article ID 8820803, 2020.

[24] R. Rust, R. Z. Weber, L. Grönnert et al., "Anti-Nogo-A antibodies prevent vascular leakage and act as pro-angiogenic factors following stroke," *Scientific Reports*, vol. 9, no. 1, pp. 1–10, 2019.

[25] C. Wiessner, F. M. Bareyre, P. R. Allegrini et al., "Anti—Nogo-A antibody infusion 24 hours after experimental stroke improved behavioral outcome and corticospinal plasticity in normotensive and spontaneously hypertensive rats," *Journal of Cerebral Blood Flow & Metabolism*, vol. 23, no. 2, pp. 154–165, 2003.

[26] L. D. Moon, "Therapeutics targeting Nogo-A hold promise for stroke restoration," *CNS & Neurological Disorders-Drug Targets (Formerly Current Drug Targets-CNS & Neurological Disorders)*, vol. 12, no. 2, pp. 200–208, 2013.

[27] J. E. Orfila, R. M. Dietz, K. M. Rodgers et al., "Experimental pediatric stroke shows age-specific recovery of cognition and role of hippocampal Nogo-A receptor signaling," *Journal of Cerebral Blood Flow & Metabolism*, vol. 40, no. 3, pp. 588–599, 2020.

[28] Y. Liu, C. Ma, H. Li et al., "Nogo-A/Pir-B/TrkB signaling pathway activation inhibits neuronal survival and axonal regeneration after experimental intracerebral hemorrhage in rats," *Journal of Molecular Neuroscience*, vol. 69, no. 3, pp. 360–370, 2019.

[29] Y. Takamatsu, K. Tamakoshi, Y. Waseda, and K. Ishida, "Running exercise enhances motor functional recovery with inhibition of dendritic regression in the motor cortex after collagenase-induced intracerebral hemorrhage in rats," *Behavioural Brain Research*, vol. 300, pp. 56–64, 2016.

[30] J. Yang, Y. Han, W. Ye, F. Liu, K. Zhuang, and G. Wu, "Alpha tocopherol treatment reduces the expression of Nogo-A and NgR in rat brain after traumatic brain injury," *Journal of Surgical Research*, vol. 182, no. 2, pp. e69–e77, 2013.

[31] H. Chen, H. L. Cao, S. W. Chen et al., "Neuroglobin and Nogo-A as biomarkers for the severity and prognosis of traumatic brain injury," *Biomarkers*, vol. 20, no. 6-7, pp. 495–501, 2015.

[32] M. Reindl, S. Khantane, R. Ehling et al., "Serum and cerebrospinal fluid antibodies to Nogo-A in patients with multiple sclerosis and acute neurological disorders," *Journal of Neuroimmunology*, vol. 145, no. 1-2, pp. 139–147, 2003.

[33] T. Karnezis, W. Mandemakers, J. L. McQualter et al., "The neurite outgrowth inhibitor Nogo A is involved in autoimmune-mediated demyelination," *Nature Neuroscience*, vol. 7, no. 7, pp. 736–744, 2004.

[34] P. Fontoura, P. P. Ho, J. DeVoss et al., "Immunity to the extracellular domain of Nogo-A modulates experimental autoimmune encephalomyelitis," *The Journal of Immunology*, vol. 173, no. 11, pp. 6981–6992, 2004.

[35] M. Simonen, V. Pedersen, O. Weinmann et al., "Systemic deletion of the myelin-associated outgrowth inhibitor Nogo-A improves regenerative and plastic responses after spinal cord injury," *Neuron*, vol. 38, no. 2, pp. 201–211, 2003.

[36] T. Liebscher, L. Schnell, D. Schnell et al., "Nogo-A antibody improves regeneration and locomotion of spinal cord–injured rats," *Annals of Neurology*, vol. 58, no. 5, pp. 706–719, 2005.

[37] W. B. Cafferty, P. Duffy, E. Huebner, and S. M. Strittmatter, "MAG and OMgp synergize with Nogo-A to restrict axonal growth and neurological recovery after spinal cord trauma," *Journal of Neuroscience*, vol. 30, no. 20, pp. 6825–6837, 2010.

[38] K. Kucher, D. Johns, D. Maier et al., "First-in-man intrathecal application of neurite growth-promoting anti-Nogo-A antibodies in acute spinal cord injury," *Neurorehabilitation and Neural Repair*, vol. 32, no. 6-7, pp. 578–589, 2018.

Hindawi
Disease Markers
Volume 2022, Article ID 4910731, 10 pages
https://doi.org/10.1155/2022/4910731

*Research Article*

# Study on $TiO_2$ Nanofilm That Reduces the Heat Production of Titanium Alloy Implant in Microwave Irradiation and Does Not Affect Fracture Healing

**Yiming Xu**,[1] **Zikai Hua**,[2] **Yun Cai**,[3] **Xianxuan Feng**,[1] **Jiajia Yang**,[4] **Jie Shen**,[5] **and Yuehong Bai**[1]

[1]*Department of Rehabilitation Medicine, Shanghai Jiao Tong University Affiliated Sixth People's Hospital, 200233, China*
[2]*Orthotek Laboratory, School of Mechatronics Engineering and Automation, Shanghai University, 200072, China*
[3]*Fudan University Affiliated Zhongshan Hospital, 200032, China*
[4]*The First Affiliated Hospital, Sun Yat-sen University, Guangzhou, 510062, China*
[5]*Medical Records and Statistics Office, Shanghai Jiao Tong University Affiliated Sixth People's Hospital, 200233, China*

Correspondence should be addressed to Jie Shen; slyysj2009@163.com and Yuehong Bai; aibyhw@126.com

Received 14 March 2022; Revised 23 March 2022; Accepted 1 April 2022; Published 13 April 2022

Academic Editor: Pei-Wen Zhu



*Background*. Metal implants can produce heat and damage adjacent tissues under microwave irradiation, which makes local metal implants in the body a contraindication for microwave therapy. However, with the wide application of titanium alloy implants which have low permeability and low conductivity, this concept has been challenged. Our team members have confirmed through previous research that continuous low-power microwave irradiation does not cause thermal damage to the surrounding tissues of the titanium alloy. Is there any other way to further increase the dose of microwave irradiation while reducing the heat production of titanium alloy implants? In this study, the effect of $TiO_2$ nanofilm on reducing the heat production of titanium alloy implants in microwave field was verified by animal experiments, and the effect of $TiO_2$ nanofilm on fracture healing was observed. *Methods*. 30 rabbits were selected. In the experiment of temperature measurement, 10 rabbits were randomly divided into experimental group ($n = 5$) and control group ($n = 5$), and the contralateral lower limb of the rabbits in experimental group was set as the sham operation group. The right femurs in the experimental group were implanted with Ti6Al4V plates coated with $TiO_2$ nanofilm, and the right femurs in the control group were implanted with common titanium alloy plates without $TiO_2$ nanofilm. The same surgical procedure was used in the sham operation group, but no plate was implanted. The temperature of the deep tissue above the metal implant was measured with an anti-interference thermocouple thermometer during 20 minutes of microwave irradiation. The other 20 rabbits were randomly divided into two groups, experimental group ($n = 10$) and control group ($n = 10$). The femoral shaft fracture models were established again. Ti6Al4V plates coated with $TiO_2$ nanofilm and common titanium alloy plates were implanted in the two groups, respectively, and both groups were exposed to continuous microwave irradiation with a power of 40 W or 60 W for 30 days after operation. The fracture healing was evaluated by X-ray at 0 day, 14 days, and 30 days after microwave irradiation, respectively. The animals were sacrificed at 30 days after operation for histopathological assessment. *Results*. The temperature in the experimental group, control group, and sham operation group increased significantly after 40 W and 60 W microwave irradiation ($2.18 \pm 0.15^\circ$C~$6.02 \pm 0.38^\circ$C). When exposed to 40 W microwave, the temperature rise of the control group was $4.0 \pm 0.34^\circ$C, which was significantly higher than that of the experimental group $2.82 \pm 0.15^\circ$C ($P < 0.01$) and the sham operation group $2.18 \pm 0.33^\circ$C ($P < 0.01$). There was no significant difference in temperature rise between the experimental group and the sham operation group ($P = 0.21$). When exposed to 60 W microwave, the temperature rise of the control group was $6.02 \pm 0.38^\circ$C, which was significantly higher than that of the experimental group $3.66 \pm 0.14^\circ$C ($P < 0.01$) and sham operation group $2.96 \pm 0.22^\circ$C ($P < 0.01$), and there was no significant difference between the experimental group and the sham operation group ($P = 0.32$). X-ray evaluation showed that there was no significant difference in callus maturity between the experimental group

and the control group at 14 days ($P = 0.554$), but there was significant difference in callus maturity between the two groups at 30 days ($P = 0.041$). The analysis of bone histologic and histomorphometric data at 30 days was also consistent with this. *Conclusion*. Under the animal experimental condition, compared with the common titanium alloy implant, the $TiO_2$ nanofilm can reduce the heat production of the titanium alloy implant in the 2450 MHz microwave field and has no adverse effect on fracture healing. This study opens up a promising new idea for the application of microwave therapy to metal implants in human body.

## 1. Introduction

Microwave is a high-frequency electromagnetic wave with wavelength from 1 mm to 1 m and frequency from 300 MHz to 300 GHz [1]. When the human body is exposed to a microwave irradiation, an induced electromagnetic field is generated in the body, which heats the tissues. It is well known that the therapeutic effect of microwave is mainly related to heat production, and microwave therapy is also known as microwave diathermy. Microwave diathermy can improve the range of motion of joints in clinical application [2]. Enhance microcirculation and protein synthesis to heal wounds [3], increase blood flow to injured tissues [4], reduce pain [5], and modify the physical properties of fibrous tissues [6]. Therefore, microwave therapy is widely used in the rehabilitation of acute injury and chronic inflammation of bone [7–9], joints [10], muscles, and tendons [11, 12].

The local metal implants in human body are generally considered to be an absolute contraindication for microwave therapy [13], which is mainly due to the secondary irradiation of tissues caused by the microwave reflection of metal and the excessive heat generated by the eddy current formed inside the metal implants in the microwave electromagnetic field, which damages the tissues adjacent to the metal implants [14, 15]. This contraindication limits the application of microwave in persistent pain, delayed healing, and infection after internal fixation [16–19].

This problem has existed since the application of microwave in clinic, and now clinicians and material engineering scientists are trying to solve it. Inspired by the fact that patients with titanium alloy implants can undergo MRI examination [20–22], our team believes that patients fixed with titanium alloy steel plate may receive microwave treatment because of the low permeability and low conductivity of titanium alloy. The following experiments verify this hypothesis. In vivo animal studies by Ye et al. [23, 24] showed that there was no obvious histological change in the skeletal muscles and nerves near the titanium alloy implant when single irradiation with 2450 MHz microwave at a lower dose (20 W~40 W) or continuous irradiation with 25 W titanium alloy fixed rabbit femoral fracture. However, with the increase of power (60 W and 80 W), acute thermal injury of skeletal muscle and nerve could be observed. The results of these studies indicate that, on the one hand, low doses microwave can be applied to fractures fixed by titanium alloy implants. On the other hand, the heat generated by microwave irradiation of titanium alloy implants is dose-dependent.

Is there any other way to further increase the microwave irradiation dose while reducing the heat generation of titanium alloy implants? Some materials scientists are attracted by surface modification and coating techniques, which have been applied to improve the performance of modern orthopaedic materials [25, 26]. Professor Hua's team from Shanghai University has designed a $TiO_2$ nanofilm that was coated on titanium alloy (Ti6Al4V) substrates by sol-gel method. Preliminary study in vitro [27] showed that the temperature rise of the sample was lower than that of the uncoated control group after the sample was radiated by 2450 MHz 25 W microwave for 10 minutes, which met the expected requirements. In order to further verify the in vivo effect of the $TiO_2$ nanofilm and observe the effect of the $TiO_2$ nanofilm on fracture healing, we designed following animal experiments.

## 2. Materials and Methods

*2.1. Sample Size.* In a previous study with a power of 40 W microwave [24], the temperature change in the deep tissue above the implant in each group of subjects obeyed a normal distribution with a standard deviation of 0.42°C. If the true difference between the experimental and control means is 1.3°C, we would need to study three experimental samples and three control samples in order to reject the zero hypothesis that the thermal change of the experimental group and the control group is equal to the probability of 0.8(power). The type I error probability associated with this null hypothesis is 0.05. In this study, there were 5 measurements for each condition.

*2.2. Animal Model.* Thirty New Zealand white rabbits weighing 3.0~3.5 kg were used in the study. Ten of 30 rabbits were used for temperature measurement trial and were randomly divided into experimental group (EG) and control group (CG), with 5 rabbits in each group. The contralateral lower limb of the rabbits in experimental group was set as the sham operation group (SOG). 20 of 30 rabbits were used for bone histology and imaging observation and were divided into EG and CG, with 10 rabbits in each group. The animals were purchased from Songlian Laboratory Animal Corporation (production license: SCXK2017-0008).

To establish an animal model of internal fixation of femoral shaft fracture in rabbits, the skin of the right lateral thigh was incised under intravenous anesthesia with pentobarbital sodium 30 mg/kg, and the fascia and skeletal muscle were separated layer by layer to the middle of the femur. The EG was implanted with a 460 mm × 42 mm "I"-shaped titanium alloy plate coated with $TiO_2$ nanofilm (Figures 1 and 2) (Zhengtai Laboratory of Shanghai University, China). The CG was implanted with titanium alloy plate without $TiO_2$ nanofilm (Synthes Company, USA). Then, a stainless steel wire saw was used to cut the middle femur corresponding to the fourth hole of the plate, with a cutting depth of about 3 mm. In the end, wash the wound, suture the wound layer by layer, and bandage it. In the SOG, only skin incision

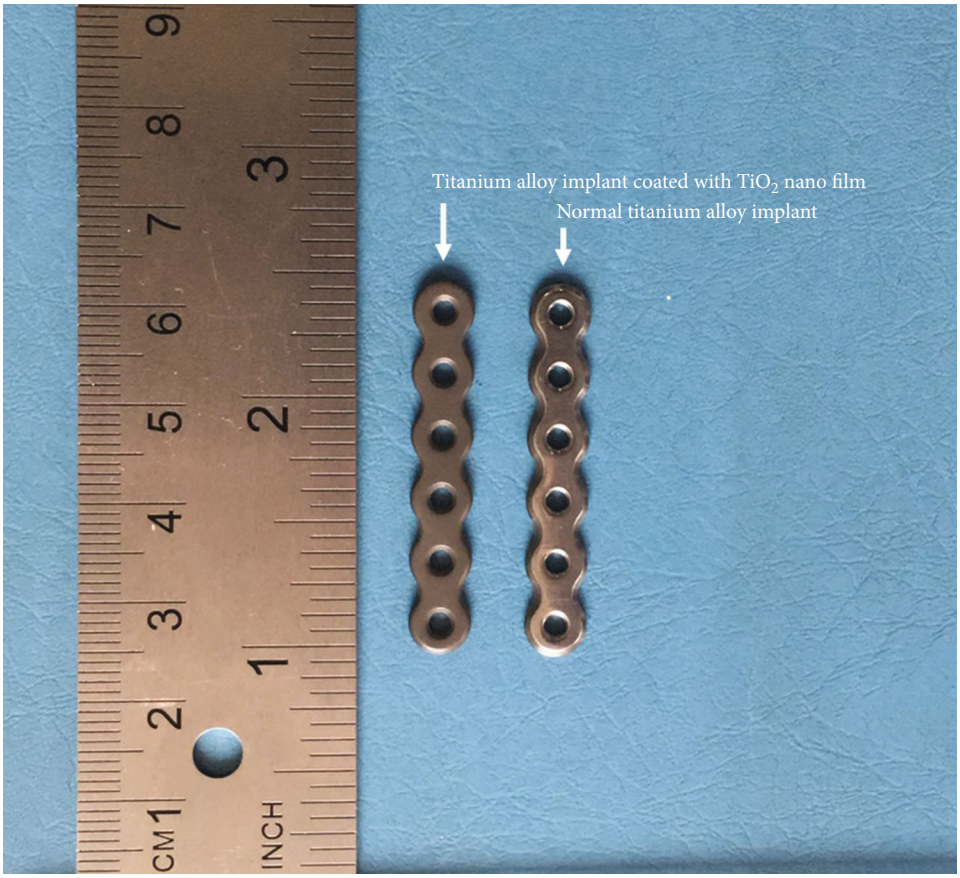


Figure 1: Plates used in the EG and the CG.

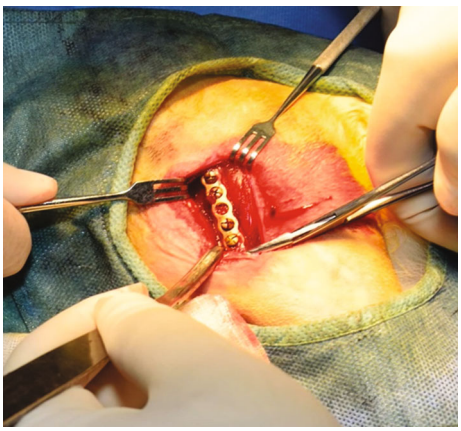

Figure 2: Implantation of titanium alloy plate into rabbit femur.

and muscle separation were performed on the left thigh to expose the femur, and no plate was implanted. Penicillin (800,000 units/day) was administered intramuscularly 3 days after surgery. At the end of the experiment, all New Zealand rabbits were sacrificed by excessive anesthesia (pentobarbital sodium).

*2.3. Microwave Irradiation and Temperature Measurement.* Three days after operation, the EG, the CG, and the SOG received the temperature measurement during microwave irradiation. The ambient temperature of the laboratory is set at 25°C. New Zealand rabbits were anesthetized with sodium pentobarbital (30 mg/kg) via the ear vein, and the original skin incision was exposed and cut. The temperature sensor of the anti-interference thermocouple thermometer (FHCME-04008, Baldwin, USA) was embedded in the deep tissue 5 mm above the central surface of the implant. Leave it for at least 3 minutes, and when the digital reading is stable, record the initial temperature. Then, a 2450 MHz microwave transmitting probe (PM-800, ITO, Japan) was placed 10 cm above the skin (Figure 3(a)), the microwave irradiation power was adjusted to 40 W, and the irradiation was started, and the irradiation time and the corresponding thermometer readings were recorded for 20 minutes. Then, the microwave therapeutic apparatus was turned off and waited for 1 hour. Observe the temperature displayed by the thermometer to recover to the initial temperature, turn on the microwave therapeutic apparatus again, adjust the microwave irradiation power to 60 W, and record the irradiation time and the corresponding thermometer reading for 20 minutes.

*2.4. Continuous Microwave Irradiation.* Twenty New Zealand rabbits in the EG and CG were exposed to 2450 MHz microwave irradiation every day from the third day after operation until histological and imaging assessment. The microwave-emitting probe was placed 10 cm above the

(a) (b)

Figure 3: (a) A 2450 MHz microwave transmitting probe was placed 10 cm above the skin, and an anti-interference thermocouple thermometer sensor (indicated by the red arrow in the figure) was inserted through the original skin incision for temperature measurement. (b) The microwave transmitting probe was placed 10 cm above the surgical incision and faced the middle of thigh during daily microwave irradiation.

incision in the thigh during daily irradiation (Figure 3(b)) at a power of 40 W for 20 minutes.

*2.5. X-Ray Assessment.* Anteroposterior and lateral radiographs of the femur were taken at 0, 14, and 30 days after microwave irradiation to evaluate the fracture healing process. The camera output voltage is 55 KV, the current is 0.3 mA, the exposure time is 3 s, and the optical density evaluation uses the same light source. The X-ray images were stored in the PC as digital image files. The X-ray images of each specimen were evaluated by three radiologists. The degree of fracture healing was based on the maturity of callus. The classification of Goldberg et al. is as follows [28]: stage 1, unhealed; stage 2, possible healing; and stage 3, radiographic healing, followed by calculation of the mean radiographic score.

*2.6. Histology and Histomorphometery.* After 30 days of microwave irradiation, 5 rabbits in each group were sacrificed, and 10 samples were taken for histological assessment. Specimens were fixed with 10% formalin and decalcified with 10% nitric acid. After embedding in paraffin, 5 $\mu$m thick longitudinal sections were prepared and stained with hematoxylin-eosin or Masson trichrome. Two slides of each specimen were examined, one stained with hematoxylin-eosin and the other stained with Masson trichrome. A group of pathologists (LZW, JQ, and DJX) blinded to trial grouping scored all stained sections based on the amount of mineralization in the fracture space using a grading system described by Perry et al. [29].

For the assessment of bone histomorphometry, the rabbits were sacrificed 30 days after microwave irradiation, and the bone tissue around the bone defect was obtained, and the bone samples were trimmed and fixed in 10% formalin for 1 week. After being rinsed with tap water, the samples were dehydrated with 70%-99% ethanol for 24 hours, respectively, and then embedded with methyl methacrylate. The polymerized tissue samples were placed in a refrigerator at 4°C for about one week, and the embedded samples were taken out. Sections were cut into 50 $\mu$m using a hard tissue microtome and stained with toluidine blue, observed by 25x optical microscope. Measurement of the fracture gap was performed by the histomorphometry software (Simple-PCI 6.0, Hamamatsu Photonics, Japan). Nomenclature and calculations for bone histomorphometry were performed in accordance with the American Association for Bone and Mineral Research reporting specifications.

*2.7. Ethics.* All experimental procedures involving animals were performed according to the protocol approved by the Animal Welfare and Ethics Committee of Shanghai Sixth People's Hospital (License No.: SYXK (HU) 2011-0128). NIH guidelines for the care and safety of laboratory animals were strictly followed. The animals were given food and water free of charge throughout the study. All procedures and measurements were performed under deep anesthesia with sodium pentobarbital (30 mg/kg).

*2.8. Statistics.* For quantitative data, the SPSS20.0 software (IBM Corporation, Armonk, NY) was used to perform unpaired $t$ test and paired sample $t$ test according to the situation. Two-tailed $P < 0.05$ was considered statistically significant between the two groups.

## 3. Result

*3.1. Temperature Changes of Tissue Adjacent to Implant during Microwave Irradiation.* When the microwave was irradiated at 40 W and 60 W, respectively, the temperature of the EG, the CG, and the SOG increased significantly (from 2.18 ± 0.15°C to 6.02 ± 0.38°C) (Table 1). Compared with the 40 W microwave groups, the temperature of the EG, the CG, and the SOG exposed to 60 W microwave increased more, and the average peak temperature differences were 0.72°C, 2.06°C, and 0.74°C, respectively (Table 1). When the microwave power was 40 W, the temperature of the CG rose by 4.0 ± 0.34°C, which was significantly higher than that of the EG 2.82 ± 0.15°C ($P < 0.01$)

Table 1: Peak temperature changes of deep tissue during microwave irradiation.

| Power | Groups | Temperature ($\bar{x}\pm s$) (°C) 0 min | 20 min | Gap | $P$ value |
|---|---|---|---|---|---|
| 40 W | Experimental group | 35.95 ± 0.24 | 38.74 ± 0.36 | 2.82 ± 0.15 | <0.01* |
| | Control group | 35.94 ± 0.24 | 39.94 ± 0.44 | 4.00 ± 0.34# | <0.01* |
| | Sham operation group | 36.08 ± 0.20 | 38.26 ± 0.29 | 2.18 ± 0.33 | <0.01* |
| 60 W | Experimental group | 35.80 ± 0.34 | 39.46 ± 0.38 | 3.66 ± 0.14 | <0.01* |
| | Control group | 35.98 ± 0.28 | 42.00 ± 0.55 | 6.02 ± 0.38# | <0.01* |
| | Sham operation group | 36.04 ± 0.32 | 39.00 ± 0.26 | 2.96 ± 0.22 | <0.01* |

*Tissue temperature after 20 minutes was statistically different from that initial temperature ($P < 0.01$). #There was significant difference between the control group and the other two groups ($P < 0.05$).

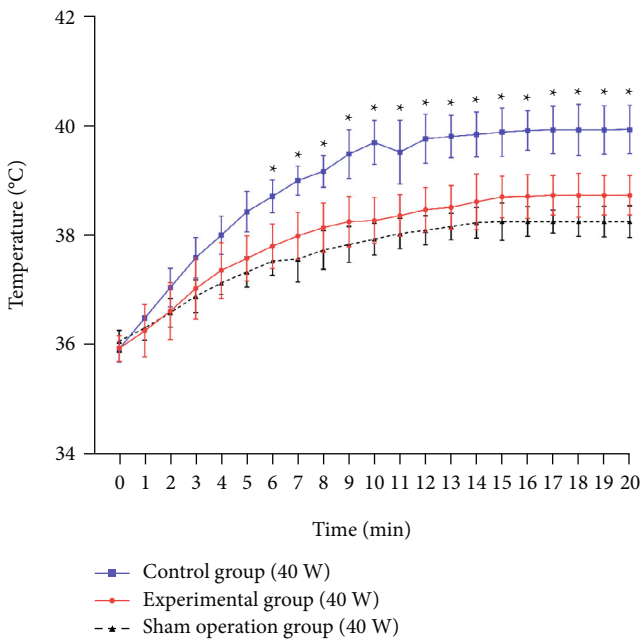


Figure 4: Temperature changes of deep tissues under 40 W microwave irradiation. The initial temperature of the three groups was basically the same. The body temperature of the three groups increased rapidly in the first 10 minutes and remained stable in the last 6 minutes. There was no significant difference between the experimental group and the sham operation group ($P = 0.21$). *There was a significant difference in temperature between the control group and the experimental group ($P < 0.05$).

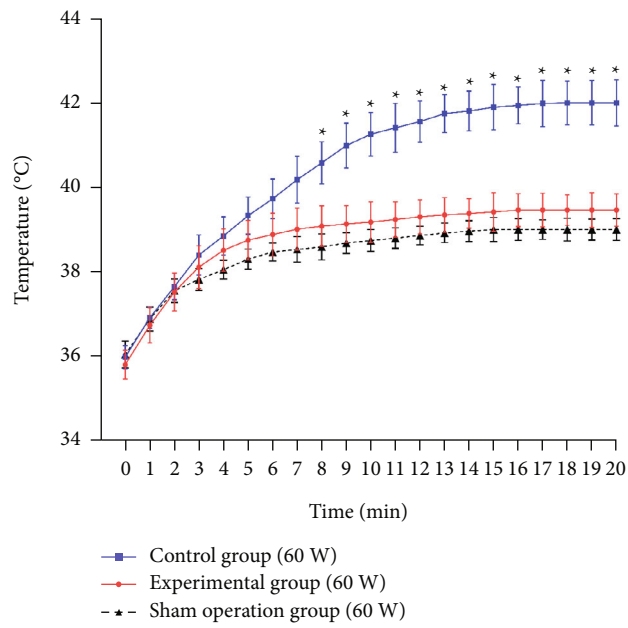


Figure 5: Temperature changes of deep tissues under 60 W microwave irradiation. The initial temperatures of the three groups are basically the same. The body temperature of the experimental group and the sham operation group tended to be stable after 6 minutes, while the body temperature of the control group continued to rise for about 15 minutes and then reached the peak. There was no significant difference between the experimental group and the sham operation group ($P = 0.32$). * There was a significant difference between the control group and the experimental group ($P < 0.05$).

and SOG 2.18 ± 0.33°C ($P < 0.01$), and there was no significant difference in temperature rise between the EG and SOG ($P = 0.21$) (Figure 4). When exposed to 60 W microwave, the temperature rise in the CG was 6.02 ± 0.38°C, which was significantly higher than that in the EG 3.66 ± 0.14°C ($P < 0.01$) and the SOG 2.96 ± 0.22°C ($P < 0.01$), and there was no significant difference between the EG and the SOG ($P = 0.32$) (Figure 5).

*3.2. X-Ray Assessment of Fracture Healing after Continuous Microwave Irradiation.* There were significant differences in fracture line density between the EG and the CG at 0, 14, and 30 days (Figure 6), indicating that the fracture healing process of the two groups was normal. The results of callus maturity measurement showed that there was no significant difference in callus maturity between the EG and the CG at 14 days ($P = 0.554$), and the callus maturity of the EG was less than that of the CG at 30 days ($P = 0.041$) (Figure 7).

*3.3. Analysis of Bone Histologic and Histomorphometric Data after Continuous Microwave Irradiation.* Bone histopathological section showed that after 30 days of microwave irradiation, bone defects in both groups healed well, periosteal reaction was obvious, and callus proliferation was obvious (Figure 8). The fracture healing histologic score was 7.00 ±

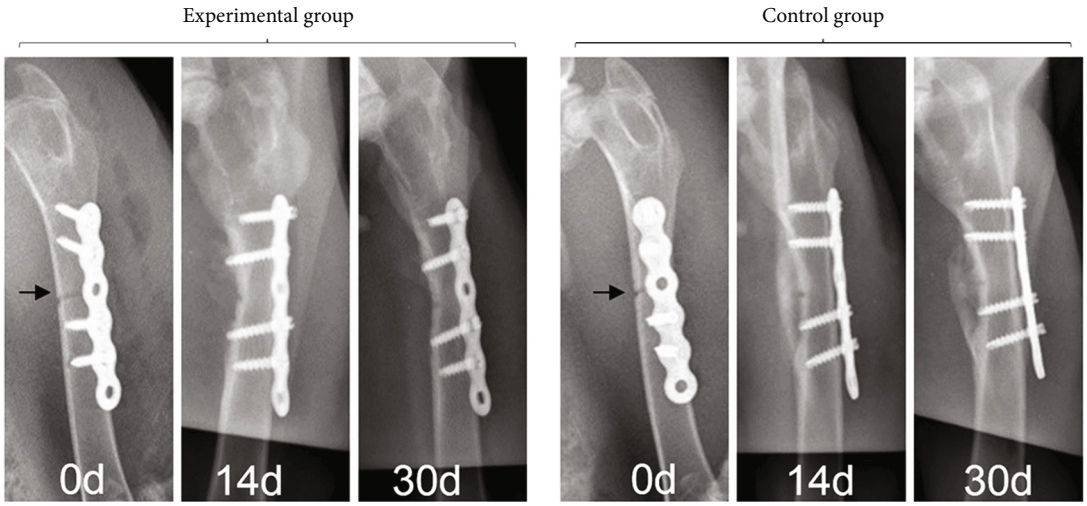


Figure 6: Radiographic images of femoral defects in rabbits at 0, 14, and 30 days. After 30 days, the fracture defects in the two groups were basically healed, and the fracture line was not obvious. Arrows: fracture line.

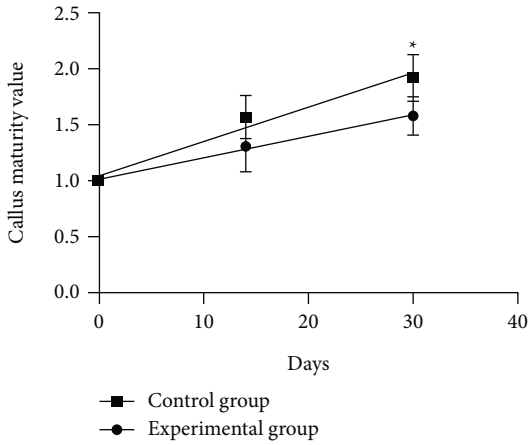


Figure 7: X-ray evaluation of fracture healing. *The maturity of callus in the control group was higher than that in the experimental group ($P < 0.05$).

0.76 in the CG and 6.12 ± 0.64 in the EG, with a statistically significant difference ($P = 0.026$).

The results of fracture healing histologic score and histomorphology after 30 days of microwave irradiation are shown in Table 2. The histologic score, bone volume, and node-terminus ratio of the CG were higher than those of the EG, and the differences were statistically significant ($P < 0.05$).

## 4. Discussion

In this study, it was found in vivo that $TiO_2$ nanofilm could reduce the heat generation of titanium alloy implants after microwave irradiation, and it was observed that $TiO_2$ nanofilm had no adverse effects on fracture healing, so it was in line with the original design.

*4.1. Heat Production Mechanism of Metallic Implant in Microwave Field.* In rehabilitation medicine, microwave therapy is a common treatment for acute injuries and chronic inflammation of bones [7–9], joints [10], skeletal muscles, and tendons [11, 12]. One of the contraindications of microwave therapy is that it cannot be applied to local metal implants [13]. There are two reasons for this. Firstly, the metal will reflect microwaves, resulting in secondary irradiation to the tissue at the treatment site [13]. Secondly, as a magnetic substance, metal generates heat in the microwave field [30]. At present, the mechanisms of heat production of metal implants in microwave fields include eddy currents and magnetic hysteresis [31–33]. Eddy current refers to the induced electromotive force generated by metal magnetic materials in the alternating magnetic field, which generates a circular current in the direction of the change of magnetic flux. Eddy currents convert the energy of electromagnetic waves into thermal energy within the metal conductor, thereby raising the temperature of the metal, that is, eddy current loss [34]. Hysteresis is a phenomenon that the change of magnetization or magnetic induction of ferromagnetic substance always lags behind the change of magnetic field intensity in the process of magnetization and demagnetization of ferromagnetic substance. Hysteresis loss is the decay and loss of energy induced by hysteresis. It is generally expressed in the form of thermal energy [35]. Hysteresis loss is related to the number of magnetic domains in the metal, and the difference between different metals is large.

In this study, titanium alloy implants were coated. The main reason is that the magnitude of eddy current loss is related to factors such as the way the magnetic field changes, the movement of the conductor, the geometry of the conductor, and the permeability and conductivity of the conductor [36, 37]. Compared with stainless steel, copper, nickel, and other metals, under the same conditions, titanium alloy has the lowest eddy current loss and heat production because of its low permeability and conductivity. In

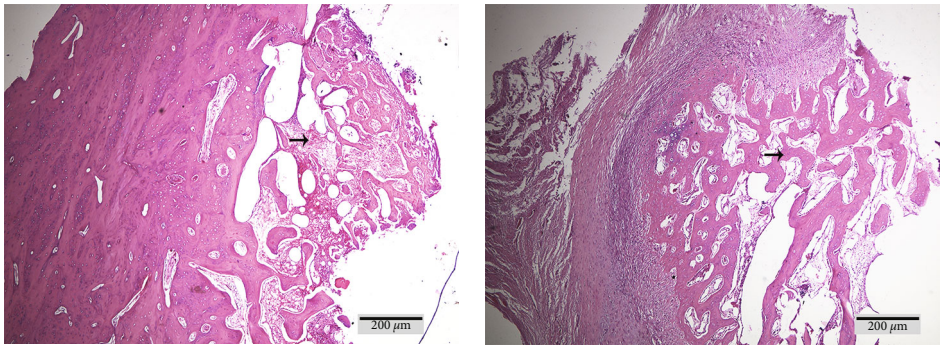


(a) (b)

Figure 8: Histological evaluation of fracture healing. (a) Experimental group and (b) control group; →: bone trabecular.

Table 2: Comparison of the histologic and histomorphometric data.

| | Experimental group | Control group | $P$ value |
|---|---|---|---|
| Histologic score | 6.12 ± 0.64 | 7.00 ± 0.76 | 0.026* |
| Bone volume (%) | 22.45 ± 8.69 | 32.73 ± 5.86 | 0.015* |
| Trabecular thickness (mcm) | 19.57 ± 2.32 | 21.14 ± 2.45 | 0.082 |
| Trabecular separation ($\mu$m) | 16.24 ± 4.15 | 14.76 ± 2.61 | 0.252 |
| Node-terminus ratio(/mm) | 3.25 ± 1.03 | 4.50 ± 0.93 | 0.023* |

*After 30 d microwave treatment, compared with the experimental group, the histologic score, bone volume, and node-terminus ratio of the control group were significantly higher ($P < 0.05$).

addition, titanium is a paramagnetic substance [38], with a small number of magnetic domains and less heat production due to hysteresis loss.

*4.2. Influence Factors of Tissues Temperature Adjacent to Metal Implants in Microwave Field.* It is obvious that the heat production of metal implants in the microwave field is the main factor for the temperature rise of adjacent tissues, but there are other important factors that can affect the temperature of tissues, including the dose of microwave, the duration of microwave irradiation, the distance between microwave probe and tissue, local blood flow, local tissue structure, and properties [3, 13]. The dose and duration of microwave irradiation are directly proportional to the tissue temperature, that is, the greater the microwave dose, the longer the irradiation time, and the higher the tissue temperature. The distance between microwave and tissue and the abundance of blood flow are inversely proportional to tissue temperature, that is, the larger the distance between microwave probe and tissue, the richer the local blood flow, the faster the flow rate, and the slower the rise of tissue temperature. The structure of tissues also affects the absorption and heat production of microwaves. Generally speaking, the temperature at the junction of different tissues increases due to the reflection and refraction of microwaves, and tissues with high dielectric constant absorb more microwaves, such as muscles, liver, and kidney [3]. The final temperature of the tissue adjacent to the metal implant in the microwave field is often the result of the combined effect of the above factors.

In addition, it should be noted that for metal implants in the microwave field, the temperature of the area around the implant is not exactly uniform. It has been shown that the temperature at both ends of the metal implant in the microwave electric field is the highest [39]. In this study, preliminary tests showed that there was no significant difference in temperature between the two ends of the metal implant and the central area, and that the distance from the implant was 5 mm compared with 10 mm. The temperature is higher at 5 mm [30], so we placed the temperature probe at 5 mm directly above the middle hole of the titanium alloy implant to obtain the most accurate temperature in this area.

*4.3. Reduction of Heat Production of Titanium Alloy in Microwave Field by $TiO_2$ Nanofilm and Its Possible Mechanism.* The results of this study showed that under 40 W and 60 W microwave irradiation, the temperature of the CG with traditional titanium alloy plate increased more than that of the EG ($P < 0.01$) and the SOG ($P < 0.01$), while there was no significant difference between the EG and the SOG ($P > 0.05$). This indicates that the $TiO_2$ nanofilm can obviously reduce the heat generated by the coated titanium alloy or/and prevent the heat generated by the titanium alloy from conducting outwards. Even if the microwave power increases, it can also play a role in blocking heat. We speculate that the mechanism may be related to the properties of $TiO_2$. $TiO_2$ is a semiconductor, and the $TiO_2$ film is used to protect against electromagnetic irradiation [40]. When the titanium alloy coated with $TiO_2$ nanofilm receives electromagnetic irradiation, its resistance is less than that of the muscle tissue and greater than that of the titanium alloy substrate. It is both a physical barrier and an electrostatic barrier at the interface between titanium alloy and muscle tissue. Therefore, it can not only reduce the occurrence of eddy current in titanium alloy but also prevent the heat generated by titanium alloy from being transmitted outside [27].

*4.4. Effect of $TiO_2$ Nanofilm on Fracture Healing.* Some studies have achieved antibacterial and accelerated fracture healing by surface modification of internal fixation materials [41]. Hu et al. [42] prepared ZnO-$TiO_2$ coating by microarc

oxidation and compared it with pure titanium, and the short-term function (adhesion, proliferation, and alkaline phosphatase activity) and long-term differentiation of rat bone marrow stem cells (bMSCs) on zinc-containing coating were significantly enhanced. In another study [43], Zn-doped $TiO_2$ nanotubes can not only inhibit the growth of bacteria but also promote the growth of osteoblasts in vitro and bone formation in vivo. There are also some recent studies showing that the addition of Fe [44] and Cu [45] elements to $TiO_2$ coatings is a potential approach that can improve the antibacterial and osteogenic properties of orthopaedic implants. But in this study, $TiO_2$ is a smooth and thin $TiO_2$ nanofilm coated on a titanium alloy (Ti6Al4V) substrate by a sol-gel method, and the effect of increasing fracture healing is not considered in the design [27]. Therefore, this study did not observe that the fracture healing of the EG was better than that of the CG. This improvement can be considered in the future.

In the present study, more callus was observed in the CG than in the EG, and we considered that it might be related to temperature. The healing process of fracture can be influenced by the local tissue temperature [46]. A moderate increase in local tissue temperature (generally considered to be less than 45°C [3]) accelerates blood flow [13], accelerates tissue metabolism [3], and promotes osteoblast differentiation [46]. Under 40 W microwave irradiation, the temperature of the CG was always higher than that of the EG, so the CG produced more callus.

*4.5. Defects of the Research.* Firstly, in the thermometry experiment, skeletal muscle and nerve specimens were not taken to observe histological changes, so the thermal injury caused by temperature rise could not be observed. Secondly, in the experiment of observing fracture healing, limited by the number of plates, we did not set up a blank control group (that is, no microwave irradiation treatment after fracture internal fixation) and a 60 W microwave irradiation group, so we cannot judge the accurate effect of $TiO_2$ film on fracture healing under different doses of microwave. Thirdly, the temperature rise of the metal implant under microwave irradiation is affected by the shape, thickness, and other factors of the implant and is limited by the size of the rabbit femur. This study only explores the heat production of the line titanium alloy plate, and the research design can be further optimized in the future.

*4.6. Implications of the Research.* The progress of material science, especially the wide application of titanium alloy implants, makes it possible to apply low-dose microwave therapy (≤40 W) to patients with titanium alloy implants, such as fracture patients with titanium alloy internal fixation [24, 30]. In this study, titanium alloy implants were coated with $TiO_2$ thin film to reduce the heat generation during microwave irradiation, so that the application dose of microwave therapy was increased (≤60 W). This study opens up a promising new idea that the contraindication of local metal implants in microwave therapy may be eliminated through further improvement of material science, so that more patients can benefit from electrotherapy.

## 5. Conclusion

Under the animal experimental condition, compared with the common titanium alloy implant, the $TiO_2$ nanofilm can reduce the heat production of the titanium alloy implant in a 2450 MHz microwave field and has no adverse effect on fracture healing. This study is a promising new method to increase the dose of microwave applied to titanium alloy implants by improving the surface properties of metal implants. However, the thermal insulation mechanism and dose-effect relationship of $TiO_2$ film in microwave field are still not clear, whether $TiO_2$ film is still effective after changing the shape, size, and thickness of titanium alloy internal fixation and whether there are other better thermal insulation coatings need more research.

## Data Availability

The study data presented may be made available from the corresponding author upon reasonable request.

## Conflicts of Interest

The authors declare that they have no competing interests.

## Acknowledgments

The authors wish to thank Dr. Shiqi Liu and Dr. Yuzhen Zou for their excellent technical assistance in preexperiment, hematoxylin and eosin staining, and histological analysis.

## References

[1] D. I. McRee, "Environmental aspects of microwave radiation," *Environmental Health Perspectives*, vol. 2, pp. 41–53, 1972.

[2] A. Rabini, D. B. Piazzini, G. Tancredi et al., "Deep heating therapy via microwave diathermy relieves pain and improves physical function in patients with knee osteoarthritis: a double-blind randomized clinical trial," *European Journal of Physical Rehabilitation Medicine*, vol. 48, no. 4, pp. 549–559, 2012.

[3] A. Giombini, V. Giovannini, A. Di Cesare et al., "Hyperthermia induced by microwave diathermy in the management of muscle and tendon injuries," *British Medical Bulletin*, vol. 83, no. 1, pp. 379–396, 2007.

[4] N. T. A. D. Sousa, E. C. D. O. Guirro, J. G. Calió, M. C. D. Queluz, and R. R. D. J. Guirro, "Application of shortwave diathermy to lower limb increases arterial blood flow velocity and skin temperature in women: a randomized controlled trial," *Brazilian Journal of Physical Therapy*, vol. 21, no. 2, pp. 127–137, 2017.

[5] D. Maiettini, V. De Angelis, L. Graziosi et al., "Sacrum colonrectal cancer metastasis: microwave ablation for palliative pain treatment," *Recenti Progressi in Medicina*, vol. 107, no. 12, pp. 673–676, 2016.

[6] B. J. deLateur, J. B. Stonebridge, and J. F. Lehmann, "Fibrous muscular contractures: treatment with a new direct contact microwave applicator operating at 915 MHz," *Archives of Physical Medicine and Rehabilitation*, vol. 59, no. 10, pp. 488–499, 1978.

[7] W. H.-S. Chang, J.-S. Sun, S.-P. Chang, and J. C. Lin, "Study of thermal effects of ultrasound stimulation on fracture healing," *Bioelectromagnetics*, vol. 23, no. 4, pp. 256–263, 2002.

[8] S. A. Leon, S. O. Asbell, H. H. Arastu et al., "Effects of hyperthermia on bone. II. Heating of bone in vivo and stimulation of bone growth," *International Journal of Hyperthermia*, vol. 9, no. 1, pp. 77–87, 1993.

[9] S. A. Leon, S. O. Asbell, G. Edelstein et al., "Effects of hyperthermia on bone. I. Heating rate patterns induced by microwave irradiation in bone and muscle phantoms," *International Journal of Hyperthermia*, vol. 9, no. 1, pp. 69–75, 1993.

[10] H. Tonomura, K. A. Takahashi, O. Mazda et al., "Effects of heat stimulation via microwave applicator on cartilage matrix gene and HSP70 expression in the rabbit knee joint," *Journal of Orthopaedic Research*, vol. 26, no. 1, pp. 34–41, 2008.

[11] A. Giombini, A. Di Cesare, M. R. Safran, R. Ciatti, and N. Maffulli, "Short-term effectiveness of hyperthermia for supraspinatus tendinopathy in athletes: a short-term randomized controlled study," *The American Journal of Sports Medicine*, vol. 34, no. 8, pp. 1247–1253, 2006.

[12] A. Giombini, G. Casciello, M. C. Di Cesare, A. Di Cesare, S. Dragoni, and D. Sorrenti, "A controlled study on the effects of hyperthermia at 434 MHz and conventional ultrasound upon muscle injuries in sport," *Journal of Sports Medicine and Physical Fitness*, vol. 41, no. 4, pp. 521–527, 2001.

[13] G. C. Goats, "Microwave diathermy," *British Journal of Sports Medicine*, vol. 24, no. 4, pp. 212–218, 1990.

[14] P. S. Ruggera, D. M. Witters, G. von Maltzahn, and H. I. Bassen, "In vitro assessment of tissue heating near metallic medical implants by exposure to pulsed radio frequency diathermy," *Physics in Medicine and Biology*, vol. 48, no. 17, pp. 2919–2928, 2003.

[15] H. Virtanen, J. Keshvari, and R. Lappalainen, "The effect of authentic metallic implants on the SAR distribution of the head exposed to 900, 1800 and 2450 MHz dipole near field," *Physics in Medicine and Biology*, vol. 52, no. 5, pp. 1221–1236, 2007.

[16] O. Levy, A. Schindler, A. Chechik, and M. Heim, "A complication of internal fixation rods in sport," *British Journal of Sports Medicine*, vol. 27, no. 1, p. 36, 1993.

[17] R. C. Gardner, "A complication of excessive compression and rigid internal fixation," *The Journal of Trauma*, vol. 12, no. 6, pp. 534–536, 1972.

[18] B. B. Greenberg, "Infratrochanteric fracture as a late complication of internal fixation of slipped capital femoral epiphysis," *Bulletin of the Hospital for Joint Diseases*, vol. 15, no. 2, pp. 188–200, 1954.

[19] N. F. SooHoo, L. Krenek, M. J. Eagan, B. Gurbani, C. Y. Ko, and D. S. Zingmond, "Complication rates following open reduction and internal fixation of ankle fractures," *The Journal of Bone and Joint Surgery American*, vol. 91, no. 5, pp. 1042–1049, 2009.

[20] A. Gill and F. G. Shellock, "Assessment of MRI issues at 3-Tesla for metallic surgical implants: findings applied to 61 additional skin closure staples and vessel ligation clips," *Journal of Cardiovascular Magnetic Resonance*, vol. 14, no. 1, p. 3, 2012.

[21] Y. Kim, M. Muruganandham, J. M. Modrick, and J. E. Bayouth, "Evaluation of artifacts and distortions of titanium applicators on 3.0-Tesla MRI: feasibility of titanium applicators in MRI-guided brachytherapy for gynecological cancer," *International Journal of Radiation Oncology • Biology • Physics*, vol. 80, no. 3, pp. 947–955, 2011.

[22] Y. F. Zou, B. Chu, C. B. Wang, and Z. Y. Hu, "Evaluation of MR issues for the latest standard brands of orthopedic metal implants: plates and screws," *European Journal of Radiology*, vol. 84, no. 3, pp. 450–457, 2015.

[23] D. Ye, Y. Xu, T. Fu et al., "Low dose of continuous-wave microwave irradiation did not cause temperature increase in muscles tissue adjacent to titanium alloy implants–an animal study," *BMC Musculoskeletal Disorders*, vol. 14, no. 1, pp. 364–364, 2013.

[24] D. Ye, Y. Xu, G. Wang et al., "Thermal effects of 2450 MHz microwave exposure near a titanium alloy plate implanted in rabbit limbs," *Bioelectromagnetics*, vol. 36, no. 4, pp. 309–318, 2015.

[25] Z. K. Hua, R. Z. Sang, and J. H. Zhang, "Micro and nano-scale surface texturing: an application in ceramic-on-ceramic artificial joint materials," *Nanoscience and Nanotechnology Letters*, vol. 4, no. 9, pp. 879–882, 2012.

[26] H. L. Cao and X. Y. Liu, "Activating titanium oxide coatings for orthopedic implants," *Surface and Coatings Technology*, vol. 233, pp. 57–64, 2013.

[27] Z. Hua, F. Tang, Y. Bai et al., "A titanium dioxide nano film encapsulation for metal orthopedic implants in diathermy rehabilitation therapy," *Nanoscience and Nanotechnology Letters*, vol. 7, no. 3, pp. 268–271, 2015.

[28] V. M. Goldberg, A. Powell, J. W. Shaffer, J. Zika, G. D. Bos, and K. G. Heiple, "Bone grafting: role of histocompatibility in transplantation," *Journal of Orthopaedic Research : Official Publication of the Orthopaedic Research Society*, vol. 3, no. 4, pp. 389–404, 1985.

[29] A. C. Perry, B. Prpa, M. S. Rouse et al., "Levofloxacin and trovafloxacin inhibition of experimental fracture-healing," *Clinical Orthopaedics and Related Research*, vol. 414, no. 414, pp. 95–100, 2003.

[30] D. Ye, Y. Xu, H. Zhang, T. Fu, L. Jiang, and Y. Bai, "Effects of low-dose microwave on healing of fractures with titanium alloy internal fixation: an experimental study in a rabbit model," *PLoS One*, vol. 8, no. 9, article e75756, 2013.

[31] I. Morales, D. Archilla, P. de la Presa, A. Hernando, and P. Marin, "Colossal heating efficiency via eddy currents in amorphous microwires with nearly zero magnetostriction," *Scientific Reports*, vol. 10, no. 1, p. 602, 2020.

[32] K. Kuroda and S. Yatsushiro, "New insights into MR safety for implantable medical devices," *Magnetic Resonance in Medical Sciences*, vol. 21, no. 1, pp. 110–131, 2022.

[33] J. Sun, W. Wang, and Q. Yue, "Review on microwave-matter interaction fundamentals and efficient microwave-associated heating strategies," *Materials*, vol. 9, no. 4, p. 231, 2016.

[34] Y. Tao, Q. Li, Q. Wu, and H. Li, "Embedding metal foam into metal-organic framework monoliths for triggering a highly efficient release of adsorbed atmospheric water by localized eddy current heating," *Materials Horizons*, vol. 8, no. 5, pp. 1439–1445, 2021.

[35] G. Pefanis, N. Maniotis, A.-R. Tsiapla, A. Makridis, T. Samaras, and M. Angelakeris, "Numerical simulation of temperature variations during the application of safety protocols in magnetic particle hyperthermia," *Nanomaterials*, vol. 12, no. 3, p. 554, 2022.

[36] S. P. Morgan Jr., "Effect of surface roughness on eddy current losses at microwave frequencies," *Journal of Applied Physics*, vol. 20, no. 4, pp. 352–362, 1949.

[37] K. Foster and M. F. Littmann, "Factors affecting core losses in oriented electrical steels at moderate inductions," *Journal of Applied Physics*, vol. 57, no. 8, pp. 4203–4208, 1985.

[38] A. N. Luiten, A. G. Mann, and D. G. Blair, "Paramagnetic susceptibility and permittivity measurements at microwave frequencies in cryogenic sapphire resonators," *Journal of Physics D: Applied Physics*, vol. 29, no. 8, pp. 2082–2090, 1996.

[39] H. Muranaka, T. Horiguchi, Y. Ueda, and N. Tanki, "Evaluation of RF heating due to various implants during MR procedures," *Magnetic Resonance in Medical Sciences*, vol. 10, no. 1, pp. 11–19, 2011.

[40] C.-H. Liang and Y.-J. Chen, "Preparation of high-performance metal-free UV/near infrared-shielding films for human skin protection," *Nanomaterials*, vol. 11, no. 8, p. 1954, 2021.

[41] X. Lin, S. Yang, K. Lai, H. Yang, T. J. Webster, and L. Yang, "Orthopedic implant biomaterials with both osteogenic and anti-infection capacities and associated in vivo evaluation methods," *Nanomedicine*, vol. 13, no. 1, pp. 123–142, 2017.

[42] H. Hu, W. Zhang, Y. Qiao, X. Jiang, X. Liu, and C. Ding, "Antibacterial activity and increased bone marrow stem cell functions of Zn-incorporated TiO2 coatings on titanium," *Acta Biomaterialia*, vol. 8, no. 2, pp. 904–915, 2012.

[43] Y. Li, W. Xiong, C. Zhang et al., "Enhanced osseointegration and antibacterial action of zinc-loaded titania-nanotube-coated titanium substrates: in vitro and in vivo studies," *Journal of Biomedical Materials Research Part A*, vol. 102, no. 11, pp. 3939–3950, 2014.

[44] Y. Tian, H. Cao, Y. Qiao, F. Meng, and X. Liu, "Antibacterial activity and cytocompatibility of titanium oxide coating modified by iron ion implantation," *Acta Biomaterialia*, vol. 10, no. 10, pp. 4505–4517, 2014.

[45] Q. Wu, J. Li, W. Zhang et al., "Antibacterial property, angiogenic and osteogenic activity of Cu-incorporated TiO coating," *Journal of Materials Chemistry B*, vol. 2, no. 39, pp. 6738–6748, 2014.

[46] L. B. Feril, K. Tachibana, K. Ogawa, K. Yamaguchi, I. G. Solano, and Y. Irie, "Therapeutic potential of low-intensity ultrasound (part 1): thermal and sonomechanical effects," *Journal of Medical Ultrasonics*, vol. 35, no. 4, pp. 153–160, 2008.